

JAERI-M

85-083

JAPANESE CONTRIBUTIONS TO IAEA INTOR WORKSHOP,

PHASE TWO A, PART 2

CHAPTER XI : CONCEPT EVOLUTION,

CHAPTER XII : DESIGN CONCEPT,

AND CHAPTER XIII : OPERATION AND TEST PROGRAMME

July 1985

Ken TOMABECHI, Noboru FUJISAWA, Hiromasa IIDA,  
Masayoshi SUGIHARA, Masahiro SEKI, Tsutomu HONDA,<sup>\*1</sup>  
Masao KASAI,<sup>\*2</sup> Yoshio SAWADA, Takeshi KOBAYASHI,  
Yutaka ITOU, Ryuta SAITO, Yasushi SEKI,  
Keiji TANI, Yoshinao SANADA,<sup>\*1</sup> Takaho UCHIDA,<sup>\*1</sup>  
Mitsunori KONDO,<sup>\*1</sup> Kunihiro OKANO,<sup>\*1</sup> Nobuo TACHIKAWA,<sup>\*1</sup>  
Nobuharu MIKI,<sup>\*1</sup> Noriyuki KOBAYASHI,<sup>\*1</sup> Katsuyuki EBISAWA,<sup>\*1</sup>  
Kusuho ASHIBE,<sup>\*1</sup> Tadashi ITIHARA,<sup>\*2</sup> Kanji OTA,<sup>\*2</sup>  
Kunihiro NAKASHIMA,<sup>\*2</sup> Kazuhiro MIYAMOTO,<sup>\*2</sup> Tadanori TSUKAMOTO,<sup>\*2</sup>  
Itiro NAKAZAWA,<sup>\*2</sup> Seiichi TSUJIMURA,<sup>\*2</sup> Akihisa KAMEARI,<sup>\*2</sup>  
Fushiki MATSUOKA,<sup>\*2</sup> Yutaka IMAMURA,<sup>\*2</sup> Yoshihisa TANAKA,<sup>\*3</sup>  
Tatsushi SUZUKI,<sup>\*3</sup> Junichi ADACHI,<sup>\*3</sup> Seiji MORI,<sup>\*3</sup>  
Toshimasa KURODA,<sup>\*3</sup> Shiro OKAZAKI,<sup>\*3</sup> Seiichiro YAMAZAKI,<sup>\*3</sup>  
Masahiro MISUMI,<sup>\*3</sup> Kensuke MOHRI,<sup>\*3</sup> Masaharu FUJII,<sup>\*3</sup>  
Fumio IIDA,<sup>\*4</sup> Shigeyoshi KINOSHITA,<sup>\*4</sup> and Tadanori MIZOGUCHI<sup>\*4</sup>

JAERI-Mレポートは、日本原子力研究所が不定期に公刊している研究報告書です。

入手の問合わせは、日本原子力研究所技術情報部情報資料課（〒319-11茨城県那珂郡東海村）あて、お申しこしください。なお、このほかに財団法人原子力弘済会資料センター（〒319-11茨城県那珂郡東海村日本原子力研究所内）で複写による実費頒布をおこなっております。

JAERI-M reports are issued irregularly.

Inquiries about availability of the reports should be addressed to Information Division, Department of Technical Information, Japan Atomic Energy Research Institute, Tokai-mura, Naka-gun, Ibaraki-ken 319-11, Japan.

© Japan Atomic Energy Research Institute, 1985

---

編集兼発行	日本原子力研究所
印 刷	日立高速印刷株式会社

Japanese Contributions  
to IAEA INTOR Workshop, Phase Two A, Part 2

Chapter XI : Concept Evolution,  
Chapter XII : Design Concept,  
and Chapter XIII : Operation and Test Programme

Ken TOMABECHI, Noboru FUJISAWA, Hiromasa IIDA, Masayoshi SUGIHARA,  
Masahiro SEKI, Tsutomu HONDA\*<sup>1</sup>, Masao KASAI\*<sup>2</sup>, Yoshio SAWADA,  
Takeshi KOBAYASHI, Yutaka ITOU, Ryuta SAITO, Yasushi SEKI, Keiji TANI,  
Yoshinao SANADA\*<sup>1</sup>, Takaho UCHIDA\*<sup>1</sup>, Mitsunori KONDO\*<sup>1</sup>, Kunihiro OKANO\*<sup>1</sup>,  
Nobuho TACHIKAWA\*<sup>1</sup>, Nobuharu MIKI\*<sup>1</sup>, Noriyuki KOBAYASHI\*<sup>1</sup>,  
Katsuyuki EBISAWA\*<sup>1</sup>, Kusuho ASHIBE\*<sup>1</sup>, Tadashi ITIHARA\*<sup>2</sup>, Kanji OTA\*<sup>2</sup>,  
Kunihiro NAKASHIMA\*<sup>2</sup>, Kazuhiro MIYAMOTO\*<sup>2</sup>, Tadanori TSUKAMOTO\*<sup>2</sup>,  
Itiro NAKAZAWA\*<sup>2</sup>, Seiichi TSUJIMURA\*<sup>2</sup>, Akihisa KAMEARI\*<sup>2</sup>, Fushiki MATSUOKA\*<sup>2</sup>,  
Yutaka IMAMURA\*<sup>2</sup>, Yoshihisa TANAKA\*<sup>3</sup>, Tatsushi SUZUKI\*<sup>3</sup>, Junichi ADACHI\*<sup>3</sup>,  
Seiji MORI\*<sup>3</sup>, Toshimasa KURODA\*<sup>3</sup>, Shiro OKAZAKI\*<sup>3</sup>, Seiichiro YAMAZAKI\*<sup>3</sup>,  
Masahiro MISUMI\*<sup>3</sup>, Kensuke MOHRI\*<sup>3</sup>, Masaharu FUJII\*<sup>3</sup>, Fumio IIDA\*<sup>4</sup>,  
Shigeyoshi KINOSHITA\*<sup>4</sup> and Tadanori MIZOGUCHI\*<sup>4</sup>

Department of Large Tokamak Research,  
Naka Fusion Research Establishment, JAERI

(Received May 31, 1985)

This report corresponds to Chapters XI, XII, and XIII of Japanese contribution report to IAEA INTOR Workshop, Phase Two A, Part 2. In the phase Two A, Part 2 workshop, we have studied critical technical issues and have also assessed scientific and technical data bases. Based on those results, the INTOR design have been modified to upgrade the design concept. The major modification items are related to plasma beta value, plasma operation scenario, reactor size reduction, neutron fluence, tritium producing blanket, and implementation of active control coils. In those chapters, the concept evolution for the design modification and main results are described.

Keywords: INTOR, INTOR Design Concept, INTOR Test Programme

---

\*1 Toshiba Corporation

\*2 Mitsubishi Group (Mitsubishi Electric Co., Mitsubishi Heavy Industries and Mitsubishi Atomic Power Industries)

\*3 Kawasaki Heavy Industries, Ltd.

\*4 Hitachi, Ltd.

IAEA INTOR ワークショップフェーズⅡA, パート2 報告書

第XI章：炉概念の修正

第XII章：設計概要

第XIII章：運転及び試験計画

日本原子力研究所那珂研究所臨界プラズマ研究部

苫米地 顕・藤沢	登・飯田	浩正・杉原	正芳
関 昌弘・本多	力 <sup>*1</sup> ・笠井	雅夫 <sup>*2</sup> ・沢田	芳夫
小林 武司・伊藤	裕・斉藤	龍太・関	泰
谷 啓二・真田	芳直 <sup>*1</sup> ・内田	孝穂 <sup>*1</sup> ・近藤	光昇 <sup>*1</sup>
岡野 邦彦 <sup>*1</sup> ・立川	信夫 <sup>*1</sup> ・三木	信晴 <sup>*1</sup> ・小林	則幸 <sup>*1</sup>
海老沢克之 <sup>*1</sup> ・芦部	楠夫 <sup>*1</sup> ・市原	直 <sup>*2</sup> ・太田	完治 <sup>*2</sup>
中島 國彦 <sup>*2</sup> ・宮本	和弘 <sup>*2</sup> ・塚本	忠則 <sup>*2</sup> ・中沢	一郎 <sup>*2</sup>
辻村 誠一 <sup>*2</sup> ・亀有	昭久 <sup>*2</sup> ・松岡	不誠 <sup>*2</sup> ・今村	豊 <sup>*2</sup>
田中 義久 <sup>*3</sup> ・鈴木	達志 <sup>*3</sup> ・安達	潤一 <sup>*3</sup> ・森	清治 <sup>*3</sup>
黒田 敏公 <sup>*3</sup> ・岡崎	士朗 <sup>*3</sup> ・山崎	誠一郎 <sup>*3</sup> ・三角	昌弘 <sup>*3</sup>
毛利 憲介 <sup>*3</sup> ・藤井	政治 <sup>*3</sup> ・飯田	文雄 <sup>*4</sup> ・木下	茂美 <sup>*4</sup>
溝口 忠憲 <sup>*4</sup>			

(1985年5月31日受理)

この報告書はIAEA主催のINTORワークショップ, フェーズⅡA, パート2の日本のナショナル・レポートの第XI, XII, XIII章に相当するものである。本フェーズでは, 幾つかの重要技術課題の検討及び科学的, 技術的データベースの評価を行った。その結果INTORの設計をアップグレードするための修正が必要となった。主要な修正点は, プラズマのベータ値, 運転シナリオ, 炉寸法の縮小, 中性子フルーエンス, トリチウム生産ブランケット, プラズマ位置制御コイルの組込みに関するものである。上記の章に於いて炉概念修正の経緯及び修正後の設計概要について述べる。

---

\* 1 (株) 東芝  
\* 2 三菱グループ  
\* 3 川重(株)  
\* 4 (株) 日立



## Contents

## Chapter XI : Concept Evolution

(K. Tomabechi, H. Iida, N. Fujisawa)

1. Introduction .....	1
2. Reduction of a gap between the design value and the predicted beta value .....	1
3. Operation scenario .....	3
3.1 Physics .....	3
3.2 Engineering benefits associated with the RF current ramp-up and quasi-steady operation .....	5
3.2.1 Volt second saving .....	
3.2.2 AC loss .....	
3.2.3 Power supply capacity .....	
3.2.4 Cyclic stress on the TF coil .....	
4. Size reduction .....	12
5. Tritium producing blanket .....	16
6. Fluence .....	20
7. Implementation of active control coil .....	20

## Chapter XII : Design Concept

1. Design specification (H. Iida, N. Fujisawa) .....	23
2. Physics basis (N. Fujisawa, M. Sugihara, T. Mizoguchi, K. Tani) .....	32
2.1 Reexamination of INTOR parameters .....	32
2.1.1 Basic models for selecting major parameters .....	
2.1.2 Toroidal beta correction without changing plasma current, plasma major radius .....	
2.2 Improvement in beta value with increasing plasma current reducing plasma major radius .....	46
2.3 Additional non-DT contributions to fuel beta value .....	49
2.4 Comments on the load due to ripple loss of alpha particles .....	50
3. Configuration (T. Uchida, T. Kobayashi, Y. Itou, F. Iida, T. Itihara, Y. Sanada, H. Iida) .....	51
3.1 Toroidal magnetic field coil design .....	51
3.2 Poloidal magnetic field coil design .....	51
3.3 Torus and cryogenic system topology .....	51
3.4 Modularization and segmentation .....	53
3.5 Support structure system .....	55
3.6 Radial build .....	57
3.7 Impurity control .....	57
4. Assembly and maintenance (M. Kondo, T. Uchida, J. Adachi, T. Kobayashi, H. Iida) .....	86
4.1 Torus dedicated sectors .....	86
4.2 Reference assembly/maintenance .....	86
4.2.1 Maintenance scenario and time evaluation .....	
4.2.2 Maintenance equipment .....	
4.3 Alternative assembly and maintenance acheme .....	120
4.4 Consideration of maintenance and assembly with vertical access .....	130

5.	RF heating and current drive	
	(R. Saito, K. Okano, N. Tachikawa, N. Miki, N. Kobayashi, S. Kinoshita, T. Honda, T. Uchida, K. Ota, K. Nakashima, K. Miyamoto)	131
5.1	ICRF heating system	131
5.1.1	Physical design of ICRF launchers	
5.1.2	Mechanical configuration of launchers	
5.1.3	Power supply system	
5.1.4	Summary	
5.2	LHRF current drive system	146
5.2.1	Structure and coupling efficiency	
5.2.2	Use of LHRF current drive launcher for heating	
5.2.3	Mechanical configuration of launcher	
5.2.4	Power supply system	
5.2.5	Summary	
5.3	ECRF auxiliary heating system	160
5.3.1	Launcher	
5.3.2	RF source and transmission system	
5.3.3	Conclusion	
6.	Operating scenario	
	(N. Fujisawa, R. Saito, Y. Itou, T. Tsukamoto, I. Nakazawa, )	166
6.1	Quasi-steady operation	166
6.2	Ignition approach duration	168
6.2.1	Introduction	
6.2.2	Comparative calculation	
6.2.3	Conclusion	
6.3	Available flux for burning	179
6.3.1	Relation between magnetic flux swing range and the maximum field	
6.3.2	Quasi-steady state operation	
6.3.3	Pulsed operation	
6.3.4	Summary	
7.	Plasma position control	
	(M. Kasai, A. Kameari, F. Matsuoka, Y. Imamura, H. Iida, N. Fujisawa)	191
7.1	Introduction	191
7.2	Vertical position control	191
7.2.1	Passive elements and active coil location	
7.2.2	Disturbance	
7.2.3	Vertical position control	
7.3	Radial and vertical position control	194
7.3.1	Formulations	
7.3.2	Stability analyses	
7.3.3	Radial and vertical position control	
7.4	Summary	202
8.	Magnets	
	(Y. Itou, F. Iida, T. Itihara, Y. Sanada)	221
8.1	TF coil system	221
8.1.1	Concept	
8.1.2	Configuration	
8.1.3	Load condition	
8.1.4	Conductor	
8.1.5	Support structure and analysis	

8.2	PF coil system .....	238
8.2.1	Concept .....	
8.2.2	Parameters .....	
8.2.3	Conductor .....	
8.2.4	Load condition .....	
8.2.5	Support structure .....	
8.3	Active position control coil .....	248
8.3.1	Concept .....	
8.3.2	Outside TF coil option .....	
8.3.3	Inside TF coil option .....	
8.4	Cryogenic system .....	255
8.4.1	AC loss .....	
8.4.2	Total loss .....	
8.4.3	Requirements of cryogenic system .....	
9.	Impurity control .....	
	(N. Fujisawa, N. Miki, M. Seki) .....	259
9.1	Introduction .....	259
9.2	Impurity control physics .....	259
9.3	Material and heat removal .....	260
9.4	Divertor physics .....	263
9.5	Divertor design .....	265
9.6	R and D items .....	280
10.	First wall and tritium producing blanket (Continuous tritium recovery) (T. Honda, H. Iida) .....	281
10.1	First wall .....	281
10.2	Tritium producing blanket (Continuous tritium recovery) .....	281
11.	First wall and tritium producing blanket (Batch tritium recovery) (Y. Tanaka, T. Suzuki, J. Adachi, T. Kuroda, S. Okazaki, S. Yamazaki, M. Misumi, K. Mohri, M. Fujii, T. Kobayashi, H. Iida) ...	284
11.1	Introduction .....	284
11.2	Selection of blanket concept .....	284
11.3	Design description .....	292
11.3.1	First wall/blanket concept .....	
11.3.2	Blanket support and piping .....	
11.3.3	Blanket maintenance concept .....	
11.4	Neutronic analysis .....	306
11.5	Thermal-hydraulic analysis .....	316
11.6	Structural analysis .....	330
11.7	Tritium recovery .....	336
11.8	Tritium permeation .....	340
12.	Tritium and vacuum .....	
	(T. Honda, K. Ebisawa, K. Ashibe, H. Iida) .....	346
12.1	Tritium system .....	346
12.2	Vacuum system .....	350
13.	Radiation shielding .....	
	(S. Mori, Y. Seki) .....	358
13.1	Shielding Criteria .....	358
13.1.1	Biological shielding criteria .....	
13.1.2	Components protection .....	
13.2	Optimization of shield thickness and composition .....	360
13.2.1	Objectives .....	
13.2.2	Calculation method .....	
13.2.3	Calculation results .....	
13.2.4	Conclusions .....	

13.3 Local heterogeneous effects .....	366
13.3.1 Objectives .....	
13.3.2 Calculation methods .....	
13.3.3 Calculation results .....	
13.3.4 Conclusions .....	
14. Facilities .....	
(H. Iida) .....	382
15. Cost .....	
(H. Iida, S. Tsujimura) .....	384

## Chapter XIII : Operation and Test Programme

(T. Honda, H. Iida, K. Tomabechi)

1. Role of INTOR tests .....	387
1.1 Plasma physics experiments in INTOR and complementary programme .....	388
1.2 Technology testing in INTOR and complementary programme .....	388
2. Operation schedule .....	391
3. Test programme .....	392
3.1 Plasma operation in stage-I and plasma experiments .....	393
3.2 Plasma engineering tests .....	393
3.3 Blanket engineering tests .....	394
3.4 Materials testing-bulk properties .....	394
3.5 Surface material tests .....	395
3.6 Surveillance tests .....	396
3.7 Nuclear tests .....	396
3.8 Electricity generation .....	397
3.9 Test module installation .....	397
3.10 Support facilities .....	398
3.11 Post-irradiation examination (PIE) facility .....	398

## 目 次

## 第XI章 炉概念の修正（苫米地，飯田浩，藤沢）

1. 序 .....	1
2. プラズマベータ限界の予測値と設計ベータ値間の差の縮少 .....	1
3. 運転シナリオ .....	3
3.1 物 理 .....	3
3.2 RFによる電流立上及び準定常運転に伴う工学的利点 .....	5
4. 炉寸法縮少 .....	12
5. トリチウム生産ブランケット .....	16
6. フルーエンス .....	20
7. プラズマ位置制御コイルの組込み .....	20

## 第XII章 設計概要

1. 設計仕様（飯田浩，藤沢） .....	23
2. 物 理（藤沢，杉原，溝口，谷） .....	32
2.1 INTORプラズマパラメータの再検討 .....	32
2.2 プラズマ電流を増加，主半径を減少させる事によるベータ値の改善 .....	46
2.3 DT以外のエレメントによるベータ値の増加量 .....	49
2.4 アルファ粒子のリップル損失による熱負荷に関するコメント .....	50
3. 炉構造（内田，小林武，伊藤，飯田文，市原，真田，飯田浩） .....	51
3.1 トロイダル磁場コイル .....	51
3.2 ポロイダル磁場コイル .....	51
3.3 トーラス及び低温真空トポロジー .....	51
3.4 トーラス分割構造 .....	53
3.5 支 持 .....	55
3.6 半径方向寸法 .....	57
3.7 不純物制御系 .....	57
4. 組立て分解補修（近藤，内田，安達，小林武，飯田浩） .....	86
4.1 トーラス分割構造 .....	86
4.2 組立て分解補修代表案 .....	86
4.3 組立て分解補修代替案 .....	120
4.4 垂直方向近接による分解補修案に関する考察 .....	130
5. RF加熱及び電流駆動（斉藤，岡野，立川，三木，小林剛，木下，本多，内田， 太田，中島，宮本） .....	131
5.1 ICRF加熱系 .....	131

5.2	L H R F 電流駆動系	146
5.3	E C R F 補助加熱系	160
6.	運転シナリオ (藤沢, 斉藤, 伊藤, 塚本, 中沢)	166
6.1	準定常運転	166
6.2	加熱フェーズの長さ	168
6.3	燃焼のためのフラックス ( $V \cdot S$ )	179
7.	プラズマ位置制御 (笠井, 亀有, 松岡, 今村, 飯田(浩), 藤沢)	191
7.1	序	191
7.2	垂直位置制御	191
7.3	半径方向及び垂直位置制御	194
7.4	結 論	202
8.	マグネット (伊藤, 飯田(文), 市原, 真田)	221
8.1	トロイダル磁場コイル	221
8.2	ポロイダル磁場コイル	238
8.3	プラズマ位置制御コイル	248
8.4	冷凍系	255
9.	不純物制御 (藤沢, 三木, 関(昌))	259
9.1	序	259
9.2	不純物制御物理	259
9.3	材料選択及び熱除去	260
9.4	ダイバータ物理	263
9.5	ダイバータ板設計	265
9.6	R & D 項目	280
10.	第1壁及びトリチウム生産ブランケット (連続回収型) (本多, 飯田(浩))	281
10.1	第一壁	281
10.2	トリチウム生産ブランケット (連続回収型)	281
11.	第1壁及びトリチウム生産ブランケット (バッチ回収型) (田中, 鈴木, 安達, 黒田, 岡崎, 山崎, 三角, 毛利, 藤井, 小林(武), 飯田(浩))	284
11.1	序	284
11.2	ブランケット概念の選択	284
11.3	設計概要	292
11.4	ニュートロニクス解析	306
11.5	熱水力設計	316
11.6	構造解析	330
11.7	トリチウム回収	336
11.8	トリチウム透過	340
12.	トリチウム及び真空 (本多, 海老沢, 芦部, 飯田(浩))	346
12.1	トリチウム系	346

12.2	真空系 .....	350
13.	遮蔽 (毛利, 関泰) .....	358
13.1	遮蔽基準 .....	358
13.2	遮蔽厚, 組成の最適化 .....	360
13.3	局所非均質効果 .....	366
14.	プラント配置 (飯田浩) .....	382
15.	コスト (飯田浩, 辻村) .....	384

### 第XIII章 運転及び試験計画 (本多, 飯田浩, 苔米地)

1.	INTORでの試験の役割 .....	387
1.1	INTORでのプラズマ物理実験及び補助プログラム .....	388
1.2	INTORでの技術試験及び補助プログラム .....	388
2.	運転計画 .....	391
3.	試験計画 .....	392
3.1	ステージ I の運転計画とプラズマ実験 .....	393
3.2	プラズマ工学実験 .....	393
3.3	ブランケット実験 .....	394
3.4	材料試験 - バルク材料 .....	394
3.5	表面材料試験 .....	395
3.6	サーベイランス・テスト .....	396
3.7	ニュークリア・テスト .....	396
3.8	発電試験 .....	397
3.9	テストモジュール組込 .....	397
3.10	補助施設 .....	398
3.11	照射後試験装置 .....	398

## Chapter XI Concept Evolution

## 1. Introduction

The conceptual design concept for INTOR was developed in the Phase One workshop. In the Phase Two A, Part 1 and 2 workshop, we have studied critical technical issues and have also assessed scientific and technical data bases. Based on those results, the INTOR design should be modified to upgrade the design concept. The major modification items are related to plasma beta value, plasma operation scenario, reactor size reduction, neutron fluence, tritium producing blanket, and implementation of active control coils. In this chapter, the concept evolution for the design modification and main results are described.

## 2. Reduction of a gap between the design value and the predicted beta limit

The total average beta value (5.6 %) of the present INTOR design is rather optimistic and somewhat beyond the critical beta limit (3.46 %) predicted from the empirical beta limit scaling ( $3.5I_p[\text{MA}]/a[\text{m}]B_T[\text{T}]$ ), which is derived from recent experimental and theoretical studies, and most of experimental data are below this limit. Narrowing down the gap between the design beta value and the predicted beta limit should be included in the design modification. One potential way for reduction of the beta gap is the increase of plasma current and the decrease of plasma major radius, based on the empirical beta scaling. Another possible way is the reduction of non-DT contributions in addition to the fuel DT beta value (4.57 %), 45 % of which is allotted to the non-DT contributions at present. As a tentative goal, the increase of the plasma current from 6.4 MA to 8.0 MA and the decrease of the plasma major radius from 5.3 m to 5.0 m are specified. The potential reduction of the reactor size can be attained with the reduction of the width of the inboard shielding blanket, the enhance of the maximum poloidal field, and the increase of toroidal and poloidal coil current densities.

Main plasma parameters are evaluated with the numerical code consisting of the simplified power balance of plasmas and engineering restriction of the reactor structure. An average ion temperature is kept to be 10 keV, at which the beta value takes nearly its minimum value. The plasma minor radius is also tried to keep the present design value of 1.2 m. The flux supplied by ohmic heating coils also retains the present value. The required increased volt-second due to the enhanced plasma current, which may be inconsistent with the retaining volt-second, is resolved by incorporating the non-inductive current ramp-up and transformer recharge with LH waves at low densities in the operation scenario.

The reduction of the plasma major radius have been achieved by the following potential engineering improvements. The first is the reduction of the inboard shield by 10 cm. The second is the increment of the maximum experience field of poloidal field coils, which use  $\text{Nb}_3\text{Sn}$  instead of  $\text{NbTi}$ . The last improvement is to increase current densities of toroidal (30 A/mm<sup>2</sup>) and poloidal (25 A/mm<sup>2</sup>) field coils. Those engineering improvements make the reduction of 0.3 m in the major radius feasible. The reduction of the excess of the average total beta value (5.6 %) beyond the critical beta limit (3.46 %) predicted by the empirical scaling is accomplished by the increase of the



plasma current, from 6.4 MA to 7.5 MA and the reduction of the plasma major radius, from 5.3 m to 5.0 m. It raises the beta limit (4.4 %) predicted by the empirical scaling. The other is the reduction of the additional beta value, which should be provided for impurities, high energy particles and thermalized helium particles, in addition to the beta value due to fuel DT ions. The additional beta value is chosen to be 30% of the DT fuel beta value (4.58 %) instead of 45 %. Then the total beta value amounts to 5.92 %, which increases from the reference value of 5.6 %.

Based on the above considerations, the simple plasma analysis numerical code yields the main plasma parameters, as shown in Table 2.1. The plasma current is selected to be 7.5 MA instead of 8 MA, the target value. The reason of this selection is partly because 8 MA, corresponding to 1.6 of the safety factor without a toroidal effect, is considered somewhat large, and partly because the large plasma current requires the large poloidal coil currents, in particular near the divertor region. 7.5 MA of the plasma current corresponds to 1.7 of the safety factor, taking account of elongation. The safety factor of 7.5 MA could be over 2, when the toroidal effects is included. The total beta value increases up to 5.92% from 5.6%. The critical beta limit predicted by the empirical scaling also increases due to the enhanced plasma current. Then, ratio of the total beta value to the critical one is reduced to 1.34 from 1.62. The excess of the total beta value beyond the critical one is also reduced to 1.35% from 2.14%.

Table 2.1 Modified main plasma parameters

Plasma major radius, $R_p$ (m)	5.0
Plasma radius, $a$ (m)/ $b$ (m)	1.2/1.92
Aspect ratio, $A$	4.167
Elongation, $K$	1.6
Triangularity, $\delta$	> 0.2
Average ion temperature, $\langle T_i \rangle$ (keV)	10
Average ion density, $\langle n_i \rangle$ ( $10^{20} \text{ m}^{-3}$ )	1.4
Total beta, $\beta_t$ (%)	5.92
Fuel beta, $\beta_f$ (%)	4.57
Plasma current, $I_p$ (MA)	7.5
Safety factor, $q_i$	1.7
Toroidal field, $B_T$ (T)	4.96
Thermonuclear power, $P_{th}$ (MW)	580
Neutron wall load, $P_n$ (MW/m <sup>2</sup> )	1.24

### 3. Operation scenario

In the present INTOR design, the plasma current is inductively driven by OH coils throughout the whole pulse of more than 200 s, including start-up, burn, and shut-down. In the design modification, the increase in the plasma current and the reduction of the plasma major radius, retaining the present inductive volt second, are incorporated to narrow the beta gap between the design value and the beta limit. It requires reconsideration of the present operation scenario, because the increased plasma current will be inconsistent with the retained inductive flux.

Remarkable progresses have been made experimentally and theoretically in non-inductive current drive with a LH wave, and the further progress may be expected in this area. Based on analyses and evaluations on this issue (see Chapter IV : RF heating and current drive), the non-inductive current ramp-up and recharging scenario with the LH wave is incorporated in the design modification to resolve the estimated problem about the required volt second and to gain engineering benefits associated with the non-inductive scenario. In this section, the modified quasi-steady operation scenario and engineering benefits associated with the quasi-steady operation are described.

#### 3.1 Physics

Non-inductive current ramp-up and transformer recharge scenario is incorporated in the modified INTOR design, and time scale for heating to ignition is also reconsidered. The modified operation scenario with non-inductive current ramp-up and transformer recharge with a LH wave is shown in Fig. 3.1-1. The operation scenario consists of seven phases; (A) start-up phase including a current ramp-up to 5.7 MA, (B) heating phase to ignition, (C) burn phase, (D) cooling phase for recharging or shutdown, (E) recharging phase for OH coils, (G) shutdown phase, and (H) dwell phase.

At the beginning of the start-up phase, plasma are produced and heated with an assist of ECRF heating with 10 MW, and plasmas are brought to a parameter region with around  $3 \times 10^{18} \text{ m}^{-3}$  in densities and 1-2 keV in temperatures. Such a low-density plasma carry well its current driven by a LH wave. Based on analyses on a current ramp-up scenario, a ramp-up time is specified  $\sim 100 \text{ s}$ , and during this period the plasma current increased up to 5.7 MA by the LH wave with a power level of 10 MW.

In the heating phase to ignition, plasmas are heated by an ICRF wave of 50 MW, and temperatures and densities are increased to the specified level of the burn phase. The plasma current is also increased from 5.7 MA to 7.5 MA inductively instead of rf drive, because of significant decrease of rf current drive efficiency in high density plasmas. The heating time is  $\sim 20 \text{ s}$ . An initial goal of a burn time is more than 1000 s, which is inductively driven. The cooling phase is an inverse process of the heating phase. The cooling time is  $\sim 20 \text{ s}$ . The prolonged cooling time may require temperature control with the ICRF wave, otherwise temperatures could drop with the shorter time of an order of confinement time. In the cooling phase, the plasma current decreased to from 7.5 MA to 5.7 MA inductively.

In the recharge phase, OH coils are recharged, while the plasma current is hold to 5.7 MA by the LH wave in plasmas with densities of around  $3 \times 10^{18} \text{ m}^{-3}$  and temperatures of 1-2 keV. The recharging time of  $\sim 200 \text{ s}$  is also

evaluated based on analyses of transformer recharge by the LH wave. In a quasi-steady operation, four phases from (B) to (E) are repeated.

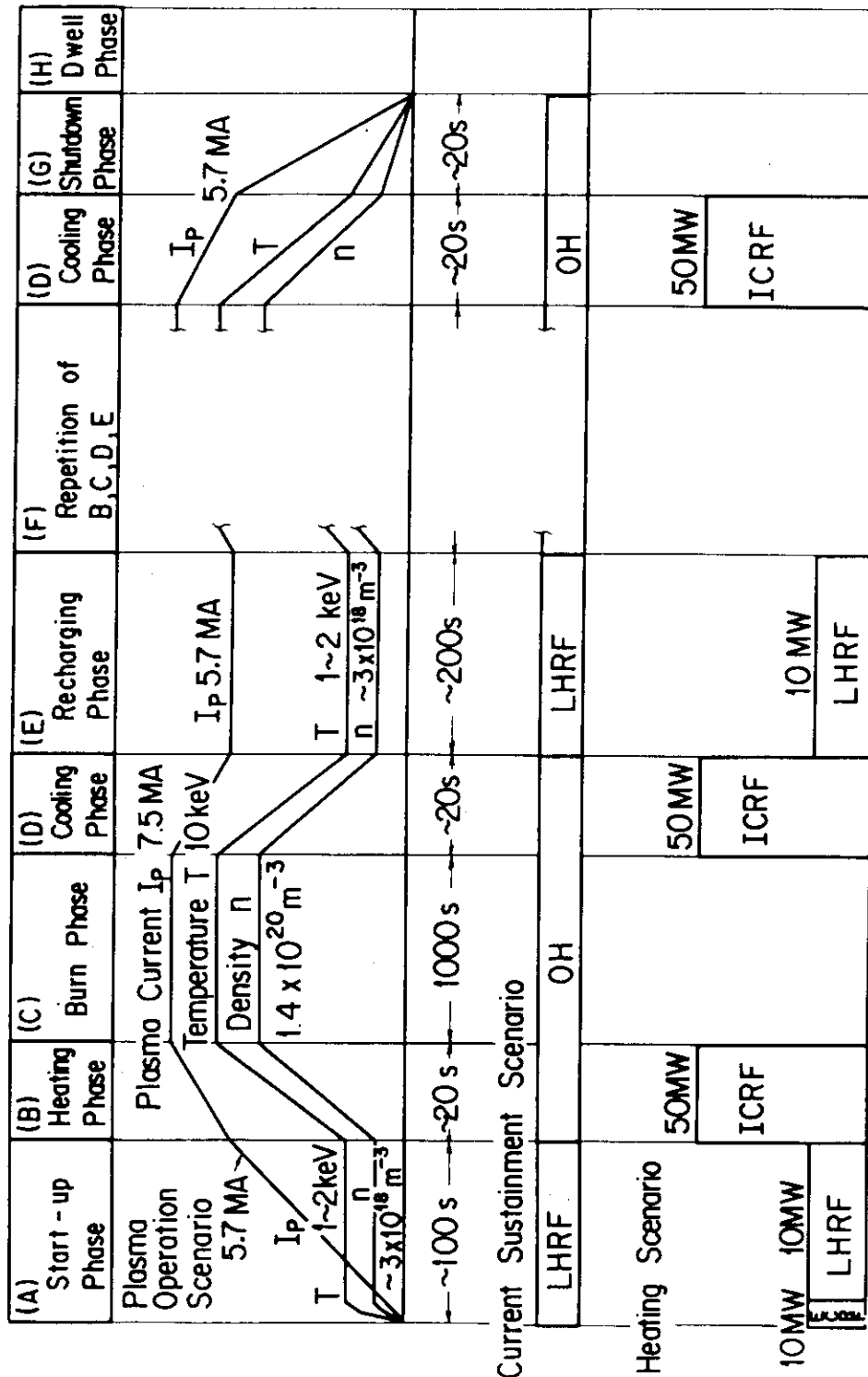


Fig. 3.1-1 Modified INTOR operation scenario

### 3.2 Engineering benefits associated with the RF current ramp-up and quasi-steady operation.

Several engineering benefits are expected associated with the plasma current ramp up by RF instead of OH coils, that is, volt second saving, decrease of AC loss in superconducting coil system and reduction of requirement for power supply.

#### 3.2.1 Volt second saving

In the conventional inductive current ramp up scenario the most part of volt second delivered by PF coil is consumed for plasma initiation and current ramp up leaving a small amount of volt second for the burning phase. When the plasma current is ramped up by RF wave injection, most of the volt second can be used for burning phase leading to a longer pulse or smaller OH coil bore then smaller reactor size. Our initial preliminary estimation of pulse length and reactor size is shown in Fig. 3.2-1. This figure shows the plasma major and minor radii in the case of RF ramp-up operation. When we assume same burn time as reference value (200 sec), plasma major radius is found to be smaller by about 80 cm than reference.

For the same reactor size as that of Phase I reference INTOR, the burn time can be about 1700 s. This estimation is made assuming full swing of OH coil.

However magnetic field analysis found some problems of superposing magnetic fields by divertor coil current and plasma current on the OH coil near divertor coil at the beginning of the burn phase. This is the disadvantage inherent to the RF ramp up scenario. Detailed explanation and results of analysis are describe in the chapter XII section 6. We show here the summay of the result in Table 3.2-1. The burn time of 957 s is obtained for the burn phase plasma current of 6.4 MA. When we increase the plasma current to 7.5 MA in order to mitigate the beta problem, 509 s of burn time is obtained. Since our RF coil system design for INTOR is not fully optimized, it should be possible to extend burn time to some extent by selecting proper division and location of divertor coils. Anyway there is certain advantage associated with RF current ramp up in extending burn time or reducing reactor size.

#### 3.2.2 AC loss

The large AC loss induced in the TF and RF coil systems was a big problem in the reference INTOR design with conventional inductive current ramp-up scenario. Even with the large number of electric breaks in the support structure, which leads to the concern about the structural integrity of the supports, the total cycle averaged AC loss exceeds 100 kW. In the case of RF current ramp up, current rise can be greatly prolonged ( 100 sec) and AC loss is dramatically reduced without significant structural problems in the support system. The design of coil support system is described in the chapter XII section 8. The result of AC loss calculation is shown in Table 3.2-2. Total cycle averaged AC loss is about 4.3 kW. This is the great advantage of the RF ramp-up scenario.

Table 3.2-1 Summary of burn time

## (a) Available flux for burning

Operation mode Plasma parameter		Quasi - steady state operation	Pulsed operation
$I_p = 7.5 \text{ MA}$ $\beta_p = 1.3$	$\phi_{\text{burn}}$	28 v.s	15 v.s
	ratio (%)	104 %	56 %
$I_p = 6.4 \text{ MA}$ $\beta_p = 2.2$	$\phi_{\text{burn}}$	45 v.s	27 v.s
	ratio (%)	167 %	100 %

## (b) Burn time

Operation mode Plasma parameter		Quasi - steady state operation	Pulsed operation
$I_p = 7.5 \text{ MA}$ $\beta_p = 1.3$	$\tau_{\text{burn}}$	509 s	273 s
	ratio (%)	89 %	48 %
$I_p = 6.4 \text{ MA}$ $\beta_p = 2.2$	$\tau_{\text{burn}}$	957 s	574 s
	ratio (%)	167 %	100 %

Table 3.2-2 AC loss of INTOR coil system

Parts		AC loss (average)
TF coils	Winding	15 [W]
	Helium vessel	240 [W]
PF coils	Winding	120 [W] *)
Coil supports	Bucking cylinder	1160 [W] *)
	Shear pannel, etc.	2770 [W] *)
	total	4305 [W]

\*) estimation value

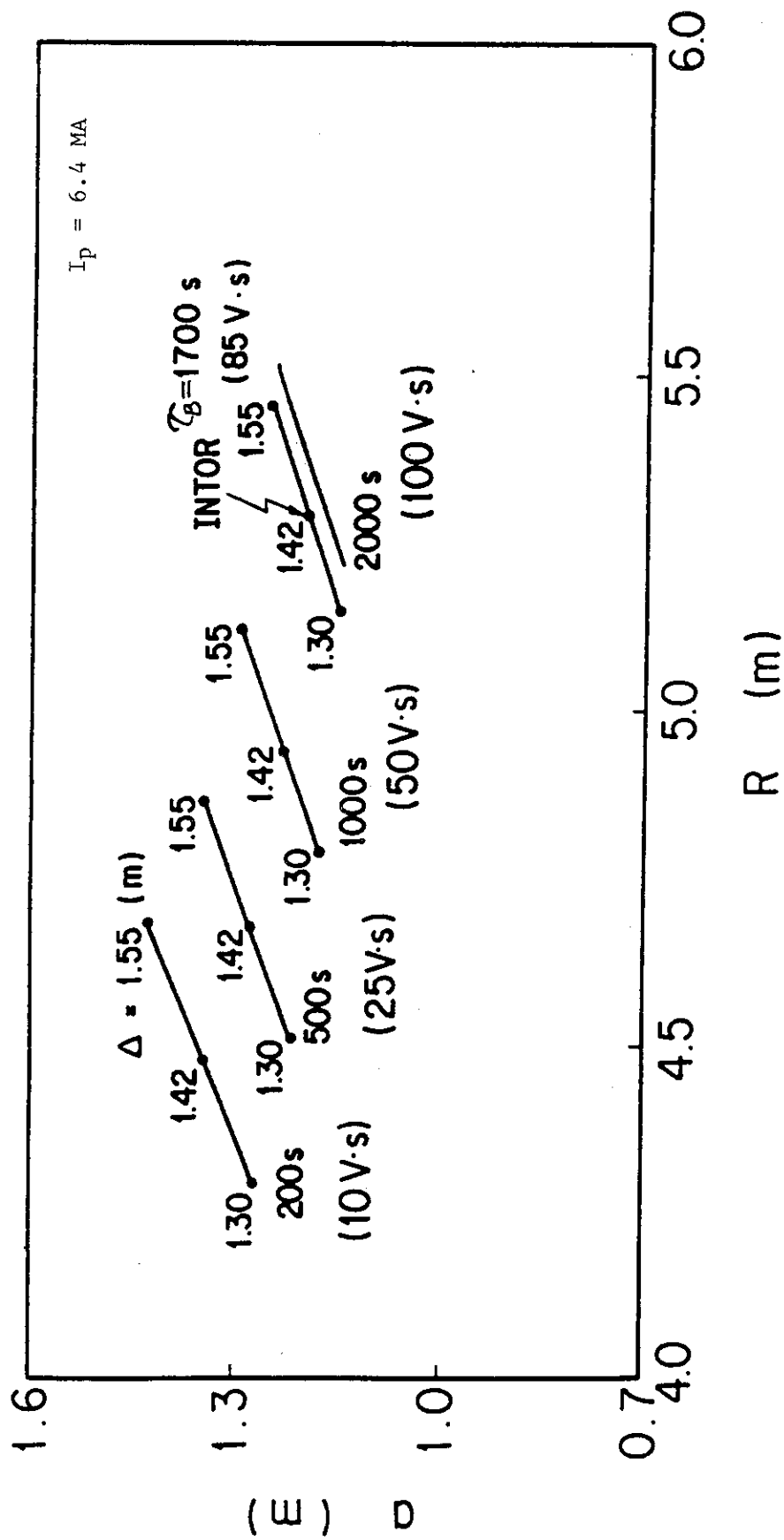


Fig.3.2-1 Reactor size ; plasma major radius R vs. minor radius a

$\Delta$  : distance bt. plasma surface and inboard TF coil vessel (1.42 m)

$T_b$  : burn time

### 3.2.3 Power supply capacity

Typical load pattern of PF coil power supply for the case of conventional inductive current ramp up scenario is shown in Fig. 3.2-2. Peak power load appears at the end of plasma current ramp-up phase ( $t=5$  s). At this time, apparent power for PF-coil power supply becomes as 2000 MVA. By adopting RF current-ramp up scenario and extend the ramp-up duration to 100 s power load at the end of current ramp up phase can be greatly reduced (600 MVA). However since there is another peak (1400 MVA) at the end of heating phase, some effort is required to reduce this peak. By extending heating phase duration and selecting proper plasma current level at the end of current ramp-up phase this peak can be reduced to about 1000 MVA. Power supply calculation is described in the chapter XII section 6. Since longer heating time requires larger power supply capacity for heating system, careful trade-off study is necessary. Our preliminary study which compares 6 s and 20 s of heating phase duration shows that the latter heating phase duration is preferable.

### 3.2.4 Cyclic Stress on the TF coil

When quasi-steady operation mode is adopted as well as current ramp up by RF, we have further possible advantage that the fatigue problem of TF coil support can be greatly mitigated. The difficulties for supporting the superconducting TF coil of large tokamak like INTOR are mainly caused by the overturning force which results from the interaction of the TF coil current and the equilibrium field. In the pulsed operation tokamak, this force acts cyclically on TF coils. The TF coil structural design criteria include conventional (primary) stress limits in addition to limits established for stress amplitude based on fatigue life consideration. It must be expected that the stress amplitude can be reduced considerably by introducing the quasi-steady state operation.

Figure 3.2-3 shows that the overturning force at low-beta phase is larger than at high-beta phase under the condition of same plasma current. This fact signifies that the amplitude of the overturning force can be reduced by sustaining the plasma current in OH coil recharging phase at lower value than the burning plasma current.



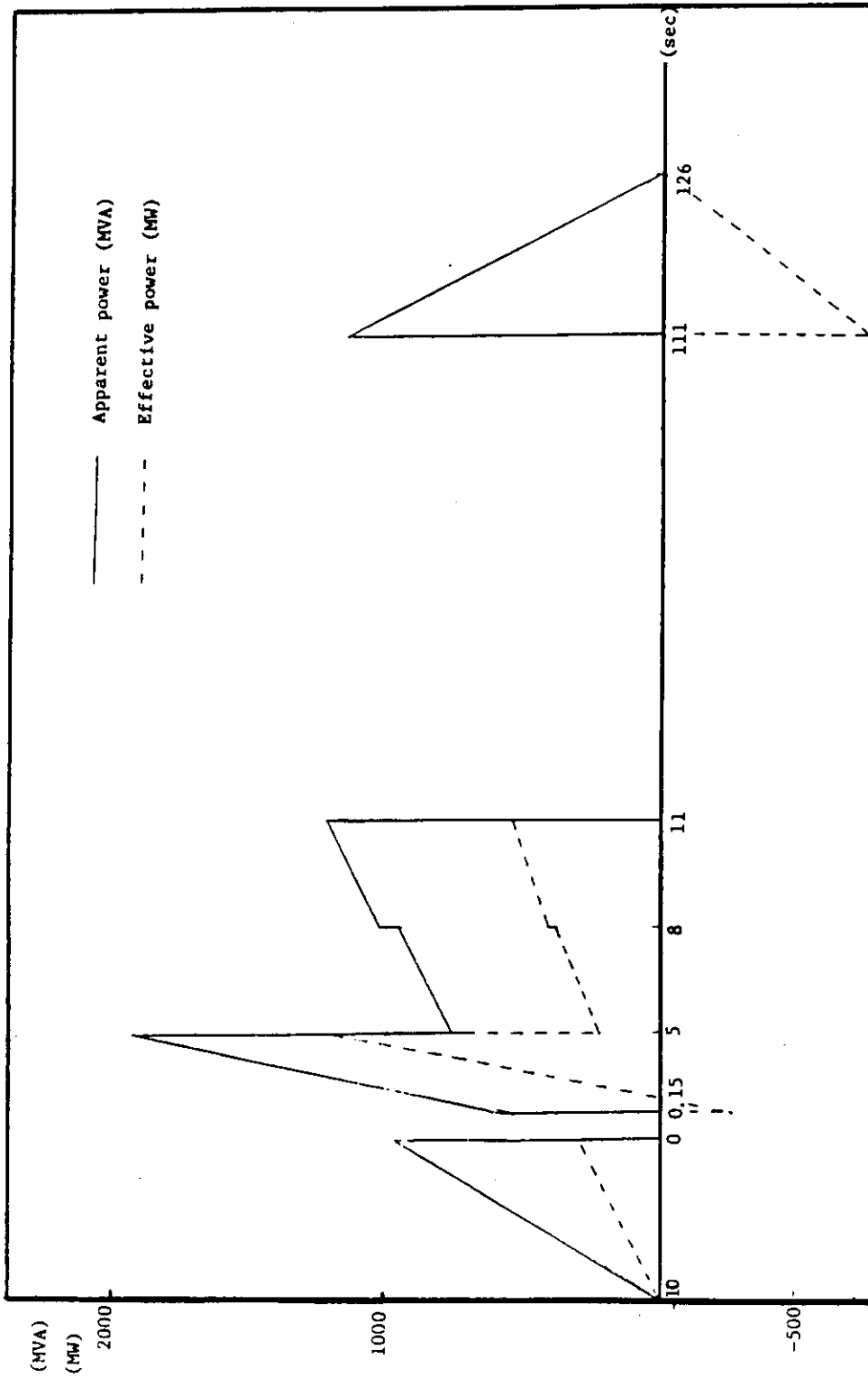


Fig.3.2-2 Load pattern of PF coil power supply for conventional pulsed reactor

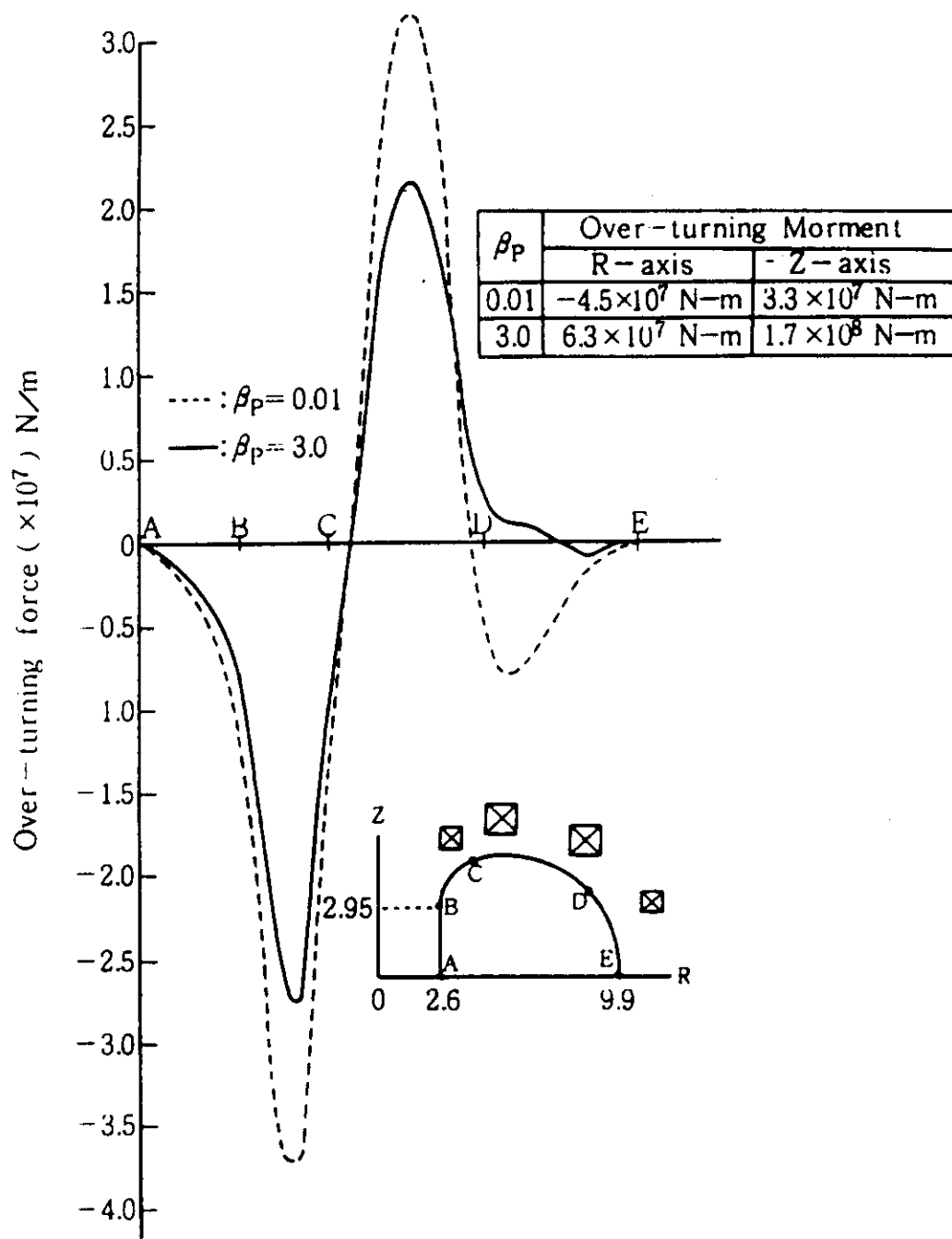


Fig.3.2-3 Overturning force distribution for low  $\beta_p$  and high  $\beta_p$

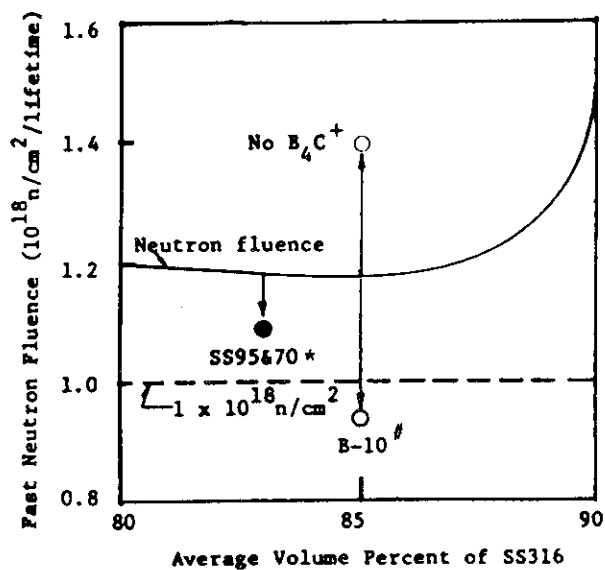
#### 4. Reactor size reduction

In order to reduce reactor size the following engineering improvements are implemented. The first is the reduction of the inboard shield by 10 cm. The second is the increment of the maximum experience field of poloidal field coils, which use  $\text{Nb}_3\text{Sn}$  instead of  $\text{NbTi}$ . The last improvement is to increase current densities of toroidal ( $30 \text{ A/mm}^2$ ) and poloidal ( $25 \text{ A/mm}^2$ ) field coils. Those engineering improvements make the reduction of 0.3 m in the major radius feasible. The inboard shield thickness is reduced by changing shield criterion for the allowable nuclear heating in TFC from 5 kW to 15 kW and optimizing shield composition. Figure 4-1 shows the result of the optimizing calculation. The composition of 85% stainless steel and 15% water is selected as the optimum point. The chapter XII section 13 describes more detailed shield calculation results.

The increase of TF coil current density from 25 to  $30 \text{ A/mm}^2$  and the maximum allowable PF coil field from 8 to 10 T resulted in the reduction of TF coil thickness by 10 cm and OH coil bore by 10 cm, respectively. TF coil and PF coil design is described in the chapter XII section 8. These engineering modification resulted in the 0.3 m of plasma major radius reduction. The comparison of the radial build between that of Phase IIA Part I and Part II is shown in Fig. 4-2. Both the reduction of the main radius 5.3 m to 5.0 m and the reduction of cross section of TF coil contribute to the reduction of the reactor structure size (diameter of the belljar) by 1 m.

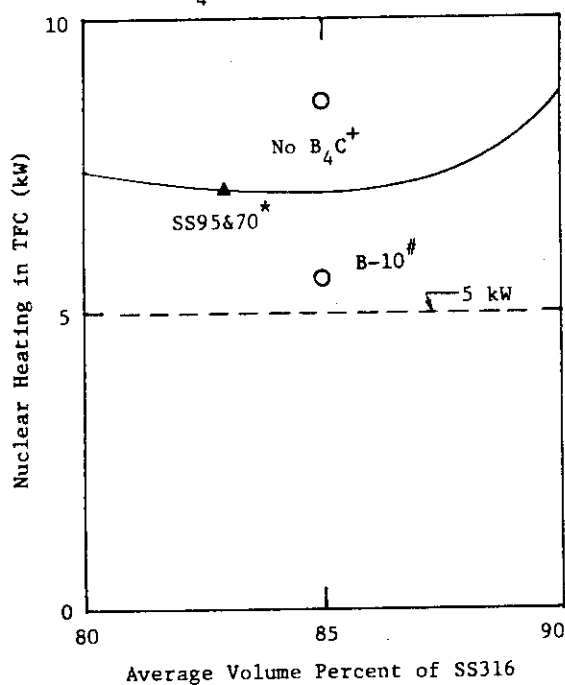
As for the vertical dimension of the reactor, the impact of the choice of impurity control system is considerable. As a reference design, the short channel type configuration of the divertor is adopted in order to reduce the reactor size as shown in Fig. 4-3. The maximum heat load on divertor plate of short channel concept is about  $5 \text{ MW/m}^2$ . This design condition is very severe from the view point of the thermal stress. If the permissible level of the maximum heat load  $2 \text{ MW/m}^2$  is adopted, the increasing length of divertor plate in horizontal direction leads to the increase in TF coil bore and the short channel divertor is not recommendable.

note : \* SS95% for Removable shield  
and 70% for Semi-permanent Shield  
+ Replace  $B_4C$  with SS80% Shield  
# Use  $B_4C$  with 100% B-10



(a) Fast neutron fluence

note : \* SS95% for Removable Shield  
and 70% for Semi-permanent Shield  
+ Replace  $B_4C$  with SS 80% Shield  
# Use  $B_4C$  with 100% B-10



(b) Nuclear heating

Fig.4-1 Dependence of TFC irradiation properties on inner shield material composition

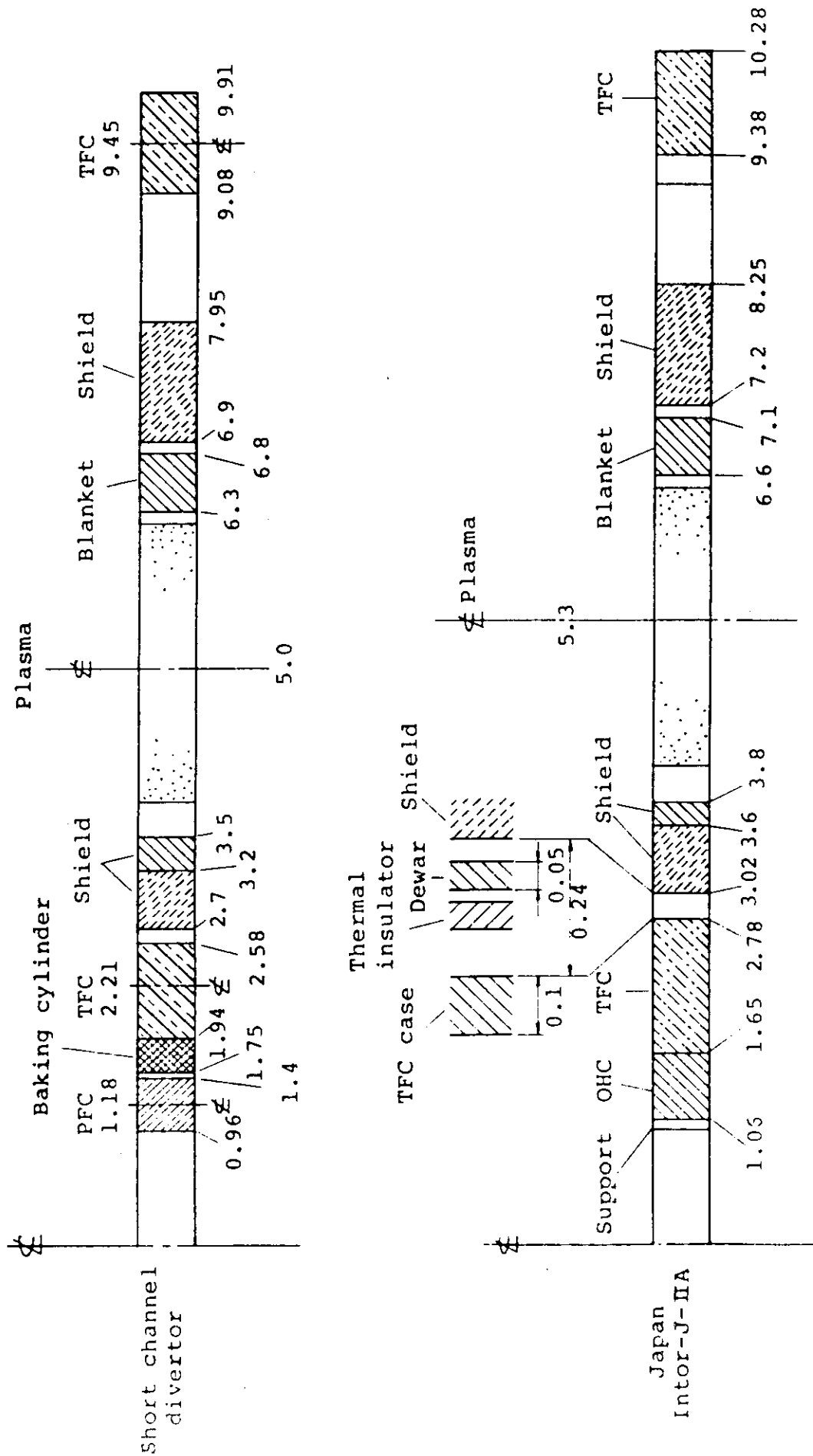


Fig.4-2 Radial build of short channel divertor concept

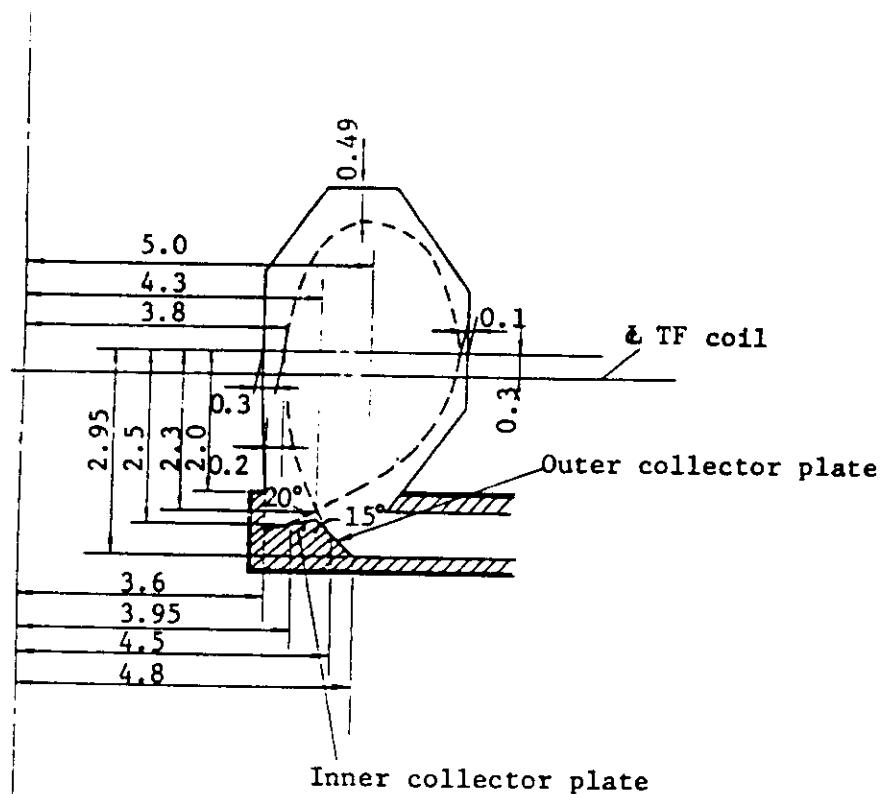


Fig.4-3(a) Profile of the divertor region (Case 1)

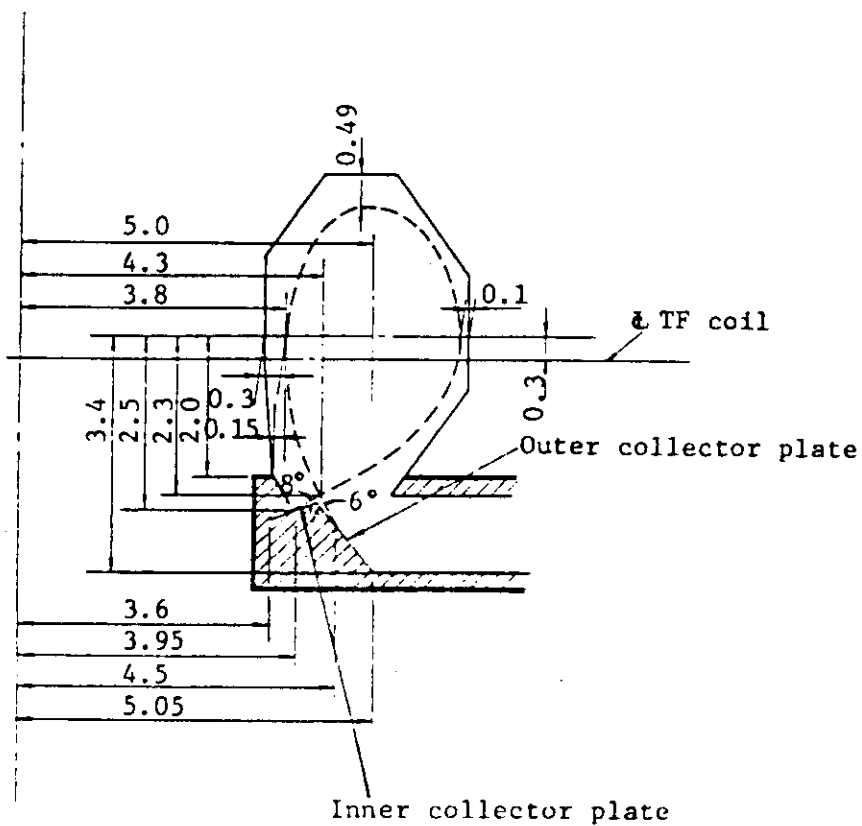


Fig.4-3(b) Profile of the divertor region (Case 2)

## 5. Tritium producing blanket

In the previous blanket design studies for INTOR, continuous tritium recovery scenario has been proposed based on economic and tritium availability considerations. However, design requirements associated with continuous tritium recovery such as the precise temperature control of breeder, lead to complexity of blanket design. A improvement of the simplicity and reliability is desired for tritium producing blanket.

In this section, batch-type tritium recovery scenario is proposed as a solution of simple and reliable tritium producing blanket, and design feasibility studies have been performed.

The design philosophies adopted for accomplishing the simplicity and reliability are as follows:

- (i) Batch-type tritium recovery scenario is adopted to simplify the temperature control mechanism of breeder.
- (ii) To provide high reliability performance of shell effect, copper alloy (Cu-Be-Ni) which offers possible advantage over pure copper in the area of radiation damage resistance is used as a shell conductor material.
- (iii) Low temperature helium gas is selected as the coolant to avoid coolant/breeder reaction in accident.
- (iv) To achieve the high tritium breeding ratio, lithium oxide ( $\text{Li}_2\text{O}$ ) and beryllium are used as a tritium breeding material and a neutron multiplier, respectively.

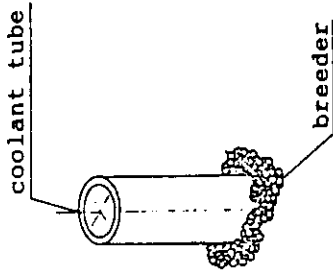
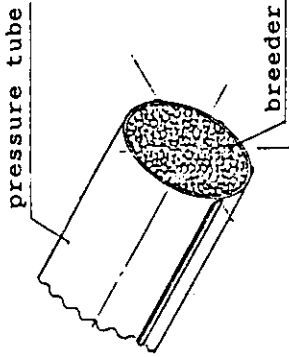
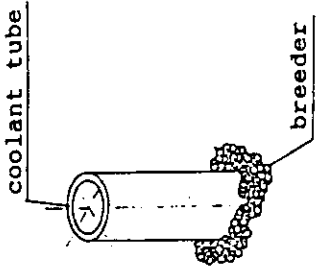
There are two major factors that reduces simplicity and reliability of blanket. One is the temperature control requirement of breeder (ex. 400 1000 °C for  $\text{Li}_2\text{O}$ ) to ensure continuous in-situ tritium recovery during reactor operation. This factor imposes installation of thermal insulation gap to provide temperature difference between breeder and coolant tube. The other is the addition of neutron multiplier and shell conductor for passive plasma stabilization with their cooling mechanism and support structure. Application of beryllium plate potentially be a candidate, since it can be used as both neutron multiplier and shell conductor. However, limited ductility of beryllium relative to other structural materials imposes some constraints on design, fabrication and reliability of the shell structure.

For the above reasons, design approaches in this selection study are focussed on simple and reliable blanket concept in the area of temperature control mechanism and neutron multiplier/shell conductor. Figure 5-1 shows an investigation of possible blanket concepts starting from simplification of temperature control mechanism of breeder. Elimination of thermal gap around cooling tube is essential for simple design of blanket. If continuous in-situ tritium recovery is a design requirement of blanket, refractory metals must be developed for the structure materials. But if the continuous in-situ recovery of bred tritium is excluded from blanket design requirements, stainless steel (or PCA), that has most developed data base for nuclear application, can be used as structure material.

As shown in Fig. 5-1 there are three options available for basic thermal hydraulic design of batch recovery blankets: (i) Water-cooled blanket, (ii) Directly-helium-cooled blanket, and (iii) Indirectly-helium-cooled blanket. Table 5-1 summarizes key features of these three-type design. Of these three concepts, indirectly-helium-cooled blanket appears most attractive and selected as the reference of the present study, because of its high potential of tritium breeding performance and easiness of periodic tritium recovery. Design study of this blanket is described in the chapter XII section 11.



Table 5-1 Comparison of design approaches for batch recovery blanket

	Water-Cooled Blanket	Directly Helium-Cooled Blanket	Indirectly Helium-Cooled Blanket
<u>Concept</u>			
<u>Features</u>	<ul style="list-style-type: none"> <li>advantages :               <ul style="list-style-type: none"> <li>low temperature of structure materials</li> <li>low pumping power</li> </ul> </li> <li>disadvantages :               <ul style="list-style-type: none"> <li>difficulty of precise coolant tube arrangement for breeder maximum temperature control</li> <li><math>\text{Li}_2\text{O}/\text{H}_2\text{O}</math> reaction</li> <li>requirement of coolant detritiation system</li> <li>change of coolant material to helium gas at tritium recovery operation</li> </ul> </li> </ul>	<ul style="list-style-type: none"> <li>minimum design considerations on the breeder temperature control</li> <li>reduction of tritium purge line</li> <li>easiness of breeder heating for tritium recovery</li> <li>complicated structure with pressure tube, sub header, manifold and so on</li> <li>requirement of large piping spaces and high pumping power</li> <li>large mass transport rate of <math>\text{Li}_2\text{O}</math></li> </ul>	<ul style="list-style-type: none"> <li>high potential of tritium breeding performance</li> <li>easiness of breeder heating for tritium recovery</li> <li>difficulty of precise coolant tube arrangement for breeder maximum temperature control</li> <li>requirement of large piping spaces and high pumping power</li> </ul>

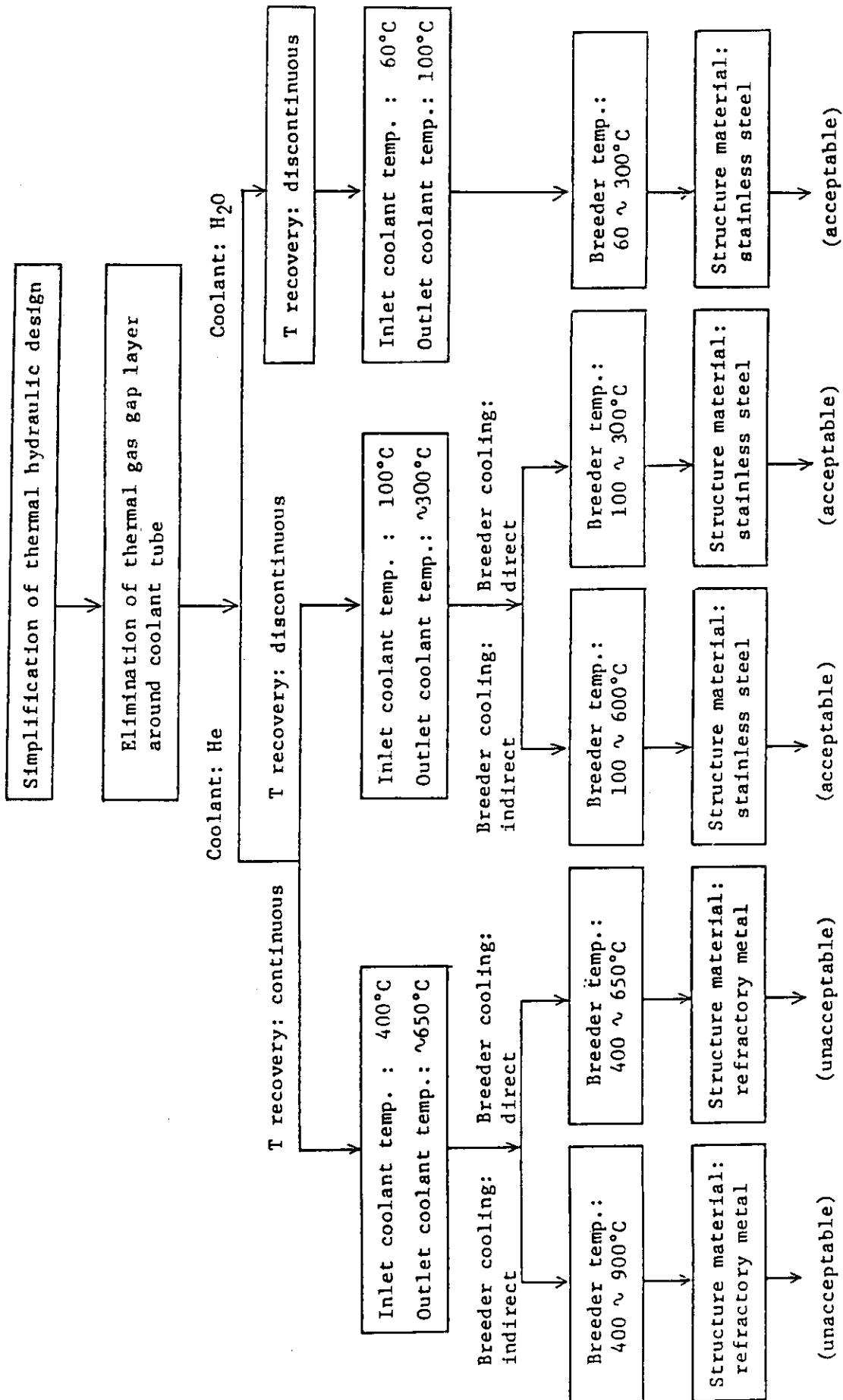


Fig.5-1 Investigation of design concepts for batch recovery blanket

## 6. Fluence

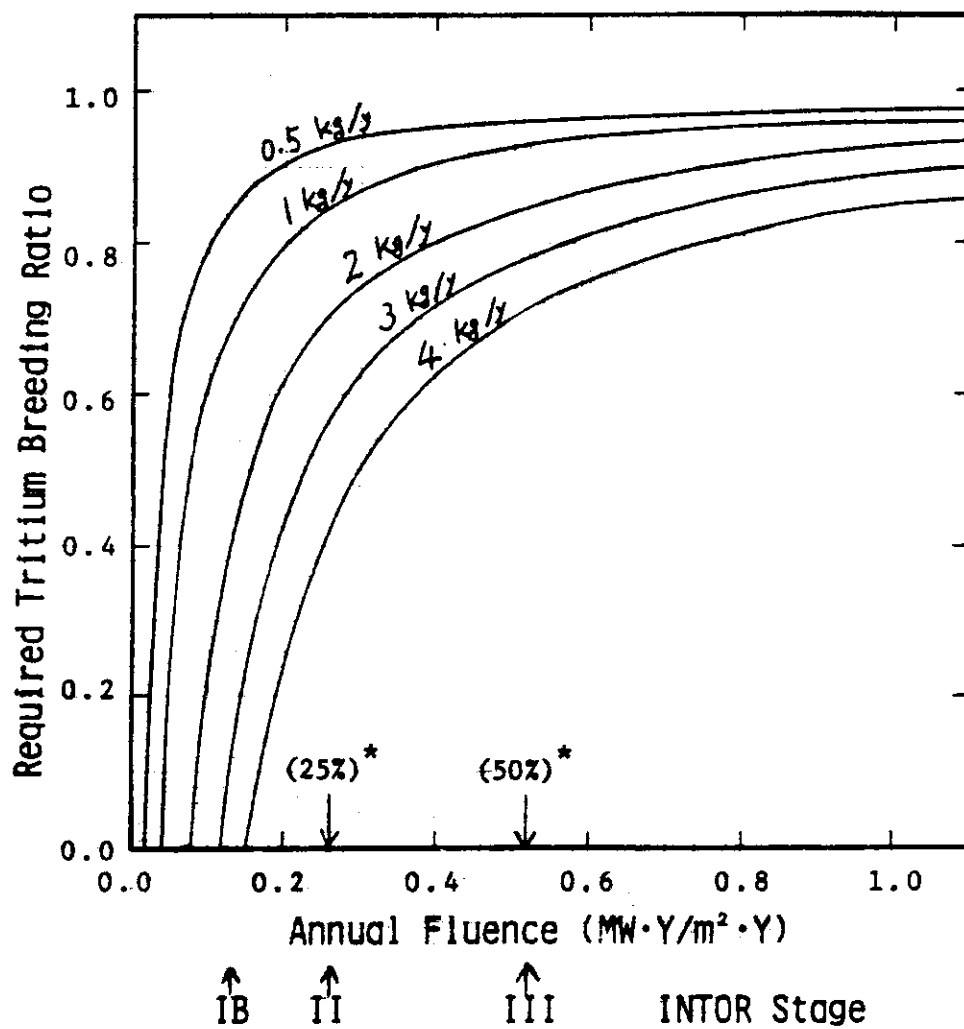
Materials tests is the one of the INTOR operation purpose. The minimum fluence required for a structural material irradiation test is said to be 3 MWY/m<sup>2</sup>. And considering fusion reactor development schedule, the irradiation test duration should not be too long. It seems that around 10 years may be the proper duration. Figure 6-1 shows the relation between required tritium breeding ratio and achievable annual fluence as the function of annual available tritium procurement. When we want 6.6 MWY/m<sup>2</sup> of fluence during 10 years operation (0.66 MWY/m<sup>2</sup>/Y), about 0.8 of tritium breeding ratio is required since the tritium procurment available in near future does not seem to exceed 3 kg/Y. Figure 6-2 shows the expected tritium supply from Heavy Water Cooled Reactor in Canada which is the only practical commercial base source. The breeding ratio of 0.8 requires installation of breeding blanket on the inboard side of reactor making reactor size increased. The fluence of 3 MWY/m<sup>2</sup> in 10 years can be achievable with the tritium breeding ratio of 0.6. Then the fluence of 3 MWY/m<sup>2</sup> is recommendable from above consideration and the finding that the fluence reduction is very effective in decreasing INTOR cost as shown in the cost benefit analysis in Phase IIA Part I.

## 7. Implementation of active control coil

Through the Phase IIA Part 1 and 2 the plasma vertical position control is discussed as one of the critical issues mainly from the viewpoint of electromagnetics. However, active control coil, which is essential component for stabilizing the plasma, has not been implemented into the mechanical configuration of the reference INTOR. The following items should be taken into consideration to determine the location of installation of the active control coil which produces the horizontal magnetic field constituent.

- (a) Active coil should be installed in the location where the magnetic field of horizontal constituent can be generated efficiently and the power supply capacity required is small enough.
- (b) Installation of the active control coil should be easy and the structure supporting the active control coil should be simple.
- (c) Radiation damage should be low enough.
- (d) Assembly and disassembly procedures should be simple and easy.

Detailed discussion is found in the chapter XII sections 3, 7 and 8.



\* Availability assuming 0.8 of duty cycle

Fig.6-1 Required tritium breeding ratio for INTOR

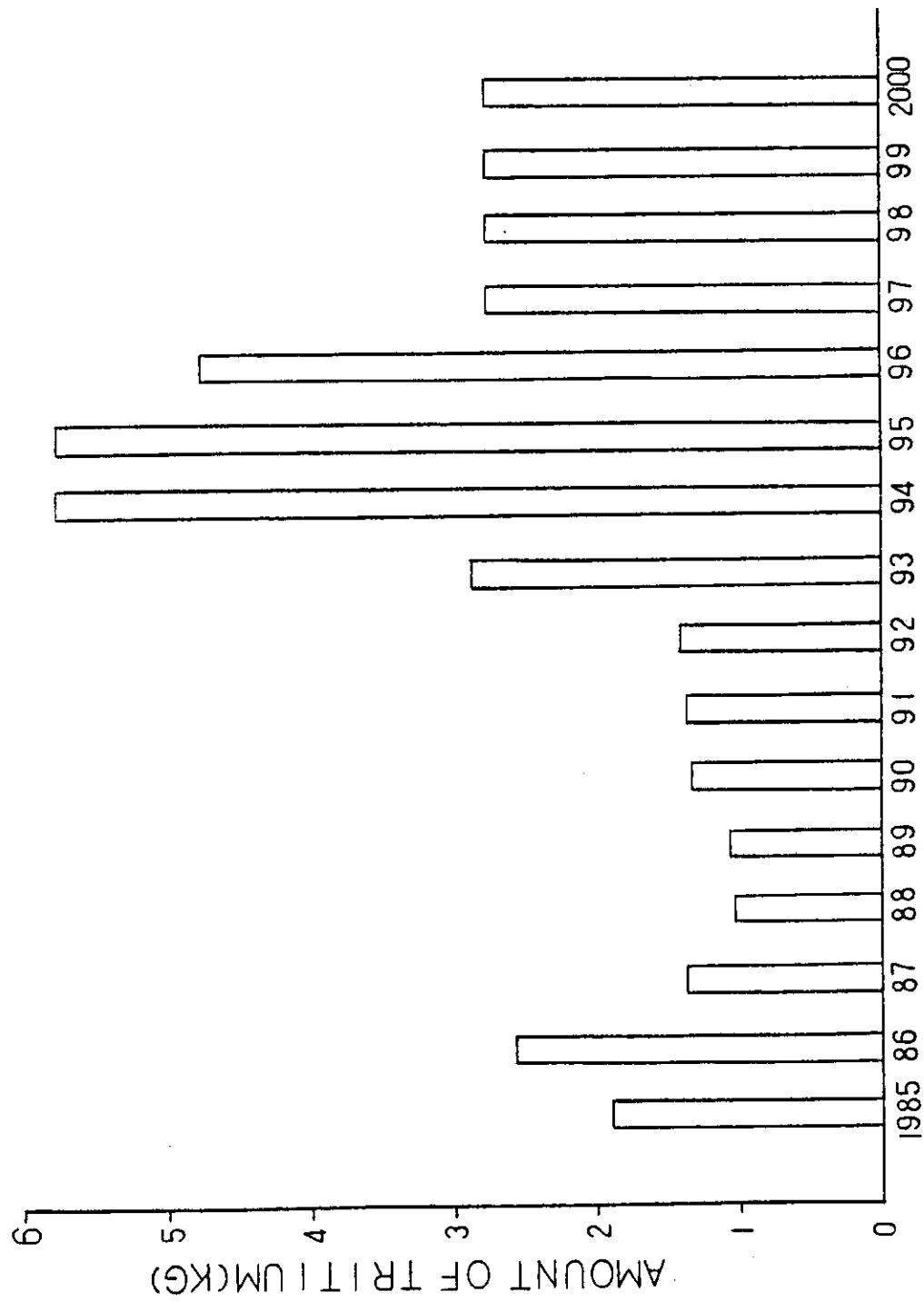


Fig.6-2 Total tritium produced each year by ONTARIO HYDRO

## Chapter XII Design Concept

### 1. Design Specifications

The INTOR design specifications that were developed and modified during Phase I and IIA Part 1 have been modified again to reflect changes in the design concept that have resulted from the Phase IIA Part 2 critical issues studies and from new information from the world-wide R and D programme. The new INTOR design specifications are listed in Table 1-1. Major changes are, increase plasma current, reduced reactor size, quasi-steady state operation mode, reduced fluence and use  $\text{Nb}_3\text{Sn}$  for PF coil conductor instead of NbTi.

TABLE 1-1 INTOR MAJOR PARAMETERS

GEOMETRY	
Chamber major radius (R)	4.9 m
Plasma major radius	5.0 m
Plasma chamber radius ( $r_w$ )	1.4 m
Plasma radius (a)	1.2 m
Plasma elongation, average (K) <sup>a,b</sup>	1.6
Plasma triangularity, average ( $\gamma$ ) <sup>a,b</sup>	0.2
Aspect ratio (A)	4.17
Plasma chamber volume <sup>c</sup>	302 m <sup>3</sup>
Plasma volume	227 m <sup>3</sup>
Plasma chamber area <sup>c</sup>	358 m <sup>2</sup>
Plasma surface area	316 m <sup>2</sup>
PLASMA	
Average ion temperature ( $\langle T_i \rangle$ )	10 keV
Average D-T ion density ( $\langle n_i \rangle$ )	$1.4 \times 10^{20} \text{ m}^{-3}$
Energy confinement time ( $\tau_E$ ) <sup>d</sup>	1.3 s
Safety factor (separatrix) ( $q_I$ ) <sup>b</sup>	1.7
Effective charge ( $Z_{eff}$ )	$\leq 1.5$
Field on chamber axis ( $B_T$ )	4.96 T
Plasma current ( $I_p$ )	7.5 MA
Toroidal field ripple ( $\delta$ ) <sup>b,e</sup>	-
Edge	0.97 %
Centre	<0.1 %
Fast alpha loss	~10 %
Beta toroidal burn average ( $\beta$ ) <sup>b,f</sup>	5.92 %
Beta poloidal ( $\beta_I$ ) <sup>b</sup>	1.3
<p>a The plasma shape is defined by the form of the separatrix.</p> <p>b For definition, see Chapter III of Phase-One report.</p> <p>c Excluding divertor.</p> <p>d At the working point, with burn control, neglecting alpha-particle and impurity corrections to the energy density.</p> <p>e All values are for peak/average maximum.</p> <p>f Allows 1.35% for impurity and alpha contributions.</p>	

Operating mode	Quasi-steady operation
Peak thermonuclear power ( $P_{th}$ )	580 MW(th)
Burn time ( $t_{burn}$ ) Stage I	~1000 s
Stages II and III	~1000 s
Recharging time ( $t_{rech}$ )	~200 s
Start-up and shut-down time ( $t_{ss}$ )	100 s
Number of pulses Stage I	$2.5 \times 10^3$
Stages II and III	$7.3 \times 10^4$
Maximum availability goal (varies with time, see INTOR operating schedule)	50 %

Major disruptions		
Number	: Stage I	30
	Stages II and III	70
Total energy deposited per disruption		
	Divertor plate <sup>g</sup>	80 MJ
	Uniform on first wall <sup>h</sup>	130 MJ
	Local on first wall <sup>i</sup>	80 MJ
Peak energy flux		
	Divertor plate	230 J·cm <sup>-2</sup>
	First wall	170 J·cm <sup>-2</sup>
Minor disruptions		
Number	: Stage I	60
	Stages II and III	350
Total energy deposited per disruption		
	Divertor	50 MJ
Energy density		
	Divertor plate	170 J·cm <sup>-2</sup>

- 25 -



TABLE 1-1 (cont.)

Time for energy deposition per disruption	20 ms
Time for current decay during disruption <sup>j</sup>	20 ms
TOROIDAL FIELD COILS	
Number	12
Conductor	(NbTi) <sub>3</sub> Sn
Stabilizer	Cu
Maximum field ( $B_{\max}$ )	~12 T
Bore height <sup>k</sup>	9.26 m
Bore width <sup>k</sup>	6.5 m
Maximum allowable nuclear heating	15 kW
Maximum radiation on insulator	$5 \times 10^9$ rad
Average conductor current density <sup>l</sup>	$2500 \text{ A}\cdot\text{cm}^{-2}$
Maximum allowable stray field	$\leq 10^{-2}$ T
POLOIDAL FIELD SYSTEM	
Total volt-seconds required	90 V s
PFC conductor	Nb <sub>3</sub> Sn
PF location (relative to TF)	outside
PF maximum allowable field at coil	~10 T
Maximum allowable stray field	$\leq 10^{-2}$ T
Field penetration time (e-folding)	
Radiation field for vertical position control <sup>m</sup>	~50 ms
Distance of passive 'shell' from separatrix (for vertical position control)	~0.3 m
Maximum rate of vertical field change in plasma	$0.5 \text{ T}\cdot\text{s}^{-1}$

j For electromechanical design purposes 20 ms should be used.

k Full bore of the container.

l Area including conductor, stabilizer and coolant flow channels, but not major structure.

m To be consistent with torus electromagnetic requirements.

TABLE 1-1 (cont.)

---

HEATING TO IGNITION	
Technique	ICRF
Mode	2nd harmonic D
Number of launchers	3 active, 1 spare
Frequency	76 MHz
Power ( $P_{rf}$ ) at start-up	50 MW
Power/area	$7 \text{ MW} \cdot \text{m}^{-2}$
Port size	$2.4 \text{ m}^2$
Pulse length for ignition	20 s
Pulse length capability	cw
CURRENT DRIVE	
Technique	LHRF
Mode	Slow wave
Number of launchers	1
Frequency	0.56 GHz
Power	10 MW
Power/area(launcher area)	$4.3 \text{ MW} \cdot \text{m}^{-2}$
(in wave guide)	$23.4 \text{ MW} \cdot \text{m}^{-2}$
Port size	$2.34 \text{ m}^2$
Pulse length for current drive	100 ~ 200 s
Pulse length capability	cw
START-UP ASSIST & CURRENT PROFILE CONTROL	
Technique	ECRF
Mode	1st harmonic, ordinary mode
Number of launchers	1
Frequency	140 GHz
Power	10 MW
Power/area (in waveguide)	$300 \text{ MW} \cdot \text{m}^{-2}$
Port size (plasma interface)	$1.3 \text{ m} \times 1.8 \text{ m}$

---

TABLE 1-1 (cont.)

---

Pulse length for start-up	10 s
Pulse length capability	cw

## IMPURITY AND PARTICLE CONTROL

Mode, impurity control	single-null, poloidal divertor
Mode, fuelling	Gas puffing, pellets

## FIRST WALL

	Continuous tritium recovery	Batch tritium Recovery
Material	SS	SS
Inboard thickness	~7 mm	7 mm
Outboard thickness	~6 mm	5 mm
Coolant	H <sub>2</sub> O	He
Maximum temperature of structure	350°C	400°C
Average neutron wall load	1.24 MW·m <sup>-2</sup>	1.24 MW·m <sup>-2</sup>
Design fluence, inboard <sup>n</sup>	3 MW·a·m <sup>-2</sup>	3 MW·a·m <sup>-2</sup>
Outboard <sup>n</sup>	3 MW·a·m <sup>-2</sup>	3 MW·a·m <sup>-2</sup>

## DIVERTOR PLATE

Surface material <sup>o</sup>	
lower plasma temperature plate	W(Mo alloy, Ta alloy)
medium plasma temperature at plate	Be(SiC, C)
Coolant	H <sub>2</sub> O
Coolant temperature(inlet/outlet)	50/100°C
Lifetime(50% availability)	≥1 a

## SHIELD

Inboard material	SS, H <sub>2</sub> O, borated steel(Pb)
Inboard thickness <sup>p</sup>	0.92 m
Outboard material	SS, H <sub>2</sub> O, borated steel, or B <sub>4</sub> C as alternative (Pb)

---

n Target: full lifetime.

o See design specification.

p Bulk shield thickness, including inboard gaps, dewars, insulation and 70 cm of actual shielding.

TABLE 1-1 (cont.)

---

Outboard thickness	1.05 m
Coolant	H <sub>2</sub> O
Maximum temperature of structure	≈100°C
Dose limit, 24 hours after shut-down <sup>q</sup>	2.5 mrem·h <sup>-1</sup>

## TEST FACILITIES

Type	Modules, segment channels
Location	Outboard
Required surface area	12 m <sup>2</sup>
Electricity production	5 ~ 10 MW

## TRITIUM FUELLING SYSTEM

Tritium flow rate	60 g·h <sup>-1</sup>
Consumption(at 25% availability)	6.5 kg·a <sup>-1</sup>
Tritium clean-up time	<3 d
Fractional burn-up	5 %
External tritium fuelling rate	$4.2 \times 10^{-21} \text{ s}^{-1}$

## TRITIUM-BREEDING BLANKET

	Continuous tritium recovery	Batch tritium recovery
Number of sectors	24	12
Position	outboard and top	Outbard and top
Neutron multiplier	Pb	Be pebble
Breeding material	Li <sub>2</sub> O pebble	Li <sub>2</sub> O pebble
Structural material	SS	SS
Coolant	H <sub>2</sub> O	He
Coolant temperature(inlet/outlet)	50/100°C	100/300°C
Thickness(including first wall)	50 cm	50 cm
Breeding ratio(objective)	>0.6	>0.6
Maximum temperature of structure	<150°C	<300°C

---

q On the outer surface of the bulk shield.

TABLE 1-1 (cont.)

Operating temperature of breeding material		
Maximum	1000°C	600°C
Minimum	400°C	100°C
Tritium purge gas	He	He
TRITIUM INVENTORY		
	Continuous tritium recovery	Batch tritium recovery
Tritium handling systems	0.4 kg	0.4 kg
Breeding blanket	0.5 ~ 1.0 kg	2.3 kg
First wall/divertor	0.1 ~ 1.0 kg	0.1 ~ 1.0 kg
Storage	2.3 kg	2.3 kg
Total	3.3 ~ 4.7 kg	5.1 ~ 6 kg
VACUUM SYSTEM		
Vacuum boundary material	SS	
Plasma chamber exhaust composition		
D-T in molecular form	94 %	
He	5 %	
Other	1 %	
Initial base pressure	$10^{-7}$ torr	
Pre-shot base pressure	$3 \times 10^{-5}$ torr	
Gas pressure(room temperature) in divertor chamber during burn	$1 \times 10^{-3}$ torr	
Pumping speed at entrance of divertor chamber pumping duct, for He and D-T, during burn	$<1 \times 10^5 \cdot s^{-1}$	
CRYOGENIC REQUIREMENTS		
Liquid He inventory	300 m <sup>3</sup>	
Liquid N <sub>2</sub> inventory	450 m <sup>3</sup>	
He liquefying requirement	1.5 m <sup>3</sup> ·h <sup>-1</sup>	

TABLE 1-1 (cont.)

---

He refrigeration heat	50 kW
N <sub>2</sub> refrigeration heat	1800 kW
POWER SUPPLY	
Stationary loads	200 MW
Energy storage	11.5 GJ

---

## 2. Physics basis

### 2.1 Reexaminations of INTOR parameters

INTOR is designed with the volume average beta value of 5.6 % which may be rather optimistic but seems to be necessary. Although systematic efforts to get high beta plasmas have been made in DIII[1], PDX[2], ISX[3] and so on, the volume average beta value of 4.5 % with 3.5 MW NBI heating power at  $B_T=6.2$  kG had been achieved at DIII experiment[4] so far. However, it is shown that there exists a universal operational boundary to the volume average beta value given by  $\beta_c(\%) = (3.0-3.5) I_p[\text{MA}] / a[\text{m}] B_T[\text{T}]$  from the data base of the present tokamak experiments. If this experimentally observed limit is decisive, the volume average beta for INTOR should be corrected to about 3.5 %. In this section, the reexaminations of INTOR reference parameters are discussed with the correction of the volume average beta.

#### 2.1.1 Basic models for selecting major parameters

##### Structural Restriction Condition

A major radius of tokamak devices are constrained to satisfy structural restriction which can be expressed as

$$R = r_v + r_c + a, \quad (1)$$

where, as shown in Fig. 2.1,  $r_v$  is the inner radius of solenoid coils which produce necessary volt-second and  $r_c$  is the structural space for poloidal and toroidal coils, shielding, vacuum chamber and support structure.

The radius of  $r_v$  is determined by the required volt-second for the full operation and the available maximum value of the poloidal magnetic field. The required volt-second  $\phi$  consists of the inductive part  $\phi_i$  and the resistive part  $\phi_r$ . The inductive flux is given as

$$\phi_i = L_p I_p = \mu_0 R \left( \ln \frac{8R}{a} + \frac{\ell_i}{2} - 2 \right) I_p, \quad (2)$$

where  $\ell_i$  is plasma inductance and  $I_p$  is plasma current. The plasma current is expressed by device parameters and safety factor  $q_\psi$ . Here, we use the following empirical expression to derive the plasma current,

$$q_\psi = q_a \left[ 1 + \frac{f_1(\gamma)}{\sqrt{A}} \right] \left[ 1 + \frac{\beta_p f_2(\gamma)}{A^{1.5}} \right], \quad (3)$$

$$q_a = \frac{2\pi}{\mu_0} \frac{a^2 B_T}{R I_p} \frac{1 + \kappa^2}{2}, \quad (4)$$

$$f_1(\gamma) = 0.16 + 0.633 \gamma,$$

$$f_2(\gamma) = 0.45 + \gamma,$$

where  $q_a$  is the safety factor by cylindrical approximation,  $\beta_p$  is the

poloidal beta,  $B_T$  the toroidal magnetic field at a magnetic axis. For the given maximum value of the toroidal magnetic field at conductor,  $B_{Tmax}$ ,  $B_T$  is expressed by

$$B_T = B_{Tmax} \{1 - (1 + \Delta/a)/A\} \quad , \quad (5)$$

where  $\Delta$  is the structural space between the inner ring of toroidal coil conductor and the plasma edge as discussed later.  $\kappa$ ,  $\gamma$  and  $A$  are the ellipticity, triangularity and aspect ratio, respectively.

On the other hand, the resistive part,  $\phi_r$ , can be divided into three phases, that is, the volt-second  $\phi_r^1$  for the break down phase,  $\phi_r^2$  for the Joule heating phase, and  $\phi_r^3$  for the burn phase.  $\phi_r^1$  may depend on  $R$  largely but it will vary with the start-up scenario. For INTOR start-up scenario,  $\phi_r^1$  is approximated as 10 V·s.  $\phi_r^2$  may be expressed as

$$\phi_r^2 = \int R I_p dt \sim 3.78 \times 10^{-6} \kappa^{\frac{1}{5}} a^{-\frac{4}{5}} R I_p^{\frac{4}{5}} \quad . \quad (6)$$

Here, we assume a typical start-up scenario of  $I_p=1$  MA/s and full bore start-up and Alcator/INTOR energy confinement scaling. The expression for  $\phi_r^3$  is given as

$$\phi_r^3 = \frac{2R}{\kappa a^2} \eta I_p t_f \sim 3.14 \times 10^{-9} \frac{R I_p}{\kappa a^2} t_f \quad , \quad (7)$$

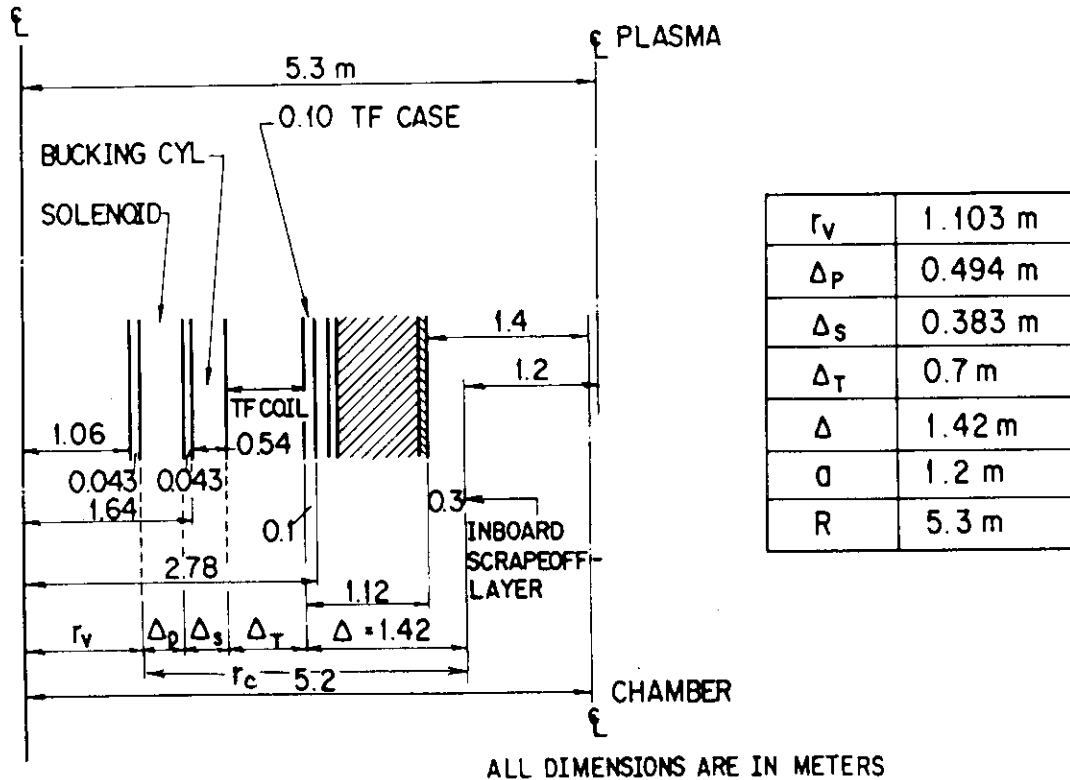


Fig. 2.1 INTOR radial build.



where  $\eta$  is the plasma resistivity and  $t_f$  the burn time. The necessary volt-second contributed by the inner most poloidal coils (OH coils) can be less than the sum of  $\phi_i$  and  $\phi_r$  since the equilibrium magnetic field coils can supply some fraction of the required volt-second. Approximating this contribution by the equilibrium vertical field  $B_v$ , it may be given as  $\pi B_v(R^2 - r_v^2)$ . However, it may greatly vary with the plasma equilibrium conditions. Here, we introduce the fraction  $f_\phi$  as a parameter and give the volt-second applied to the OH coils,  $\phi_{OH}$ , such as

$$\phi_{OH} = f_\phi \phi = f_\phi (\phi_i + \phi_r). \quad (8)$$

Given the maximum field of the OH coils as  $B_{pmax}$  and the thickness of the winding as  $\Delta_p$ , the radius  $r_v$  is evaluated by

$$2 \pi B_{pmax} (r_v^2 + r_v \Delta_p + \frac{\Delta_p^2}{3}) = \phi_{OH}. \quad (9)$$

The second and third terms of the left hand side are derived by assuming that the magnetic field decays linearly inside the conductor.

The structural space,  $r_c$ , is given as

$$r_c = \Delta_p + \Delta_s + \Delta_T + \Delta, \quad (10)$$

where  $\Delta_p$  and  $\Delta_T$  are the thickness of the OH coil and toroidal coil conductors respectively,  $\Delta_s$  is the space for the bucking cylinder, and  $\Delta$  is the space between the inner ring of toroidal coil conductor and plasma inner edge, as shown in Fig.2.1.  $\Delta_p$ ,  $\Delta_s$  and  $\Delta_T$  are determined by the coil design and is almost uniquely determined by the thickness of the shield for the coils.

### Self-ignition condition

The plasma and device parameters are obtained by solving the simplified power balance equation:

$$\frac{3}{2} knT \left( \frac{1}{\tau_{Ee}} + \frac{1}{\tau_{Ei}} \right) + P_{br} + P_{sy} = \frac{1}{4} n^2 \langle \sigma v \rangle E_\alpha f_r \left( 1 + \frac{5}{Q} \right), \quad (11)$$

where  $\tau_{Ee}$  and  $\tau_{Ei}$  are electron and ion energy confinement times.  $P_{br}$  and  $P_{sy}$  are the bremsstrahlung and synchrotron radiation power losses given as

$$P_{br} = 1.41 \times 10^{-38} Z_{eff} n_e^2 T_e^{1/2} \quad (12)$$

and

$$P_{sy} = 6.38 \times 10^{-16} B_T^{2.5} T_e^2 \left( \frac{n_e}{aA} \right)^{1/2}. \quad (13)$$

$E_\alpha$  and  $\langle \sigma v \rangle$  are alpha particle energy produced by DT fusion reaction and its reaction rate, respectively.  $f_r$  is the numerical fraction, which represents the effect of density and temperature profiles on fusion power production.  $Q$  is the energy multiplication factor defined by  $Q = P_{fusion}/P_{in}$  where  $P_{in}$  is the external heating power.

The empirical Alcator scaling law is used for the electron confinement time and the neoclassical scaling law for the ion confinement time. The numerical coefficient of these scaling laws are introduced as a parameter to represent the ambiguity of the scaling law;

$$\tau_{Ee} = C_E \times 1.1 \times 10^{-20} n a^2 \quad (14)$$

$$\tau_{Ei} = C_E \times 4.7 \times 10^{18} \frac{B_T^2 T_i^{0.5} a^2}{n q_\psi^2 A^{1.5}} \quad (15)$$

It is noted that the coefficients with  $C_E=1$  satisfy experimental results in JFT-2 and JFT-2a.

Representing the plasma density by the definition of the volume average beta with the fuel fraction of beta,  $f_\beta$ , which is defined as  $f_\beta = \beta_{\text{fuel}}/\beta$ , we can rewrite the energy balance equation (11),

$$\begin{aligned} & 5.145 \times 10^{-25} \frac{A^{1.5} T^{0.5} q_\psi^2}{C_E B_T^2 a^2} + 1.41 \times 10^{-34} \frac{T^2}{C_E f_\beta^2 \beta^2 B_T^4 a^2} \\ & + 4.61 \times 10^{-39} \frac{T^{2.5}}{(f_\beta \beta)^{1.5} B_T^{0.5} a^{0.5} A} + 1.42 \times 10^{-25} T^{0.5} \\ & = 1.44 f_r \left(1 + \frac{5}{Q}\right) \langle \sigma v \rangle \quad (16) \end{aligned}$$

From the present experimental results, it has been proposed that there is a universal operational boundary to volume averaged beta given by  $\beta_c = (3.0-3.5) \times 10^{-8} I_p / a B_T$ . We introduce the coefficient  $C_\beta$  as a parameter on the beta scaling such as

$$\beta = C_\beta \times 3.3 \times 10^{-8} \frac{I_p}{a B_T}, \quad (17)$$

where  $C_\beta=1$  represents the marginal beta within the operational boundary. By changing the parameter  $C_\beta$  along with  $C_E$ , the energy balance are checked and the plasma parameters for INTOR are reexamined.

#### Determination of numerical fractions and coefficients for the reference design of INTOR

The radial build of INTOR reference design is shown in Fig.2.1. The plasma major radius is 5.3 m and the plasma minor radius is 1.2 m. The thickness of the solenoid coils and TF coils are  $\Delta_p=0.494$  m and  $\Delta_T=0.70$  m, respectively. The space between them is also given as  $\Delta_s=0.383$  m, and  $\Delta=1.42$  m. The sum of these values, that is,  $r_c = \Delta_p + \Delta_s + \Delta_T + \Delta$  is fixed constant in this parameter study.

According to the reference operation scenario, the plasma is started up

with ohmic heating under an assist of ECRF pre-heating and ICRF heating during 11 seconds and the burn time is at most 200 seconds. In the burn phase, the plasma current is 6.4 MA and the plasma temperature is 10 keV. It is shut down for the following 11 seconds. The required volt-second for the full operation is designed to 110 V.s. To evaluate  $r_V$ , we set  $B_{Tmax}=10.68$  T (the peaked field is 12 T),  $B_{pmax}=7.27$  T (the peaked field is 8 T) and the burn time is 200 sec. The ellipticity is 1.6 and the triangularity is 0.3. The safety factor by cylindrical approximation,  $q_a$ , is 2.1. From the radial build as shown in Fig.2.1,  $r_V$  is 1.103 m. Substituting  $B_{pmax}$  and  $r_V$  into Eq.(9), we obtain  $\phi_{OH}=85.0$  V.s. The fraction,  $f_\phi$ , is therefore  $85.0/110.0 = 0.77$  and this value is fixed in the following.

The total toroidal beta for the INTOR is 5.6 %. On the other hand, using the reference parameters of  $I_p=6.4$  MA,  $B_T=5.4$  T,  $a=1.2$  m, the critical beta  $\beta_C$  [ $\beta_C=3.5I_p(\text{MA})/a(\text{m})B_T(\text{T})$ ] is given to 3.46 %. In this sense, the coefficient  $C_\beta$  of Eq.(17) is 1.72 for the present design. Also, another two parameters such as the numerical fraction of the profiles  $f_r$  and the fuel fraction of beta  $f_\beta$  are estimated as  $f_r=1.712$  and  $f_\beta=0.691$ . Substituting these parameters and  $Q=\infty$  into Eq.(16), one can obtain the R-a diagram which satisfies the self-ignition condition. The coefficient  $C_E$  of the energy confinement scaling is finally determined in such a way that the device size of  $R=5.3$  m and  $a=1.2$  m can satisfy the self-ignition condition and one can find  $C_E=0.769$ .

In summary, the present INTOR reference parameters can be obtained with the following conditions as shown in Table 2.1

Table 2.1 Fractions and coefficients for INTOR reference design.

Fraction or Coefficient	Value
$f_\phi = \frac{\text{volt-sec produced by OH coils}}{\text{required volt-sec.}}$	0.772
$f_r$ : (numerical fraction of the pressure and temperature profiles)	1.712
$f_\beta = \frac{\text{DT fuel beta}}{\text{total beta}} = \frac{\beta_{\text{fuel}}}{\beta}$	0.691
$C_\beta$ : (coefficient for beta scaling)	1.7166
$C_E$ = (coefficient for energy confinement)	0.769

### 2.1.2 Toroidal beta correction without changing plasma current, minor and major radii

#### Parameter survey

There are many plasma and device parameters to be varied in determining the device size. To realize the trend how these parameters affect device size, parameter survey is carried out on the basis of the reference parameters. The results are shown in Fig.2.2. The increase of the elongation reduces the plasma minor radius but not major radius. The decrease of the safety factor reduces both of the plasma minor and major radii. The reduction of the shield width or increase of the maximum poloidal field reduces the plasma major radius mainly. The dependence of the device size on  $C_E$  and  $C_\beta$  are almost the same. As  $C_E$  or  $C_\beta$  increases, the device size is reduced both in minor and major radii and vice versa.

#### Toroidal beta correction

Figure 2.3 shows  $\beta - \beta_c$  diagram, where  $\beta_c = 3.5 I_p(\text{MA}) / a(\text{m}) B_T(\text{T})$  is the experimental beta limit. The present toroidal beta is higher than this limit by a factor of 1.7. To reduce the present toroidal beta below the limit without changing the plasma major and minor radii,  $P_0$  must move to  $P_0^1$  as shown in Fig.2.3. If the coefficient  $C_E$  is kept constant at 0.769 and  $C_\beta$  is reduced from 1.72 to 1.0,  $P_0$  will move to  $P^1$  where beta satisfies the  $\beta_c$  limit but the plasma major and minor radii are changed. Hence, to recover the original plasma major and minor radii, the energy confinement or some other parameters have to be improved. Fig.2.4 shows equi- $C_\beta$  lines and equi- $C_E$  lines, which satisfy the self-ignition condition, on the  $\beta - \beta_c$  space. With keeping the same plasma size, the energy confinement time must be improved more than two times when  $C_\beta$  is decreased from 1.72 to 1.0 and the toroidal beta is reduced to about 3.2 %. It is noted that, if we allow some improvement of beta limitation, e.g.  $C_\beta \sim 1.3$ , then it is enough to increase the energy confinement coefficient  $C_E$  to 1.05.

In Fig.2.5, we show the effect of the fuel fraction of beta  $f_\beta$ . Figure 2.5(a) shows the case of the reference design, that is,  $f_\beta = 0.691 (=1/1.45)$ . The results has already been discussed above. If  $f_\beta$  is improved to 0.769 ( $=1/1.3$ ), the toroidal beta of 4.90 % can ignite the plasma with same plasma parameters and with same value of  $C_E$ . As a result, the improvement of  $C_E$  will be needed from 0.769 only to 1.32. Similarly, when  $f_\beta = 0.833 (=1/1.2)$ , beta should be 4.48 % and the required improvement of  $C_E$  should be from 0.769 to only 1.05 as shown in Fig.2.5(c).

If one allows to change another parameters such as the elongation, safety factor, shield width and so on but keeping the same plasma major and minor radii, there may exist several methods to reduce beta below  $\beta_c$ . Figure 2.5(d) shows one of the examples. Here, the elongation changes 1.6 to 1.7, the safety factor changes 1.74 to 2.60 and the shield width reduces from 1.42 to 1.30 as well as  $C_E$  improves 0.769 to 1.10. In Fig.2.6, these path of  $P_0 \rightarrow P^N \rightarrow P_0^N$  ( $N=1,2,3,4$ ) is shown on the  $R$ - $a$  plane, and final plasma parameters at  $P_0^N$  ( $N=0,1,2,3,4$ ) are listed on Table 2.2.

#### Other energy confinement scaling

Although the Alcator scaling law is used for the INTOR reference design,

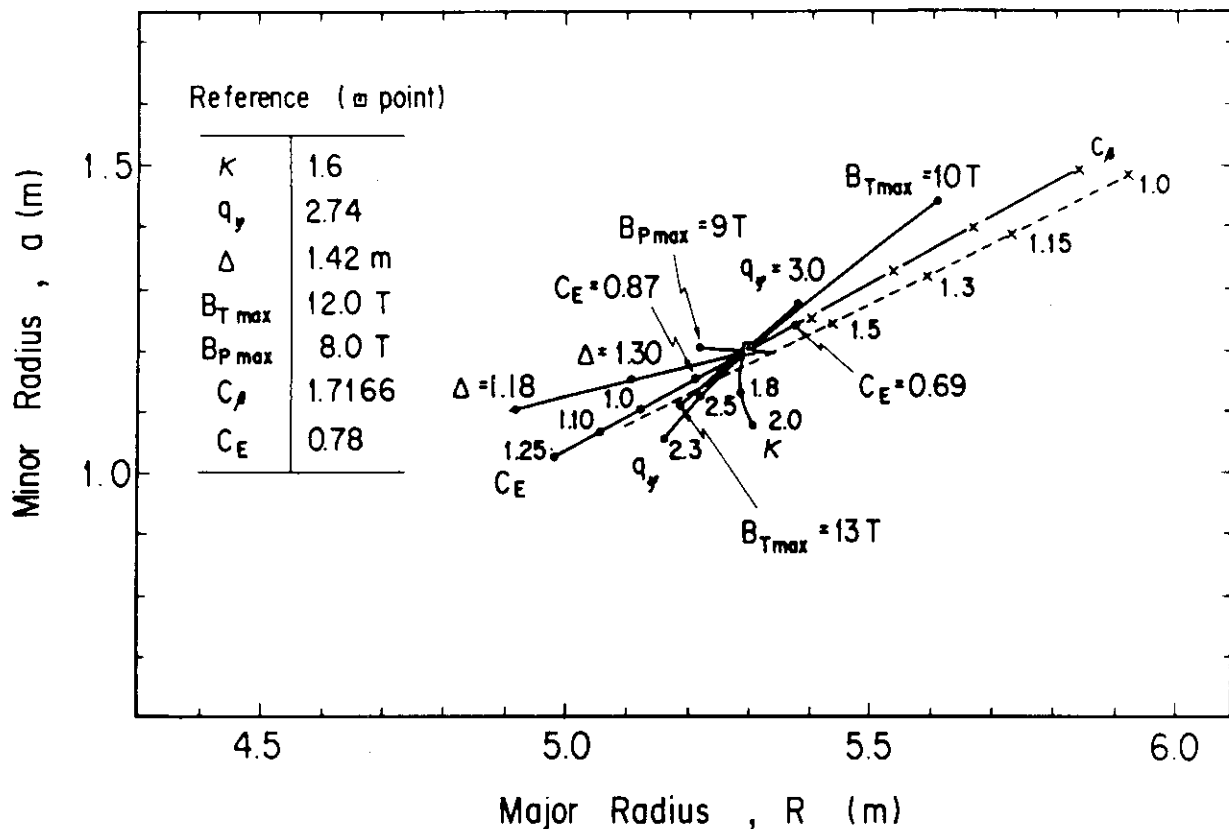


Fig. 2.2 The trend of plasma size by changing various parameters on the basis of INTOR reference.

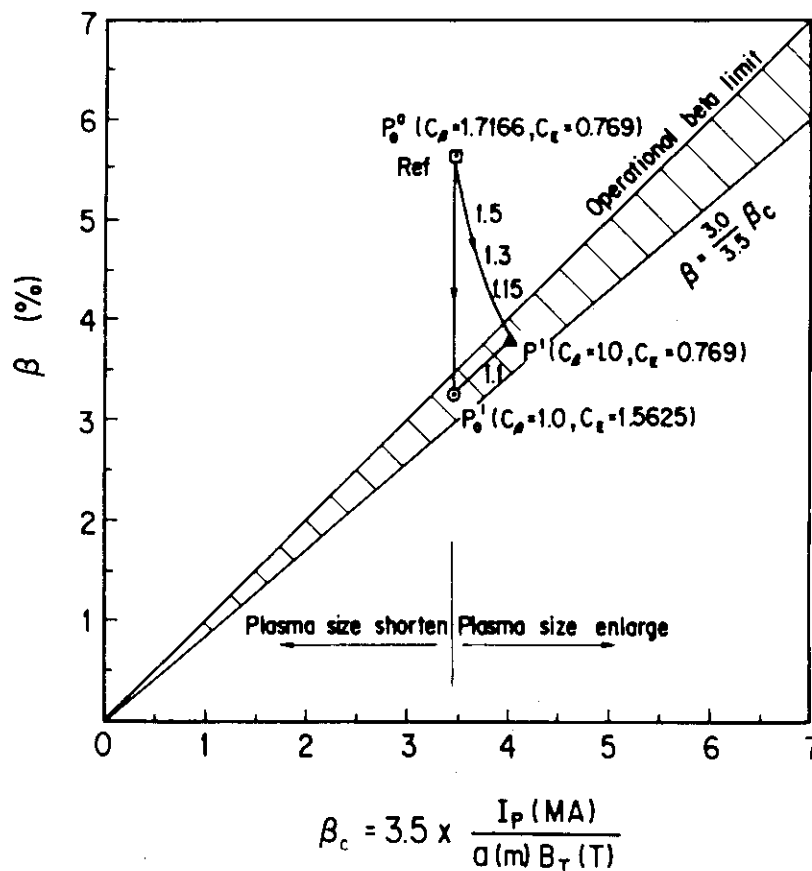


Fig. 2.3 The volume average toroidal beta versus the critical beta limit.

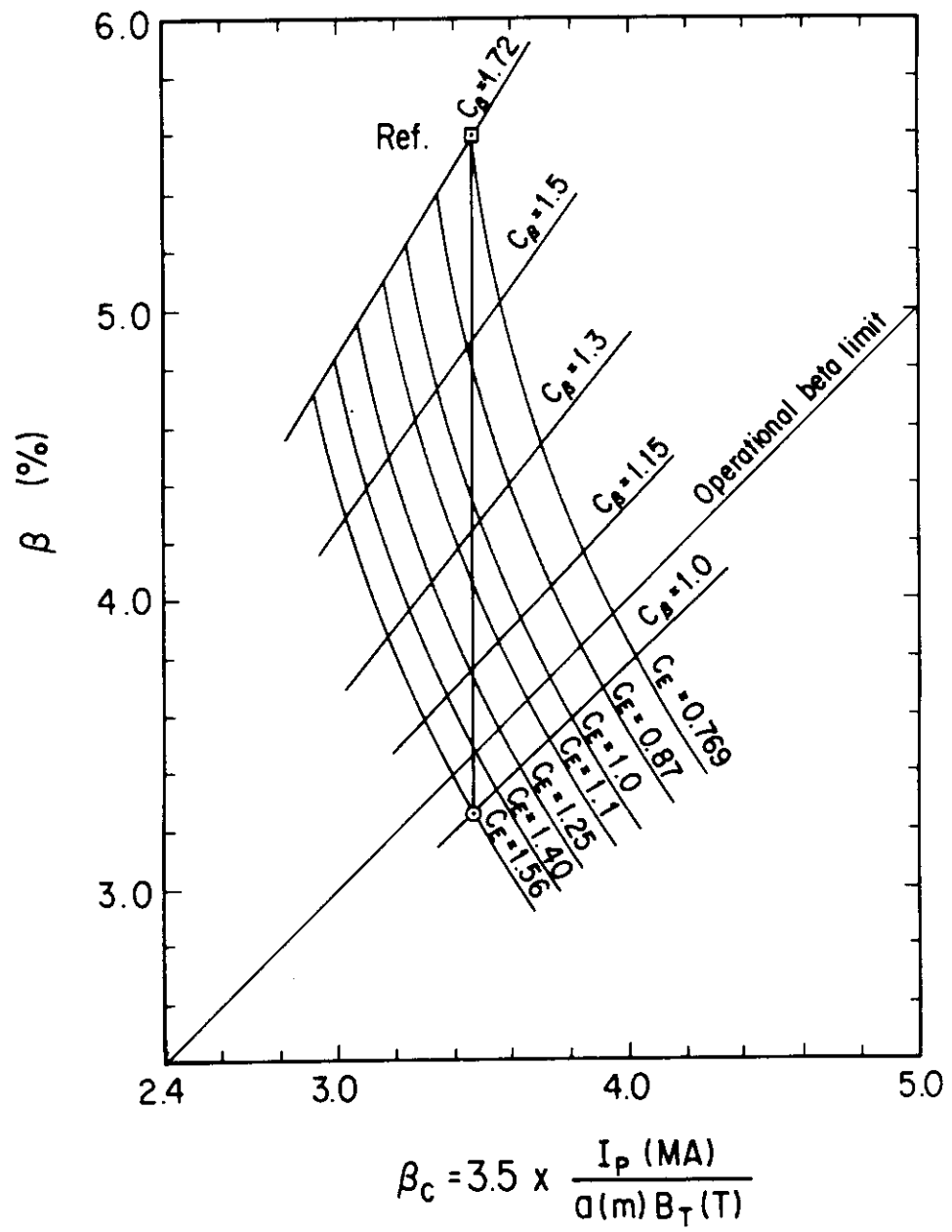


Fig. 2.4 Equi- $C_\beta$  lines and equi- $C_E$  lines on the  $\beta - \beta_c$  plane.

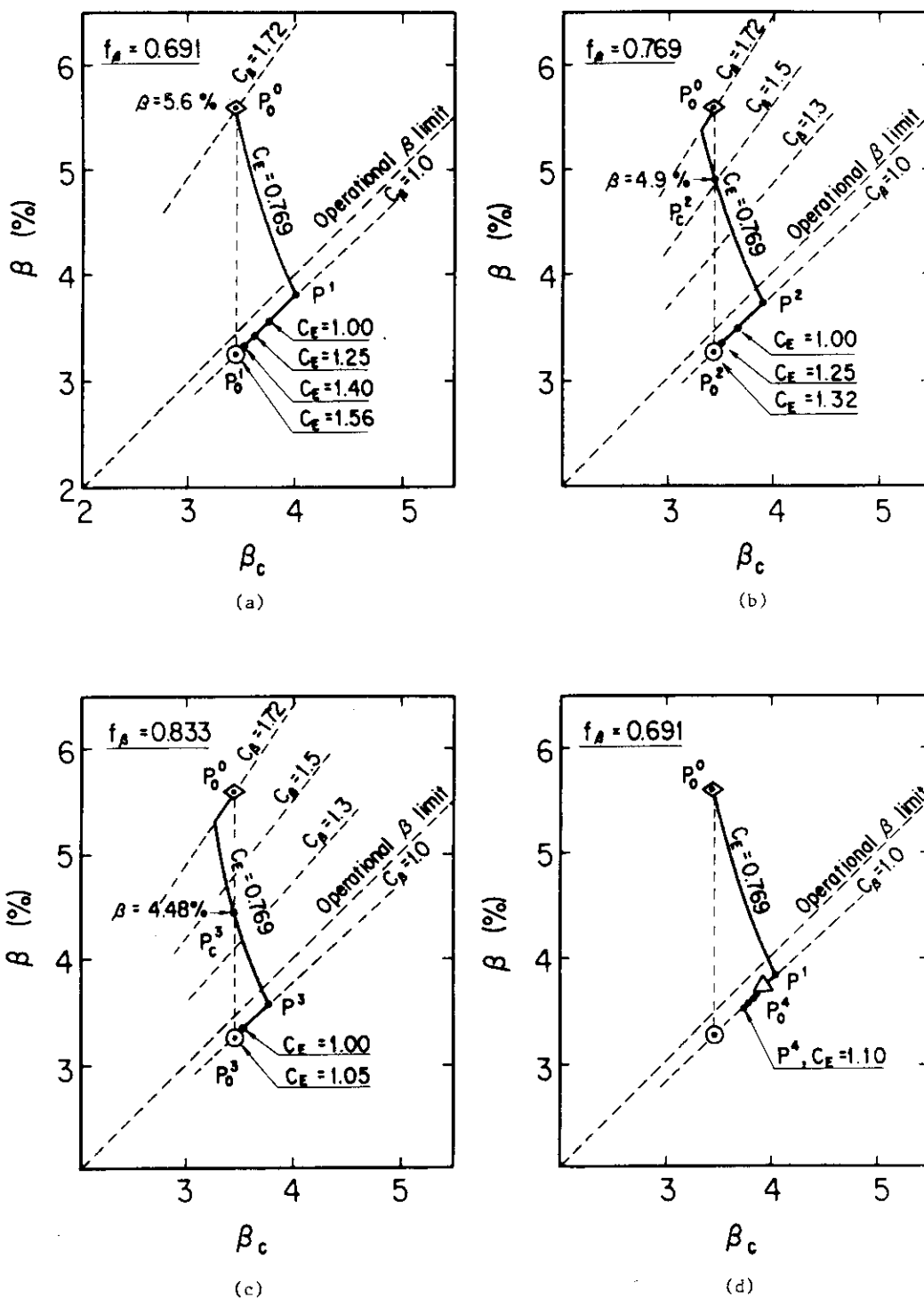


Fig. 2.5 Paths for R during the beta value of 5.6 % to comfortable beta value.

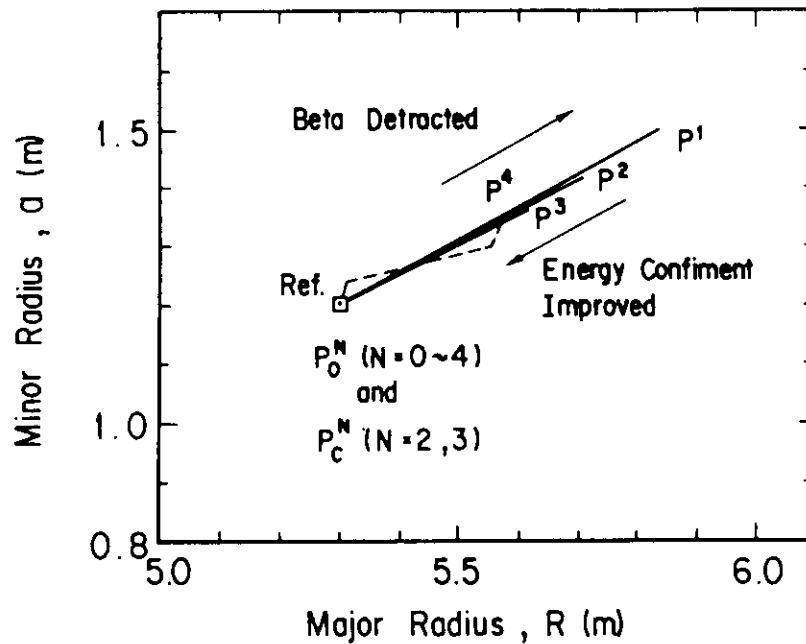


Fig. 2.6 Plasma major and minor radii at the conditions  $P^N$  and  $P_0^0$  in Fig. 2.5.

Table 2.2 List of plasma parameters with reduction of beta values without changing plasma minor and major radii, and plasma current.

	I	$P_0^0$	$P_0^1$	$P_0^2$	$P_0^3$	$P_0^{4*}$	$P_c^2$	$P_c^3$
R (m)	5.3	5.29	5.30	5.30	5.30	5.29	5.31	5.30
a (m)	1.2	1.20	1.20	1.20	1.20	1.20	1.21	1.20
$B_T$ (T)	5.4	5.40	5.40	5.40	5.40	5.60	5.40	5.40
$I_p$ (MA)	6.4	6.36	6.38	6.38	6.38	7.52	6.46	6.38
$\beta_c$	3.46	3.44	3.45	3.45	3.45	3.91	3.47	3.44
$\beta$ (%)	5.6	5.57	3.25	3.25	3.25	3.69	4.90	4.48
$P_{out}$ (MW)	620	610	209	259	304	333	597	594
$P_{wall}$ (MW/m <sup>2</sup> )	1.3	1.23	0.42	0.52	0.61	0.64	1.19	1.18
$n$ ( $10^{20}$ m <sup>-3</sup> )	1.4	1.39	0.81	0.90	0.98	1.00	1.36	1.35
$f_p$	—	0.691	0.691	0.769	0.833	0.691	0.769	0.833
$C_p$	—	1.7166	1.00	1.00	1.00	1.0	1.50	1.38
$C_E$	—	0.769	1.569	1.32	1.05	1.10	0.769	0.769

\*  $x=1.7$ ,  $q_p=2.60$ ,  $\Delta=1.30$  m



the energy confinement law in tokamaks is a very controversial issue. The interpretation of the experimental observations, in particular with intense neutral beam heating, has not yet converged to a generally accepted picture by now. We introduce other well-established scaling laws and discuss only the results in our studies.

For an Ohmically heated, low beta tokamak, the confinement time is well described by the scaling proportional to density like the Alcator scaling. Recent experimental results presented from Alcator-C, TFTR[5] et al. show that the electron confinement is rather consistent with so-called neo-Alcator energy confinement scaling:

$$\tau_{Ee} = C_E \times 1.15 \times 10^{-21} \bar{n}_e R^{2.3} a^{0.8} \quad (18)$$

On the other hand, the data base analysis on ISX-B[6] showed that energy confinement correlates with plasma current and not at all with plasma density. One of the simplest form for representing this current dependence is the Mirnov scaling law given as

$$\tau_{Ee} = C_E \times 0.145 \times 10^{-6} a I_p \quad (19)$$

We analyze the self-ignition conditions for each scaling law replacing Eq.(14) by Eq.(18) or (19). All of fractions and coefficients except  $C_E$  shown in Table 2.1 are the same while  $C_E=1.0$ . The neo-Alcator scaling law allows us that, if the present level of volume averaged toroidal beta,  $C_\beta=1.72$ , could be kept, the plasma size will be made much smaller than that of the reference, as shown in Fig 2.7. Even the beta reduces to the present experimental limit by taking  $C_\beta=1.0$  and the energy confinement keeps the same, the plasma major and minor radii are 4.93 m and 1.00 m, respectively. Furthermore, if the reference plasma size is held unchanged, the coefficient of the neo-Alcator scaling allows a margin of 1.74 on the energy confinement for ignition even for beta of 3.25 % with  $C_\beta=1$ .

Keeping the fractions except  $C_E$  unchanged in Table 2.1, the plasma and device parameters which satisfy the self-ignition condition with the Mirnov scaling with  $C_E=1$  is fairly similar to those with the Alcator scaling as shown in Fig.2.8 and Table 2.3. However, when the volume average beta reduces below 3.25 % by taking  $C_\beta=1.0$ , the increase of the plasma size with the Mirnov scaling law is less than that with the Alcator scaling law. As noted in Eq.(19), the Mirnov scaling law does not correlate with the plasma density, so that the electron energy confinement with the Mirnov scaling law is little affected by the density as well as the beta. Necessary improvement on the energy confinement is, then, 1.76 compared with 2.05 for the Alcator scaling. Hence, the Mirnov scaling may have a little advantage for the requirement of the energy confinement when the volume average beta is reduced but plasma size is held.

#### Conclusive remarks

The volume average toroidal beta of the INTOR reference is considerably higher than the experimentally observed beta limit. The beta correction is recommended. With the same fuel fraction of beta as the reference, the energy confinement has to be improved more than two times if the beta reduces from

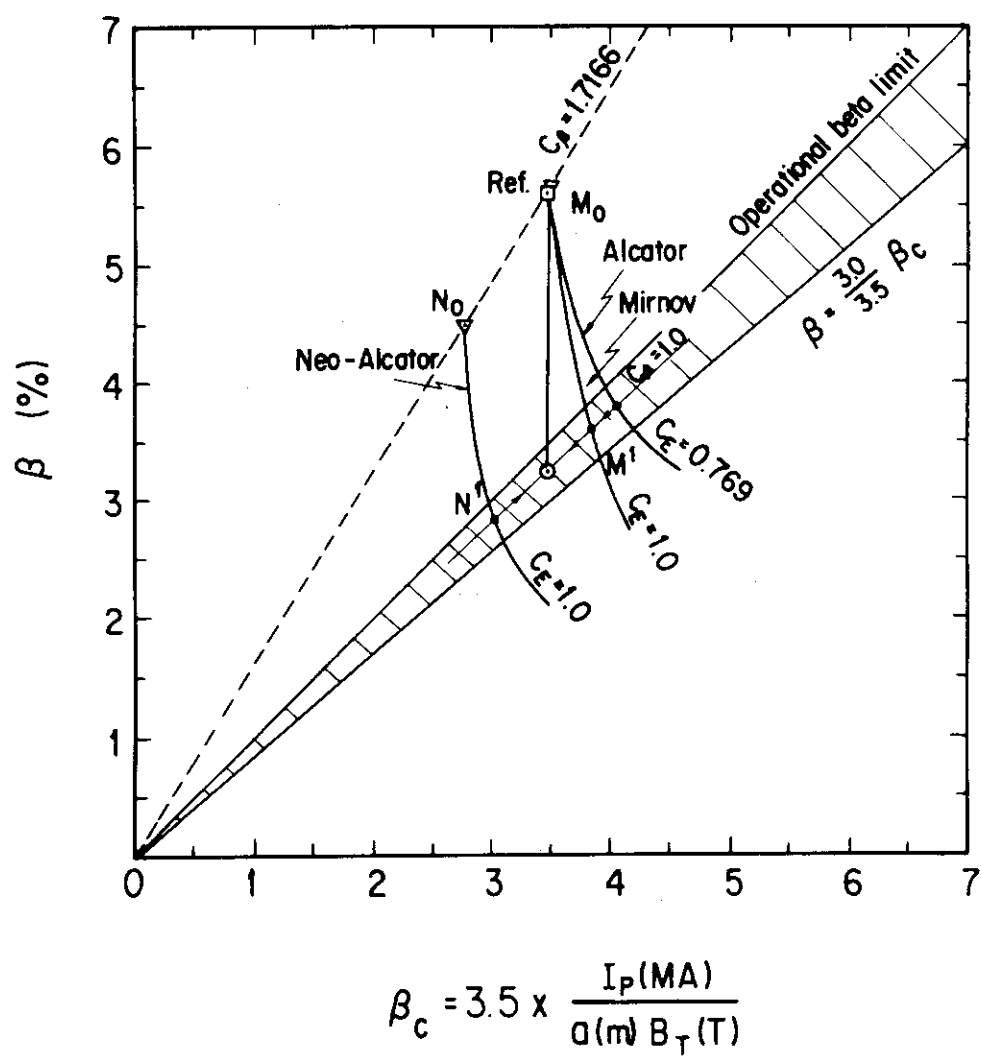


Fig. 2.7  $\beta - \beta_c$  diagram with different energy confinement scaling laws.

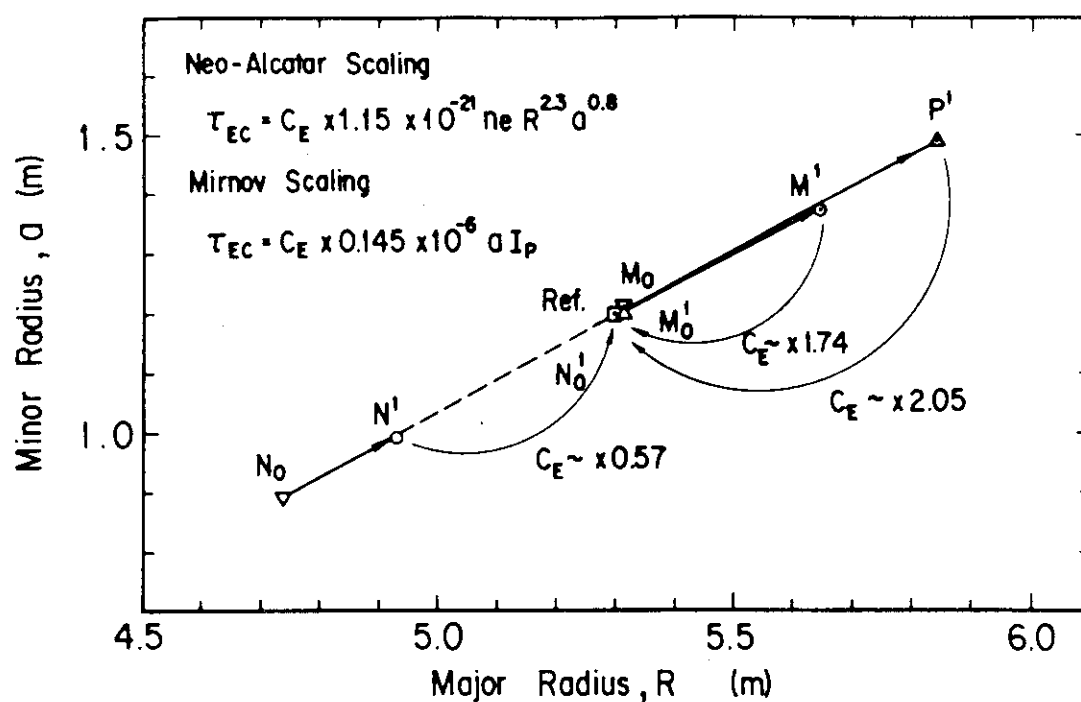


Fig. 2.8 R-a Diagram satisfying self-ignition condition with neo-Alcator and Mirnov scalings.

Table 2.3 List of plasma parameters with various scalings.

	Ref.	$N_0$	$N'$	$M_0$	$M'$	$N'_0$	$M'_0$
$R$ (m)	5.3	4.74	4.93	5.32	5.64	5.30	5.30
$a$ (m)	1.2	0.89	1.00	1.21	1.38	1.20	1.20
$B_T$ (T)	5.4	5.47	5.44	5.40	5.38	5.39	5.40
$I_P$ (MA)	6.4	3.83	4.64	6.48	8.11	6.38	6.41
$\beta_c$	3.46	2.74	2.99	3.47	3.82	3.46	3.46
$\beta$ (%)	5.6	4.44	2.82	5.62	3.60	3.23	3.23
$P_{out}$ (MW)	620	203	104	636	356	204	210
$P_{wall}$ (MW/m <sup>2</sup> )	1.3	0.58	0.26	1.27	0.60	0.42	0.42
$n$ ( $\times 10^{20}$ m <sup>-3</sup> )	1.4	1.14	0.72	1.40	0.89	0.82	0.81
$C_\beta$	—	1.7166	1.00	1.7166	1.00	1.00	1.00
$C_E$	—	1.00	1.00	1.00	1.00	0.57	1.74

$$f_p = 0.691$$

5.6 % to 3.25 %. The energy confinement time of the reference design is 1.4 sec and that of our calculation based on the fractions shown in Table 2.1 is 1.69 sec. Hence, the energy confinement time become 3.46 sec, when beta is reduced to 3.25 %, which is a little risky. If the additional beta is improved up to 1/1.2, the required energy confinement time is 2.33 sec even in the beta of 3.25 %. If the beta of 4.48 % being the case of  $C\beta = 1.38$  and the additional beta of 1/1.2 can be achieved, the energy confinement time of 1.69 sec is enough for the self-ignition, and the plasma parameters in these cases are shown in Table 2.2. If we cannot improve neither of energy confinement nor fuel fraction of beta, but have to reduce confinement pressure, plasma major and minor radii should be increased to a reasonable size.

#### References for subsection 2.1

- [1] (a) M. Nagami, et al., in Plasma Physics and Controlled Nuclear Fusion Research (Proc. 9th Int. Conf. Baltimore, 1982) Vol. 1, IAEA, Vienna (1983) 27. (b) M. Nagami, et al., Nuclear Fusion, Vol. 24 (1984) 183.
- [2] D. Johnson, et al., in Plasma Physics and Controlled Nuclear Fusion research (Proc. 9th Int. Conf. Baltimore, 1982) Vol. 1, IAEA, Vienna (1983) 9.
- [3] M. Murakami, et al., in Plasma Physics and Controlled Nuclear Fusion Research (Proc. 9th Int. Conf. Baltimore, 1982) Vol. 1, IAEA, Vienna (1983) 57.
- [4] K. H. Burrell, et al., Nuclear Fusion 23 (1983) 536.
- [5] (a) B. C. Blackwell, et al., in Plasma Physics and Controlled Nuclear Fusion Research (9th Int. Conf. Baltimore, 1982) Vol. 1, IAEA, Vienna (1983). (b) R. J. Hawryluk et al., PPPL-2108.
- [6] (a) D. W. Swain and G. H. Neilson Nuclear Fusion 22 (1982) 1015. (b) G. H. Neilson, et al., Nuclear Fusion 23 (1983) 285.

## 2.2 Improvement in beta value with increasing plasma current and reducing plasma major radius

Two main goals were proposed in the INTOR workshop to try to reduce the excess of the total beta value over the critical beta limit predicted from the empirical scaling law. One is the reduction of the plasma radius, and the other is the increase of the plasma current, based on the empirical beta limit scaling obtained from experimental and theoretical studies (see Chapter VIII, Physics). As a tentative goal of the plasma current, 8 MA is specified. The potential reduction of the reactor size can be attained with reducing the spaces of some components in the torus inboard, which will be realized with more advanced engineering concepts. The reduction of the width of the shielding blanket is one of the possible candidates, and the enhance of the maximum poloidal field is another candidate, and the other is the increase of toroidal and poloidal coil current densities.

Main plasma parameters are obtained from the numerical code mentioned in the previous section, which consist of the simplified power balance of plasmas and engineering restriction of the reactor structure. An average ion temperature is kept to be 10 keV, at which the beta value takes nearly its minimum value. The plasma minor radius is also tried to keep the present design value of 1.2 m. The flux supplied by ohmic heating coils also retains the present value. The required increased volt-second due to the enhanced plasma current, which is inconsistent with the retaining volt-second, is resolved by incorporating the non-inductive current ramp-up and transformer recharge with LH waves at low densities in the operation scenario.

The reduction of the plasma major radius have been achieved by the following potential engineering improvements. The first is the reduction of the inboard by 10 cm shield, which is described in the section 13, Optimization of the inboard shield. The second is the increment of the maximum experience field of poloidal field coils, which use Nb<sub>3</sub>Sn instead of NbTi. The last improvement is to increase of the current densities of toroidal (30 A/mm<sup>2</sup>) and poloidal (25 A/mm<sup>2</sup>) field coils. The last two items are discussed in the section 8, Magnets. Those engineering improvements make the reduction of 0.3 m in the major radius feasible.

The reduction of the excess of the average total beta value (5.6 %) beyond the critical beta limit (3.4 %) predicted by the empirical scaling ( $3.5I_p[\text{MA}]/a[\text{m}]B_T[\text{T}]$ ) is accomplished by the following two considerations. The one is the increase of the plasma current, from 6.4 MA to 7.5 MA and the reduction of the plasma major radius, from 5.3 m to 5.0 m, which raises the beta limit (4.4 %) predicted by the empirical scaling. The other is the reduction of the additional beta value, which should be provided for impurities, high energy components, and helium ions, in addition to the beta value due to fuel DT ions. The additional beta value is chosen to be 30% of the DT fuel beta value (4.58 %). Then the total beta value amounts to 5.92 %, which increases from the reference value of 5.6 %.

Taking account of the above considerations, the simple plasma analysis numerical code yields the main plasma parameters, as shown in Table 2.4. The plasma current is selected to be 7.5 MA instead of 8 MA, the target value. The reason of this selection is partly because 8 MA, corresponding to 1.6 of the safety factor without a toroidal effect, is considered somewhat large, and partly because the large plasma current requires the large poloidal coil

currents, in particular near the divertor region, which is discussed in the section 6, Optimization of the burn time. 7.5 MA of the plasma current corresponds to 1.7 of the safety factor, taking account of elongation. The safety factor of 7.5 MA could be over 2, when the toroidal effects is included. The total beta value increases up to 5.92% from 5.6%. The critical beta limit predicted by the empirical scaling also increases due to the enhanced plasma current. Then, ratio of the total beta value to the critical one is reduced to 1.34 from 1.62. The excess of the total beta value beyond the critical one is also reduced to 1.35% from 2.14%. Those reduction is partly due to the increased plasma current, and partly due to the reduced additional beta value to the fuel DT beta value.

In the above study on specifying the major parameters, the self-ignition is evaluated with an assumption that the electron power loss follows the modified INTOR/Alcator scaling law, in which the numerical coefficient is changed so that the scaling can reproduce experimental results of JFT-2 and DIVA tokamaks. The energy confinement scaling, however, is significantly controvercial at present, and no definite scaling can be specified. As for as the energy confinement performance is concerned, it is informative to evaluate the confinement performance with an ignition margin, the ratio of alpha heating power to plasma power loss due to transport, based on various proposed scaling. The evaluation of the confinement performance is shown in Table 2.5.

Table 2.4 Modified main plasma parameters

Plasma major radius, $R_p$ (m)	5.0
Plasma radius, $a$ (m)/ $b$ (m)	1.2/1.92
Aspect ratio, $A$	4.167
Elongation, $K$	1.6
Triangularity, $\delta$	> 0.2
Average ion temperature, $\langle T_i \rangle$ (keV)	10
Average ion density, $\langle n_i \rangle$ ( $10^{20} \text{ m}^{-3}$ )	1.4
Total beta, $\beta_t$ (%)	5.92
Fuel beta, $\beta_f$ (%)	4.57
Plasma current, $I_p$ (MA)	7.5
Safety factor, $q_I$	1.7
Toroidal field, $B_T$ (T)	4.96
Thermonuclear power, $P_{th}$ (MW)	580
Neutron wall load, $P_n$ (MW/m <sup>2</sup> )	1.24

Table 2.5 Summary of energy confinement time scaling laws

$$\tau_E = C B^{\alpha_B} P^{\alpha_P} I^{\alpha_I} n_e^{\alpha_n} T^{\alpha_T} K^{\alpha_K} a^{\alpha_a} R^{\alpha_R} q^{\alpha_q} M^{\alpha_M}$$

(in s, T, MW, MA, keV,  $10^{20} \text{ m}^{-3}$ , m)

Scaling	C	$\alpha_B$	$\alpha_P$	$\alpha_I$	$\alpha_n$	$\alpha_T$	$\alpha_K$	$\alpha_a$	$\alpha_R$	$\alpha_q$	$\alpha_M$	$\tau_E$ (INTOR)*	I**
INTOR	0.5				1.0			2.0				(1.4)	1.5
T-II (OH)	0.023	-0.33			1.0			0.21	2.63	1.17	0.42	(5.0)	5.2
Neo-Alc	0.071				1.0			1.0	2.0	0.5	0.5	(8.3)	8.7
Goldston	0.033		-0.5	1.0			0.5	-0.37	1.75		0.5	0.7	0.7
Kaye	0.055	-0.09	-0.58	1.24	0.26		0.28	-0.49	1.65		0.5	1.0	1.0
ASDEX-L	0.033	-0.11	-0.33	1.0	-0.11		0.5	-0.22	1.11		0.33	0.4	0.4
CTT	0.12		-0.72	1.44	0.28			-0.16	1.44		0.5	1.3	1.4
Perkins	0.13	-0.1	-0.6	0.9	0.6			0.4	1.7		0.5	1.5	1.6
T-11 (T-10)	0.014				1.0	-0.5		0.25	2.75	1.0	0.5	2.0	2.1
PDX-L	0.016			1.0			0.5	-0.37	1.75		0.5	3.8	4.0
Mod. GMS	0.39			1.0				1.0			0.5	5.5	5.7
ASDEX-H	0.065			1.0					1.0		0.5	3.9	4.1
* INTOR	B	$P_a$	$I_p$	$\bar{n}_e$	T	K	a	R	$q_I$	$M_I$	$\tau_E$		
Parameters:	4.96	116	7.5	1.9	10	1.6	1.2	5.0	1.7	2.5	(1.4)		

\*\* Ignition margin,  $I = P / P_{\text{loss}}$ ,  $P_{\text{loss}} = 3\bar{n}_e T (1 + n_{DT}/\bar{n}_e) / 2\tau_E$

### 2.3 Additional non-DT contributions to fuel DT beta value

The total average beta value (5.6 %) of the present INTOR design somewhat beyond the critical beta limit (3.46 %) predicted from the empirical beta scaling. Narrowing the gap between the design value and the predicted limit of beta values are tried in the previous sections. One way for narrowing is changing the plasma parameters, i.e. increasing the plasma current to 7.5 MA from 6.4 MA, and reducing the major radius to 5.0 m from 5.3 m. Another way is the reduction in non-DT contributions in addition to fuel DT beta value, that are from impurities, thermal alpha particles, energetic alpha particles, and energetic ions generated during heating to ignition. The present additional beta is allotted by 45 % of the average beta value (4.57 %) for thermal DT ions and associated electrons. Here, the additional beta is reconsidered.

Assuming that impurities have same temperatures and profiles of DT ions and electrons, and that impurities are fully ionized, the beta contribution from the impurities is

$$\beta_{\text{imp}} = \frac{Z_k + 1}{2Z_k} \frac{Z_{\text{eff}} - 1}{Z_k - Z_{\text{eff}}} \beta_{\text{DT}}.$$

As helium ions have small contribution to the effective ionic charge, they are neglected in evaluating beta contribution as impurities. Their contribution to beta is independently evaluated later. For oxygen impurities, this yields

$$\beta_{\text{imp}} = \begin{cases} 0.094 \beta_{\text{DT}} & (Z_{\text{eff}}=2.0) \\ 0.043 \beta_{\text{DT}} & (Z_{\text{eff}}=1.5) \end{cases}.$$

For carbon impurities, this also yields

$$\beta_{\text{imp}} = \begin{cases} 0.135 \beta_{\text{DT}} & (Z_{\text{eff}}=2.0) \\ 0.065 \beta_{\text{DT}} & (Z_{\text{eff}}=1.5) \end{cases}.$$

In the specification of the INTOR design, the effective ionic charge is specified less than 1.5. Based on those consideration, it is concluded that the beta contribution from the impurities is less than 10 % of the DT beta.

The beta contribution for thermalized alpha particles is

$$\beta_{\text{He}} = 1.5 \frac{n_{\text{He}}}{n_{\text{DT}}} \beta_{\text{DT}}.$$

Here, helium ions are assumed to have same profile as DT ions. This yields

$$\beta_{\text{He}} = \begin{cases} 0.15 \beta_{\text{DT}} & (10 \%) \\ 0.075 \beta_{\text{DT}} & (5 \%) \end{cases}.$$

In the INTOR specification, the helium concentration is considered 5 - 10 %. From the above evaluations, it is concluded that the beta contribution from thermalized alpha ions is around 10 % of the DT beta value.

For energetic alpha particle, the beta contribution is simply assumed without detailed calculations,  $\beta_{\text{alph}}=0.1 \beta_{\text{DT}}$ .

Based on the above evaluations, the additional beta value for impurities and helium particles, and energetic alpha particles is concluded to be 30 % of the fuel DT beta value.



## 2.4 Comments on the heat load due to ripple loss of alpha particles

It has been reported that the maximum heat load on the first wall due to ripple loss of charged fusion products in a reactor tokamak with TF ripple  $\delta \sim 1\%$  might reach the order of  $1 \text{ MW/m}^2$  [1]. In INTOR with  $\delta \sim 1\%$ , the separatrix is in the ergodic orbit region (GWB criterion for fast ion loss [2]). Most of particles on the ergodic orbit, however, can hit the first wall before entering into the divertor, because the radial position of the separatrix is close to the inner edge of the torus and the radial excursion from the magnetic surface of suprathreshold alpha particles near the separatrix is very large. This means some kind of mechanism to remove the heat load in the first wall for a reactor with long duty cycle of burning, which makes the design of reactor to be very difficult.

The above mentioned heat load had been estimated under assumption that the plasma boundary completely touches the first wall without any gap between them. In a real tokamak reactor, however, there is a finite gap  $r_g$  between the separatrix surface and the first wall which is about  $0.1 \langle a \rangle$  in INTOR where  $\langle a \rangle$  is the average minor radius. This may alleviate the heat load by  $\sim 20\%$  because of the enlargement of the surface area. The additional time for loss particles to travel  $\Delta r_g$  may also reduce the loss fraction of charged fusion products.

The effect of non-circular cross section on the loss of alpha particles seems to be very interesting. The ergodic orbit region and the diffusion coefficient of alpha particles on ergodic orbits in a non-circular cross sectional plasma are still unresolved. High effects both on the magnetic surface and on the guiding-center orbits must be taken into consideration for the more accurate estimation of loss of charged fusion products. For the precise calculation of heat load map on the first wall of a reactor with poloidal divertor, the magnetic field derived by a MHD equilibrium code must be used as an axis-symmetric component of the field to follow the orbit.

### References for subsection 2.4

- [1] TANI, K., TAKIZUKA, T., AZUMI, M., KISHIMOTO, H., Nucl. Fusion 23 (1983) 567.
- [2] GOLDSTON, R.J., WHITE, R.B., BOOZER, A.H., Phys. Rev. Lett 47 (1981) 647.

### 3. Configuration

The conceptual design of the reactor structure is carried out in taking into account the following points.

- ① Reduction of the reactor size
- ② Simplification of the reactor structure
- ③ Simplification of the disassembly and assembly procedures.

The short channel divertor concept is adopted as the reference design of the reactor structure. The vertical cross sectional view of the reactor structure and the horizontal cross sectional view in midplane of the reactor structure are shown in Fig. 3.1 and in Fig. 3.2 respectively.

#### 3.1 Toroidal magnetic field coil design

The number and the bore size of TF coil is determined in taking into account the accessibility and the maintainability for the remote handling of the blanket and divertor.

The TF coil main parameters are shown in Table 3.1. The type of superconductor in TF coil is a cable in conduit type (NbTi<sub>3</sub>)Sn conductor with a supercritical helium forced cooling. The number of TF coil amounts to 12. The bore of the TF coil is 6.5 m width × 9.26 m height. The bore size is slightly reduced in comparison with that of phase IIa Part 1 (6.6 m width × 9.3 m height).

The configuration of the TF coil is shown in Fig. 3.3. The cross-sectional view of the TF coil at the midplane is shown in Fig. 3.4. The size of cross section of TF coil winding part is 512 mm × 704 mm. The size of cross section of the support structure of the TF coil winding is 830 mm × 1300 mm. The shear panel installed between the TF coils is shown in Fig. 3.5. The region of installation of shear panel is different for the upper part and for the lower part of TF coil.

#### 3.2 Poloidal magnetic field coil design

The main parameters of PF coil are shown in Table 3.2. All the PF coils are located outside of TF coil. The location of PF coil is shown in Fig. 3.6. Nb<sub>3</sub>Sn superconductor is used with a supercritical helium forced cooling system. The largest size of cross section of the PF coils is 1 m × 1 m (coil number 15 and 16) and the largest radius of the PF coils is 10.3 m (coil number 9 and 18).

#### 3.3 Torus and cryogenic system topology

- (1) The combined type vacuum boundary concept is adopted in order to reduce the radial build of the inner side of the plasma. This vacuum boundary concept is shown in Fig. 3.7.

The vacuum boundary of the plasma chamber is located on the inner side of the shield structure. The outer part of the shield structure is connected with the torus access port through which the blanket and divertor sectors are retracted. The access port is connected with the window part of the outer side of the belljar. In the torus access port, the access door is installed to form the plasma vacuum chamber.

By virtue of the access port and the access door, the connection between divertor sectors and blanket sectors is carried out only mechanically, so the assembly and disassembly procedures become simple. The vacuum seal is carried out around the access door without T shaped sealing. It is desirable to avoid the T shaped seal where the electromagnetic forces of blanket and divertor might act on. The vacuum seal carried out around the access door is more reliable than T shaped sealing. The shielding structure where the bellows are installed is shown in Fig. 3.8.

The vacuum seal of the access door is carried out by lip seal as shown in Fig. 3.9. The mechanical connection between the access door and the access port is performed by the tie bar as shown in Fig. 3.9. The connecting structure between the access port and the belljar is shown in Fig. 3.10. The connection is carried out by bellows in order to avoid the thermal stress due to thermal expansion of the torus at the time of bake out.

## (2) Torus resistance

In order to estimate the one turn resistance, the following model of the plasma vacuum enclosure and the cryostat (belljar) are taken into consideration as shown in Fig. 3.11. Concerning the plasma vacuum enclosure, one turn resistance ( $0.2 \text{ m}\Omega$ ) can be obtained with 12 bellows. Concerning the belljar structure, one turn resistance ( $0.2 \text{ m}\Omega$ ) can be sustained with help of the thin plate.

The resistance of a plate is shown as

$$R = \rho \cdot \frac{L}{A}$$

The resistance of a disk is shown as

$$R = \rho \cdot \frac{2\pi}{t}$$

The integrated one turn resistance  $R_t$  is given as

$$\frac{1}{R_t} = \sum \frac{1}{R}$$

here, L: length of a plate  
A: cross sectional area  
t: thickness of a plate  
 $\rho$ : specific resistance

( $69 \times 10^{-6} \Omega \cdot \text{cm}$  (at room temperature) ----- SS316L)  
( $129 \times 10^{-6} \Omega \cdot \text{cm}$  (at room temperature) ----- Inconel 625)

The basic configuration of the bellows (SS316L) is as follows.

thickness of the plate :	2 mm
pitch :	40 mm
height :	65 mm
number of convexities :	8

The belljar of 2 mm thickness is made from Inconel 625. The belljar is consist of cylindrical part, belljar dome and belljar bottom. The thin plate of the belljar is supported with the reinforcement as shown in Fig. 3.12.

The integrated resistance amounts to  $R_t = 0.12 \times 10^{-3} (\Omega)$ . This value satisfies the required one turn resistance: 0.2 m $\Omega$ .

### 3.4 Modularization and segmentation

#### (1) Segmentation of torus (blanket)

The TF coil bore size is reduced in comparison with that of phase IIa Part I (6.6 m  $\times$  9.3 m). The reduction of TF coil size does not permit the blanket replacement by 1 segment/TF coil. The blanket should be segmented as 2 sectors/TF coil. The reduced TF coil bore size is 6.5 m  $\times$  9.26 m. The horizontal cross sectional view at  $Z = 0$  and  $Z = -3350$  mm planes of the segmented structures are shown in Fig. 3.13 and Fig. 3.14. The blanket structures between TF coils are of equal toroidal span. Each blanket sector which is supported with outer shield structure is connected by flange with the semi-permanent shield-post in order to form the torus configuration. From the view point of simplification and reliability of assembly and disassembly procedures, the retraction of the first blanket sector is carried out by single straight line motion and the retraction of the second one is carried out by two straight line motions. Each access port installed between the torus and the coil cryostat serves two blanket sectors which can be removed one after another. The concept of this retraction concept is shown in Fig. 3.15.

#### (2) Segmentation of divertor

When the assembly and disassembly of divertor is carried out, the large structures such as RF heating system is intact. The access to the divertor is performed under the RF heating duct. The segmentation of divertor structure is shown in Fig. 3.16. The divertor is segmented as 2 sectors/TF coil. As shown in Fig. 3.16, though the divertor plate structures between TF coil are of almost equal toroidal span, the divertor plate support structures are of unequal span. Each sector is retracted one after another by single straight line motion as shown in Fig. 3.17.

#### (3) Shell conductor

The shell conductors are installed just behind the first wall in

each blanket sector. The shell conductor structures between TF coils are independent. The electrical connection of the shell conductor between two segmented blankets is performed at the outer side of the shield structure with help of the connecting bars as shown in Fig. 3.18.

#### (4) Active control coil

The following items should be taken into consideration to determine the location of installation of the active control coil which produces the horizontal magnetic field constituent.

- (a) Active coil should be installed in the location where the magnetic field of horizontal constituent can be generated efficiently.
- (b) Mutual inductance between the shell conductor and the active control coil should be as low as possible.
- (c) Installation of the active control coil should be easy and the structure supporting the active control coil should be simple.
- (d) Radiation damage should be low
- (e) Assembly and disassembly procedures should be simple and easy.

The examples of the active control coil installed inside of TF coil are shown in Fig. 3.19 ~ Fig. 3.21. One example of the active coil installed outside of TF coil is shown in Fig. 3.22.

- (i) Examination from the view point of reactor structure and reactor construction.

The active control coil arrangement of Case 1 is shown in Fig. 3.19. The active control coils ① ①' are installed in the shield structure which plays a role of plasma vacuum boundary. This location is chosen in order to avoid the interference with the shield post.

The installation of the active control coil is carried out after the construction of shielding structure and the winding of coils and insulation in torus structures.

The active control coil arrangement of Case 2 is shown in Fig. 3.20. Though the active control coil ② ②' are installed also in the shield structure, they interfere with the shield post as shown in Fig. 3.24. This interference between the active control coil and the shield post makes the torus construction more difficult and the jointing part of the shield post with the semi-permanent shield will be less robust. In this case, as the semi-permanent shield and the shield post are separated, the joining of the shield post with the semi-permanent shield will be performed after the installation

of the torus shield structure and the installation of the active control coils.

The active control coil arrangement of Case 3 is shown in Fig. 3.21. The active control coils (3) (3') require the vacuum enclosures which should surround the active control coils because the active control coils penetrates into the side wall of the access port.

The active control coils (4) (4') of Case 4 shown in Fig. 3.21 are installed between the shield and the TF coil. In this case, after the winding of the active control coil, the shield structure is constructed and the active control coils are installed on the shield structure. The difficulty in the installation is that the lower shear panel between TF coils is already installed before installation of the lower active control coil.

The active control coils installed outside of the TF coils (Case 5 and Case 6) are shown in Fig. 3.22. There is no problem for both Case 5 and Case 6 on the construction and the installation of the upper active control coil. However, the lower active control coil (5') in Case 5 interferes with the vacuum duct. The lower active control coil (6') in Case 6 interferes with the TF coil support legs.

- (ii) Examination from the view point of the performance of plasma control.

In this section, only the comparisons of the active control coil between outside of TF coil bore and inside of TF coil bore are briefly mentioned. The detailed analyses on the performance of the plasma control are discussed in 7.

In the case of the active control coil installed in TF coil bore, the maximum displacement of plasma is 0.54 cm, the power supply capacity is  $60\text{ V} \times 90\text{ kA}$ . In the case of the active control coil installed outside of TF coil bore, the maximum displacement of plasma is 0.54 cm, the power supply capacity is  $180\text{ V} \times 180\text{ kA}$ .

### 3.5 Support structure system

#### (1) TF coil support

##### (i) Force to the torus center (Centering force)

The force to the torus center in the toroidal field magnet is supported by the pressure acting on the center support cylinder. The support by the pressure acting between the surface of wedge part of the magnet cases is not expected here because of the uncertainty of its reliability, though the adoption of the wedge effect can reduce the space necessary for support structure.

## (ii) Overturning force

The toroidal torsion force (overturning force) in the TF coil is supported by the support beams installed between TF coils.

## (iii) Gravity

The gravity of the TF coils is supported from both the torus center and the outside of the torus. At the torus center, TF coils are supported with the support leg which also supports the PF coils. At the outside of the torus, each TF coil has an independent support leg. These support legs have a shield layer of FRP cylinder located between the floor of 300°K and the structures of 4.2K in order to reduce the heat penetration. These support legs are equipped also with the slide mechanism which serves to relax the resulting thermal stress of TF coils at the time of cooling or elevation of temperature. The concept of the support leg is shown in Fig. 3.25.

## (2) PF coil support

## (i) Electromagnetic force

The hoop force resulting in PF coil is sustained by the PF coil's own structures. The out of plane force acting on the PF coils (coil number 1~6, 10~16) is supported with the support structure which is located between the center support cylinder and the TF coil. As regard to the other PF coils, they are supported by the arms on the toroidal field coils.

## (ii) Gravity

The support concept of the gravity of PF coils is the same as that of electromagnetic force. PF coils can slide freely in radial direction in order to relax the thermal stress due to the temperature difference at the time of cooling or elevation of temperature.

## (3) Torus support

The supporting of the torus is carried out by means of the vacuum duct standing from the floor. This combined concept of the support leg and the vacuum duct permits to obtain the space for the lower support beam between TF coils. This support leg can support the gravity of the shield, blanket, divertor and the plasma vacuum chamber. The support leg can slide freely in the radial direction on the base in order to permit the thermal expansion at the time of bake out as shown in Fig. 3.26. On the slide surface, a low friction material is employed.

## (4) Blanket support

The electromagnetic force acting on the blanket sector is finally supported by the semi-permanent shield structure. The directions of the electromagnetic force acting on the outer side of the shield

are shown in Fig. 3.27. As support system, both the bolts and the shear key on the flange are used. As shown in Fig. 3.28, the load  $F_R$  is supported by the bolts as tensile load, the load  $F_y$  is supported by the shear keys which are installed upper and lower part of the blanket.

### 3.6 Radial build

The comparison of the radial build between that of Phase IIA Part I and Part II is shown in Fig. 3.29. Both the reduction of the main radius 5.3 m to 5.0 m and the reduction of cross section of TF coil contribute the reduction of the reactor structure size (diameter of the belljar) by 1 m.

### 3.7 Impurity control

The impact of the choice of impurity control system is considerable on the reactor structure especially on the reactor size. As reference design, the short channel type configuration of the divertor is adopted in order to reduce the reactor size as shown in 3.30. The divertor is segmented as 2 sectors/TF coil which is discussed already in 12.3.4. The horizontal sectional view of the divertor is shown in Fig. 3.16. The maximum heat load on divertor plate of short channel concept is about  $5 \text{ MW/m}^2$ . This design condition is very severe from the view point of the thermal stress. If the permissible level of the maximum heat load  $\sim 2 \text{ MW/m}^2$  is adopted, the increasing length of divertor plate in horizontal direction leads to the increase in TF coil bore and in the diameter of belljar as shown in Fig. 3.31.



Table 3.1 Major characteristics of the TF magnet system

1. Total ampere-turns	124 MAT
2. No. of coils	12
3. Ampere-turns per coil	10.3 MAT
4. Plasma major radius	5.0 m
5. Field at plasma axis	4.96 T
6. Cooling method	Supercritical helium forced cooling
7. Grading concept	No grade
8. Winding configuration	Pancakes
9. Superconductor	Cable in conduit type (NbTi) <sub>3</sub> Sn conductor
10. No. of turns per coil	352
11. No. of pancakes per coil	22
12. Operation current	29.4 kA
13. Critical current	60 kA (at 12 T, 5 K)
14. Avg. winding current density	28.7 A/mm <sup>2</sup>
15. Maximum field	11.5 T
16. Inductance	~45 H
17. Magnetic field energy	~20 GJ
18. Electromagnetic force	
Hoop force	940 MN
Centering force	304 MN
Vertical force	208 MN

Table 3.2 Specification of poloidal field coil system

Number of coils	18
Concept of power supply	Hybrid
Magnetomotive force/coil	0.18 MAT (#9 coil) ~ 20.2 MAT (#16 coil)
Cooling method	Supercritical helium forced cooling
Superconducting cable	Cable in conduit type Nb <sub>3</sub> Sn conductor
Operating current	35.7 (kA)
Critical current	80 (kA)
Average current density	24.7 (A/mm <sup>2</sup> )
Maximum field	9.83 T
Support concept	Outer coils supported by TF coils. Inner coils by the center post and TF coils.

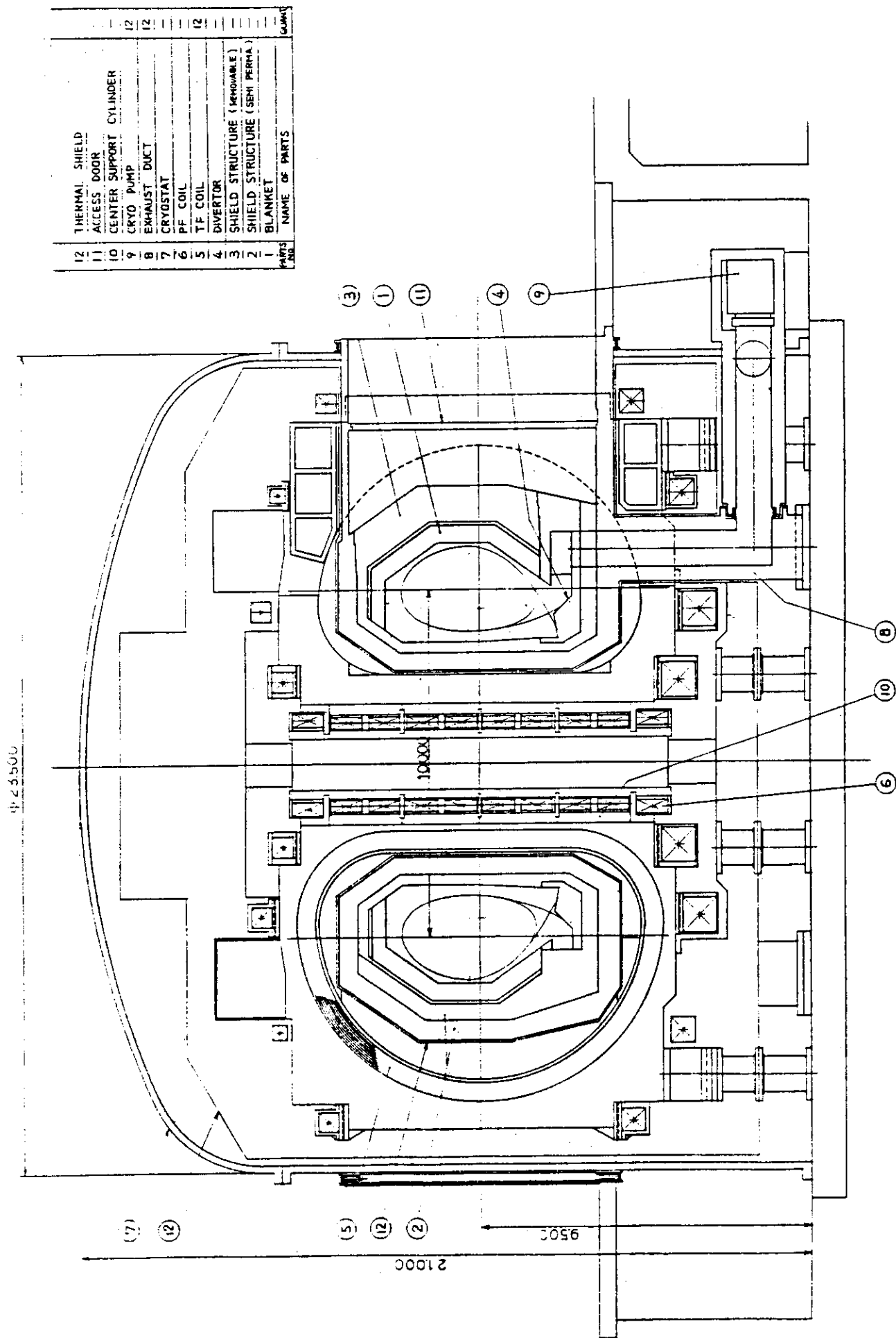


Fig. 3.1 Vertical view of INTOR

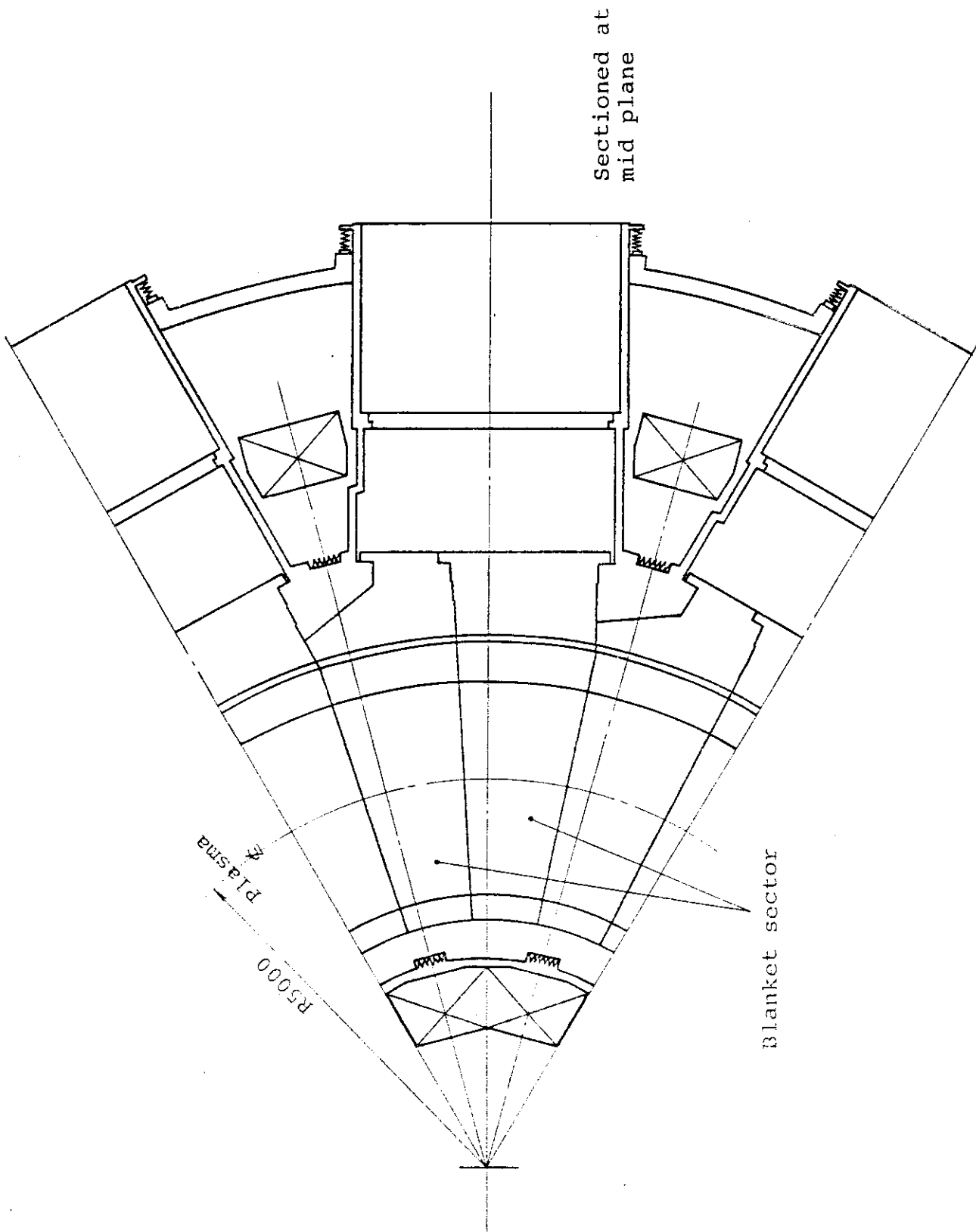


Fig. 3.2 Horizontal cross sectional view of INTOR

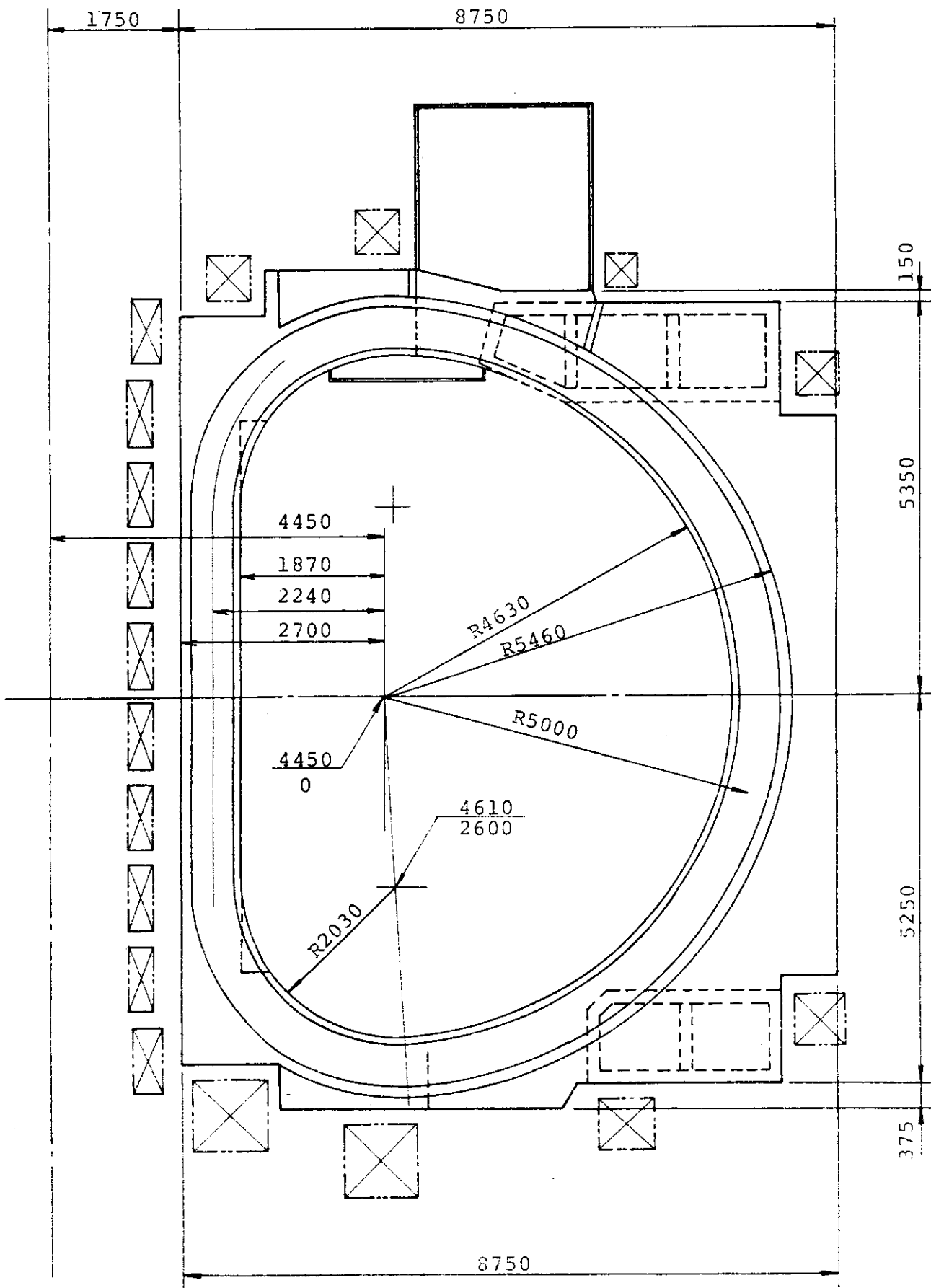
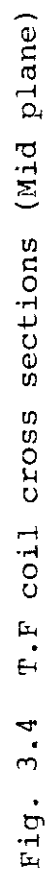


Fig. 3.3 T.F coil configuration



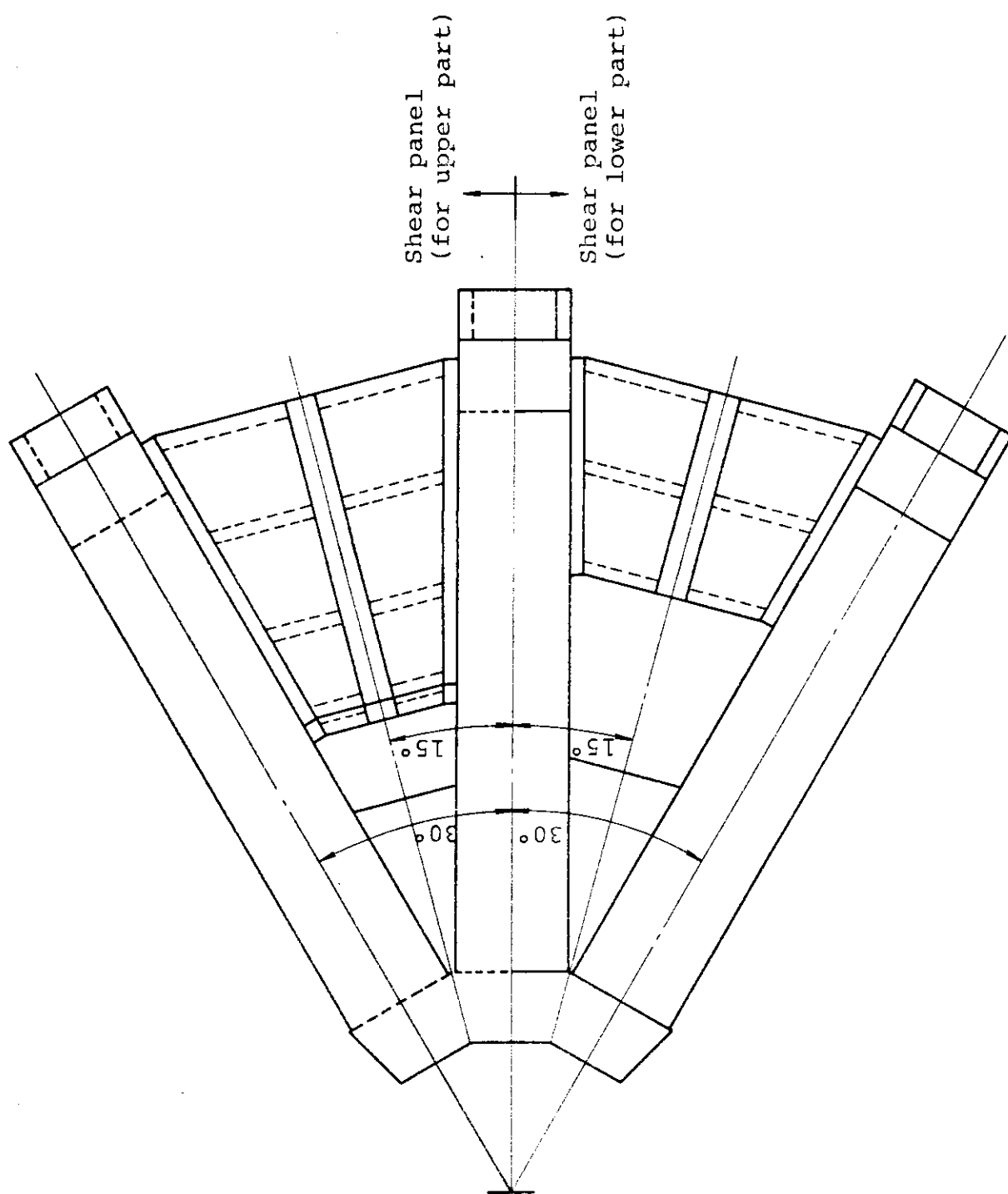


Fig. 3.5 Configuration of T.F. coil shear panel

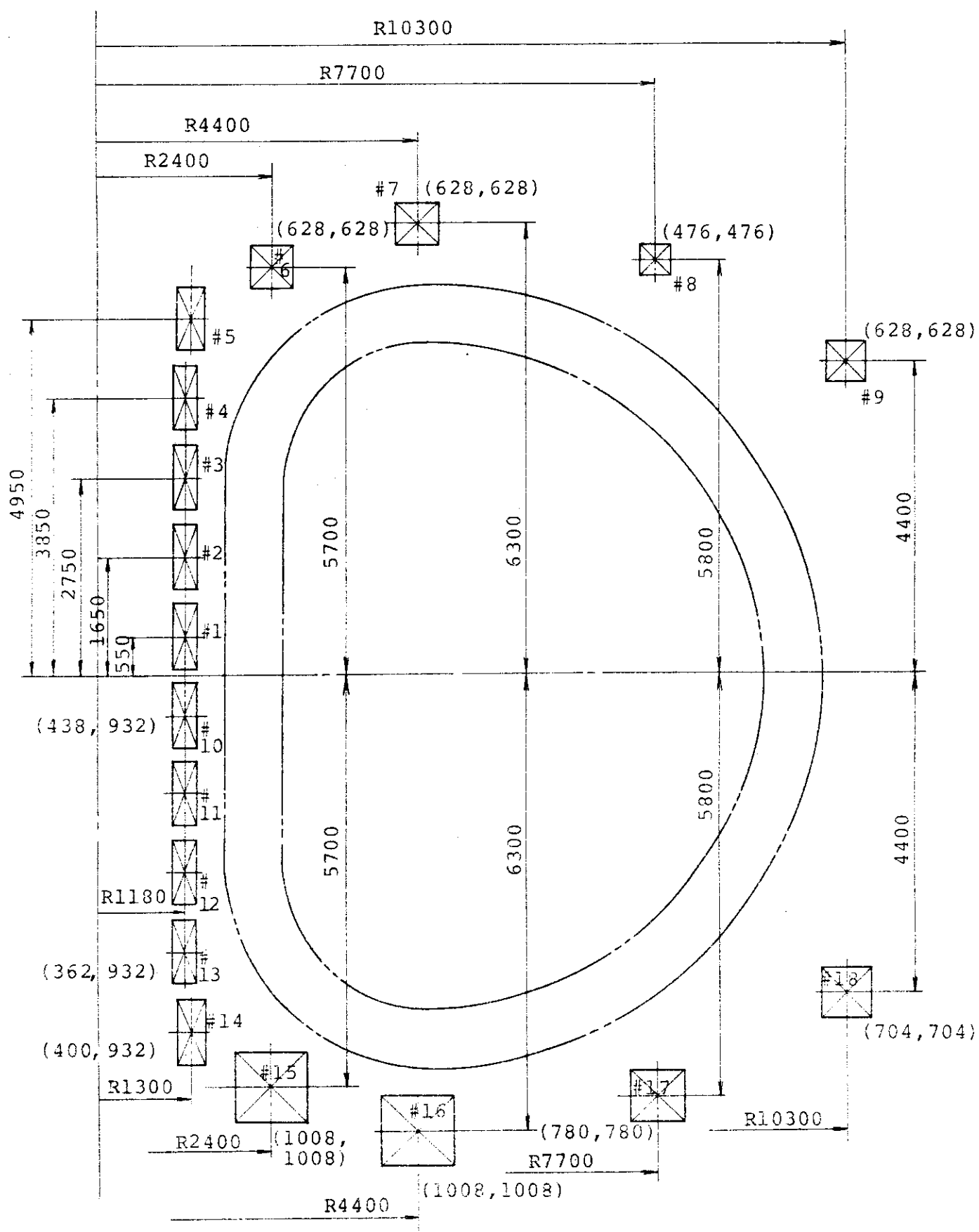


Fig. 3.6 Poloidal coil location and dimensions



Semi-permanent  
shield (Vac. chamber)

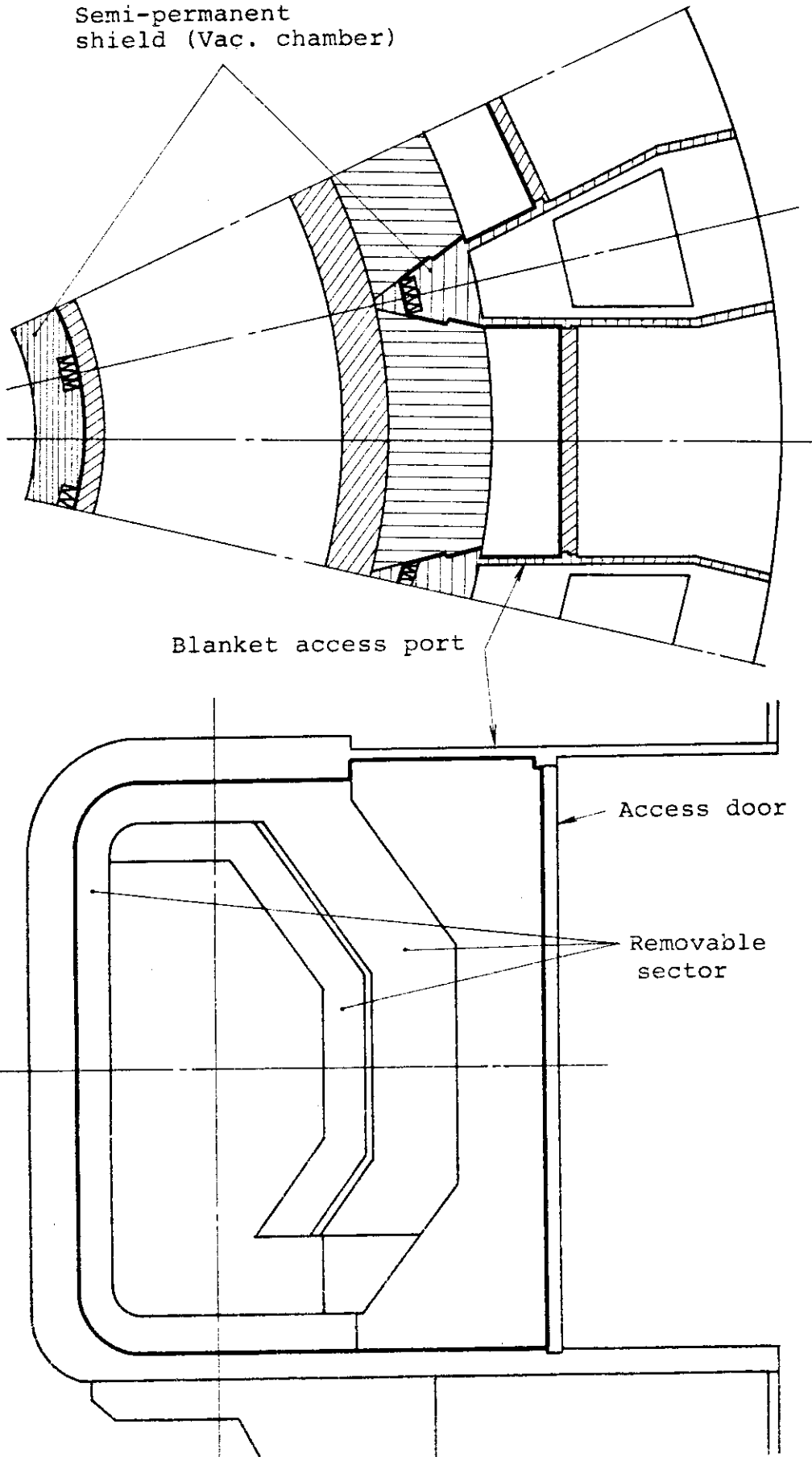


Fig. 3.7 Vacuum boundary of plasma chamber

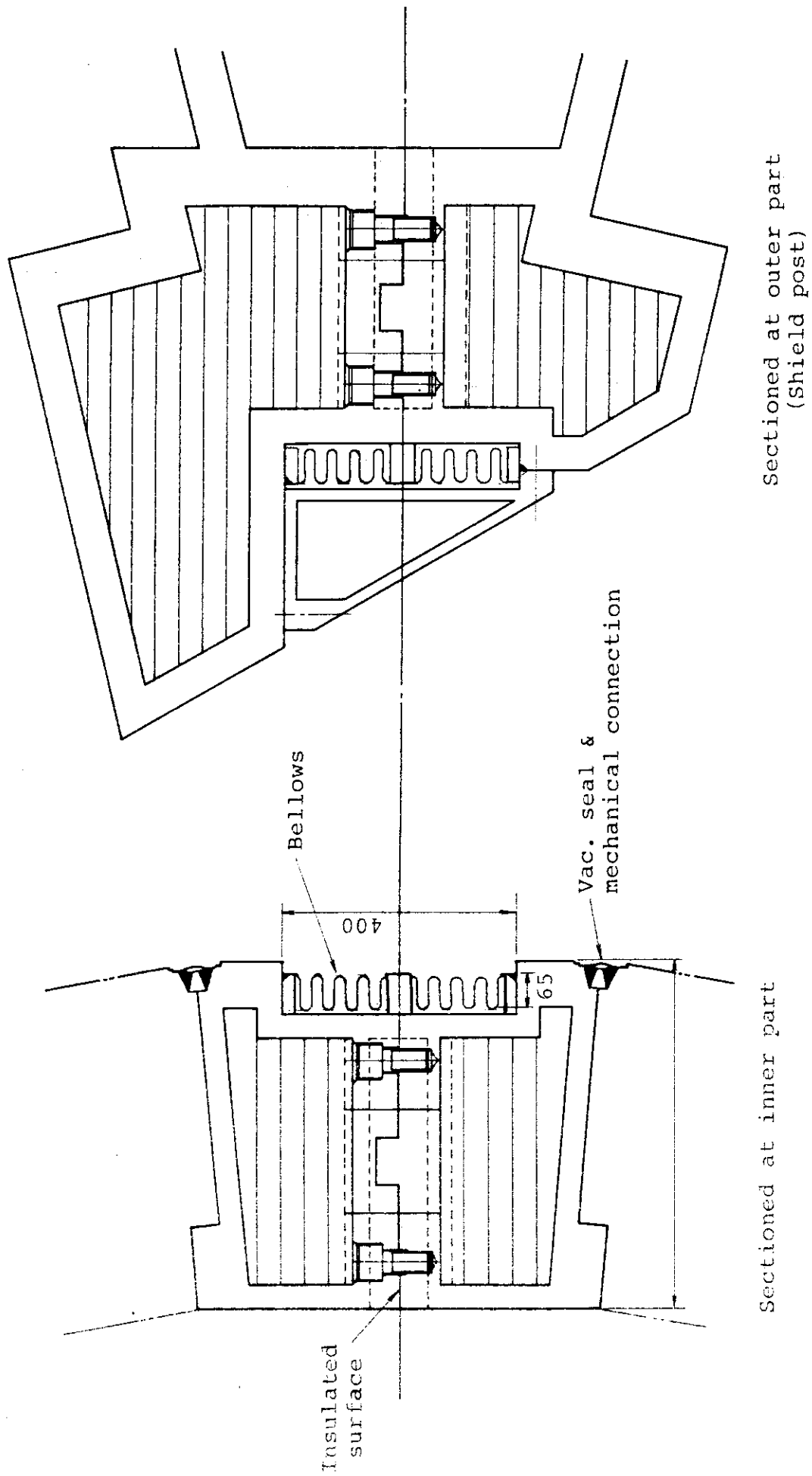


Fig. 3.8 FER shield structure

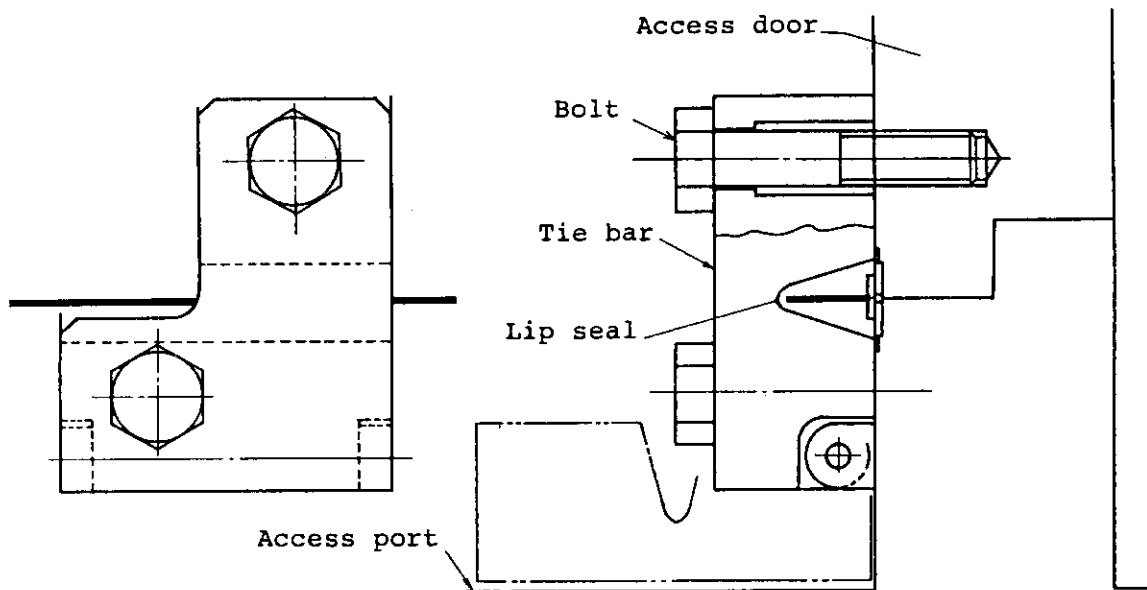


Fig. 3.9 Vacuum seal and tie bar for access door

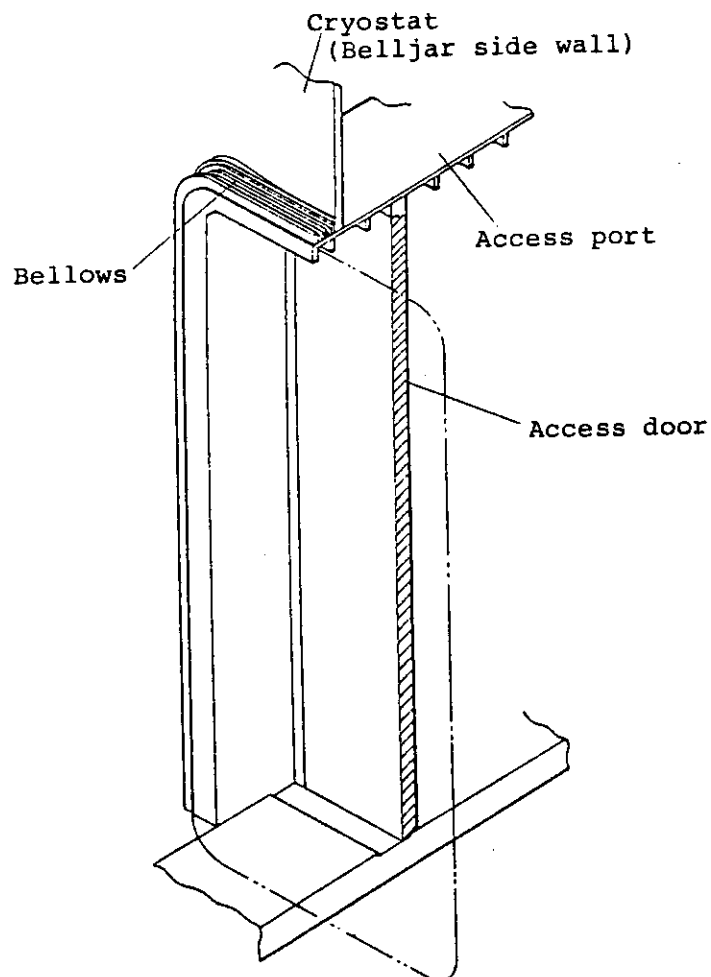
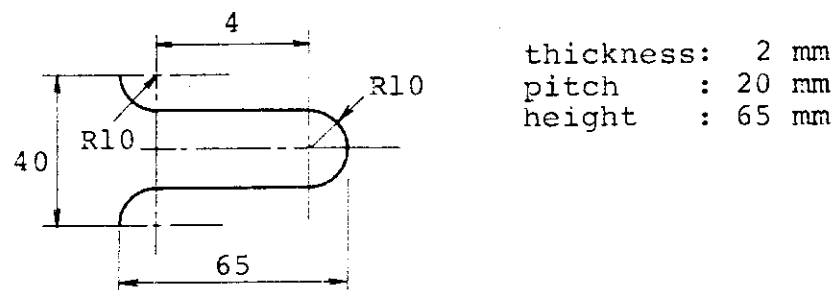


Fig. 3.10 Configuration of torus access port



Basic configuration of bellow

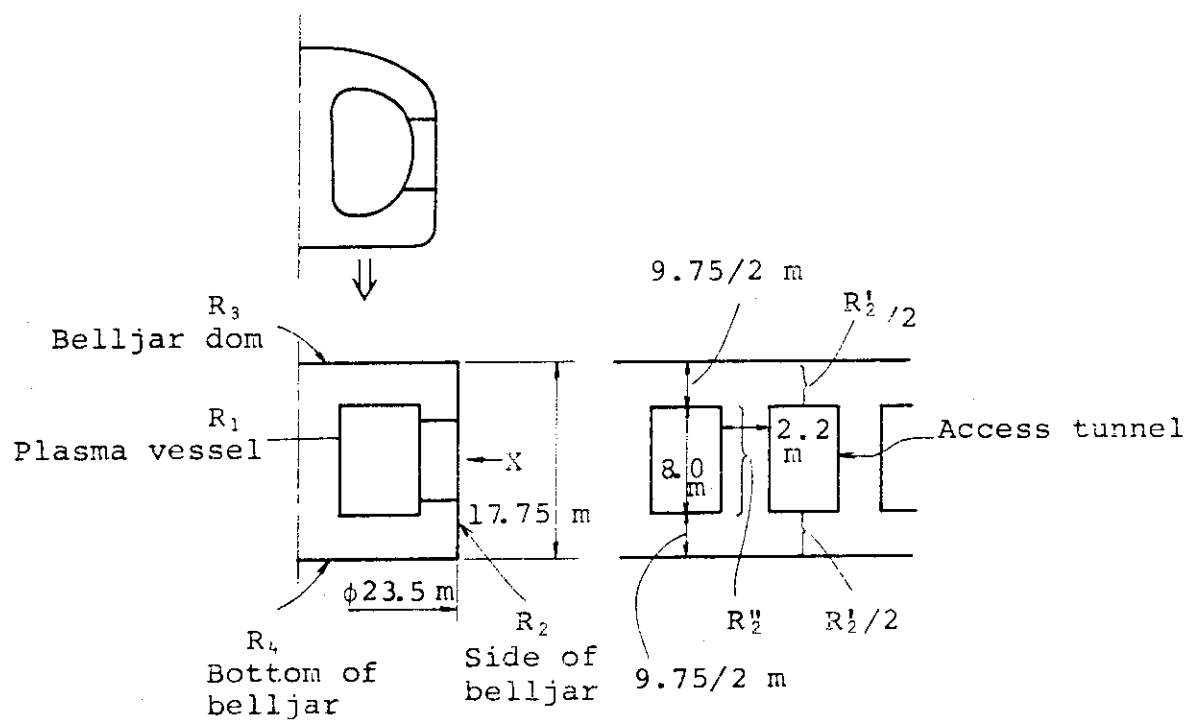


Fig. 3.11 Composition of loop resistance

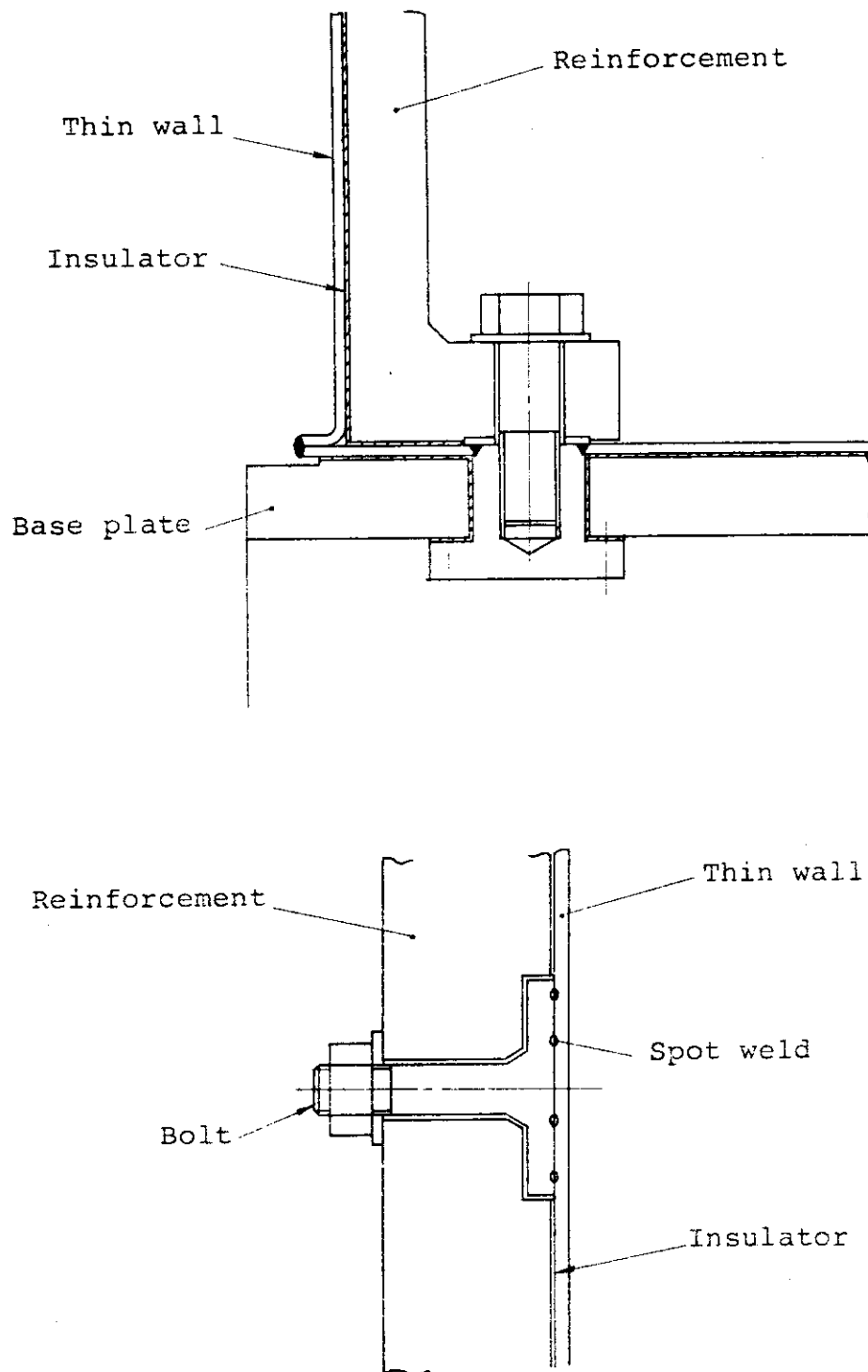


Fig. 3.12 Concept of vacuum wall (Thin wall type)

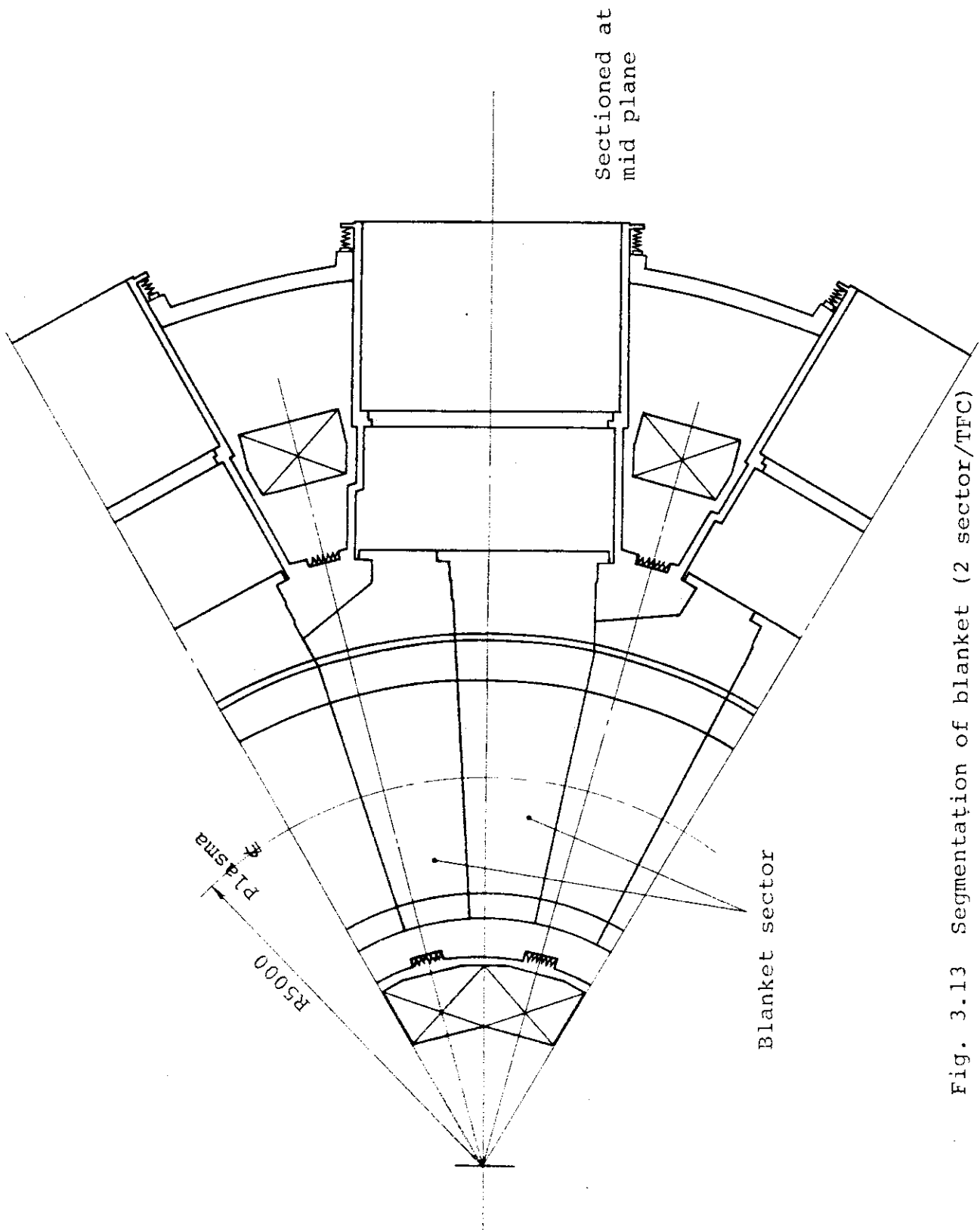


Fig. 3.13 Segmentation of blanket (2 sector/TFC)

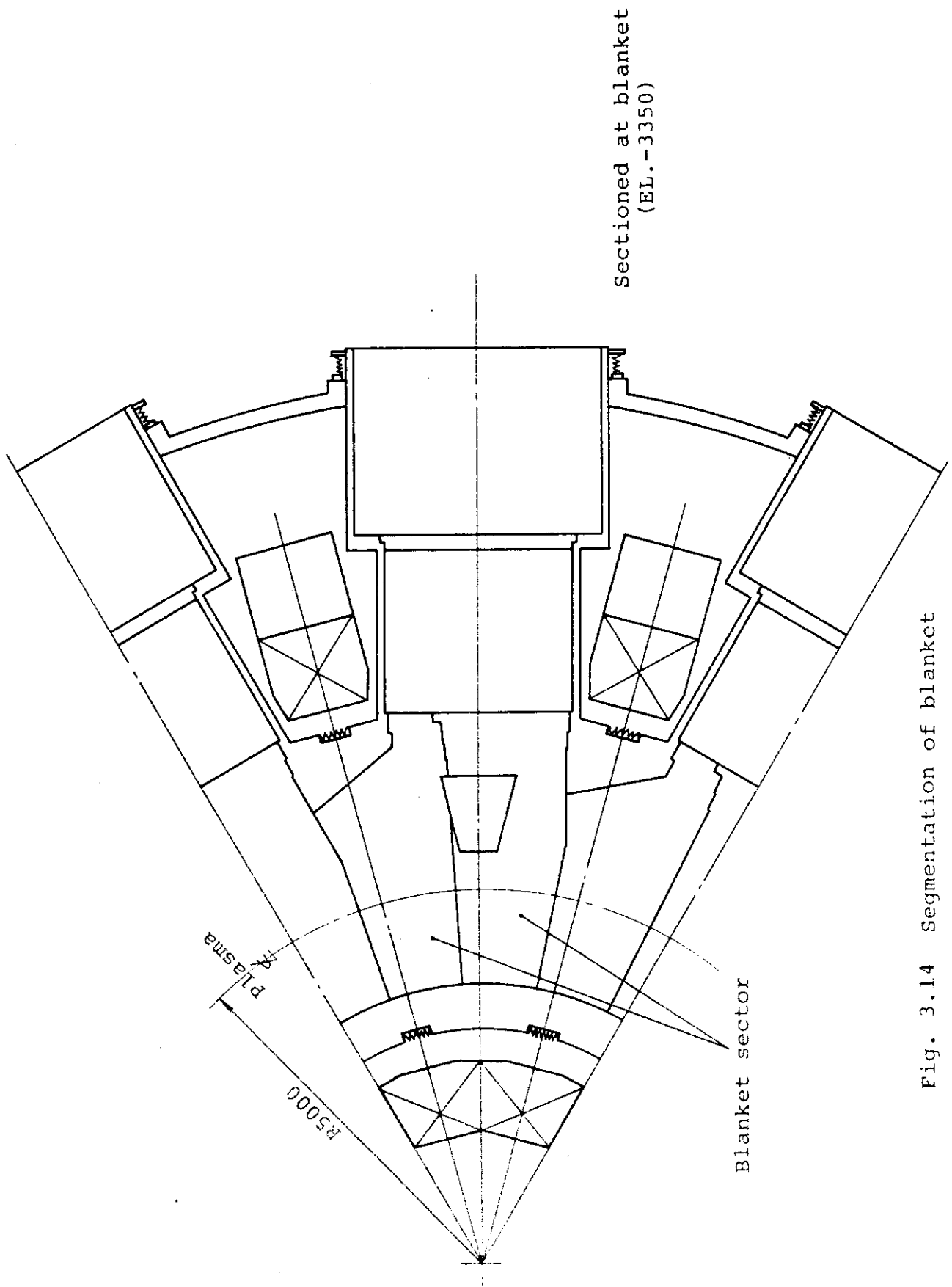


Fig. 3.14 Segmentation of blanket

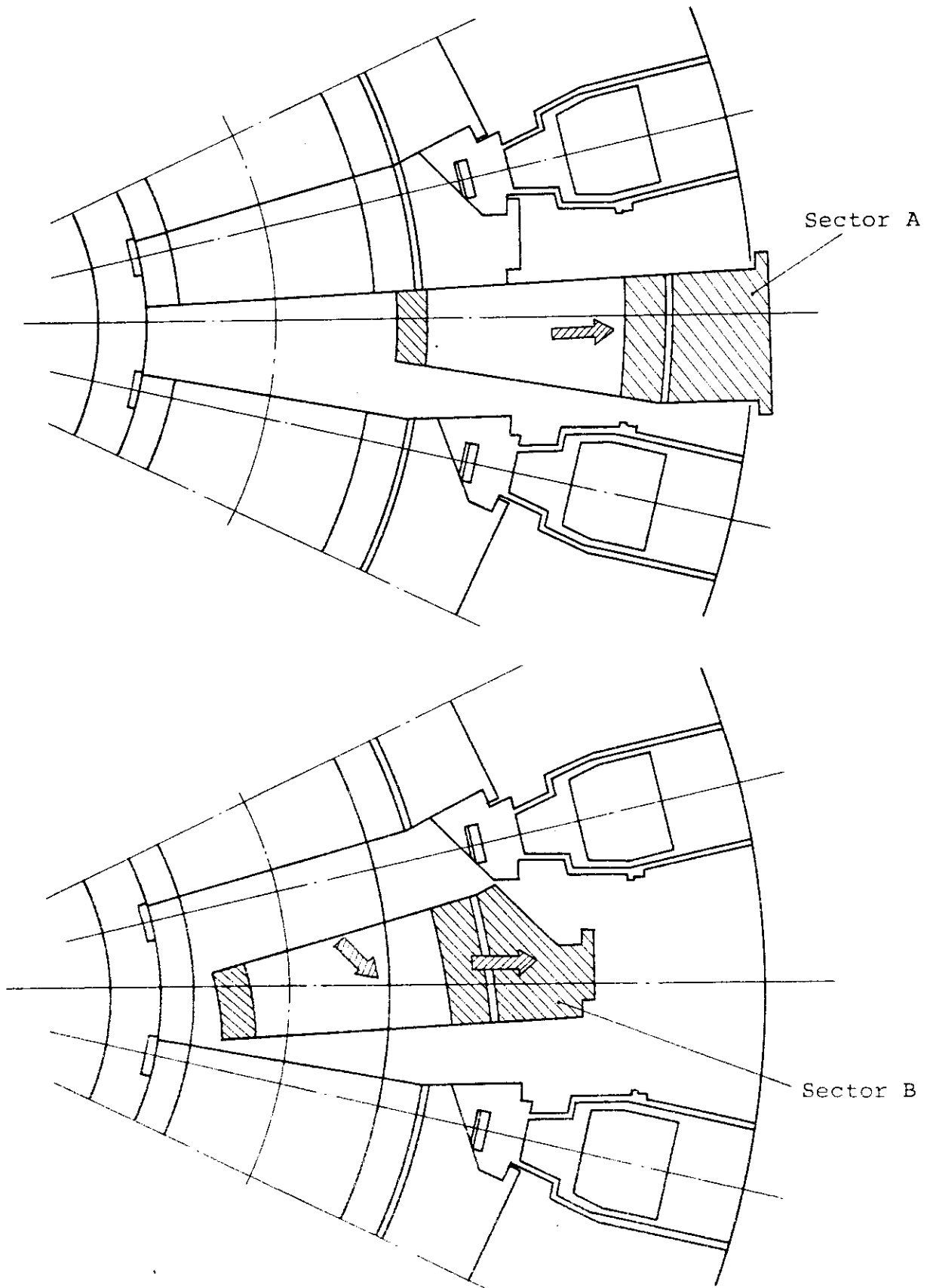


Fig. 3.15 Blanket replacement concept.



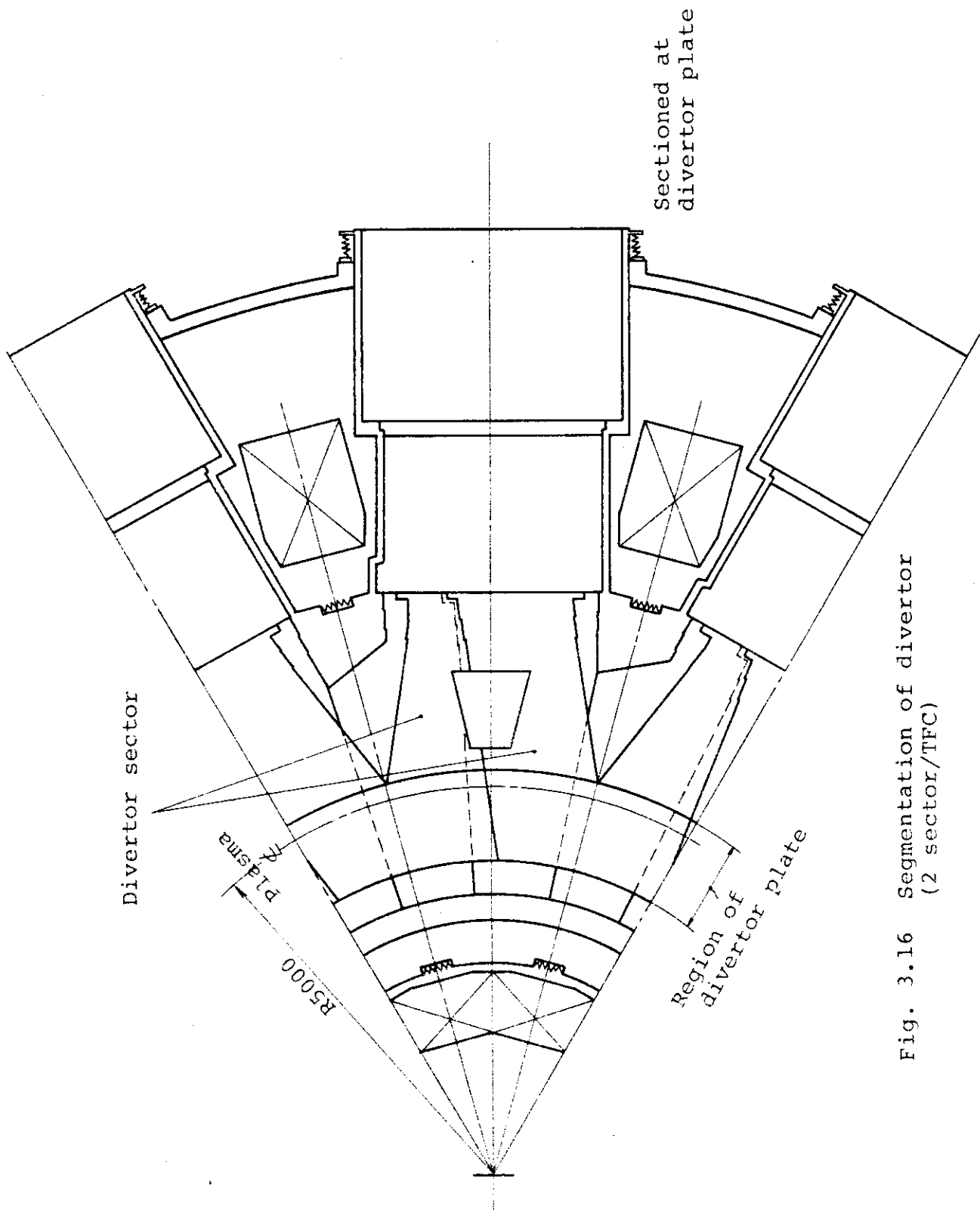


Fig. 3.16 Segmentation of divertor  
(2 sector/TFC)

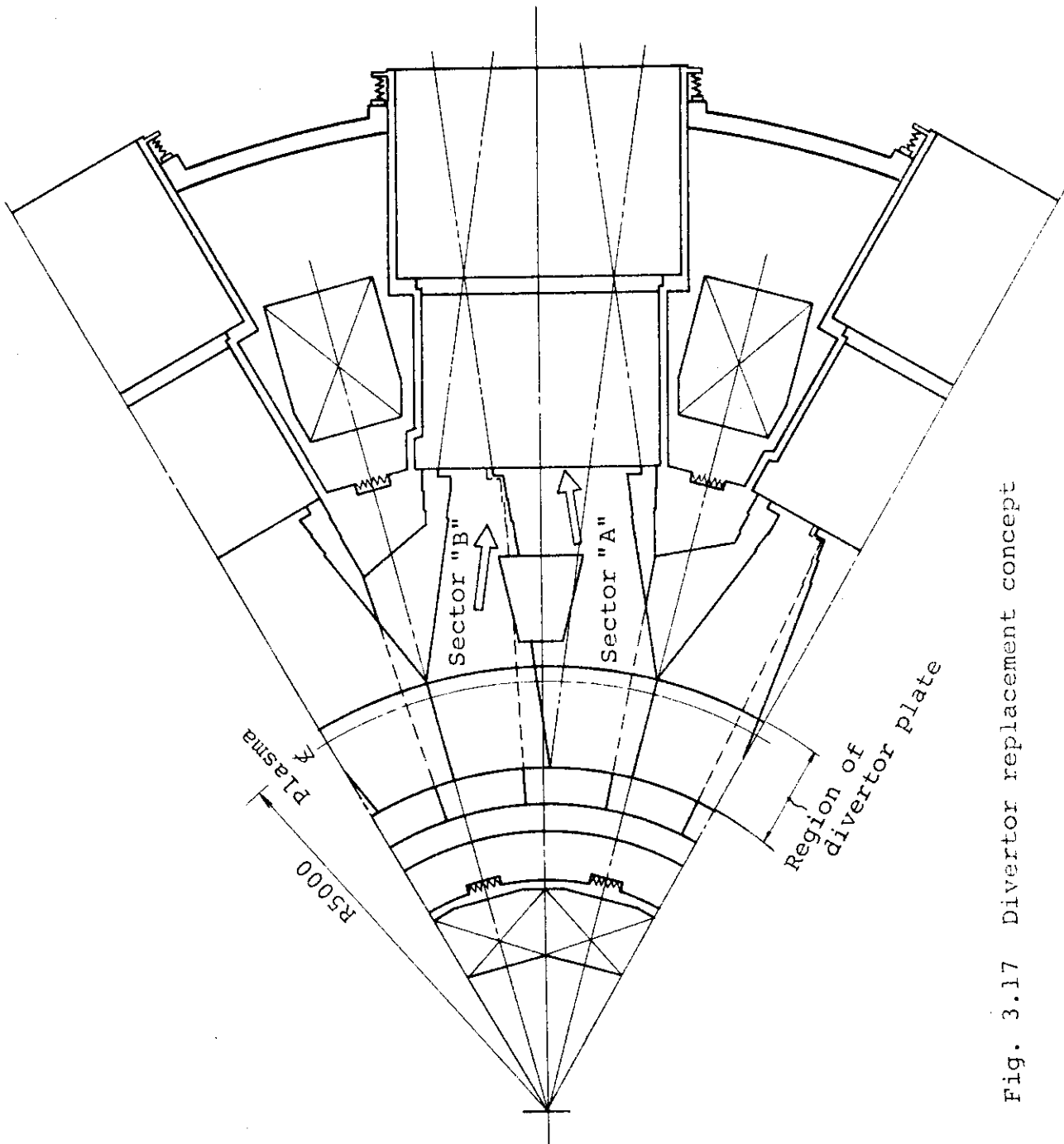


Fig. 3.17 Divertor replacement concept

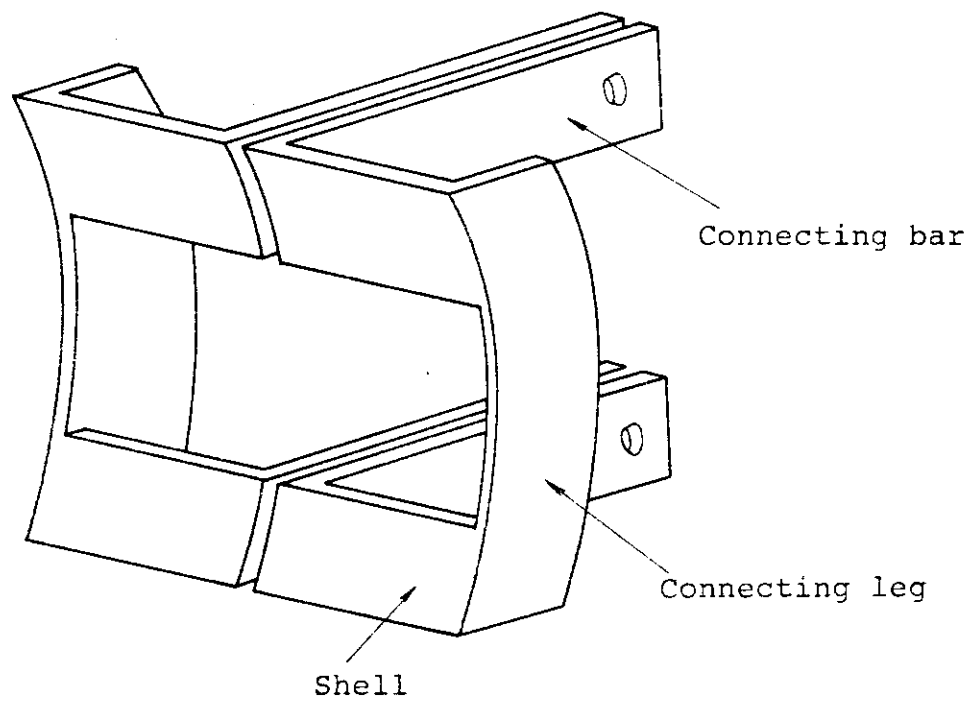


Fig. 3.18 Schematic drawing of shell conductor

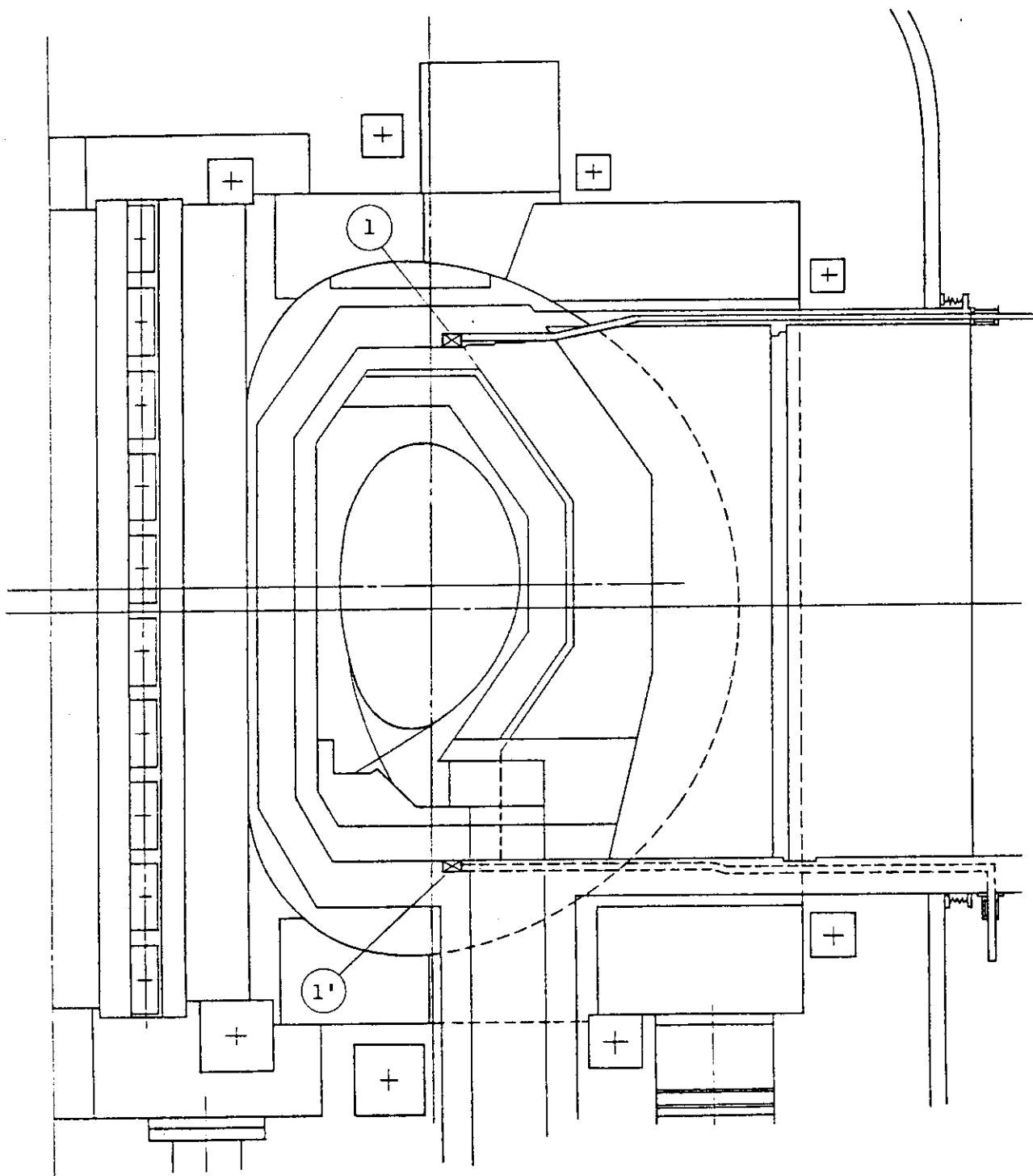


Fig. 3.19 Location of active coil (Case 1)

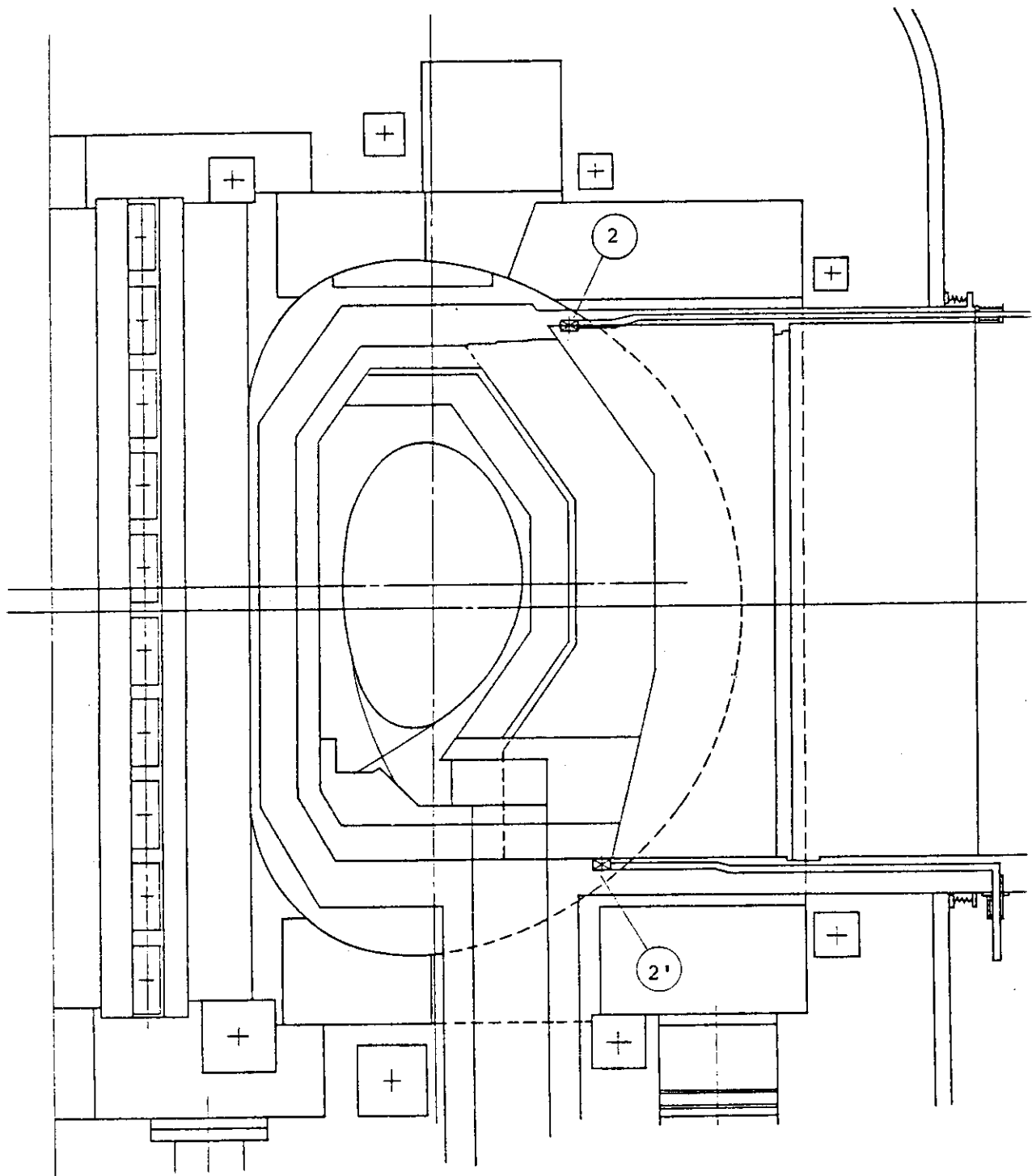


Fig. 3.20 Location of active coil (Case 2)

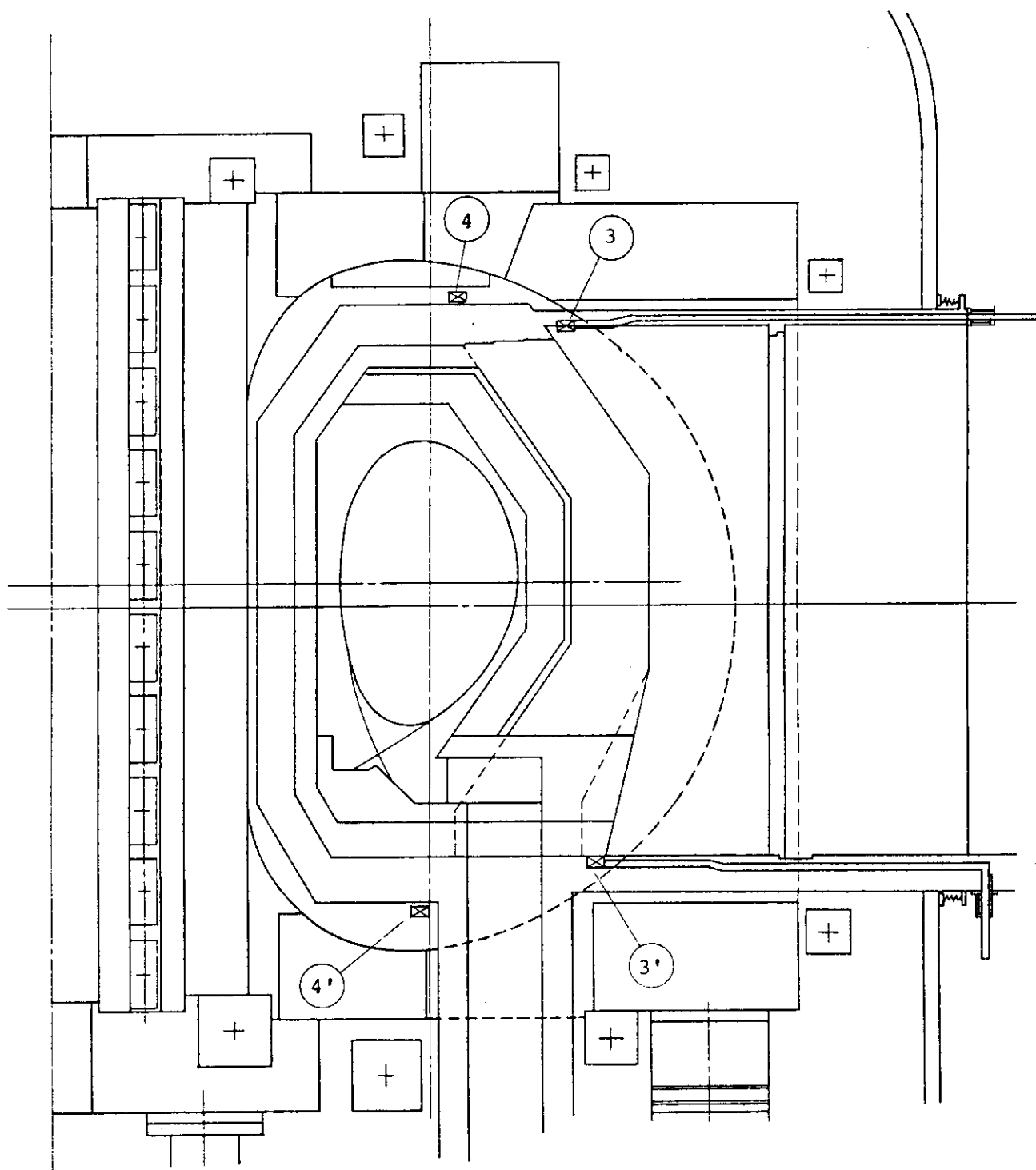


Fig. 3.21 Location of active coil (Case 3)  
(Case 4)

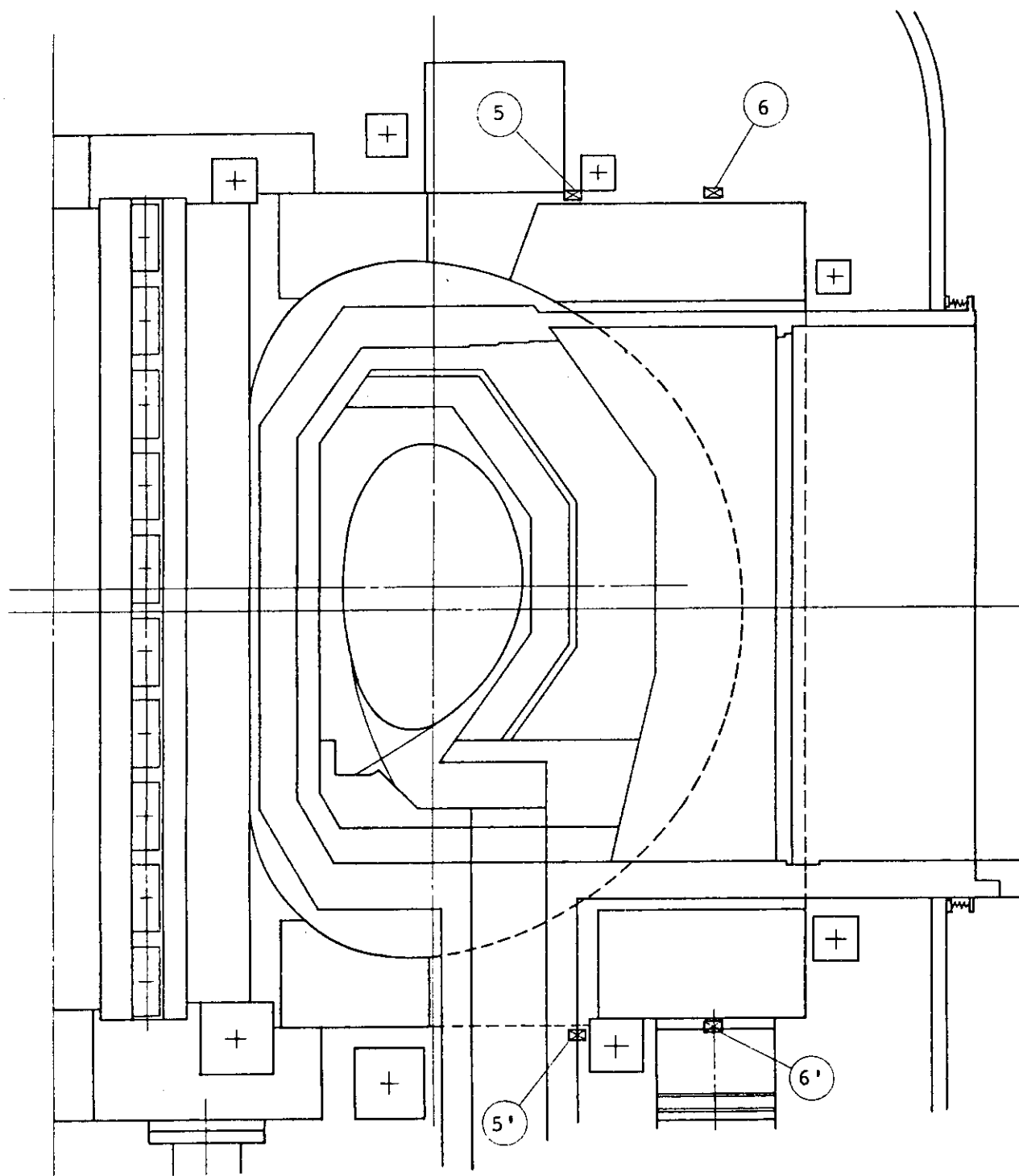


Fig. 3.22 Location of active coil (Case 5)  
(Case 6)

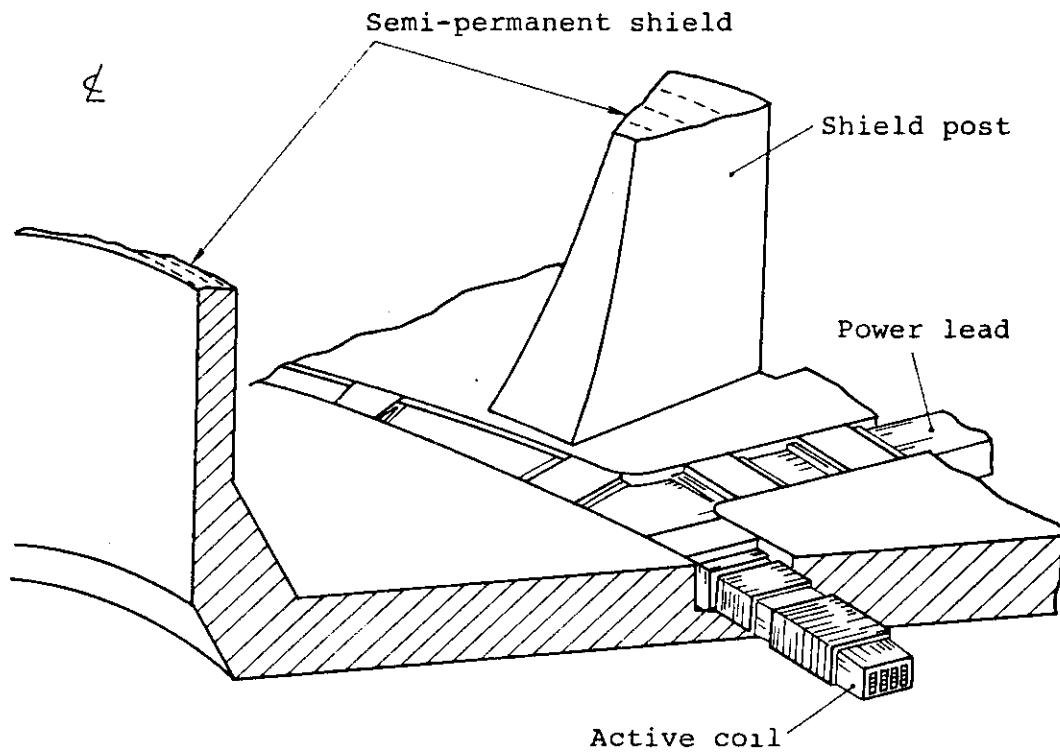


Fig. 3.23 Active coil configuration (Case 1)

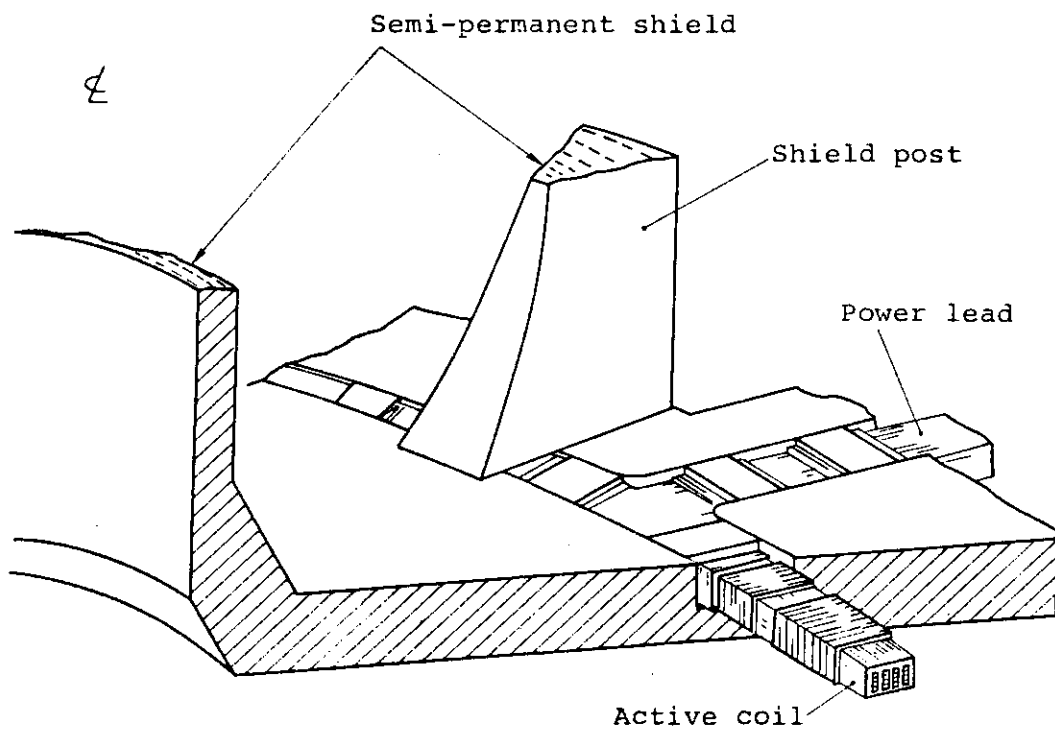


Fig. 3.24 Active control coil configuration (Case 2)



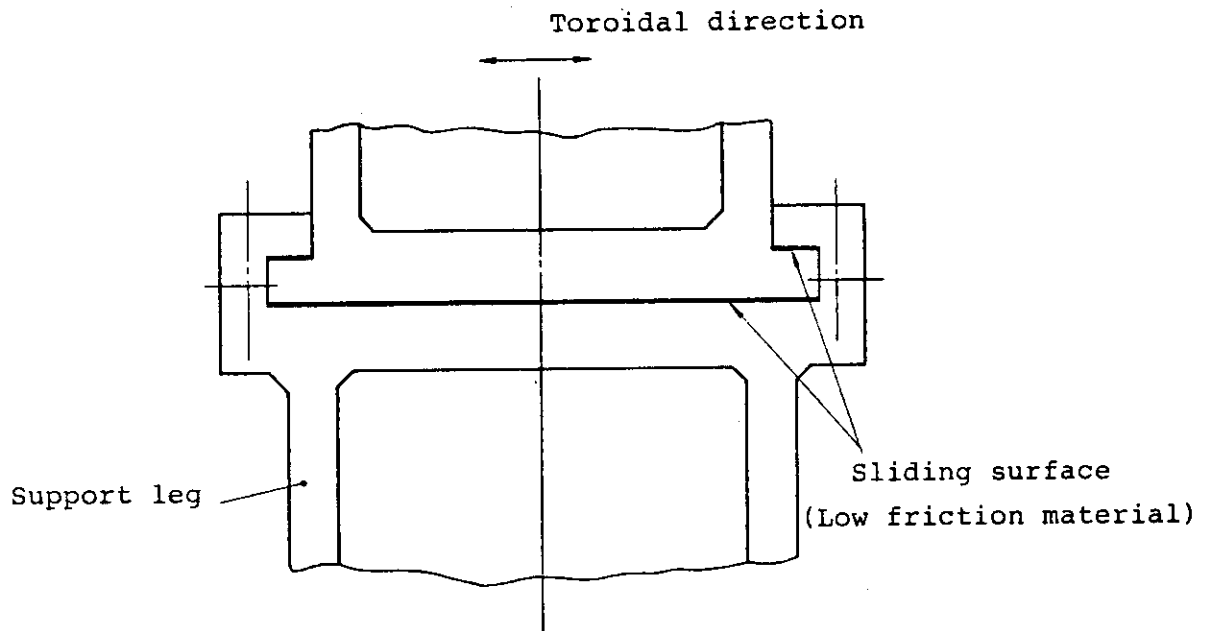


Fig. 3.25 Support structure of magnet

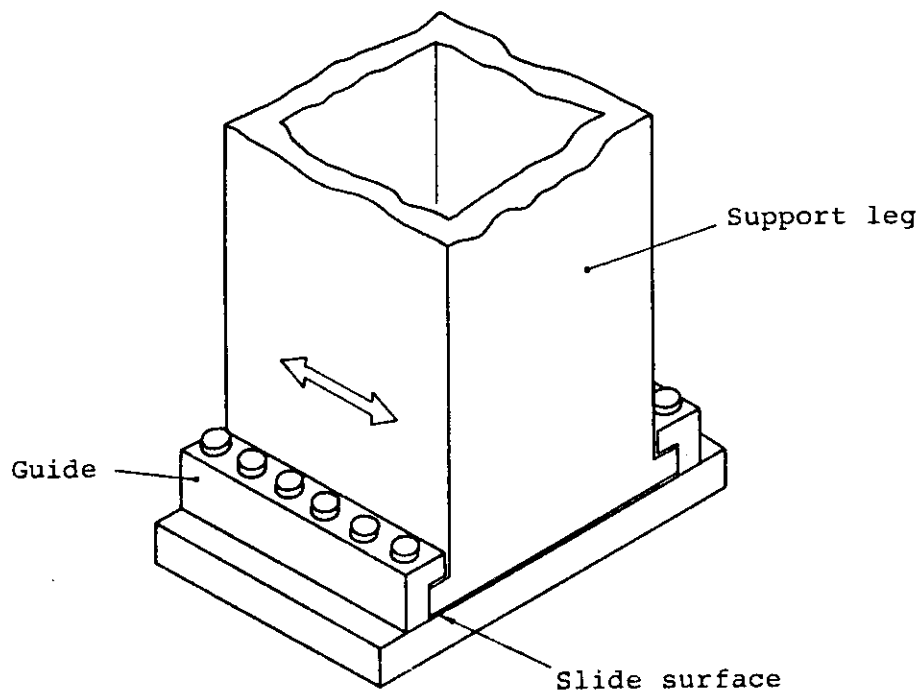


Fig. 3.26 Concept of torus support leg

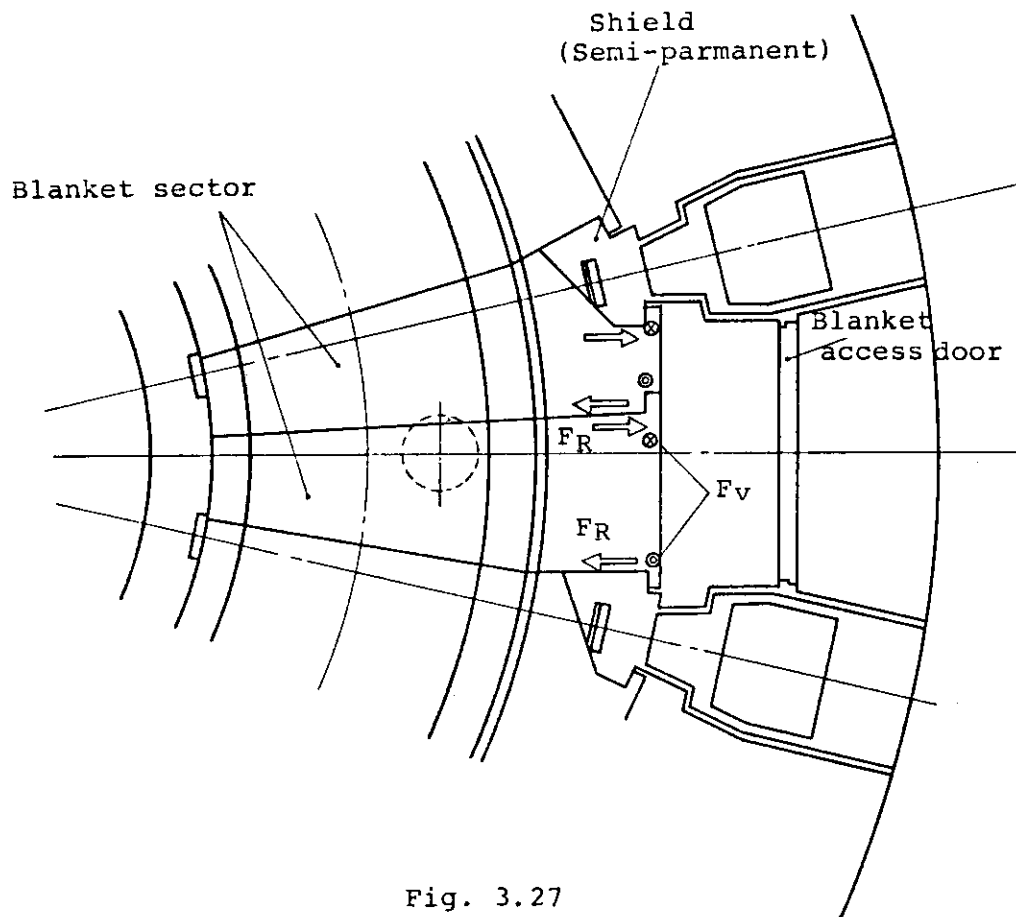


Fig. 3.27

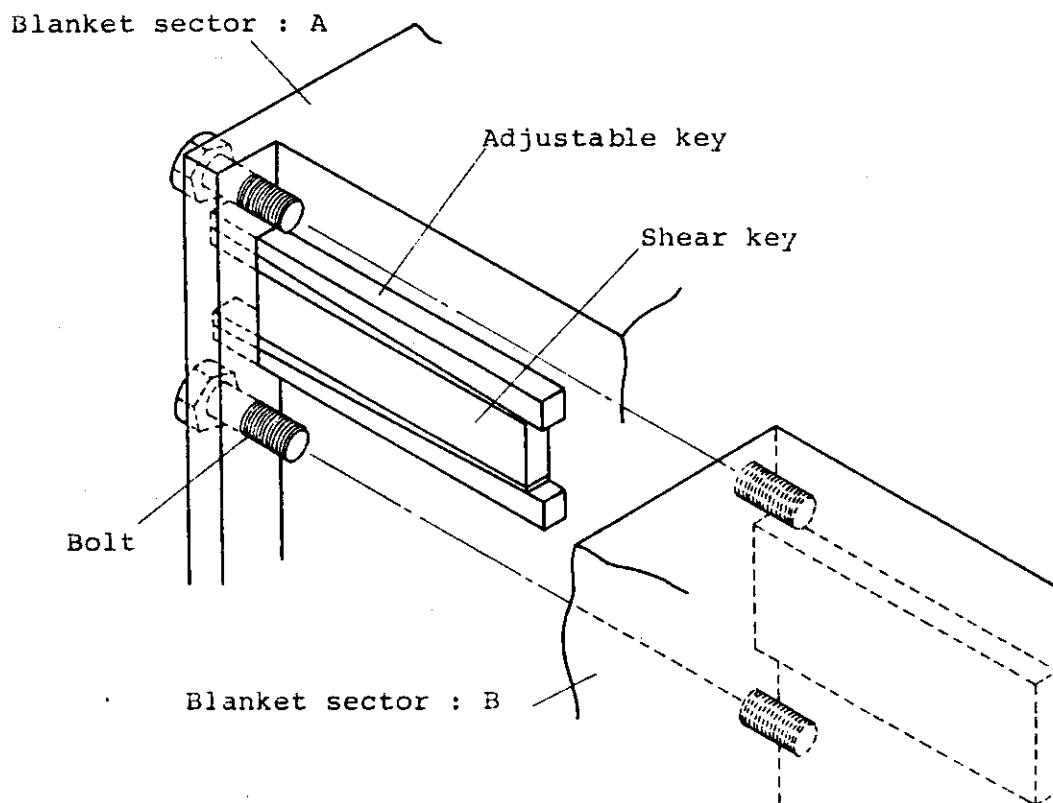


Fig. 3.28 Connecting structure of torus sector

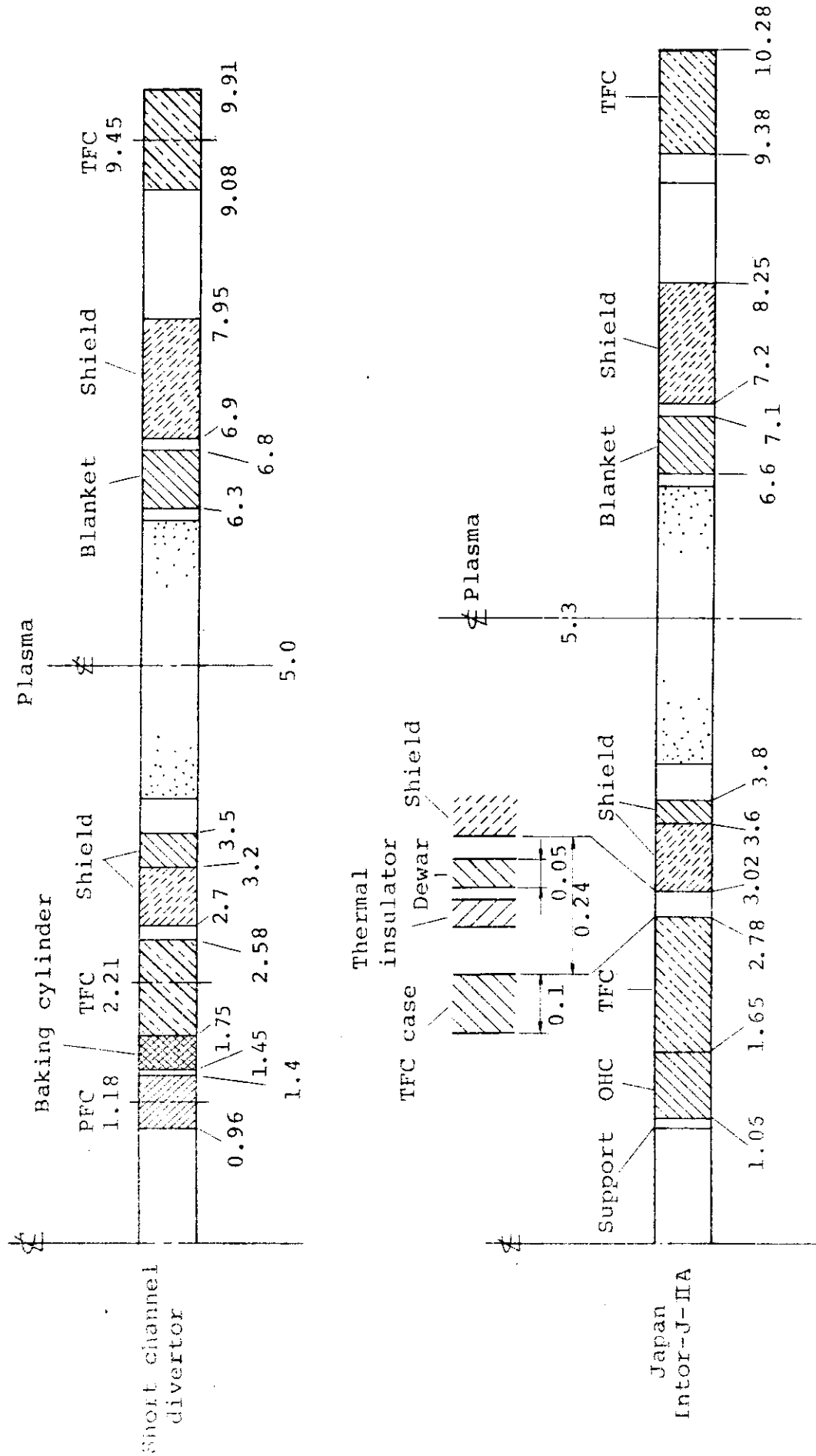


Fig. 3.29 Radial build of short channel divertor concept

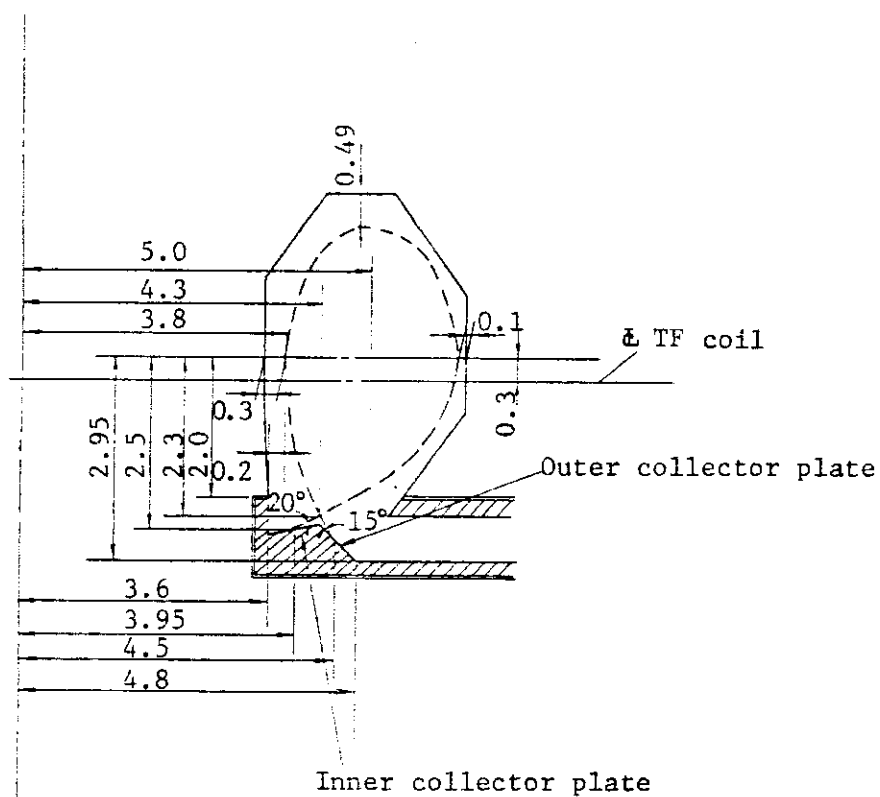


Fig. 3.30 Profile of the divertor region (Case 1)

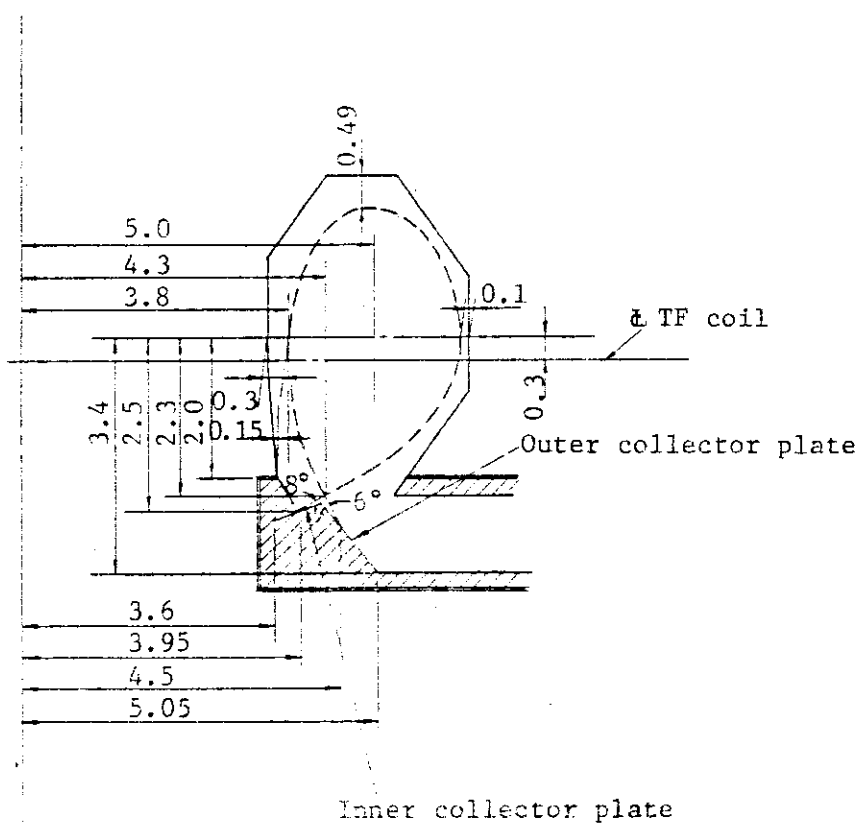


Fig. 3.31 Profile of the divertor region (Case 2)

## 4. Assembly and Maintenance

### 4.1 Torus Dedicated Sectors

#### (1) Torus(blanket) segmentation

Torus(blanket) consists of 24 sectors. (The number of sectors between TF coils is 2.)

Figure 4.1 shows the blanket structure between TF coils. Each blanket structure between TF coils is of equal toroidal span. Each blanket sector which is supported with outer shield structure is connected by flange with semi-permanent shield-post in order to form the torus configuration.

In this concept, each access port serves two blanket sectors which can be removed one after another. The retraction of the first blanket sector is carried out by single straight line motion, the retraction of the second one is carried by two straight line motions.

#### (2) Divertor segmentation

The segmentation of divertor structure is shown in Fig. 4.2. The divertor is segmented as 2 sectors/TF coil and each sector is retracted one after another by single straight oblique line motion.

### 4.2 Reference Assembly/Maintenance

#### 4.2.1 Maintenance scenario and time evaluation

##### (1) Time necessary for access

###### (a) Requirements for access

There are two requirements for access. One is TF coil shutdown time and the other is baking time for removal of tritium.

###### (b) Time for baking

The first wall/blanket/shield are baked using each cooling pipe : high temperature air is flowed into each pipe and they are heated to 150°C. Time for heating to 150°C is 32 hours. Baking is continued for 168 h (1 week). Total time for baking, therefore, needs 200 h (9 days).

###### (c) Time for access

It is possible to begin TF coil shutdown and baking at the same time. Time for TF coil shutdown needs 20 hours. On the other hand, time for baking needs 200 hours. Therefore, time for access needs 200 hours.

- (2) Specific tasks which can be accomplished by hands-on operation  
Hands-on operation is considered as follows;

- (a) Opening/closing of valves
- (b) Connecting/disconnecting of cables of power supply
- (c) Hanging wire on crane hook
- (d) Positioning and installation of auto welder, cutter, etc.
- (e) Visual inspection of various work

- (3) Components considered for maintenance and replacement  
In this consideration the scheduled and the unscheduled maintenance are divided as follows,

Scheduled Divertor, ICRF, LHRF, ECRF, Blanket

Unscheduled TF coil, PF coil, Semi-permanent shield

- (4) Scheduled intervention and time evaluation

- (a) Divertor

Table 4.1 shows the procedure of divertor replacement, and table 4.6 shows the time evaluation for replacement. Time for replacement needs about 19 days.

- (b) Blanket

Table 4.2 shows the procedure of blanket replacement, and table 4.7 shows the time evaluation for replacement. Time for replacement needs about 26 days.

- (c) ICRF

Figures 4.3 and 4.4 show installation of ICRF launcher and replacement of ICRF, respectively. Table 4.3 shows the replacement procedure of all ICRF components, and table 4.8 shows the time evaluation for replacement. When the replacement of blanket which is at the same port as RF is needed, all RF components must be removed before the removal of blanket. Time for replacement needs about 33 days. And disassembly procedures (1) to (9) and assembly procedures (5) to (11) are only needed, when the disassembly/assembly of antenna which is routine work is done. Time for replacement needs 21 days.

- (d) LHRF

Figures 4.5 and 4.6 show installation of and replacement of LHRF, respectively. Table 4.4 shows the replacement procedure of all

LHRF components, and table 4.9 shows the time evaluation for replacement. In both tables disassembly procedures (1) to (9) and assembly procedures (5) to (11) are only needed as same as ICRF replacement, when the disassembly/assembly of launcher is done. Time for replacement needs about 21 days (33 days) as same as that of ICRF.

(e) ECRF

Figures 4.7 and 4.8 show installation of and replacement of ECRF, respectively. Table 4.5 shows the replacement procedure of all ECRF components; and table 4.10 shows the time evaluation for replacement. In both tables, disassembly procedures (1) to (7) and assembly procedures (5) to (9) are only needed as same as ICRF(LHRF) replacement, when the disassembly/assembly of module-A is done. Time for replacement needs about 18 days (28 days).

(5) Unscheduled intervention and time evaluation

Table 4.11 shows the procedure of large scaled maintenance. The procedure of reassembly is basically the opposite procedure of disassembly. The replacement of semi-permanent shield, TF coil, and PF coil must be done up to procedure 12, procedure 16, and procedure 17, respectively.

#### 4.2.2 Maintenance equipment

(1) Access door carrier

Fig. 4.9 shows the access door carrier. As shown in the figure, the access door is jacked up by the clamp arms and removed with the access door carrier.

(2) Bolt runner

Fig. 4.10 shows the bolt runner. This bolt runner runs on the guide rail of the access door and connects mechanically between the access door and the access tunnel. It could be installed and removed easily by the articulated manipulator. Fig. 4.11 shows the access door structure for maintenance.

(3) Auto lip seal welder

Fig. 4.12 shows the auto lip seal welder. It is also installed on the same guide rail of the access door as the bolt-runner by the articulated manipulator.

Welding ----- TIG  
 Shield gas ----- Ar  
 Speed of welding --- 80 cm/min.  
 Weight ----- 10 kg

## (4) Auto lip seal cutter

Fig. 4.13 shows the auto lip seal cutter. It is also installed on the same guide rail as the bolt-runner.

Cutting ----- nibbling

Cutting speed ---- 15 cm/min.

## (5) Auto pipe welder

Fig. 4.14 shows the cross section of the cooling pipe.

Fig. 4.15 shows the auto pipe welder installed on the cooling pipe by the articulated manipulators.

## (6) Overhead manipulator

There are two types of manipulators.

One is power manipulator as shown in Fig. 4.16.

The other is bilateral servo manipulator.

	load capacity
servo manipulator	25 kg
power manipulator	100 kg

## (7) Multi-joint inspection system

This system is developed for the in-vessel and out-vessel inspection. (Fig. 4.17)

<u>USE</u>	◦ Inspection
<u>ARM</u>	◦ Articulated (Universal joint type)
	◦ 17 degrees of freedom
	◦ 1 kg capacity at the tip
<u>CONTROL</u>	◦ Program control
<u>SENSORS</u>	◦ Touch(56), Position(17)
	Limit(34)
<u>ACTUATORS</u>	◦ DC motor
<u>REMARK</u>	This system is a prototype of in-vessel inspection.

MAIN SPECS

Joint Type	Universal Joint
Number of Joint	8
Degree-of-Freedom	17
Number of Sensors	107
Motor Type	DC Motor
Number of Motors	17
Total Length	2250 mm
Weight	23 kg



(8) In-vessel inspection system

Figures 4.18 and 4.19 show the in-vessel inspection system. The prototype of this system is the multi-joint inspection system.

(9) Others

- Overhead crane
- Divertor retraction vehicle
- Blanket retraction vehicle
- Floor-mobile manipulator
- NDT system
- Support frame and several jigs

Table 4.1 Divertor replacement procedure

**\*\* Disassembly \*\***

1. Shutdown and baking
2. Start the cooling of decay heat
3. Transfer and position the bolt-runner on the guide rail of the access door (Articulated manipulator, Transfer vehicle)
4. Disconnect the bolts on the access door (Bolt-runner)
5. Remove the bolt-runner (Articulated manipulator; Transfer vehicle)
6. Transfer and position the auto seal cutter on the guide rail of the access door (Articulated manipulator, Transfer vehicle)
7. Cut the seals on the access door (Auto seal cutter)
8. Remove the auto seal cutter (Articulated manipulator, Transfer vehicle)
9. Position the access door carrier
10. Clamp and remove the access door (Access door carrier)
11. Transfer and position the torque wrench on the divertor flange (Articulated manipulator, Transfer vehicle)
12. Disconnect the bolts of the divertor flange (Torque wrench)
13. Remove the torque wrench (Articulated manipulator, Transfer vehicle)
14. Transfer and position the auto pipe cutter on the cooling pipe (Articulated manipulator, Transfer vehicle)
15. Cut the cooling pipe (Auto pipe cutter)
16. Position the divertor retraction vehicle under the divertor A
17. Remove the divertor A (Divertor retraction vehicle)
18. Position the divertor retraction vehicle under the divertor B
19. Remove the divertor B (Divertor retraction vehicle)

**\*\* Assembly \*\***

1. Install the divertor B (Divertor retraction vehicle)
2. Install the divertor A (Divertor retraction vehicle)
3. Transfer and position the auto pipe welder on the cooling pipe (Articulated manipulator, Transfer vehicle)
4. Weld the cooling pipe (Auto pipe welder)
5. Transfer and position the torque wrench on the divertor flange (Articulated manipulator, Transfer vehicle)

---- At the same time of this work, non-destructive test of the cooling pipes is carried out.----

Table 4.1 (continued)

6. Connect the bolts of the divertor flange (Torque wrench)
7. Remove the torque wrench  
(Articulated manipulator, Transfer vehicle)
8. Install the access door (Access door carrier)
9. Transfer and position the auto seal welder on the guide rail of the access door (Articulated manipulator, Transfer vehicle)
10. Weld the seals on the access door (Auto seal welder)
11. Remove the auto seal welder  
(Articulated manipulator, Transfer vehicle)
12. Transfer and position the bolt-runner on the guide rail of the access door (Articulated manipulator, Transfer vehicle)
13. Connect the bolts on the access door (Bolt-runner)
14. Remove the bolt-runner  
(Articulated manipulator, Transfer vehicle)
15. Bake, evacuate, and NDT

Table 4.2 Blanket replacement procedure

**\*\* Disassembly \*\***

1. Shutdown and baking
2. Start the cooling of decay heat
3. Transfer and position the bolt-runner on the guide rail of the access door (Articulated manipulator, Transfer vehicle)
4. Disconnect the bolts on the access door (Bolt-runner)
5. Remove the bolt-runner (Articulated manipulator, Transfer vehicle)
6. Transfer and position the auto seal cutter on the guide rail of the access door (Articulated manipulator, Transfer vehicle)
7. Cut the seals on the access door (Auto seal cutter)
8. Remove the auto seal cutter  
(Articulated manipulator, Transfer vehicle)
9. Position the access door carrier
10. Clamp and remove the access door (Access door carrier)
11. Transfer and position the torque wrench on the blanket flange and the divertor flange  
(Articulated manipulator, Transfer vehicle)
12. Disconnect the bolts of the blanket flange and the divertor flange  
(Torque wrench)
13. Remove the torque wrench  
(Articulated manipulator, Transfer vehicle)
14. Transfer and position the auto pipe cutter on the cooling pipe  
(Articulated manipulator, Transfer vehicle)
15. Cut the cooling pipe (Auto pipe cutter)
16. Position the divertor retraction vehicle under the divertor A
17. Remove the divertor A (Divertor retraction vehicle)
18. Position the divertor retraction vehicle under the divertor B
19. Remove the divertor B (Divertor retraction vehicle)
20. Position the blanket retraction vehicle under the blanket sector-A
21. Remove the blanket sector-A (Blanket retraction vehicle)
22. Position the blanket retraction vehicle under the blanket sector-B
23. Remove the blanket sector-B (Blanket retraction vehicle)

Table 4.2 (continued)

**\*\* Assembly \*\***

1. Install the blanket sector-B (Blanket retraction vehicle)
2. Install the blanket sector-A (Blanket retraction vehicle)
3. Install the divertor B  
(Divertor retraction vehicle)
4. Install the divertor A  
(Divertor retraction vehicle)
5. Transfer and position the auto pipe welder on the cooling pipe  
(Articulated manipulator, Transfer vehicle)
6. Weld the cooling pipes (Auto pipe welder)
7. Transfer and position the torque wrench on the blanket flange and  
the divertor flange  
(Articulated manipulator, Transfer vehicle)
8. Connect the bolts of the blanket flange and the divertor flange  
(Torque wrench)
9. Remove the torque wrench  
(Articulated manipulator, Transfer vehicle)
10. Install the access door (Access door carrier)
11. Transfer and position the auto seal welder on the guide rail of  
the access door (Articulated manipulator, Transfer vehicle)
12. Weld the seals on the access door (Auto seal welder)
13. Remove the auto seal welder  
(Articulated manipulator, Transfer vehicle)
14. Transfer and position the bolt-runner on the guide rail of the  
access door (Articulated manipulator, Transfer vehicle)
15. Connect the bolts on the access door (Bolt-runner)
16. Remove the bolt-runner  
(Articulated manipulator, Transfer vehicle)
17. Bake, evacuate, and NDT

Table 4.3 Replacement of ICRF antenna

**\*\* Disassembly \*\***

- (1) Shutdown
- (2) Bake and evacuate for tritium removal
- (3) Cool for the removal of decay heat
- (4) Disconnect the bolts of connecting part-A (See Fig. 4.3)
- (5) Cut the lip seal of connecting part-A
- (6) Install the sub-support structure (See Fig. 4.4)
- (7) Cut the vacuum seal between the access door and the antenna
- (8) Cut the cooling pipes
- (9) Remove the antenna
- [10] Remove the support and the sub-support structure
- [11] Remove the access door
- [12] Disconnect the bolts between the support structure for the shield of the antenna and the floor
- [13] Remove the shield with support structure

**\*\* Assembly \*\***

- [1] Install the shield with support structure
- [2] Connect the bolts between the support structure for the shield of the antenna and the floor
- [3] Install the access door
- [4] Install the support and the sub-support structure
- (5) Install the antenna
- (6) Connect(weld) the cooling pipes and NDT
- (7) Weld the vacuum seal between the access door and the antenna, and NDT
- (8) Remove the sub-support structure
- (9) Weld the lip seal of connecting part-A and NDT
- (10) Connect the bolts of connecting part-A
- (11) Bake and evacuate

Table 4.4 Replacement procedure of LHRF launcher

**\*\* Disassembly \*\***

- (1) Shutdown
- (2) Bake and evacuate for tritium removal
- (3) Cool for the removal of decay heat
- (4) Disconnect the bolts of connecting part-A (See Fig. 4.5)
- (5) Cut the lip seal of connecting part-A
- (6) Install the sub-support structure (See Fig. 4.6)
- (7) Cut the vacuum seal between the access door and the antenna
- (8) Cut the cooling pipes
- (9) Remove LHRF launcher
- [10] Remove the support and the sub-support structure
- [11] Remove the access door
- [12] Disconnect the bolts between the support structure for the shield of the antenna and the floor
- [13] Remove the shield with support structure

**\*\* Assembly \*\***

- [1] Install the shield with support structure
- [2] Connect the bolts between the support structure for the shield of the antenna and the structure
- [3] Install the access door
- [4] Install the support and the sub-support structure
- (5) Install LHRF launcher
- (6) Connect(weld) the cooling pipes and NDT
- (7) Weld the vacuum seal between the access door and the antenna, and NDT
- (8) Remove the sub-support structure
- (9) Weld the lip seal of the connecting part-A, and NDT
- (10) Connect the bolts of the connecting part-A
- (11) Bake and evacuate

Table 4.5 Replacement procedure of ECRF

**\*\* Disassembly \*\***

- (1) Shutdown
- (2) Bake and evacuate for tritium removal
- (3) Cool for the removal of decay heat
- (4) Remove the module-B with the overhead crane
- (5) Cut the vacuum seal between the access door and the module-A
- (6) Cut the cooling pipes
- (7) Withdraw and remove the module-A
- [8] Remove the support structure
- [9] Remove the access door
- [10] Disconnect the bolts between the support structure for the shield of the module-A and the floor
- [11] Remove the shield with support structure

**\*\* Assembly \*\***

- [1] Install the shield with support structure
- [2] Connect the bolts between the support structure for the shield of the module-A and the floor
- [3] Install the access door
- [4] Install the support structure
- (5) Install the module-A
- (6) Weld the cooling pipes and NDT
- (7) Weld the vacuum seal between the access door and the module-A and NDT
- (8) Install the module-B
- (9) Bake and evacuate



Table 4.6 Time required for divertor replacement

**\*\* Disassembly \*\***

1 ~ 2	After shutdown, start baking and the cooling of decay heat	200 hours
3 ~ 5	Disconnect the bolts on the access door	8 hours
6 ~ 8	Cut the vacuum seals on the access door	2 hours
9 ~ 10	Remove the access door	5 hours
11 ~ 13	Disconnect the bolts between the divertor flanges	16 hours
14 ~ 15	Cut the cooling pipes	6 hours
16 ~ 17	Remove the divertor A	10 hours
18 ~ 19	Remove the divertor B	10 hours
		<hr/> 257 hours

**\*\* Assembly \*\***

1	Install the divertor B	20 hours
2	Install the divertor A	20 hours
3 ~ 4	Weld the cooling pipes	5 hours
5 ~ 7	Connect the bolts between the divertor flanges	16 hours
8	Install the access door	10 hours
9 ~ 11	Weld the vacuum seals on the access door	2 hours
12 ~ 14	Connect the bolts on the access door	8 hours
15	Bake, evacuate, and NDT	104 hours
		<hr/> 185 hours

Sum total: 442 hours  
(19 days)

Table 4.7 Time required for blanket replacement

**\*\* Disassembly \*\***

1 ~ 2	After shutdown, start baking and the cooling of decay heat	200 hours
3 ~ 5	Disconnect the bolts on the access door	8 hours
6 ~ 8	Cut the vacuum seals on the access door	2 hours
9 ~ 10	Remove the access door	5 hours
11 ~ 12	Disconnect the bolts between the blanket flanges and the divertor flanges	46 hours
14 ~ 15	Cut the cooling pipes	18 hours
16 ~ 17	Remove the divertor A	10 hours
18 ~ 19	Remove the divertor B	10 hours
20 ~ 21	Remove the blanket sector-A	15 hours
22 ~ 23	Remove the blanket sector-B	15 hours
		<hr/> 329 hours

**\*\* Assembly \*\***

1	Install the blanket sector-B	30 hours
2	Install the blanket sector-A	30 hours
3	Install the divertor B	20 hours
4	Install the divertor A	20 hours
5 ~ 6	Weld the cooling pipes	17 hours
7 ~ 9	Connect the bolts between the blanket flanges and the divertor flanges	46 hours
10	Install the access door	10 hours
11 ~ 13	Weld the vacuum seals on the access door	2 hours
14 ~ 16	Connect the bolts on the access door	8 hours
17	Bake, evacuate and NDT	104 hours
		<hr/> 287 hours

Sum total: 616 hours  
(26 days)

Table 4.8 Time required for ICRF replacement

**\*\* Disassembly \*\***

(1)~(3)	After shutdown, start baking and the cooling of decay heat	200 h
(4)~(5)	Cut the connecting part-A	15 h
(6)	Install the sub-support structure	8 h
(7)~(9)	Remove the antenna	63 h
[10]	Remove the support and the sub-support structure	40 h
[11]	Remove the access door	26 h
[12]~[13]	Remove the shield with support structure	50 h
		<hr/> 402 h

**\*\* Assembly \*\***

[1]~[2]	Install the shield with support structure	75 h
[3]	Install the access door	45 h
[4]	Install the support and the sub-support structure	47 h
(5)~(7)	Install the antenna	86 h
(8)	Remove the sub-support structure	6 h
(9)~(10)	Connect the connecting part-A	22 h
(11)	Bake, evacuate, and NDT	104 h
		<hr/> 385 h

Sum total: 787 h  
(33 days)

Table 4.9 Time required for LHRF replacement

**\*\* Disassembly \*\***

(1)~(3)	After shutdown, start baking and the cooling of decay heat	200 h
(4)~(5)	Cut the connecting part-A	15 h
(6)	Install the sub-support structure	8 h
(7)~(9)	Remove the launcher	63 h
[10]	Remove the support and the sub-support structure	40 h
[11]	Remove the access door	26 h
[12]~[13]	Remove the shield with support structure	50 h
		<hr/> 402 h

**\*\* Assembly \*\***

[1]~[2]	Install the shield with support structure	75 h
[3]	Install the access door	45 h
[4]	Install the support and the sub-support structure	47 h
(5)~(7)	Install the launcher	86 h
(8)	Remove the sub-support structure	6 h
(9)~(10)	Connect the connecting part-A	22 h
(11)	Bake, evacuate, and NDT	104 h
		<hr/> 385 h

Sum total: 787 h  
(32 days)

Table 4.10 Time required for ECRF replacement

**\*\* Disassembly \*\***

(1)~(3)	After shutdown, start the cooling of decay heat	200 h
(4)	Remove the module-B	32 h
(5)~(7)	Remove the module-A	24 h
[8]	Remove the support structure	28 h
[9]	Remove the access door	26 h
[10]~[11]	Remove the shield with support structure	34 h
		<hr/> 344 h

**\*\* Assembly \*\***

[1]~[2]	Install the shield with support structure	51 h
[3]	Install the access door	45 h
[4]	Install the support structure	42 h
(5)~(7)	Install the module-A	34 h
(8)	Install the module-B	48 h
(9)	Bake, evacuate, and NDT	104 h
		<hr/> 324 h

Sum total: 668 h  
(28 days)

Table 4.11 Procedure of large scaled maintenance

1. Shutdown and baking
2. Disconnect the electric line
3. Remove the belljar dome
4. Remove the upper PF coils
5. Remove the upper intercoil support beam
6. Remove the RF
7. Remove the access door
8. Cut the cooling pipes
9. Remove the upper part of the vacuum boundary of cryostat
10. Remove the divertor
11. Remove the blanket module
12. Remove the shield structure
13. Remove the support leg for torus (shield)
14. Lower the lower PF coils on the floor
15. Remove the lower intercoil support beam
16. Remove the TF coils
17. Remove the lower PF coils

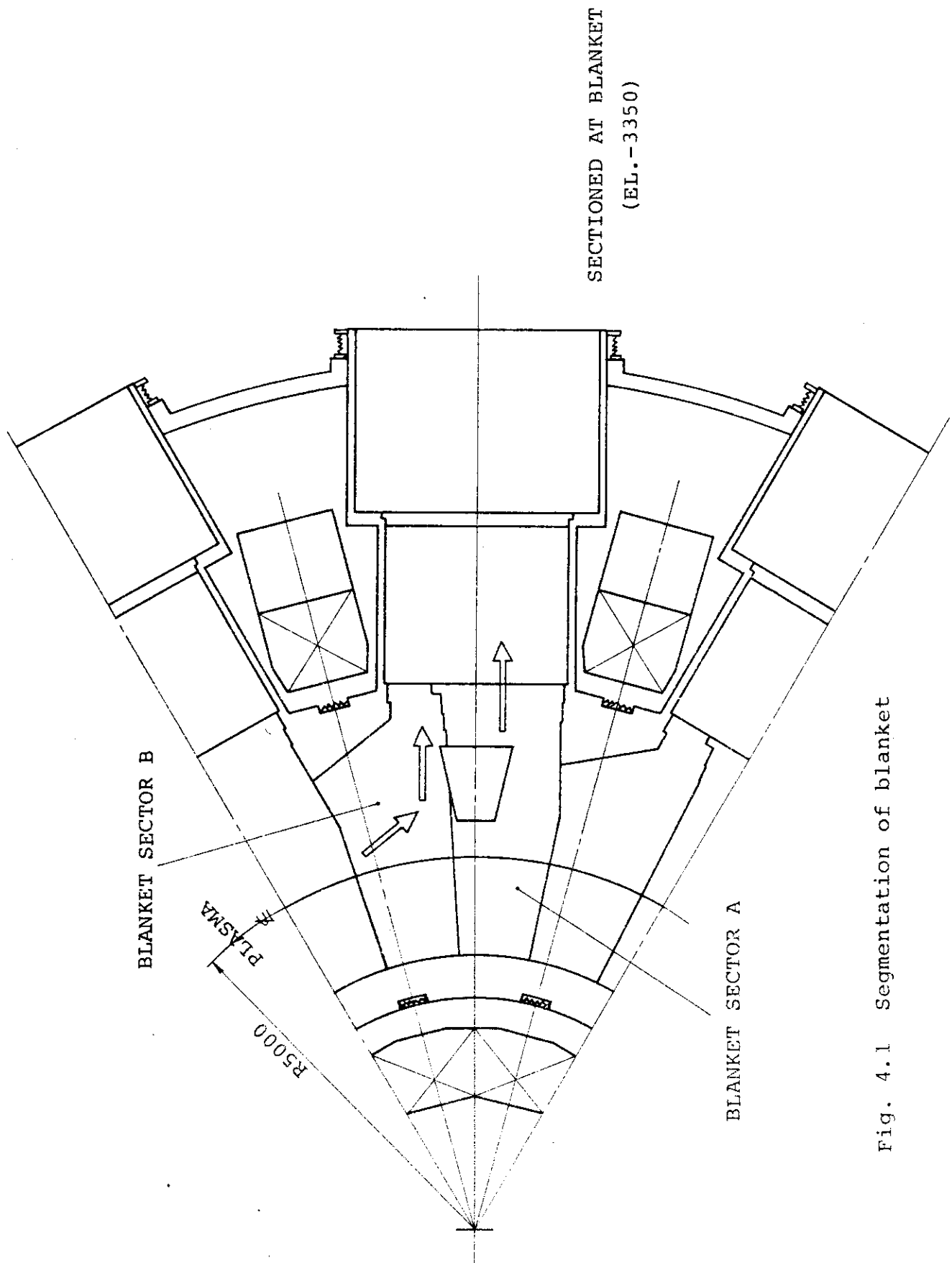


Fig. 4.1 Segmentation of blanket

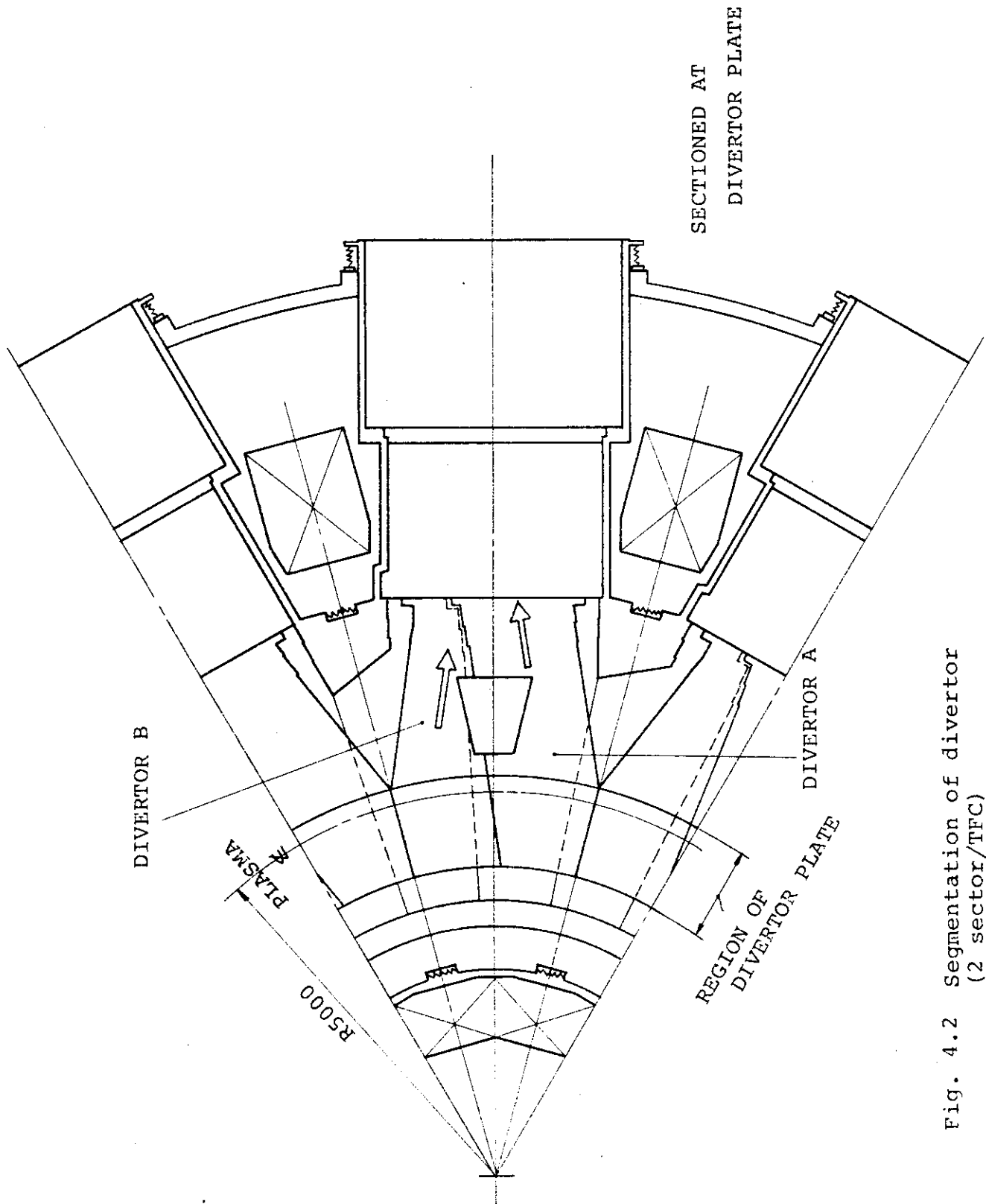


Fig. 4.2 Segmentation of divertor  
(2 sector/TFC)

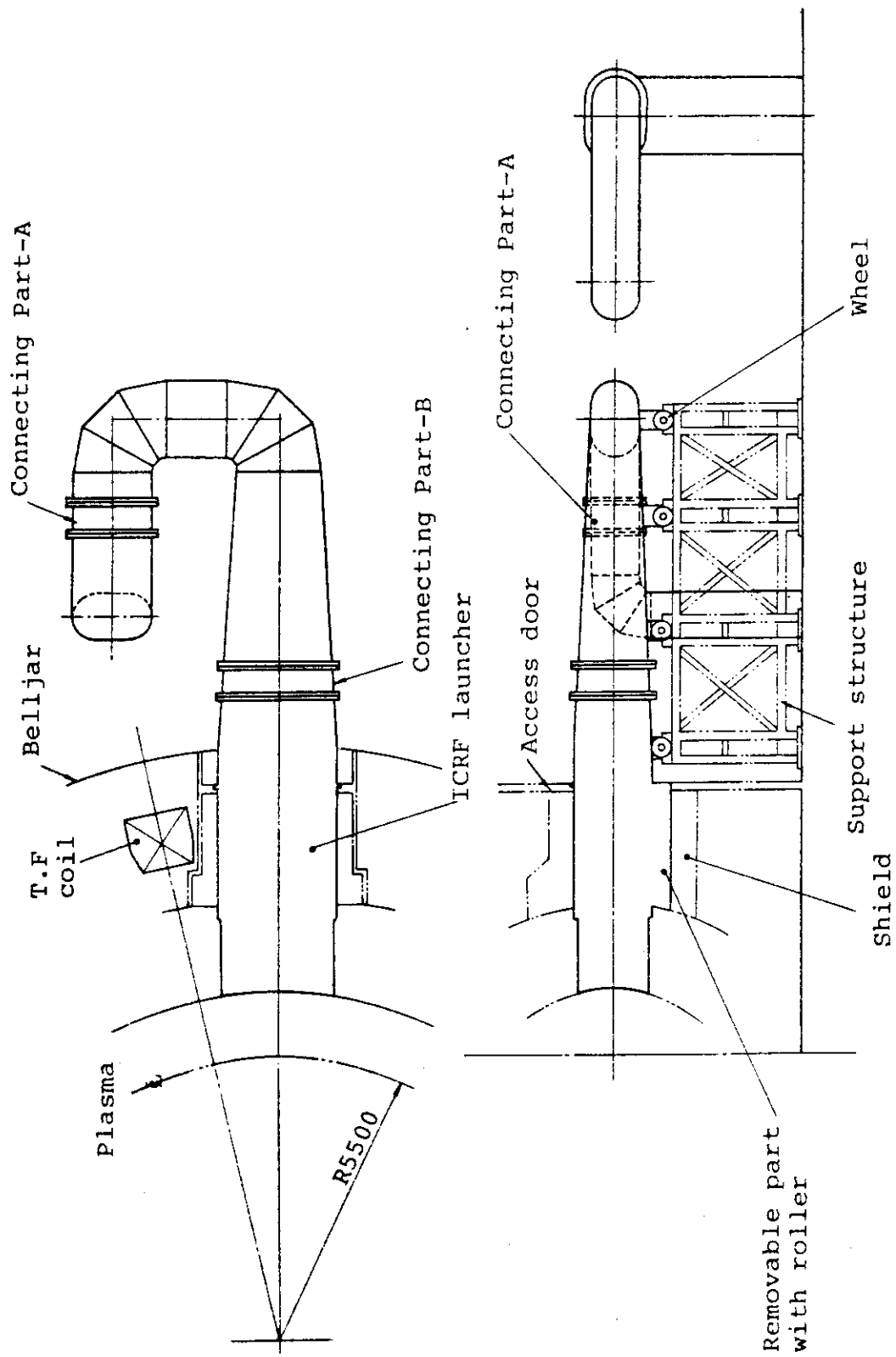


Fig. 4.3 Installation of ICRF launcher



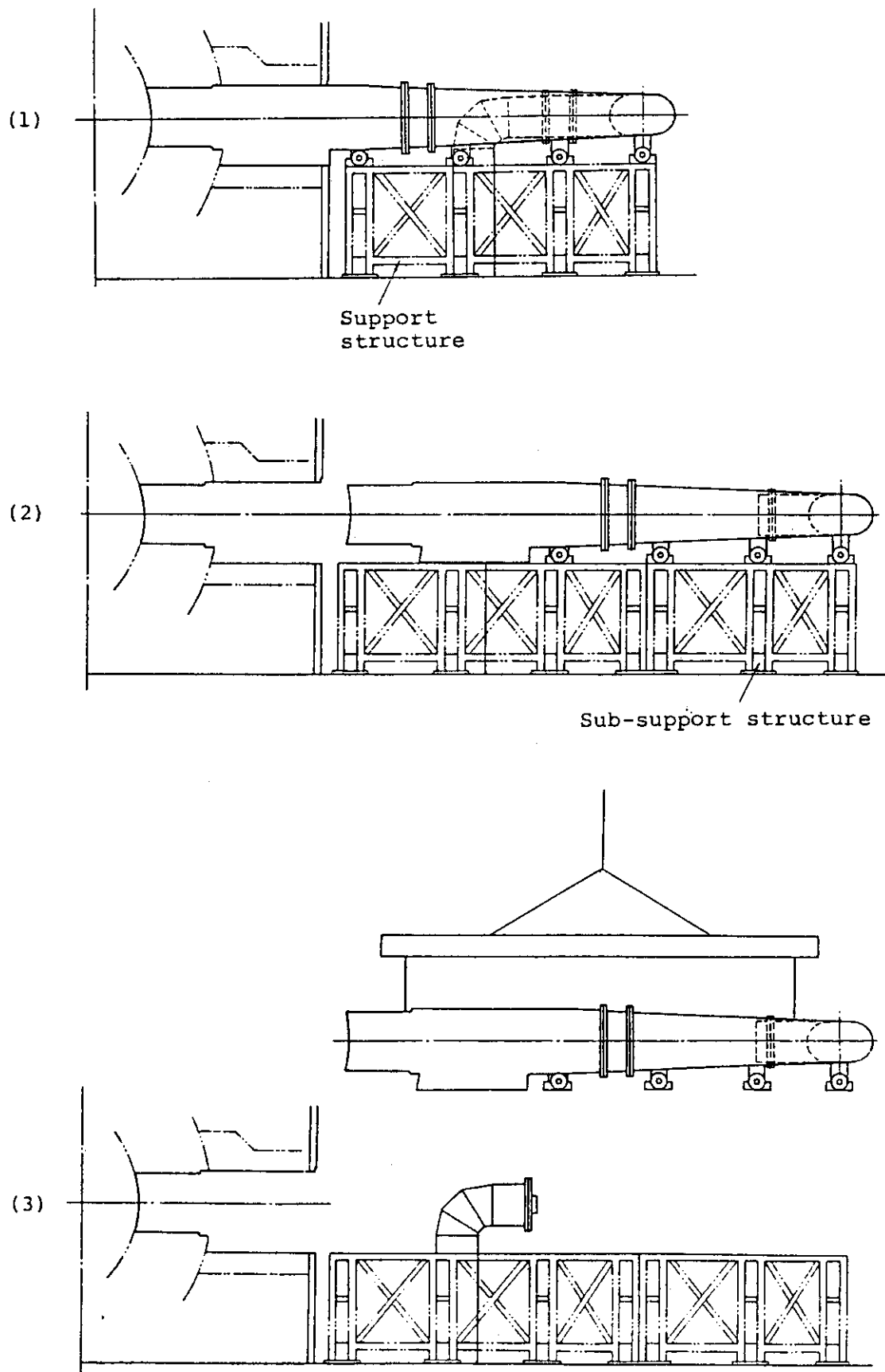


Fig. 4.4 Replacement of ICRF

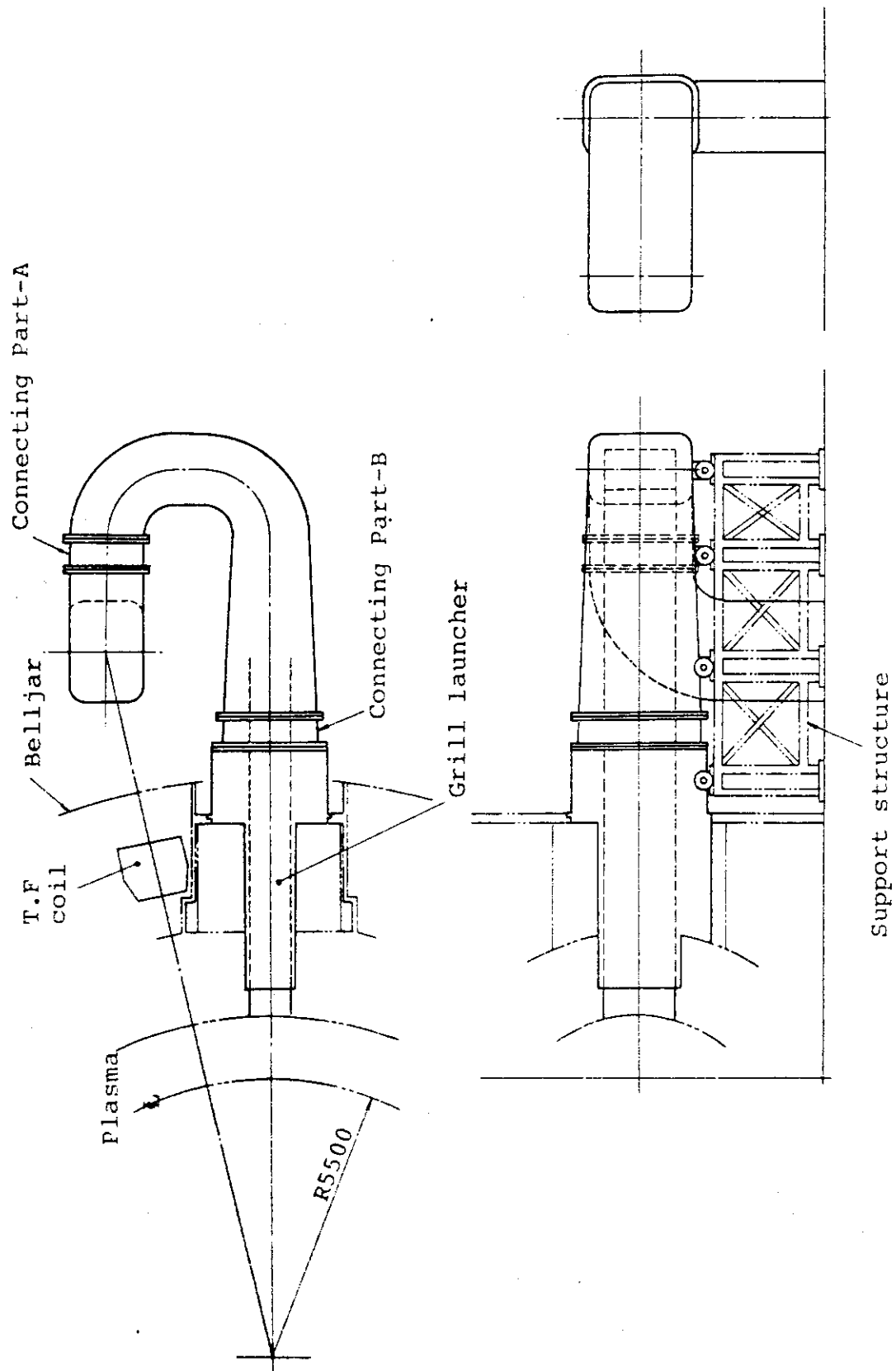


Fig. 4.5 Installation of LHRF

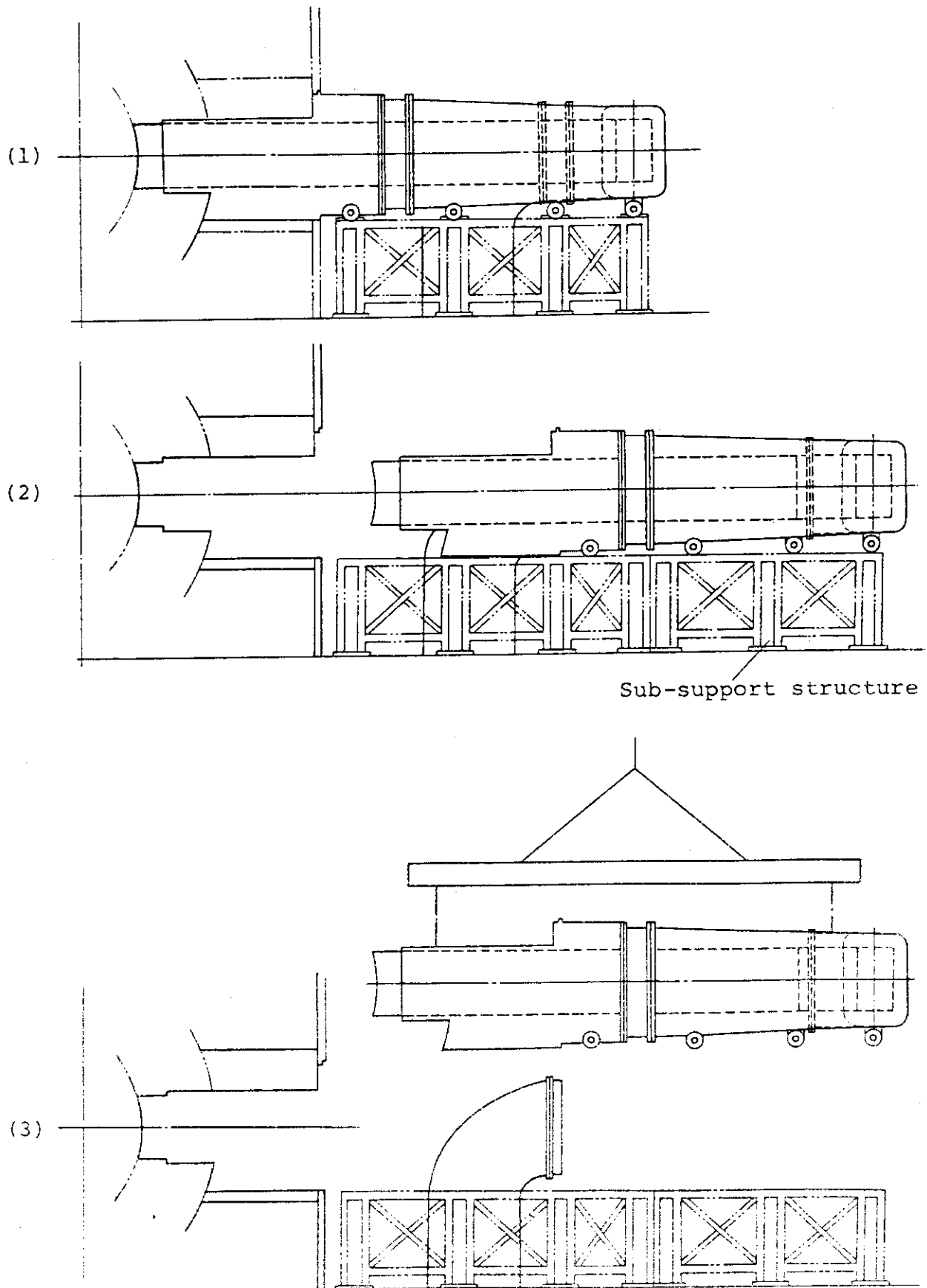


Fig. 4.6 Replacement of LHRF

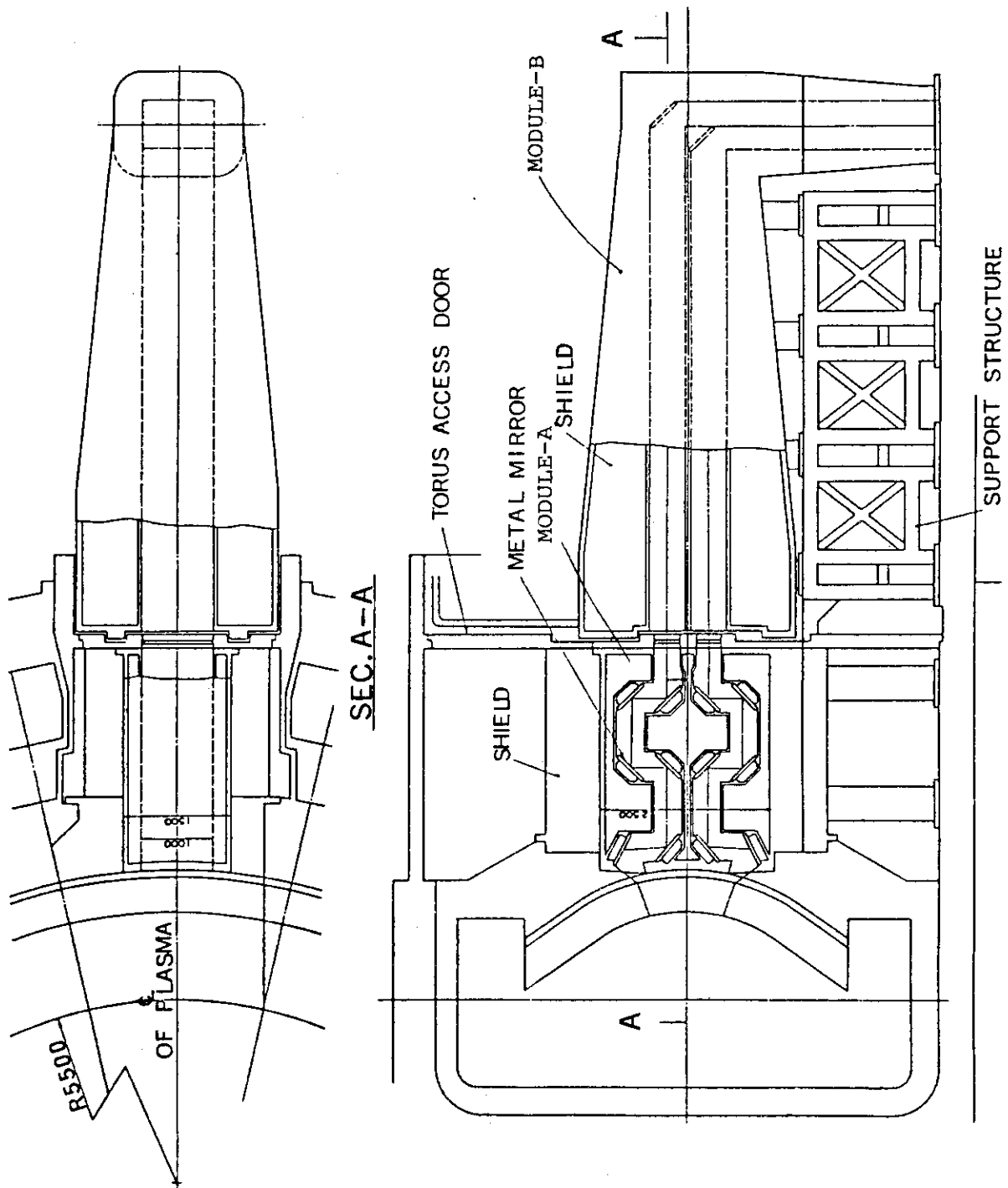


Fig. 4.7 Installation of ECRF

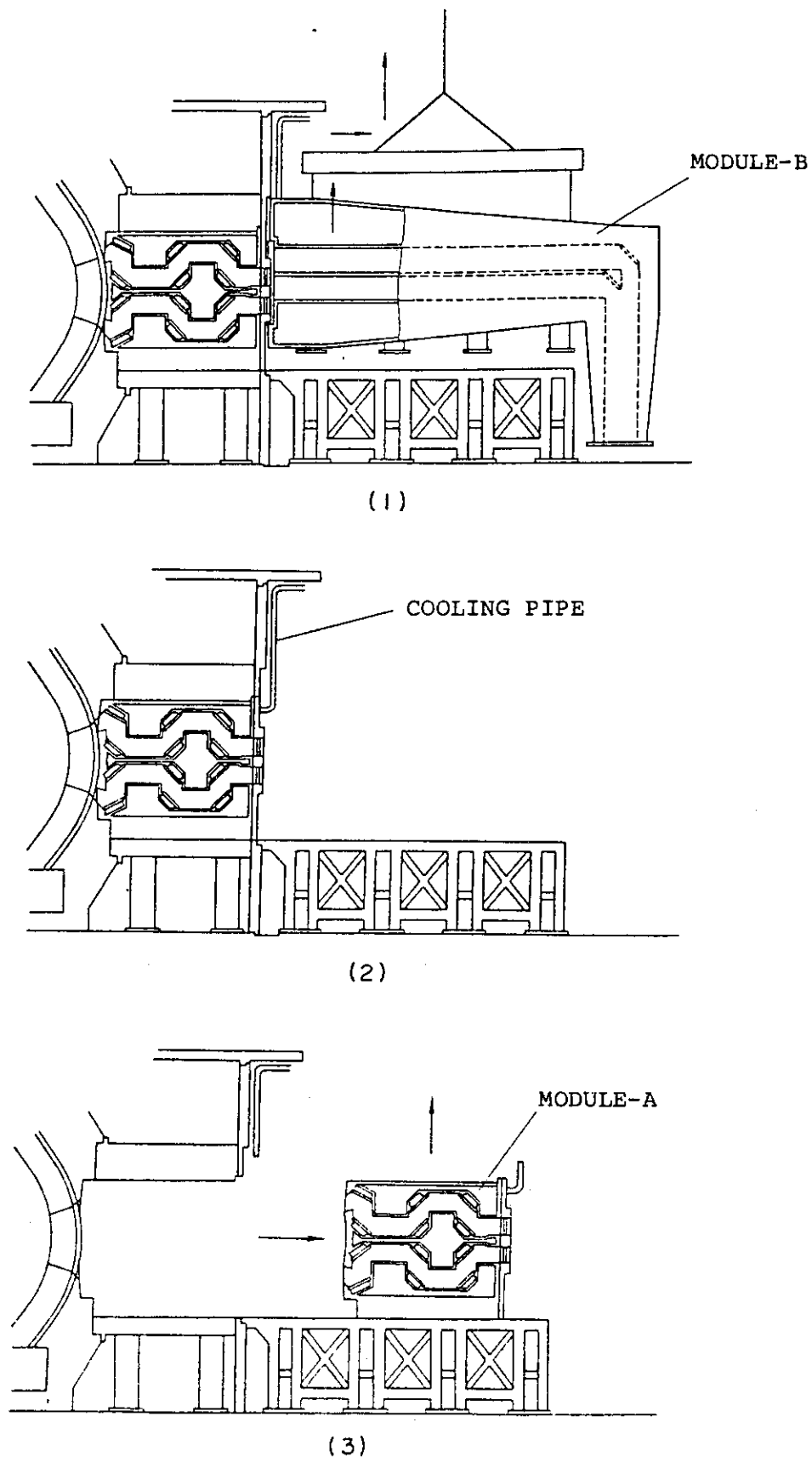


Fig. 4.8 Replacement of ECRF

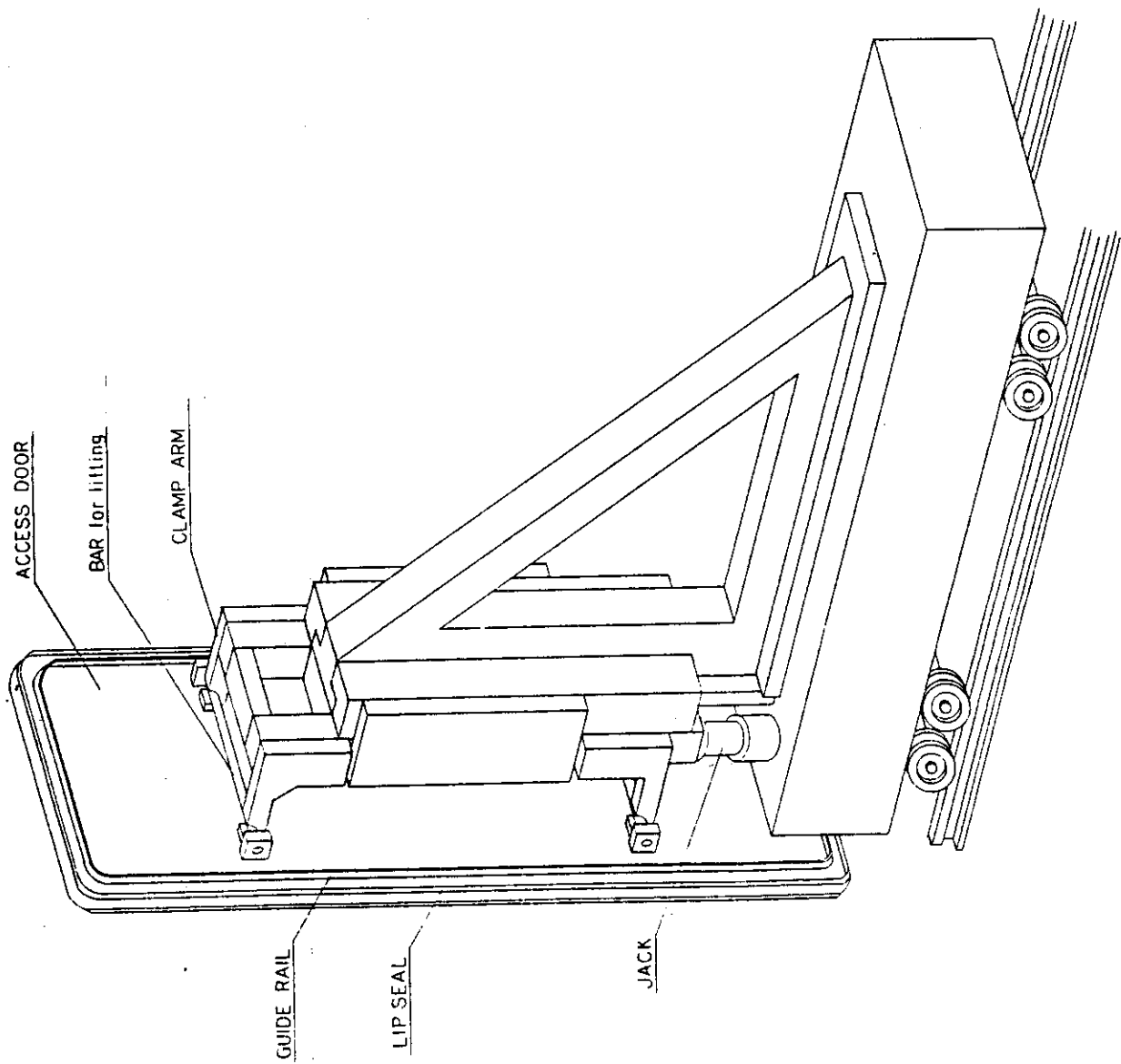


Fig. 4.9 Access door carrier

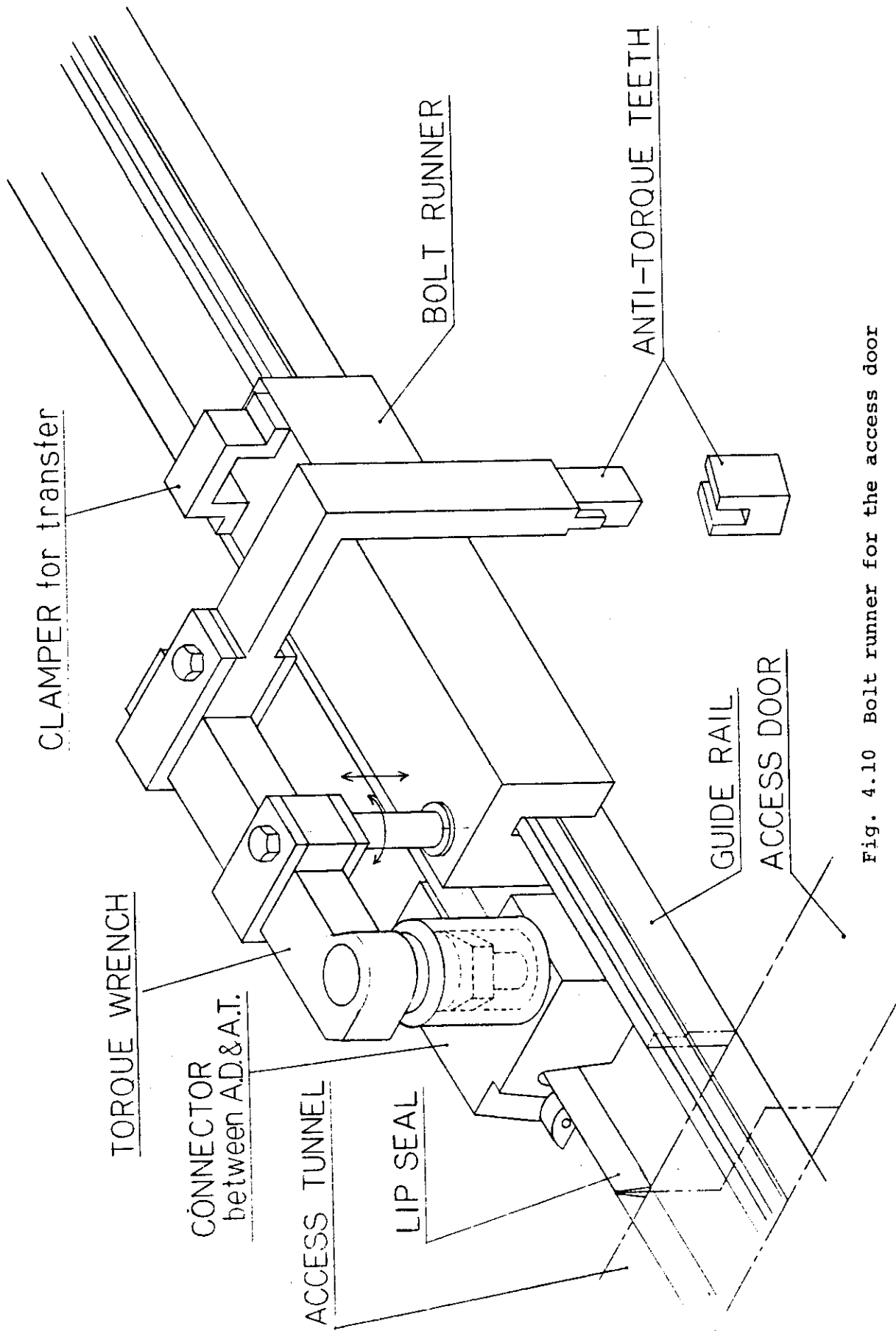


Fig. 4.10 Bolt runner for the access door

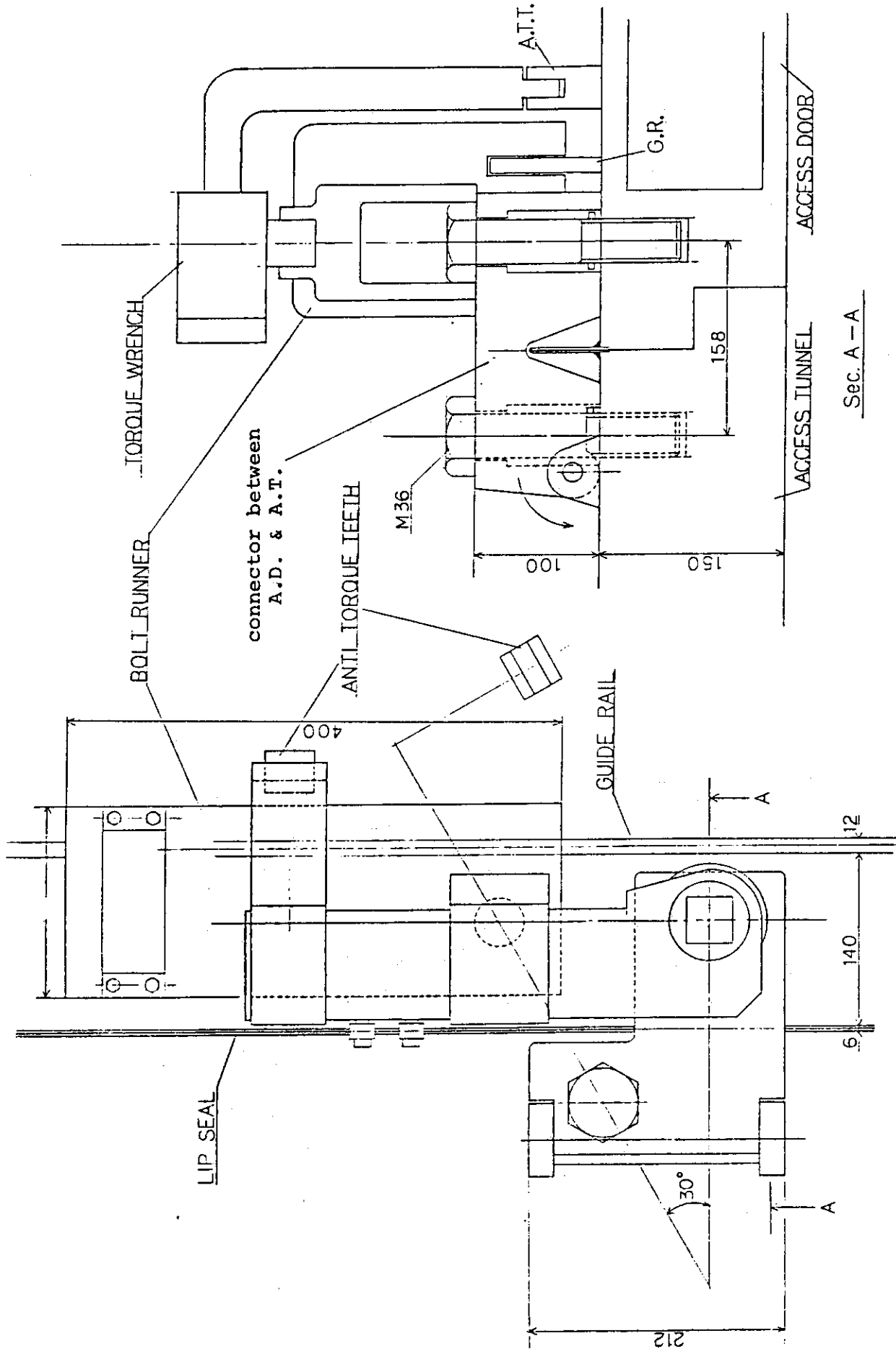


Fig. 4.11 Access door structure for maintenance



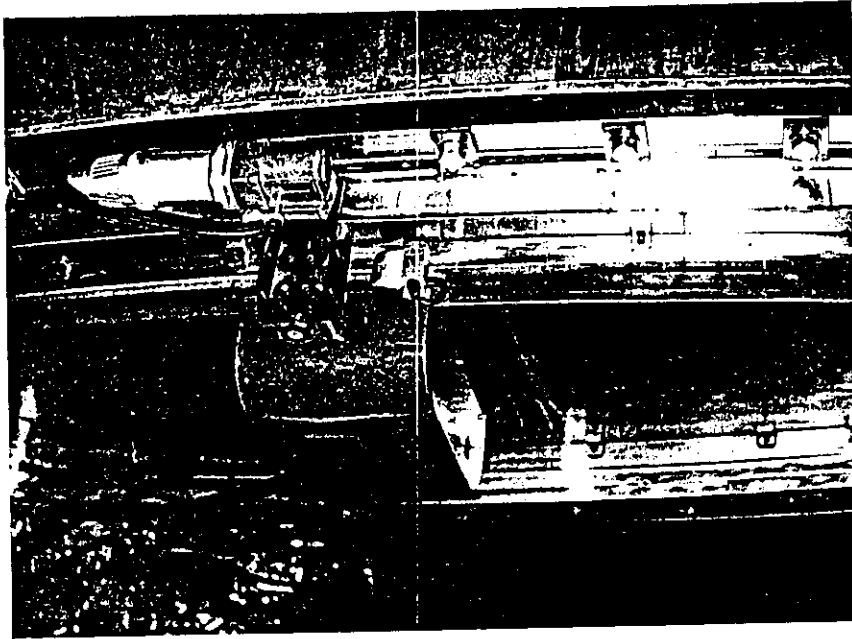


Fig. 4.13 Auto lip seal cutter on the access door

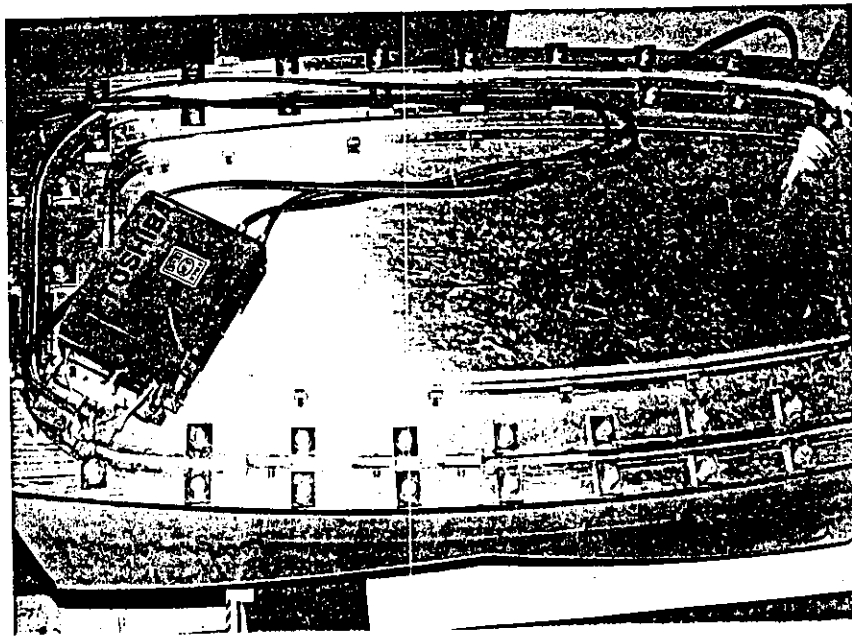


Fig. 4.12 Auto lip seal welder on the access door

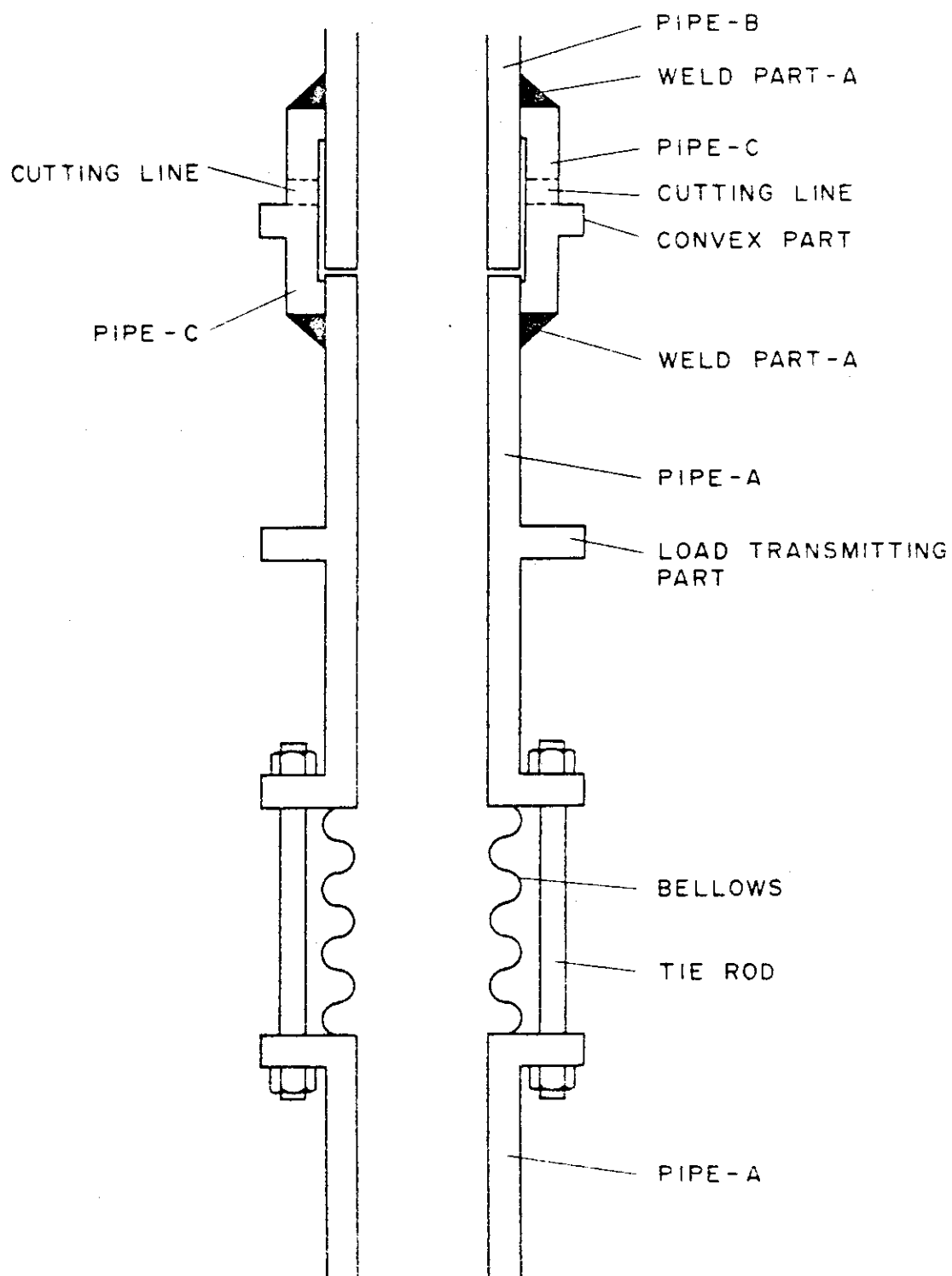


Fig. 4.14 Cooling pipe structure for maintenance

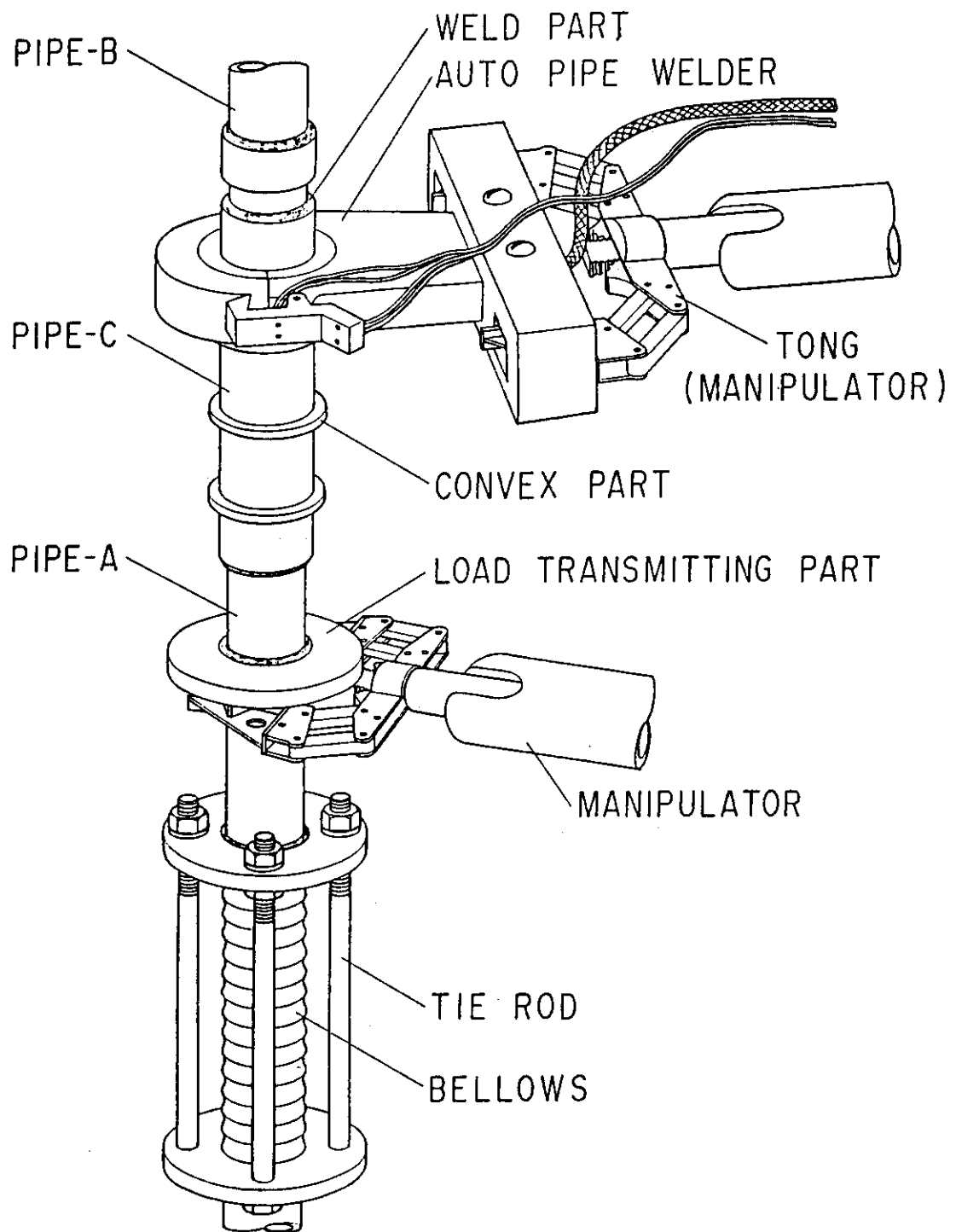


Fig. 4.15 Cooling pipe welding concept

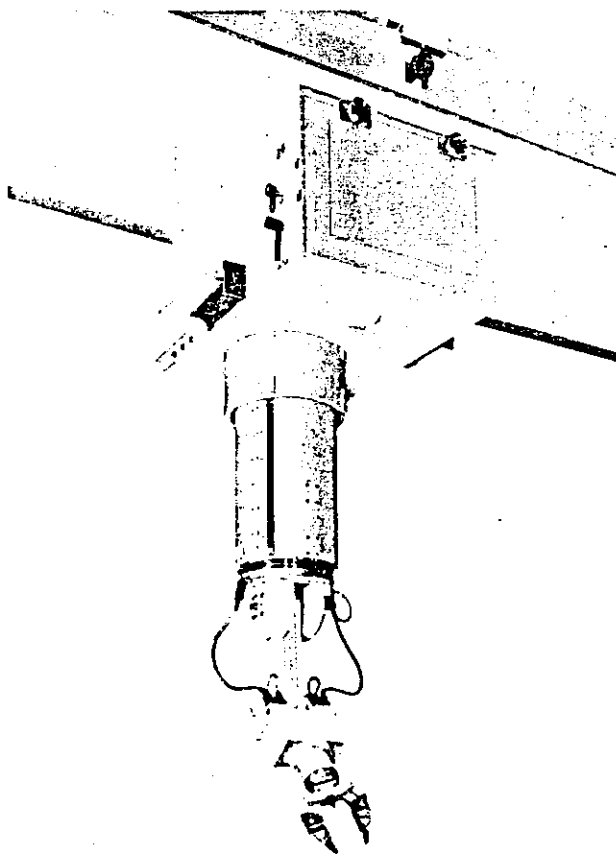


Fig. 4.16 Power manipulator (overhead crane type)

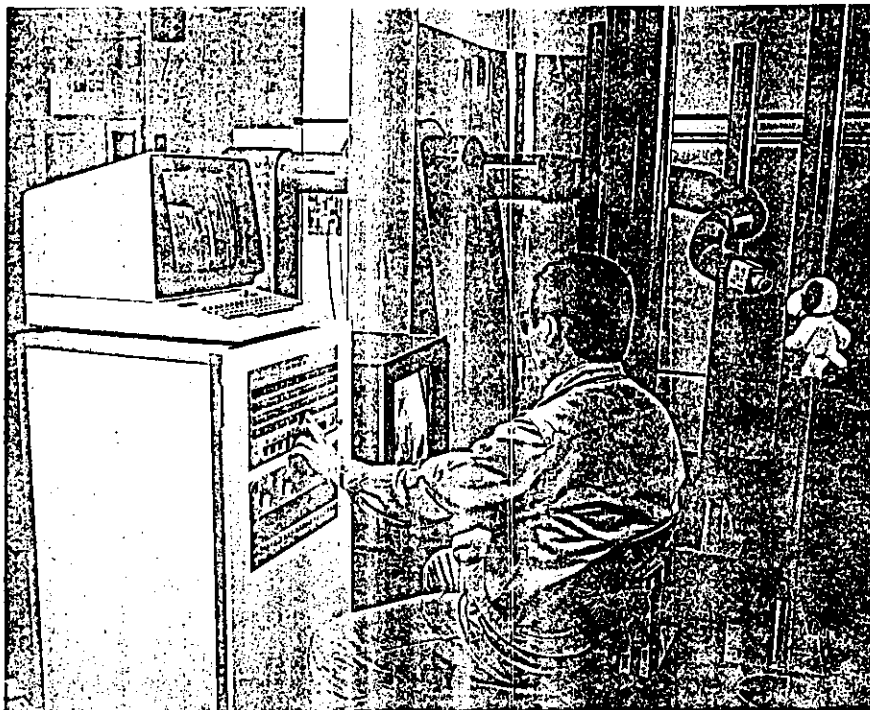


Fig. 4.17 Multi-joint inspection system

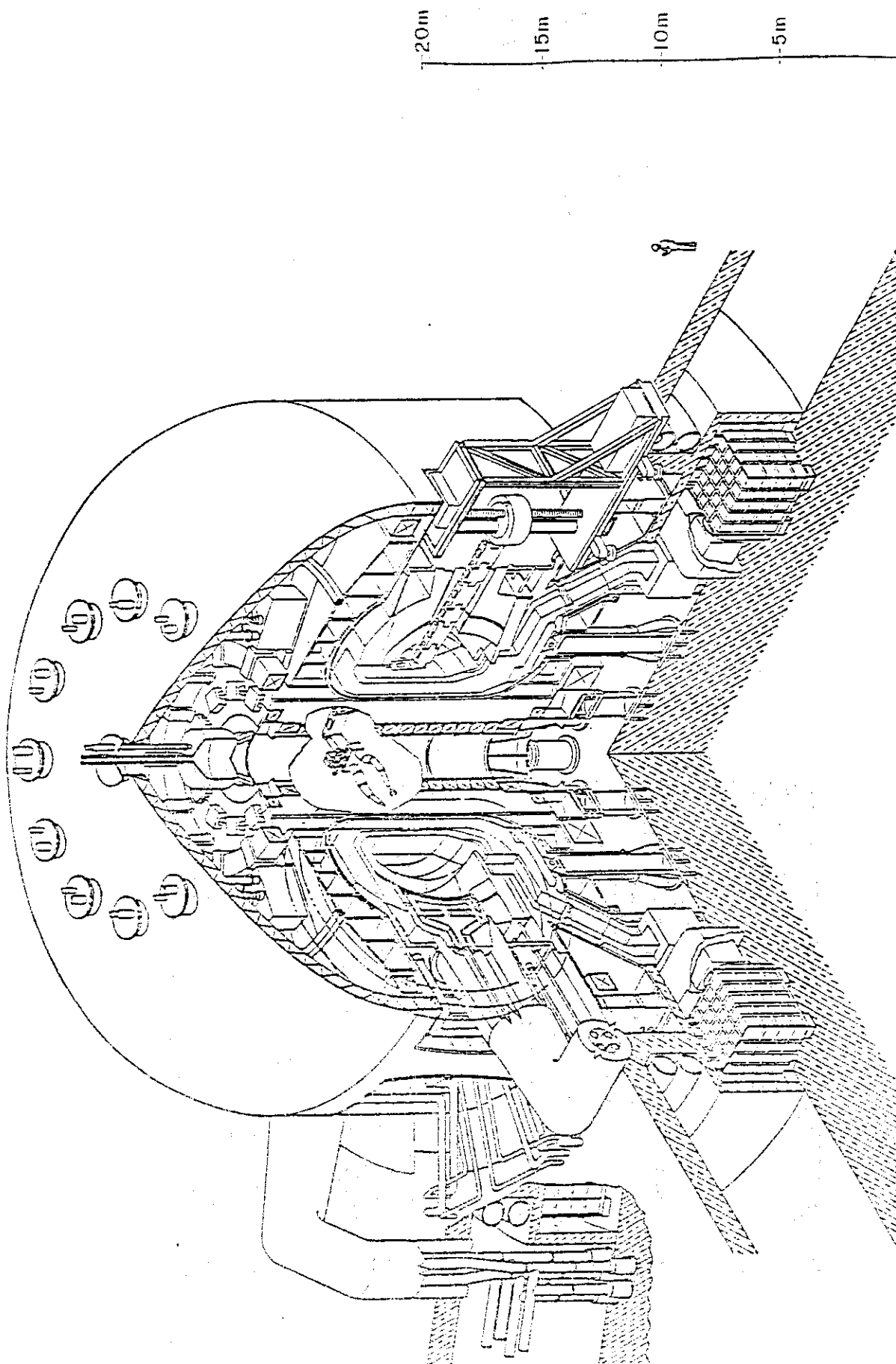


Fig. 4.18 In-vessel inspection system

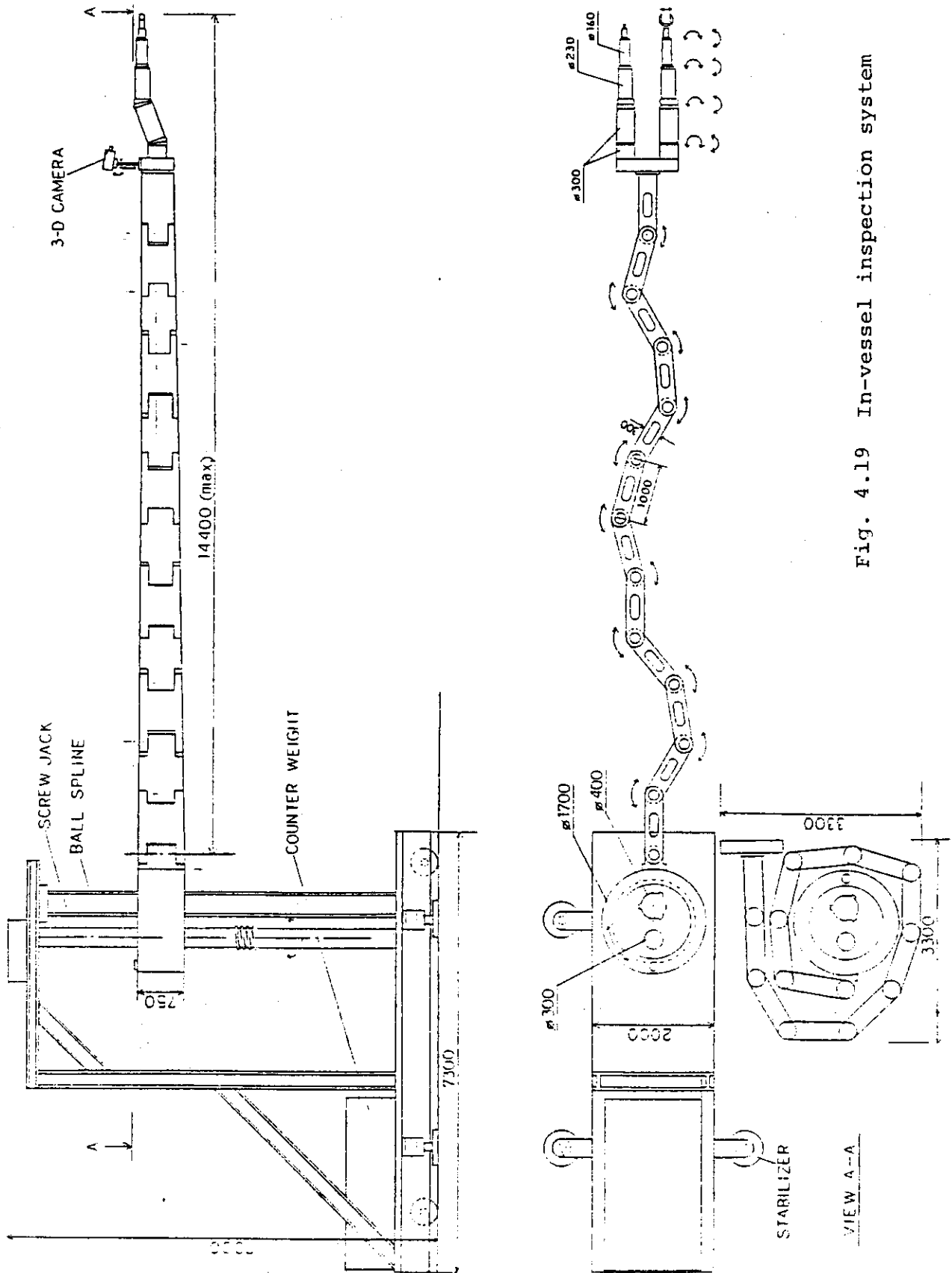


Fig. 4.19 In-vessel inspection system

### 4.3 Alternative assembly and maintenance scheme

The objective of the study is to develop a new design concept with a reliable, feasible and simple maintenance scheme.

#### (1) Basic considerations

Maintenance considerations must be established at the outset of the reactor design study as the fundamental feature in the development of the reactor configuration.

Following basic maintenance philosophy was established for the conceptual design.

- ① The maximum dose rate of  $2.5 \text{ mrem h}^{-1}$  is specified in the reactor room 24 hours after shutdown so that "hands-on" maintenance is performed for normal operation without removing the torus shield.
- ② The tokamak will be designed to be maintained and repaired by the use of existing technology or that developed in the near future for remote maintenance equipment such as manipulators, viewing systems and transfer mechanisms.

#### (2) Torus segmentation and maintenance scheme

Torus segmentation is the important consideration for maintenance. Torus segmentation equal to the number of TF coils is desirable to establish the simplest and the most reliable maintenance scheme with single straight-line radial motion. However, removal of all of the first wall region by single straight-line motion needs the enlarged TF coils. In order to avoid the unnecessary enlargement of TF coils, a part of the first wall is remained in the reactor with permanent shield.

It is supposed that a part of the first wall which is eroded less than  $0.1 \text{ mm}$  during the lifetime of INTOR ( $3 \text{ MW}\cdot\text{y}/\text{m}^2$ ) can be considered as a permanent structure. Erosion thickness of the first wall on coordinate along poloidal direction from null point is shown in Fig. 4.20. Charge exchange particles are distributed locally in the vicinity of the divertor. The erosion thickness of the first wall within  $1 \text{ m}$  in distance from null point is estimated more than  $0.1 \text{ mm}$  as shown in this figure, and this part of the first wall must be removed for maintenance.

Increase of about  $300 \text{ mm}$  in bore of TF coils enables this part of the first wall to be withdrawn with radial straight motion through the access port. Thus, the bore of the TF coil is  $6.8 \text{ m} \times 9.26 \text{ m}$ . Plan sectional views in this configuration are shown in Fig. 4.21.

The reliability of the first wall integrated with permanent shield is obtained by placing it a little behind normal first wall position.

The divertor is also segmented into 12 sectors toroidally and withdrawn with single straight-line radial motion. In order to enlarge the space for divertor removal, the outboard shield is supported by the support shelves provided in the permanent shield post. It is lifted up from the shelves by the lifting jack inserted into the divertor access port when removed. Concept of torus segmentation is illustrated in Fig. 4.22.

#### (3) Maintenance

##### 1) Design conditions

- ① Personnel access to the outside of the shield is possible after 24 hours of reactor shut-down.
- ② Tight containment transfer units are not used, since the plasma chamber and the components to be transferred is sufficiently backed out before breaking the vacuum boundary and cooled during the maintenance.

- ③ Defective components are transferred to the maintenance facility for repair and replacement and are substituted by spare components.
- ④ Weights of a blanket module and a divertor module are 270 tons and 50 tons, respectively.

## 2) Maintenance procedure

The removal procedure of the blanket module is shown in Table 4.12 and concept of blanket module removal in Fig. 4.23.

As special shield plugs are inserted into the space, where the components such as the divertor module and the duct of the heating system are placed during normal operation, unsealing the plasma vacuum boundary, disconnecting the bolts and releasing the clamps of the components could be performed by personnel access.

The divertor module is extracted with divertor shield structure by a multi-cylinder jack. This shield is extended outward for divertor removal as shown in Fig. 4.24.

## 3) Blanket module transfer machine

The blanket module transfer machine is shown in Fig. 4.25.

The blanket module transfer machine is composed of roller forks and a travelling system. The roller forks are inserted under the blanket module and jack it up a little to transfer it. The roller forks comprise lifting jacks and endless rollers with side rollers to ensure the direction of motion.

Periodic travelling mechanism by hydraulic cylinders is adopted for the travelling system. Hooks in front of the travelling system, biting projections placed at regular intervals, are pulled by the hydraulic cylinders to travel.

Water is used as fluid for the hydraulic system of the hydraulic cylinders and the lifting jacks, considering easy treatment after its leakage in the plasma vacuum vessel. A hydraulic circuit of the blanket module transfer machine is shown in Fig. 4.26.

Velocities of the hydraulics cylinder and the lifting jack are as follows;

Hydraulic cylinder	
Normal operation	200 mm/min
Slow operation	10 mm/min
No-load operation	300 mm/min
Lifting jack	
Normal operation	10 ~ 15 mm/min
Slow operation	5 mm/min

The transfer equipment, which has the same kind of mechanism as the blanket module transfer machine, has been developed to transport the VENUS (Versatile NLHEP and Universities Spectrometer) in the TRISTAN (Transposable Ring Intersecting Storage Accelerators in Nippon) project. The equipment can move a total weight of about 2,200 tons with an accuracy of less than  $\pm 0.5$  mm of adjusting error.



Table 4.12 Removal Procedure of Blanket Module

Sequence	Procedure
1	Shut down the reactor.
2	Bake out the components in the vacuum vessel.
3	Cut the lip seal welds of the divertor cassette and the access door.
4	Disengage the connection of the divertor cassette.
5	Drain the coolant pipes.
6	Remove the jumpers of the coolant pipes outside the access door and set the air cooler to the coolant pipes.
7	Unload the divertor transfer machine and set the divertor cassette.
8	Remove the divertor cassette and load it.
9	Unload the shield plug and insert it into the divertor access port by the divertor transfer machine.
10	Cut the lip seal welds of the heating system.
11	Disengage the connection of the heating system.
12	Remove the heating system and load it by the overhead crane.
13	Unload the shield plug and insert it into the duct shield of the heating system.
14	Disengage the connection of the duct shield.
15	Remove the duct shield.
16	Unload the shield plug and insert it into the duct for the heating system.
17	Remove the shield plug under the blanket module to insert the roller forks.
18	Disengage the connection of the blanket module.
19	Lift up the outboard shield of the blanket module from the supporting shelves of the permanent shield by the lifting jack included in the shield plug for the divertor access port.
20	Unload the blanket module transfer machine and insert the roller forks under the blanket module.
21	Lift up the blanket module and remove it by the blanket module transfer machine.
22	Unload the shield plug and insert it into the access port, when the blanket module remains to be removed for a long time.

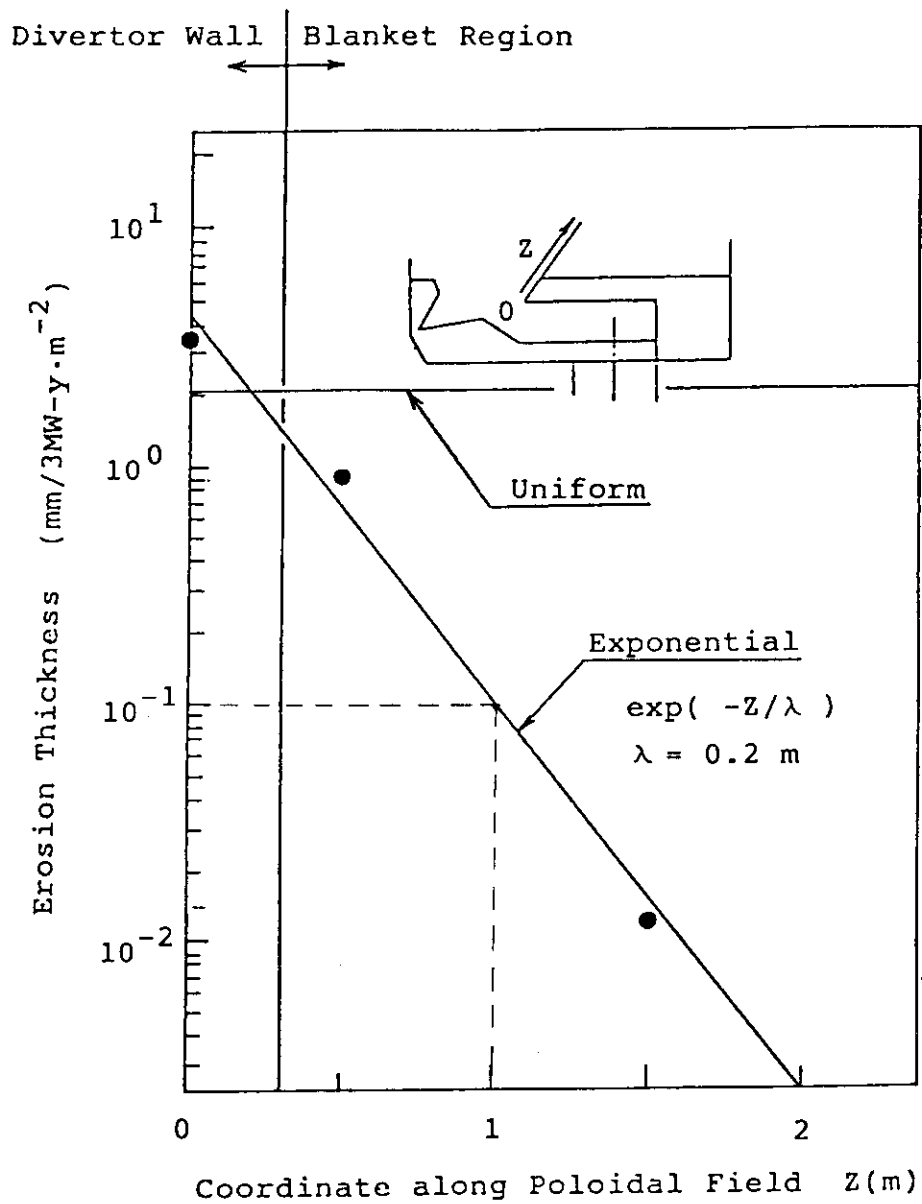


Fig. 4.20      Erosion Thickness of First Wall  
 (316 Type S.S.)

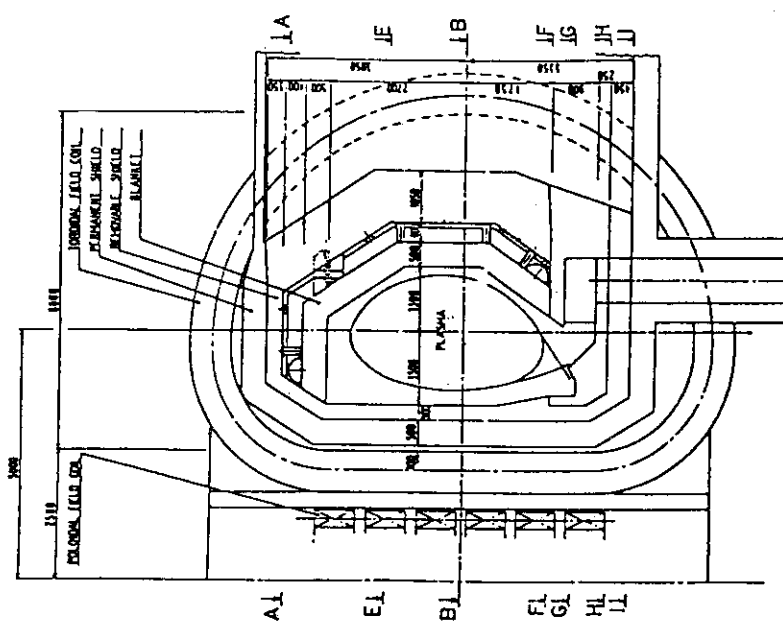
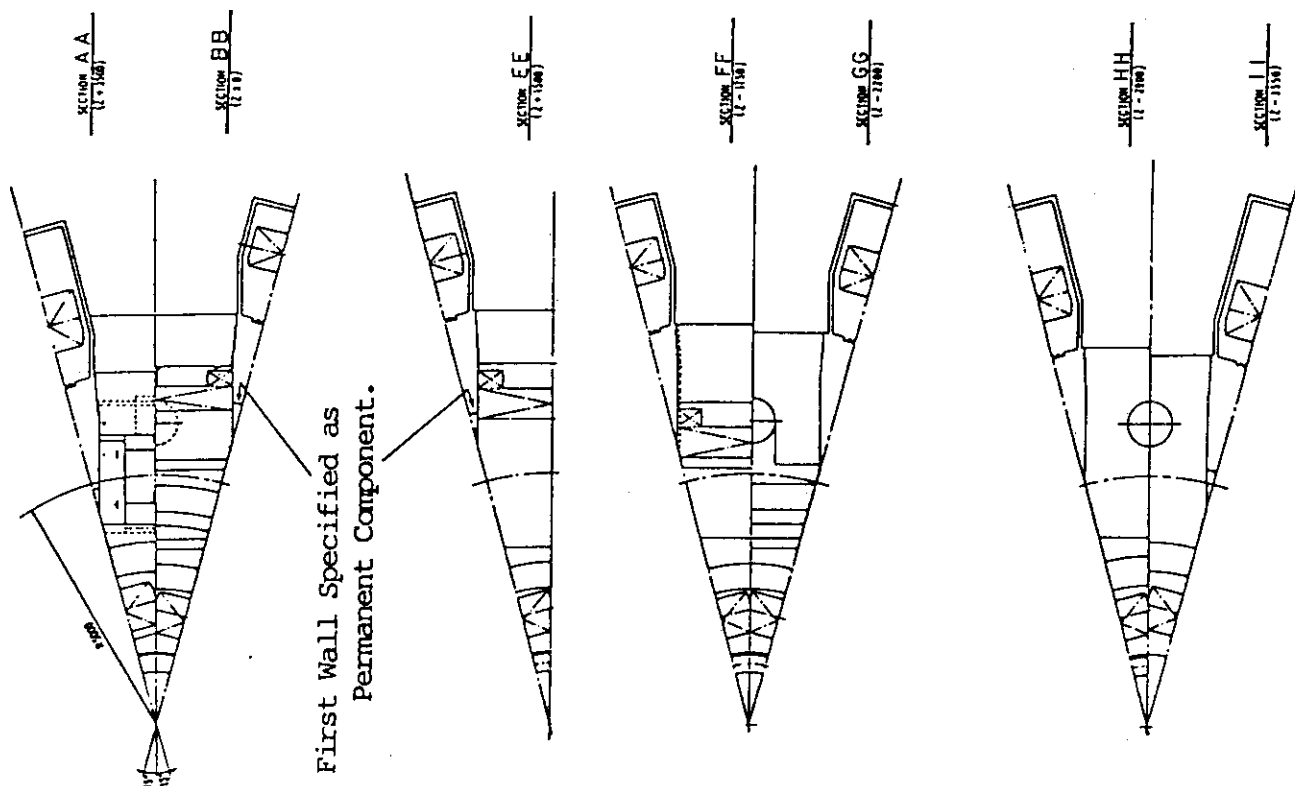


Fig. 4.21

Torus Concept with Removable Blanket Module  
equal to the Number of TF Coils



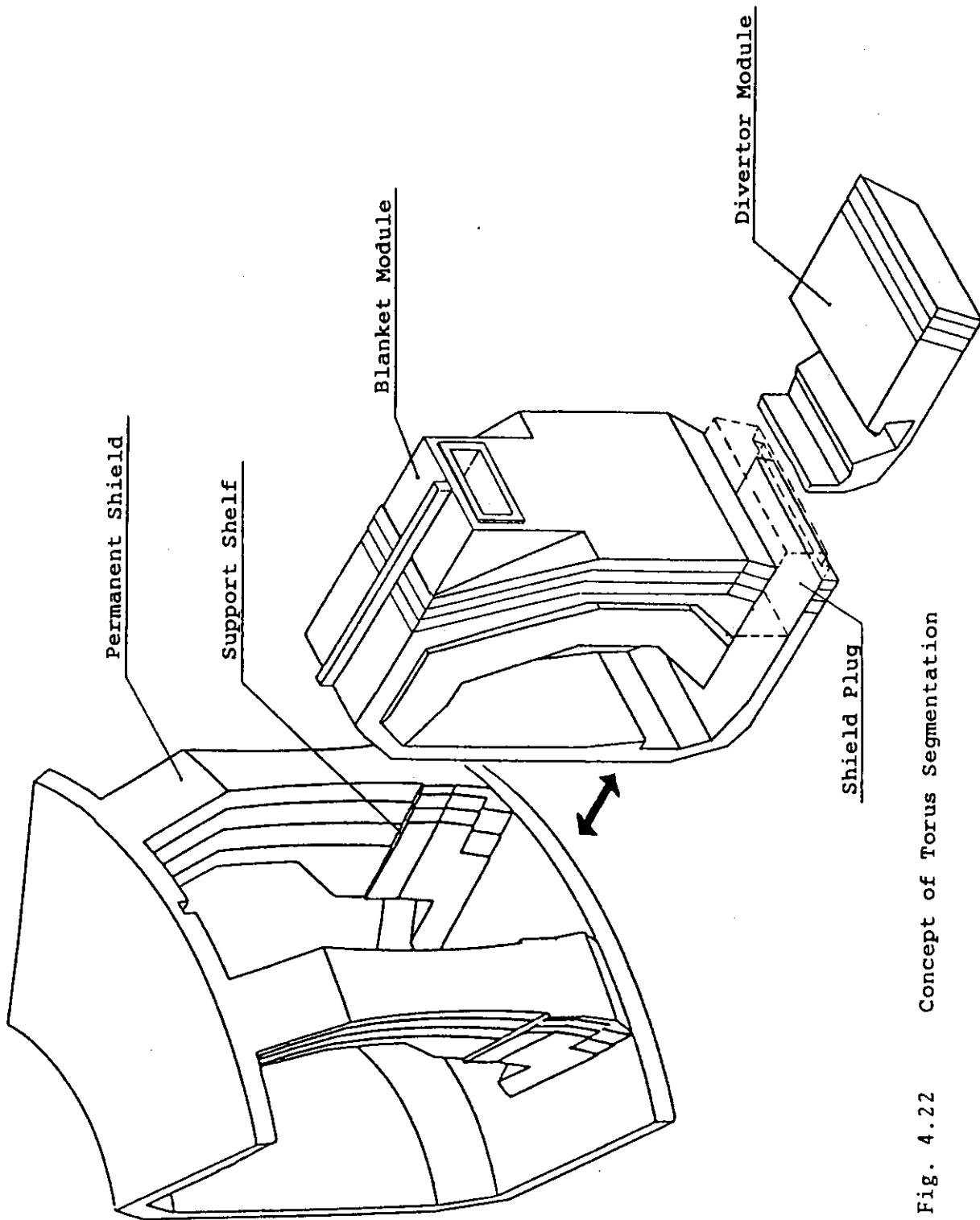
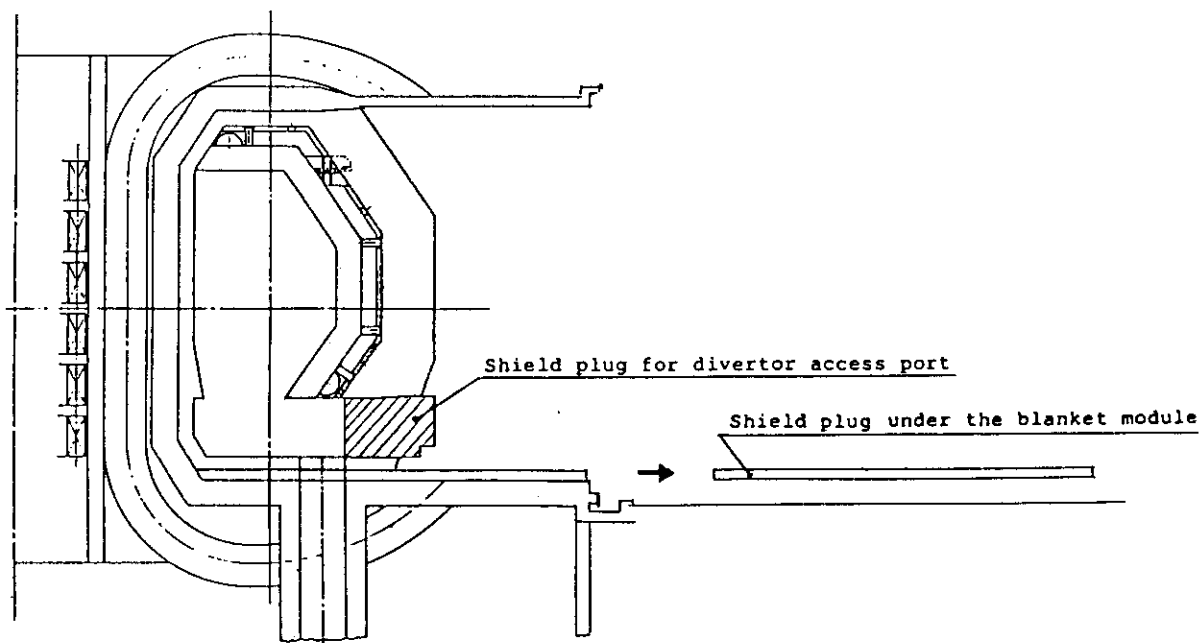
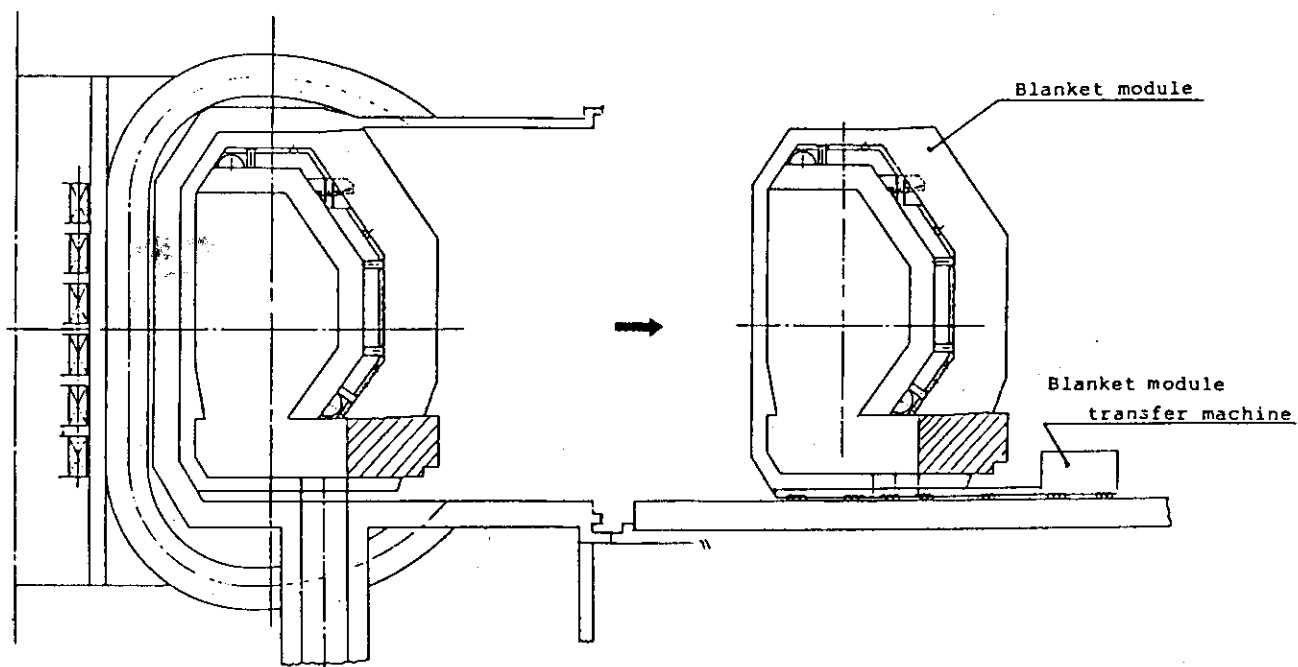


Fig. 4.22 Concept of Torus Segmentation



- 1) Remove the shield plug under the blanket module



- 2) Remove the blanket module by the blanket module transfer machine

Fig. 4.23 Removal Concept of Blanket Module

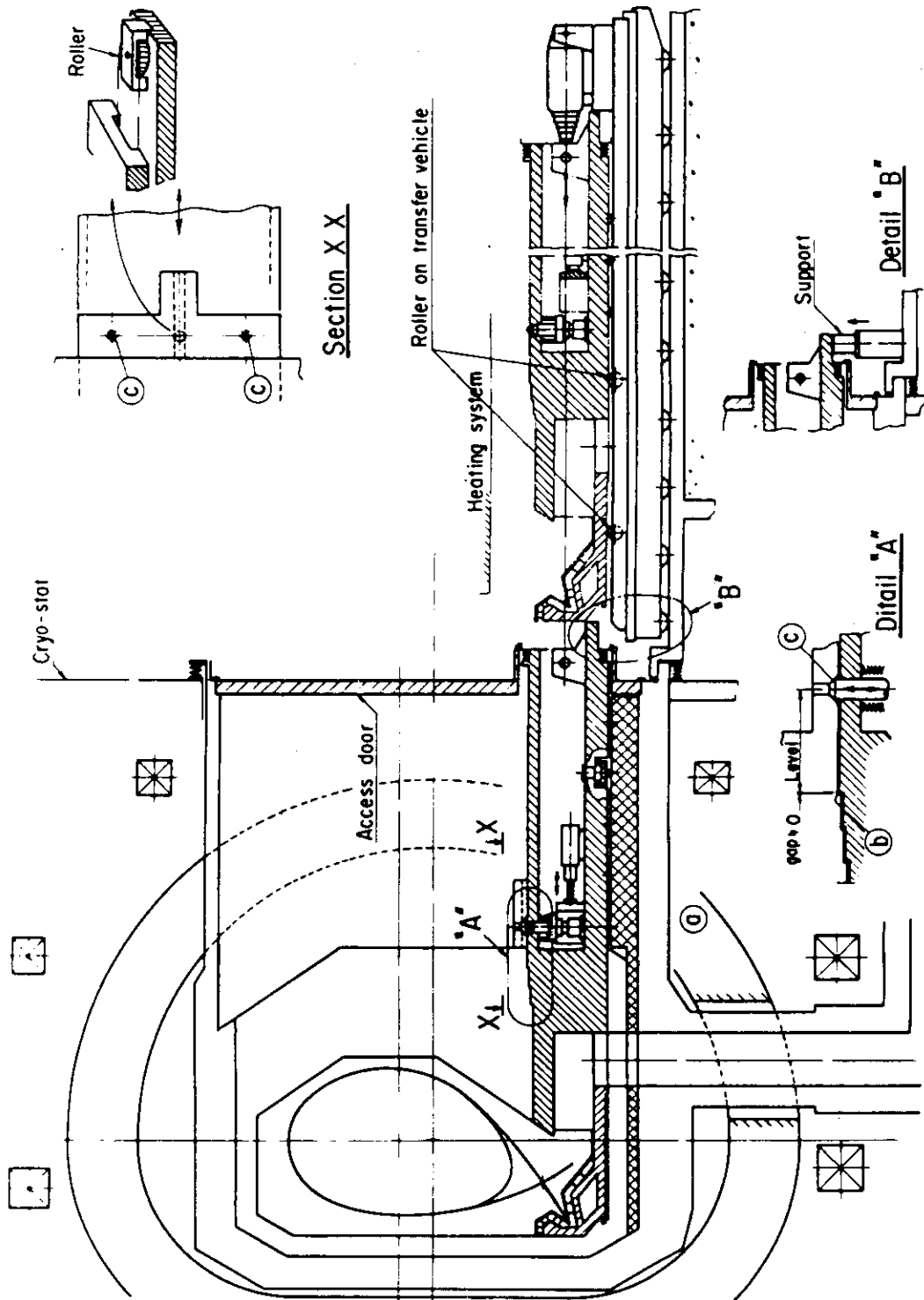


Fig. 4.24 Removal Concept of Diver tor

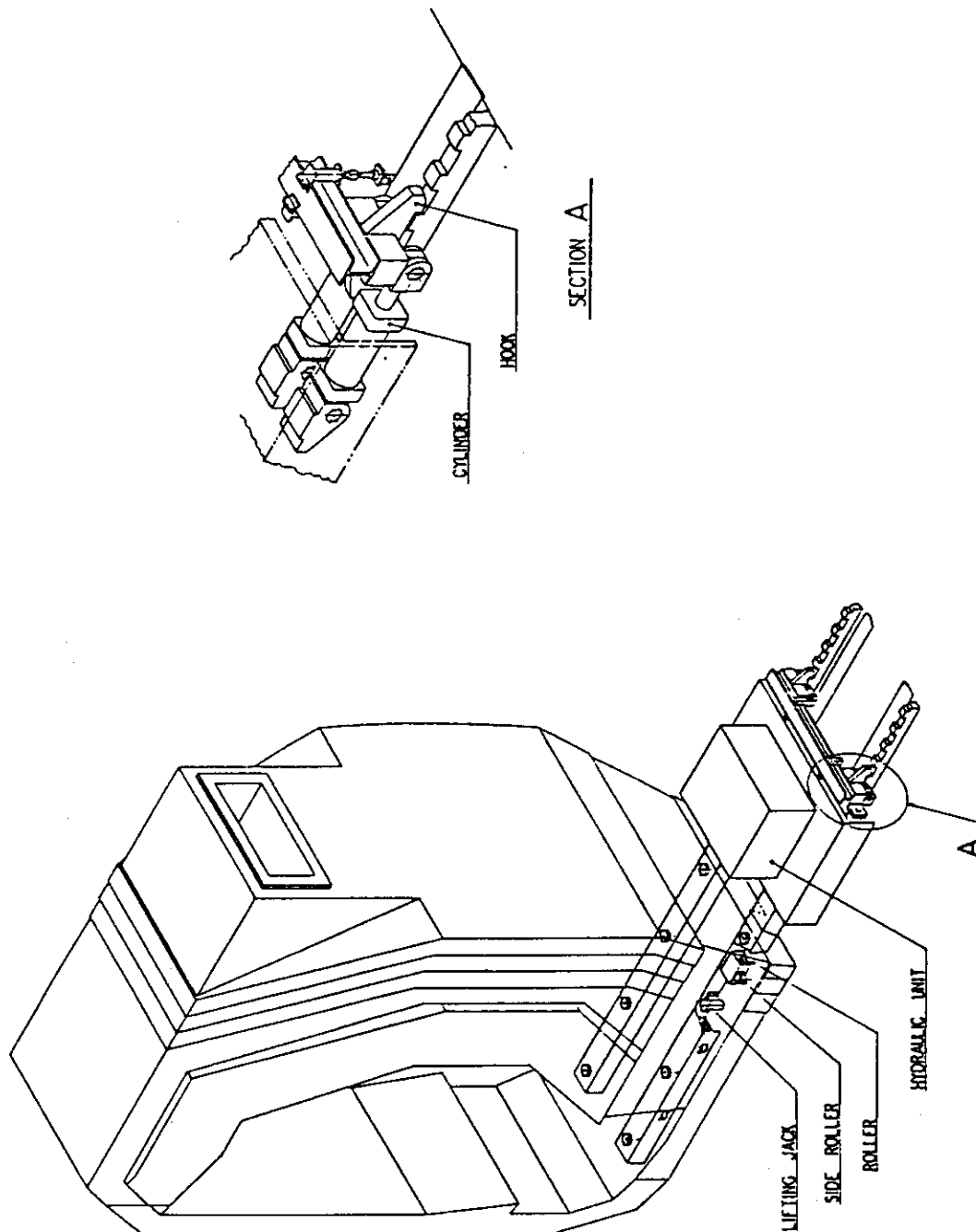


Fig. 4.25 Blanket Module Transfer Machine

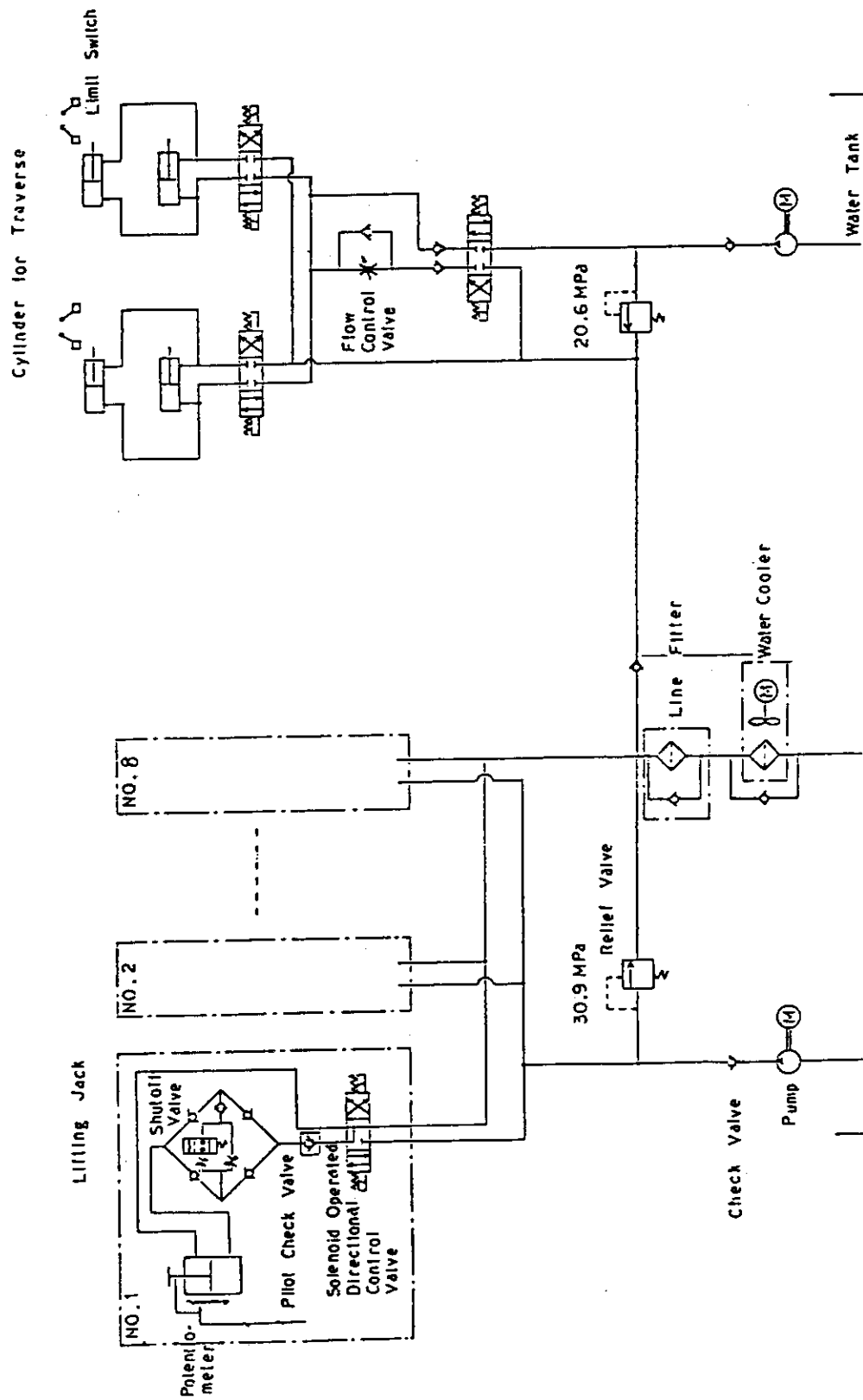


Fig. 4.26 Hydraulic Circuit of Blanket Module Transfer Machine



#### 4.4 Consideration of maintenance and assembly scheme with vertical access

Maintenance and assembly scheme with vertical access has the possibility to reduce the device size and cost. In this scheme, segmented blanket modules are removed through an overhead access port without the requirement for disassembling other torus sectors. Some evaluation for this scheme was carried out.

The possible main advantages of this approach for replacing the blankets are considered as follows.

- ① Reduction of the TF coils dimension and PF coils' ampere-turns may be achieved. Shear panels of the TF coils located at outboard region may result in facilitating the support of them.
- ② Special-purpose transfer machine for blanket module replacement could be eliminated by using the overhead crane
- ③ This approach allows the possibility that the blanket modules are removed independently from the divertor cassette

On the contrary, this approach has the following problems to be resolved in the actual reactor design.

- ① As shell conductors or active coils for plasma vertical stabilization become partial because of the small-segmented blankets, it may be impossible to control the plasma vertical stability. It is necessary to connect segmented conductors or coils, which results in the complicated torus structure.
- ② As blanket is segmented into small modules and is separated from shield, it is difficult to support the blanket modules solidly only at the top of the torus. Although it may be possible to join the blanket modules and shields if fully remote handling is adopted, solid support with high accuracy can not be expected.
- ③ The lifting device which can position very precisely the blanket module will become very large, and so its cost will be high and the reactor building will become very large.
- ④ The containment transfer cask, if needed, will be very complicated and large to contain the lifting device, the handling devices, jigs and tools, etc. in it. If the cask is transferred by the overhead crane, the reactor hall will be very high.
- ⑤ The small blanket module segmented toroidally may be divided into upper and lower parts by the plasma heating duct. In this case, the support structure and the maintenance of the lower part seem to be difficult.

Although the above problems should be examined more in detail, it is anticipated that they will be very difficult from point of engineering view compared with the maintenance scheme with horizontal access. Therefore the feasibility of reliable reactor concept appears to be doubtful.

## 5. RF Heating and Current Drive

Basic parameters of RF heating/current drive system are shown in Table 5 - 1, based on the scenario described in chapter 6. In this chapter, the conceptual design of each RF system is described, including the physical design of launchers.

The results shows that the RF systems are feasible as a quasi-steady state operation.

### 5.1 ICRF Heating System

#### 5.1.1 Physical design of ICRF launchers

We propose loop-antenna launchers for ICRF heating system. The advantages of this type of launchers are; (1) high power density on couplers, (2) easy shielding of neutron flux, (3) suppression of small  $k_{\parallel}$  part of waves less than  $k_0 = \omega/c$  by antenna phasing, etc. Injection of over 15 MW through an 1.8 m  $\times$  1.3 m port is attainable by optimization of antenna design.

We show, in Figure 5.1-1 the ICRF launcher which consists of  $2 \times 2$  loop-antennae. It has been designed for FER but is identical for INTOR. We have used a three dimensional antenna-plasma coupling code including effects of antenna feeders to analyze the coupling characteristics of the launchers. The RF current distribution on the antenna is given by the phase constant  $\beta = \omega/\sqrt{LC}$ , where L and C are the inductance and capacitance of antenna. The value of  $\beta$  is not determined in self-consistent method (the effects of plasma are neglected). Cold plasma and single pass model are assumed. Wave fields are Fourier-decomposed in y and z direction and we solve wave equation numerically in radial direction up to some distance (typically 20 cm) from the Faraday shield.

Owing to the available port size, the antenna length L and the antenna width w for  $2 \times 2$  loop antenna launchers are restricted up to  $L=0.8$  m and  $w=0.3$  m, respectively. The distance between plasma boundary (separatrix) and Faraday shield is fixed same to the thickness of scrape off layer (15 cm for FER). Then, the parameters for the optimization are the distance between (1) Faraday shield and antenna conductor,  $\delta_{fa}$ , (2) antenna conductor and return conductor,  $\delta_{ar}$ . The loading impedance,  $Z = Z_R + iZ_I$ , depends on these distances. Figure 5.1-2-a shows these dependences on  $\delta_{fa}$  with a relatively large value of  $\delta_{ar}$  (30 cm), where the RF power supplies with  $0-\pi/0-\pi$  phasing. The magnitude of  $Z_R$  over 25 ohm is obtained with  $\delta_{fa} = 3$  to 4 cm. The antenna characteristic length reaches 1/2 with  $\delta_{fa} = 3.2$  cm, so that the imaginary part of loading impedance of the antenna for the co-axial tube,  $Z_I$ , is minimized. As a result, extremely low value of VSWR in co-axial tube can be obtained. With  $\delta_{fa}$  less than 4 cm, VSWR is less than 1.7 as shown in Figure 5.1-2-b, where we assumed the characteristic impedance of co-axial tube,  $Z_0 = 30(\text{ohm}) = Z_L = |Z|$ . On the other hand, a current maximum of the half wave-length antenna is situated near the antenna feeder. It should enhance an excitation of TEM mode by the feeder current, then the small  $k_{\parallel}$  part of waves may increase. It is convenient to define  $\eta_2 =$

$ZR_2/ZR$ , where  $ZR_2$  is a loading resistance integrated from  $k_0$  to  $\infty$ . The value  $\eta_2$  is also shown in Figure 5.1-2-a. With  $0-\pi/0-\pi$  phasing, we can obtain  $\eta_2$  large enough ( $>0.8$ ) to be acceptable.

We have finally chosen  $\delta_{fa} = 4$  cm owing to an electrical breakdown limit between Faraday shield and antenna conductor and in order to reduce RF loss on the Faraday shield (Table 5.1-1). It is found that injection of over 15 MW/port (3.75 MW/antenna) is attainable. The maximum voltage of standing wave on antenna conductor is about 15 kV (7.5 kV/cm between Faraday shield and antenna) and the voltage in co-axial tube is also very low (17 kV) because of the low VSWR (less than 1.7).

### 5.1.2 Mechanical configuration of launcher

#### (1) Outline of ICRF launcher

The overview of ICRF launcher and Bird's-eye view of ICRF launcher are shown in Fig. 5.1-3 and Fig. 5.1-4, respectively. The launcher is composed of the antenna conductor, the Faraday shields, the return conductor and the coaxial cable. The cross-shaped structure is installed into the jacket to reinforce it and support the return conductor, the coaxial cable and cooling headers. The all antenna elements and coaxial cable have cooling channels. For the purpose of radiation shielding, stainless steel pebbles are packed between the cross-shaped support structure and the jacket. Cooling water flows through the space among the pebbles to remove the nuclear heat generation.

#### (2) Electromagnetic force and stress

Eddy current is induced in the jacket, the Faraday shields, the antenna conductor and the coaxial cables during a plasma disruption. Electromagnetic forces due to the interaction between the eddy current  $i$  and toroidal and poloidal magnetic field are shown in Fig. 5.1-5. As it is shown in Fig. 5.1-5-(A) electromagnetic forces  $F_t$  on the side position and  $F_p$  on the front surface of the Faraday shield are considered. Electromagnetic stresses result from  $F_t$  and  $F_p$  are estimated from the beam model which is shown in Fig. (A)-(3). Electromagnetic forces  $F_t$  and  $F_p$  act on the side of the coaxial cable, as they are shown in Fig. (B)-(2). Consequently electromagnetic force causes torsion to the coaxial cable (Fig. (B)-(3)). Electromagnetic forces  $F_t$  and  $F_p$  on the antenna conductor are shown in Fig. 5.1-5-(C). Since the force of  $F_p$  is much smaller than that of  $F_t$ , we evaluate only the force  $F_t$ . As the force  $F_t$  causes torsion to the antenna support structure, shear stresses occur at the center of the antenna support. Eddy current and electromagnetic force on the jacket are shown in Fig. 5.1-5-(D) which are derived from the FEM analysis. Analytical conditions and results of the electromagnetic forces and stresses are listed in Table 5.1-2. Resultant stress are so small that there is no problem.

## (3) Thermal analysis

Thermal analysis for the faraday shield is performed under the condition of 1) radiation from plasma ( $15 \text{ W/cm}^2$ ), 2) alpha particle ripple loss ( $14.5 \text{ W/cm}^2$ ), 3) nuclear heat generation ( $10 \text{ W/cc}$ ) and 3) RF loss ( $1 \text{ W/cm}^2$ ). The temperature and stress distribution are shown in Fig. 5.1-6. The maximum stress of  $156 \text{ MPa}$  occurs at the corner of cooling channel is smaller than  $3S_m (=360 \text{ MPa})$ , according to the ASME Sec. III. Both terminal end of the faraday shield is bended so as to reduce the thermal stress due to stretching of the faraday shield as shown in Fig. 5.1-1.

## (4) Repair and maintenance

The replacement concept is shown in Fig. 5.1-7.  
The replacement procedure is shown as follows:

## - Disassembly -

- 1) Shutdown.
- 2) (Bake and evacuate for tritium removal).
- 3) Cool for the removal of decay heat.
- 4) Disconnect the bolts of connecting part-A.
- 5) Cut the lip seal of connecting part-A.
- 6) Install the sub-support structure.
- 7) Cut the vacuum seal between the access door and the antenna.
- 8) Cut the cooling pipes.
- 9) Remove the antenna.

## - Assembly -

- 1) Install the antenna.
- 2) Connect (weld) the cooling pipes and NDT.
- 3) Weld the vacuum seal between the access door and the antenna, and NDT.
- 4) Remove the sub-support structure.
- 5) Weld the lip seal of connecting part-A and NDT.
- 6) Connect the bolts of connecting part-A.
- 7) Bake and evacuate.

## 5.1.3 Power supply system

The power supply system of ICRF is shown in Fig. 5.1-8. One of the advantage of ICRF heating is the availability of the high power vacuum tube of the output power of MW class. For the power amplifier of  $81 \text{ MHz}$ , TH-518 or X-2170 is presently available. Their output power is more than  $1 \text{ MW}$ . It is necessary to drive the antenna of one port with the power of about  $15 \text{ MW}$ . As it is usually acceptable that the power efficiency of the RF amplifier is  $65\%$ , the power transport efficiency is about  $90\%$ , and the power factor of the power supply is about  $85\%$ , the A.C. power supply for the total RF output power of  $60 \text{ MW}$  including the redundancy requires the capacity of  $121 \text{ MVA}$ . Required capacity pattern is shown in Fig. 5.1-9, since the ICRF heating system is operated in the beginning and the end of  $1000 \text{ sec}$  burn time.

#### 5.1.4 Summary

We have designed a new launcher for ICRF heating, which consists of  $2 \times 2$  loop-antennae. Owing to the reduced size of access port, the size of antennae are also reduced by 40% in area as compared with the previous design (Phase IIa). In order to maximize the antenna power density, we adopt 'half wave length resonant antenna', which will allow us an extremely low value of VSWR and to minimize the peak voltage in co-axial tube. Injection power of 15 MW/port is attainable with the maximum electric field less than 7.5 kV/cm on the antenna conductor and the peak voltage less than 17 kV in co-axial tube.

We estimate stresses due to thermal inputs from plasmas and electromagnetic forces during a plasma major disruption. The calculation of the thermal stresses includes the heat load due to 1) radiation from plasmas, 2) nuclear volume heating, 3) RF loss and 4) ripple loss of Alpha-particles with space dependence. A cooling system to remove these thermal flux is designed and additional stresses due to the pressure of liquid coolant is taking into account. In order to estimate the electromagnetic forces, we assumed the characteristics of the current decay as  $\exp(-t/\tau)$   $\tau=15$  ms.

These stress calculations are carried out on the Faraday shield, antenna conductor, return conductor, cooling jacket and co-axial tube. We have confirmed all the stresses calculated are small enough to be acceptable in comparison with the stress criteria of 316 SS.

All the components of antenna and co-axial tube are fixed on a cross-shaped structure which supports the launcher casing.

In the calculations on the antenna-plasma coupling, we assumed moderate density of scrape off plasma ( $>3 \times 10^{17} \text{ m}^{-3}$  at the surface of shield). As most of characteristics of scrape off layer in divertor operations are still unknown, the present result can be somewhat optimistic. More experimental data on the coupling characteristics between the antenna and the diverted plasma are required, and these informations will be obtained by the coming experiments of JT-60.

Table 5 - 1 Basic parameters of RF heating/current drive

	MAIN HEATING	CURRENT DRIVE	START-UP ASSIST/ PROFILE CONTROL
Wave	ICRF	LHRF	ECRF
Mode	2nd harmonic D	Slow mode	1st harmonic, 0 mode
Frequency	76 MHz	0.56 GHz	140 GHz
Power	50 MW	10 MW	10 MW
Duration	~ 20 s	~ 200 s	10 s

Table 5.1-1

width of ant. conductor w	:	0.3 m
length of ant. conductor L	:	0.8 m
distance between ant. & shield $\delta_{fa}$	:	0.04 m (0.03 m)
thickness of Faraday shield t	:	0.02 m
distance between ant. & return $\delta_{ar}$	:	0.3 m
number of antennae/port	:	$2 \times 2$
antenna spacing (in toroidal)	:	0.6 m
antenna phasing	:	$0-\pi/0-\pi$
loading impedance Z/ohm	:	$25.61 + i13.26$ $(31.14 + i 1.83)$
antenna phase length (for 81 MHz)	:	$0.8 \pi (\pi)$
VSWR	:	1.65 (1.07)

( ) ;  $\delta_{fa} = 0.03$  m.

Table 5.1-2 Electromagnetic force and stress of ICRF launcher

	Faraday shield Fig. 5.1.2-3-(A)	Coaxial cable Fig. 5.1.2-3-(B)	Antenna conductor Fig. 5.1.2-3-(C)	Jacket Fig. 5.1.2-3-(D)
Analytical condition	$I_p = 5.7 \times \frac{\tau_{ex} - t}{\tau_{ex}} \text{ MA}$ $\tau_{ex} = 15 \text{ ms}$ $B_t = 4.3T, \quad B_p = 0.55T$	$I_p = 5.7 \times \frac{\tau_{ex} - t}{\tau_{ex}} \text{ MA}$ $\tau_{ex} = 15 \text{ ms}$ $B_t = 4.0T, \quad B_p = 0.58T$	$I_p = 5.7 \times \frac{\tau_{ex} - t}{\tau_{ex}} \text{ MA}$ $\tau_{ex} = 15 \text{ ms}$ $B_t = \frac{5.2m \times 5.3T}{R}$	
Eddy current	2.98 A	2.48 kA	33.7 kA	580 kA (at L5 in Fig. (1))
Electromagnetic force	$F_t = 1310 \text{ kgf/m (Fig. (2))}$ $F_p = 167 \text{ kgf/m (Fig. (2))}$	$F_t = 1.11 \times 10^3 \text{ kgf (Fig. (2))}$ $F_p = 161 \text{ kgf (Fig. (2))}$ $T = 7.7 \times 10^4 \text{ kgf} \cdot \text{mm (Fig. (3))}$	$F_t = 4.23 \times 10^3 \text{ kgf (Fig. (2))}$ $F_p = 567 \text{ kgf (Fig. (2))}$ $T = 1.27 \times 10^6 \text{ kgf} \cdot \text{mm (Fig. (3))}$	0.3 kg/mm
Stress	$\sigma = 1.4 \text{ kg/mm}^2 \text{ (by } F_t)$ $\sigma = 4.1 \text{ kg/mm}^2 \text{ (by } F_p)$	$\tau = 0.3 \text{ kg/mm}^2$	$\tau_{\text{max}} = 4.0 \text{ kg/mm}^2 \text{ (Fig. (3))}$	$\tau_{\text{side}} = 3.2 \text{ kg/mm}^2$ $\tau_{\text{upper}} = 0.4 \text{ kg/mm}^2$ $\tau_{\text{lower}}$



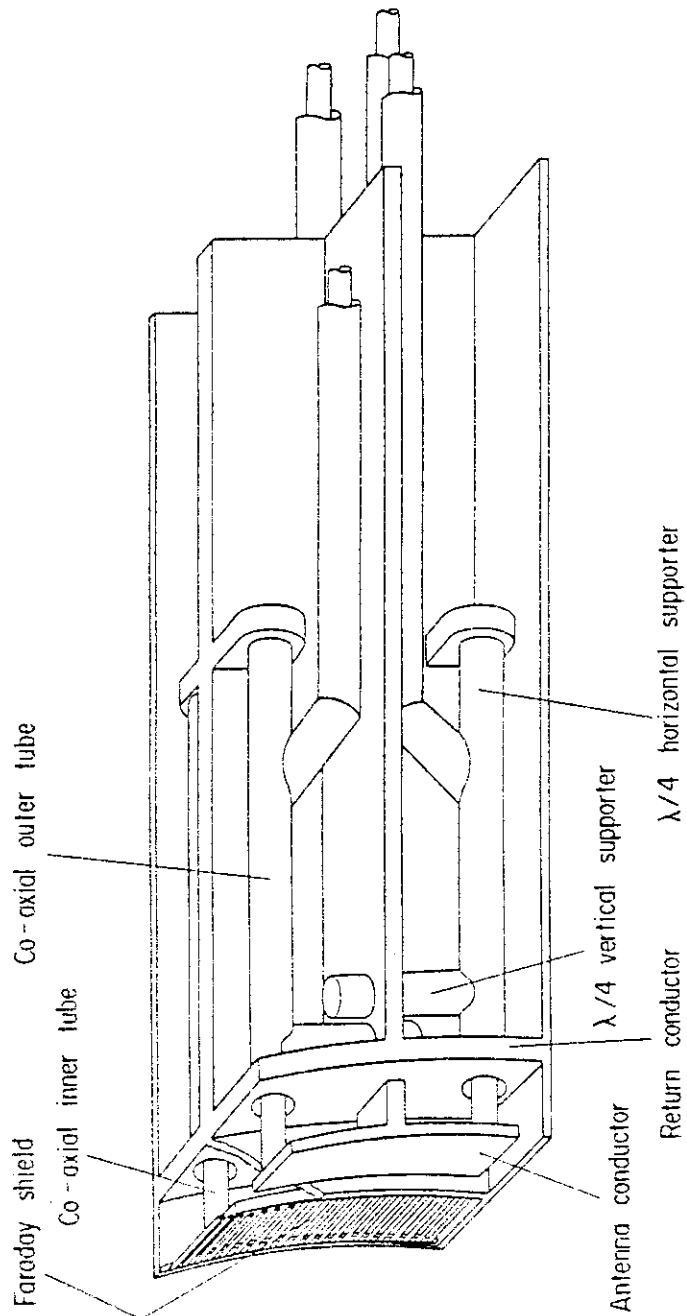
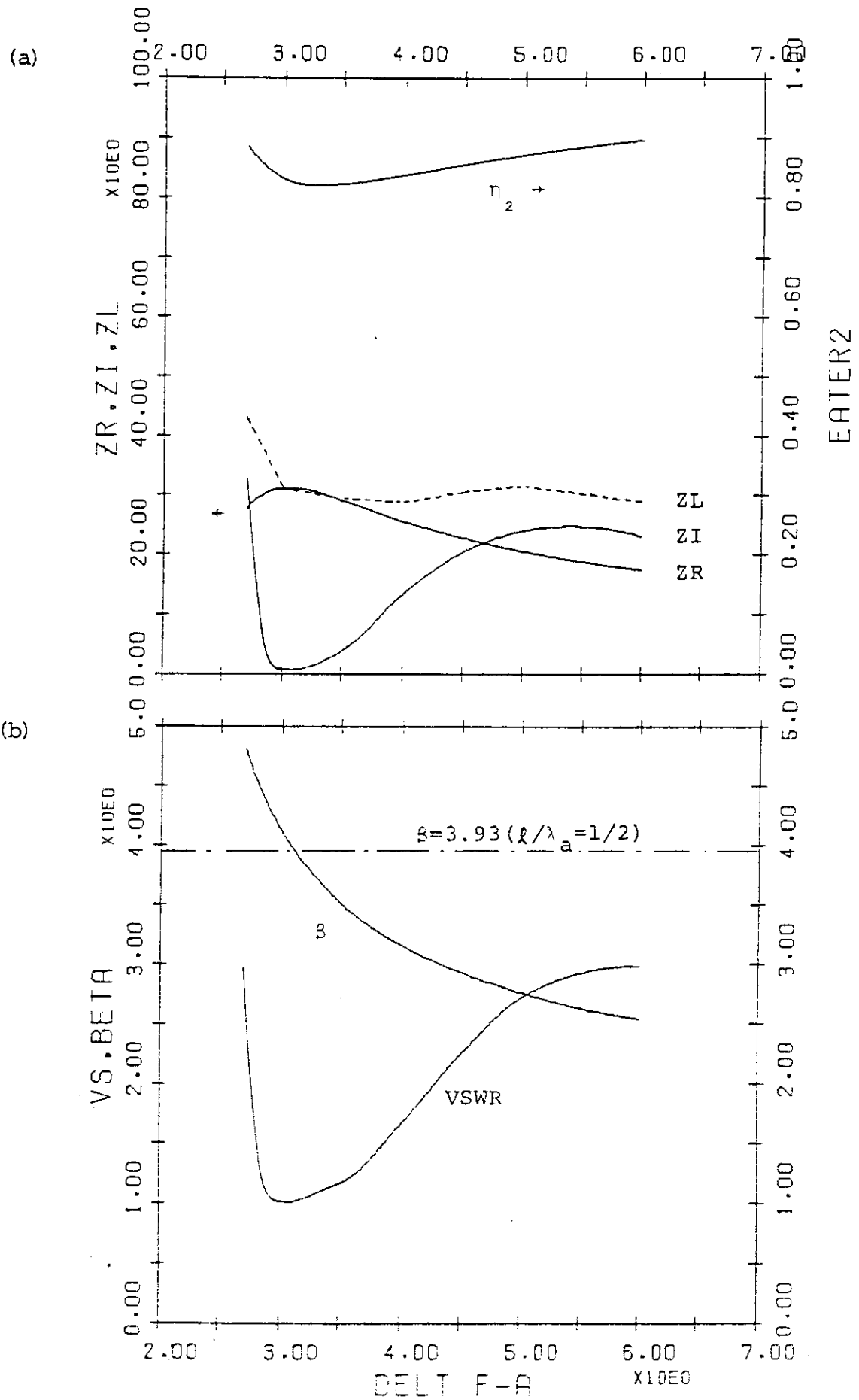


Fig. 5.1-1 ICRF Launcher (loop-antenna type)



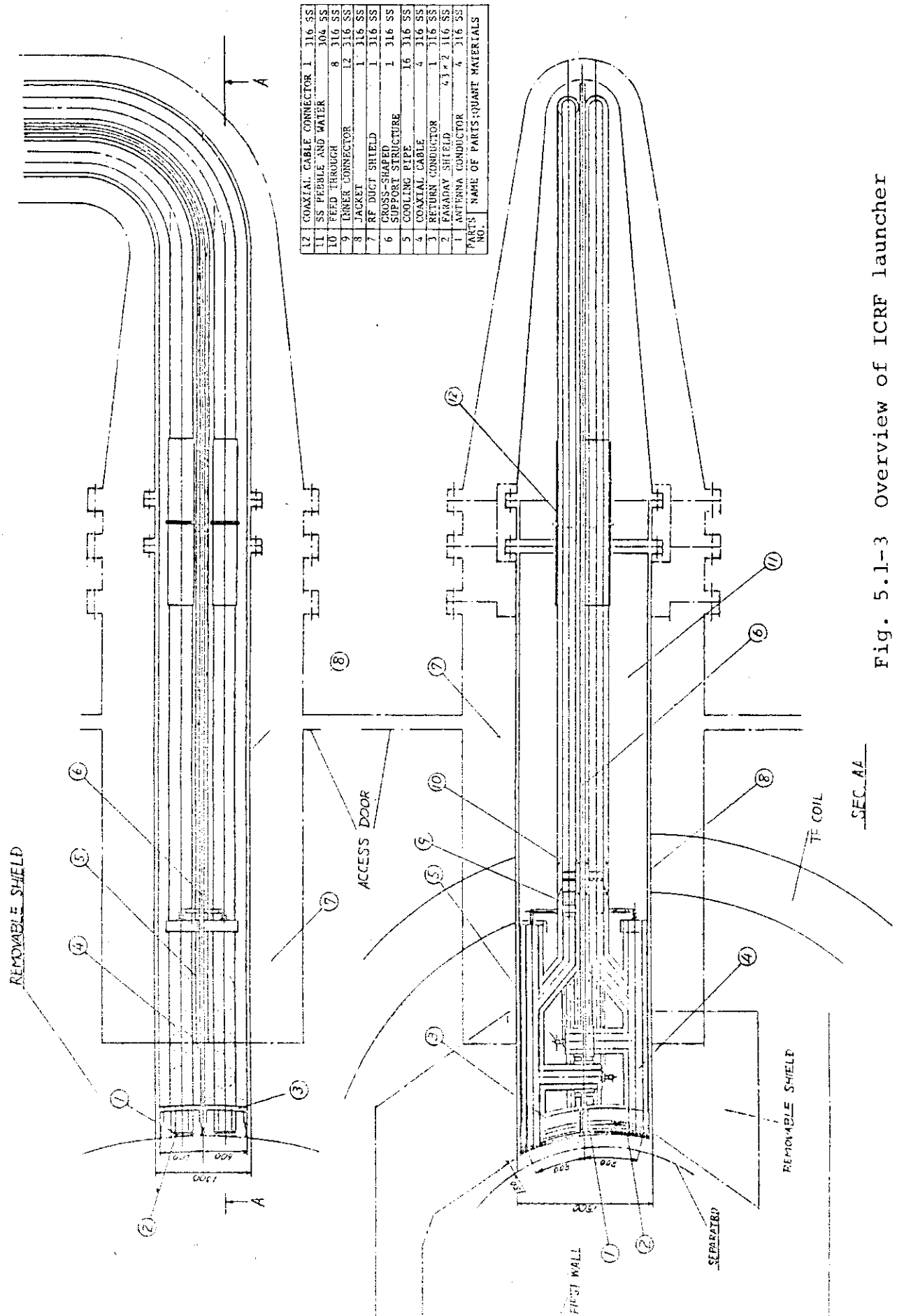


Fig. 5.1-3 Overview of ICRF launcher

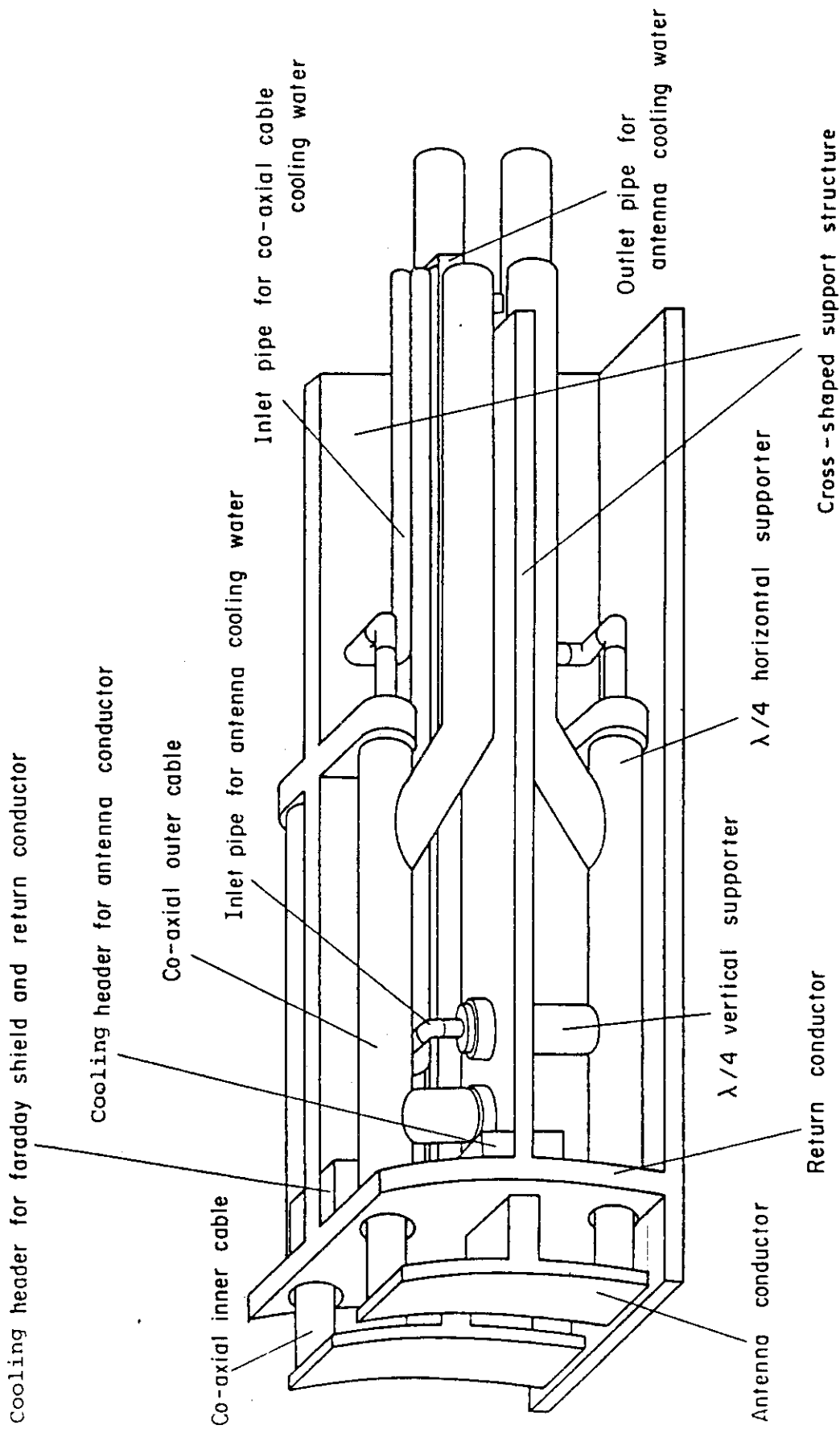
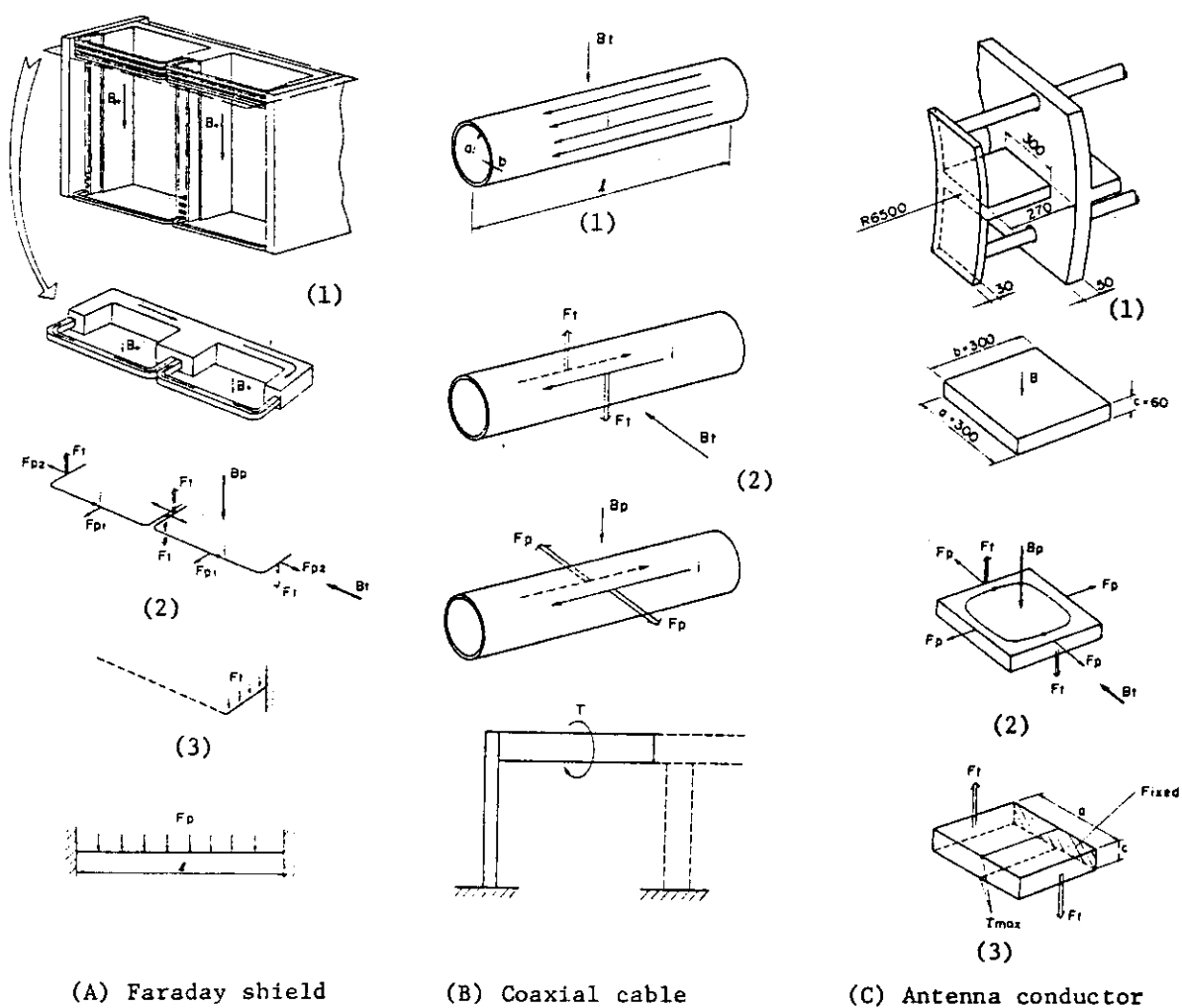


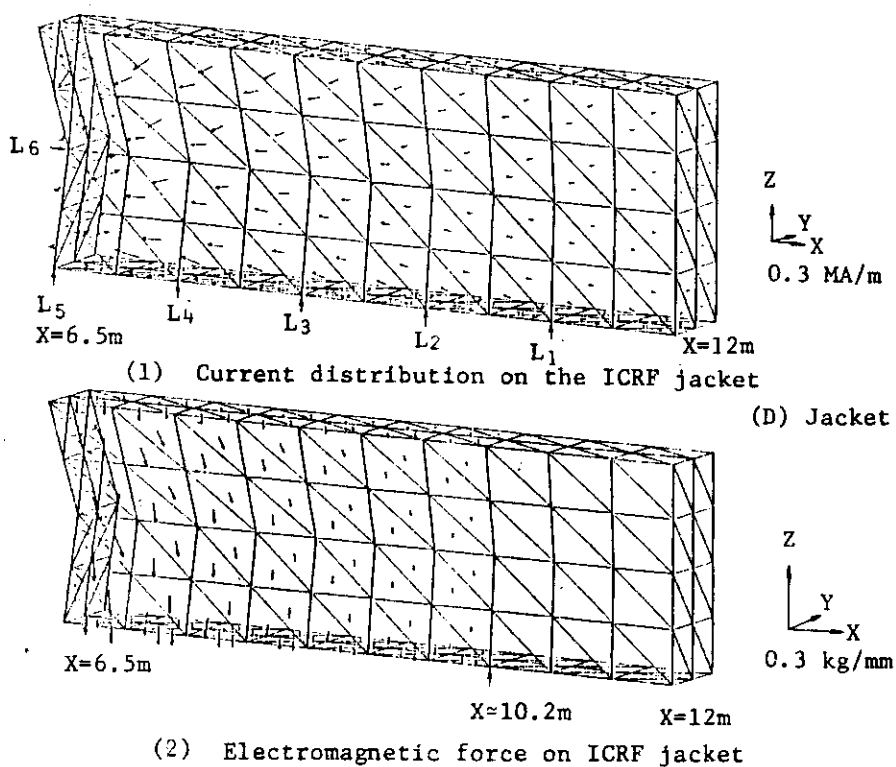
Fig. 5.1-4 Bird's-eye view of ICRF LAUNCHER



(A) Faraday shield

(B) Coaxial cable

(C) Antenna conductor



(D) Jacket

Fig. 5.1-5 Electromagnetic force

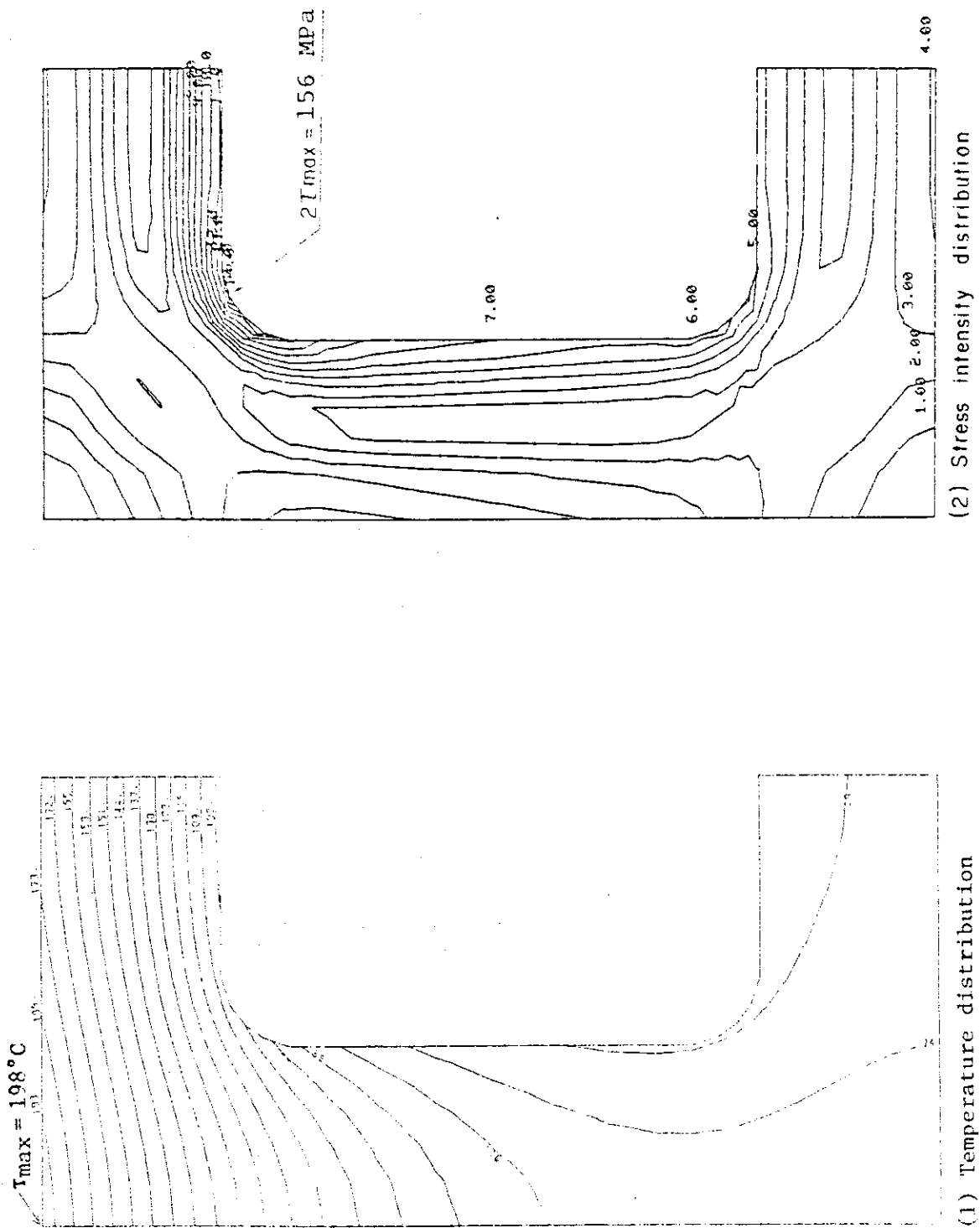


Fig. 5.1-6 Temperature and stress distribution of faraday shield

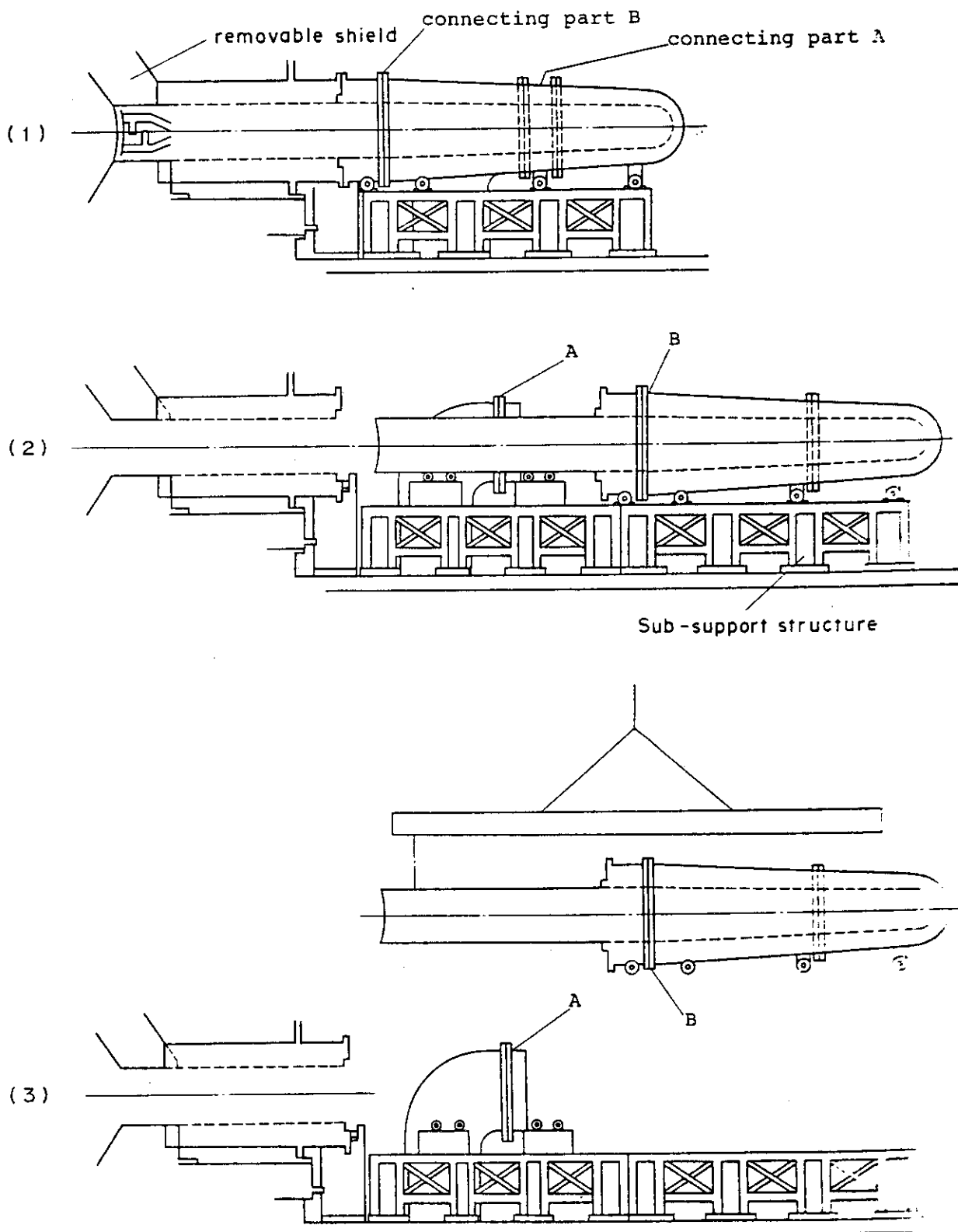


Fig. 5.1-7 Replacement of ICRF Launcher

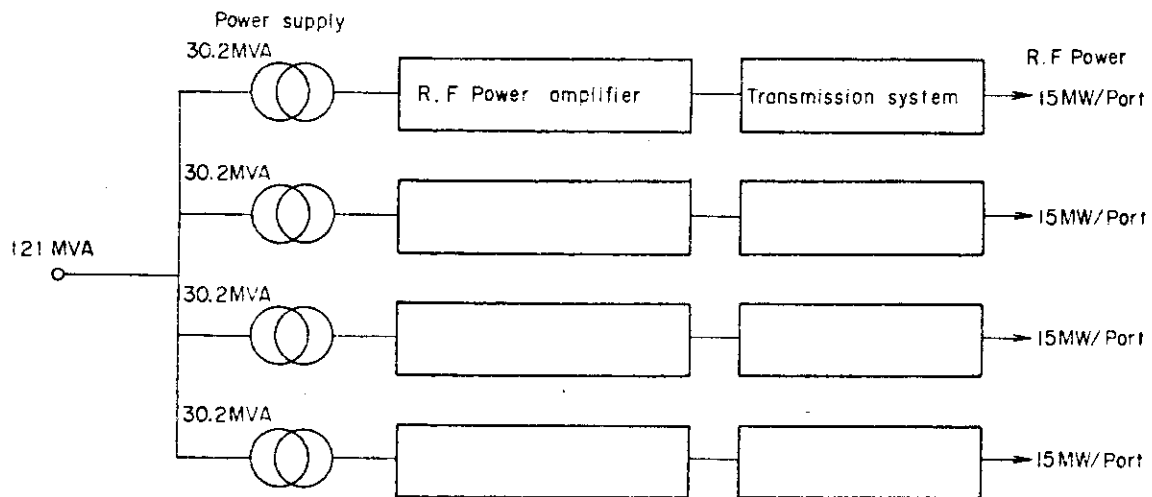


Fig. 5.1-8 Schematic diagram of power supply

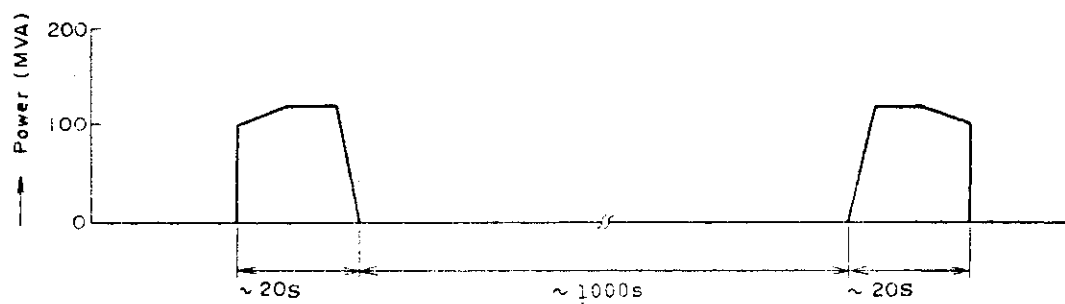


Fig. 5.1-9 Power and operation pattern



## 5.2 LHRF Current Drive System

### 5.2.1 Structure and coupling efficiency of LHRF launcher for current drive

A quasi-steady state operation scenario is proposed to simplify the reactor engineering. High average  $n_{\parallel}$  and broad wave spectrum is favorable for minimizing the recharge time of OH coils or the supplied energy. We propose phased LHRF launcher for current drive. The typical schematics of the launcher is shown in Fig. 5.2-1. The special feature of this system are as follows:

- (1) Wave frequency is equal to  $2f_{\text{LHCD}} = 0.56$  GHz for avoiding the parametric instability, where  $f_{\text{LHCD}}$  is the lower hybrid frequency in the low density plasma (order of  $10^{18}\text{m}^{-3}$ ) during the recharging phase. The frequency is lower than that for the plasma heating (2 GHz) required for higher plasma density and is more effective for good coupling efficiency.
- (2) The width of grill elements array in the toroidal direction is smaller than the permissible rf port width (1.3 m) determined from the view point of required biological shield thickness.

We now look into the coupling properties changing the number of grills, the vacuum distance, and the phase difference between neighboring waveguides with the other parameters held fixed.

First we consider the characteristics of the spectrum width, as a function of the number of grills ( $N$ ) in toroidal direction. As shown in Fig. 5.2-2, the width become larger as the number of grills decreases, and approximately the product of the width and  $N$  is constant. In the figure  $n_{\parallel}$  is the refractive index in the toroidal direction. Smaller number of waveguides is preferable for the waveguide fabrication technique. And since broader spectrum, as long as its main part satisfies the accessibility condition ( $n_{\parallel} \geq 1$ ), is required the smaller number of waveguides is preferable. Thus  $N = 8$  appears to be best for the current drive.

In evaluating coupling efficiency, a figure of merit we took is the fractional intensity  $(1-R)F$  of the LH wave, where  $R$  is the average reflection coefficient and  $F$  is the fraction of  $n_{\parallel} > 1$  in the transmitted spectrum. The transmission coefficient  $1-R$  and the fractional intensity  $(1-R)F$  are shown in Fig. 5.2-3, as a function of central peak  $n_{\parallel 0}$  in the spectrum which varies with the phase difference  $\Delta\phi$ . As  $n_{\parallel 0}$  increases in the region of  $n_{\parallel 0} > 2$ ,  $1-R$  and  $(1-R)F$  decrease. This is because decay length  $\lambda_x$  of the evanescence wave in the vacuum region changes inversely with the refractive index  $n_{\parallel}$  in the toroidal direction,

$$\lambda_x = \frac{c}{f \sqrt{n_{\parallel}^2 - 1}}$$

where  $c$  is the light velocity and  $f$  is the wave frequency. At  $\pi/2$  ( $n_{\parallel 0} = 3$ ) 53.6% of the wave energy is reflected by evanescence region between the waveguide and plasma and 77.6% of the transmission energy usefully generates plasma current.

Finally, we consider the behavior of  $1-R$  and  $(1-R)F$  as the vacuum distance varied, keeping  $\Delta\phi = \pi/2$ . These results are shown in Fig. 5.2-4, which illustrates that the coupling efficiency increases for the shorter vacuum distance.

The launcher design for the quasi-steady state current drive and the coupling efficiency for a typical plasma-edge conditions ( $x_p$  and  $dn_e/dx$ ) are summarized in Table 5.2-1. In order to accommodate up to 10 MW of current drive the waveguide-averaged intensity is only  $3.49 \text{ kW/cm}^2$  and maximum electric field  $7.06 \text{ kV/cm}$ .

### 5.2.2 Use of LHRF current drive launcher for heating

Most important restriction for determining the wave frequency is that  $f \gtrsim 2f_{\text{LHCD}}$  is satisfied for avoiding the parametric instability. That if we select  $f = 2 \text{ GHz}$  which is the twice of lower hybrid frequency in the high density plasma of the heating phase, LHRF heating may be also possible by the same LHRF system.

We now consider the coupling properties for 2 GHz. It is desirable to keep the septum  $d_p$  as thin as possible, but waveguide fabrication difficulties limit it to  $d_p = 1.0 \text{ cm}$ . For the phase difference  $\Delta\phi$  needed to define a travelling wave for current drive, it is necessary to satisfy  $F \gg 0.5$ , so we select the phase difference of  $\pi/2$ . The transmission coefficient  $1-R$  and the fractional intensity  $(1-R)F$  are shown in Fig. 5.2-5 as a function of  $n_{\parallel 0}$  which varies with the waveguide opening  $b_p$ . As  $n_{\parallel 0}$  increases,  $(1-R)F$  decreases. At  $b_p = 0.25 \text{ cm}$  ( $n_{\parallel 0} = 3$ ) only about 6% of the energy is used to generate usefully plasma current. This is 1/7 of the coupling efficiency for the lower frequency (0.56 GHz) LHRF launcher, and the excessively large power is required for the rf sources. Since it causes certain trouble in realizing the economical reactor. It is not recommendable to use the same LHRF launcher for the both of plasma heating and current drive.

### 5.2.3 Mechanical configuration of launcher

#### (1) Outline of LHRF current drive system

The overview of LHCD launcher is shown in Fig. 5.2-6. The launcher is composed of 32 waveguides (laterally 4 × vertically 8), 32 ceramic windows, several ribs and a jacket. In order to reduce the neutron damage of the ceramic windows, multi-bended waveguides are used. Since the heat flux to the launcher surface is very high and the coolant path between the waveguides is narrow (4 mm), we have chosen the bended cooling channels which consists of some rib panels and wings. These concept is shown in Fig. 5.2-7. The ceramic window is placed at the plasma side before ECR zone.

#### (2) Electromagnetic force and stress

Eddy current is induced in the jacket and the waveguides during a plasma disruption. Electromagnetic forces due to the interaction between the eddy current  $i$  and toroidal and poloidal magnetic field are shown in Fig. 5.2-8. As the jacket of LHCD launcher is as same as that of ICRF launcher in size, we consider the electromagnetic forces and stresses only in the case of waveguides.

First we consider the current  $i$  induced by the variation of  $B_{\perp}$  ( $=0.25T$ ) as shown in Fig. 5.2-8-(a). The electromagnetic forces  $F_p$  and  $F_t$  occurs on the waveguide due to the interaction between the eddy current  $i$  and toroidal and poloidal magnetic field as shown in Fig. 5.2-8-(b). The force  $F_t$  and  $F_p$  cause the shear stress at the corner of the waveguide.

$$\tau = \frac{F_t + F_p}{2t\ell} = 0.07 \text{ kgf/mm}^2$$

here,  $t$  : thickness of waveguide

$\ell$  : length of waveguide

Electromagnetic stresses are negligible from these considerations.

#### (3) Thermal analysis

Thermal analysis for the first wall of LHCD launcher is performed under the condition of 1) radiation from plasma ( $15 \text{ W/cm}^2$ ), 2) Alpha particle ripple loss ( $14.5 \text{ W/cm}^2$ ), 3) nuclear heat generation ( $10 \text{ W/cc}$ ), 3) RF loss ( $0.45 \text{ W/cm}^2$ ).

The maximum temperature and the thermal stress of the first wall, 4 mm in thickness, are  $180^\circ\text{C}$  and  $16 \text{ kg/mm}^2$ , respectively. According to the ASME Sec. III, thermal stress of  $16 \text{ kg/mm}^2$  is smaller than  $3S_m$  ( $=36 \text{ kg/mm}^2$ ).

#### (4) Repair and maintenance

The replacement concept is shown in Fig. 5.2-9. The replacement procedure is shown as follows:

- Disassembly -

- 1) Shutdown.
- 2) (Bake and evacuate for tritium removal).
- 3) Cool for the removal of decay heat.
- 4) Disconnect the bolts of connecting part-A.
- 5) Cut the lip seal of connecting part-A.
- 6) Install the sub-support structure.
- 7) Cut the vacuum seal between the access door and the antenna.
- 8) Cut the cooling pipes.
- 9) Remove LHCD launcher.

- Assembly -

- 1) Install LHCD launcher.
- 2) Connect (weld) the cooling pipes and NDT.
- 3) Weld the vacuum seal between the access door and the antenna, and NDT.
- 4) Remove the sub-support structure.
- 5) Weld the lip seal of the connecting part-A, and NDT.
- 6) Connect the bolts of the connecting part-A.
- 7) Bake and evacuate.

#### 5.2.4 Power supply system

The power supply system of LHCD system is shown in Fig. 5.2-10. As 50% power efficiency of the RF amplifier, 60% power transport efficiency and 85% power factor of the rectifier and transformer can be usually acceptable, the A.C. power supply requires the capacity of 78 MVA. Required capacity pattern is shown in Fig. 5.2-11, since the LHCD system is operated in the beginning and the recharging phase of 200 sec.

#### 5.2.5 Summary

We have designed a grill launcher for LHRF current-drive, which composed of  $4 \times 8$  wave guides. Using this launcher with  $\pi/2$  phasing gives average  $n$ -index  $n_0 = 3$  and 46.4% of the wave energy is transmitted into the plasmas through the evanescent layer. The 77.4% of this transmitted energy is absorbed by the electrons carrying the currents.

We estimate stresses due to thermal inputs from plasmas and electro-magnetic forces during a plasma disruption. It is found that the stresses due to the electro-magnetic force are very small in any cases owing to its grill structure. On the other hand, it is difficult to remove heat flux on the surface of grill launcher facing plasma. We have designed a water cooling system of this grill surface, which consists of some rib panels and wings to bend the flow. With the wall thickness of waveguide of 3 mm and the thickness of water pass of 4 mm, we found that the thermal flux on the grill surface is removable and the total stresses can be less than the stress criteria of SUS 316 according to the ASME Sec. III, where the total stresses include the thermal stresses.

ses due to 1) radiation from plasmas, 2) nuclear volume heating, 3) RF loss, 4) ripple loss of Alpha particles with space dependence and the stresses due to the pressure of the cooling water.

The ceramics window should be placed at the plasma side before ECR zone. Using 'multi-bended waveguides' will effectively reduce the neutron damage of these ceramics.

Our calculations of RF-plasma coupling is based on the moderate density of plasma scrape off layer. If its density is extremely low, the coupling efficiency of the launcher can be more pessimistic. The coming experiments of JT-60 will give us more informations on the characteristics of the scrape off plasma in divertor operations.

Table 5.2 -1 Specifications of the launching system  
for LHRF current drive

Quantity	Unit	Value	Explanation
$f$	GHz	0.56	Wave frequency
$b_p$	cm	3.50	Narrow guide opening
$d_p$	cm	1.00	Septum
$h_p$	cm	38.10	Vertical guide opening
$N$		8	Number of grill elements
$M$		4	Number of arrays stacked in the poloidal direction
$\Delta\phi$		$\pi/2$	Phase difference
$n_{//0}$		2.98	Central peak in the spectrum
$\Delta n$		1.37	FWHM of the spectrum
$dn_e/dx$	$\text{cm}^{-4}$	$10^{11}$	Edge density gradient
$x_p$	cm	0.50	Vacuum distance
$R$		0.377	Average reflection coefficient
$F$		0.670	Spectral fraction lying with in the range of $n_{//} > 1$
$P_{CD}$	MW	10.0	LH wave for current drive
$p$	$\text{kW}/\text{cm}^2$	3.49	Wave intensity at antenna
$E_{\text{max}}$	$\text{kV}/\text{cm}$	7.06	Maximum electric field at antenna

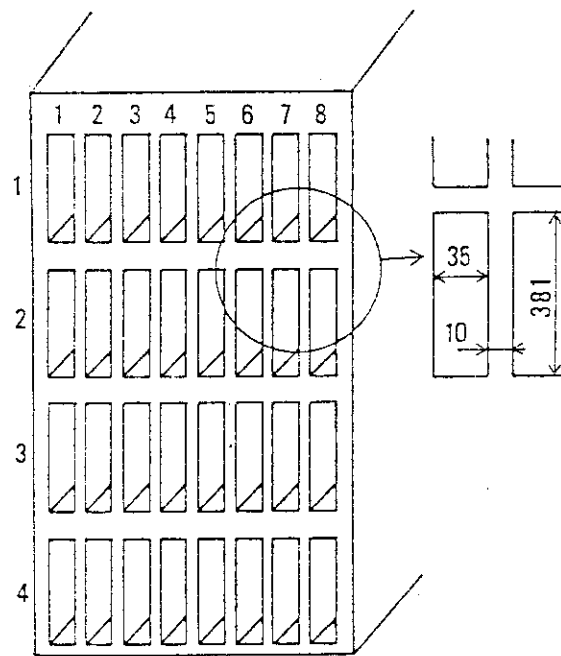


Fig. 5.2 -1 Simplified schematics of the launching system for LHRF current drive. The launcher is composed of 32 waveguides (horizontally 8 x vertically 4).

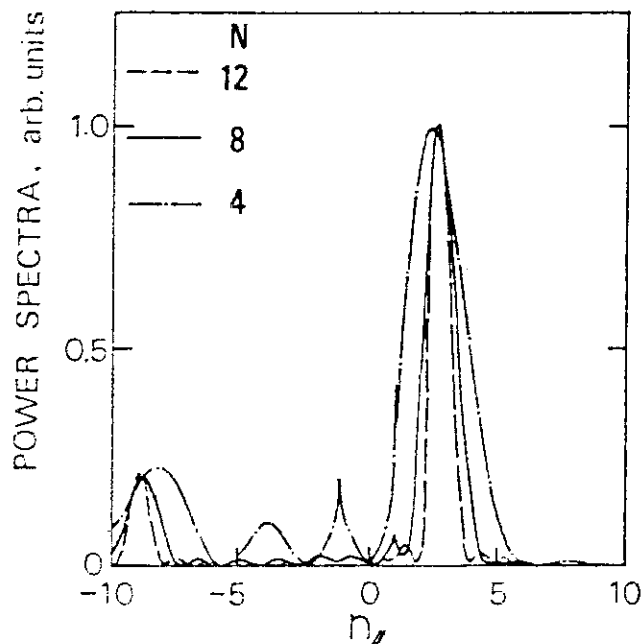


Fig. 5.2 -2 Power spectra for differing numbers of grill elements,  $N$ .  
Wave frequency  $f = 0.56\text{GHz}$ , narrow guide opening  $b_p = 3.50\text{cm}$ , septum  $d_p = 1.00\text{cm}$ , vacuum distance  $x_p = 1.00\text{cm}$ , edge density gradient  $dn_e/dx = 10^{11}\text{cm}^{-4}$ , phase difference  $\Delta\Phi = \pi/2$ .

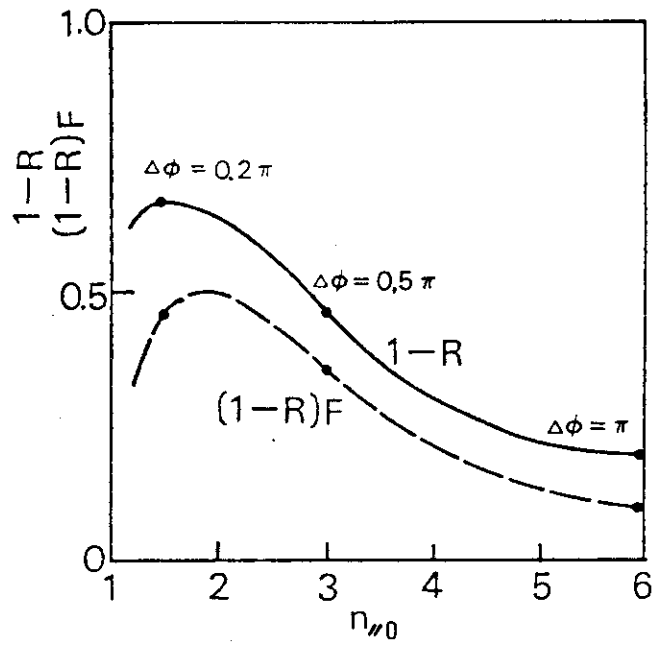


Fig. 5.2 -3 Transmission coefficient of the antenna,  $1-R$ , and fractional intensity of the LH wave for current drive,  $(1-R)F$ , versus central peak in the spectrum,  $n_0 = 5.95 \Delta\phi / \pi$ .  $f = 0.56\text{GHz}$ ,  $b_p = 3.50\text{cm}$ ,  $d_p = 1.00\text{cm}$ ,  $x_p = 1.00\text{cm}$ ,  $dn_e/dx = 10^{11}\text{cm}^{-4}$ ,  $N = 8$ .

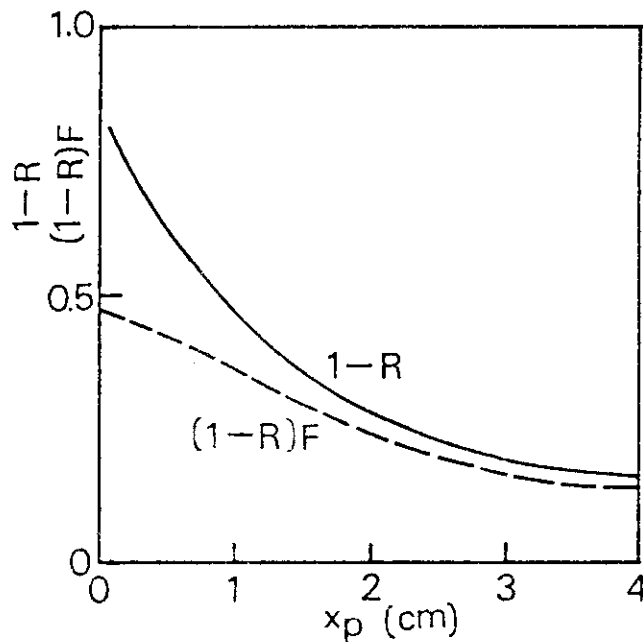


Fig. 5.2 -4 Transmission coefficient of the antenna,  $1-R$ , and fractional intensity of the LH wave for current drive,  $(1-R)F$ , versus vacuum distance,  $x_p$ .  $f = 0.56\text{GHz}$ ,  $b_p = 3.50\text{cm}$ ,  $d_p = 1.00\text{cm}$ ,  $dn_e/dx = 10^{11}\text{cm}^{-4}$ ,  $N = 8$ ,  $\Delta\phi = \pi/2$ .



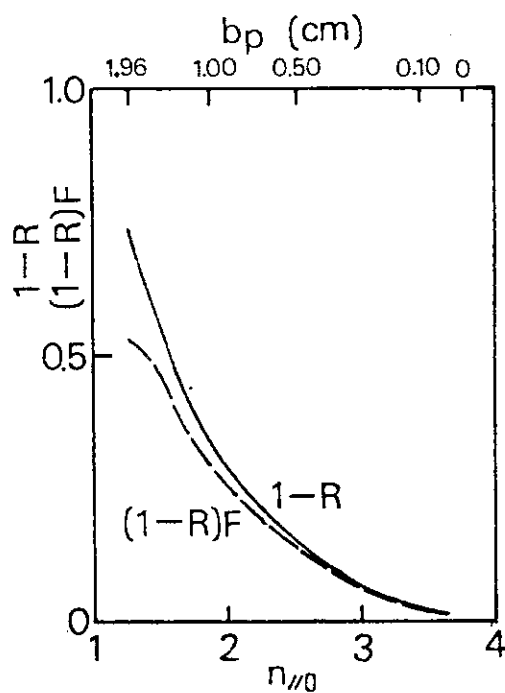


Fig. 5.2 — 5 Transmission coefficient of the antenna,  $1-R$ , and fractional intensity of the LH wave for current drive,  $(1-R)F$ , versus central peak in the spectrum,  $n_{//0} = 3.75/(b_p + 1)$ .  $f = 2\text{GHz}$ ,  $\Delta\phi = \pi/2$ ,  $d_p = 1.00\text{cm}$ ,  $x_p = 0.50\text{cm}$ ,  $dn_e/dx = 10^{11}\text{cm}^{-4}$ ,  $N = 8$ .

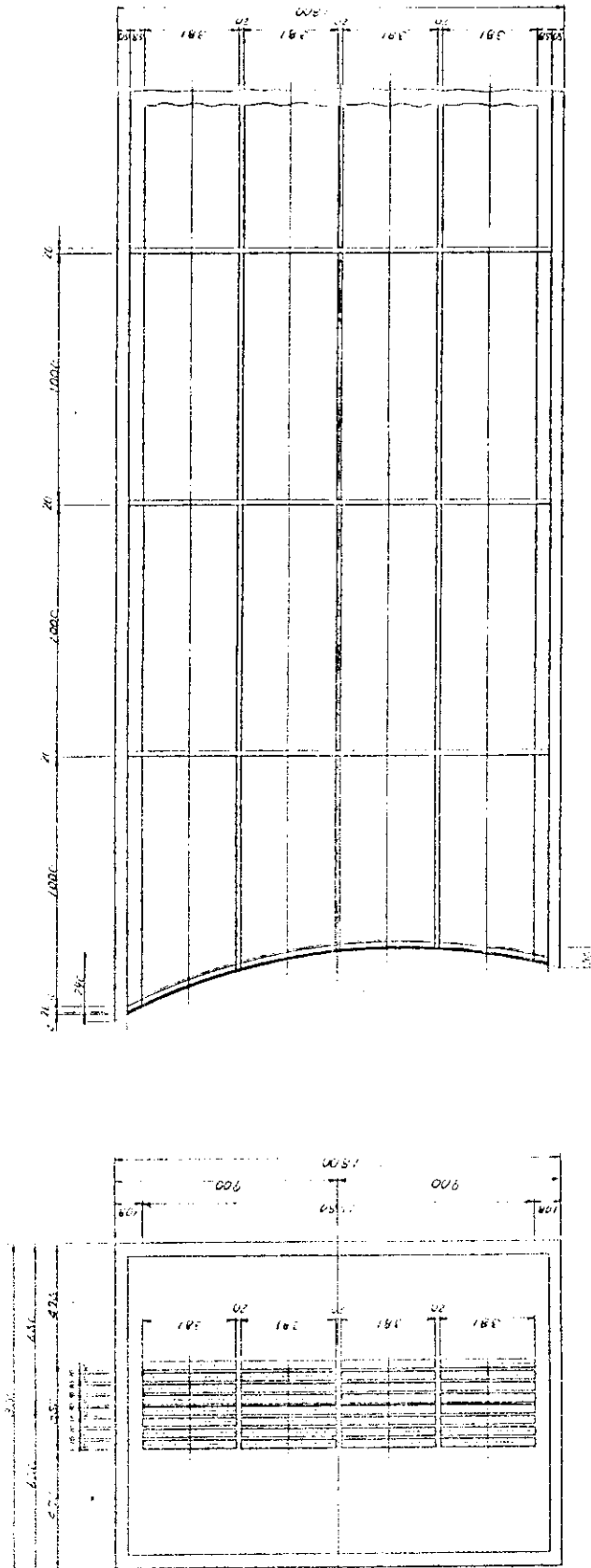


Fig. 5.2-6 LHRF current drive launcher

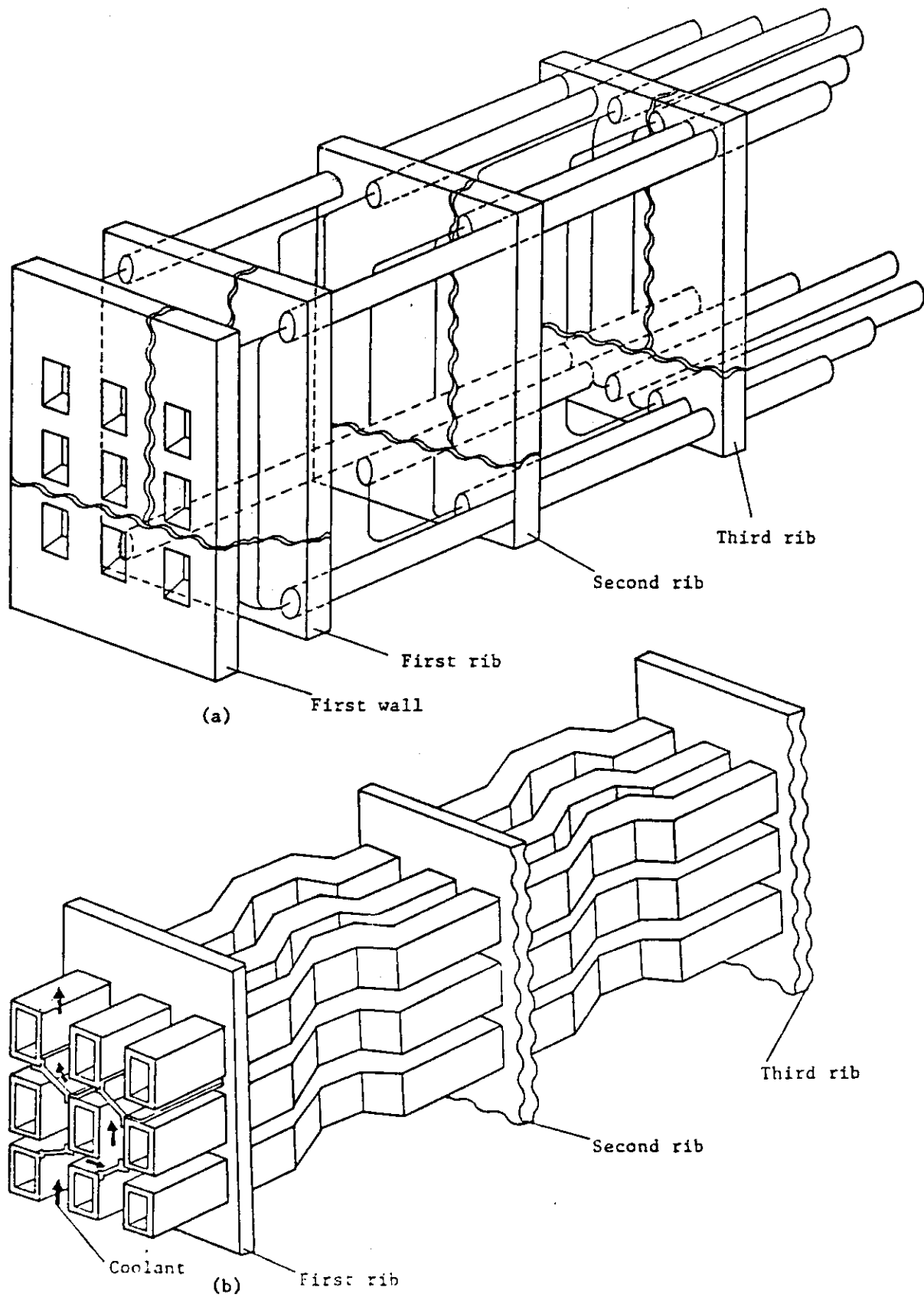
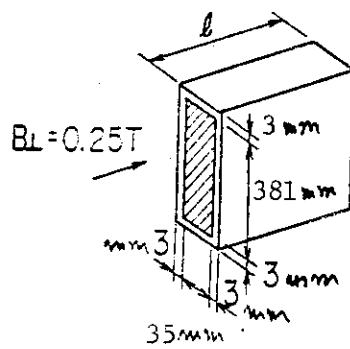
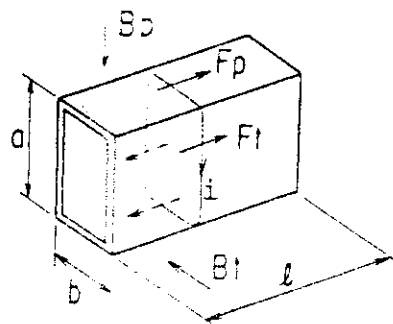


Fig. 5.2-7 Bird's eye view of waveguide cooling concept



(a)



(b)

$i = 869 \text{ kA}$   
 $B_p = 0.53 \text{ T}$   
 $B_t = 4.4 \text{ T}$   
 $F_t = 1468 \text{ N}$   
 $F_p = 19 \text{ N}$

Fig. 5.2-8 Electromagnetic force on waveguide

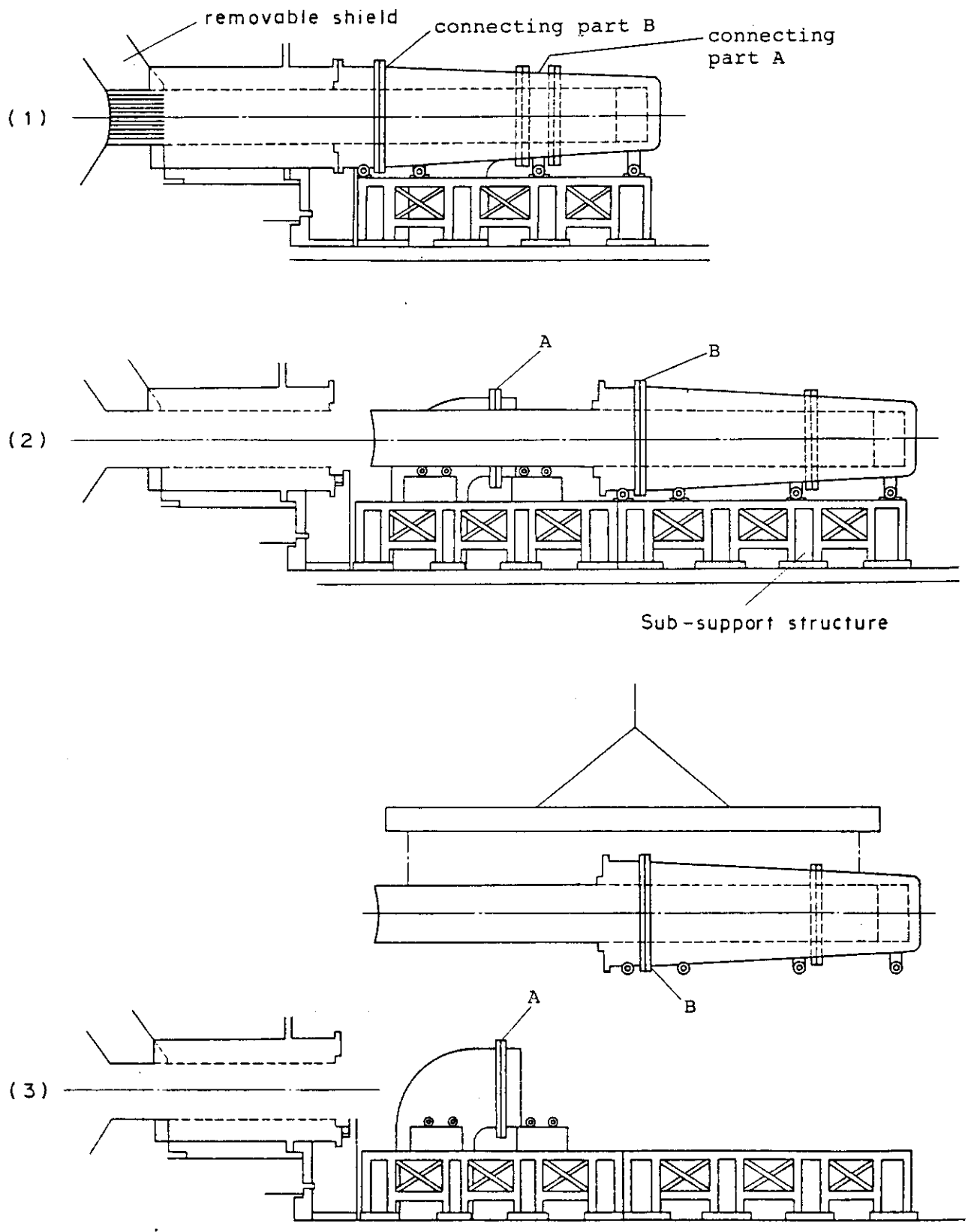


Fig. 5.2-9 Replacement of LHCD Launcher

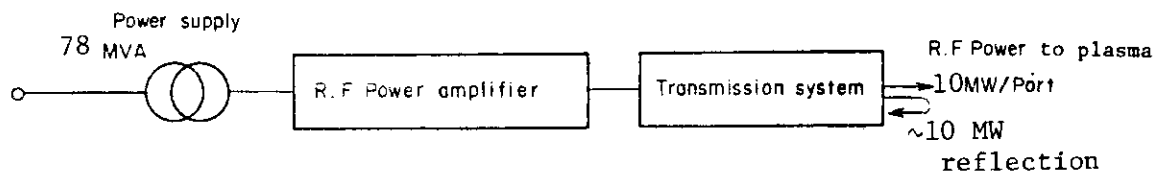


Fig. 5.2-10 Schematic diagram of power supply

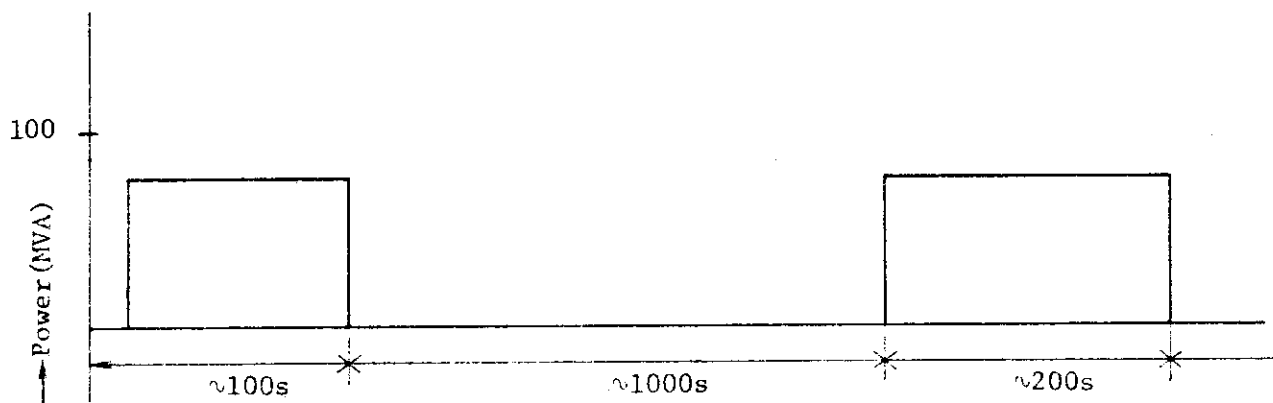


Fig. 5.2-11 Power and operation pattern

### 5.3 ECRF auxiliary heating system

#### 5.3.1 Launcher

##### (1) Launching concept consideration

For ECRF auxiliary heating system, the following function are expected; current start up assist, current profile control, pre-ionization and electron heating. It is required to shift the energy deposition region in the plasma depending on these function, and the radiated direction of the rf power beams should be controled. To alter the rf power beam direction, reflection angle of the beam wave guide reflector is adjusted. In the INTOR design, a frequency of 140 GHz and a power of about 10 MW for 10 sec are required. In the ECRF auxiliary heating system, a primary component is a oscillator. There are no high-power and long-pulse radiation sources at these frequency range at the present time. The most promising millimeter wave radiation sources now are gyrotrons. In the present design, it is assumed that gyrotrons delivering the power of 200 kW in the TE<sub>04</sub> mode will be available. Supposing the rf power loss in the oversized circular wave guide transmission line, approximately 100 of these gyrotrons is required for 10 MW injection.

The rf power is injected in ordinary mode from the outboard side through the duct in blanket and shield. The cross-section of the duct is 1.3 m × 1.8 m, and the horizontal length is about 8 m. So in the duct, the transmission of the rf power by the beam wave guide system is not practical. In this design, the following options are adopted.

- ① The rf power is transfered by a bundle of circular wave guides and finally reflected as a bundle of the rf power beams.
- ② This bundle of beams are shifted below the mid plane.
- ③ To decrease the transmission loss in the launcher, the number of elbows and reflectors should be minimalize unless other restraints are applied.
- ④ The main components to be repaired are windows, reflectors and its actuator. Windows should not be placed in the direct sight of the plasma but for the accessibility in the area outside the bulk shielding. The configuration of the ECRF launcher is shown in Fig. 5.3-1 and Fig. 5.3-2.

##### (2) Launcher configuration

###### 1) Beam wave guide

Beam wave guide consists of the horn antenna and two reflectors called the first reflector and the second reflector. The rf power radiated by each wave guide in transmission line is reflected by the first reflector. The reflection angle is adjusted so that each beam axis is directed to come together in the vertical plane. This bundle of the rf beams is reflected by the second reflector which is plane reflector and rotates around the axis parallel to the magnetic field by the actuator. Rotated angle of the second reflector is adjusted to shift the bundle of the rf power beams toward a point where the rf energy is expected to be concentrated. In this configuration, the rf power is launched by 108 horns of aperture 50 mm. Distance from the first reflector is 250 mm, the aperture of the first reflector

is 100 mm and the second reflector is 1.4 m  $\times$  1.2 m. These reflectors receive the radiation power from the plasma, and the nuclear heating by neutron and gamma ray. The rear side is cooled by water.

## 2) Mode converter and elbow

The necessary components for a transmission line in the launcher are mode converter, elbow and window. The power is transmitted in the low-loss TE<sub>01</sub> mode. Mode converter is needed to transfer the TE<sub>01</sub> mode to the TE<sub>11</sub> mode. Since the loss rate of TE<sub>11</sub> mode is high, the transmission length after the converter must be short. Mode converter is positioned at the end of the transmission line. For mode conversion, the periodic curvature perturbation method is applied. Conversion efficiency of 90% of these mode converter is calculated, supposing the diameter of 20 mm and length of 2.8 m. These mode converters are arranged in the 9  $\times$  12 array in the wave guide container which contains the water for cooling and shielding. The window is placed behind the bulk shield, so transmission line must be bent. Tapered miter elbow type is used, and aperture width is 60 mm. Diffraction loss of 0.04 dB is estimated.

## (3) Power loss estimation

The estimation of power loss in a transmission line is shown in Table 5.3-1. The power loss in the beam wave guide is caused by the beam diffraction and the surface roughness. Ohmic loss is negligible. The spill over from the finite aperture depends on the distance and aperture. In this design, the edge power level of a dominant mode is -20 dB and the spill over loss is calculated approximately to be 0.1 dB. The conversion loss to the higher mode is estimated to be comparable to the spill over loss. Supposing the surface roughness is 30  $\mu$ , power loss is estimated to be 0.15 dB.

## (4) Maintenance

To replace the window, the shielding duct flange with the window assembly is debolted and wave guide are disconnected at the elbow which is made up of the reflector with the horn and the horn. The latter is inserted to the former and jointed together. The bundle of the wave guides shaped L is lifted out. To replace the reflector, the duct flange is lifted up and launching assembly with wave guide, mode converter and so on, is pulled out from the shielding duct.

## 5.3.2 RF source and transmission system

### (1) System configuration

It is assumed that gyrotrons delivering the beam power 200 kW will be available. Approximately 100 of these gyrotrons are required. Each gyrotron requires a 90 kV, 8 A DC power supply and series regulator. Taking into account of the protection capacity, a high voltage DC power supply with a few series regulator can drive 20 gyrotrons. Each gyrotron output power is transmitted by the circular waveguide as TE<sub>01</sub> mode. The oscillation mode is assumed to be the TE<sub>01</sub> mode, so mode converter is needed to transform the mode from TE<sub>04</sub> to TE<sub>01</sub>. Other components is similar to the present system. Estimated power loss is shown in Table 5.3-1.



(2) Total efficiency

It is assumed that gyrotron efficiency is 30 %, transmission loss is 3 dB. Approximately 70 MW of the DC power is required and AC power is about 80 MVA.

5.3.3 Conclusion

Assuming that the oscillator out-put power and the window capacity is of the order of 200 kW, ECRF launcher concept is developed. In the transmission system, the existing technology can be scaled up except the window which has much uncertainty of design condition such as heat load and radiation damage.

If the output power level of the oscillator would be much larger than that of 200 kW, the beam wave guide system will be promising.

Table 5.3-1 Estimation of the transmission loss (per line)

Component	Diameter (mm)	Length (m)	Ohmic loss (dB)	Mode conversion loss (dB)	Number	Total insertion loss (dB)
Circular waveguide	20	100	0.70	$\sim 0.1$	---	0.8
Mode converter $TE_{04}-TE_{01}$	37	3.3	0.02	0.22	1	0.24
Mode converter $TE_{01}-TE_{11}$	20	2.8	0.29	0.46	1	0.75
Miter Bend	60	1.0	$\sim 0$	0.04	10	0.4
Window	$\sim 60$	---	$\sim 0.3$	---	1	$\sim 0.3$
Mode filter	---	---	$\sim 0.1$	---	1	$\sim 0.1$
Waveguide taper	---	$\sim 0.5$	$\sim 0$	$\sim 0$	4	$\sim 0$
Horn antenna	---	---	$\sim 0$	$\sim 0$	1	$\sim 0$
Total						2.59

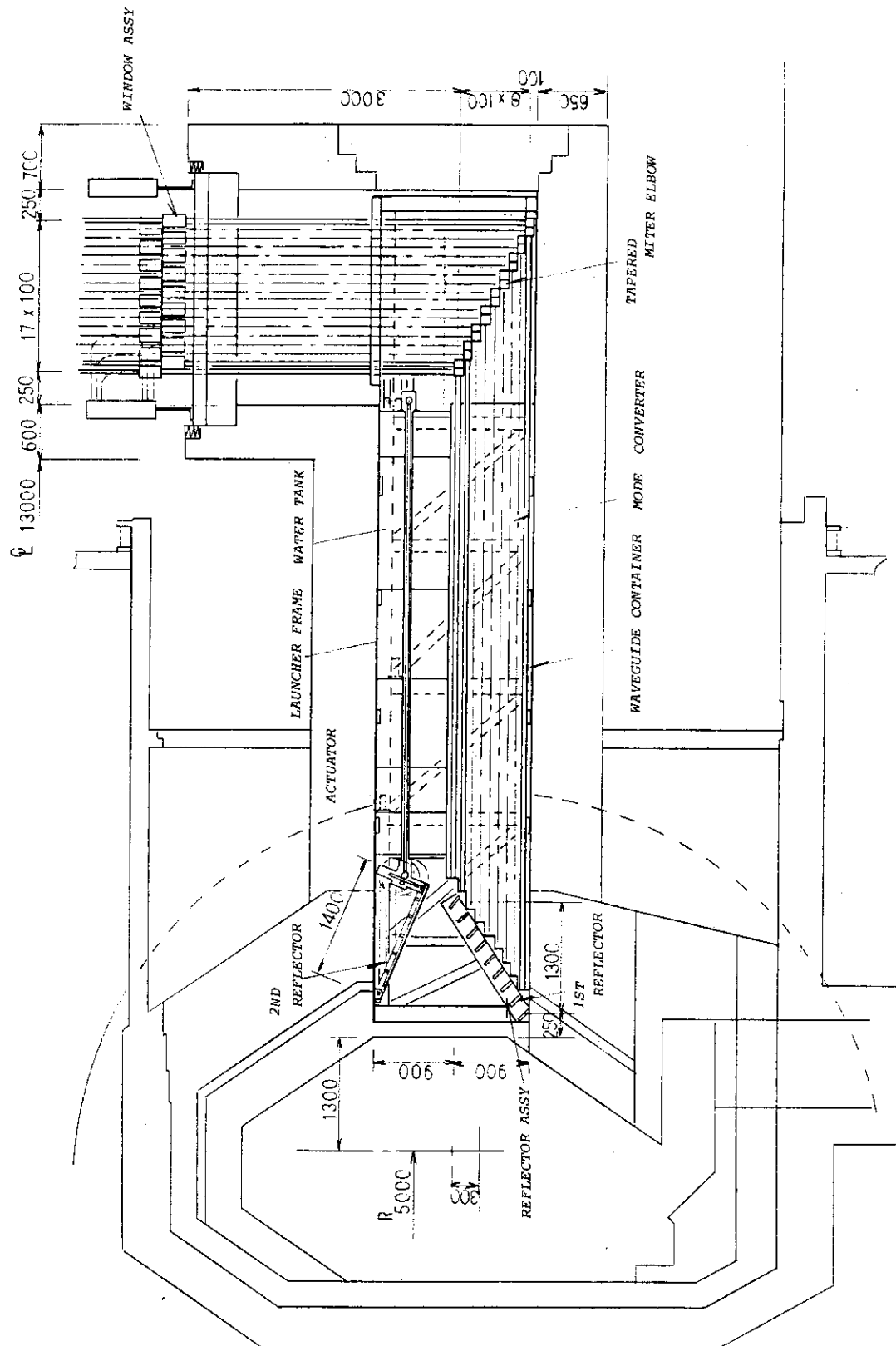


Fig. 5.3-1 ECRF launcher configuration

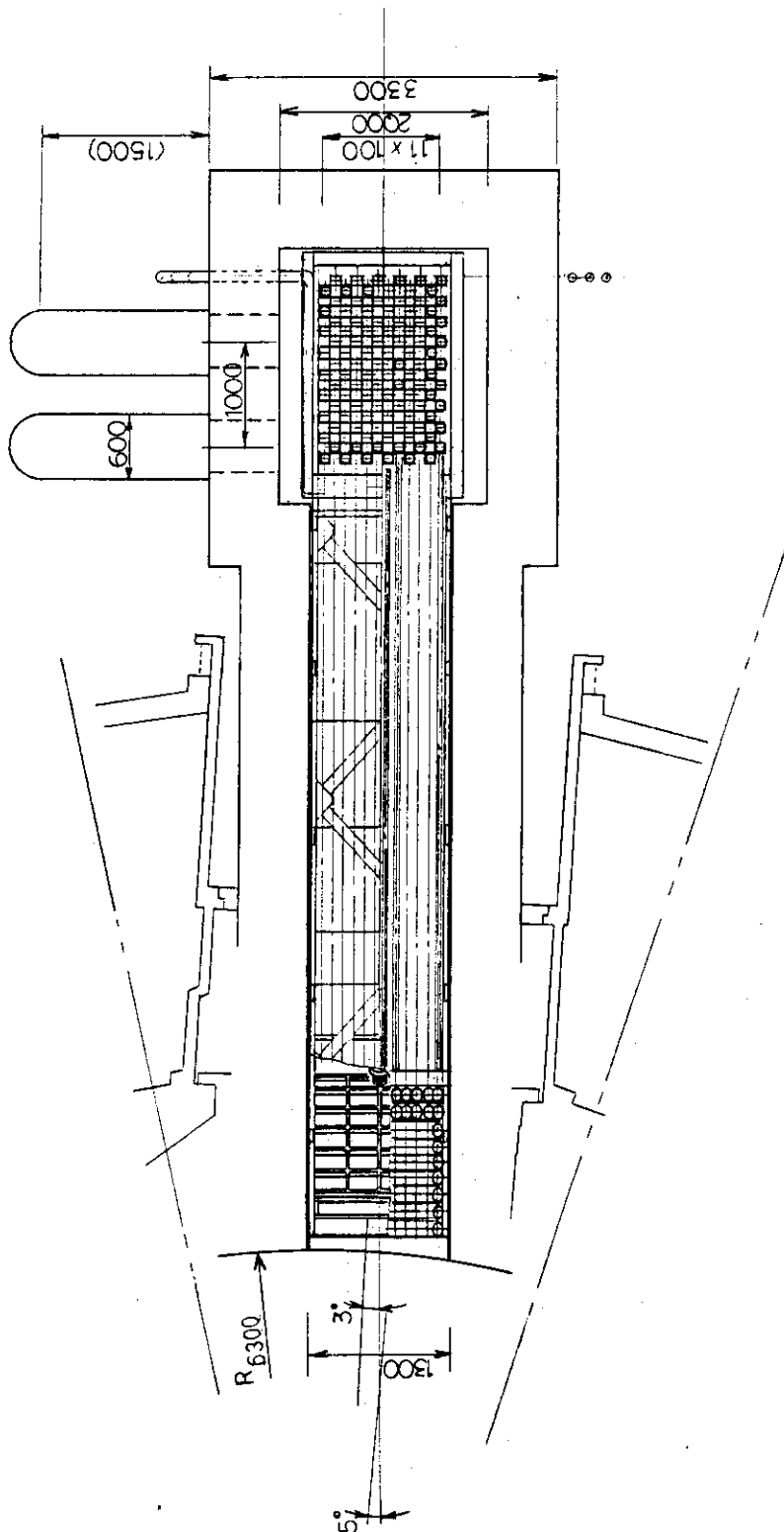


Fig. 5.3-2 ECRF launcher configuration (plane view)

## 6. Operation scenario

### 6.1 Quasi-steady operation

Non-inductive current ramp-up and transformer recharge scenario is incorporated in the modified INTOR design to narrow down the gap between the design beta value and the beta limit predicted by the empirical beta scaling, as presented in the section 2, and to gain engineering benefits associated with the non-inductive current drive scenario. This means modification of the present operation scenario with inductive current drive. We also reconsider the time scale for heating to ignition, which is discussed in the next section from a viewpoint of optimizing power supply.

The modified operation scenario with non-inductive current ramp-up and transformer recharge with a LH wave is shown in Fig. 6.1-1. The operation scenario consists of seven phases; (A) start-up phase including a current ramp-up to 5.7 MA, (B) heating phase to ignition, (C) burn phase, (D) cooling phase for recharging or shutdown, (E) recharging phase for OH coils, (G) shutdown phase, and (H) dwell phase.

At the beginning of the start-up phase, plasma are produced and heated with an assist of ECRF heating with 10 MW, and plasmas are brought to a parameter region with around  $3 \times 10^{18} \text{ m}^{-3}$  in densities and 1-2 keV in temperatures. Such a low-density plasma carry well its current driven by a LH wave. Based on analyses on a current ramp-up scenario (see Chapter IV, RF heating and current drive), a ramp-up time is specified  $\sim 100 \text{ s}$ , and during this period the plasma current increased up to 5.0 MA by the LH wave with a power level of 10 MW.

In the heating phase to ignition, plasmas are heated by an ICRF wave of 50 MW, and temperatures and densities are increased to the specified level of the burn phase. The plasma current is also increased from 5.7 MA to 7.5 MA inductively instead of rf drive, because of significant decrease of rf current drive efficiency in high density plasmas. The heating time is  $\sim 20 \text{ s}$ , which is discussed in the next section.

An initial goal of a burn time is more than 1000 s, which is inductively driven. The preliminary study on a scenario about poloidal coil currents shows that the burn time is considerably limited to less than 1000 s, but the longer burn time may be possible by optimizing currents of PF coils. The cooling phase is an inverse process of the heating phase. The cooling time is  $\sim 20 \text{ s}$ . The prolonged cooling time may require temperature control with the ICRF wave, otherwise temperatures could drop with the shorter time of an order of confinement time. In the cooling phase, the plasma current decreased to from 7.5 MA to 5.7 MA inductively.

In the recharge phase, OH coils are recharged, while the plasma current is hold to 5.7 MA by the LH wave in plasmas with densities of around  $3 \times 10^{18} \text{ m}^{-3}$  and temperatures of 1-2 keV. The recharging time of  $\sim 200 \text{ s}$  is also evaluated based on analyses of transformer recharge by the LH wave (see also Chapter IV, RF heating and current drive). The reason why the plasma current is reduced to 5.7 MA in the recharging phase is because of reducing a difference between forces on the TF coils during high- and low-beta plasmas. In a quasi-steady operation, four phases from (B) to (E) are repeated.

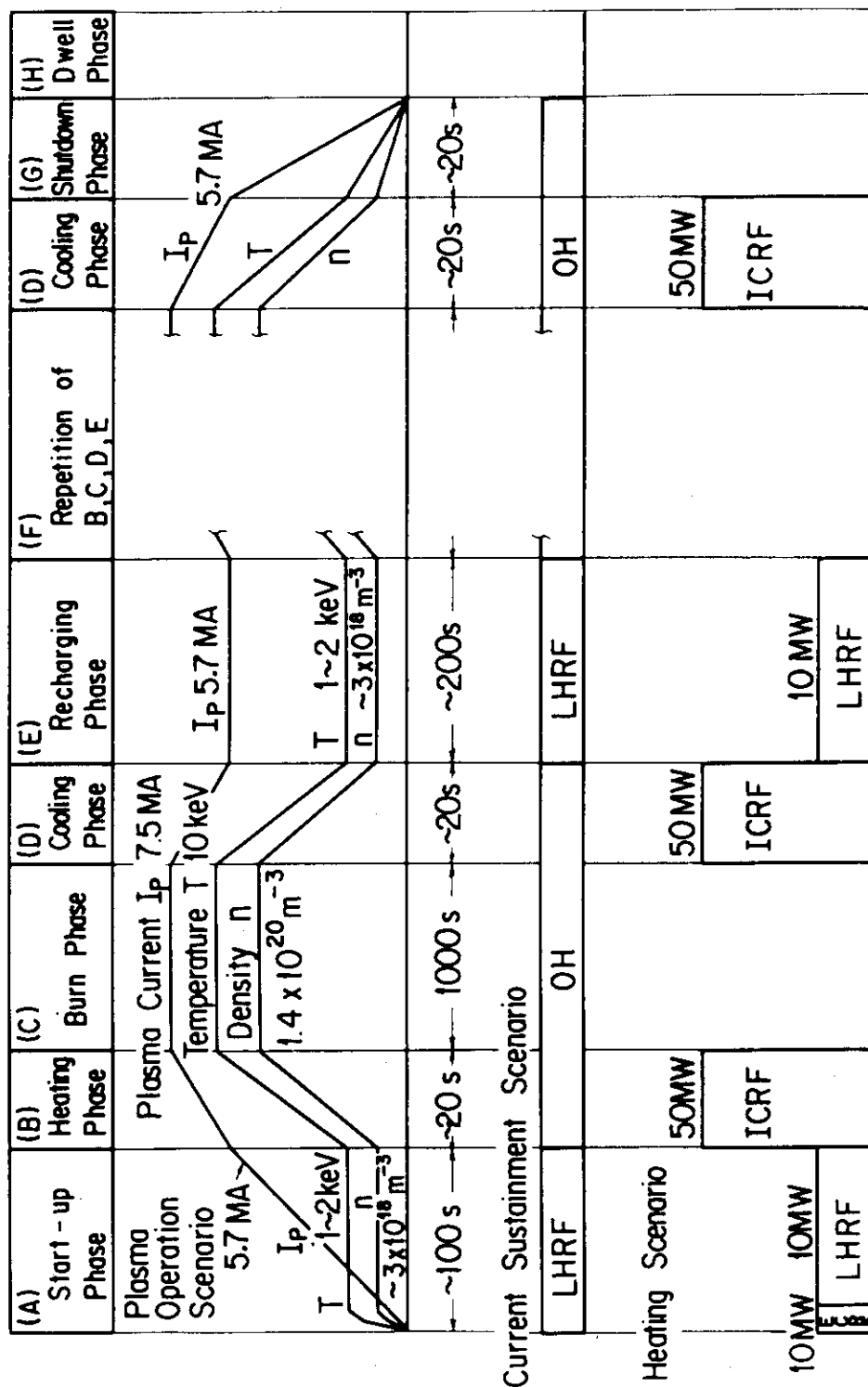


Fig. 6.1-1 Modified INTOR operation scenario

## 6.2 Ignition approach duration

### 6.2.1 Introduction

The capacity and energy required for power supplies of PF system and heating systems are closely related to the operating scenario of plasma. In the scenario with RF current ramp up critical phase for the power supply system is the ignition approach phase (heating phase). Longer duration of this phase requires smaller system but larger energy storage system for plasma heating.

In this chapter, we compare operating scenarios with the ignition approach duration of  $T_h = 6$  sec and  $T_h = 20$  sec from the point of minimizing power supply requirement.

### 6.2.2 Comparative calculation

#### (1) Specification

- ① PF coil current scenarios are shown in Table 6.2-1.
- ② Specification of heating systems is shown in Table 6.2-2.

#### (2) Study

- ① It is assumed that flywheel motor generators deliver the electric power to all systems except LHRF current drive system, which is delivered by utility lines because of large energy requirement.
- ② It is assumed that the capacity of generators equals to the maximum value of instantaneous apparent powers caused by means of axisymmetric phase control for thyristor convertors.
- ③ The calculated output of thyristor convertors is presented by Table 6.2-3. Figure 6.2-1 ~ 3 show load patterns which are computed by the PF simulator.
- ④ From the capacity and energy required for power supplies of PF system and heating systems as shown in Table 6.2-4, we can get the specification of the flywheel motor generators shown in Table 6.2-5.
- ⑤ A cost scaling of thyristor convertor systems and flywheel motor generators is assumed as follows,
  - Thyristor convertor system ; 32 K\$/MW
  - FWMG system ; (16 K\$/MVA) + (4 K\$/MJ)

### 6.2.3 Conclusion

We studies comparing  $T_h = 6$  sec and  $T_h = 20$  sec. Table 6.2.6 shows cost ratios for the above two cases. We conclude  $T_h = 20$  sec is better.

Table 6.2-1 PF coil current scenarios

Time(sec) $T_h=6$ sec ( $T_h=20$ sec)		0.0	100	106 (120)	606 (620)	612 (640)	712 (740)
coil current (MAT)	Coil No. 1	0.0	-1.617	-4.254	-9.434	-7.907	-1.617
	2	0.0	-1.617	-4.254	-9.434	-7.907	-1.617
	3	0.0	-1.617	-4.254	-9.434	-7.907	-1.617
	4	0.0	4.725	2.835	-2.457	-1.701	4.725
	5	0.0	5.025	3.015	-2.613	-1.809	5.025
	6	0.0	6.296	5.294	3.614	4.256	6.296
	7	0.0	5.298	5.943	5.271	4.482	5.298
	8	0.0	-3.492	-1.590	-1.786	-3.730	-3.492
	9	0.0	0.414	-3.632	-3.828	0.176	0.414
	10	0.0	-1.617	-4.254	-9.434	-7.907	-1.617
	11	0.0	-1.617	-4.254	-9.434	-7.907	-1.617
	12	0.0	4.625	2.775	-2.405	-1.665	4.625
	13	0.0	4.725	2.835	-2.457	-1.701	4.725
	14	0.0	5.025	3.015	-2.613	-1.809	5.025
	15	0.0	15.660	14.930	13.250	13.620	15.660
	16	0.0	18.210	20.210	19.530	17.400	18.210
	17	0.0	-9.405	-6.941	-7.137	-9.643	-9.405
	18	0.0	-5.736	-10.260	-10.450	-5.974	-5.736
plasma $I_p$ (MA)		0.0	5.700	7.500	7.500	5.700	5.700



Table 6.2-2 Specifications of heating system for INTOR

	Main heating	Current drive	Start-up assist
Wave	ICRF	LHRF	ECRF
Mode	2nd harmonic D	slow mode	1st harmonic, 0 mode
Frequency	76 MHz	0.56 GHz	140 GHz
Power injection	50 MW	10 MW	10 MW
Duration	6 ~ 20 sec	100 sec	5 sec
Efficiency	0.45	0.15 (Including 50% reflection loss)	0.13
Power factor	0.85	0.85	0.85

Table 6.2-3 Convertors of PF system for INTOR

unit [MW]

COIL NO.	$T_h = 6 \text{ sec}$		$T_h = 20 \text{ sec}$	
	Forward	Reverse	Forward	Reverse
1	0	19.5	0	5.9
2	0	19.4	0	5.9
3	0	18.8	0	5.7
4	8.0	4.2	2.4	1.3
5	8.0	4.2	2.4	1.3
6	12.3	0	4.0	0
7	5.4	0	5.4	0
8	0	11.0	0	3.4
9	15.2	134.7	4.6	40.4
10	0	19.2	0	5.8
11	0	18.3	0	5.5
12	7.5	3.9	2.3	1.2
13	7.0	3.7	2.1	1.1
14	6.8	3.5	2.4	1.2
15	23.6	0	23.6	0
16	96.7	0	54.3	0
17	0	63.1	0	22.1
18	0	394.1	0	118.3
TOTAL	190.5	717.6	103.5	219.1

Table 6.2-4 Capacity and energy required for various P/S

	Capacity required (MVA)		Energy required (MJ)		Remarks
	$T_h = 6 \text{ sec}$	$T_h = 20 \text{ sec}$	$T_h = 6 \text{ sec}$	$T_h = 20 \text{ sec}$	
PF coil P/S	655	225	8887		
ECRF P/S	91		385		Heating time = 5 sec
LHRF P/S	79		13400		Heating time = 100 sec
ICRF P/S	131		1332	4444	

Table 6.2-5 Specification of MG sets

For use	Spec. of MG	
	$T_h = 6\text{sec}$	$T_h = 20 \text{ sec}$
PF coil P/S	(*) $222^{\text{MVA}} - 3^{\text{GJ}} - 3^{\text{SETS}}$	(*) $80^{\text{MVA}} - 3^{\text{GJ}} - 3^{\text{SETS}}$
ICRF P/S (Including ECRF P/S)	$230^{\text{MVA}} - 1.8^{\text{GJ}} - 1^{\text{SETS}}$	$115^{\text{MVA}} - 2.5^{\text{GJ}} - 1^{\text{SETS}}$

(\*) With lowering reactive power by means of asymmetric phase control for thyristors

Table 6.2-6 Cost ratio of power supplies

	Cost ratio	
	$T_h = 6\text{sec}$	$T_h = 20 \text{ sec}$
PF coil P/S (Including convertor)	6.8	4.5
ICRF P/S (Including ECRF P/S)	1.0	2.2

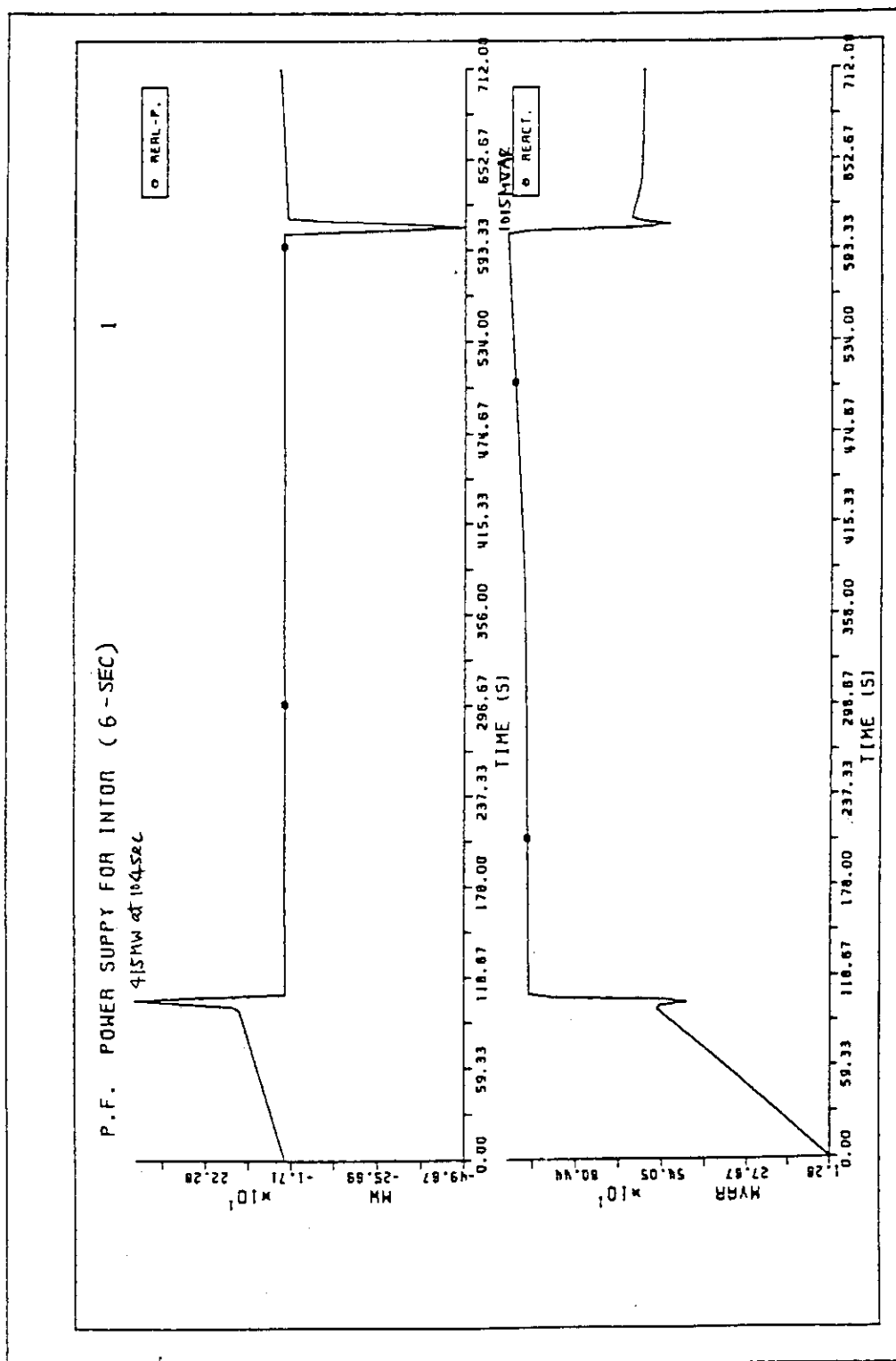


Fig. 6.2 -1 Load pattern with symmetric phase control of PF system  
(  $T_h = 6 \text{ sec}$  )

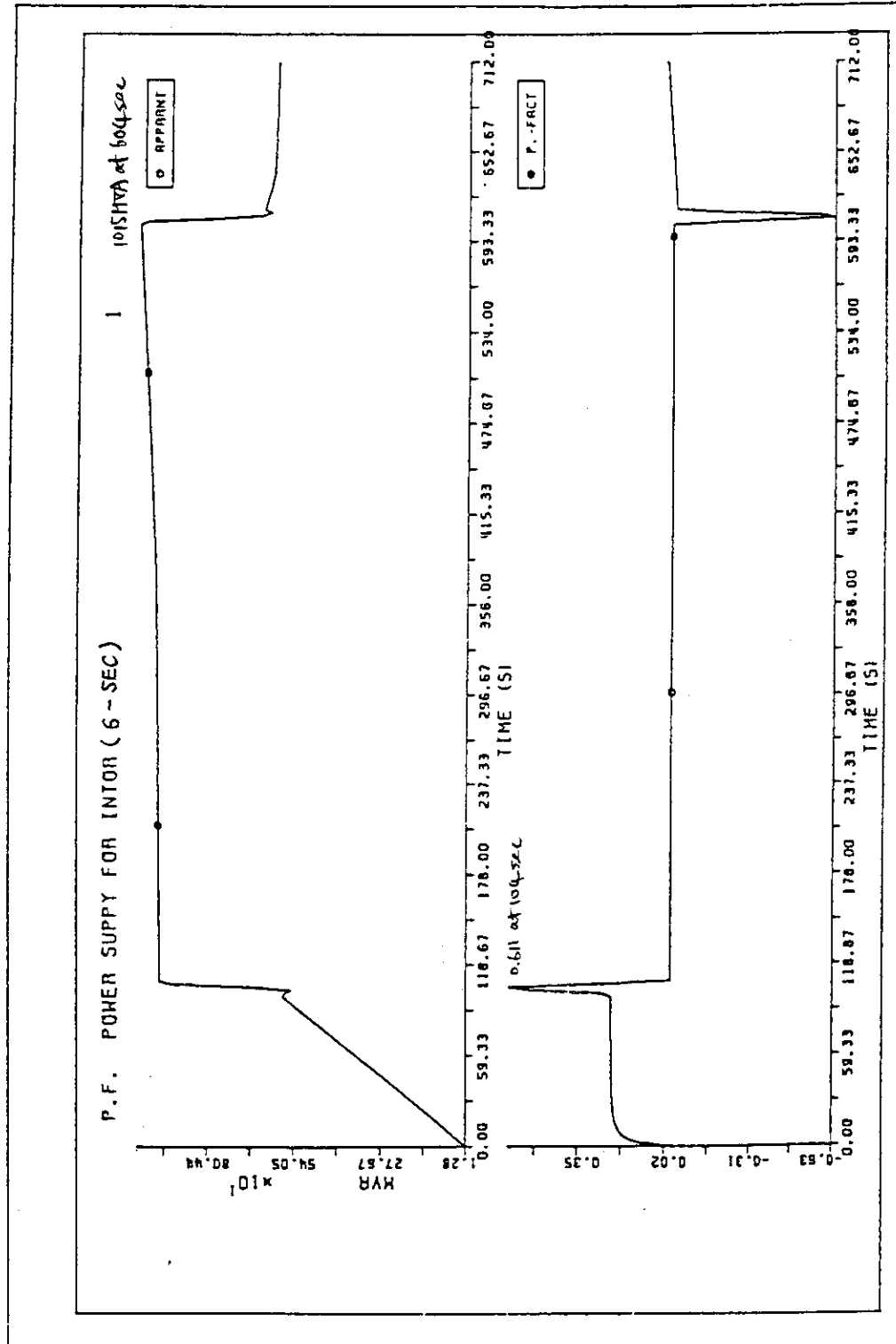


Fig. 6.2 -1 Load pattern with symmetric phase control of PF system  
(  $T_h = 6 \text{ sec}$  )

CONTINUED

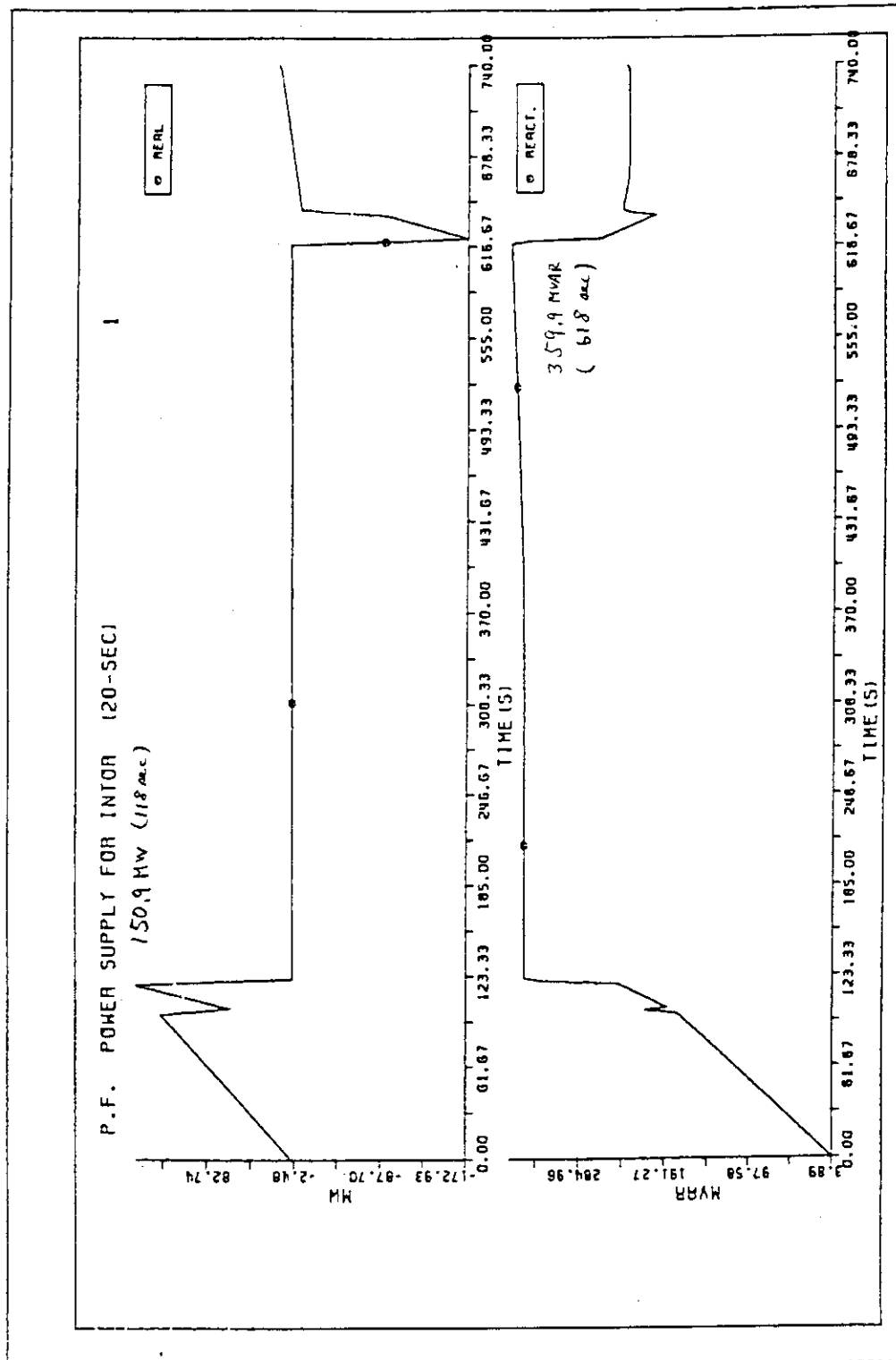


Fig. 6.2 -2 Load pattern with symmeric phase control of PF system

 $(T_h = 20 \text{ sec})$

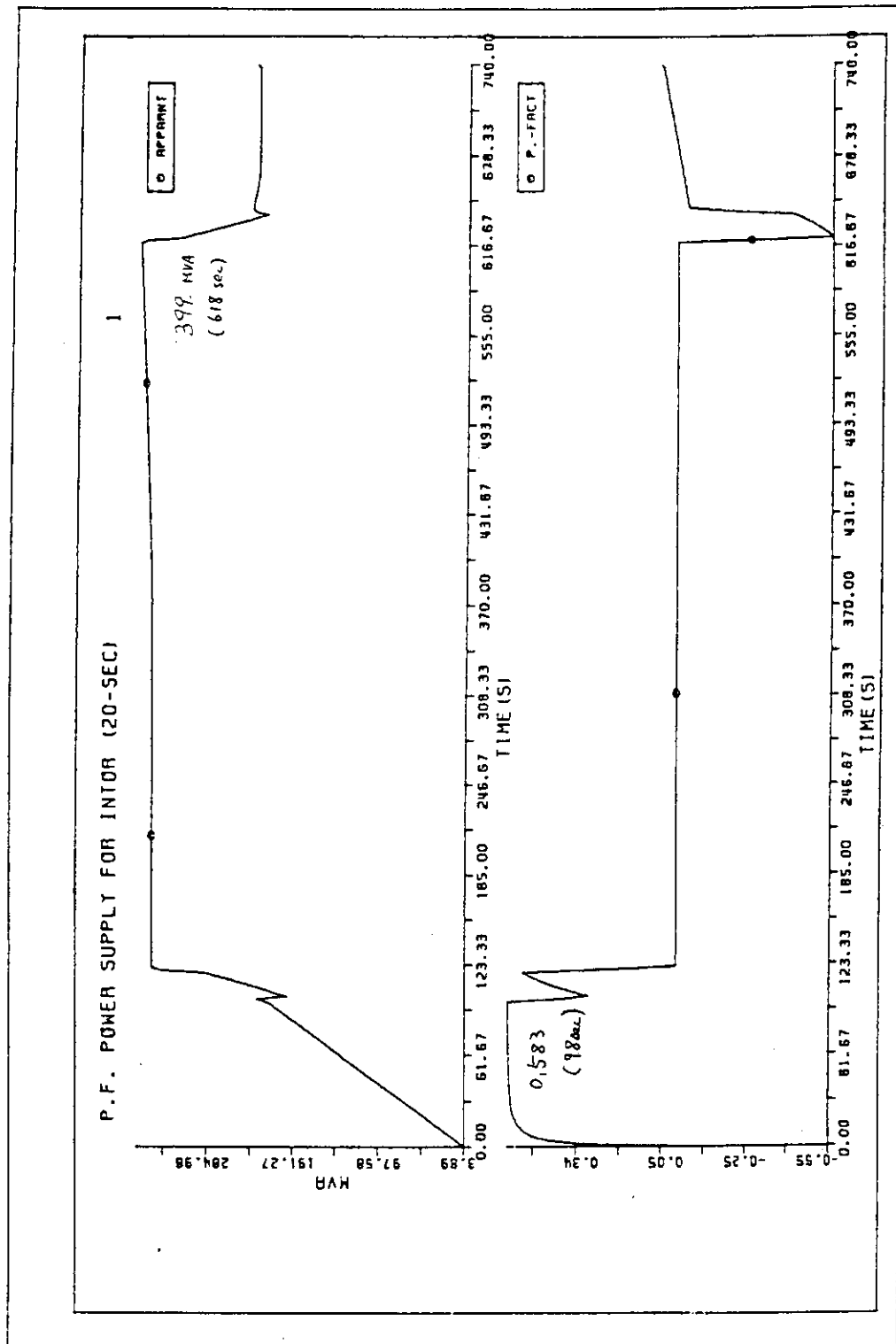


Fig. 6.2 -2 Load pattern with symmetric phase control of PF system  
(  $T_h = 20 \text{ sec}$  )

CONTINUED



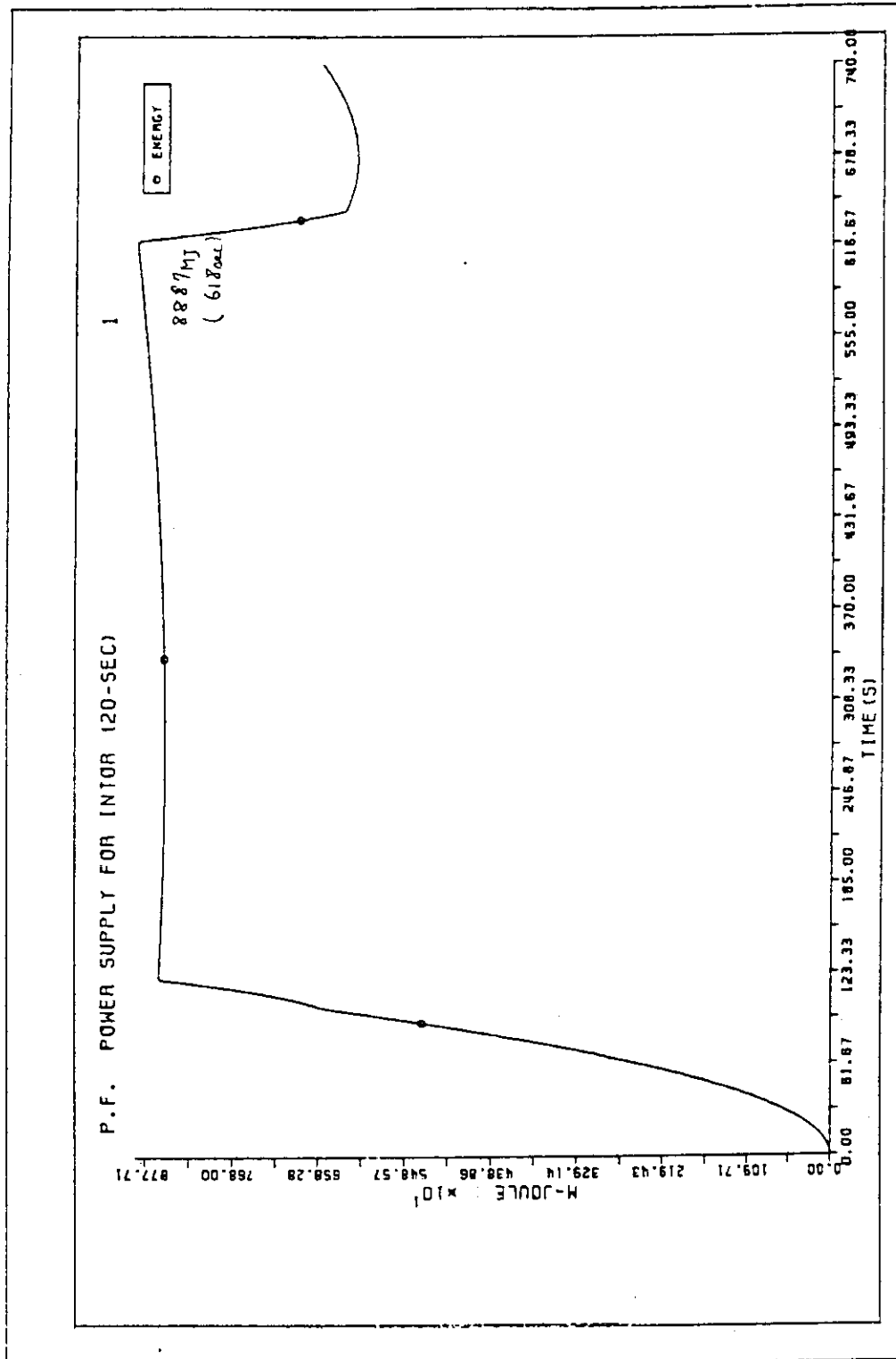


Fig. 6.2 -3 Load pattern with symmetric phase control of PF system  
(  $T_h = 20$  sec )

### 6.3 Available flux for burning

#### 6.3.1 Relation between magnetic flux swing range and the maximum field

In the scenario of quasi-steady state operation described in 6.1, higher magnetic field will act on the poloidal field coil, especially inboard OH coils, than in the case of conventional pulsed operation at the beginning of burn phase. This can be explained using Fig. 6.3-1 as follows.

The point ① in Fig. 6.3-1 is the start point of burn phase and the point ② or ③ is the end point of burn. The plasma current during burn should be sustained by OH flux change. The direction of OH coil current at beginning of burn is same as of the plasma current. And the divertor coils are continuously excited and their current direction is also same as of plasma current. So there is the external field "B<sub>EX</sub>" generated by the plasma current and divertor coils on the OH coil windings. At the point ①, the direction of B<sub>EX</sub> is almost same as that of OH coil windings "B<sub>OH</sub>", and opposite at the point ② or ③. Therefore B<sub>OH</sub> at start of burn should be less than B<sub>max</sub> (the maximum allowable field).

On the other hand in the case of pulsed operation it is possible to excite the OH coils to B<sub>max</sub> because there is no plasma current, then no divertor coil current at the pulse start. When the plasma and divertor coil currents rise to significant level, the OH coil current will be very small or current direction is inverted.

For the end of burn phase there may be some risk in fully swinging OH coil to -B<sub>max</sub> regardless of whether operation mode is quasi-steady state or pulsed, that is, it may be dangerous to select point ③ for the end of burn because of possible sudden loss of B<sub>EX</sub> by plasma disruption. Then ② is better selection. Therefore B<sub>OH</sub> cannot be fully swung from B<sub>max</sub> to -B<sub>max</sub> especially in the case of quasi-steady state operation.

In order to use the OH flux change efficiently and to obtain the longer burn time under the limit of magnetic field, it is important to estimate B<sub>EX</sub> accurately and to determine the proper operation points. The evaluation of B<sub>EX</sub> and determination of the operation points are performed as follows.

The current of each PF coil is determined by the requirements of plasma equilibrium and the generation of OH flux. From the plasma equilibrium requirement, the current of each PF coil {I<sub>i</sub><sup>EF</sup>} can be approximately expressed as

$$\{I_i^{EF}\} = \{C_{1i}^{EF}\} \phi_{EF} + (\{C_{2i}^{EF}\} \beta_p + \{C_{3i}^{EF}\}) I_p \quad \text{-----} \quad (1)$$

where  $\phi_{EF}$  is the interlinking flux with plasma,  $\beta_p$  is the poloidal beta value and  $I_p$  is the plasma current. The suffix "i" means the PF coil number and {C<sub>1~3i</sub><sup>EF</sup>} are constants values which are determined depending on the locations of PF coils and the shape of plasma.

In the same way as the equilibrium, the current for the OH flux {I<sub>i</sub><sup>OH</sup>} is expressed as

$$\{I_i^{OH}\} = \{C_i^{OH}\} \phi_{OH} \quad \text{-----} \quad (2)$$

where  $\{C_i^{OH}\}$  is constant which is also determined for the given location of PF coils.

Next we consider the magnetic field  $B_i$  on each PF coil winding. The fractions of  $B_i$  due to  $\{I_i^{EF}\}$ ,  $\{I_i^{OH}\}$  and  $I_p$  are expressed as follows for given  $\beta_p$ .

$$B_i^{EF} \propto \{I_i^{EF}\}$$

$$\therefore B_i^{EF} = K_{1i} \phi_{EF} + K_{2i} I_p \quad \text{-----} \quad (3)$$

$$B_i^{OH} \propto \{I_i^{OH}\}$$

$$\therefore B_i^{OH} = L_i \phi_{OH} \quad \text{-----} \quad (4)$$

$$B_i^{Pl} \propto I_p$$

$$\therefore B_i^{Pl} = M_i I_p \quad \text{-----} \quad (5)$$

then

$$\begin{aligned} B_i &= B_i^{EF} + B_i^{OH} + B_i^{Pl} \\ &= K_{1i} \phi_{EF} + (K_{2i} + M_i) I_p + L_i \phi_{OH} \end{aligned} \quad \text{-----} \quad (6)$$

where  $K_{1i}$ ,  $K_{2i} + M_i$  and  $L_i$  are coefficient for  $\phi_{EF}$ ,  $I_p$ , and  $\phi_{OH}$  respectively. And these values are vectors in two dimensions of perpendicular (radial direction) and parallel components to the torus axis.

Only  $K_{2i}$  is dependent on  $\beta_p$ . But after deciding the plasma parameters of the burn phase and/or the recharging phase, the term of " $(K_{2i} + M_i) I_p$ " is reduced to the constant vector.

Then we pay attention to the allowable OH flux change " $\Delta\phi_{OH}$ " under the condition of the limiting field strength " $B_{max}$ ". First, we consider the case in which the only  $i$ th PF coil's operation is restricted by maximum allowable field  $B_{max}$ .

From the eq. (6), and the restriction  $|B_i| \leq B_{max}$

$$\begin{aligned} B_i^2 &= (B_i^r)^2 + (B_i^z)^2 \\ &= D_i \phi_{OH}^2 + 2F_i \phi_{OH} + G_i \leq B_{max}^2 \end{aligned} \quad \text{-----} \quad (7)$$

where  $B_i^r$  and  $B_i^z$  are perpendicular and parallel components of  $B_i$  respectively. And  $D_i$  is constant value for the given locations of PF coils.  $F_i$  and  $G_i$  are functions of  $\phi_{EF}$ . Fig. 6.3-2 shows the relation between  $B_i^2$  and  $\phi_{OH}$  schematically. Allowable OH flux change  $\Delta\phi_{OH}$  shown in the figure is variable and depends on the value of  $\phi_{EF}$ . In order to obtain the maximum flux change,  $\phi_{OH}$  should be determined by minimizing the value of " $G_i(\phi_{EF}) - \{F_i(\phi_{OH})\}^2/D_i$ ".

Now we consider the actual PF coil system which has many coils. As shown in Fig. 6.3-3, it is necessary to find out the range of  $\Delta\phi_{OH}$  in which all PF coils simultaneously satisfy the condition of  $B_{max}$ . It is known as the results of many case of calculation that the critical value of  $B_{max}$  always appears on certain coils. They are the OH coil located in midplane, the divertor coil and the nearest coil to the divertor coil.

### 6.3.2 Quasi-steady state operation

The operational scenario of the quasi-steady state operation is shown in Fig. 6.1. In this paragraph, we consider the optimum scheme of operation. During the cyclic operation of burn and recharging phases, the plasma current is kept in the range from 7.5 MA to 5.7 MA. However the total magnetic flux  $\phi_t$  is conserved for the interval when the plasma current is sustained by OH flux (i.e. from the start of heating to the end of cooling). This is expressed as

$$\phi_t = \phi_p + \phi_{OH} + \phi_{EF} + \int v_p dt = \text{const.} \quad \text{----- (8)}$$

where  $\phi_p$  is the inductive flux of plasma current and  $v_p$  is the one-turn voltage of plasma.  $\int v_p dt$  is called the resistive flux, it is estimated about 3 V.s during each phase of heating and cooling. The location of PF coils is shown in Fig. 8.2-1 and Fig. 6.3-4 shows the allowable flux change  $\Delta\phi_{OH}$  during the burn phase and the recharging phase.  $\Delta\phi_{OH}$  depends on  $\phi_{EF}$ . And also  $\Delta\phi_{OH}$  depends on the plasma current, as shown by the broken lines ①, ② and ③ in Fig. 6.3-4. The value shown in this figure is the maximum value of  $\Delta\phi_{OH}$ , but at the operation it is impossible to obtain the full range because of the necessity of satisfying eq. (8). Considering this restriction, the operation scheme is described on the  $\phi_{OH}$ ,  $\phi_{EF}$  diagram like Fig. 6.3-5. Figure (a) and (b) correspond to the burn phase and the recharging phase respectively. In the figure the solid lines show the upper limit of maximum field 10 T on #13, #14 and #15 coils, and the broken lines show the lower limit (-10T) on #1 coil.

The circular and triangular symbols are the operation points presenting as follows;  $\bullet \rightarrow \circ$  is the heating phase,  $\circ \rightarrow \Delta$  is the burn phase,  $\Delta \rightarrow \blacktriangle$  is the cooling phase and  $\blacktriangle \rightarrow \circ$  is the recharging phase. The values of  $\phi_p$  are 57 V.s at the recharging phase and 80 V.s at the burn phase. The end point of the burning phase is selected 5 V.s higher than the lower limit of #1 coil as shown in figure (a) preventing the field of #1 coil from overshooting the limite value at the plasma disruption.

From this consideration, the obtained flux is 28 V.s for sustaining the burning plasma. This corresponds to the burn time of about 509 s. And Fig. 6.3-6 shows the magnetic field on the PF coils at the operation points. The maximum values appear on #14 coil at the end of recharge and on #1 coil at the end of burn. These values are lower than the limit field of 10 T.

### 6.3.3 Pulsed operation

Next we consider the burn time of the pulsed operation of inductive current ramp-up scenario, through the same process of the quasi-steady state operation described above paragraph. The plasma current is ramped up to 5 MA spending 8 V.s before heating and to 6.4 MA spending additional

3 V.s before reaching the burn phase. The current of the burning plasma is the same as the previous design. The values of  $\phi_p$  are 50 V.s at 5 MA and 72 V.s at 6.4 MA.

Fig. 6.3-7 shows the allowable range of OH flux as a function of  $\phi_{EF}$ . Solid line ① shows that of the initial excitation of OH coils with no plasma current. The line ① indicates that the OH coils have a ability to generate about 90 V.s for  $\Delta\phi_{OH}$  when  $\phi_{EF}$  equals zero. However, in the same way as the quasi-steady state operation, the effective OH flux for burn is restricted by the allowable operation scheme. The scheme is shown in Fig. 6.3-8 on the  $\phi_{OH}$ ,  $\phi_{EF}$  diagram. (a), (b), and (c) in the figure is the burn phase, the phase just before heating or just after cooling, and the initial excitation respectively. The result shows that 27 V.s of OH flux is obtained for burning. This means that 574 s duration of burn time is possible.

#### 6.3.4 Summary

In order to compare the deference between the quasi-steady state operation and the pulsed operation two other cases are considered. They are as follows;

- a) Pulsed operation with the burn phase plasma current of 6.4 MA
- b) Quasi-steady state operation with the burn phase plasma current of 7.5 MA

The operation schemes of case a) and b) are shown in Fig. 6.3-9 and Fig. 6.3-10 respectively. The results are summarized in Table 6.3-1. (a) shows the available flux for burning and (b) shows the burn time. The burn time in (b) is not proportional to the available flux in (a) because of the deference of the one-turn voltage of burning plasma between 6.4 MA and 7.5 MA. Percent ratios in the table show the comparison with the case of pulsed operation of  $I_p = 6.4$  MA. Changing the operation scenario from the inductive current ramp-up the quasi-steady state operation, it is possible to extend the burn time more than 170%.

In the case of the quasi-steady state operation of  $I_p = 7.5$  MA, plasma current just before heating phase is selected to be 5.7 MA, while in the other cases the current is 5 MA. When the current of recharging phase is selected to be 5 MA as same as other three cases, the available flux for burning will be larger by about 10 %.

In the consideration above, we do not mention about the dependency on the location of PF coils and only consider the case shown in Fig. 8.2-1. There are two divertor coils in this configuration. They are #15 and #16 coils. The magnetic field on #15 coil winding is higher because not only high Amper-turns of #15 coil but also the field owing to #16 coil which locate just outside the #15 coil. And this situation makes difficulty to obtain the wide range of  $\phi_{OH}$ . However, it is known that dividing the divertor current into three coils instead of two will make the range of  $\phi_{OH}$  wider, through the experience of FER design study.

Table 6.3-1 Summary of burn time.

(a) Available flux for burning

Operation mode Plasma parameter		Quasi - steady state operation	Pulsed operation
$I_p = 7.5 \text{ MA}$ $\beta_p = 1.3$	$\phi_{\text{burn}}$	28 v.s	15 v.s
	ratio (%)	104 %	56 %
$I_p = 6.4 \text{ MA}$ $\beta_p = 2.2$	$\phi_{\text{burn}}$	45 v.s	27 v.s
	ratio (%)	167 %	100 %

(b) Burn time

Operation mode Plasma parameter		Quasi - steady state operation	Pulsed operation
$I_p = 7.5 \text{ MA}$ $\beta_p = 1.3$	$\tau_{\text{burn}}$	509 s	273 s
	ratio (%)	89 %	48 %
$I_p = 6.4 \text{ MA}$ $\beta_p = 2.2$	$\tau_{\text{burn}}$	957 s	574 s
	ratio (%)	167 %	100 %

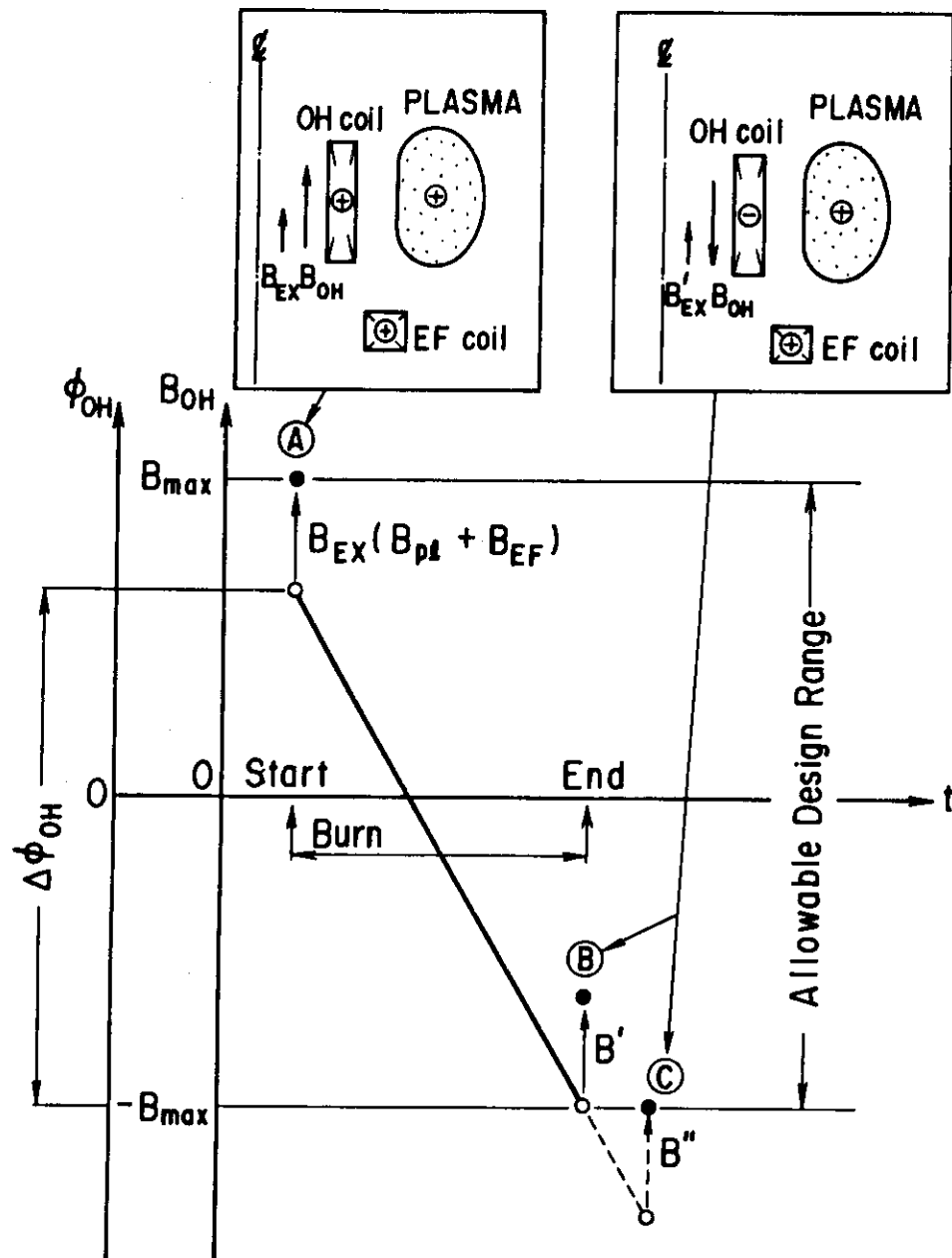


Fig. 6.3-1 Swing range of OH field on Quasi-steady operation reactor

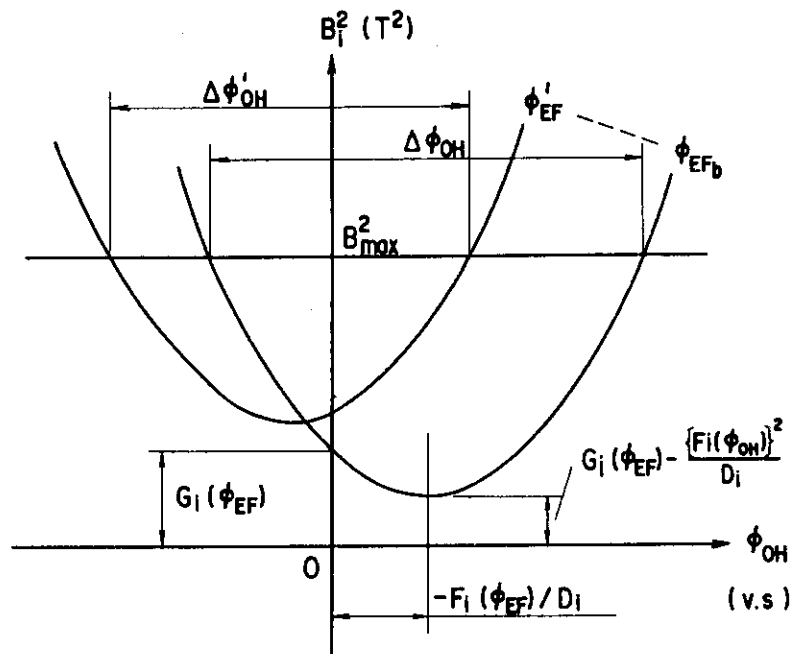


Fig. 6.3-2. Allowable OH flux change ( $B_i^2$  vs  $\phi_{OH}$ )

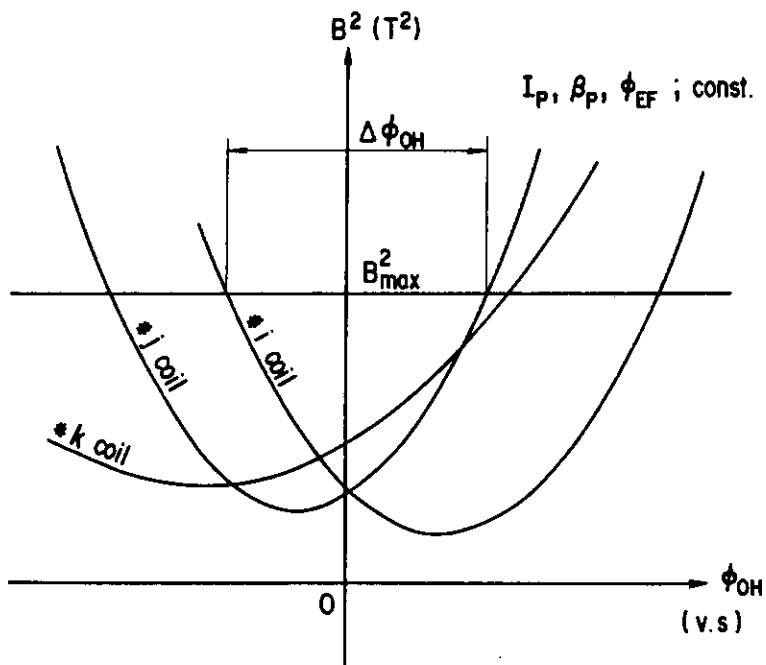


Fig. 6.3-3. Allowable range of  $\phi_{OH}$



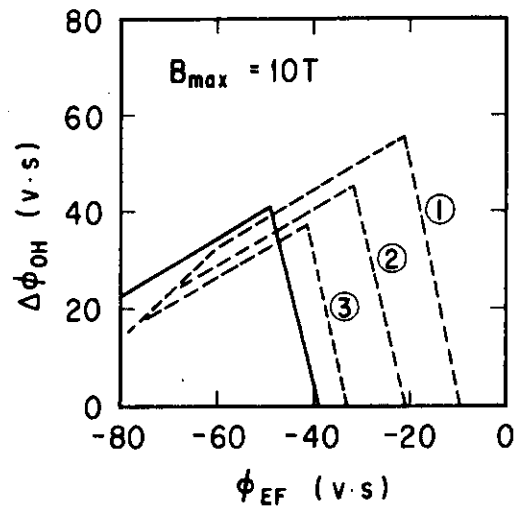


Fig. 6.3-4  $\Delta\phi_{OH}$ ,  $\phi_{EF}$  diagram  
 Solid line shows the OH flux for  
 burning phase  $\beta_p = 1.3$ ,  $I_p = 7.5$  MA.  
 Broken lines show for recharging  
 phase  $\beta_p = 0.1$ , ①, ② and ③ are for  
 $I_p = 5.0$ ,  $5.7$  and  $6.3$  MA respectively

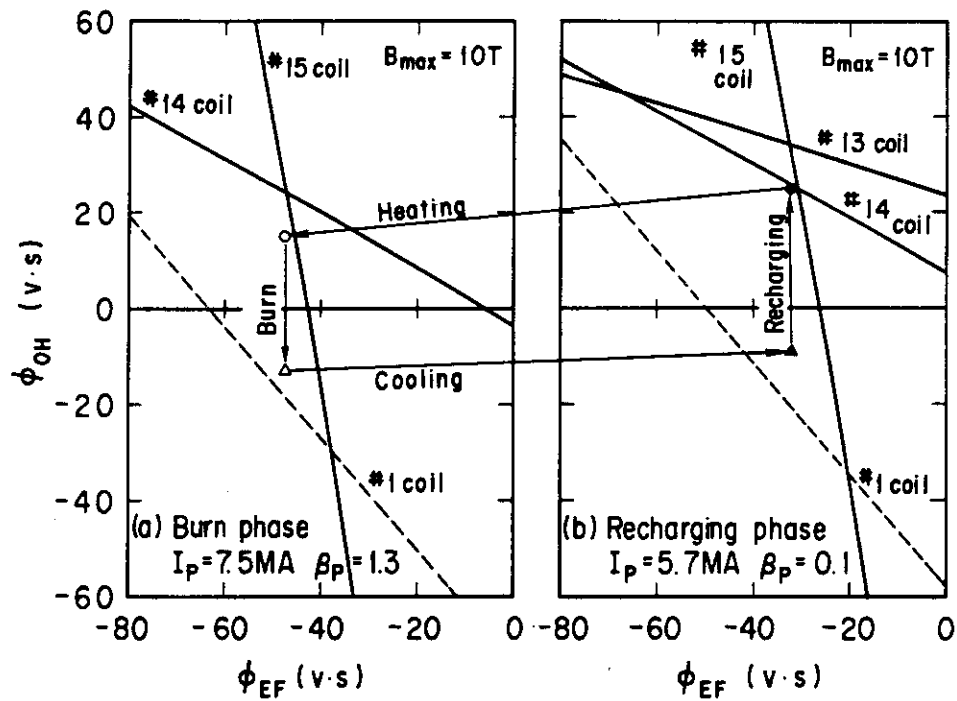


Fig. 6.3-5 Operation scheme on  $\phi_{OH}$ ,  $\phi_{EF}$  diagram  
 Solid lines show the upper limit of #13, #14 and #15 coil and  
 broken lines show the lower limit of #1 coil  
 (●→○ Ignition approach, ○→Δ Burn, Δ→▲ Cooling, ▲→○ Recharging)

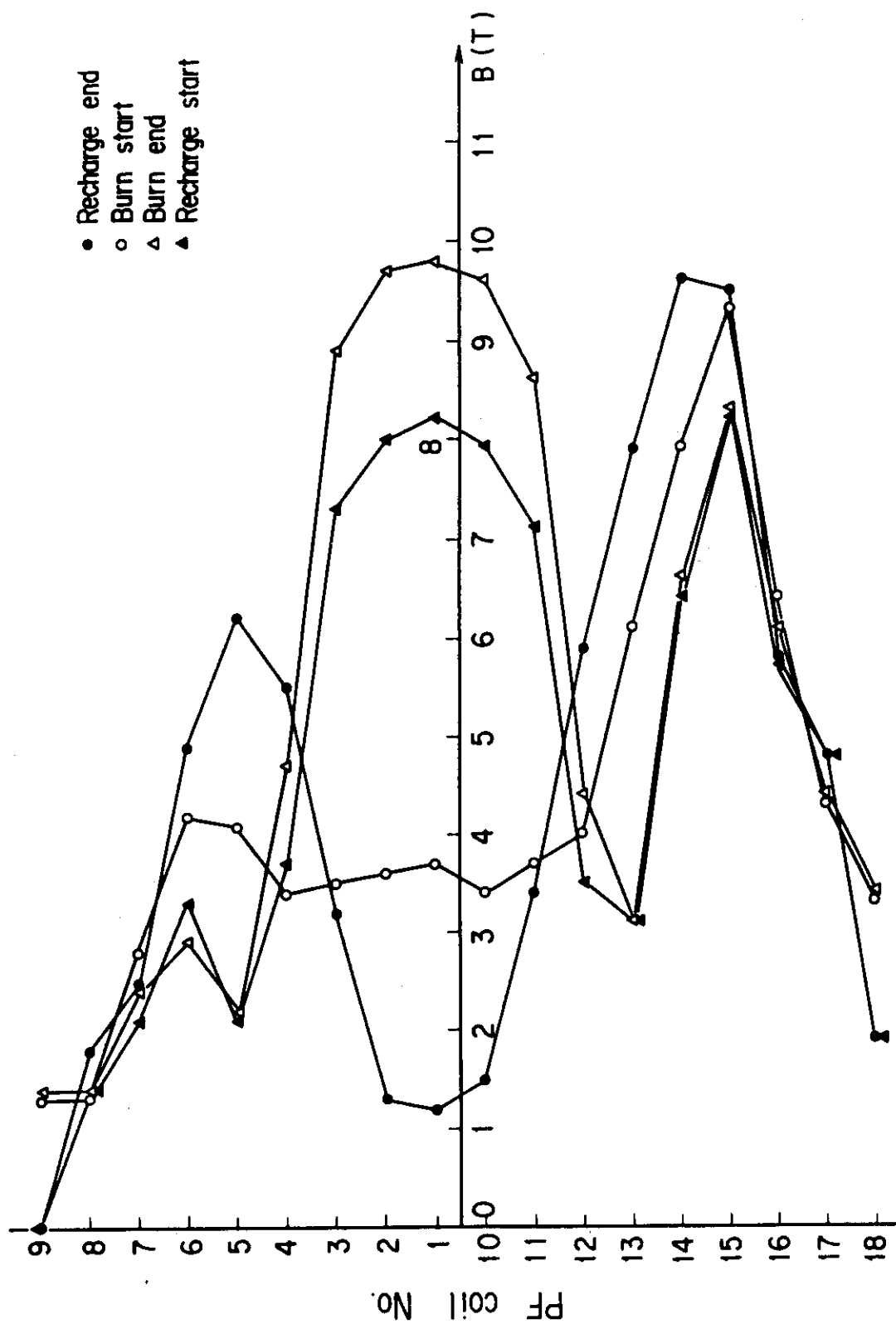


Fig. 6.3-6 Magnetic field on PF coil winding

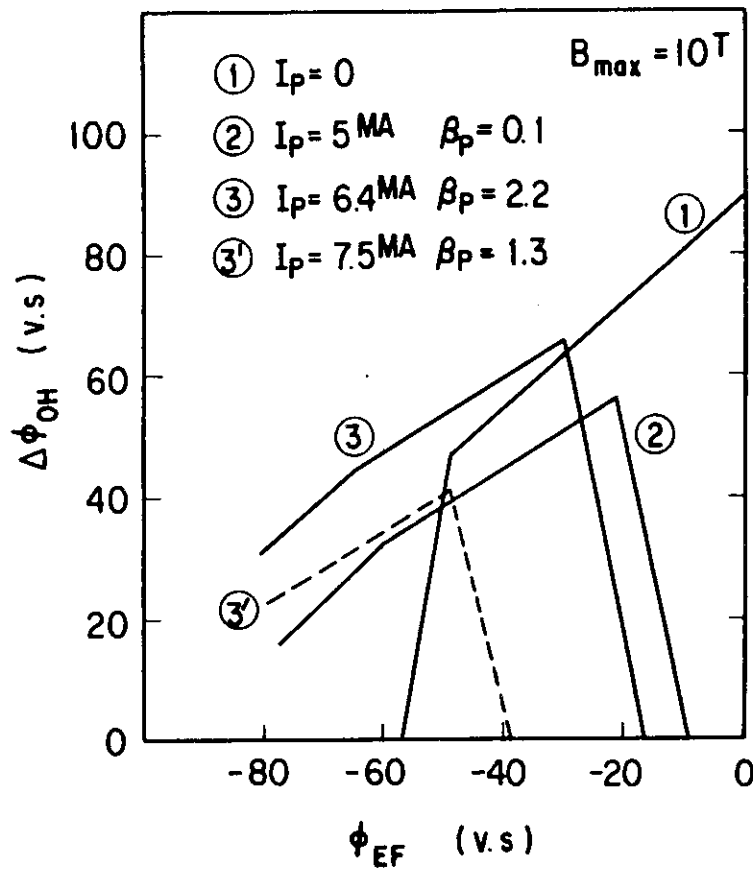


Fig.6.3-7  $\Delta\phi_{OH}, \phi_{EF}$  diagram of pulsed operation  
 Solid line ① shows the allowable range of OH flux at the initial excitation for pulsed operation.  
 Solid line ② shows the case of low  $\beta_p$  plasma.  
 ③ and ③' show the OH flux for burning phase.  
 ③ shows the case of pulsed operation  $I_p = 6.4 \text{ MA}$   $\beta_p = 2.2$ .  
 ③' shows the case of the plasma parameters  $I_p = 7.5 \text{ MA}$   $\beta_p = 1.3$  of quasi-steady operation.

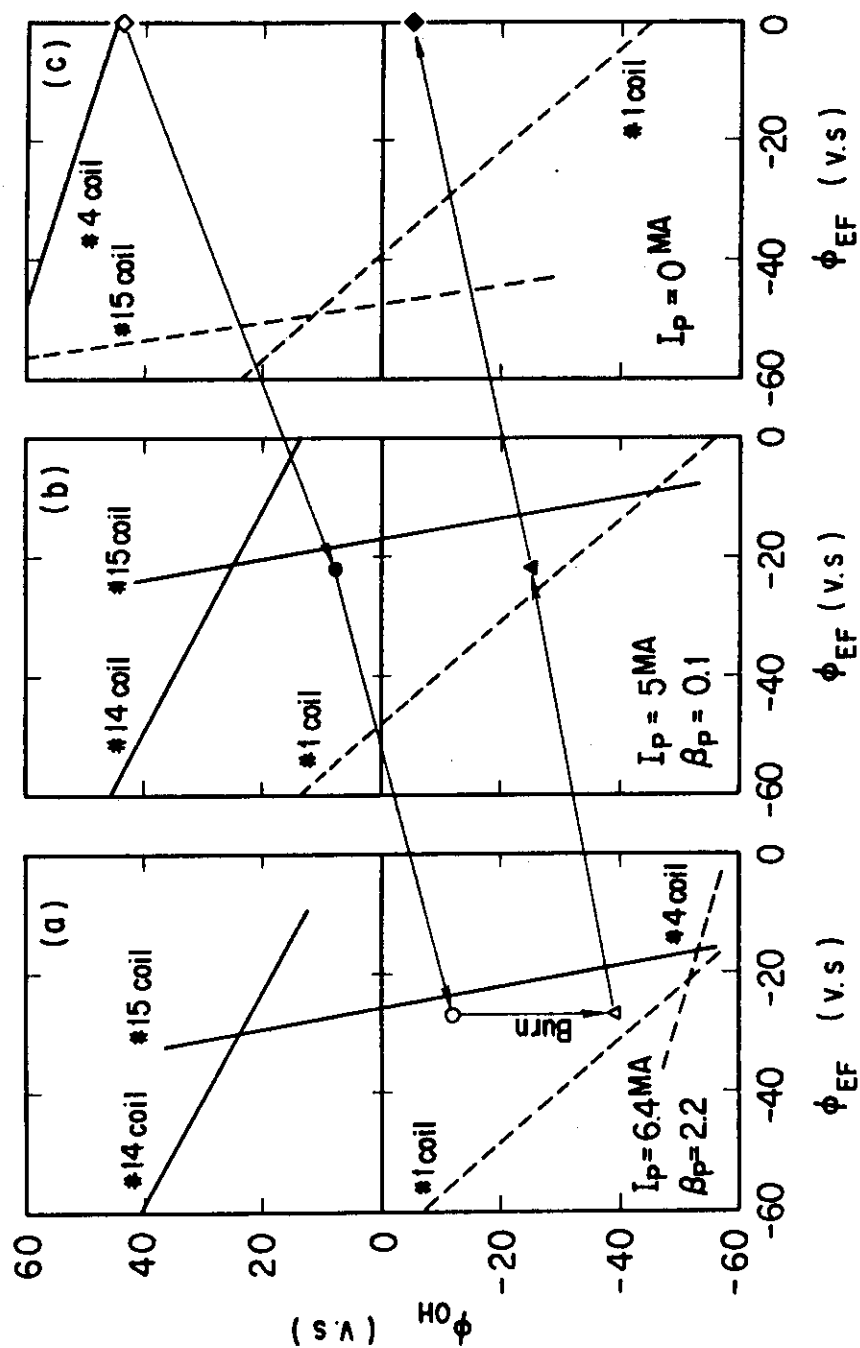


Fig. 6.3-8 Operation scheme of pulsed operation on  $\phi_{OH}$ ,  $\phi_{EF}$  diagram (a), (b), and (c) is the burning phase, the phase of before heating or after cooling, and the initial excitation respectively. Solid lines show the upper limit and broken lines show the lower limit corresponding to the maximum field ( $\pm 10 \text{ T}$ )

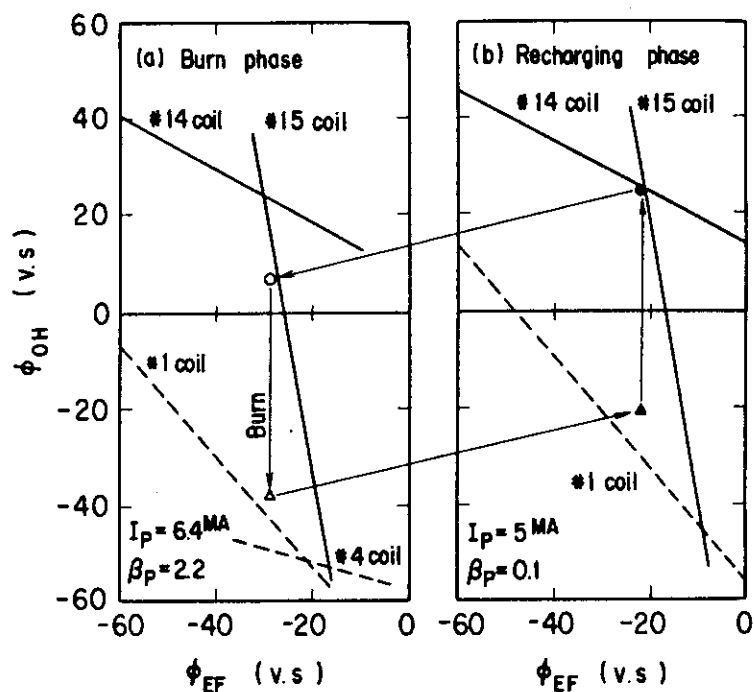


Fig.6.3-9 Operation scheme of quasi-steady state operation on  $\phi_{OH}$ ,  $\phi_{EF}$  diagram.

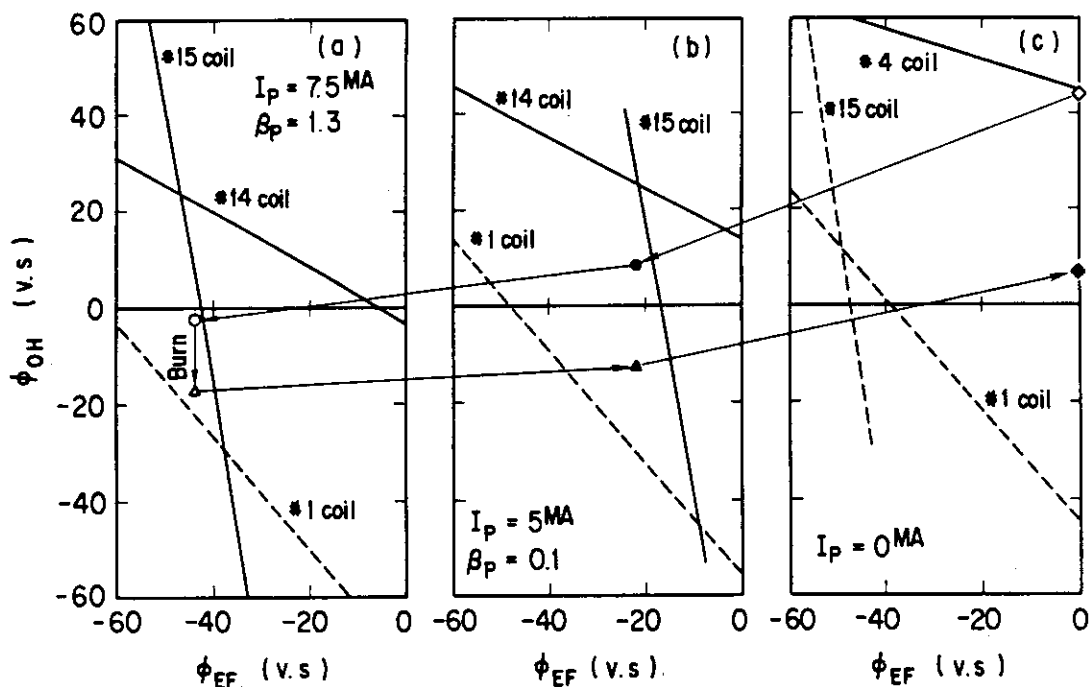


Fig.6.3-10 Operation scheme of pulsed operation on  $\phi_{OH}$ ,  $\phi_{EF}$  diagram.  
The case of burning plasma parameters  $I_p = 7.5 \text{ MA}$ ,  $\beta_p = 1.3$ .

## 7. Plasma Position Control

### 7.1 Introduction

The design of high conductive shells and active control coils is one of the critical issues in transient electromagnetics, since vertically elongated plasmas are positionally unstable against vertical movements without feedback control. The location of active control coils will provide significant impacts on the design and assembling/disassembling of future tokamaks. The active coils outside the toroidal field coils (outer active coils) would make the active coil design and their initial assembling easy, though fairly large power will be required for plasma position control. In this system, the shielding effect of poloidal field coils against the control field by active coils is so large that it should be taken into account in estimating the required power. One turn toroidal resistance of more than  $0.1 \text{ m}\Omega$  will be also needed to penetrate the control field in case of outer active coils, whether a scenario of noninductive plasma current ramp-up is adopted or not [1]. On the other hand, the active coils inside the toroidal field coils inner active coils will mitigate the requirements for control power and conductive shell design and will not necessary require high one turn toroidal resistance, though the active coil design and their installation will be difficult as compared with the case of outer active coils.

Considering these problems, parametric studies on plasma position control are carried out for the INTOR (INTOR-Japan) and the FER designed in JAERI. Figure 7.1.1 shows a bird's-eye view of the INTOR drawn by TORSAC (Tokamak Reactor System Analysis Code). The main parameters of the INTOR-Japan are summarized in Table 7.1.1 together with the FER parameters. The results of the parametric studies for the FER are shown in the following sections, since they provide good information to the INTOR design studies because of the similarity of these two parameter sets. However, in the FER design, there is a gap between the adjacent conductive shells due to the center post as shown in Fig. 7.1.2. Total gap length amounts to about 15 % of total length in the toroidal direction at mid plane. It should be noticed that these gaps reduce the stabilization property of passive elements significantly.

Section 7.2 describes the studies on vertical position stabilization for both INTOR-Japan and FER systems. Section 7.3 describes the studies on the control of both vertical and radial position in asymmetric systems in the vertical direction, where vertical and radial displacements interfere each other. In this section, the simulations of plasma displacement at saw tooth instabilities and disruptions are shown. The conclusions are summarized in section 7.4.

### 7.2 Vertical Position Control

#### 7.2.1 Passive Elements and Active Coil Location

Torus structure of Japanese INTOR design is electrically divided into 12 sectors, though it consists of 24 blanket/shield modules. Figure 7.2.1 shows our half sector model of passive elements. Copper conductive shells of 2 cm in thickness are installed in only outboard blanket modules as shown in Fig. 7.2.1. The width of toroidal bar and side wall of Cu shell are 1m and 0.75m, respectively. In analyzing

shell properties of passive elements, plasma toroidal current distribution is taken into account based on plasma equilibrium calculations. Figure 7.2.2 represents the stabilizing property of passive elements for both high beta ( $\beta_p = 1.3$ ) and low beta ( $\beta_p = 0.1$ ) cases. The growth times of plasma vertical movement,  $\gamma^{-1}$ , are  $\sim 320$  msec and  $\sim 200$  msec for high beta and low beta cases, respectively.

Two candidate positions are considered for active control coil installation, i.e. (1) outside the toroidal field coils (TFC) (outer active coils), (2) between shields and TFC (inner active coils). In order to control both vertical and radial plasma positions, active coils are located at outer-upper and outer-lower portions of plasma as shown in Fig. 7.2.3. Since the INTOR plasma is asymmetric to the mid plane, upper and lower poloidal field coils with same radial position can not be connected in series and each poloidal field coils has its own power supply. In such a system, the mutual inductance can not be zero between vertical position control coils and poloidal field coils (EF coils and OH coils), and poloidal field coils shield the magnetic field of vertical position control coils. Figure 7.2.4 shows the shielding property of passive elements including poloidal field coils. The curve (a) represents the shielding function [2] of passive elements without poloidal field coils in cases of both inner and outer active coils. Only one curve is drawn for inner and outer active coil cases, since the shielding functions are almost same between these two cases. The curves (b) and (c) represent the shielding functions of passive elements including poloidal field coils for inner and outer active coil cases, respectively. This shielding property of the poloidal field coils will significantly increase the required power for plasma position control.

### 7.2.2 Disturbance

The required power and/or power supply capacity for plasma position control depend strongly on a disturbance condition, though it is hard to specify the disturbance in the vertical direction. However, in asymmetric systems, an averaged radial magnetic field in plasma is not generally cancelled, when plasma moves in the radial direction (see section 7.3). In the INTOR designed at JAERI, a radial displacement of 1 cm is estimated to induce approximately 5.5 Gauss at high beta phase (flat-top phase) and 5.1 Gauss at low beta phase (re-charging phase), respectively. A rapid displacement in the radial direction could be expected at MHD activities such as saw tooth instability and fish bone instability. Assuming the time scale of this radial displacement as an order of 1 msec, we specified the disturbance condition as the following radial field,  $B_d$ .

$$B_d = B_{do}(1 - e^{-t/\tau_{Bd}}) \quad (7.2.1)$$

$$B_{do} = 10 \text{ Gauss}, \tau_{Bd} = 1 \text{ msec}$$

### 7.2.3 Vertical Position Control

Simulation analyses of plasma vertical position are performed to estimate the required power, coil voltage and coil current. A plasma toroidal current profile is taken into account to calculate the mutual inductances between plasma and coils and passive elements. Our

mathematical model of vertical position control system is described in reference [2]. PID action is used for our analyses of vertical position control. A integrating action time,  $T_I$ , is set to 0.25 sec for all simulations to make a offset small enough at 1 sec after control is started. Gain,  $G$ , and derivative action time,  $T_D$ , are determined so that the resonant value of closed loop transfer function,  $M$ , is set to 1.3. The voltage limitation is applied to active control coils in our simulations, since the requirement for power supply is mitigated by limiting the peak voltage of active coils which is generated at initial stage of feedback control simulation.

Figure 7.2.5 (a) and (b) show the simulation results of high beta ( $\beta_p=1.3$ ) case (flat-top phase) controlled by outer active coils. The time evolutions of plasma vertical position, active coil current and voltage are drawn. In Fig. 7.2.5 (a), passive effects of poloidal field coils are taken into account, and the required voltage, current and power supply capacity ( $V_{\max} \times I_{\max}$ ) of active coils are 180 V, 177.5 kA and 32 MVA, respectively. In Fig. 7.2.5 (b), the shielding effects of poloidal field coils are neglected. In this case, the voltage, current and power supply capacity are 125 V, ~107.5 kA and ~13.5 MVA, respectively. The maximum plasma displacement is ~0.55 cm in both cases. Since poloidal field coils shield the radial magnetic field produced by active coils, the poloidal field coils enlarge the required power supply capacity of active coils by a factor of 2.5 in our outer coil case.

Figure 7.2.6 (a) and (b) show the results of high beta, inner active coil case with and without the shielding effect of PFC. In inner active coil case, the coil voltage, current and power supply capacity are 60 V, ~90 kA and ~5.4 MVA, respectively (Fig. 7.2.6 (a)). The power supply capacity in inner active coil case is approximately one sixth of that in outer active coil case. However, the maximum plasma displacement is also ~0.55 cm in inner active coil cases (both (a) and (b)) which is almost same value as that in outer active coil cases. This is due to the fact that a maximum displacement depends mainly on a stabilizing property of passive elements, a decay index- $n$  ( $n$ -index) and a disturbance condition and not strongly on an active coil location when a disturbance is rapidly applied to plasma, since a maximum displacement is obtained at early stage of feedback control where the effect of feedback control is insufficient [1]. Comparing with the results in Fig. 7.2.6 (a) and (b), it can be seen that the shielding effect of PFC enlarges the required power supply capacity by approximately 20 % in our inner active coil case.

In Fig. 7.2.7 and 7.2.8, the simulation results of low beta ( $\beta_p=0.1$ ) phase (re-charging phase) are shown for outer and inner active coil cases, respectively. At low beta phase, the required power supply capacities are approximately 52 MVA and 9.8 MVA in outer and inner active coil cases, respectively. The maximum plasma displacement is approximately 1 cm in both cases. At low beta phase, both the required power supply capacity and the maximum displacement are increased as compared with high beta case, since the value of the  $n$ -index is smaller ( $n=-1.956$ ) than that ( $n=-1.35$ ) in high beta case.

Our simulation results for INTOR-Japan are summarized in Table 7.2.1. We also summarize the results for JAERI FER in Table 7.2.2. The maximum displacements,  $\delta Z_{\max}$ , are larger in the FER case than in INTOR case. These larger displacements in FER case is due to the center posts



which produce the gaps between the adjacent blanket modules as mentioned in section 7.1. In addition to this gap effect, smaller n-index ( $n=-2.548$ ) of the FER enlarges the displacements in low beta cases. By comparing the power supply capacity of the case number 1, 5 and 6, it can be seen that the shielding effect of PF coils depends on the active coil location. Active coils should be located as far from PF coils towards TF coils as possible, when they are installed outside TF coils. Outer active coil system becomes impractical from a view point of required power if bellows are not used to gain toroidal one turn resistance as seen from the results of the case 8 and 10 in Table 7.2.2. This is due to the shielding effect of vacuum vessel. If high conductive shells are not required, a large technical benefit will be obtained. The parametric studies for the FER case shows that the required power supply capacity of conductive shell-less cases will be a few times as large as that of conductive shell cases when active coils are located outside TFC. An implactically large power supply capacity (815 MVA) is required at low beta phase because of small n-index ( $n=-2.548$ ). Assuming that the n-index can be increased to  $n=-2.0$  which is close to INTOR value, the power supply capacity will decrease to approximately 220 MVA which is still large, as shown in the case 16. However, if a disturbance condition would be mitigated at low beta phase as described in the following section, a shell-less system will not be necessarily impractical or a requirement for shell design will be mitigated even in outer active coil case.

On the other hand, the power supply requirement is largely mitigated in inner active coil cases. Then, this system will provide a wide variety in the design of torus structures such as a vacuum vessel without bellows or blanket modules without conductive shells.

### 7.3 Radial and Vertical Position Control

#### 7.3.1 Formulations

The kinetic equation of plasma radial movement is simply expressed as eq.(7.3.1) by using the Shafranov formula [3].

$$M_p \ddot{R}_p = \frac{\mu_0 I_p^2}{2} \left( \ell_n \frac{8R_p}{A_p} + \beta_p + \frac{\ell_i - 3}{2} \right) + F_R \quad (7.3.1)$$

where,  $M_p$  : plasma mass  
 $R_p$  : plasma major radius  
 $A_p$  : plasma minor radius  
 $I_p$  : plasma current  
 $\beta_p$  : poloidal beta  
 $\ell_i$  : normalized internal inductance  
 $F_R$  : radial force by external field  
 $\mu_0$  : permeability

When a plasma is displaced in both radial and vertical direction by  $\delta R_p$  and  $\delta Z_p$ , respectively, external vertical field in a plasma,  $B_Z(R+$

$\delta R_p, Z+\delta Z_p$ ), is expressed as eq. (7.3.2).

$$B_z(R+\delta R_p, z+\delta z_p) = B_z(R, z) + \frac{\partial B_z}{\partial R} \delta R_p + \frac{\partial B_z}{\partial z} \delta z_p + B_{zd} \quad (7.3.2)$$

Where,  $B_z(R, Z)$  is a external vertical field in a plasma at equilibrium position,  $B_{zd}$  is a disturbance radial field.

Multiplying eq. (7.3.2) by plasma toroidal current density,  $i_p(R, Z)$ , and integrating it in plasma region, we obtain the equation of external radial force,  $F_R$ , at plasma displacement as eq.(7.3.3).

$$F_R = 2\pi I_p (R_p B_v - n \delta R_p - k \delta z_p) + 2\pi I_p R_p B_{vd} \quad (7.3.3)$$

Here,  $B_v$  is equilibrium vertical field, and  $R_p, n, k$  and  $B_{vd}$  are defined as the following equations.

$$R_p = \frac{1}{I_p B_v} \int R \cdot i_p(R, z) \cdot B_z(R, z) dR dz \quad (7.3.4)$$

$$\begin{aligned} n &= - \frac{1}{I_p B_v} \int R \cdot \frac{\partial B_z}{\partial R} \cdot i_p(R, z) dR dz \\ &= - \frac{1}{I_p B_v} \int R \cdot \frac{\partial B_R}{\partial z} \cdot i_p(R, z) dR dz \end{aligned} \quad (7.3.5)$$

$$\begin{aligned} k &= - \frac{1}{I_p B_v} \int R \frac{\partial B_z}{\partial z} i_p(R, z) dR dz \\ &= \frac{1}{I_p B_v} \int \frac{\partial}{\partial R} \{ R \cdot B_R(R, z) \} i_p(R, z) dR dz \end{aligned} \quad (7.3.6)$$

$$B_{vd} = \frac{1}{I_p R_p} \int R \cdot i_p(R, z) \cdot B_{zd}(R, z) dR dz \quad (7.3.7)$$

The  $n$  defined by eq.(7.3.5) is a natural expansion of the decay index- $n$  value ( $n$ -index). The  $k$  represents the strength of the interaction between radial and vertical displacements and becomes zero if the external field is completely symmetric with respect to mid plane ( $Z=0$  plane). However, if the external field is asymmetric like INTOR plasma, the  $k$  does not become zero and plays important role. We call this  $k$  as  $k$ -index in this paper.

Linearizing eq.(7.3.1), the following equation is obtained for plasma radial movement.

$$\begin{aligned}
& \{2\pi B_v (1 - \frac{1}{\Lambda_0} n) - \frac{\mu_0 I_p}{4R_p} - \frac{7}{6} \mu_0 I_p \frac{\beta_p}{R_p}\} \delta R_p - 2\pi B_v k \delta z_p \\
& - (2\pi R_p B_v + \mu_0 I_p \beta_p) \frac{\delta I_p}{I_p} + I_p \left( \sum_i \frac{\partial M_{pi}}{\partial R_p} \frac{\delta I_i}{I_p} + \sum_k \frac{\partial M_{pk}}{\partial R_p} \frac{\delta I_k}{I_p} \right) \\
& = - \frac{\mu_0 I_p}{2} \delta \beta_p - \frac{\mu_0 I_p}{4} \delta \ell_i - 2\pi R_p B_v d
\end{aligned} \tag{7.3.8}$$

where,  $M_{pi}$  : mutual inductance between plasma and the i-th coil

$M_{pk}$  : mutual inductance between plasma and the k-th eddy current mode

$I_i$  : the i-th coil current

$I_k$  : eddy current of the k-th mode

$\Lambda_0$  in eq. (7.3.8) is defined by eq. (7.3.9).

$$\Lambda_0 = -4\pi R_p B_v / (\mu_0 I_p) \tag{7.3.9}$$

In deriving eq.(7.3.8), plasma mass,  $M_p$ , is neglected and  $a^2/R$  is kept constant (conservation of toroidal flux in a plasma) and  $\beta_p$  scales as  $1/(I_p^2 R^{2/3})$  (adiabatic compression/decompression). The  $\delta \beta_p$  in eq.(7.3.8) represents the  $\beta_p$  change due to the change in plasma thermal energy.

The equation of plasma vertical movement is represented by eq.(7.3.10).

$$2\pi B_v n \delta z_p - 2\pi B_v k \delta R_p + I_p \left( \sum_i \frac{\partial M_{pi}}{\partial z_p} \frac{\delta I_i}{I_p} + \sum_k \frac{\partial M_{pk}}{\partial z_p} \frac{\delta I_k}{I_p} \right) = 2\pi R_p B_v R_d \tag{7.3.10}$$

The second term in eq.(7.3.10) represents the coupling between radial and vertical movement.

Other equations needed for simulation are circuit equations of plasma current, active and passive coils and eddy currents as expressed by the following equations.

$$(L_p \dot{I}_p) + \sum_i (M_{pi} \dot{I}_i) + \sum_k (M_{pk} \dot{I}_k) + \eta_p I_p = 0 \tag{7.3.11}$$

$$L_i \dot{I}_i + (M_{pi} \dot{I}_p) + \sum_j (M_{ij} \dot{I}_j) + \sum_k (M_{ik} \dot{I}_k) + \eta_i I_i = V_i \tag{7.3.12}$$

$$\tau_k \dot{I}_k + (M_{pk} \dot{I}_p) + \sum_i (M_{ik} \dot{I}_i) + I_k = 0 \tag{7.3.13}$$

Where,  $L_p$  : plasma self inductance

$\eta_p$  : plasma resistance

$L_i$  : self inductance of the i-th coil

$M_{ij}$  : mutual inductance between the i-th coil and the j-th coil

$M_{ik}$  : mutual inductance between the i-th coil and the k-th

## eddy current mode

 $\eta_i$  : resistance of the i-th coil $I_j$  : the j-th coil current $\tau_k$  : time constant of the k-th eddy current mode

## 7.3.2 Stability Analyses

Due to the coupling between radial and vertical movement as described in Section 7.3.1, the stability criteria should be somewhat modified. From eqs.(7.3.8), (7.3.10) and (7.3.11), the following stability criteria without feedback control can be derived.

$$n\{n - 1 - \frac{\Lambda_o}{2\Lambda}(1 - \frac{2\beta_p}{\Lambda_o})^2 + \frac{1}{2\Lambda_o} - \frac{7}{3} \frac{\beta_p}{\Lambda_o}\} + k^2 < 0 \quad (7.3.14)$$

$$\Lambda = L_p / \mu_o R_p$$

Assuming that  $\lambda n(8R_p/a_p)$  is large enough, eq.(7.3.14) is simplified as eq.(7.3.15).

$$n(n - \frac{3}{2}) + k^2 < 0 \quad (7.3.15)$$

When k-index is zero, we can obtain well known stability criteria " $0 < n < 3/2$ ". Equation (7.3.15) shows that the stability of plasma position is deteriorated when there is a interaction between radial and vertical movements.

In unstable case, the growth rate,  $\gamma_g$ , of plasma movement without feedback control is the root of the equation given by  $\det A(\gamma_g) = 0$ . Where,  $A(s)$  is defined as eq.(7.3.16).

$$A(S) = \begin{pmatrix} A_{11}(S), A_{12}(S), A_{13}(S) \\ A_{12}(S), A_{22}(S), A_{23}(S) \\ A_{13}(S), A_{23}(S), A_{33}(S) \end{pmatrix} \quad (7.3.16)$$

$$\text{where, } A_{11}(S) = 2\pi B_v \{n + N_z(S)\}$$

$$A_{12}(S) = -2\pi B_v \{k - K(S)\}$$

$$A_{13}(S) = -2\pi B_v B_z(S)$$

$$A_{22}(S) = 2\pi B_v \{1 - \frac{1}{2\Lambda_o} - n + N_R(S)\} - \frac{7}{6} \mu_o I_p \frac{\beta_p}{R_p}$$

$$A_{23}(S) = -2\pi R_p B_v \{1 - B_R(S)\} - \mu_o I_p \beta_p$$

$$A_{33}(S) = L_p \{1 - K_p(S)\}$$

$$N_z(S) = \sum_k \frac{S\tau_k}{1+S\tau_k} \{-\frac{I_p}{2\pi R_p B_v \tau_k} (\frac{\partial M_{pk}}{\partial z_p})^2\} \quad (7.3.17)$$

$$N_R(s) = \sum_k \frac{S\tau_k}{1+S\tau_k} \left\{ -\frac{I_p}{2\pi R_p B_p v_k} \left( \frac{\partial M_{pk}}{\partial R_p} \right)^2 \right\} \quad (7.3.18)$$

$$K(s) = \sum_k \frac{S\tau_k}{1+S\tau_k} \left\{ -\frac{I_p}{2\pi R_p B_p v_k} \frac{\partial M_{pk}}{\partial R_p} \frac{\partial M_{pk}}{\partial z_p} \right\} \quad (7.3.19)$$

$$B_R(s) = \sum_k \frac{S\tau_k}{1+S\tau_k} \left\{ -\frac{I_p M_{pk}}{2\pi R_p B_p v_k} \cdot \frac{\partial M_{pk}}{\partial R_p} \right\}$$

$$B_z(s) = \sum_k \frac{S\tau_k}{1+S\tau_k} \left\{ -\frac{I_p M_{pk}}{2\pi R_p B_p v_k} \cdot \frac{\partial M_{pk}}{\partial z_p} \right\} \quad (7.3.21)$$

$$K_p(s) = \sum_k \frac{S\tau_k}{1+S\tau_k} \frac{M_{pk}^2}{L_p \tau_k} \quad (7.3.22)$$

In eq.(7.3.16), the stabilizing effects of active coils and poloidal field coils are neglected.

Figures 7.3.1 and 7.3.2 show the growth rate of plasma position movement for high beta phase and low beta phase, respectively. In the curves (b), the k-index is neglected. From these figures, it can be seen that the radial-vertical coupling increases the growth rate of position movements. The growth rates obtained from the curves (b) in Fig. 7.3.1 and 7.3.2 are close to those obtained from the curves in Fig. 7.2.2.

The K(s) function defined by eq.(7.3.19) represents the interaction between two direction through eddy currents. If passive structures are perfectly symmetric with respect to Z=0 plane, K(s) becomes zero. The K(s) functions of the INTOR-Japan are shown in Fig. 7.3.3 for both high beta phase and low beta phase. The absolute values of these K(s) functions are small as compared with the corresponding k-index. So the asymmetry of the passive elements does not largely affect on the coupling of plasma radial and vertical movements. The  $N_R(s)$  function defined by eq. (7.3.18) expresses the stabilization property of passive elements in the radial direction. Fig. 7.3.4 shows the  $N_R(s)$  function of the INTOR-Japan for high and low beta phases. High conductive shells seem not to be largely effective to mitigate plasma radial movements.

### 7.3.3 Radial and Vertical Position Control

While it is generally hard to name probable disturbance that would yield directly vertical movements of plasmas, it is rather easy to list up probable causes which would result in plasma radial movements. Among them are changes of the plasma current distribution and the plasma thermal energy during saw tooth, fish bone, minor disruption or major disruption. These disturbances generate vertical movements of plasmas through the mechanisms mentioned above.

Then, for realistic analyses and clear issue identification on

radial and vertical position control of an asymmetric plasma, it seems to be appropriate procedures to give, as the initial perturbation, a change which directly causes radial movements of the plasma resulting from the perturbation.

The initial rapid changes in  $Z_p$ ,  $R_p$  and  $I_p$  can be expressed by the following equations for the rapid changes in poloidal beta and normalized internal inductance,  $\ell_i$ .

$$\begin{pmatrix} \delta z_p \\ \delta R_p \\ \delta I_p / I_p \end{pmatrix} = \begin{pmatrix} 0.063 \\ 0.174 \\ -0.463 \end{pmatrix} \delta \ell_i + \begin{pmatrix} 0.096 \\ 0.224 \\ 0.012 \end{pmatrix} \delta \beta_p \text{ at high } \beta_p \quad (7.3.23)$$

$$\begin{pmatrix} \delta z_p \\ \delta R_p \\ \delta I_p / I_p \end{pmatrix} = \begin{pmatrix} 0.051 \\ 0.129 \\ -0.608 \end{pmatrix} \delta \ell_i + \begin{pmatrix} 0.113 \\ 0.222 \\ 0.004 \end{pmatrix} \delta \beta_p \text{ at low } \beta_p \quad (7.3.24)$$

It can be seen that the radial displacement at low beta phase is smaller than that at high beta phase for the same change in  $\ell_i$ . Assuming the rapid change of  $\delta \ell_i = 0.1$  for example, the initial displacements of  $\delta R_p$  are calculated as 1.74 cm and 1.29 cm in case of high  $\beta_p$  and low  $\beta_p$ , respectively. Since the initial displacements of 1.74 cm and 1.29 cm induce the radial field of 9.5 Gauss and 6.6 Gauss, the power supply requirements will decrease by ~10 % and ~56 % in high  $\beta_p$  and low  $\beta_p$  case, respectively.

With these considerations, simulation analyses have been carried out for the following cases:

- a) When a change of plasma current distribution during saw tooth is given as the initial perturbation.
- b) When changes of plasma thermal energy and plasma current distribution during plasma disruption are given as the initial perturbation.

#### (1) Plasma Position Control at Saw-Tooth

Though the power supply requirement depends largely on the magnitude of  $\ell_i$  change (it is proportional to the second power of the disturbance magnitude), we simply assumed the  $\ell_i$  change of 0.1 with a time constant of 1 msec. That is,  $\delta \ell_i(t)$  is given by the following equation.

$$\delta \ell_i(t) = -\delta \ell_{i0} (1 - e^{-t/\tau_\ell}) \quad (7.3.25)$$

$$\delta \ell_{i0} = 0.1, \tau_\ell = 1 \text{ msec}$$

The disturbance of  $\delta \ell_{i0} = 0.1$  may be somewhat large, since our preliminary estimation shows that  $\ell_i$  will decrease by  $\leq 0.05$  per the change of 0.1 in safety factor at magnetic axis. So our disturbance condition stands safety side for estimating the power supply requirements.

Simulation results of plasma position control for  $\ell_i$  perturbation at saw-tooth are shown in Fig.7.3.5 ~ 7.3.9. The active coils are located outside the TF coils for all cases. The voltage of Ohmic

heating (OH) coils is limited to 10 V except the result in Fig. 7.3.9, where the OH coil voltage limit is 1 V. The same voltage is applied to both active coils for position control. P action is used in feedback control simulations for simplicity. The power supply capacity for both vertical and radial position control,  $P_{SRV}$ , is 88 MVA in high beta case as shown in Fig. 7.3.5. The shielding effect of the PF coils is included in this result. The power supply requirement for only vertical position stabilization,  $P_{SV}$ , can be estimated by the following equation.

$$P_{SV} = |I_1 - I_2|_{\max} \times |V|_{\max} \quad (7.3.26)$$

where,  $I_1$  : current of No.1 active coil

$I_2$  : current of No.2 active coil

$|I_1 - I_2|_{\max}$  : maximum absolute value of  $I_1 - I_2$

$|V|_{\max}$  : maximum absolute value of coil voltage

By using eq.(7.3.26), the  $P_{SV}$  is estimated as 36 MVA in case of Fig. 7.3.5. This estimated value is close to the power supply requirement of the case 1 shown in Table 7.2.1. In case of low beta, the  $P_{SRV}$  and  $P_{SV}$  are ~67 MVA and ~27 MVA, respectively as shown in Fig. 7.3.6. Both power supply requirements are smaller than those of high beta case, and the  $P_{SV}$  is approximately a half of that shown in Table 7.2.1. This result is consistent with the estimations mentioned previously. In order to study the shielding effect of the PF coils, the result of position control simulation without the PF coil is shown in Fig. 7.3.7. Both  $P_{SRV}$  and  $P_{SV}$  are approximately 2~3 times as small as those with the PF coils. This is almost same result obtained in Section 7.2. By comparing the vertical displacements shown in Fig. 7.3.7 and 7.3.8, it can be seen that the vertical displacement is generated mainly by the asymmetric external equilibrium field and the effect of the asymmetry of passive structures is small. At the abrupt reduction of  $\ell_i$ , plasma current increases as shown in Fig. 7.3.5~7.3.8. When plasma is moving toward inboard side, the increment in plasma current assists to stop the moving and makes radial position control easy. Fig. 7.3.9 shows this fact. The simulation parameters are the same as those in case of Fig. 7.3.5 except the voltage limit of OH coils which is set to 1V in Fig. 7.3.9. The  $P_{SRV}$  and  $P_{SV}$  are calculated as ~36 MVA and ~8.5 MVA, respectively. The  $P_{SV}$  becomes approximately the fourth of that obtained in Section 7.2.3.

## (2) Plasma Displacements at Disruption

As for abnormal losses of the plasma thermal energy at disruptions, in the following analyses for FER we have assumed that the thermal energy be lost by 40 % with a time constant of 5 msec at disruption. According to the assumption, we have used, as the initial perturbation, a decrease in  $\beta$  by 40 % with a time constant of 5 msec. Furthermore the normalized plasma internal inductance,  $\ell_i$ , has been assumed to decrease by approximately 40 % (from 0.8 to 0.5) with a time constant of 5 msec in order to simulate the plasma current flattening during the transport phase. Then the time-evolving changes of  $\beta_p$  and  $\ell_i$ ,  $\delta\beta_p(t)$  and  $\delta\ell_i(t)$ , are given by the following equations,

$$\delta\beta_p(t) = -\delta\beta_{po}(1 - e^{-t/\tau_d}) \quad (2.4.2)$$

$$\delta\ell_i(t) = -\delta\ell_{io}(1 - e^{-t/\tau_d}) \quad (2.4.3)$$

$$\tau_d = 5 \text{ msec.}$$

Fig. 7.3.10 through 7.3.15 present simulation results for the JAERI FER, which are all for high  $\beta$  operations. The active coils are located inside the TF coils, and the shielding effects of the PF coils are neglected for all cases. The results with copper shells installed inside the blanket are shown in Fig. 7.3.10 through 7.3.13, and those without copper shells in Fig. 7.3.14 and 7.3.15. In Fig. 7.3.10 which gives simulation results for the case without active position control at a disruption, it is observed that the plasma shrinks mainly radially in the first stage of disruption, and next moves downward. Both radial and vertical displacements increase to  $\sim 30$  cm in 50 msec after disruption initiation. Thus the asymmetry of the plasma causes vertical movements of the plasma in addition to radial displacements. Due to asymmetry of the external equilibrium field with respect to the mid-plane, radial displacements of the plasma destroy the equilibrium in the vertical direction, and result in vertical movements of the plasma. The coupling between radial and vertical displacements is measured by the k-index defined in Section 7.3.1. The simulation results with the k-index set to be zero are shown in Fig. 7.3.11. In this case the vertical displacement is less than 1/10 of that obtained in Fig. 7.3.10. The reason vertical movements are yielded even with the k-index assumed to be zero is attributed to asymmetry of the reactor structures surrounding the plasma. That is, radial fields to cause vertical movements are generated by eddy currents on the asymmetric structures induced by radial movements of the plasma. However it is observed, through comparison between Fig. 7.3.10 and 7.3.11, that the effects of the asymmetry of structures are minor. (Ref. Section 7.3.2)

Fig. 7.3.12 and 7.3.13 describes simulation results of the cases with radial and vertical position control working. No voltage limits are given to the active control coils in the former case, while the voltage limit of  $\pm 200$  V is incorporated in the latter. In the case without voltage limits, though it is possible to control the plasma position, the power supply requirements necessary to restore the plasma position amounts to an unrealistic value of  $\sim 1.7 \times 10^4$  MVA. On the contrary, with the voltage limit of  $\pm 200$  V ( $\pm 50$  V for OH coils), the power supply requirement is reasonable (65 MVA for 50 msec duration). However the radial and vertical displacements,  $\delta R_p$  and  $\delta Z_p$ , have turned out to be relatively large values,  $\sim -30$  cm and  $\sim -26$  cm, respectively, at 50 msec after disruption starts.

Results for the cases without copper shells are shown in Fig. 7.3.14 and 7.3.15. No position control is incorporated in the former case, and the latter case uses position control by active control coils with a voltage limit of  $\pm 200$  V. Comparison of the results indicated in these figures with those in Fig. 7.3.10 and 7.3.13 leads to the observation that, while the effects of copper shells on  $\delta R_p$  are not so large,  $\delta Z_p$  is affected substantially by existence of copper shells. For example,  $\delta R_p$  of the case without shells is larger only by  $\sim 5$  cm than that of the case having shells. On the other hand, as for  $\delta Z_p$ , the cases without shells result in large values such as  $\sim -82$  cm (with no position control incorporated) and  $\sim -63$  cm (with position control working), which are approximately 2.5 times larger than those of with copper shells.



#### 7.4 Summary

Parametric studies on plasma position control are performed for INTOR and FER designed at JAERI. The following conclusions are obtained.

- 1) Poloidal field coils shield the magnetic field produced with active control coils. This effect increases the power supply requirement for position control by  $\sim 20\%$  in inner active coil cases and  $\sim 150\%$  at least in outer active coil cases. The active coil location should be carefully selected in case of outer active coils not to have strong interaction with poloidal field coils.
- 2) Outer active coils would be able to control plasma position within a practical power level ( $< 100\text{MVA}$ ). However, one turn toroidal resistance of  $\sim 0.1\text{ m}\Omega$  will be required to suppress the increase in shielding property of vacuum vessel against magnetic field of active coils.
- 3) In case of inner active coils, the requirement of power supply is approximately  $1/10 \sim 1/5$  as small as that in case of outer active coils. Bellows or conductive shells are not required in this case.
- 4) Asymmetric external fields by PF coils and eddy currents with respect to the mid plane ( $Z=0$ ) displace plasma in the vertical direction when plasma moves rapidly in the radial direction, while the effect of eddy currents induced by plasma radial movements is minor.
- 5) The power supply requirement at low beta phase is smaller than that at high beta phase ( $1/2 \sim 1/4$ ) if normalized plasma internal inductance is reduced as a disturbance, though the opposite results are obtained if the same disturbance field is applied to plasma at both phases.
- 6) Plasma moves largely toward divertor plates as well as inboard first wall, at plasma disruptions. In the case without conductive shell, the magnitude of vertical displacement is about three times as large as that in the case with high conductive shells.

#### 7.5 Reference

- [1] M. Kasai, K. Ueda, S. Niikura, H. Iida, N. Fujisawa, et.al., "Japanese Contribution to INTOR Workshop phase 2 A (part 2) Session X Group C", 15-26 October 1984.
- [2] A. Kameari, "Control of Plasma Vertical Position in Tokamak Reactors", Nuclear Engineering and Design/Fusion, to be published.
- [3] V. S. Mukovatov and V. D. Shafranov, Nucl. Fusion 11 (1971) 605.

Table 7.1.1 Main parameters of JAERI FER and INTOR-Japan

	JAERI FER	INTOR-Japan
Major Radius (m)	5.3	5.0
Minor Radius (m)	1.12	1.2
Plasma Current (M)		
flat-top phase	5.7	7.5
re-charging phase	4.3	5.7
Poloidal Beta		
flat-top phase	2.6	1.3
re-charging phase	0.1	0.1
n-index		
flat-top phase	-1.272	-1.35
re-charging phase	-2.548	-1.956
k-index		
flat-top phase	0.52	0.5787
re-charging phase	1.30	1.0
Vertical Field (T)		
flat-top phase	-0.465	-0.474
re-charging phase	-0.198	-0.25536

Table 7.2.1 Summary of voltage, current and power capacity

in vertical position control for INTOR-Japan

Case	Coil	PFC	$\beta$	$V_{\max}$	$I_{\max}$	$V_{\max}$	$I_{\max}$	$\delta Z_{\max}$
				(v)	(kA)	(MVA)		(mm)
1	Outer	with	High	180	177	32		5.4
2	Outer	W/O	High	125	107	13		5.5
3	Inner	with	High	60	90	5.4		5.4
4	Inner	W/O	High	60	74	4.4		5.4
5	Outer	with	Low	270	196	53		10.1
6	Outer	W/O	Low	100	114	11		10.3
7	Inner	with	Low	170	98	17		9.8
8	Inner	W/O	Low	75	79	5.9		10.1

\* Disturbance field is 10 Gauss with 1 msec rise time

Table 7.2.2 Summary of voltage, current and power capacity  
in vertical position control<sup>1)</sup> for JAERI FER

Case	Coil	Bellows	Shell	$\beta$	V <sub>max</sub> (V)	I <sub>max</sub> (kA)	V <sub>max</sub> I <sub>max</sub> (MVA)	$\delta Z_{max}$ (mm)
1	Outer	with	with	High	150	215	32	11.6
2	Inner	with	with	High	40	66	2.6	11.5
3	Outer	with	with	Low	400	361	144	53.1
4	Inner	with	with	Low	100	122	12	55.6
5	Coil A <sup>2)</sup>	with	with	High	400	604	242	12.2
6	Coil B <sup>3)</sup>	with	with	High	150	281	41	11.3
7 <sup>4)</sup>	Outer	with	with	Low	200	259	52	26.6
8	Outer	w/o	with	High	1000	748	748	9.4
9	Inner	w/o	with	High	60	126	7.6	10.7
10	Outer	w/o	with	Low	2000	1068	2136	34.3
11	Inner	w/o	with	Low	150	222	33	41.1
12	Outer	with	w/o	High	300	271	81	16.1
13	Inner	with	w/o	High	80	85	6.8	16.9
14	Outer	with	w/o	Low	1500	543	815	40.8
15	Inner	with	w/o	Low	300	190	57	48.9
16 <sup>4)</sup>	Outer	with	w/o	Low	600	372	223	26.7

1) Disturbance field is 10 Gauss with 1 msec rise time.

2) (R,Z) = (9.75,  $\pm 5.1$ )

3) (R,Z) = (7.52, 5.05), (7.42, -5.0)

4) n-value is assumed to be -2.0.

\* When disturbance of  $l_i$  is assumed to be 0.1, V<sub>max</sub>, I<sub>max</sub> and  $\delta Z_{max}$  are multiplied by 2.1 in high  $\beta$  case or by 0.46 in low  $\beta$  case.

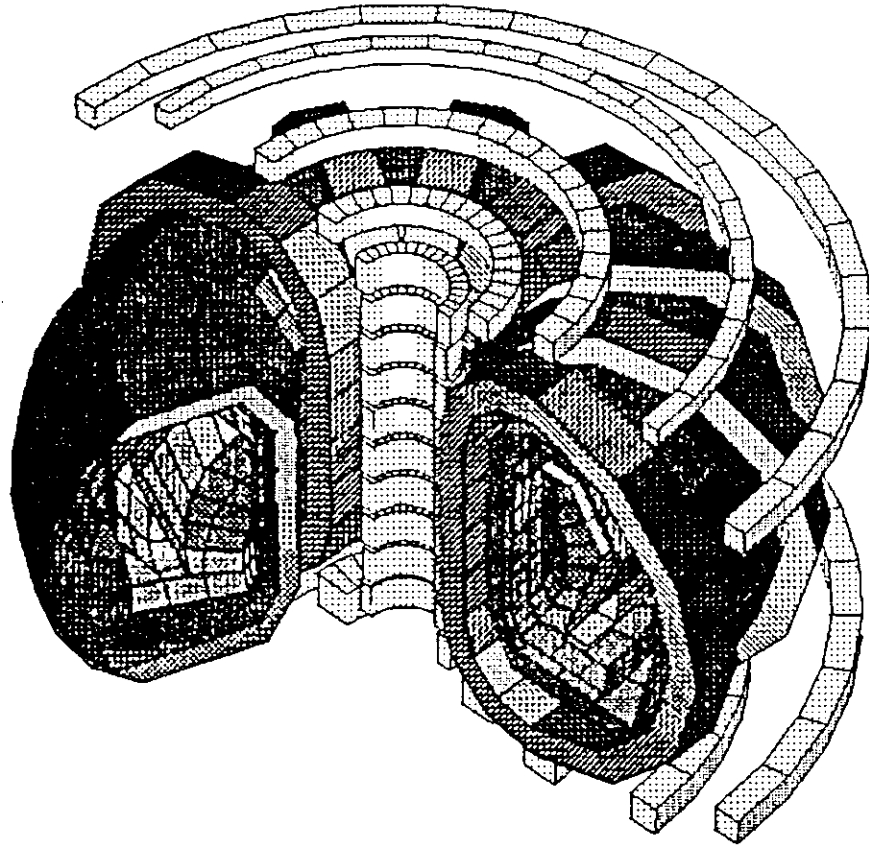


Fig. 7.1.1 Bird's-eye view of INTOR-Japan.

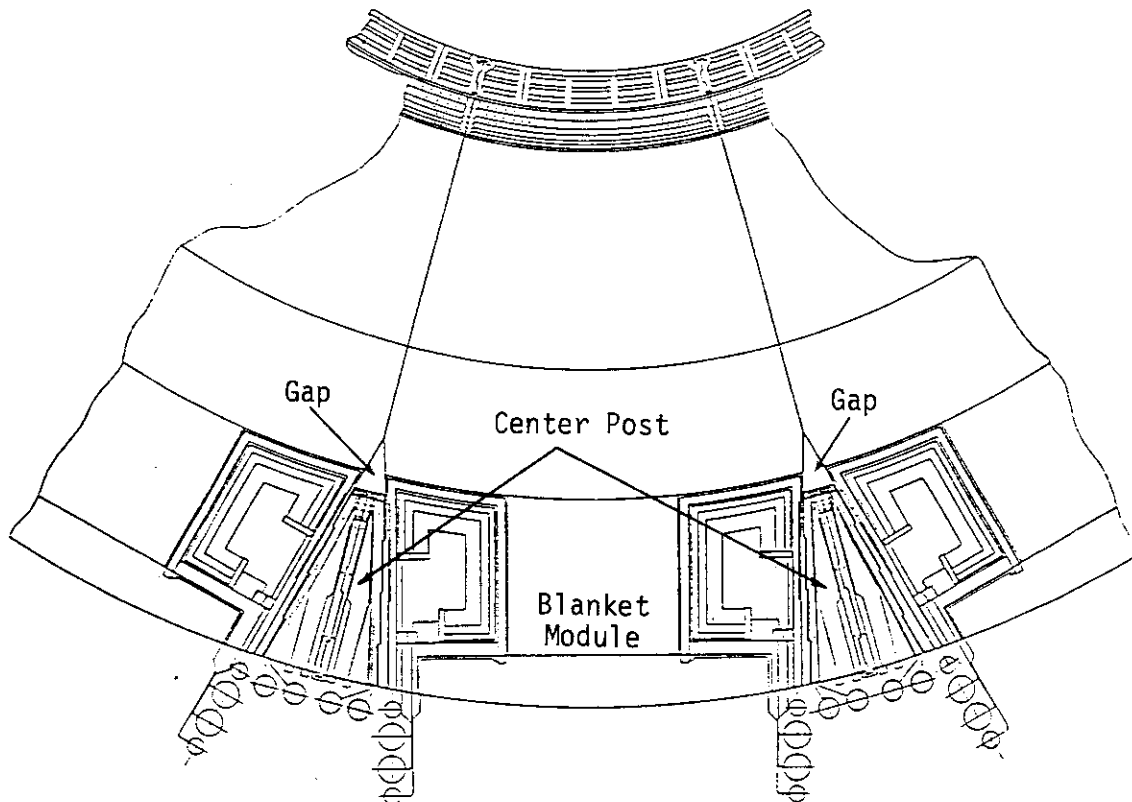
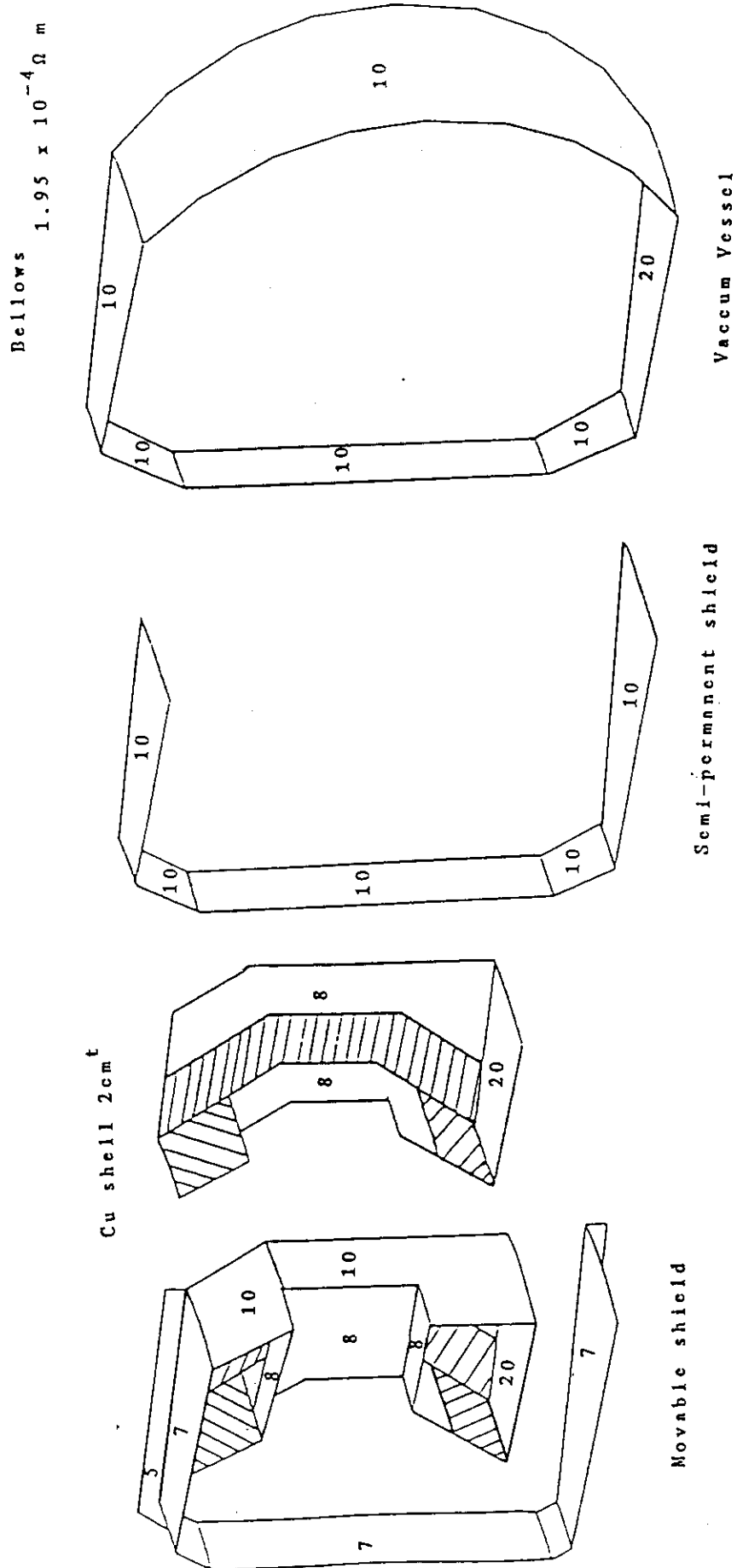


Fig. 7.1.2 Plan view of JAERI FER.



\* The numbers in the figure are the thickness (cm) of stainless steel.  
Resistivities of copper and stainless steel are  $2 \mu\Omega \text{ cm}$  and  $75 \mu\Omega \text{ cm}$ , respectively.

Fig. 7.2.1 Half sector model of INTOR passive elements.

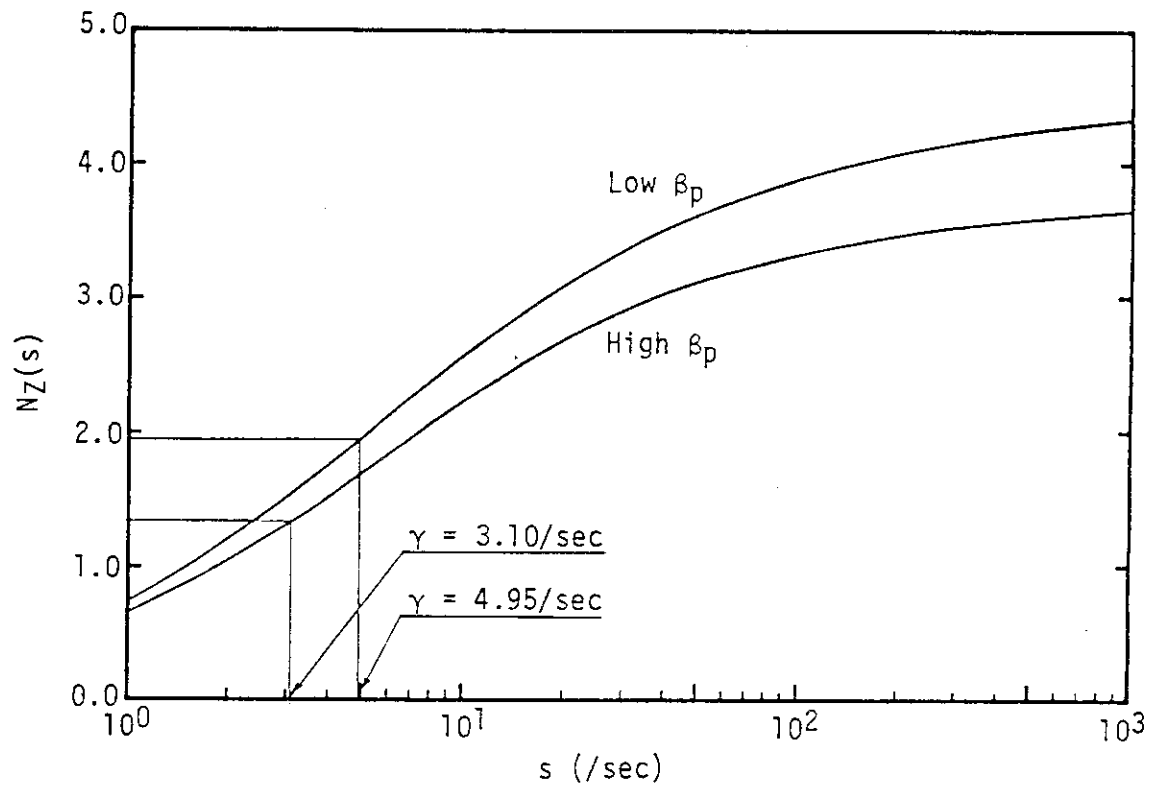
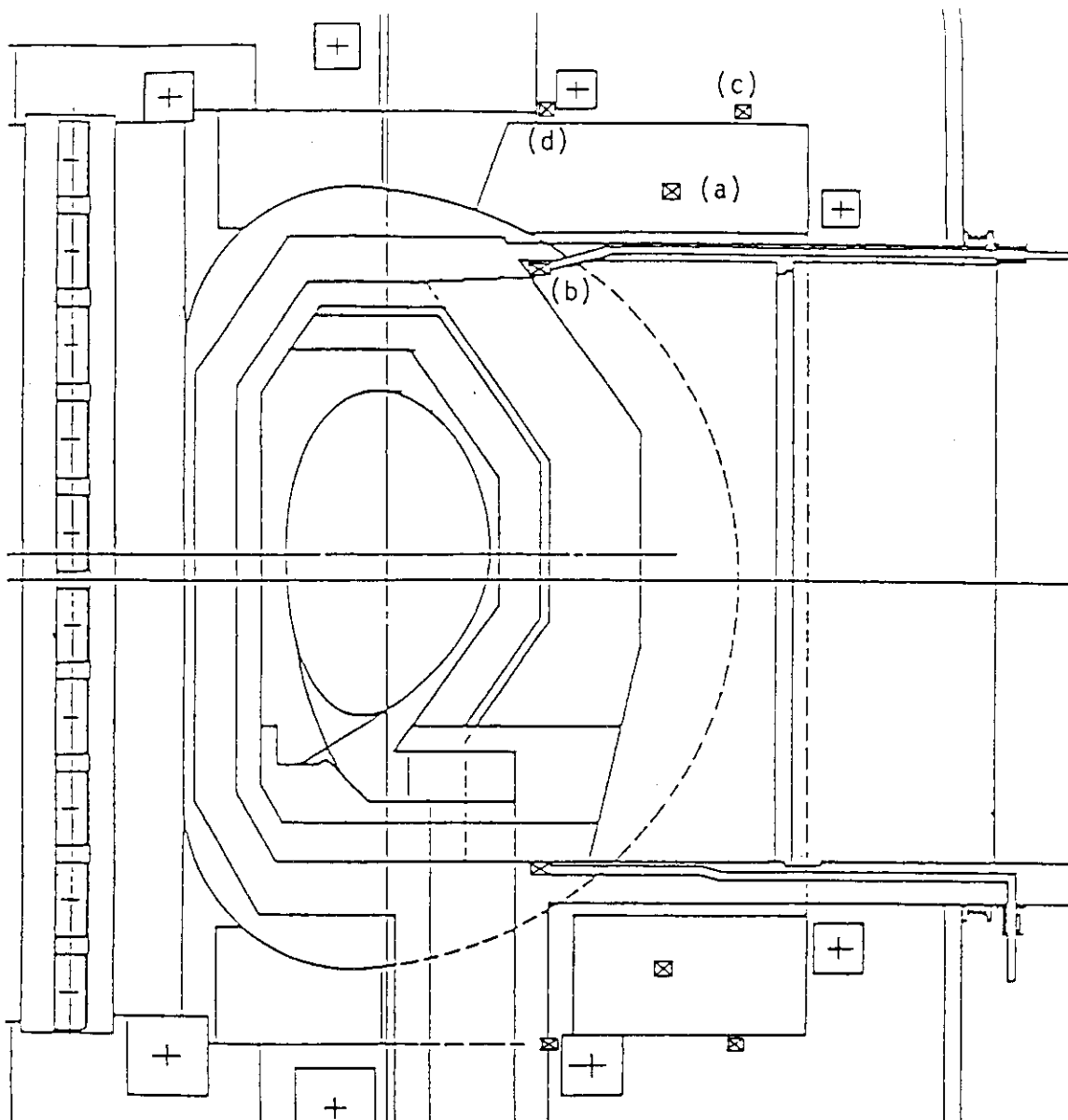


Fig. 7.2.2 Stabilizing properties of passive elements in cases of high beta ( $\beta_p = 1.3$ ) and low beta ( $\beta_p = 0.1$ ) phases.



- (a) Standard Outer Active Coil Location  
INTOR (8.2m,  $\pm 4.2$ m) FER (8.75m,  $\pm 4.25$ m)
- (b) Standard Inner Active Coil Location  
INTOR (7.0m,  $\pm 3.6$ m) FER (7.25m,  $\pm 3.25$ m)
- (c) Case 1 Outer Active Coil Location  
FER (9.75m,  $\pm 5.10$ m)
- (d) Case 2 Outer Active Coil Location  
FER (7.52m, 5.05m) (7.42m, -5.00m)

**Fig. 7.2.3 Schematic view of active coil locations.**

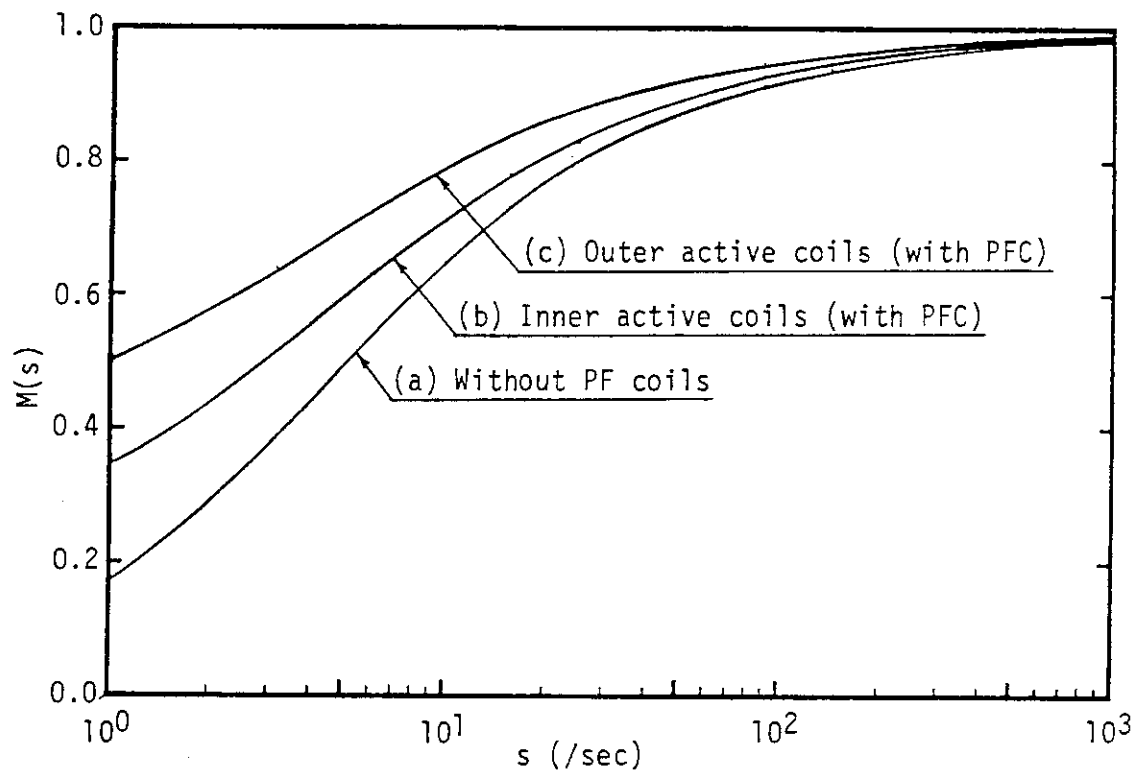


Fig. 7.2.4 Shielding properties of passive elements.



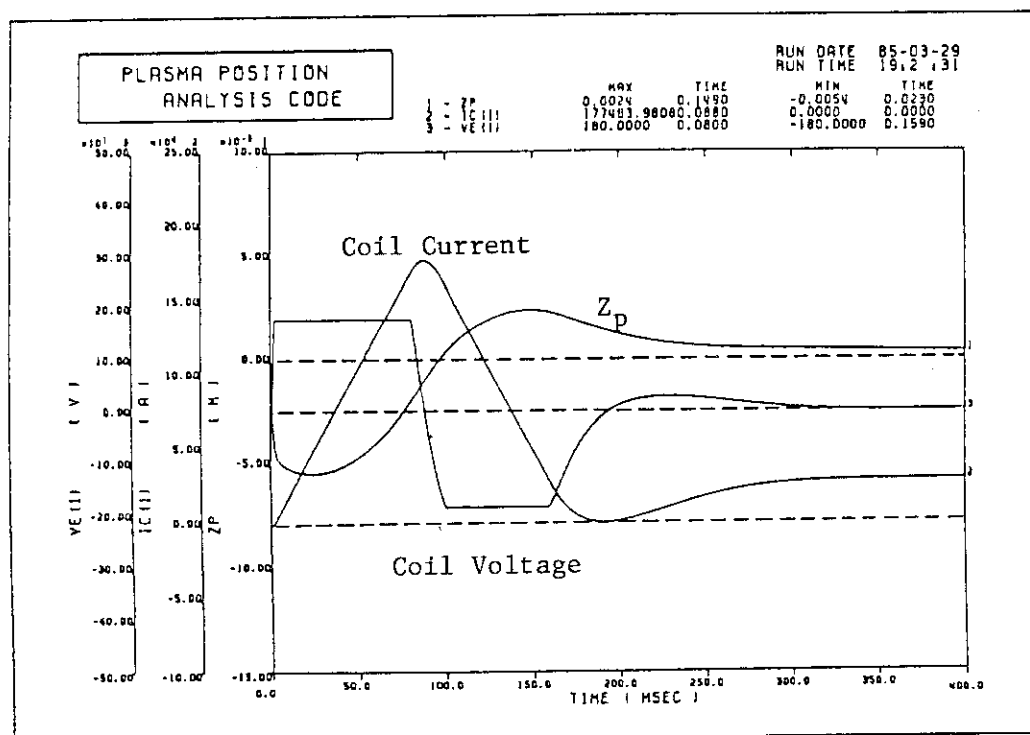


Fig. 7.2.5 (a) Simulation result of vertical position control by outer active coils in high beta case. Shielding properties of PF coils are taken into account.

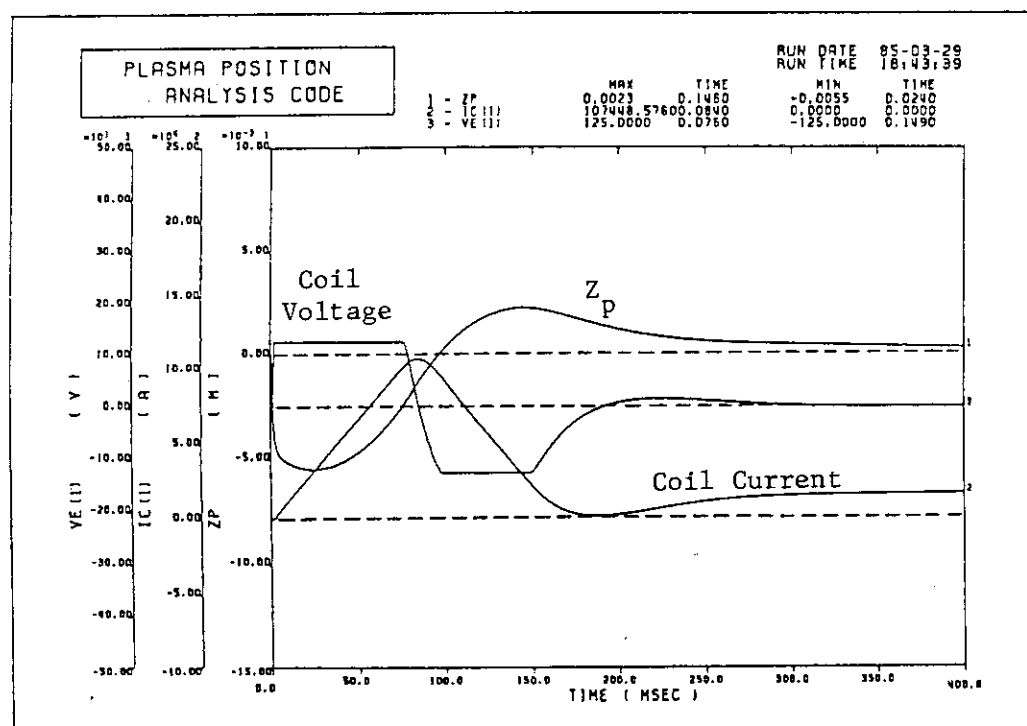


Fig. 7.2.5 (b) Simulation result of vertical position control by outer active coils in high beta case. Shielding properties of PF coils are neglected.

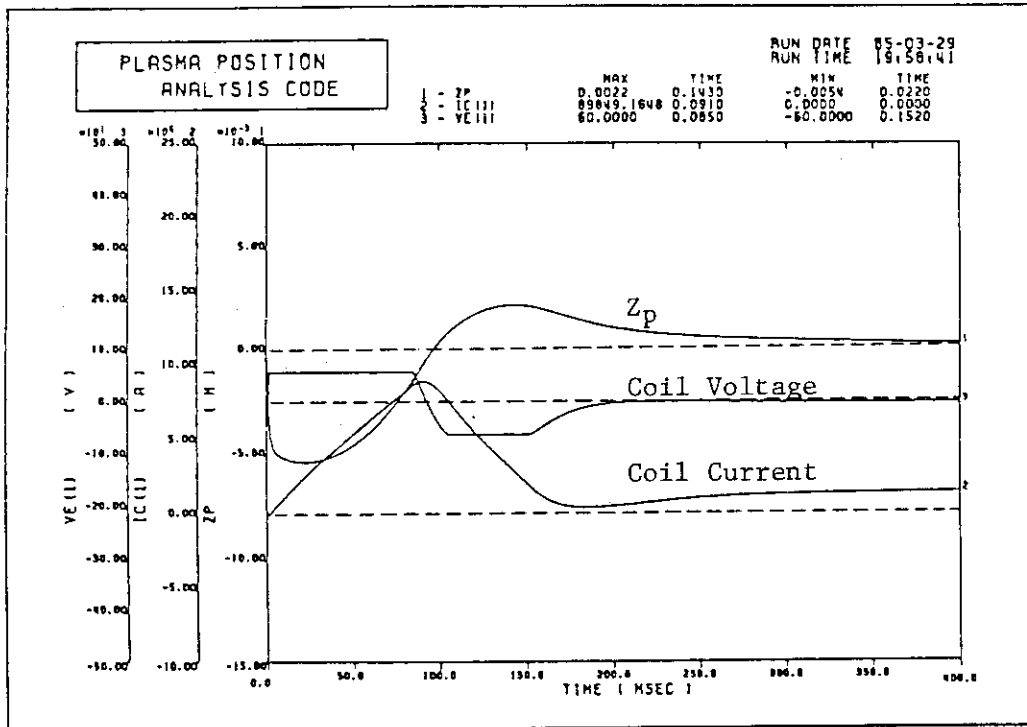


Fig. 7.2.6 (a) Simulation result of vertical position control by inner active coils in high beta case. Shielding properties of PF coils are taken into account.

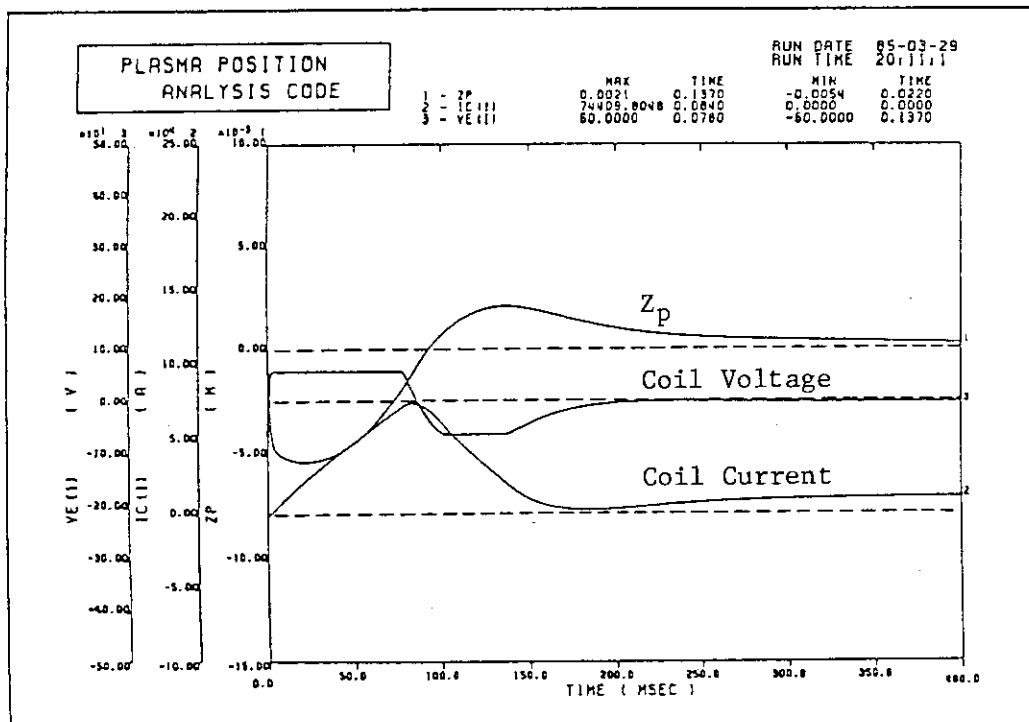


Fig. 7.2.6 (b) Simulation result of vertical position control by inner active coils in high beta case. Shielding properties of PF coils are neglected.

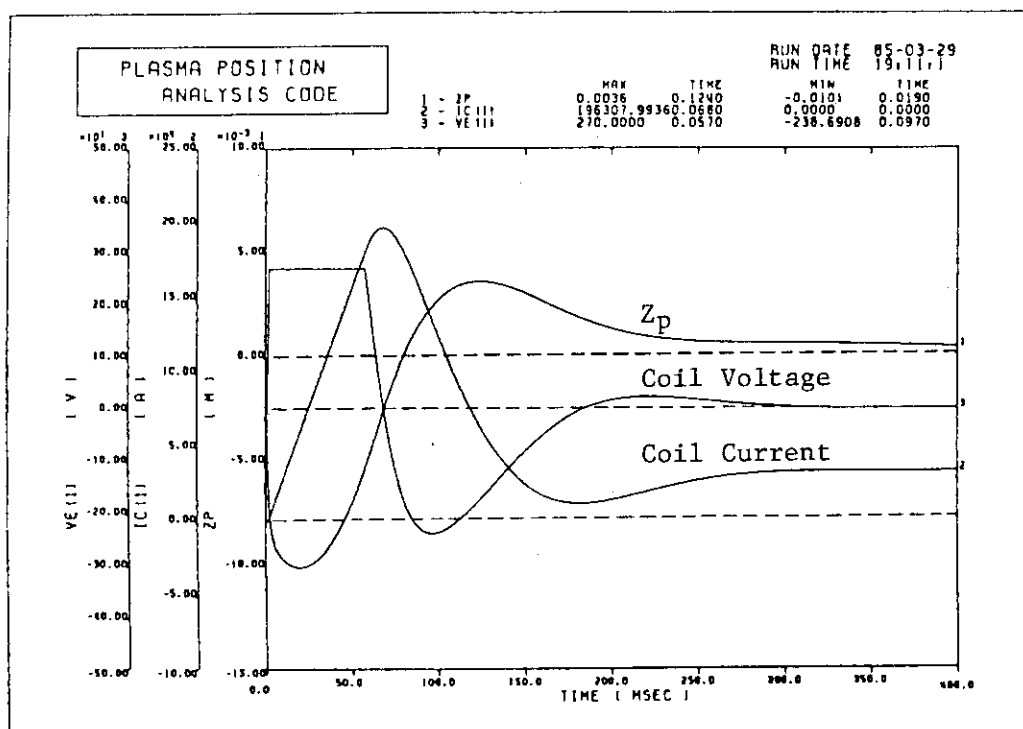


Fig. 7.2.7 Simulation result of vertical position control by outer active coils in low beta case. Shielding properties of PF coils are taken into account.

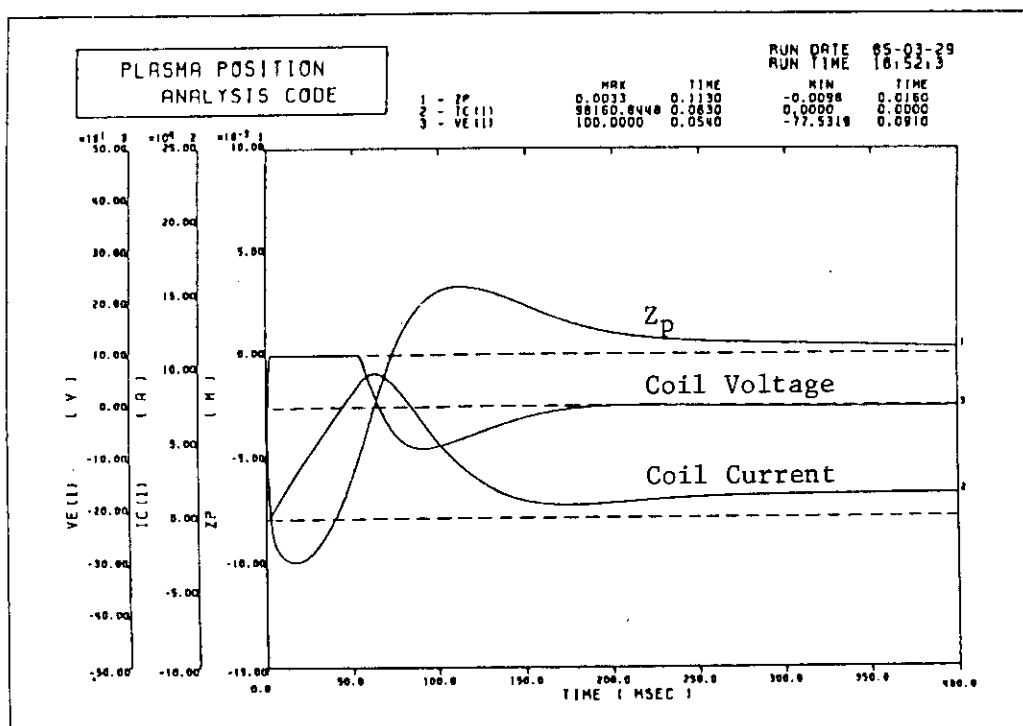


Fig. 7.2.8 Simulation result of vertical position control by inner active coils in low beta case. Shielding properties of PF coils are taken into account.

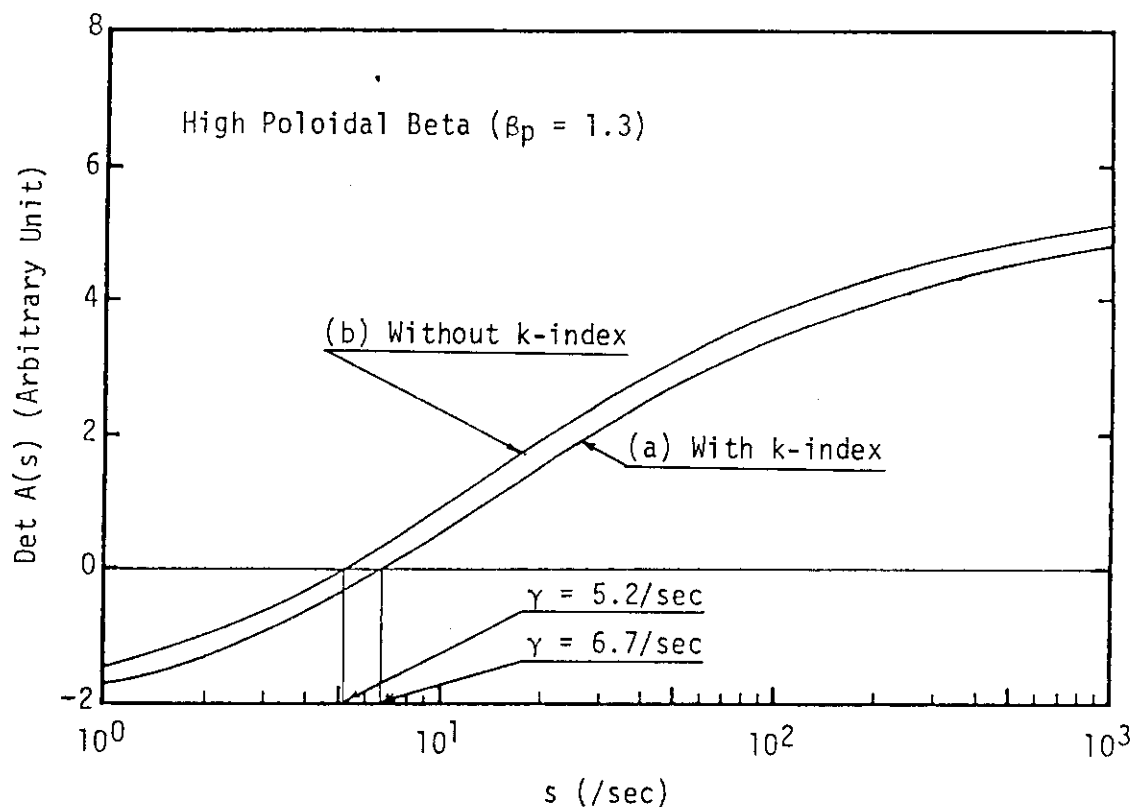


Fig. 7.3.1 Growth rates of plasma position movements at high beta phase with and without k-index.

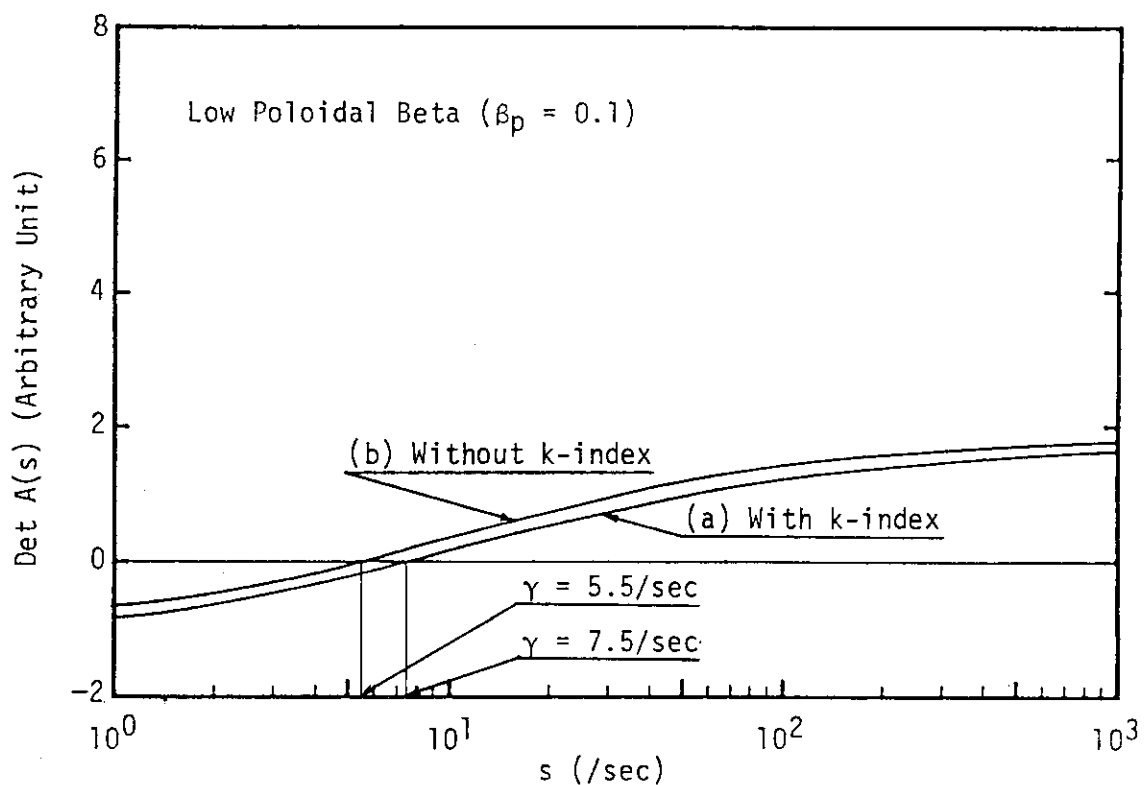


Fig. 7.3.2 Growth rates of plasma position movements at low beta phase with and without k-index.

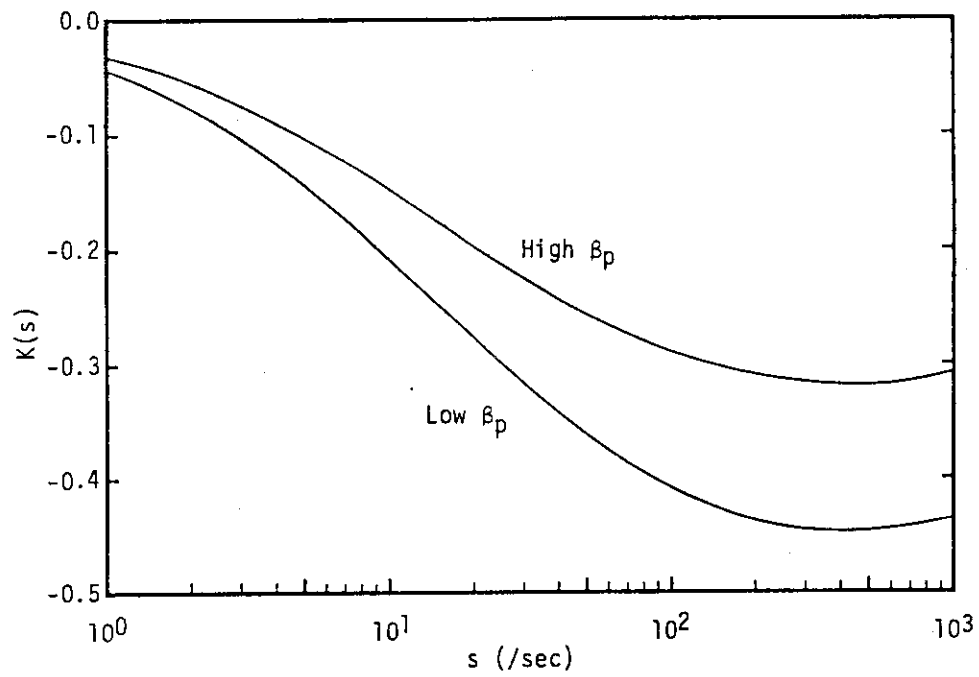


Fig. 7.3.3 Coupling functions,  $K(s)$ , between radial and vertical movements in high beta and low beta cases.

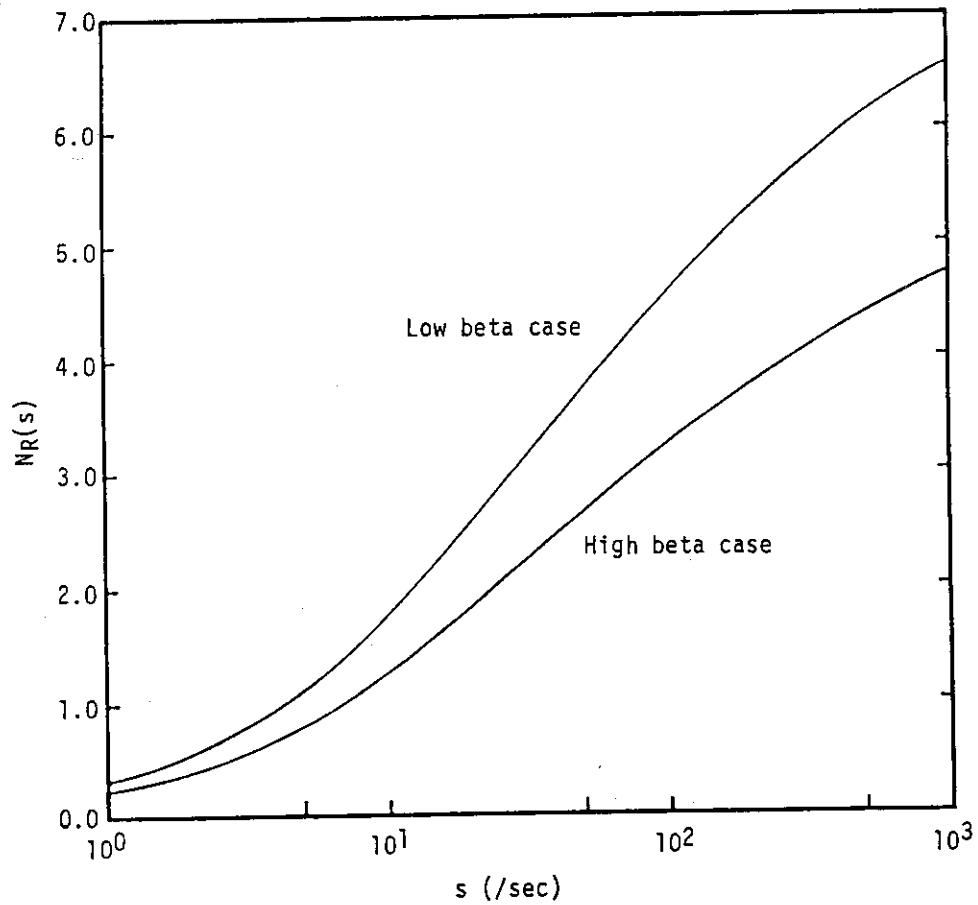


Fig. 7.3.4 Stabilizing functions,  $N_R(s)$ , in the radial direction at high beta and low beta phases

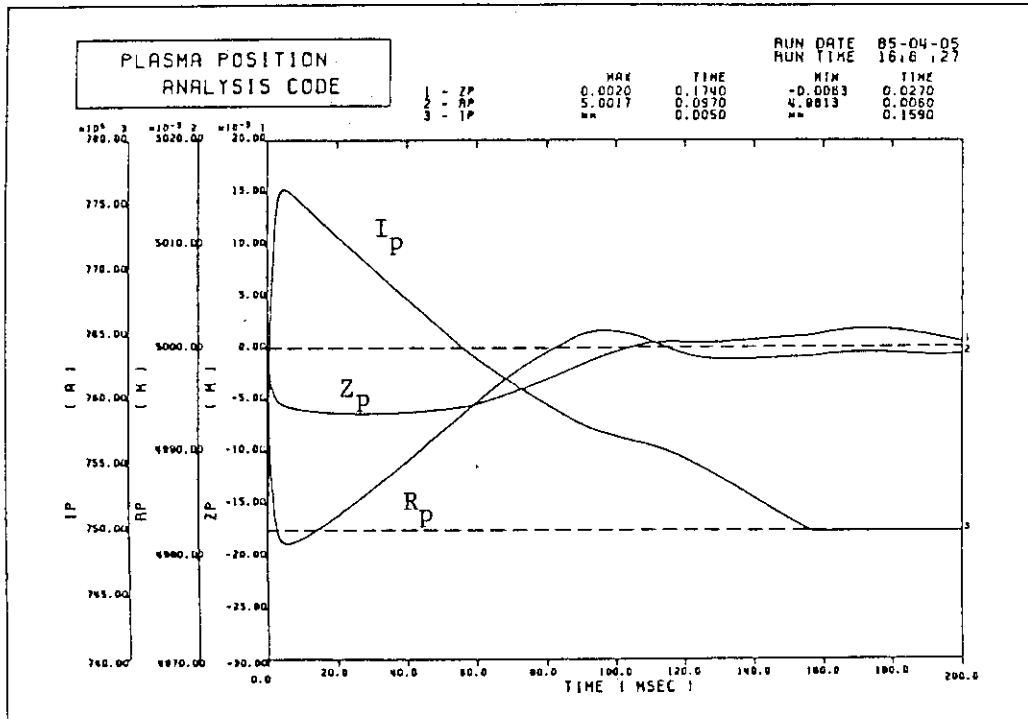


Fig. 7.3.5 Simulation result of plasma vertical and radial position control by outer active coils including the shielding effects of PF coils in high beta case.

$\delta Z_{pmax} : 6.3\text{mm}$ ,  $\delta R_{pmax} : 18.7\text{mm}$ ,  $I_{1max} : 294\text{kA}$ ,  $I_{2max} : 294\text{kA}$ ,  
 $|I_1 - I_2|_{max} : 24\text{kA}$ ,  $V_{max} : 150\text{V}$ ,  $P_{SRV} : 88\text{MVA}$ ,  $P_{SV} : 36\text{MVA}$

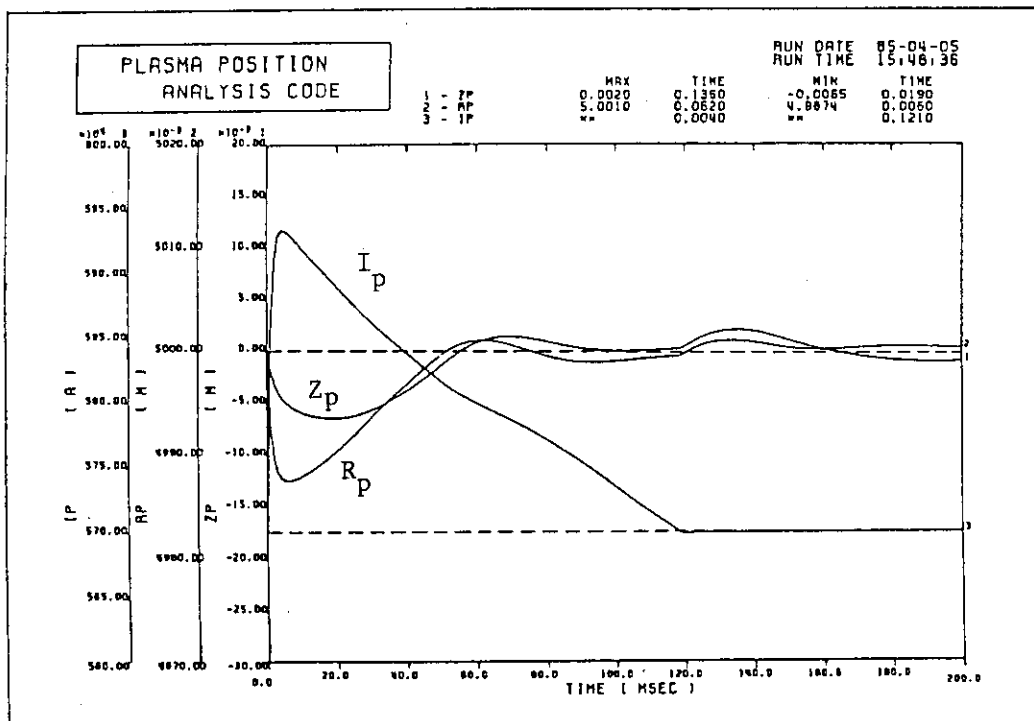


Fig. 7.3.6 Simulation result of plasma vertical and radial position control by outer active coils including the shielding effects of PF coils in low beta case.

$\delta Z_{pmax} : 6.5\text{mm}$ ,  $\delta R_{pmax} : 12.6\text{mm}$ ,  $I_{1max} : 196\text{kA}$ ,  $I_{2max} : 196\text{kA}$ ,  
 $|I_1 - I_2|_{max} : 160\text{kA}$ ,  $V_{max} : 170\text{V}$ ,  $P_{SRV} : 67\text{MVA}$ ,  $P_{SV} : 27\text{MVA}$

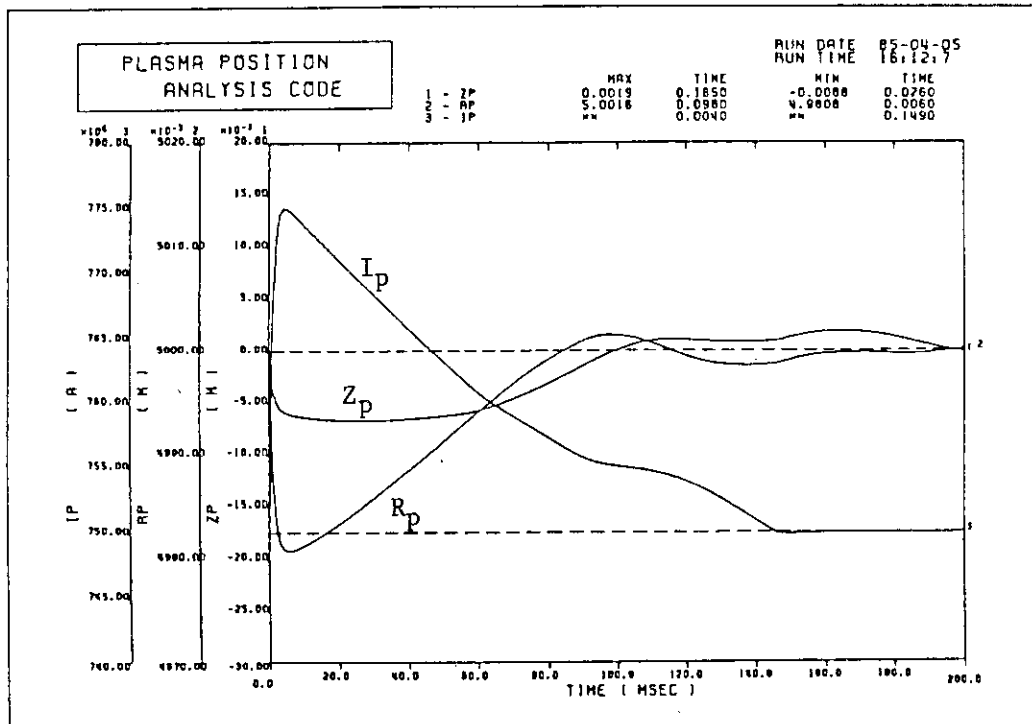


Fig. 7.3.7 Simulation result of plasma vertical and radial position control by outer active coils neglecting the shielding effects of PF coils in high beta case.

$\delta Z_{pmax} : 6.8mm$ ,  $\delta R_{pmax} : 19.2mm$ ,  $I_{1max} : 172kA$ ,  $I_{2max} : 175kA$ ,  
 $|I_1 - I_2|_{max} : 150kA$ ,  $V_{max} : 110V$ ,  $P_{SRV} : 38MVA$ ,  $P_{SV} : 17MVA$

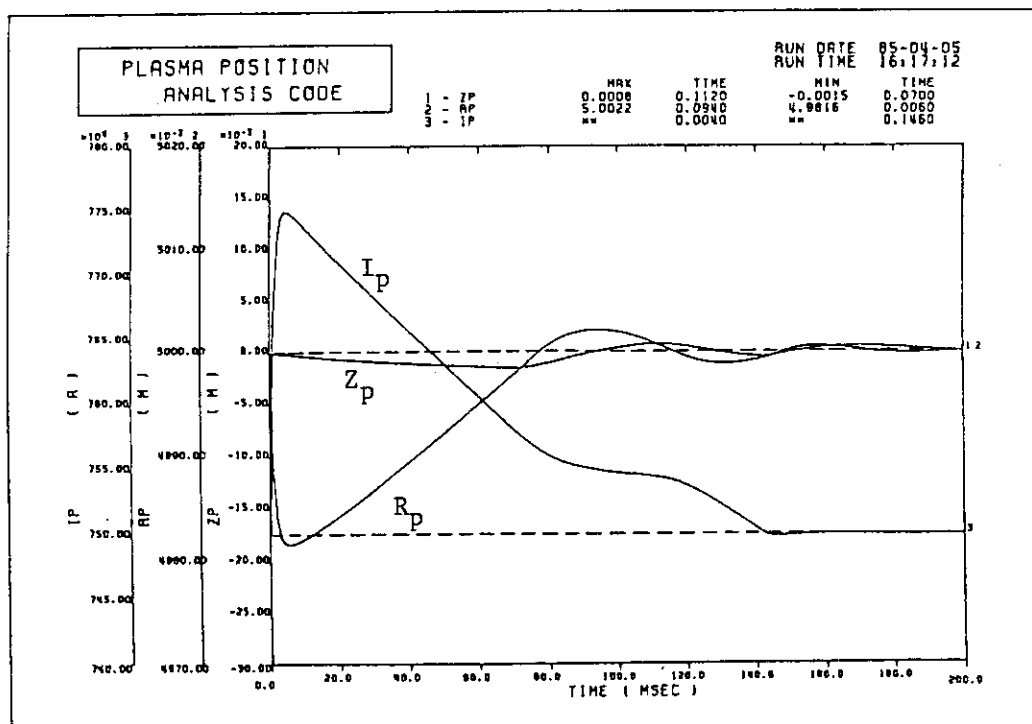


Fig. 7.3.8 Simulation result of plasma vertical and radial position control by outer active coils neglecting the shielding effects of PF coils in high beta case. The k-index is assumed to be zero in this simulation.

$\delta Z_{pmax} : 1.5mm$ ,  $\delta R_{pmax} : 18.4mm$ ,  $I_{1max} : 151kA$ ,  $I_{2max} : 140kA$ ,  
 $|I_1 - I_2|_{max} : 44.6kA$ ,  $V_{max} : 110V$ ,  $P_{SRV} : 32MVA$ ,  $P_{SV} : 4.5MVA$

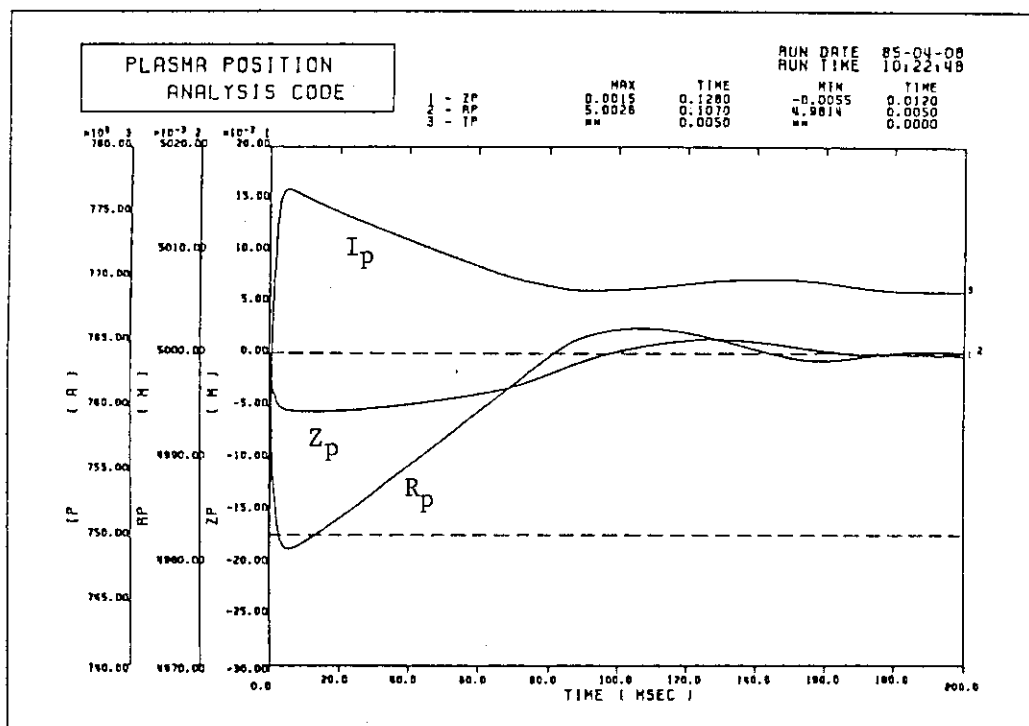


Fig. 7.3.9 Simulation result of plasma vertical and radial position control by outer active coils including the shielding effects of PF coils in high beta case. The voltage limit of OH coils is set to 1V in this simulation.

$\delta Z_{pmax} : 5.5\text{mm}$ ,  $\delta R_{pmax} : 18.6\text{mm}$ ,  $I_{1max} : 195\text{kA}$ ,  $I_{2max} : 160\text{kA}$ ,  
 $|I_1 - I_2|_{max} : 85\text{kA}$ ,  $V_{max} : 100\text{V}$ ,  $P_{SRV} : 36\text{MVA}$ ,  $P_{SV} : 8.5\text{MVA}$



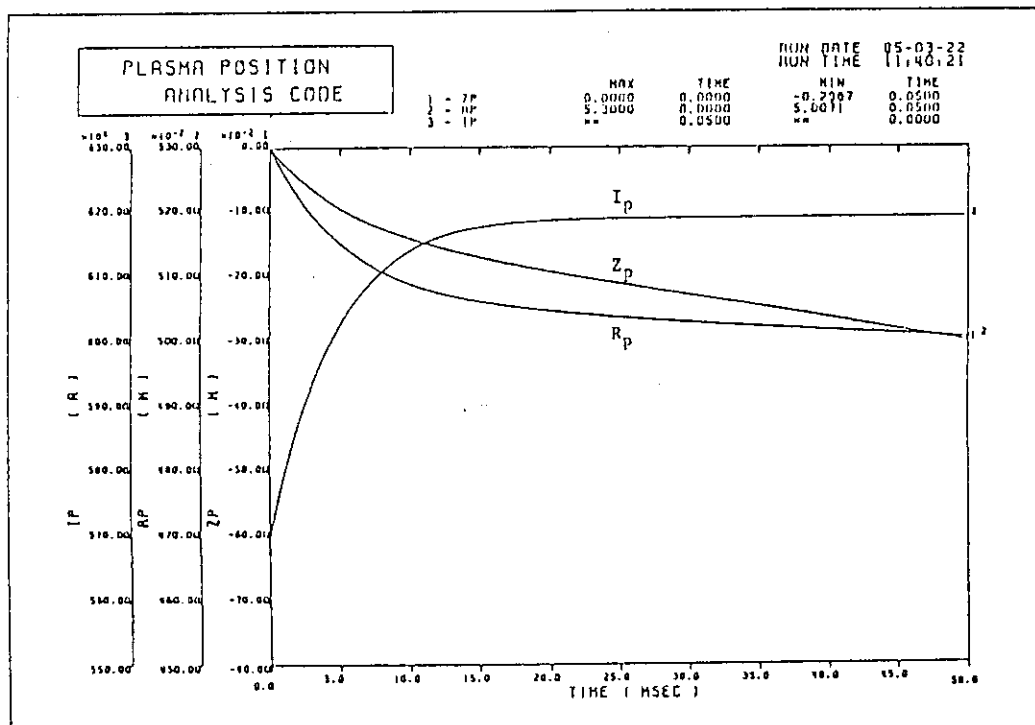


Fig.7.3.10 Simulation results of plasma position movements at disruption. Plasma positions and current are not controlled in this figure. High conductive shells are installed in blanket modules.  $\beta_p$  and  $\ell_i$  are reduced by 40% with a time of 5 msec.

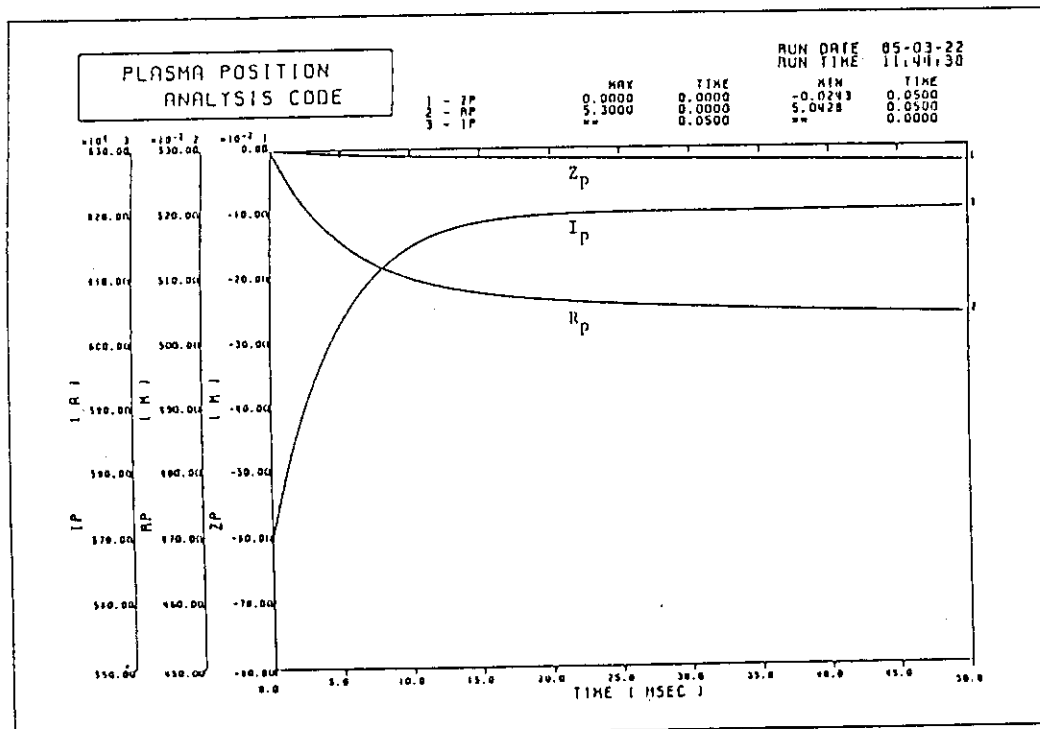


Fig.7.3.11 Simulation result of plasma position movements at disruption. Simulation conditions are the same as those in figure 3.7.10 except that the k-index is set to zero in this calculation.

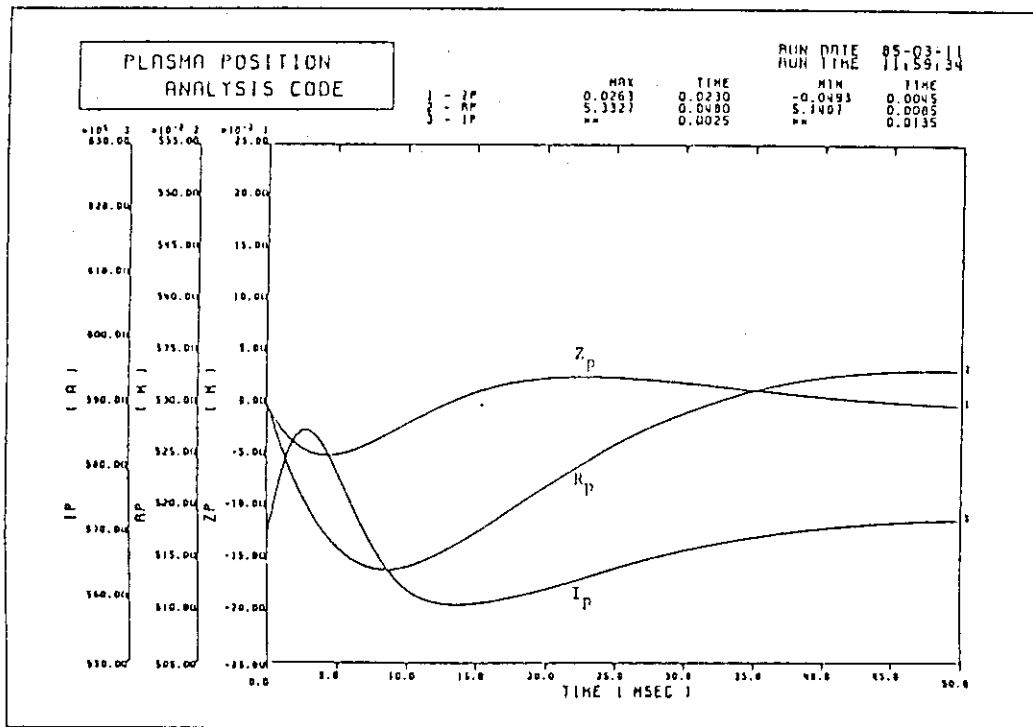


Fig.7.3.12 Simulation results of plasma position control by inner active coils at disruption. Since active coil voltages is not limited, impractically large power is required.

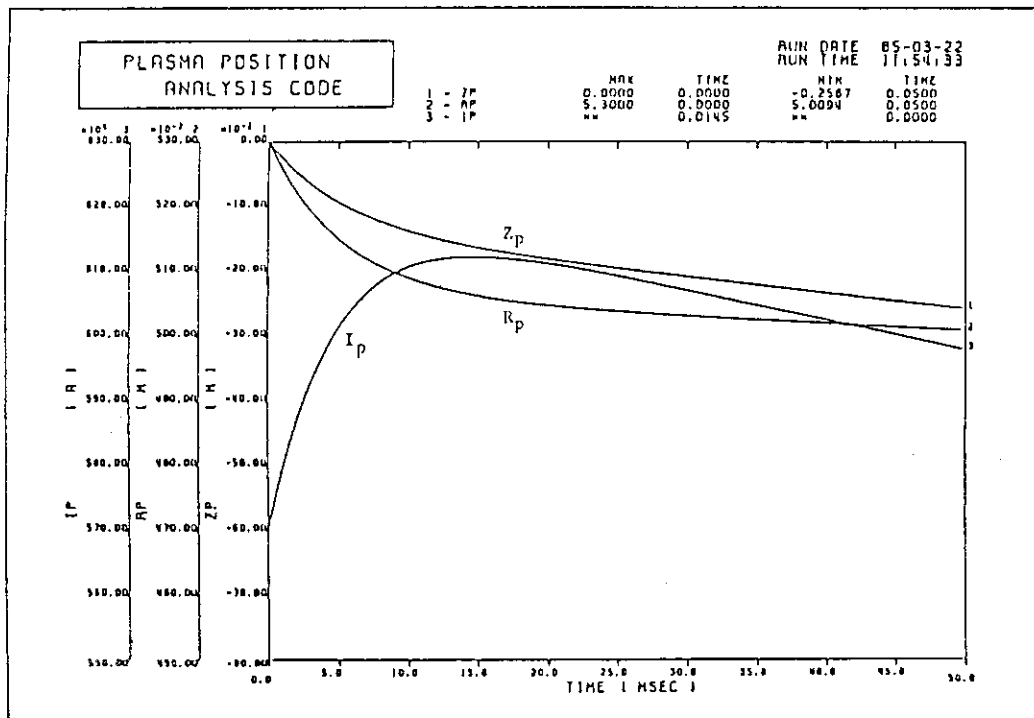


Fig.7.3.13 Simulation results of plasma position control by inner active coils at disruption. Active coil voltage is limited to  $\pm 100$  V.

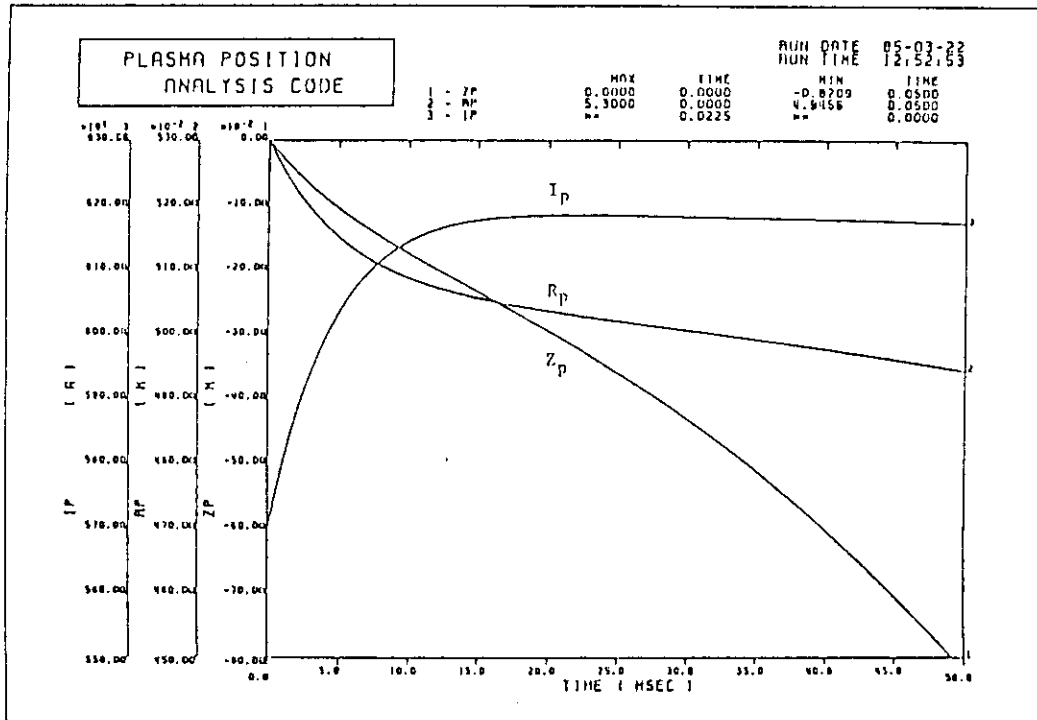


Fig.7.3.14 Simulation results of plasma position movements at disruption. Plasma position and current are not controlled in this calculation. There is no conductive shell in blanket modules. More than 2.5 times larger displacement is observed in the vertical position comparing with the results in figure 3.7.10.

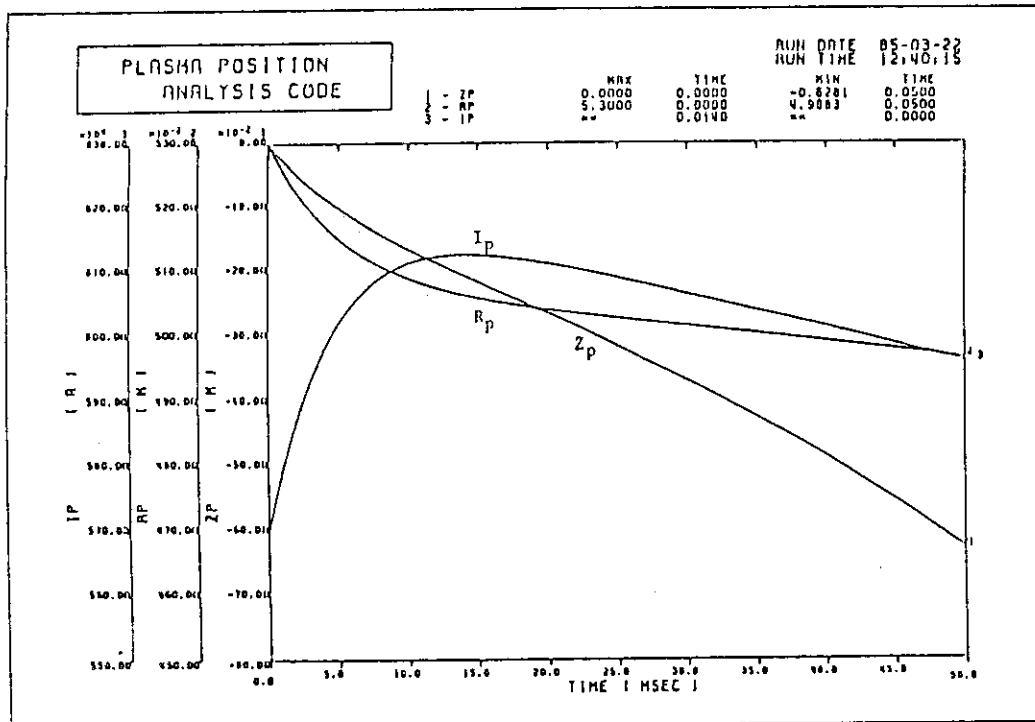


Fig.7.3.15 Simulation result of plasma position control by inner active coils at disruption. There is no conductive shell in blanket modules. Active coil voltage is limited to  $\pm 200$  V in this case.

## 8. Magnets

### 8.1 TF coil system

#### 8.1.1 Concept

New magnet system design concept is developed with the following objects;

- 1) Size reduction of TF and PF coils
- 2) Adoption of forced flow type conductor (Cable in conduit)

Efforts were made to obtain smaller TF coil than the Phase-IIA Part 1 reference size in order to realize a compact and low cost experimental reactor. Comparison of this TF coil system with that selected in Phase-IIA Part 1 shown in Table 8.1-1. The reduction of the thickness of the TF coil inboard leg contributed in obtaining the smaller plasma major radius.

The major requirement for the INTOR TF magnet is to provide total ampere-turns of 124 MAT required to generate the 4.96 T field at plasma axis. The key design issues of TF magnet are the establishment of cryogenic stability and mechanical rigidity for the enormous electromagnetic force. Besides those, there are many conflicting constraints; AC losses, coil protection against normal zone propagation, electrical insulation, joint requirements, fabricability, economics, etc.

There are many discussion with regard to the cooling method of large bore TF magnet. We adopted a forced cooling method in this phase. The reason for this choice is that forced cooling magnets have some interesting advantages and potentialities especially concerning with the heat transfer characteristics, mechanical integrity or high rigidity of the magnet for large electromagnetic force, high voltage endurance, etc., overcoming the difficulties of supplying the supercritical helium and cooling down the large magnet.

Table 8.1-2 illustrate detailed design specifications.

### 8.1.2 Configuration

TF coil configuration are shown in Fig. 8.1-1 to Fig. 8.1-3. One coil has 22 pancakes, each insulated by insulation tape and resin impregnated glass tape. One pancake is wound with 16 turns. The overall current density in the winding of TF magnet is  $28.7 \text{ A/mm}^2$  and the maximum field is 11.5 T at the magnet bore.

The number and bore of TF coil is determined, taking into account accessibility and maintainability for the remote handling of blanket, etc. and also considering the achievement of an acceptable field ripple at plasma region.

The elevation view of TF coil is shown in Fig. 8.1-1 and Fig. 8.1-2. Fig. 8.1-4 indicates toroidal field distributions at a center line of a toroidal coil and between toroidal coils on a mid-plane. The attained field ripple is  $\pm 0.97\%$  at  $R=6.2 \text{ m}$ . Fig. 8.1-5 shows toroidal field distribution along coil perimeter. The maximum field is 11.52 T at coil perimeter 2.6 m from the center of inboard leg.

### 8.1.3 Load condition

In-plane force distribution of TF coil is shown in Fig. 8.1-6. The total hoop force per coil is 940 MN and centering force and vertical force  $F_z$  are 304 MN and  $\pm 208 \text{ MN}$  respectively. Besides those electromagnetic forces which are caused by TF coil itself, TF coil must be sustained against out-of-plane force which is caused by the interaction between TF coil current and poloidal field. Fig. 8.1-7 gives the out-of-plane force distributions at recharge and burn phase.

Maximum force 26 MN at burn phase appears on the lower half of coil due to divertor coil field.

Unbalanced out-of-plane force is caused by the single null divertor coil.

### 8.1.4 Conductor

Cable in conduit type superconductor is adopted in order to get high rigidity of coil winding.

Selected superconducting material is  $(\text{NbTi})_3\text{Sn}$  because of its good characteristics at high field over 10 T.

Fine Nb filament diameter is  $\phi 5 \mu\text{m}$  and there are 1193 filaments in a strand which diameter  $\phi 0.87 \text{ mm}$ . Bronze ratio and copper ratio are 2.5 and 2.0 respectively. The surface of strand is insulated by inorganic material  $\text{CuO}$  in order to suppress AC loss heat load. There are 567 strands in stainless steel conduit and supercritical helium flows inside conduit. Void fraction is 40% in the conductor. The detailed specifications of cable in conduit type conductor for TF coil are listed in Table 8.1-3 and the concept of superconductor is illustrated in Fig. 8.1-8. Operation current of this conductor is 29.4 kA at the field of 11.5 T and its critical current at 12 T, 5 K is 60 kA. Limiting current and stability margin for this cable in conduit type conductor are 32.1 kA and  $0.8 \text{ J/cc}$  respectively.

The designed conductor critical current 60 kA is two times higher than operation current 29.4 kA and Limiting current 32.1 kA is higher than operation current. Stability margin  $0.8 \text{ J/cc}$  is enough cryostable for this cable in conduit type conductor.

### 8.1.5 Support structure and analysis

TF coil system must be designed to be cryogenically stable for operating current and to be sufficiently rigid to support the electromagnetic force.

The magnetic hoop force are supported by the TF coil case and stainless-steel conduits of the winding. The coil case and support structure have a thick-walled stainless-steel structure.

The centering force is supported by the bucking cylinder. The cross-section of bucking cylinder is a 12-sided regular polygon with a circular central hole. The cylinder has 6 axial segments which contain a single radial insert of dielectric material, e.g. G-10, to suppress the eddy currents.

To withstand the overturning force, an inter-coil support structure is used. The inter-coil support structure is located upper and lower part connecting the adjacent TF coils.

The weight of coil system is held by Glass-epoxy cylinder with liquid nitrogen temperature heat intercept on the base of cryostat.

The support structure system is shown in Fig. 8.1-9 and Fig. 8.1-10.

In order to estimate the overall stress on TF coil and structure support, stress analysis has been carried out using FEM code SAP-V. The analytical model is shown in Fig. 8.1-11. The resulting deformations are shown in Fig. 8.1-12 and Fig. 8.1-13.

In case of hoop force loading, the maximum deformation is 7.1 mm and the maximum stresses of winding and coil case are 547 MPa and 360 MPa, respectively.

In case of overturning force loading, the maximum deformation of toroidal direction is about 28 mm and maximum stresses of winding and coil case are 203 MPa and 355 MPa, respectively.

The results of overall stress analysis for both hoop and overturning force show that the TF coil support structure can provide allowable stress level for normal operation mode. However, the TF coil and support have the high stress level which are closely related to upper limitation.

Table 8.1-1 Comparison of TF coil systems

Items	INTOR-M	INTOR-J-IIA
a) TF coil bore	6.5 m × 9.26 m	6.6 m × 9.3 m
b) Magnet cross section	512 mm thick × 740 mm wide	maximum 700 mm thick × 949 mm wide
c) Current density	28.7 A/mm <sup>2</sup>	19.4 A/mm <sup>2</sup>
d) Plasma major radius	5.0 m	5.2 m
e) Number of coils	12	12
f) Number of torus sector	24	24
g) Torus replacement	Mid plane access with straight line motion for removal of each sector	Mid plane access with straight line motion for removal of each sector

Table 8 1-2 Major characteristics of the TF magnet system

1. Total ampere - turns	124 MAT
2. No. of coils	12
3. Ampere - turns per coil	10.3 MAT
4. Plasma major radius	5.0 m
5. Field at plasma axis	4.96 T
6. Cooling method	Supercritical helium forced cooling
7. Grading concept	No grade
8. Winding configuration	Pancakes
9. Superconductor	Cable in conduit type (NbTi) <sub>3</sub> Sn conductor
10. No. of turns per coil	352
11. No of pancakes per coil	22
12. Operation current	29.4 KA
13. Critical current	60 KA (at 12T, 5K)
14. Avg. winding current density	28.7 A/mm <sup>2</sup>
15. Maximum field	11.5 T
16. Inductance	~45 H
17. Magnetic field energy	~ 20 GJ.
18. Electromagnetic force	
Hoop force	940 MN
Centering force	304 MN
Vertical force	208 MN

Table 8.1-3 Characteristics of the superconductor for TFC

NO	Item	sign	unit	12 T conductor
1.	Superconducting material		—	(NbTi) <sub>3</sub> Sn
2.	Strand diameter	$\phi_{Dw}$	mm	0.87
3.	Filament diameter (Number of filaments)		$\mu\text{m}$	5 (2852)
4.	Bronze ratio		—	2.5
5.	Copper ratio		—	2.0
6.	No. of strands	n	—	$3^4 \times 7 = 567$
7.	Superconducting material area of strands	$A_{sc}$	mm <sup>2</sup>	111.1
8.	Copper area of strands	$A_{cu}$	mm	222.2
9.	Total area of strands	$A_{co}$	mm <sup>2</sup>	333.3
10.	Operation current	$I_d$	KA	29.4
11.	Critical current at 12T, 5K	$I_c$	KA	60.0
12.	S.S. Conduit outer dimensions	a	mm	30 x 30
13.	S.S. Conduit inner dimensions	b	mm	23.5 x 23.5
14.	S.S. Conduit area	$A_{sus}$	mm <sup>2</sup>	343.7
15.	Insulation thickness	t <sub>ins</sub>	mm	1.0
16.	Helium area	$A_{He}$	mm <sup>2</sup>	222.2
17.	Volume fraction of copper in strands	$f = A_{cu} / A_{co}$	—	0.667
18.	Volume fraction of metal in the cable space	$f_{co} = \frac{A_{co}}{A_{co} + A_{He}}$	—	0.6
19.	Cable space area $A = A_{co} + A_{He}$	A	—	555.5
20.	Void fraction $f_{He} = 1 - f_{co}$	$f_{He}$	—	0.4
21.	Limiting current	$I_B$	KA	32.1
22.	Stability margin	$\Delta H$	J/cc	0.8
23.	Minimum winding radius	R	mm	2160
24.	Maximum winding strain	$\epsilon$	%	0.74



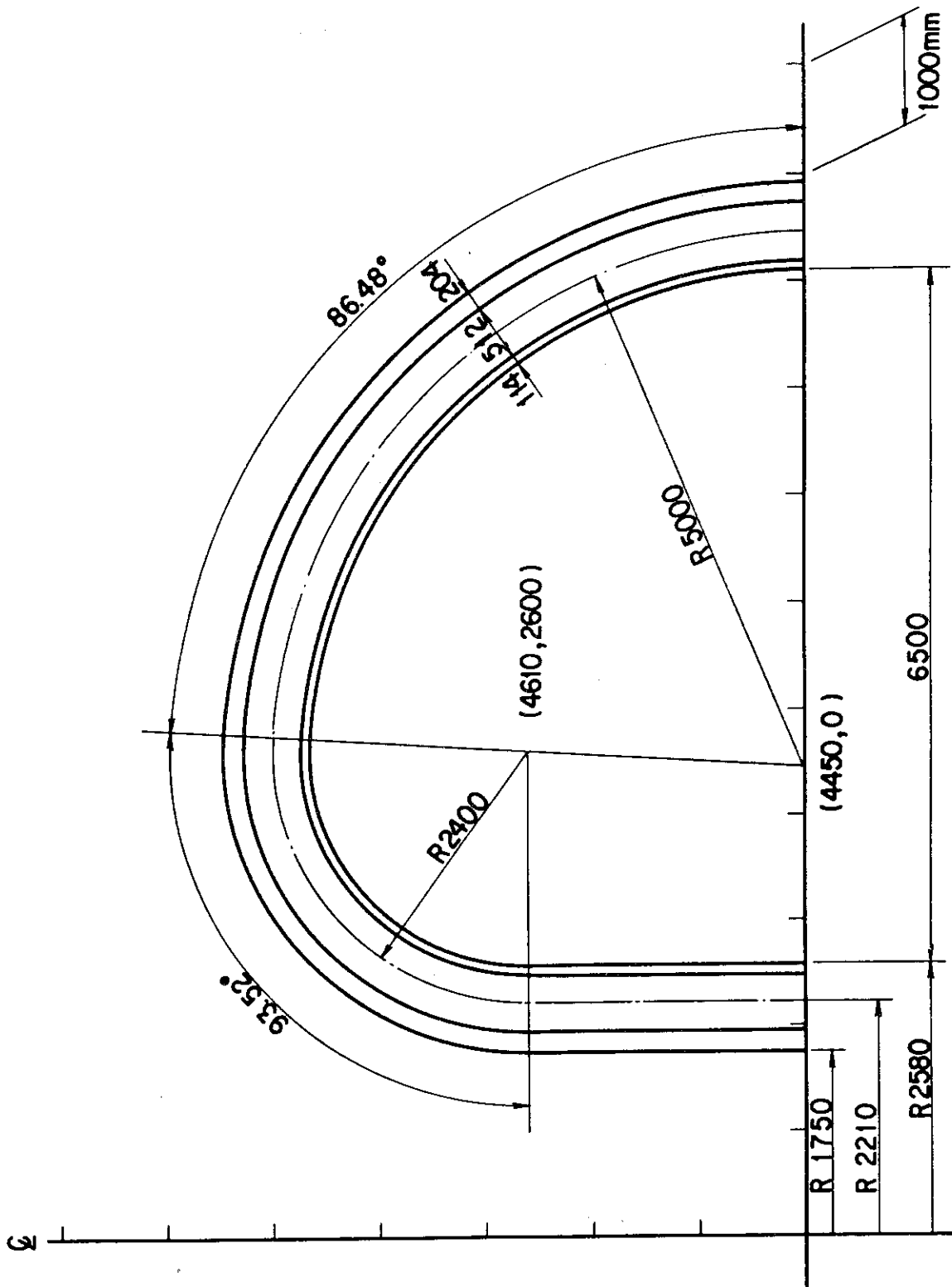


Fig. 8.1-1 TF coil dimension

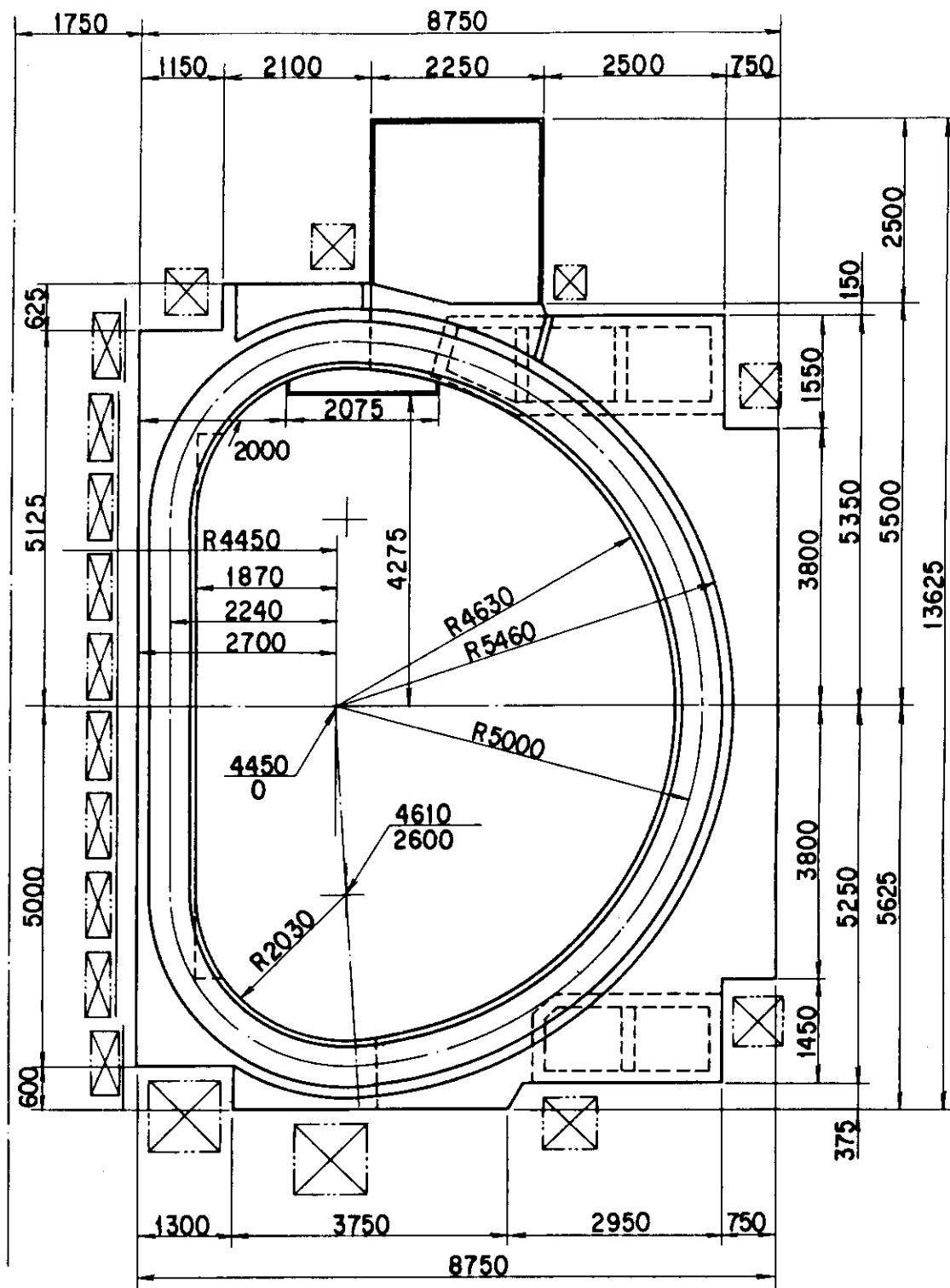


Fig. 8-1-2 TF Coil configuration

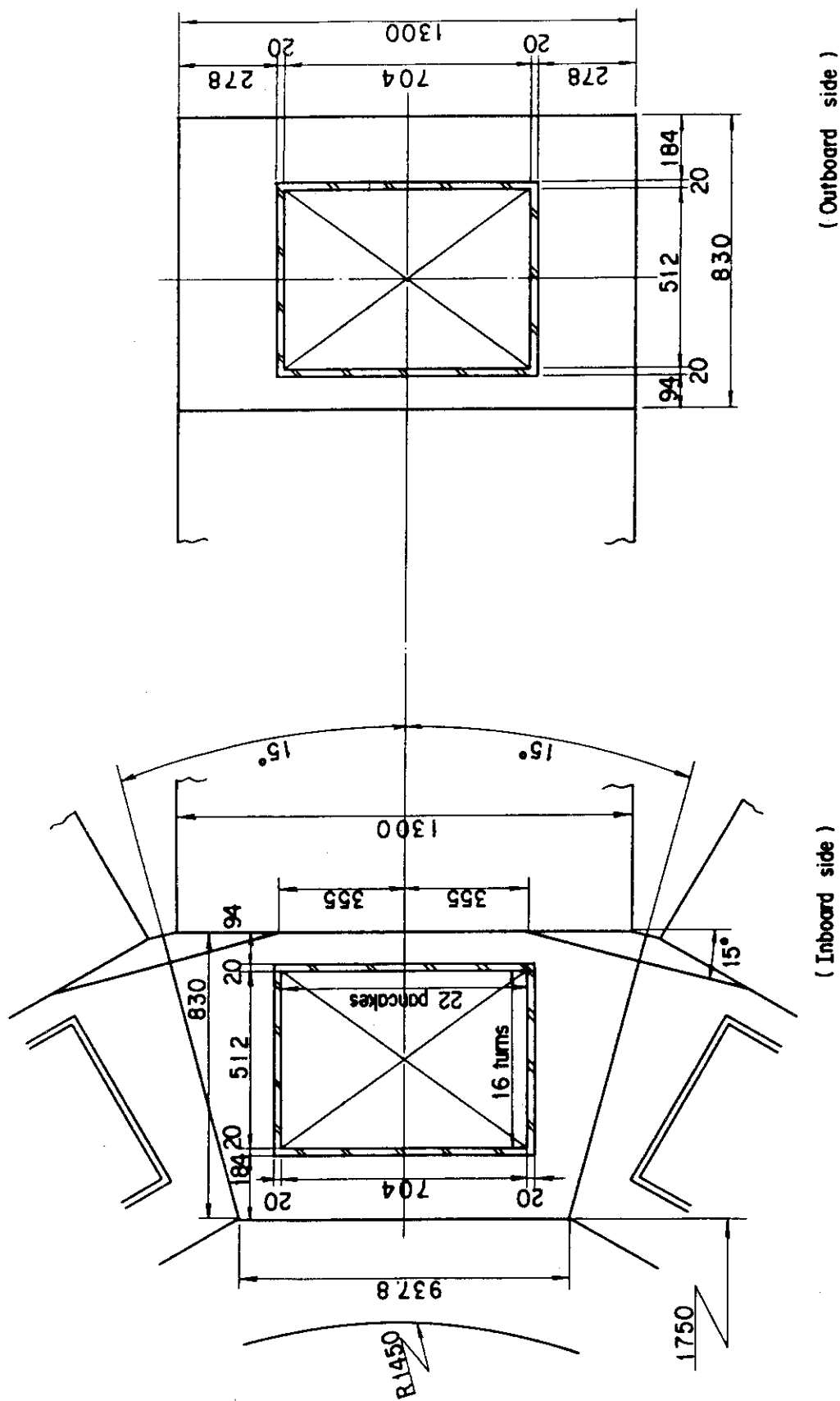


Fig. 8.1-3 TF Coil cross sections

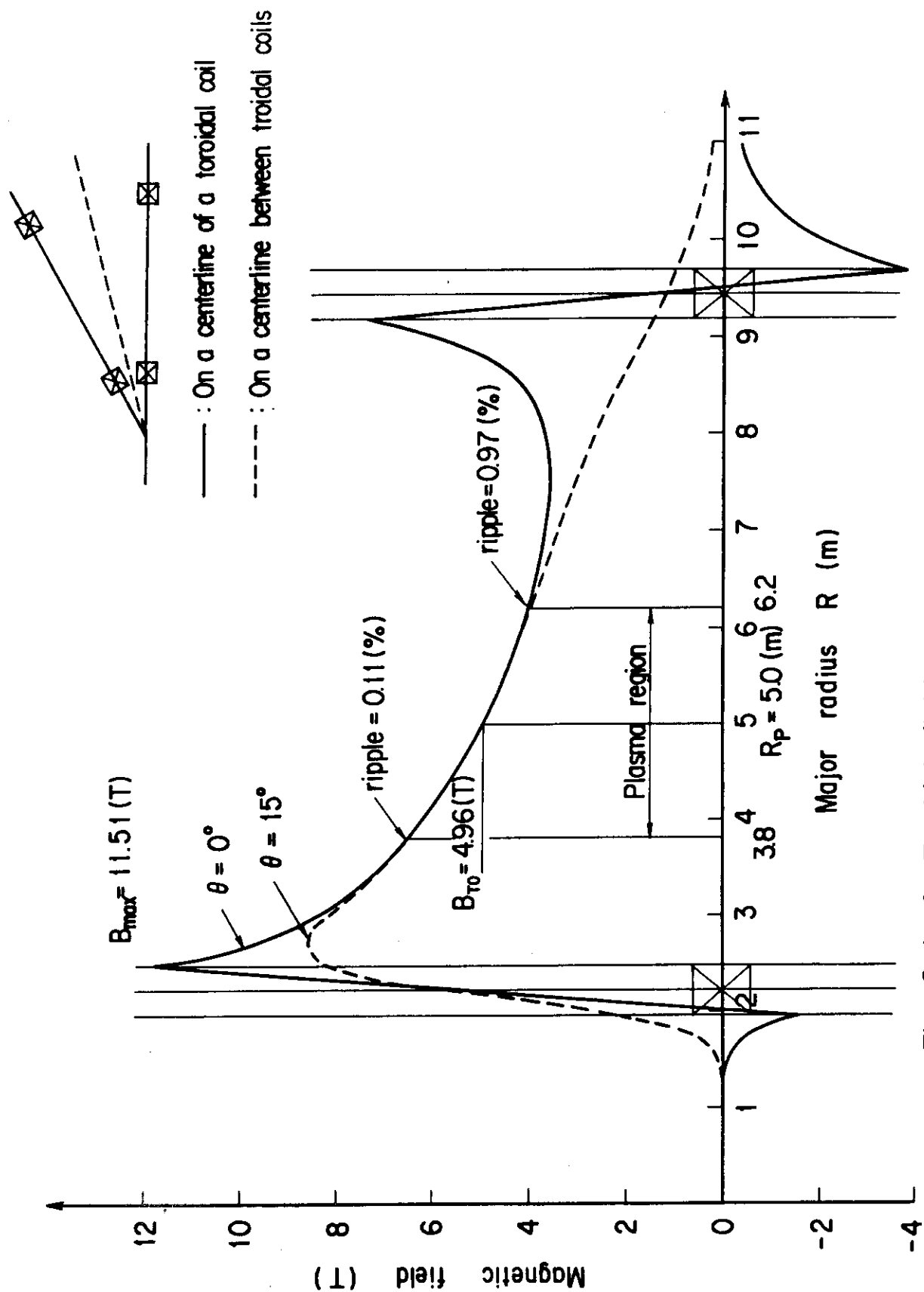


Fig. 8.1-4 Toroidal field distribution on a mid - plane

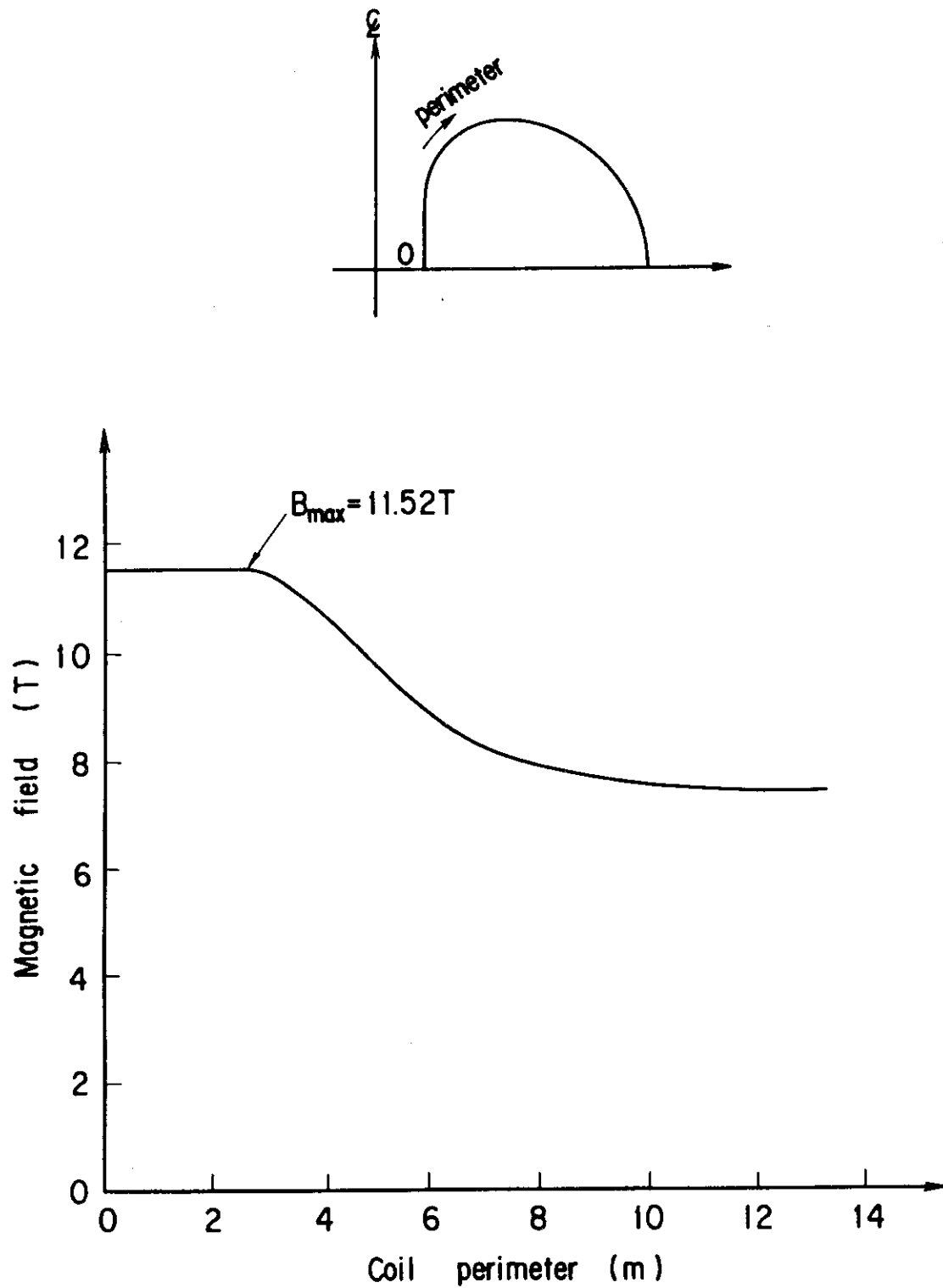


Fig.8.1-5 Toroidal field distribution along coil perimeter

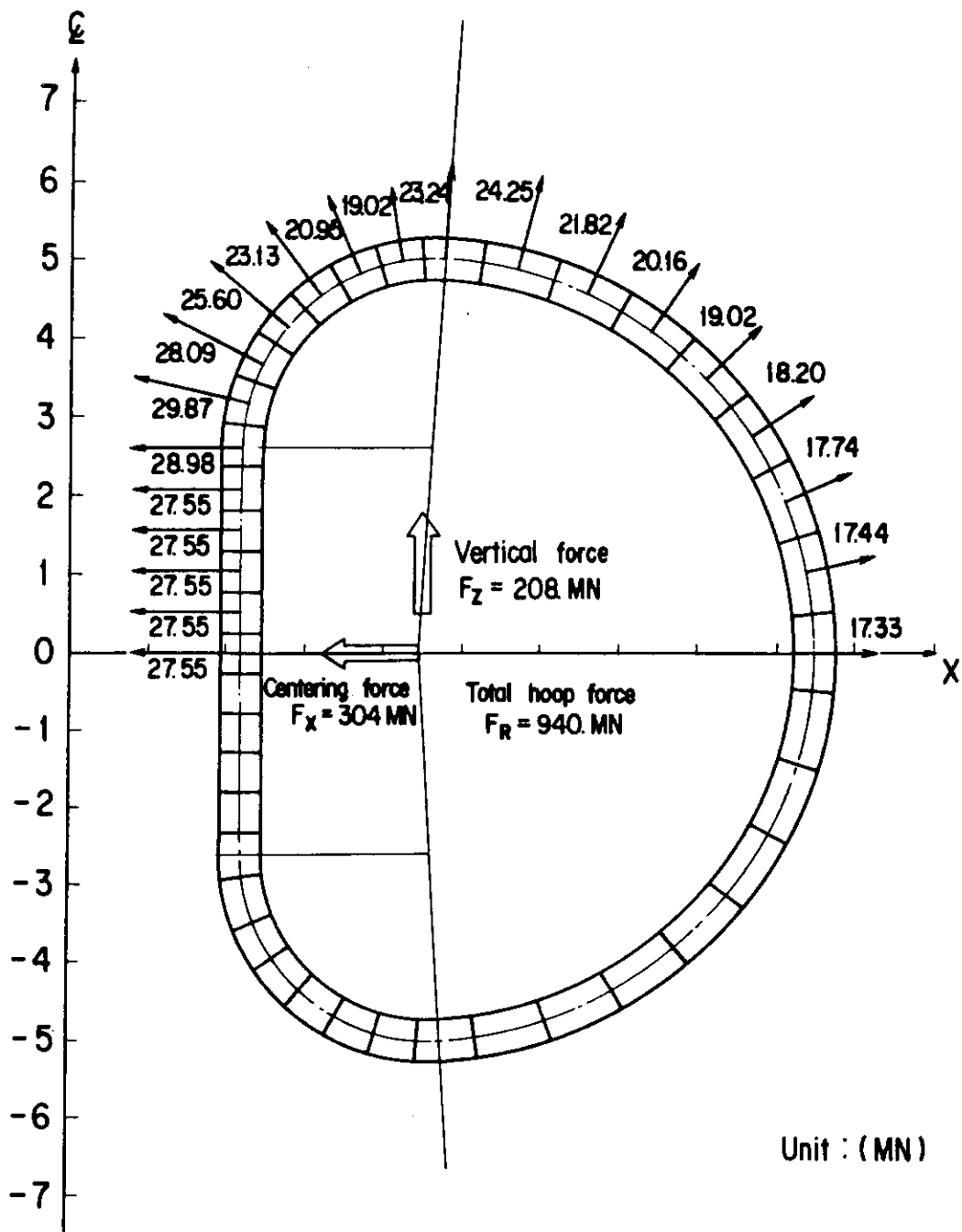


Fig. 8.1-6 In-plane force distribution along coil mid-plane

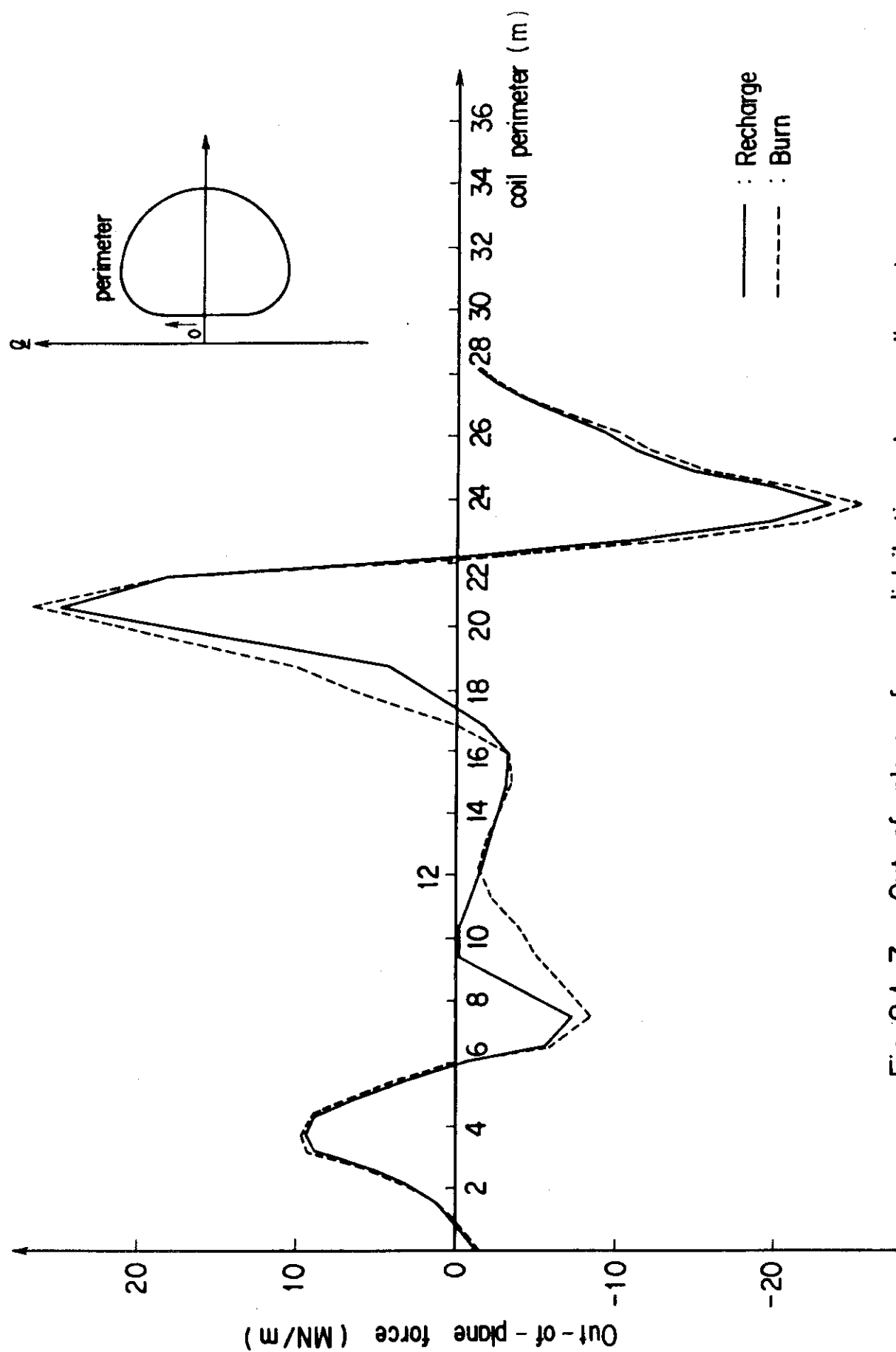


Fig. 8.1-7 Out-of-plane force distribution along coil perimeter

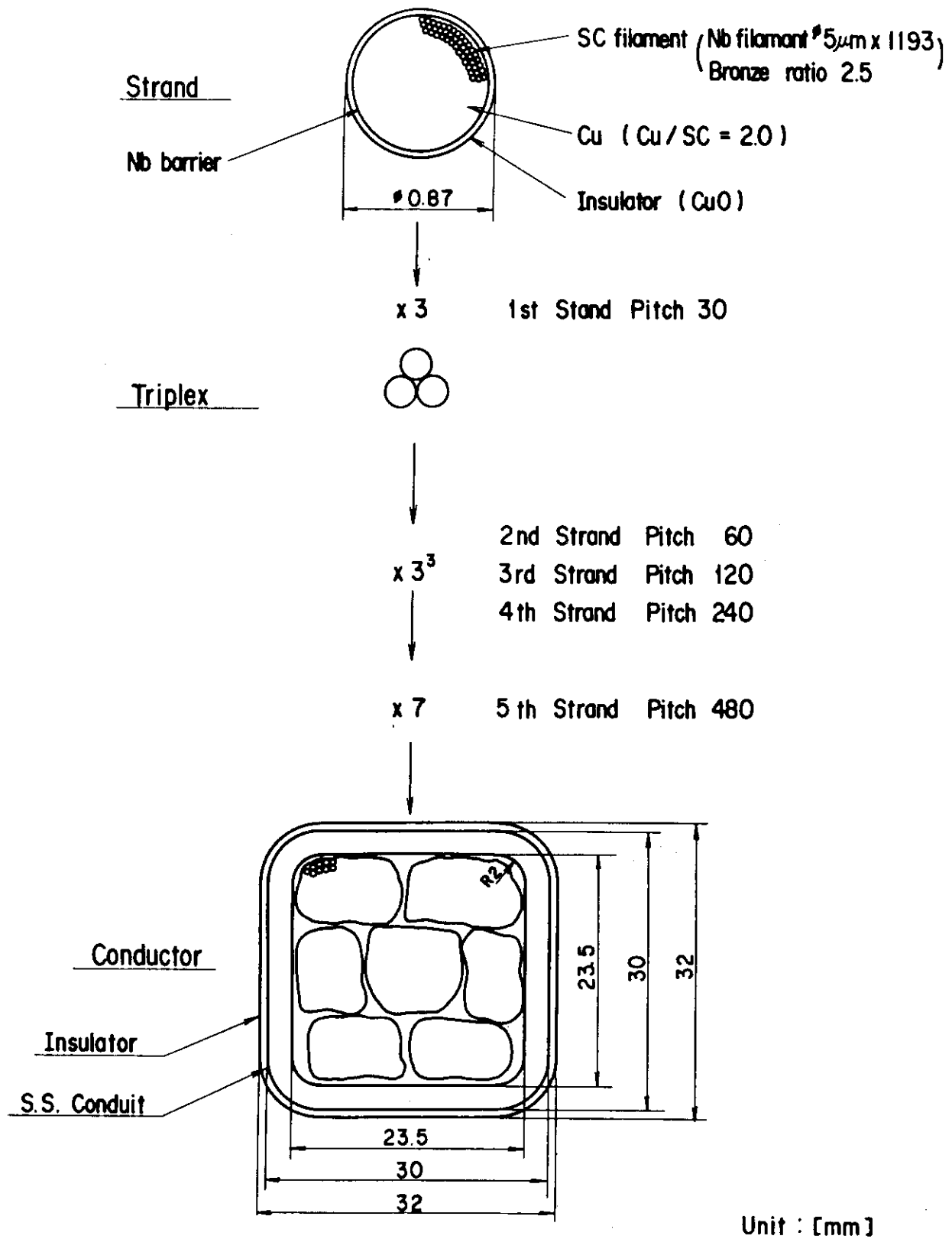


Fig.8.1-8 SC Conductor of TF Coil for INTOR



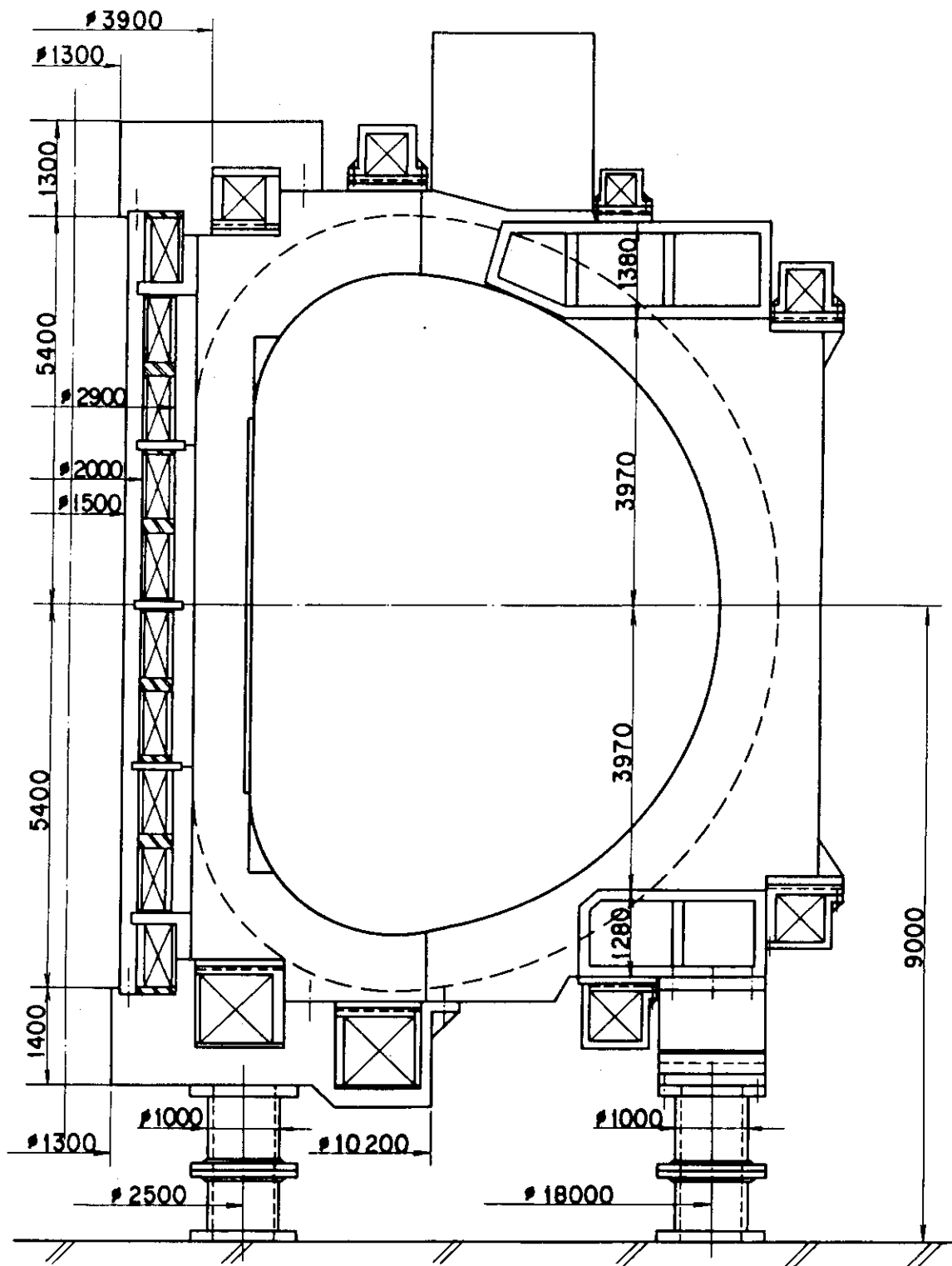


Fig. 8.1-9 Structure of TF and PF Coil Support System

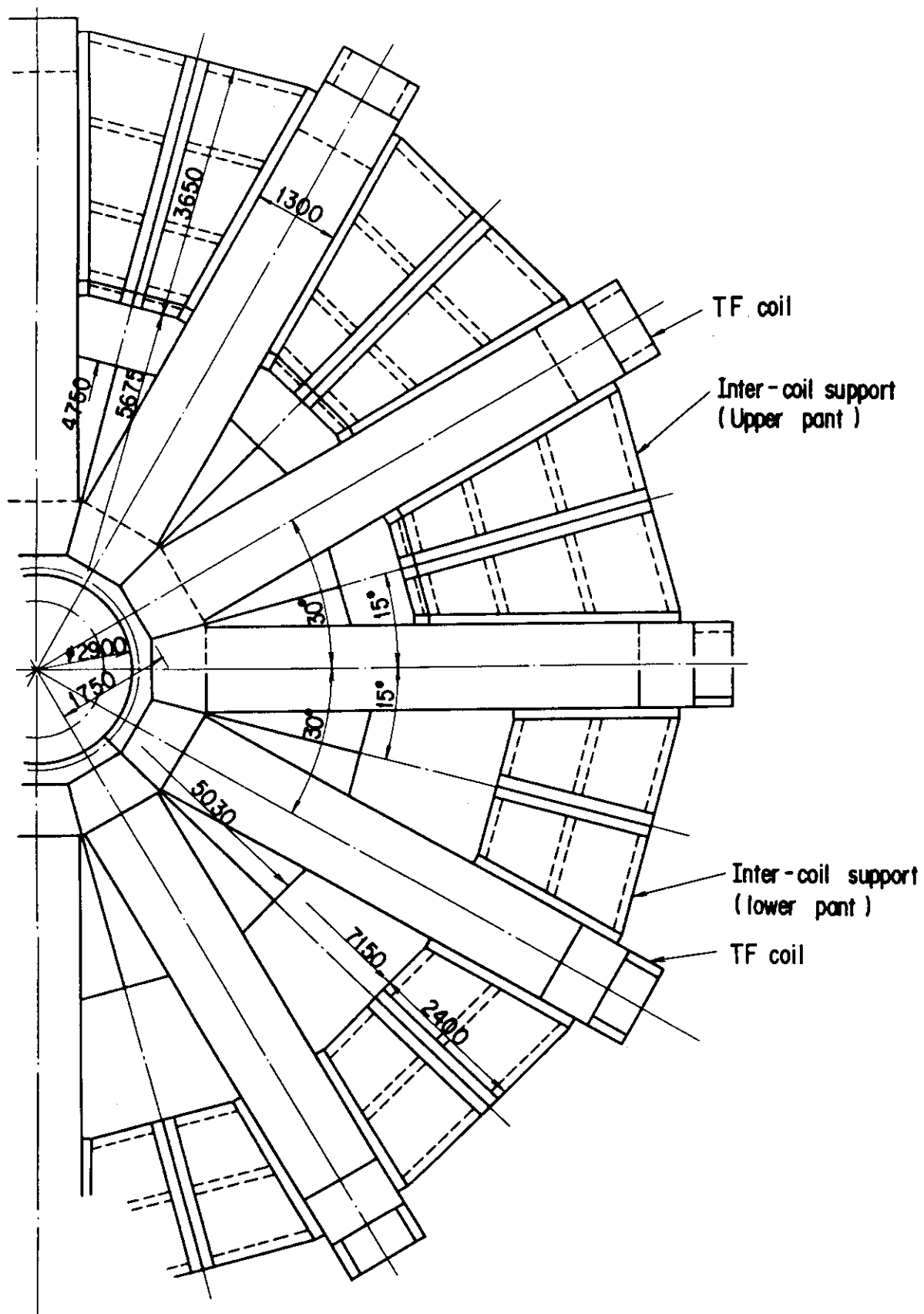


Fig. 8-1-10 Structure of TF Coil Support System  
( Bucking Cylinder and Inter-coil Support )

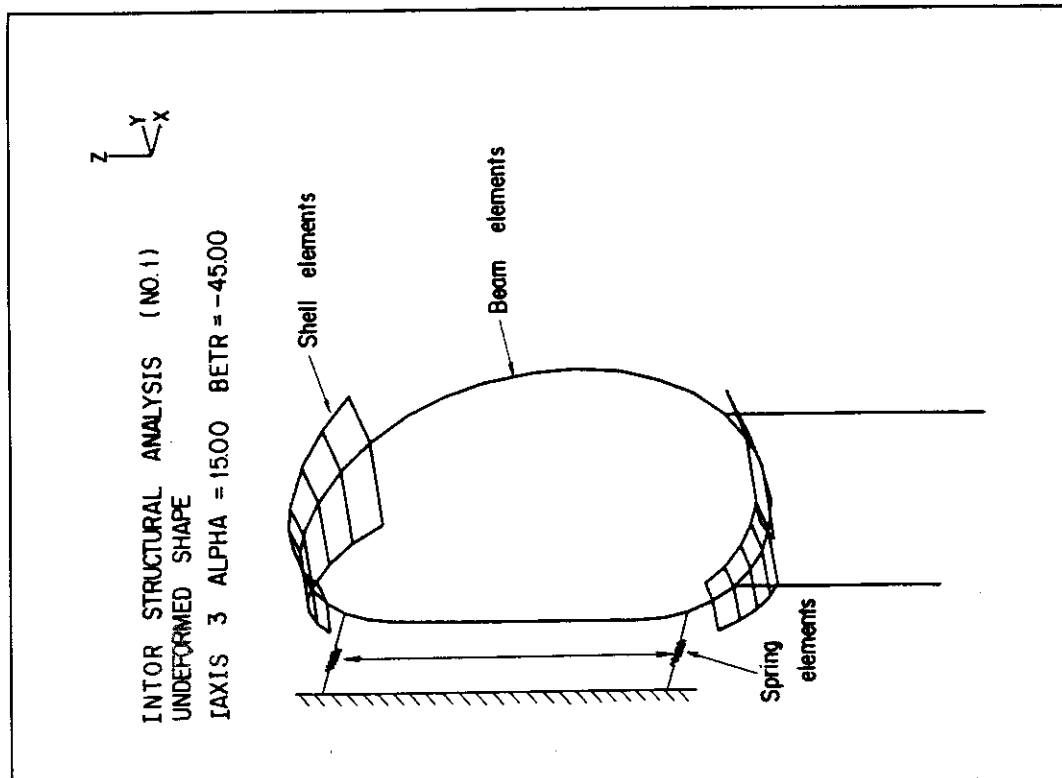


Fig. 8-1-11 Analysis Model

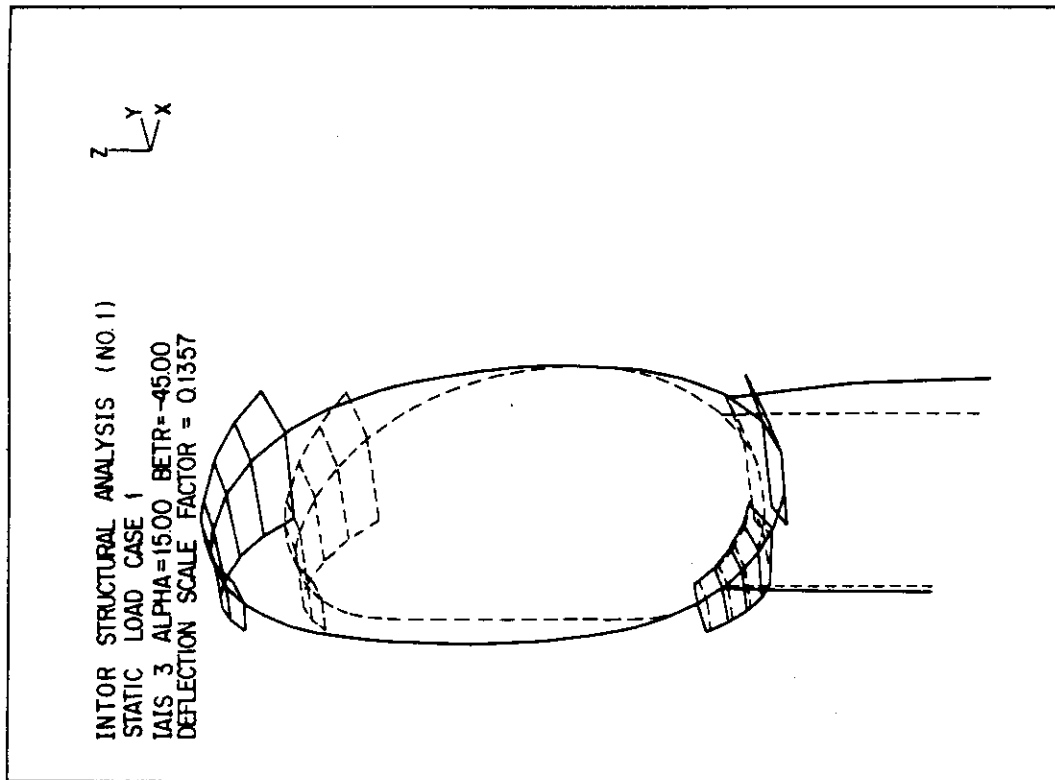


Fig. 8-1-12 Deformation due to hoop force

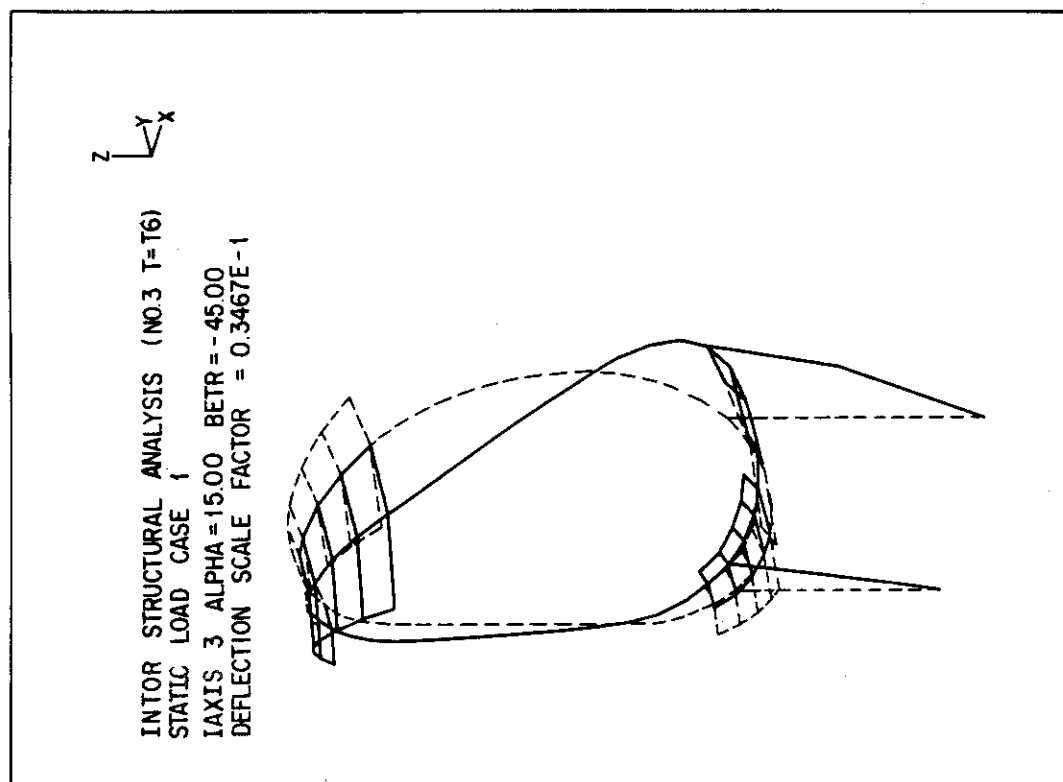


Fig. 8.1-13 Deformation due to overturning force

## 8.2 PF Coil System

### 8.2.1 Concept

Design concept and main characteristics of the PF coils are described.

The supercritical helium forced-flow system is selected for the cooling system of the superconducting coils. This cooling system is expected to have winding stiffness and strength higher than those of bath cooling system, and to have ability to endure high voltage with vacuum-impregnation technique. The type of superconductor is Internally Cooled Cable Superconductor (ICCS). The maximum field on the windings is targetted to reach 10 T. Therefore, for higher field PF coils  $\text{Nb}_3\text{Sn}$  is employed as superconducting materials. On the other hand for the lower field PF coils  $\text{NbTi}$  alloy is employed. The current density of the windings and coil current are  $25 \text{ A/mm}^2$  class and 35 kA class respectively.

The ring coils are hybrid coils; they are operated for both OH current and EF current. In order to maximize the OH flux and minimize the winding field, five central solenoid coils are operated as hybrid coils, and other solenoid coils are used for OH current only.

All of the PF coils bear their extensive magnetic force by themselves. The solenoid coils are located within the bucking cylinder, simplifying support structure for the centering force of TF coils and the piping of the solenoid coils. The solenoid coils are supported by distributively arranged shelves against the vertical magnetic forces.

### 8.2.2 Parameters

The locations of PF coils are shown in Fig. 8.2-1, and is symmetric about the mid plane. The vertical location of outer most coils is limited by inhibited zone which the access parts to the blanket require.

The cyclic operation pattern is shown in Fig. 8.2-2. The duration of burning phase is 500 s, and the recharging phase 100 s. The EF flux is mainly generated by ring coils, and less by five solenoid coils, #1, 2, 3, 10, 11 coils. These situation is shown in typical current pattern, Fig. 8.2-3. In this figure, #5 PF coil is a typical OH coil, #16 PF coil is a typical EF coil, and #1 PF coil is one of the five solenoid coils mentioned above. The difference between #1 and #5 PF coils current indicates the EF current in #1 PF coil, and is about one third of #16 PF coil current. The EF flux by solenoid coils helps design current distribution of PF coils that should maximize OH flux and minimize field on the PF coils. Maximum field on the PF coils, maximum current density are intended to be 10T and  $25 \text{ A/mm}^2$  respectively. Maximum current of the PF coils, which is concerned with coil voltage and manufacturing ability for both superconductor and coil winding.

Selected major parameters are shown in Table 8.2-1. Although most of parameter values in this table are much smaller than the design guidelines above mentioned, some of them are close to the margine. Most critical values related with the guide lines are, 9.83 T of winding field,  $24.7 \text{ A/mm}^2$  of current density, 35.73 kA of coil current, which occur in #1 solenoid coil at the same time. The maximum stored magnetic energy in the PF coil system is 8.9 GJ at the end point of burning phase. The maximum voltage applied by power supplies is 3.6 kV. On top of the above design guidelines, mechanical stress due to electromagnetic force can be a restricting factor as described in 8.2.5.

### 8.2.3 Conductor

The conductor design chosen for PF coil is almost same as those for TF coil except Nb barrier configuration for reduction of AC losses. The forced cooling coil does not require a helium can which is another advantage for PF coil design.

Fine Nb filament diameter is  $\phi 5 \mu\text{m}$  and there are 3012 filaments in a strand which diameter  $\phi 0.89 \text{ mm}$ . Bronze ratio and copper ratio are 2.5 and 2.0 respectively. Each group of fine filaments is enclosed by Nb barrier to decouple each other. The surface of strand is insulated by inorganic material CuO in order to suppress AC loss heat load. There are 567 strands in stainless steel conduit and supercritical helium flows inside conduit. Void fraction is 40% in the conductor. The detailed specifications of cable in conduit type conductor for PF coil are listed in Table 8.2-2 and the concept of superconductor and the cross section of PF coil are illustrated in Fig. 8.2-4 and Fig. 8.2-5. Operation current of this conductor is 40.0 kA at the field of 10 T and its critical current at 10T, 5 K is 80 kA. Limiting current and stability margin for this conductor are 41.6 kA and 0.8 J/cc respectively.

### 8.2.4 Load Condition

Main loads on the PF coils are extensive and vertical electromagnetic forces induced by the PF coil currents themselves. Fig. 8.2-6 (a) shows extensive magnetic force  $F_R$ , (volumetric integral of radial component) and Fig. 8.2-6 (b) shows vertical magnetic force  $F_z$ , (volumetric integral of vertical component) at four time points in a cyclic operation. Large forces occur at ring coils located in lower half region of the torus. Unbalanced force is loaded on solenoid coils to push up/down vertically as a whole. Because in solenoid coils vertical forces are not symmetric about the equator plane.

### 8.2.5 Support structure

PF coils system must be designed to be cryogenically stable and to sufficiently rigid to support the magnetic force, similarly to TF coil system design.

The PF coils are enclosed in a common cryostat together with TF coils. In this way, there is a simple separation between the warm and cold parts.

The magnetic hoop force are mainly supported by stainless-steel conduits of the winding, because of absence of coil case. The hoop force of No.17 coil produce a maximum hoop stress, about 420 MPa.

To withstand the out-of-plane force (vertical direction force), there are two support systems as follows;

- (1) PF coils in the outboard region

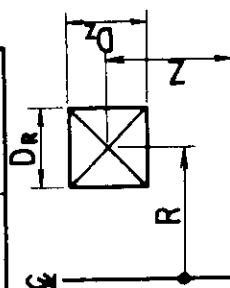
The out-of-plane forces are supported by TF coil structure as shown in Fig. 8.1-9.

- (2) OH coils in the inboard region

The out-of-plane forces are supported by the insulated fan-shaped shelves connected with bucking cylinder and support poles. Each axial side of bucking cylinder and poles are fixed to the TF coil using lower and upper support frames, as shown in Fig. 8.2-7.

Table 8.2-1 PF Coil Parameters

Coil No.	Coil Position		$n_{\text{max}}$ (MAT)	$B_{\text{max}}$ (T)	Conductor Type	No. of Turns	Max. Current (kA)	Max. Current Density (A/mm <sup>2</sup> )	Cross Section		Length of Cooling Path (m)
	R (m)	Z (m)							$D_R$ (mm)	$D_Z$ (mm)	
1	1.18	0.55	9434	9.83	F.F.	264	35.73	24.7	418	912	163
2	1.18	1.65	9434	9.71	F.F.	264	35.73	24.7	418	912	163
3	1.18	2.75	9434	8.89	F.F.	264	35.73	24.7	418	912	163
4	1.18	3.85	4725	5.50	F.F.	216	21.88	15.1	342	912	134
5	1.3	4.95	5025	6.24	F.F.	240	20.94	14.5	380	912	163
6	2.4	5.7	6296	4.86	F.F.	256	24.59	17.0	608	608	241
7	4.4	6.3	5943	2.77	F.F.	256	23.21	16.1	608	608	221
8	7.2	5.8	3730	1.89	F.F.	144	25.90	17.9	456	456	271
9	10.3	4.4	3828	1.37	F.F.	256	14.95	10.4	608	608	259
10	1.18	-0.55	9434	9.58	F.F.	264	35.73	24.7	418	912	163
11	1.18	-1.65	9434	8.60	F.F.	264	35.73	24.7	418	912	163
12	1.18	-2.75	4625	5.89	F.F.	216	21.41	14.8	342	912	134
13	1.18	-3.85	4725	7.86	F.F.	216	21.88	15.1	342	912	134
14	1.3	-4.95	5025	9.60	F.F.	240	20.94	14.5	380	912	163
15	2.4	-5.7	1566	9.47	F.F.	676	23.17	16.0	988	988	196
16	4.4	-6.3	2021	6.38	F.F.	676	29.90	20.7	988	988	180
17	7.2	-5.8	9643	4.83	F.F.	400	24.11	16.7	760	760	226
18	10.3	-4.4	1045	3.36	F.F.	324	32.25	22.3	684	684	291



note : F.F. means Forced Flow Cooling.

Table 8-2-2 Characteristics of the superconductor for PFC

NO	I tem	sign	unit	10 T conductor
1	Superconducting material		—	Nb <sub>3</sub> Sn
2	Strand diameter	D <sub>w</sub>	mm	0.89
3	Filament diameter (Number of filaments)		μm	5 (3012)
4	Bronze ratio		—	2.5
5	Copper ratio		—	2.0
6	NO. of strands	n	—	3 <sup>4</sup> x 7 = 567
7	Superconducting material area of strands	A <sub>sc</sub>	mm <sup>2</sup>	117.6
8	Copper area of strands	A <sub>cu</sub>	mm <sup>2</sup>	235.2
9	Total area of strands	A <sub>co</sub>	mm <sup>2</sup>	352.8
10	Operation current	I <sub>d</sub>	KA	40.0
11	Critical current at 10T, 5K	I <sub>c</sub>	KA	80.0
12	S.S. Conduit outer dimensions	a	mm	36 x 36
13	S.S. Conduit inner dimensions	b	mm	24.2 x 24.2
14	S.S. Conduit area	A <sub>sus</sub>	mm <sup>2</sup>	708
15	Insulation thickness	t <sub>ins</sub>	mm	1.0
16	Helium area	A <sub>He</sub>	mm <sup>2</sup>	235.2
17	Volume fraction of copper in strands	$f = A_{cu}/A_{co}$	—	0.667
18	Volume fraction of metal in the cable space	$f_{co} = \frac{A_{co}}{A_{co} + A_{He}}$	—	0.6
19	Cable space area $A = A_{co} + A_{He}$	A		588
20	Void fraction $f_{He} = 1 - f_{co}$	f <sub>He</sub>		0.4
21	Limiting current	I <sub>B</sub>	KA	41.6
22	Stability margin	ΔH	J/cc	0.8
23	Minimum winding radius	R	mm	1000
24	Maximum winding strain	ε	%	1.8



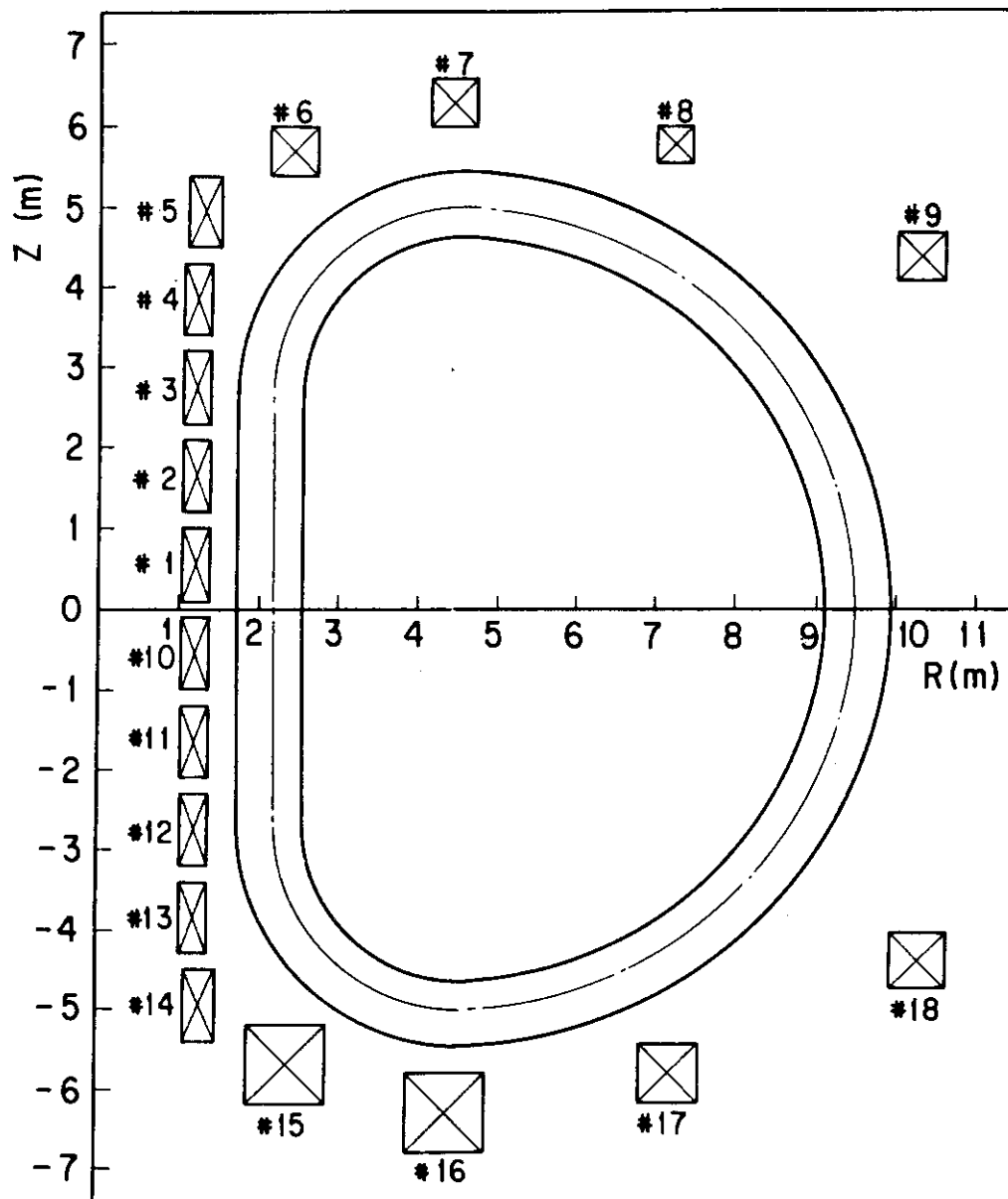


Fig. 8-2-1 Location of PF coils

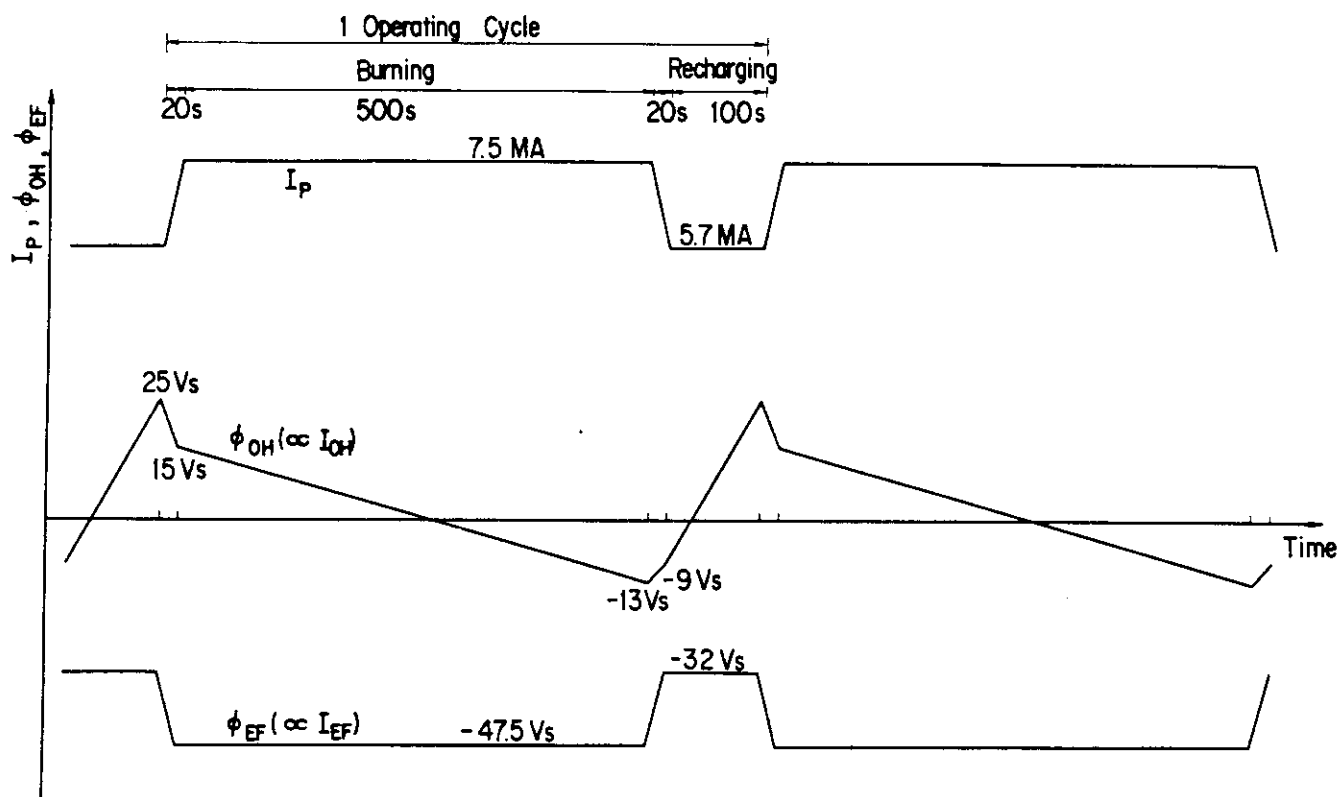


Fig. 8-2-2 Operating Pattern of PF Coils

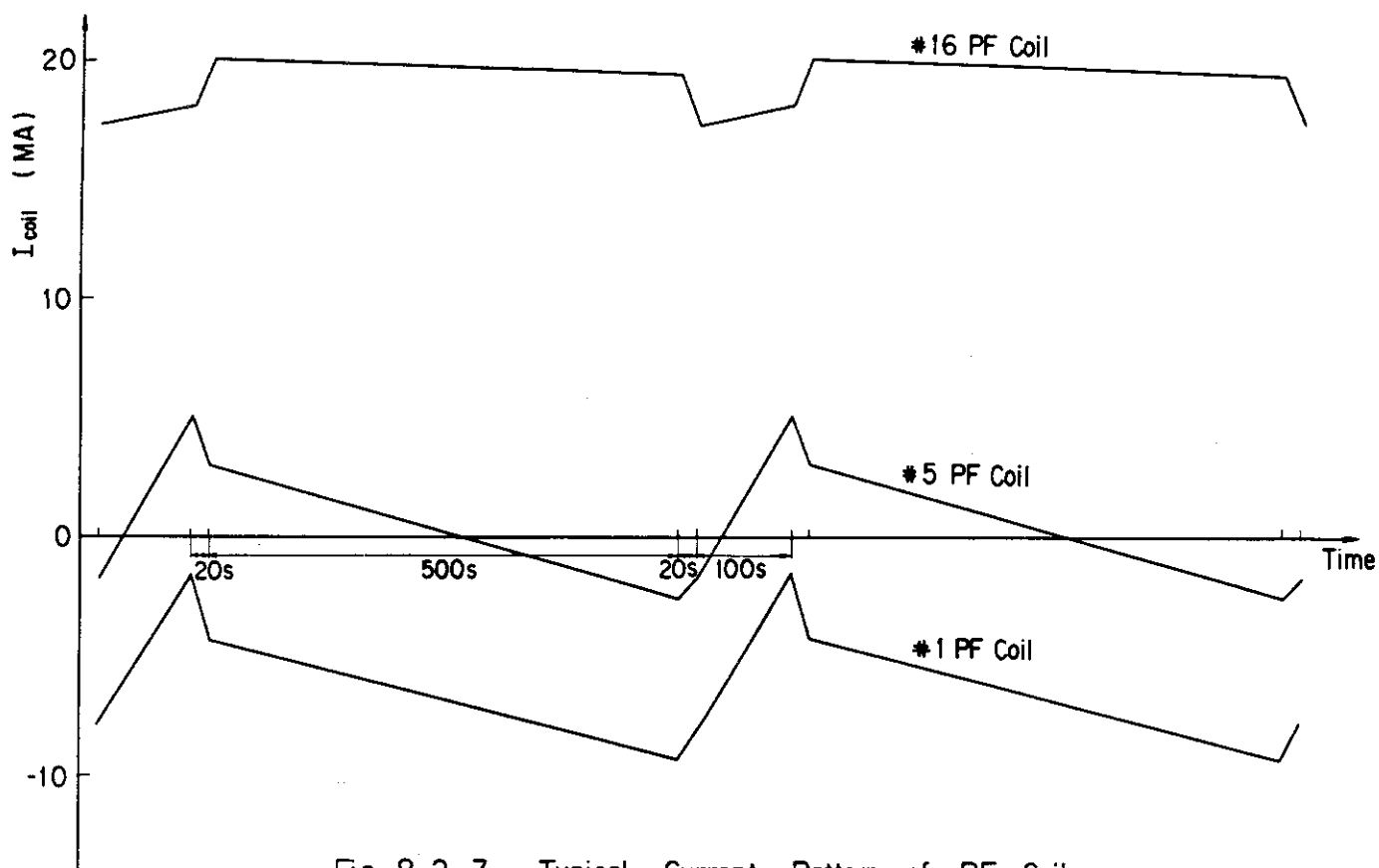


Fig. 8-2-3 Typical Current Pattern of PF Coils

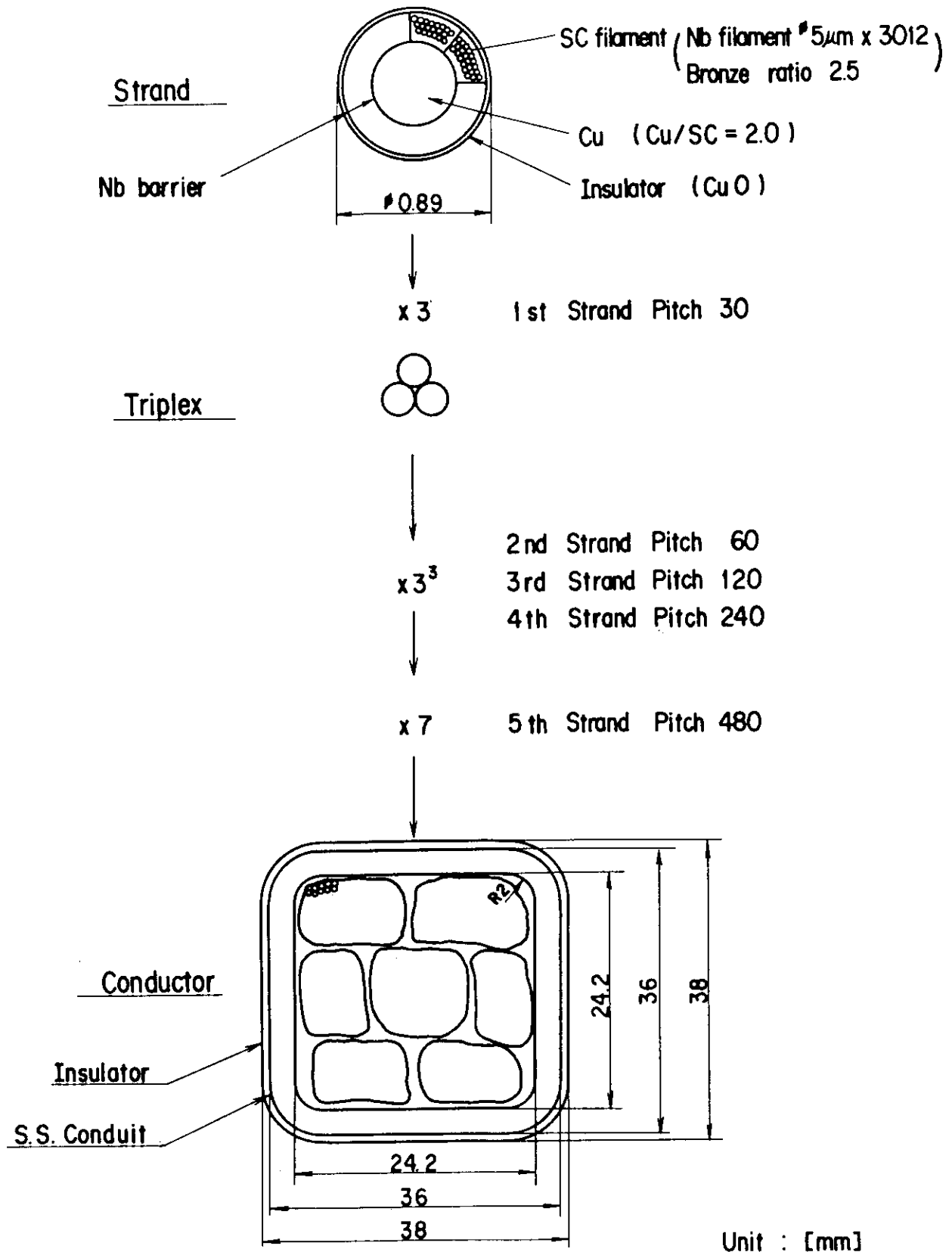


Fig.8.2-4 SC Conductor of PF coil for INTOR

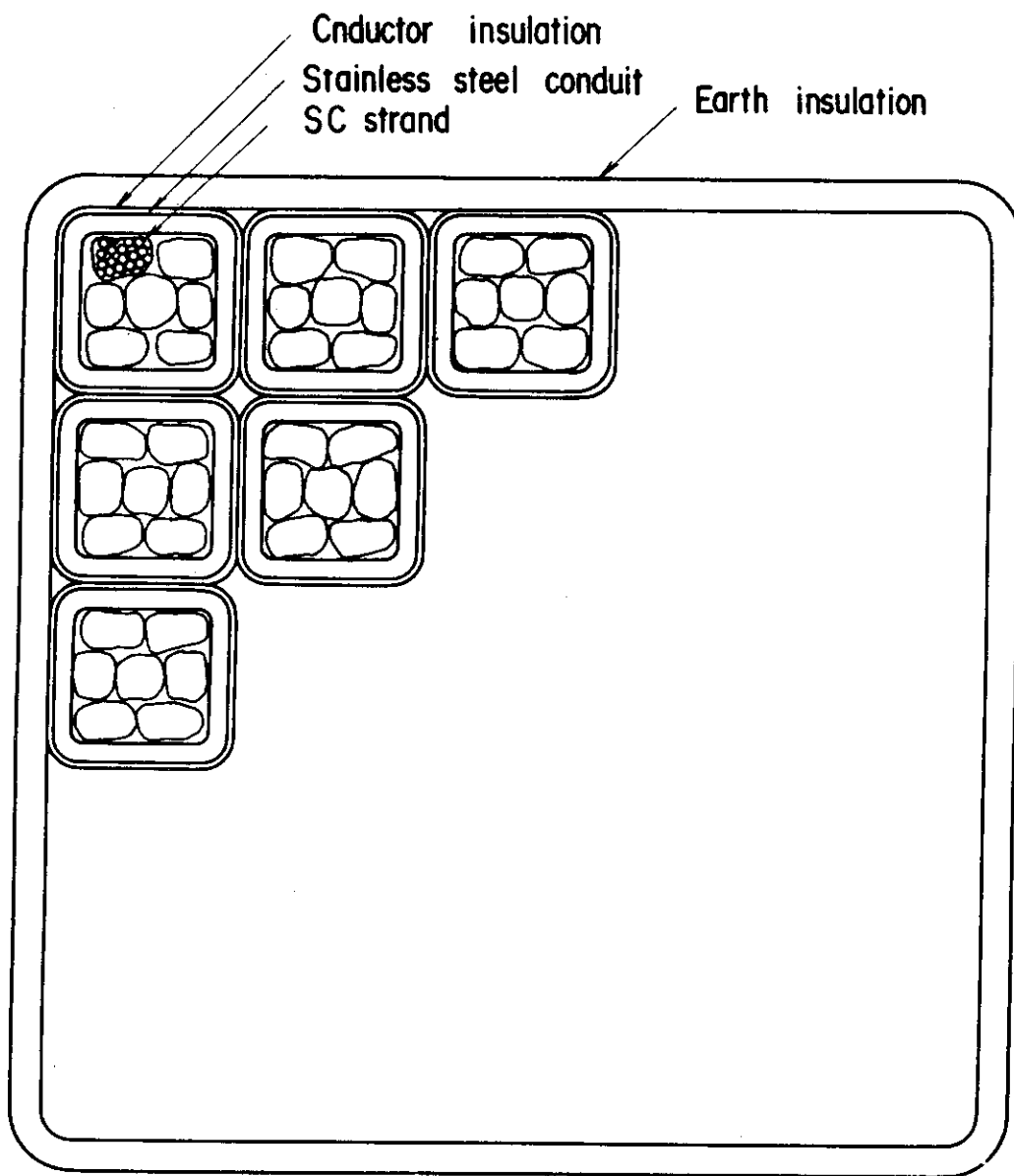


Fig. 8.2-5 Cross section of PF coil for INTOR

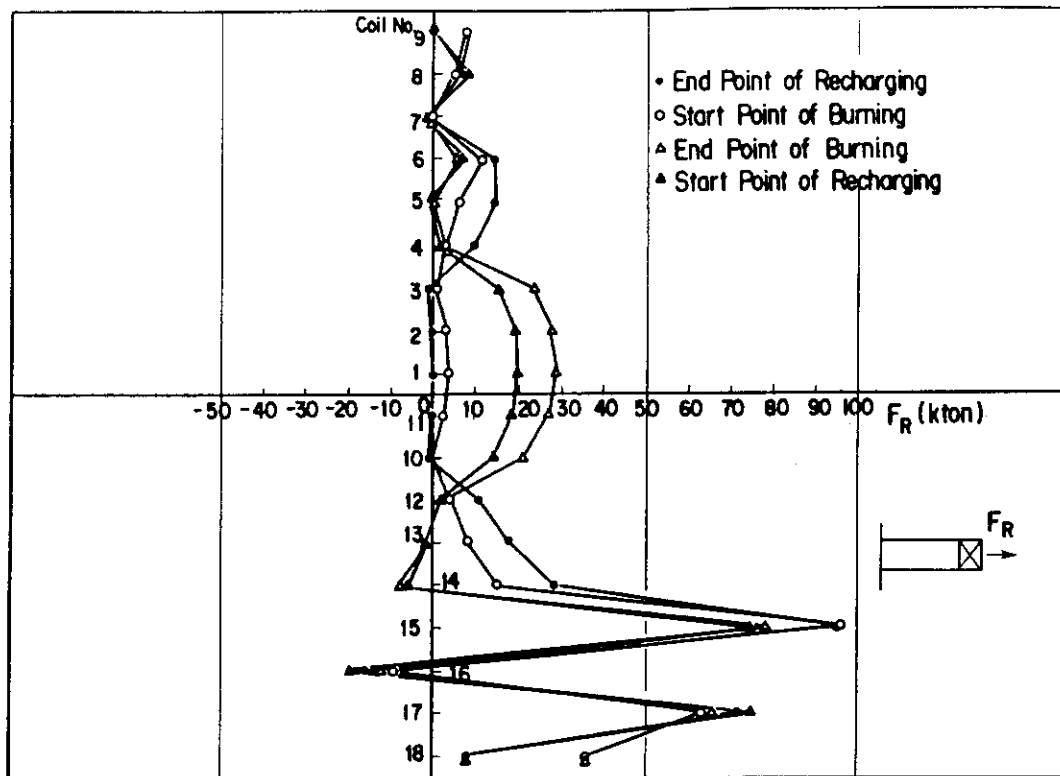
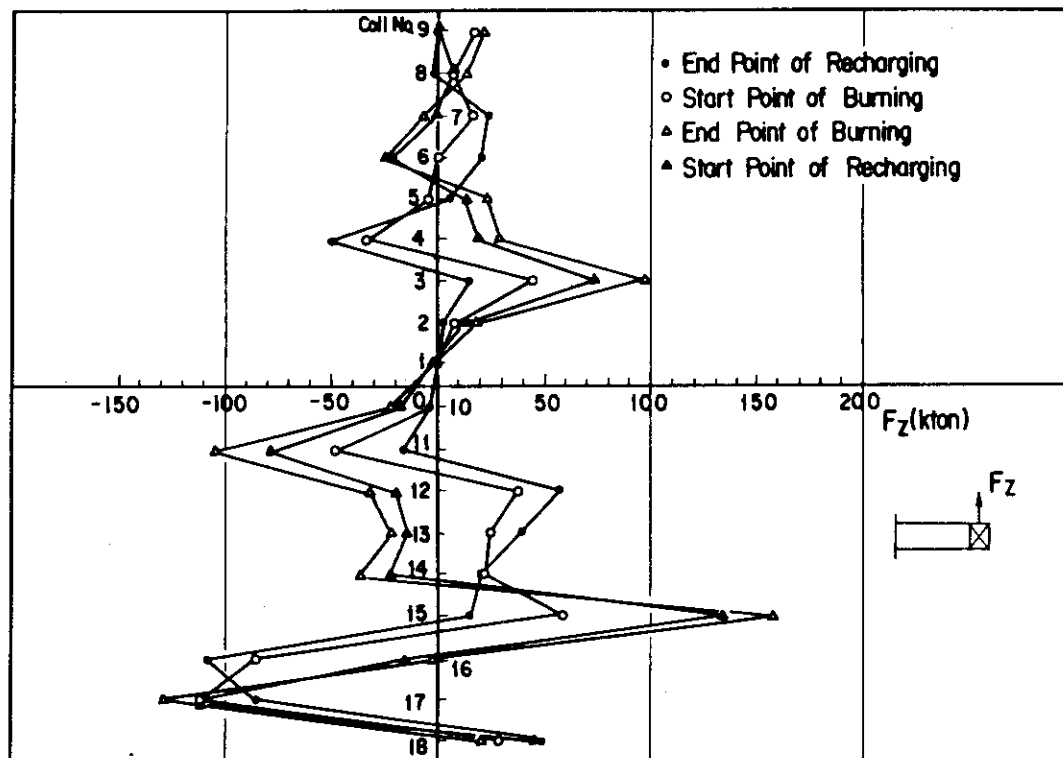
(a)  $F_R$  Component(b)  $F_Z$  Component

Fig. 8-2-6 Magnetic Forces of PF Coils

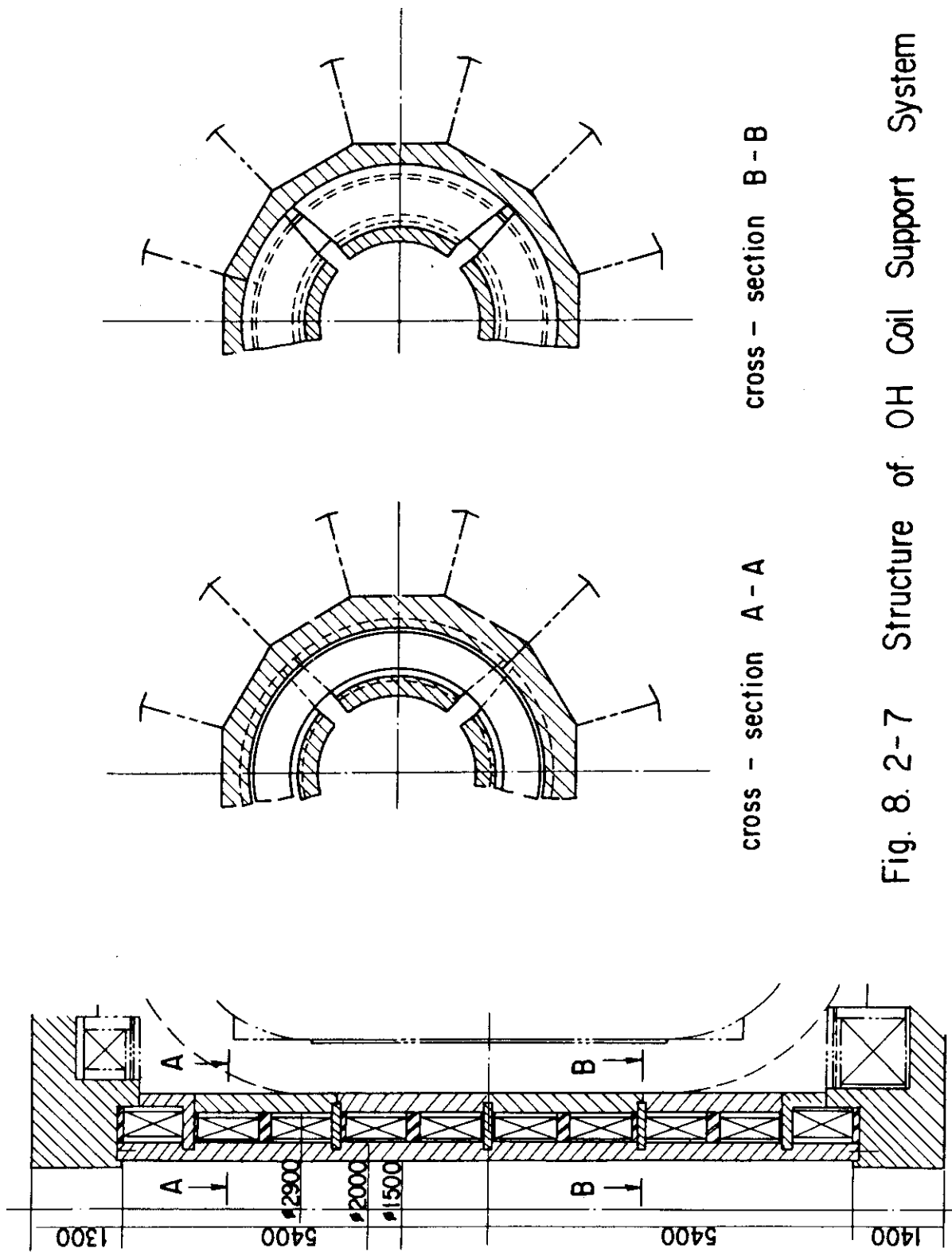


Fig. 8. 2-7 Structure of OH Coil Support System

### 8.3 Active position control coil

#### 8.3.1 Concept

Impacts of installation of the active position control coils depending on the coil location were discussed conceptually at the last workshop<sup>1)</sup>.

On the design of the reactor configuration concerning the active control coil, the major problem is the selection of the coil location which can be inside or outside of the TF coils. Following two cases were studied here.

Case 1      Outside TF coil

Case 2      Within shield (inside TF coil bore)

In case 1, the coil will be constructed with superconducting conductor, on the other hand in case 2, it must be copper coil with direct cooling by water.

The required Ampere-turn of the active coil and the current pattern are significantly affected by the characteristics of the passive shell which is installed in the blanket. And these specifications should be determined from the electromagnetic transient analysis of the plasma. In this consideration, the conceptual specifications, which are shown in Table 8.3-1, are assumed.

The value of the Ampere-turn in the case 1 is about three times larger than that of the previous estimation<sup>1)</sup>, because of taking into consideration of the additional shielding effect by the superconducting PF coils.

#### reference

- 1) INTOR Workshop Phase 2 Part 2 Session X  
Japanese Contribution to Disciplinary Group G Task 4

### 8.3.2 Outside TF Coil Option

In case of the outside TF coil option, the active position control coils (simply called active coils) should be superconducting coils in order to reduce heat flux coming into TF/PF coils system and to match the thermal contraction of TF/PF coils and the active coils. The possible location of active coils is the following two positions, case 1-1 and case 1-2 shown in Fig. 8.3-1. Based on the conceptual specifications in Table 8.3-1, the parameters of the active coils shown in Table 8.3-2 are determined.

The active coils have several problems; (1) AC loss greater than the other coils, (2) High voltage induced in the neighbouring PF coils, (3) AC loss in the TF coil support structure. AC loss of the active coils is 2 mW/cc or 25 W/coil, which are about ten times greater than those of a TF coil. Rapid alternation of the active coil current induces electromotive force in the neighbouring PF coils. In case 1-1, it is estimated to be about 29 kV and in case 1-2 48 kV, and these values make the design of the PF coil difficult. Another AC loss problem occurs at the TF coil supporting structures. The additional AC loss by the active coils is about 20 kW. It is five times greater than the total AC losses in normal operation without position control.

### 8.3.3 Inside TF coil option

In case of internal location of the TF coils, the design of the active control coil will depend on whether the coil will be set on the removable component or on the semi-permanent component. On the removable component, partial coil will be adopted. On the other hand, ring coil will be adopted on the semi-permanent component.

Fig. 8.3-2 shows the schematic view of the active control ring coil within the semi-permanent shield. In this case, it is necessary to connect the coil conductors and cooling tubes after the installation of the coil on the semi-permanent shield. And it is more difficult to maintain the active control ring coil after DT operation than in the case of partial coil. However, there will be the possibility that some maintenance equipments will be able to approach to the coil through the access door by the development of robotics. From a viewpoint of vacuum technology, such as sealing, a canned type coil is preferable, but it is undesirable for space reduction. The coil shown in Fig. 8.3-2 is an example of bare type coils.

Fig. 8.3-3 shows a typical cross section of the active control coil; a) and b) are conductor and coil assembly respectively. The conductor material is silver bearing oxygen free copper. Maximum current density reaches about 10 A/mm<sup>2</sup> and the average joule loss of the conductor is about 0.5 W/cm<sup>2</sup>. This value is about ten times higher than the value of nuclear heating. The cooling pipe is soldered to the conductor to remove these heat loss with water.

Inorganic material such as ceramics will be applied for turn-to-turn and ground insulation. Multi turn conductors (four turns in this case in Fig. 8.3-3) and these insulator will be combined with coil binder. After that, subassembled coil will be installed in the groove which is prepared on the plasma side surface of the semi permanent shield.

In order to consider the mechanical property of this coil, the hoop stress of the conductor is estimated. The coil current of 50 kA generates about 5 ton/m of mechanical load in 1 T of poloidal magnetic field. This load generates about 5 kg/mm<sup>2</sup> of average hoop stress on each conductor.



This estimation implies some difficulty on final design, because the conductor will be softened by connecting process such as welding during the installation of the coil.

Table 8.3-1 Conceptual specifications of active position control coil

Position Items	Case 1 Outside TF coil	Case 2 Inside TF coil bore
Recommendation to coil position	Close to the plasma & far from other PF coils	Within shield
Ampere-Turn/coil	250 kAT	50 kAT
Voltage / turn	200 V/T	100 V/T
Wave form	AC ~ 10 Hz duty ~ 1/5	AC ~ 10 Hz duty ~ 1/5
Radiation condition	$< 10^8$ rad	$\sim 10^9$ rad
Nuclear heating	$\sim 10^{-6}$ W/cc	$\sim 10^{-2}$ W/cc

Table 8.3-2 Parameters of the active position control coil in case of outside TF coil option

Items	Case 1 - 1	Case 1 - 2
Location	R = 10.0 m Z = $\pm 5.5$ m (Near #9, #18 PF Coils)	R = 8.0 m Z = $\pm 5.4$ m (Near #8, #17 PF Coils)
Dimensions of Cross Section	114 mm x 114 mm	
Maximum Coil Current	27.8 kA	
No. of Turns	9	
Winding Current Density	19.2 A/mm <sup>2</sup>	
Applied Voltage	1.8 kV	
Maximum Field	0.76 T + 2.1 T (Back ground)	
Rate of Field	$\sim 30$ T/s	
Cooling	SHE Forced - flow	
ICCS Superconductor	Superconducting Material NbTi Basic Strand $\phi 0.1$ mm Filament Diameter $\phi 0.1 \mu\text{m}$ Conduit Dimension 36mm square 2mm Thickness Void Ratio $\sim 40\%$	

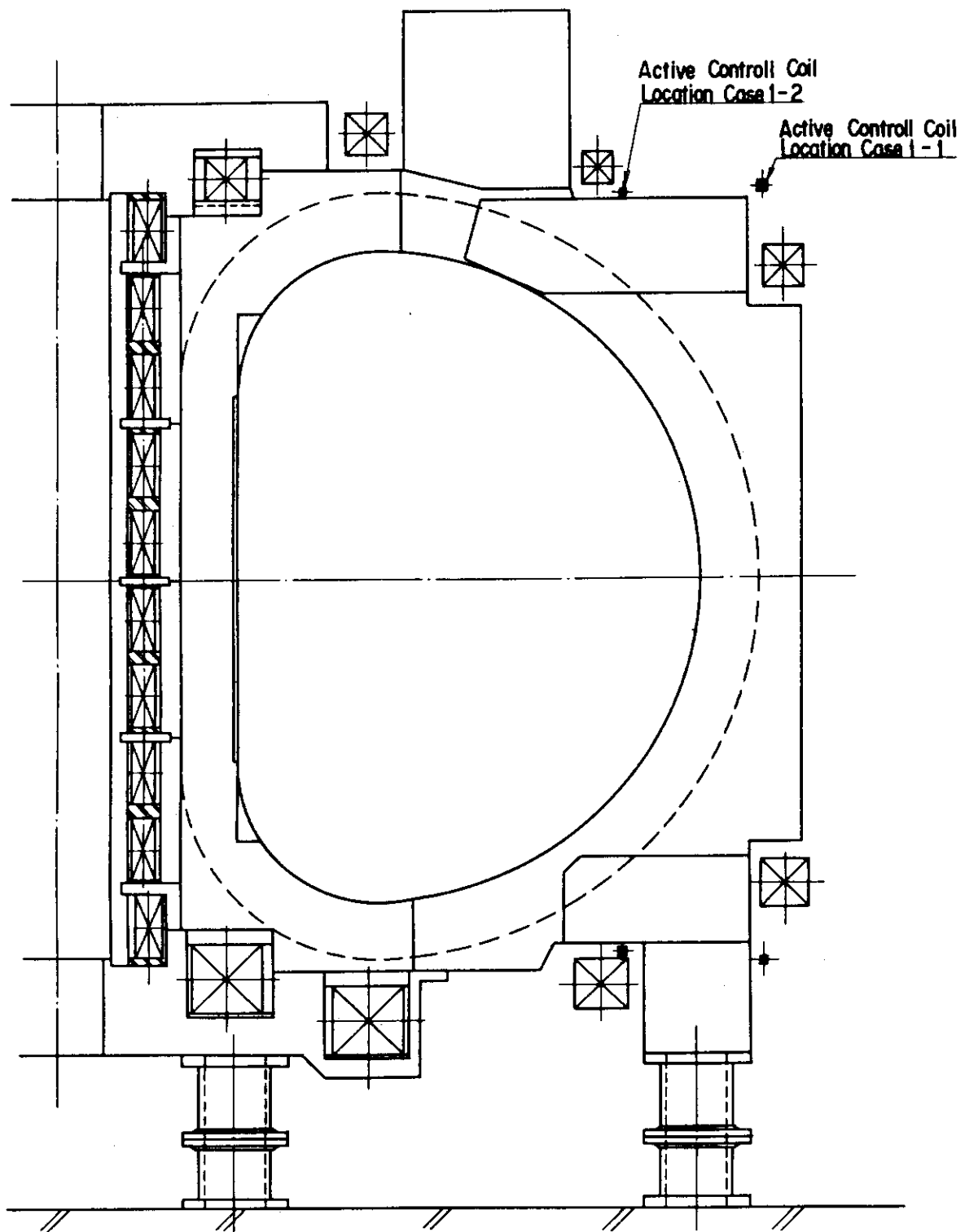


Fig. 8.3-1 Active Position Control Coil Location ( Outside TF Coil Option )

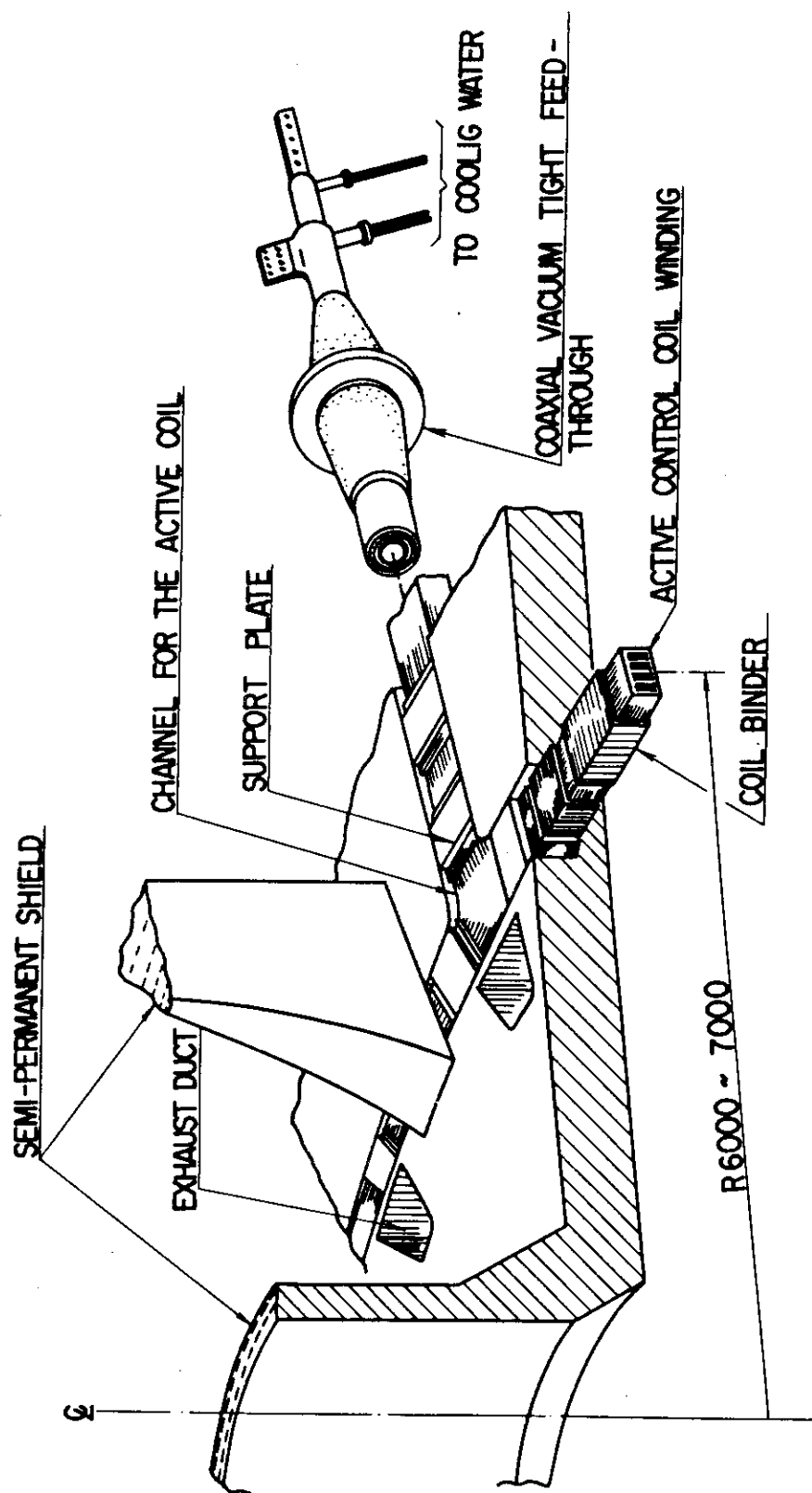


Fig.8.3-2 SCHEMATIC VIEW OF THE ACTIVE CONTROL RING COIL  
WITHIN THE SEMIPERMANENT SHIELD

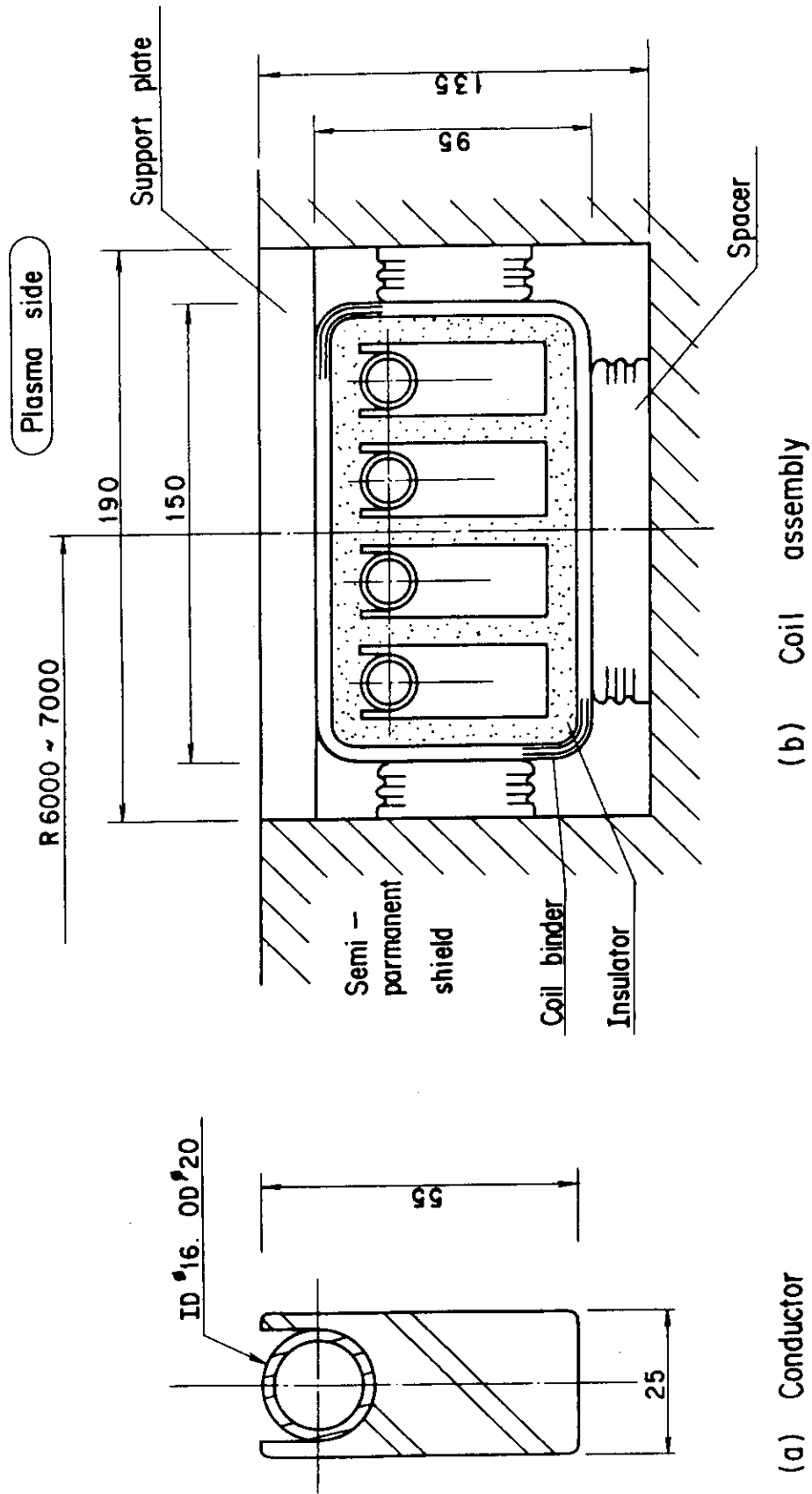


Fig.8-3-3 Cross - sectional view of active control coil

## 8.4 Cryogenic system

### 8.4.1 AC loss

The cycle averaged AC losses of INTOR coil system are summarized in Table 8.4-1. The loss of the coil supports is the largest,  $Q = 2.77$  kW. By using the cable in conduit type conductor in which strands are insulated each other, the AC loss of the coil winding is reduced remarkably, 15 W for TF coils winding and 120 W for PF coils winding respectively. AC loss formulas are listed in table 8.4-2. In comparison with the pulse operation mode, it is clear that Quasi-steady state operation mode reduced the AC loss of coil system remarkably.

### 8.4.2 Total loss

The total heat load at 4 K on the coils and structure is calculated to be about 20.7 kW as shown in Table 8.4-3. There are some additional heat load for cryogenic system as follows;

- (1) Heat load of current leads 400 l/h at 4.2 K
- (2) Heat load of cryogenic pumps 6 kW
- (3) Heat load of transfer lines 3 kW

where, additional heat loads are estimated from the Japanese FER design calculation.

Therefore, total heat load of the coil system will be about 30 kW at 4.5 K and 4000 l/h at 4.2 K.

### 8.4.3 Requirement of cryogenic system

The choice of forced-flow superconductor for the TF and PF coils requires the large cryogenic pump capacity to reduce a power loss. The requirements of pump unit are shown in Table 8.4-4.

The total heat loads of 30 kW at 4.5 K plus 400 l/h liq. He, require the large refrigeration and liquefaction capacity of 50 kW at 4.5 K or 15000 l/h at 4.2 K for the cryogenic system as shown in Table 8.4-4. The system will have three units, each two unit will have a capacity of 20 kW at 4.5 K or 6000 l/hr at 4.2 K for the main system, the other unit will have that of 10 kW at 4.5 K or 3000 l/h at 4.2 K for the stand-by operation system during no current charge. This system also has a sufficient capacity of cooling down the coils and structures within a month.

Table 8.4-1 AC loss of INTOR coil system

Parts		AC loss (average)
TF coils	Winding	15 [W]
	Helium vessel	240 [W]
PF coils	Winding	120 [W] *)
Coil supports	Bucking cylinder	1160 [W] *)
	Shear pannel, etc.	2770 [W] *)
total		4305 [W]

\*) estimation value

Table 84-2 AC loss formulas

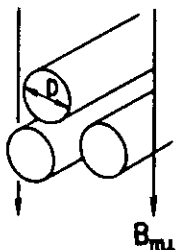
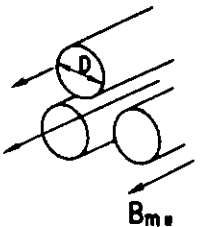
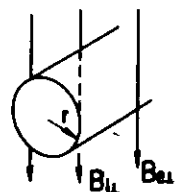
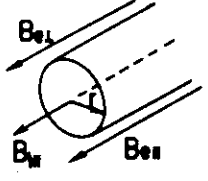
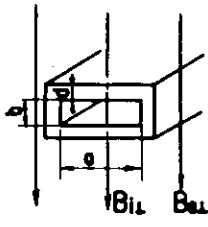
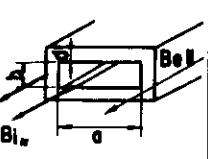
AC loss	No	Models	Formulas	Notes
Hysteresis loss	1		$Q_L = \frac{B_m^2}{2\mu_0} \cdot 2 \cdot \left( \frac{2\beta}{3} - \frac{\beta^2}{3} \right) \cdot A_{sc} \quad (J/cycle \cdot m)$ $[\beta \leq 1]$ $Q_L = \frac{B_m^2}{2\mu_0} \cdot 2 \cdot \left( \frac{2}{3\beta} - \frac{1}{3\beta^2} \right) \cdot A_{sc} \quad (J/cycle \cdot m)$ $[\beta \geq 1]$ $\beta_L = \frac{\pi B_m}{2\mu_0 J_c D}$	$A_{sc}$ : Area of S.C. material ( $m^2$ ) $\left[ A_{sc} = N \cdot \pi D^2 / 4 \right]$ $N$ : No. of filaments $J_c$ : Critical current density ( $A/m^2$ ) $D$ : Filament diameter (m) $B_m$ : Oscillating field amplitude (T)
	2		$Q_L = \frac{B_m^2}{2\mu_0} \cdot \left( \frac{2\beta}{3} - \frac{\beta^2}{3} \right) \cdot A_{sc} \quad (J/cycle \cdot m)$ $[\beta \leq 1]$ $Q_L = \frac{B_m^2}{2\mu_0} \cdot \left( \frac{2}{3\beta} - \frac{1}{3\beta^2} \right) \cdot A_{sc} \quad (J/cycle \cdot m)$ $[\beta \geq 1]$ $\beta_L = \frac{B_m}{\mu_0 J_c D}$	
Eddy current loss	1		$P_{eL} = 16 \cdot \sum \frac{\tau_n}{kn^2} \cdot \frac{B_m^2}{2\mu_0} \cdot A_c \quad (W/m)$ $\tau_n = \frac{\mu_0 r^2}{\rho kn^2} \quad (sec)$	$r$ : Conductor radius (m) $A_c = \pi r^2$ ( $m^2$ ) $J_0(k_n) = 0$ : Bessel function $k_1 = 2.405$ $k_4 = 11.792$ $k_2 = 5.520$ $k_5 = 14.931$ $k_3 = 8.654$ $k_6 = 18.071$
	2		$P_{eH} = 8 \cdot \sum \frac{\tau_n}{kn^2} \cdot \frac{B_m^2}{2\mu_0} \cdot A_c \quad (W/m)$ $\tau_n = \frac{\mu_0 r^2}{\rho kn^2} \quad (sec)$	
	3		$P_{eL} = \frac{a+2b}{4(a+b)} \cdot \frac{a}{d} \cdot \tau_L \cdot \frac{B_m^2}{2\mu_0} \cdot A_c \quad (W/m)$ $\tau_L = \frac{\mu_0 a d}{4\rho} \quad (sec)$	$d$ : Conductor width (m) $A = 2d(a+b)$ ( $m^2$ )
	4		$P_{eH} = \frac{ab}{d(a+b)} \cdot \tau_H \cdot \frac{B_m^2}{2\mu_0} \cdot A_c \quad (W/m)$ $\left[ d \ll a, b \right]$ $\tau_H = \frac{\mu_0 d a b}{2\rho(a+b)} \quad (sec)$	

Table 8-4-2 AC loss formuluss (cont.)

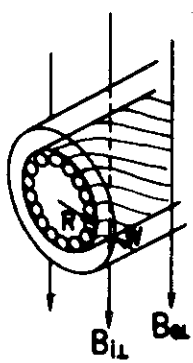
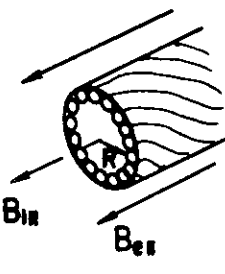
AC loss	No	Models	Formules	Note
Filament Coupling loss	1		<ul style="list-style-type: none"> <li>• <math>P_{c1} = 4 \cdot \tau_L \cdot \frac{B_{LH}^2}{2\mu_0} \cdot A_{scB}</math> (W/m)</li> <li>• <math>\tau_L = \frac{\mu_0}{2\rho_{eff}} \left( \frac{l_p}{2\pi} \right)^2</math> (sec)</li> <li>• <math>\frac{1}{\rho_{eff}} = \frac{1}{\rho_L} + \frac{W}{R} \cdot \frac{1}{\rho}</math> (1/Ωm)</li> <li>• <math>\rho_L = \frac{1+\lambda}{1-\lambda} \rho</math></li> </ul>	<p><math>A_{sc}</math>: Cross section of S.C. area (m<sup>2</sup>)  <math>\left[ A_{sc} = \pi R^2 \right]</math>  <math>l_p</math>: Twist pitch (m)  <math>R</math>: Radius of S.C. area (m)  <math>W</math>: Width of surrounding conductor (m)  <math>\rho_{eff}</math>: Effective resistivity (Ωm)  <math>\rho_L</math>: Perpendicular resistivity (Ωm)  <math>\lambda</math>: Proportion of S.C. material</p>
	2		<ul style="list-style-type: none"> <li>• <math>P_{c2} = \frac{R}{D} \cdot \tau_H \cdot \frac{B_{LH}^2}{2\mu_0} \cdot A_{scB}</math> (W/m)</li> <li>• <math>\tau_H = \frac{\mu \cdot R D}{2\rho_H} \cdot \left( \frac{2\pi R}{l_p} \right)^2</math> (sec)</li> <li>• <math>\rho_H \sim \rho_L</math></li> <li>• <math>\left( P_{c2} = \frac{1}{\rho_H} \left( \frac{\pi}{l_p} R^2 \right)^2 B f^2 \right)</math></li> </ul>	



Table 8-4-3 Heat Load on the Coil System

Item	AC loss Average (kW)	Joint loss (kW)	Radiation and Conduction (kW)	Nuclear heating Average (kW)	Total heat load Average (kW)
TF Coil	0.26	0.6	1.0	11.7	13.56
PF Coil	0.12	0.7	0.4	—	1.22
Support Structure	3.93	—	2.0	—	5.93
Total	4.31	1.3	3.4	11.7	20.71

Table. 8-4-4 Main parameters of Cryogenic System

He Ref./ Liq. System

Main System Capacity 40 kW at 4.5 K or 12000 l/h

Sub System Capacity 10 kW at 4.5 K or 3000 l/h

Cryogenic Pump (working at 4.5 K)

Supply Pressure 10 atm

Return Pressure 9 atm

Flow Rate 1000 g/sec (One Unit)

## 9 Impurity control

### 9.1 Introduction

The INTOR impurity control system studies have focussed on the development of an impurity control system which would be able to provide adequate heat removal and He pumping for INTOR while satisfying the requirements for 1) minimum plasma contamination by impurities, 2) reasonable component lifetime ( $1 \geq$  year), and 3) minimum size and cost. The major systems examined were poloidal divertors and pumped limiters. The poloidal divertor was chosen as the reference option since it offered the possibility of low sputtering rates due to the formation of a cool, dense plasma near the collector plates. Estimates of the sputtering rates associated with pumped limiters indicated that they would be too high for a reasonable system. Development of an engineering design concept was done for the poloidal divertor.

### 9.2 Impurity control physics

The INTOR impurity and particle control system must be able both to absorb the 124 MW of alpha particle heating power and to remove the alpha particles at the rate they are produced. This must be accomplished without contamination of the plasma by impurities and without a large erosion rate of the first wall components and with reasonable pumping requirement. The major candidate systems studied were a poloidal divertor and a pumped limiter. The studies have consisted of an assessment of the experimental data base for impurity control systems based on current experiments, the use of sophisticated computational models to extrapolate to operating parameters and performance for INTOR. The major systems studies have been the poloidal divertor.

The major impurity control problem is likely to be sputtering of collector plate materials by energetic plasma ions and charge exchange neutrals. The energy of the plasma ions that strike the collector plate is largely determined by the sheath potential which is several times (2-4) the electron temperature of the plasma near the collector plate. Based on extrapolations from experiments and the use of computational and analytic models, it is expected that the temperature at the plasma edge of INTOR should be 100-200 eV. The edge density should be  $1-3 \times 10^{19} \text{ m}^{-3}$ . Thus the sheath potential and ion energy for the plasma that is incident on a limiter should be in the 300-800 eV range which will lead to large sputtering rates for the limiter.

If the temperature of the plasma near the collector plate can be reduced to 20-30 eV, then materials can be found which have sputtering thresholds above the incident ion energy. A promising way of producing a low temperature plasma is to increase the recycling rate. Both modelling calculations and experiments on Doublet III indicate that this can be accomplished by the use of a suitably designed poloidal divertor. A cool, dense plasma ( $n_e > 10^{20} \text{ m}^{-3}$ ,  $T_e < 10 \text{ eV}$ ) can be produced near the collector plate by intense localized recycling of the plasma and neutral gas. The low temperature of the diverted plasma minimizes the erosion, and the high density of the plasma provides a high neutral density which eases the helium pumping speed requirements.

### 9.3 Discussion of materials and heat removal issues

The divertor is composed of a protective material, heat sink, and supporting structure. The protective material is tungsten with 1 mm or 3 mm thickness. Copper and copper alloy is considered for the heat sink material. The tungsten is brazed or plasma-sprayed to the heat sink. These multi-layer structures have cooling channels in the copper heat sink, and are cooled by water.

To keep the plate temperature low, the divertor plate is preferred to be cooled by low temperature water with high velocity. Heat transfer coefficient of water in the divertor cooling channels is shown in Fig. 9.3-1. The coefficient is  $3.2 \times 10^4$  W/m<sup>2</sup>K for the velocity of 7 m/s.

The burn time is increased to 1000 s in the design modification from 200 s in the reference design. The steady temperature is established at the end of the burn phase in the reference operation. Therefore the temperature distribution at the end of the burn phase for the design modification is assumed to be the same as that for the reference operation.

Figures 9.3-2 and 9.3-3 show the experimental apparatus and results for thermal cycling test of W-Cu duplex conducted in JAERI. The surface heat flux was estimated to be 0.72 MW/m<sup>2</sup>. The junction (W-Cu interface) temperature attains nearly a steady state value at 1 min after initiation of heating.

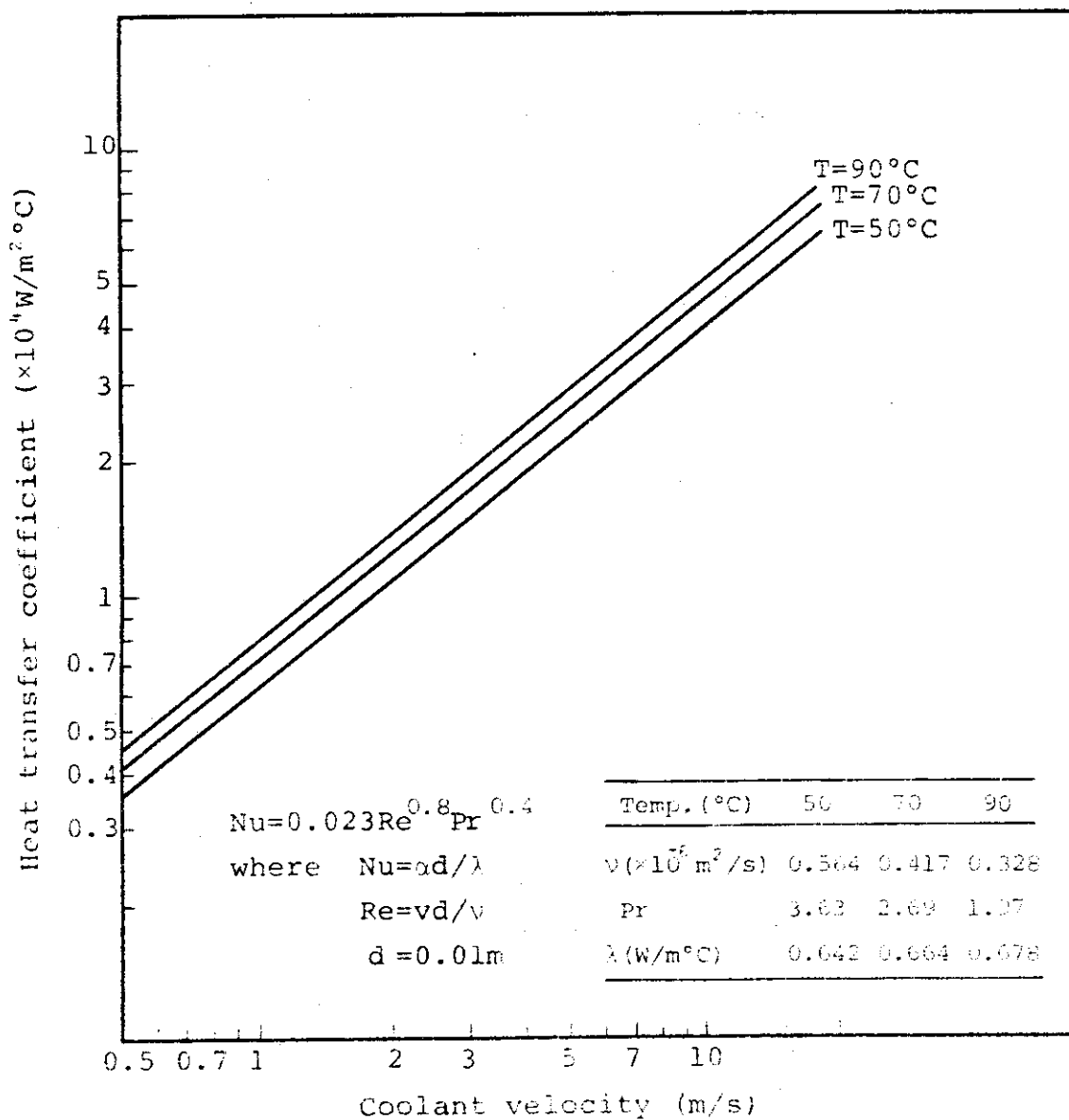


Fig. 9.3-1 Heat transfer coefficient of diverter cooling channel

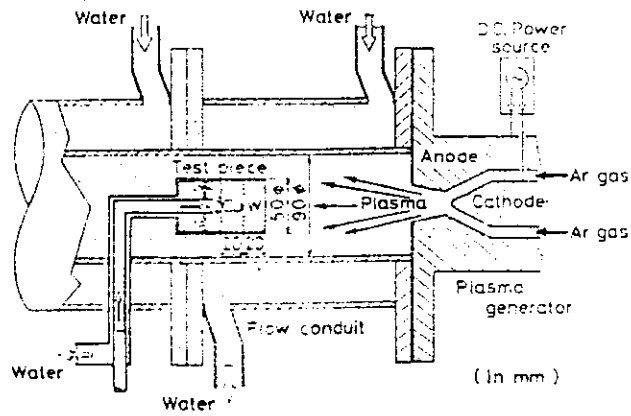


Fig. 9.3-2 Experimental apparatus

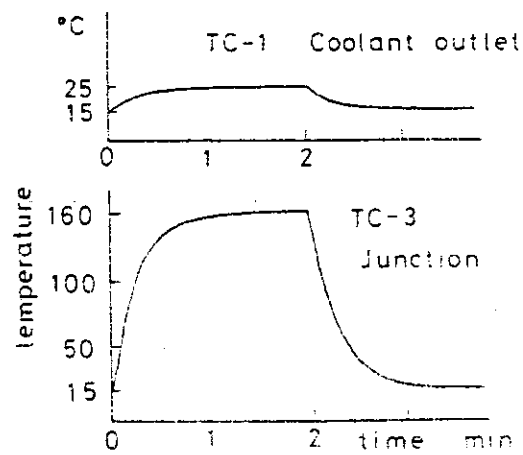


Fig. 9.3-3 Temperature traces

#### 9.4 Divertor physics

Various concepts on the impurity control have been widely assessed since the Zero Phase Workshop. Among them, the divertor concepts were evaluated to have great potential, especially the poloidal divertor was assessed to be the most promising for the INTOR impurity control. During those years, many new tokamaks went into operation and provided new useful informations, and understandings on impurity control has made great progresses. In a divertor concept, a quite new operating regime. The high-density and low-temperature divertor plasmas were observed in Doublet III experiments with a single-null poloidal configuration for the first time. Their parameters are in a quite new regime different from the past divertor plasmas, and they have several interesting features beneficial to impurity control by the divertor concept.

- (1) The density in the divertor region increases nonlinearly with a density increase of the main plasma. The density near the collector plate increases to the order of  $10^{20} \text{ m}^{-3}$ .
- (2) The high-density near the collector plate reduces the divertor plasma temperature there below 10eV.
- (3) Radiation losses from the divertor region also increase with changes in the density and temperature. They significantly reduce the input power to the collector plate.
- (3) Along with the changes in the divertor plasma parameters, neutral hydrogen gas pressures were also observed to be remarkably enhanced.
- (4) Changing magnetic configurations from limiter to divertor operation, considerable impurity reduction in the main plasmas were attained by the divertor operation. Especially, the reduction in metal impurities is observed to be remarkable.
- (5) Even in NBI heated discharges, similar phenomena to Joule heating were obtained.
- (6) The high-density divertor operation is compatible with the so-called H-mode discharges with good confinement time.

The high-density, low-temperature divertor plasma is caused by highly recycling particles in the divertor chamber, and the high recycling divertor concept have great advantages for impurity control. The low plasma temperature near the collector plate could results in significant reduction in an amount of released impurity from it. The high density plasma, moreover, could be effective in avoiding penetration of released impurities from the plate. The strong radiation in the divertor chamber could also certainly ease difficulties in the heat removal of the collector plate. The pumping requirement for helium ash could also be reduced by the neutral gas compression around the divertor plasma. Based on those favorable experimental results, it may be concluded that the high recycling divertor concept has some more credible features for impurity control than the conventional divertor and other impurity control concepts at present.

In order to discuss the possibility of the cold and dense divertor operation, a two dimensional program for the divertor plasma and neutral particles has been developed. The divertor plasma is strongly influenced by the neutral particles emitted from the divertor plate and traversing the divertor chamber through ionization and charge exchange reactions. Therefore, a self-consistent modelling is necessary for the description of the divertor plasma and neutral particles. The divertor plasma is described by the fluid equations and the neutral particle transport in the divertor chamber is solved

by the Monte Carlo simulation. The interactions between the divertor plasma and neutral particles are self-consistently solved by an iterative procedure.

The numerical simulation based on the above model was compared with the Doublet III experiments under 1 MW NBI heating. The main features of the D-III experiments were successfully reproduced, such as (a) formation of high density and low temperature plasmas, (b) strong radiative cooling of the divertor plasmas, and (c) nonlinear dependence of the divertor plasma density on the main plasma density.

The numerical simulation also gives the dual equilibrium solutions of the divertor plasma in the limited range of the ion flux entering the divertor. The origin of the dual solutions can be explained by a simplified modelling of the neutral particle recycling in the divertor plasma.

The divertor operating condition for INTOR was investigated based on the two dimensional program, solving consistently the divertor plasma and neutral particles. Simple analytic model is also developed to clarify the dual structure of the solution of the numerical code. The numerical results strongly suggest that the cold plasma layer less than 10 eV could be produced in front of the divertor plate, provided that the particle confinement time of the main plasma is shorter than 1.7 s. The evaluation of the backflow fraction of the neutrals indicated the low effective pumping speed of about  $2 \times 10^4$  l/s to keep the 5% concentration of the helium ash in the main plasma. When the real divertor geometry, e.g. open divertor shape, is taken into account, however, the required pumping speed should be increased up to  $10^5$  l/s from the parametric studies on divertor geometry. These low temperature and the required pumping speed conditions indicate that the divertor throat length of about 50 cm and the void width 5-25 cm between the first wall and the divertor plasma edge could be enough. The sputtering erosion of the divertor plate and the other inside wall of the divertor seems not to be a serious problem, since the electron temperature could be reduced to less than 10 eV near the divertor plate.

The dependence of formation of cold and dense divertor plasmas on divertor geometry is studied with the simple analytic model to reduce the size of the divertor chamber. In the open geometry, cold and dense divertor plasmas are observed to be produced in a wide range of the incoming ion flux to the divertor. Temperatures at the plate become below 10 eV. The key problem of the open geometry is that the range of the incoming flux, where triple equilibrium states are observed, becomes wide, e.g. probability in production of low-density and high-temperature divertor plasmas becomes high, which must be avoided in an operation. If the width of the void is retained narrow, it can be predicted that the short divertor of 50 cm length could produce cold and dense plasmas at the divertor plate. Even if the width of the gap is not so narrow, the low temperature plasmas at the plate can be obtained with some appropriate control measures, such as gas fuelling into the divertor chamber.

## 9.5 Divertor design

### 1. Operating conditions

Operation schedule for the design modification is given in Table 9.5-1. The burn time is assumed to increase from 200s to 1000s, and the integral wall loading is taken to decrease from 6 MW-y/m<sup>2</sup> to 3 MW-y/m<sup>2</sup>. The resultant annual number of shots is  $1.3 \times 10^4$  for Stage III.

Engineering specifications to be used for the divertor design are given in Table 9.5-2. These conditions are unchanged from the reference conditions of Phase IIA Part 2. The distributions of heat and particle fluxes on the two divertor plate are shown in Fig. 9.5-1 and Fig. 9.5-2 for plate perpendicular to the separatrix. The inner and outer plates have the peak heat fluxes of 14 MW/m<sup>2</sup> and 18 MW/m<sup>2</sup> normal to the separatrix, respectively.

### 2. Mechanical configuration for reduced channel length divertor

The plasma configuration based upon the Japanese physics prediction is shown in Fig. 9.5-3. The plasma major radius has been taken to be 5.0 m. The plasma vertical shift has been taken to be 0.3 m from TF coil system midplane. The major radius of null-point is 4.3 m. The angles between the inner/outer separatrix lines and the horizontal axis are 30° and 60°, respectively.

The specification for the reduced channel length divertor are:

- To maintain  $\geq 40$  cm from the null point to the divertor
- To limit the angle of incidence between the flux lines and the divertor plate to 15° or less on the inboard plate and to 10° or less on the outboard plate.

Two divertor configurations have been considered. Length of divertor channel has been taken to be 40 cm for these configurations. They are:

- 1) The angle between plate and separatrix is set to be 8° for the inboard plate and 6° for the outboard plate (See Fig. 9.5-4). This configuration satisfies the above-mentioned specification. Under these geometrical conditions, the peak heat flux is about 2 MW/m<sup>2</sup>. Heat flux distribution on divertor plate is shown in Fig. 9.5-5.
- 2) The angle between plate and separatrix is set to be 20° for the inboard plate and 14.5° for the outboard plate (See Fig. 9.5-6). The resultant peak heat flux is about 5 MW/m<sup>2</sup>. Heat flux distribution on divertor plate is shown in Fig. 9.5-7.

Table 9.5-3 summarizes the heat and particle fluxes on divertor plate. The parametric analysis of the divertor plate has been carried out in the engineering study. Table 9.5-4 shows the divertor operating conditions used for engineering analysis.

### 3. Lifetime analysis

The plate is composed of a protective material of 1 mm or 3 mm thick tungsten, heat sink of copper or copper alloy, and supporting structure



of 316SS.

Table 9.5-5 shows the erosion rate of divertor plate. The estimated erosion rate does not include the effect of the redeposition of the sputtered impurity ions.

The lifetime of the divertor plate has been estimated by the erosion of plasma side material and fatigue life of heat sink.

The estimated lifetimes of plates with the copper and copper alloy heat sink are shown in Table 9.5-6 and Table 9.5-7, respectively. The design fatigue curve with the safety factor of 3 on strain range or 20 on life is employed. The stress range used for evaluating the lifetime is the result from elastic analysis.

The lifetime due to fatigue is shorter than the lifetime due to erosion, except for the copper alloy with 1 mm thick tungsten tiles. The divertor plate lifetimes under the heat flux of  $5 \text{ MW/m}^2$  are very short. Therefore, the peak heat flux of  $5 \text{ MW/m}^2$  may be unacceptable even for the long pulse operation. The divertor plate lifetimes under the heat flux of  $2 \text{ MW/m}^2$  are 1.8 year for the copper heat sink with 1 mm thick tungsten tiles, and 8 year (over reactor life) for the non-annealed copper alloy with 3 mm thick tungsten tiles.

Table 9.5-8 shows a comparison of the lifetime in the long pulse operation with the lifetime in the reference operation. The fatigue life of the divertor plate is 5 times longer than that in the reference operation. The fatigue life for the copper heat sink increases from 0.35 year to 1.8 year in going from 200s burn time to 1000s burn time. The fatigue life for the non-annealed copper alloy is over the reactor lifetime under the long pulse operation condition.

#### 4. Conclusion

The major conclusions of the study are:

- 1) The peak heat flux of  $5 \text{ MW/m}^2$  may be unacceptable even for the long pulse operation.
- 2) The fatigue life of the divertor plate in the long pulse operation is 5 times longer than that in the reference operation. The divertor plate lifetimes under the heat flux of  $2 \text{ MW/m}^2$  are 1.8 year for the copper heat sink, and over reactor lifetime for the non-annealed copper alloy.
- 3) In order to limit the peak heat flux to about  $2 \text{ MW/m}^2$ , the angle between plate and separatrix should be set to be  $8^\circ$  for the in-board plate and  $6^\circ$  for the outboard plate. This configuration requires the large height of divertor chamber. The maximum height between plate and null-point is 1.1 m.

Table 9.5-1 INTOR staged operation schedule

Stage	Years	Emphasis	Availability	Annual 14 MeV neutron fluence <sup>a</sup> (MW·a/m <sup>2</sup> )	Annual number of shots <sup>b</sup>	Total number of shots
IA	1	Hydrogen plasma operation Engineering check-out	10%		$2.5 \times 10^3$	$2.5 \times 10^3$
IB	1	D-T plasma operation	15%	0.156	$3.8 \times 10^3$	$3.8 \times 10^3$
II	3	Engineering testing	25%	0.26	$6.3 \times 10^3$	$1.9 \times 10^4$
III	4	Upgraded engineering testing	50%	0.52	$1.26 \times 10^4$	$5.04 \times 10^4$

<sup>a</sup> Based on 1000 s shots and 80% duty cycle  $\sim 600$  MW(th) flat-top power,  $1.3$  MW/m<sup>2</sup> average neutron wall loading and the indicated availability.

<sup>b</sup> The requirement on Stage III is to accumulate  $\sim 3$  MW·a/m<sup>2</sup> after the end of Stage II. This could be achieved in several ways; the case given here is only a representative one.

Table 9.5-2 Engineering specifications for the high recycling regime of the single-null poloidal divertor

Outer scrape-off and divertor target		
Scrape-off temperature (at the separatrix in the main chamber)	$T_e = 130; T_i = 200$ [eV]	
Scrape-off density (at the separatrix in the main chamber)	$\approx 6 \times 10^{19} \text{ m}^{-3}$	
Total power conducted into scrape-off plasma	80 MW	
Peak temperature at target	$T_e \approx 20; T_i \approx 20$ [eV]	
Power to outer divertor throat (conducted)	$\approx 40$ MW	
Total power to each target	34.5 MW	
(a) due to kinetic energy of DT plasma	16.2 MW	(peaked)
(b) due to recombination of DT ions at surface	9.8 MW	(peaked)
(c) radiation from diverted plasma	6.5 MW	(uniform)
(d) radiation from main plasma	2 MW	(uniform)
Peak power load to outer plate (target perpendicular to magnetic surfaces)	18 MW/m <sup>2</sup>	
Peak power load to inner plate (target perpendicular to magnetic surfaces)	14 MW/m <sup>2</sup>	
Power profile ( $\exp^{-1}$ decay length to magnetic surfaces)	Outer	Inner
outboard of separatrix	3 cm	3.5 cm
inboard of separatrix	1 cm	1.2 cm
Total ion flow to target	$4.5 \times 10^{24}/\text{s}$	
Composition - 49% D <sup>+</sup> , 49% T <sup>+</sup> , 2% He <sup>2+</sup>		
Peaked ion flux density [target perpendicular to magnetic surfaces]	$1.05 \times 10^{24}/\text{m}^2/\text{s}$	

Table 9.5-2 Engineering specifications for the high recycling regime of the single-null poloidal divertor (continued)

Flux density profile ( $\exp^{-1}$ decay length $\perp$ to magnetic surfaces)	Outer	Inner
outboard	9.4 cm	11.0
inboard	1.5 cm	1.8
Radiation to outer target		
Radiation to each target	6.5 MW	
From main plasma	2 MW	
Predicted movement of intersection of separatrix with the target (in direction $\perp$ to magnetic surfaces)	$\pm 1.5$ cm	
<u>Divertor chamber walls</u>		
Total charge exchange on all divertor walls	2 MW	
Total radiation on all divertor walls	3 MW	
Both power load and sputtering by charge exchanged DT are small within the chamber. Erosion is due predominantly to helium atoms backscattered from the divertor target.		
Erosion peak - close to the position at the wall which faces the intersection of the separatrix with the target.		
Peak erosion rate: SS wall (100% availability) 3-6 mm/y		
<u>First wall (assessment of uniform conditions)</u>		
Radiation	49 MW	
Charge exchange	1 MW	
Total flux density of charge exchange atoms	$5 \times 10^{20}/\text{m}^2/\text{s}$	
Sputtering rate (from SS wall)	$2.3 \times 10^{18}$ atoms/ $\text{m}^2/\text{s}$	
Sputtering by charged particles	Negligible	

Table 9.5-3 Heat and particle flux on divertor plate

Peak energy flux to divertor plate normal to separatrix			
outboard	(MW/m <sup>2</sup> )	18	
inboard	(MW/m <sup>2</sup> )	14	
Peak ion flux to divertor plate normal to separatrix			
outboard	(m <sup>-2</sup> s <sup>-1</sup> )	1.05 × 10 <sup>24</sup>	
inboard	(m <sup>-2</sup> s <sup>-1</sup> )	1.05 × 10 <sup>24</sup>	
Inclination of divertor plate to separatrix			
outboard		6°	14.5°
inboard		8°	20°
Peak energy flux normal to divertor plate			
outboard	(MW/m <sup>2</sup> )	1.9	4.5
inboard	(MW/m <sup>2</sup> )	2.0	4.8
Peak ion flux normal to divertor plate			
outboard	(m <sup>-2</sup> s <sup>-1</sup> )	1.1 × 10 <sup>23</sup>	2.6 × 10 <sup>23</sup>
inboard	(m <sup>-2</sup> s <sup>-1</sup> )	1.5 × 10 <sup>23</sup>	3.6 × 10 <sup>23</sup>

Table 9.5-4 Divertor operating conditions used for engineering analysis

<u>Engineering</u>			
Plasma side material			
Material	W		
Thickness (mm)	1, 3		
Bond type	Brazing, plasma spraying		
Heat sink material	Cu, Cu-0.6Be-2.5Co		
First wall material	SS		
Inclination of divertor plate to separatrix			
Outboard	6°	14.5°	
Inboard	8°	20°	
<u>Heat loads (MW/m<sup>2</sup>)</u>			
Peak, Collector plate surface	2	5	
First wall	0.1	0.1	
<u>Particle fluxes (m<sup>-2</sup>s<sup>-1</sup>)</u>			
Ions, Middle of collector plate	$1.5 \times 10^{23}$	$3.6 \times 10^{23}$	
CX, First wall	$5 \times 10^{20}$	$5 \times 10^{20}$	

Table 9.5-5 Erosion rate of divertor plate

Stage		I	II	III
<u>Operating conditions</u>				
Particle flux on plate	( $\text{m}^{-2}\text{s}^{-1}$ )			
Case 1 <sup>(1)</sup>			$1.5 \times 10^{23}$	
Case 2			$3.6 \times 10^{23}$	
Electron temperature on plate	(eV)		20	
Duty cycle	(%)	81	81	81
Availability	(%)	12.5	25	50
<u>Erosion rate of tungsten<sup>(2)</sup></u>				
	(mm/y)			
Case 1		0.07	0.15	0.3
Case 2		0.18	0.38	0.7

(1) Inclination of divertor plate to separatrix

Case 1: 6° (outboard), 8° (inboard)

Case 2: 14.5° (outboard), 20° (inboard)

(2) Self sputtering and redeposition is not included.

Table 9.5-6 Lifetime of divertor plate with copper heat sink for stage III operation

		<u>1 mm thick tungsten tiles</u>		<u>3 mm thick tungsten tiles</u>	
		Case 1 <sup>(1)</sup>	Case 2 <sup>(1)</sup>	Case 1	Case 2
<u>Life due to erosion</u>					
Erosion by sputtering	(mm/y)	0.3	0.7	0.3	0.7
Life	(y)	3.4	1.4	10	4.1
<u>Fatigue life of heat sink</u>					
Heat flux	(MW/m <sup>2</sup> )	2	5	2	5
Stress range	(MPa)	227	534	300	585
Life	(y)	1.8	0.1	0.6	0.08

(1) Inclination of divertor plate to separatrix

Case 1: 6° (outboard), 8° (inboard)

Case 2: 14.5° (outboard), 20° (inboard)

Table 9.5-7 Lifetime of divertor plate with Cu-0.6Be-2.5Co heat sink  
for stage III operation

		1 mm thick tungsten tiles		3 mm thick tungsten tiles	
		Case 1(1)	Case 2(1)	Case 1	Case 2
<u>Life due to erosion</u>					
Erosion by sputtering	(mm/y)	0.3	0.7	0.3	0.7
Life	(y)	3.4	1.4	10	4.1
<u>Fatigue life of heat sink</u>					
Heat flux	(MW/m <sup>2</sup> )	2	5	2	5
Stress range	(MPa)	381	813	426	898
Life <sup>(2)</sup>	(y)	16	~0.8(3)	8	~0.8(3)

(1) Inclination of divertor plate to separatrix

Case 1: 6° (outboard), 8° (inboard)

Case 2: 14.5° (outboard), 20° (inboard)

(2) Using the fatigue curve under stress control condition for the  
as-received material (not annealed)

(3) Assuming that number of allowable cycles under 0.7% strain range  
is 10<sup>4</sup> cycles.

Table 9.5-8 Comparison of the lifetime in long pulse operation  
with the lifetime in the reference operation  
(Heat flux = 2 MW/m<sup>2</sup>)

	Reference <sup>(1)</sup>		Long pulse <sup>(1)</sup>	
<u>Tungsten tile thickness (mm)</u>	1	3	1	3
<u>Life due to erosion</u>				
Erosion by sputtering (mm/y)	0.3	0.3	0.3	0.3
Life ( y )	3.4	10	3.4	10
<u>Fatigue life of heat sink</u>				
◦ Cu heat sink				
Stress range (MPa)	227	300	227	300
Life ( y )	0.35	0.11	1.8	0.6
◦ Cu alloy heat sink				
Stress range (MPa)	381	426	381	426
Life <sup>(2)</sup> ( y )	3.2	1.6	16	8

(1) Reference : 200s burn time

Long pulse : 1000s burn time

(2) Life for the as-received material (not annealed)



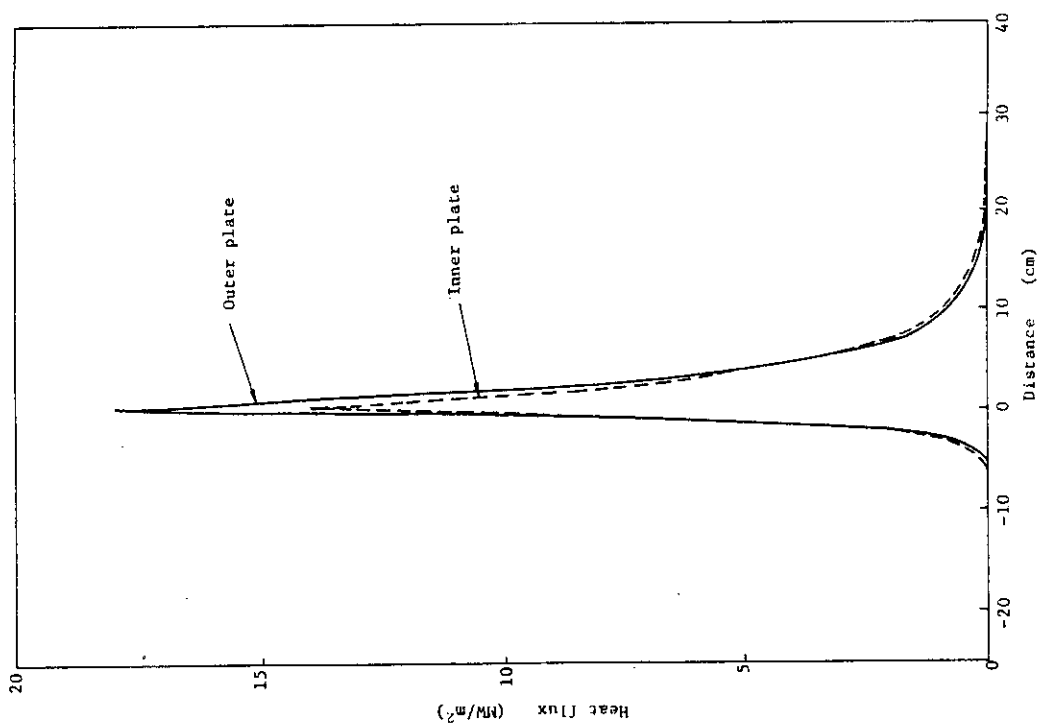


Fig. 9.5-1 Heat flux distribution perpendicular to the separatrix at the location of the collector plates

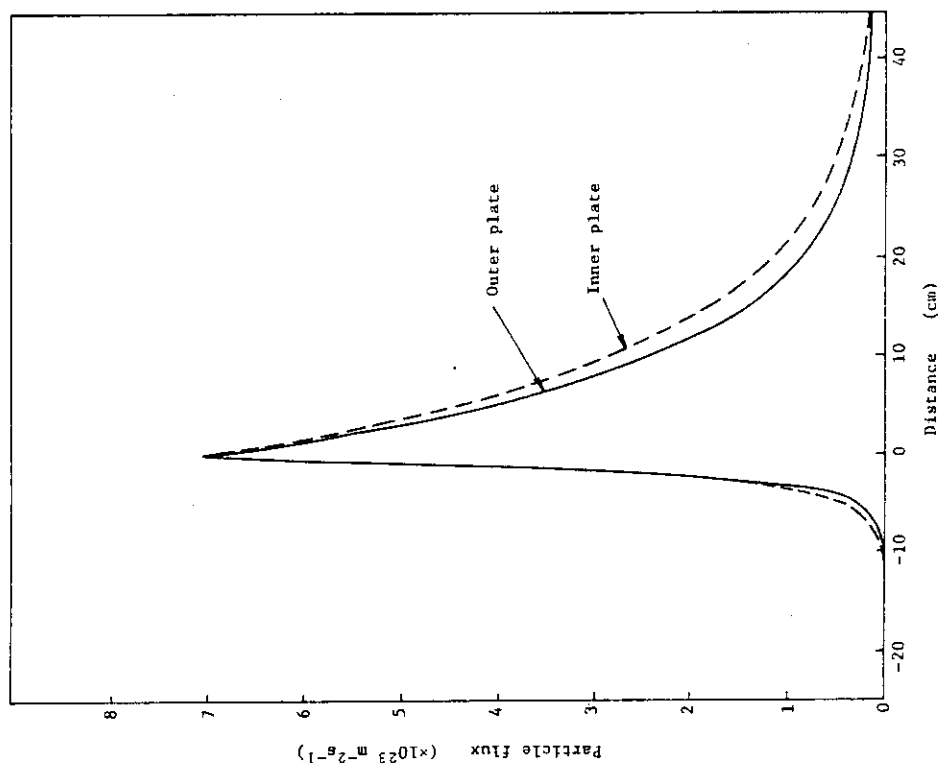


Fig. 9.5-2 Particle flux distribution perpendicular to the separatrix at the location of the collector plates

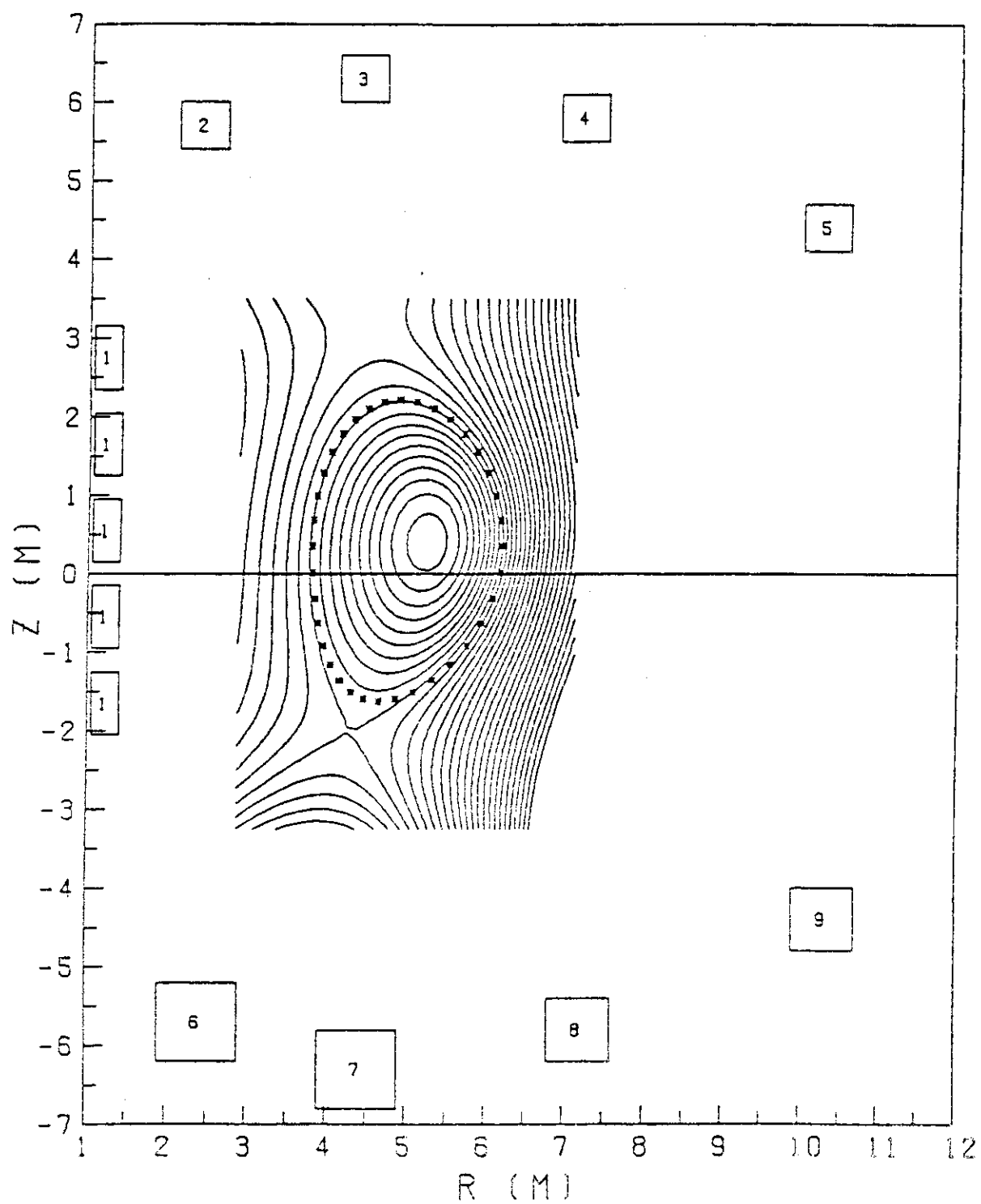


Fig. 9.5-3 Equilibrium poloidal field configuration

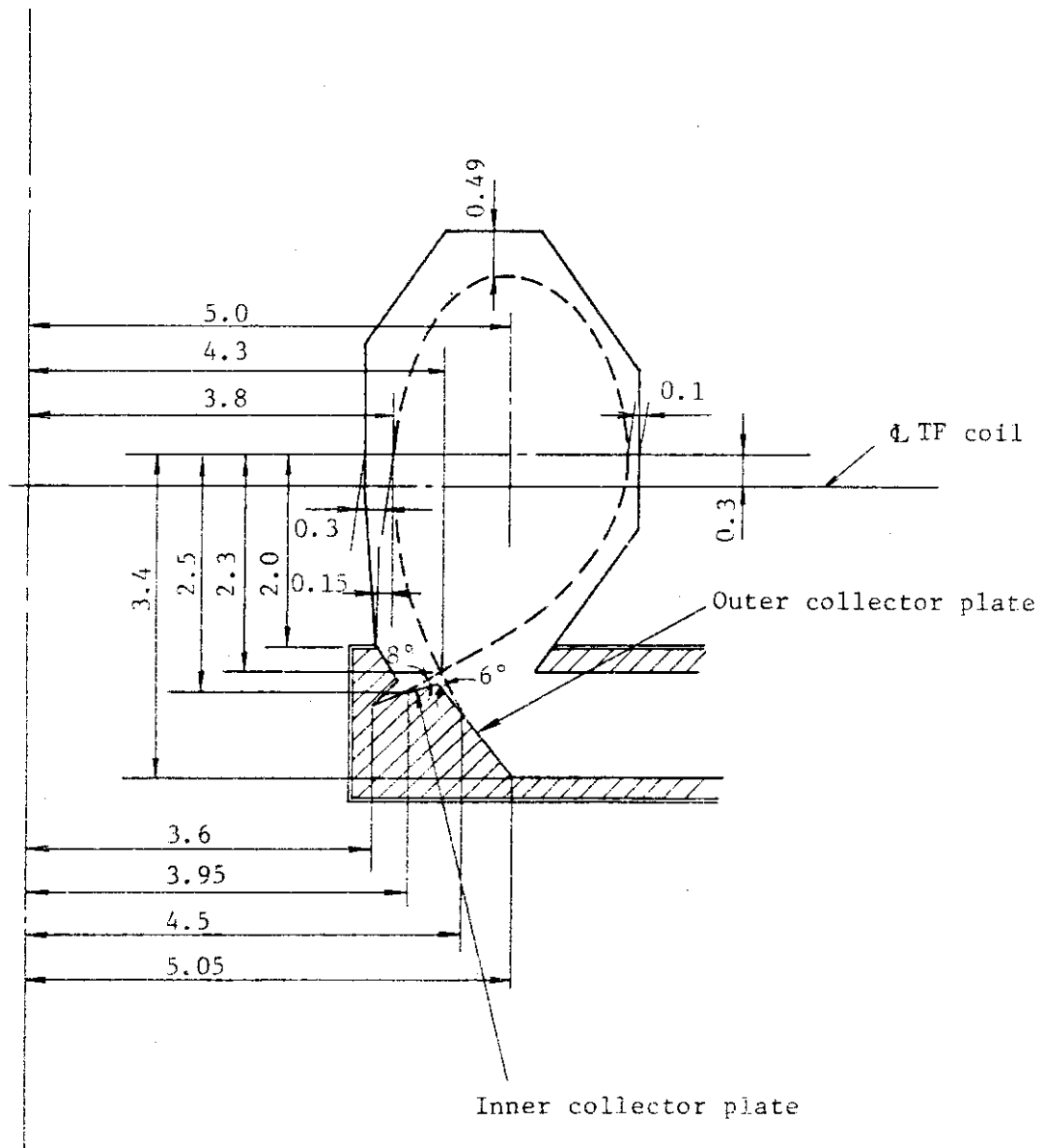


Fig. 9.5-4 Profile of the divertor region (Case 1)

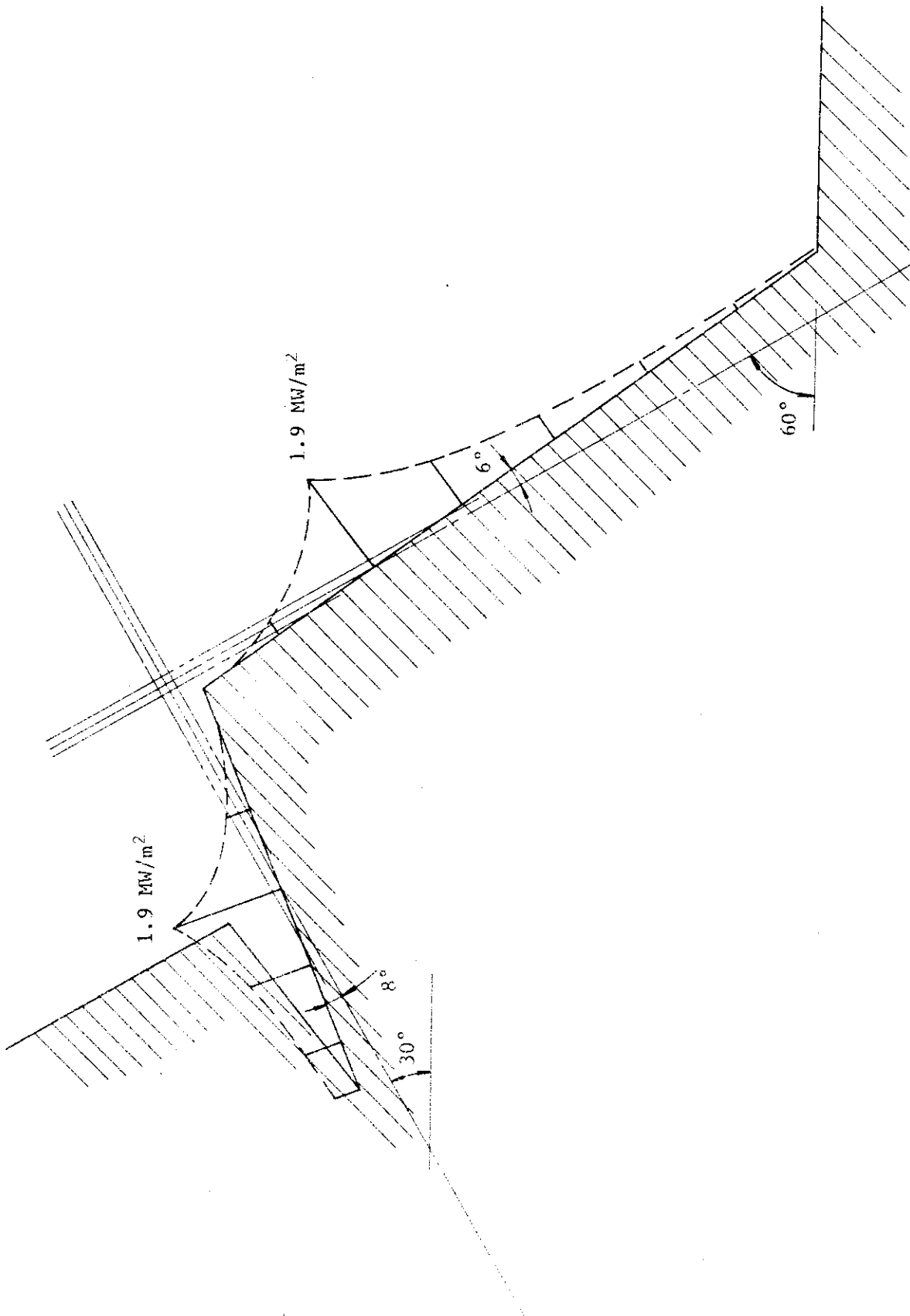


Fig. 9.5-5 Heat flux distribution on divertor plate (Case 1)

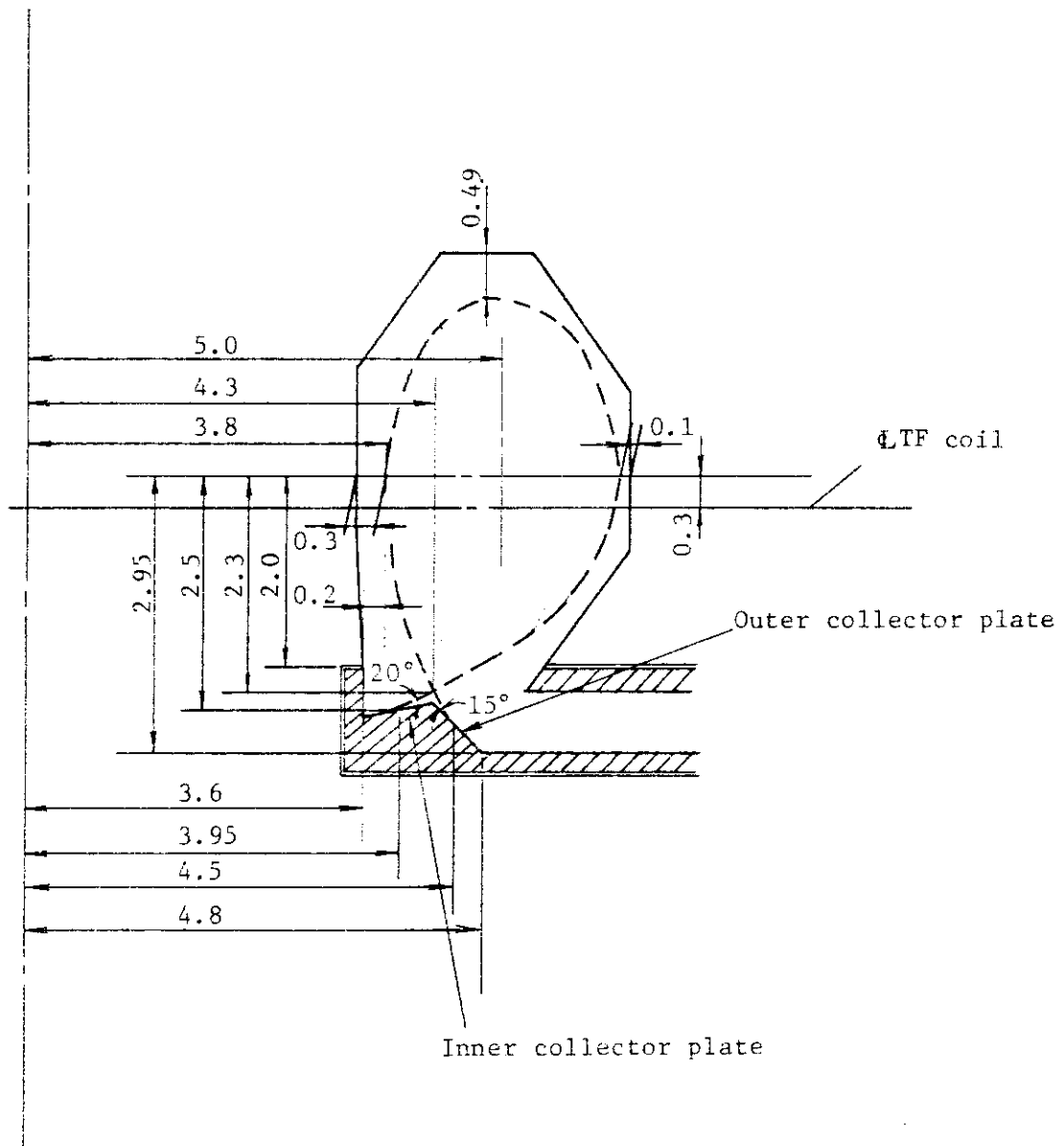


Fig. 9.5-6 Profile of the divertor region (Case 2)

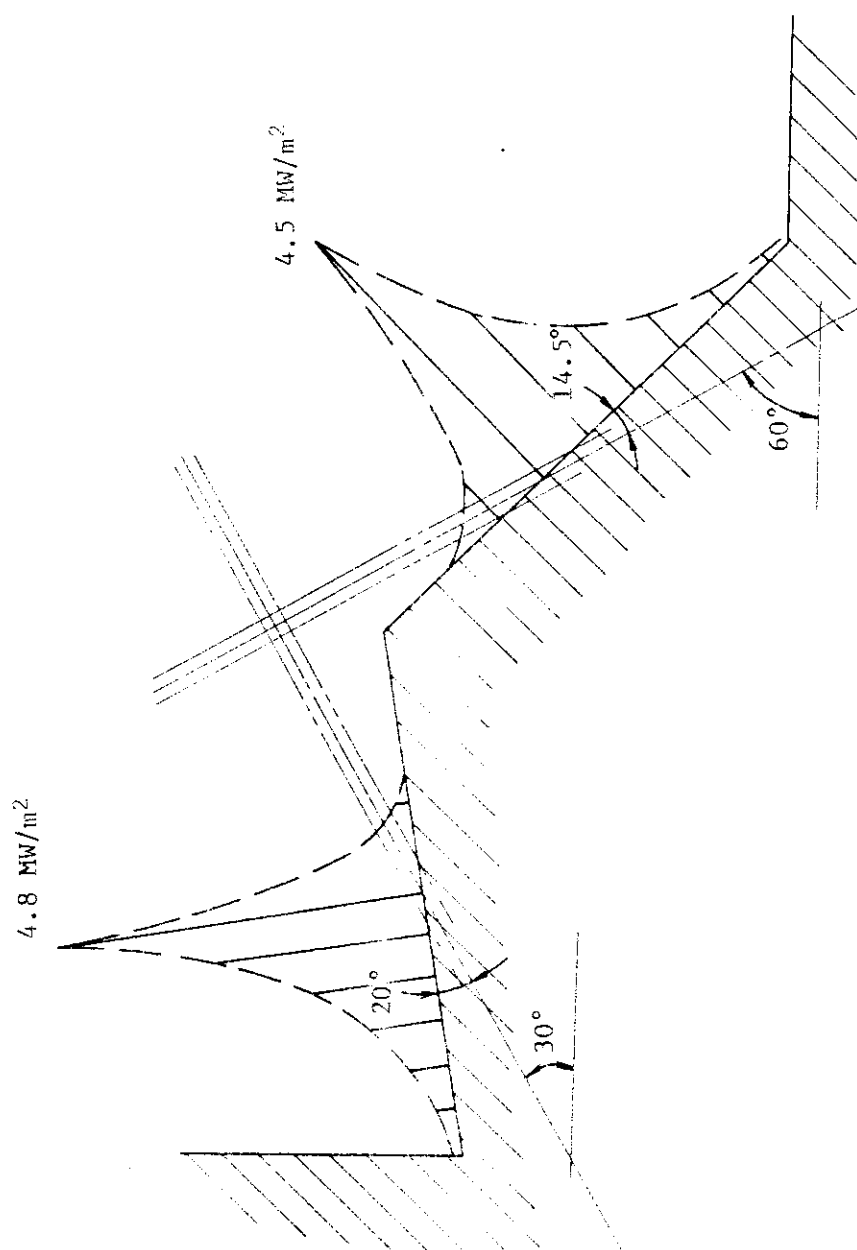


Fig. 9.5-7 Heat flux distribution on divertor plate (Case 2)

#### 9.6 R&D items

There are still many R&D items in both physics and engineering. Physically, investigation of conditions necessary for low edge temperature operation is important. Engineering R&D items include development of reliable bonding techniques of tungsten to copper heat sink.

## 10 First wall and tritium producing blanket (continuous tritium recovery)

### 10.1 First wall

The first wall system consists of ① an outboard region that serves as the major fraction of the plasma chamber surface and receives particle and radiation heat fluxes from the plasma and radiative heating from the divertor, ② an inboard region that receives radiative and particle fluxes during plasma burn and a fraction of the plasma and magnetic energy during a disruption.

The reference concept for first-wall is a water-cooled stainless-steel panel. Figure 10.1 shows the first wall structure. The first wall is integral with the blanket.

### 10.2 Tritium producing blanket (continuous tritium recovery)

Incorporation of a tritium-breeding blanket in the INTOR design is based on both economic and tritium availability considerations. From the engineering point of view, the tritium-breeding blanket is limited to the outboard and upper regions of INTOR.

The reference blanket concepts are based on  $\text{Li}_2\text{O}$ . A lead neutron multiplier is incorporated into the blanket design to achieve the desired breeding ratio as shown in Fig. 10.2.

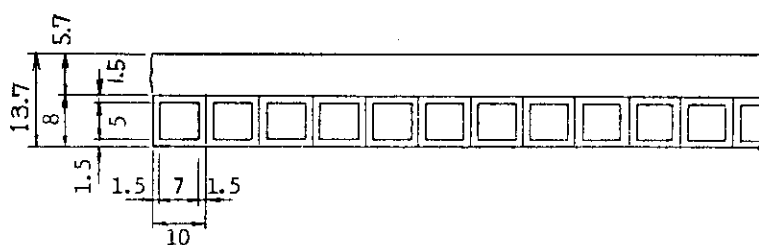
The first wall is structurally integral with the blanket. Low-temperature water coolant is used for all blanket regions.

Tritium is removed from the ceramic breeder by a low-pressure,  $\approx 0.1$  MPa helium purge stream. The breeder temperature is maintained between 400 and 1000°C to facilitate tritium release by arranging the distribution of cooling tubes (see Fig. 10.3). A 5 cm thick lead neutron multiplier is located between the breeding region and the first wall as shown in Fig. 10.4. Thickness of neutron multiplier is limited within 5.0 cm considering cooling capability of cooling tubes in panel. A water-cooled panel, which separates the lead from the breeder materials, provides cooling for adjacent regions. The lead is also cooled on the front side by the water-cooled first wall which also serves as part of the blanket containment.

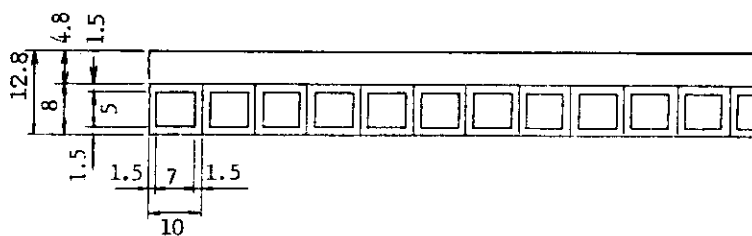
The main design parameters of the breeding blanket are as follows.

(a) Thickness of tritium breeding blanket	50 cm
(b) Structural material	SS316
(c) Filling material	$\text{Li}_2\text{O}$
(d) Neutron multiplier	Pb
(e) Maximum temperature of structure material	350°C
(f) Breeding material temperature	400~1000°C
(g) Tritium breeding ratio	0.65
(h) Coolant	$\text{H}_2\text{O}$
(i) Enrichment of $^6\text{Li}$	30%





(a) Inboard first wall



(b) Outboard first wall

Fig. 10.1 First wall

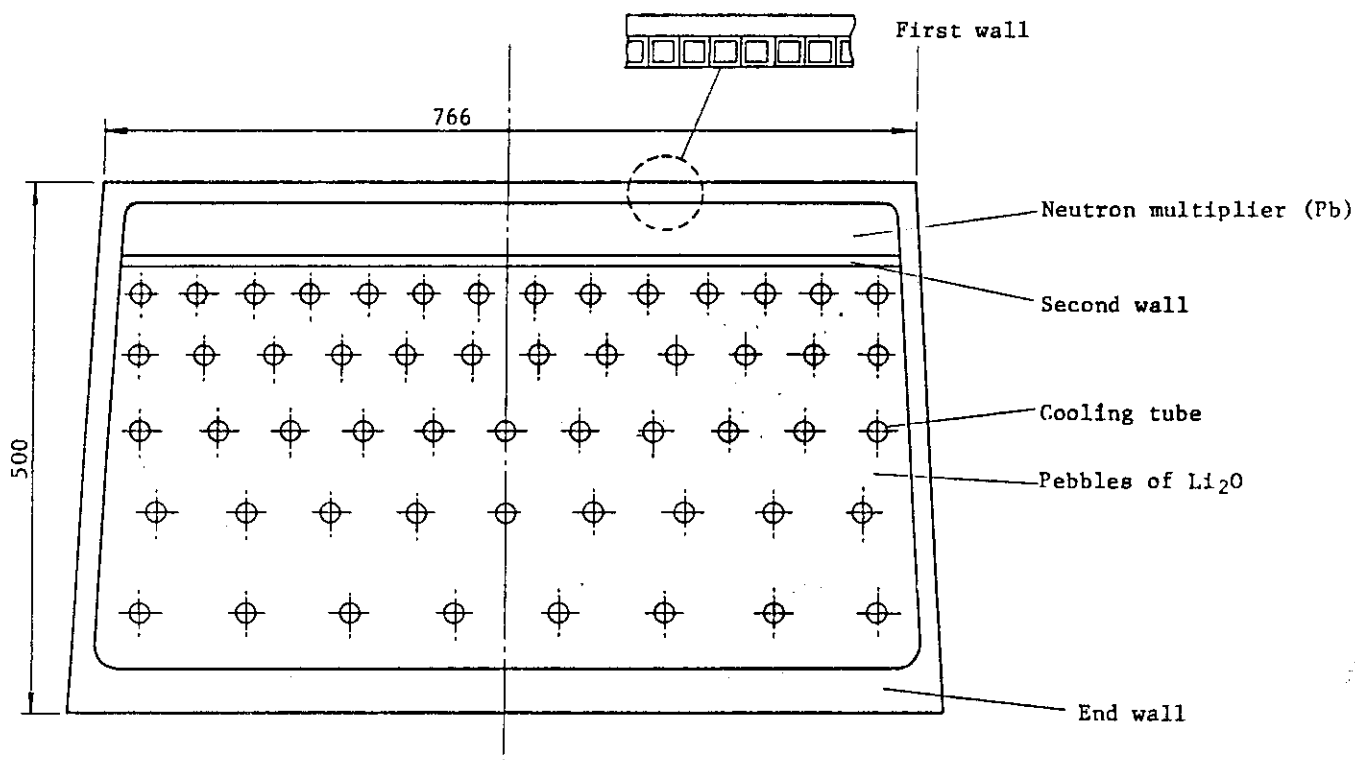


Fig. 10.2 Cross sectional view of tritium producing blanket

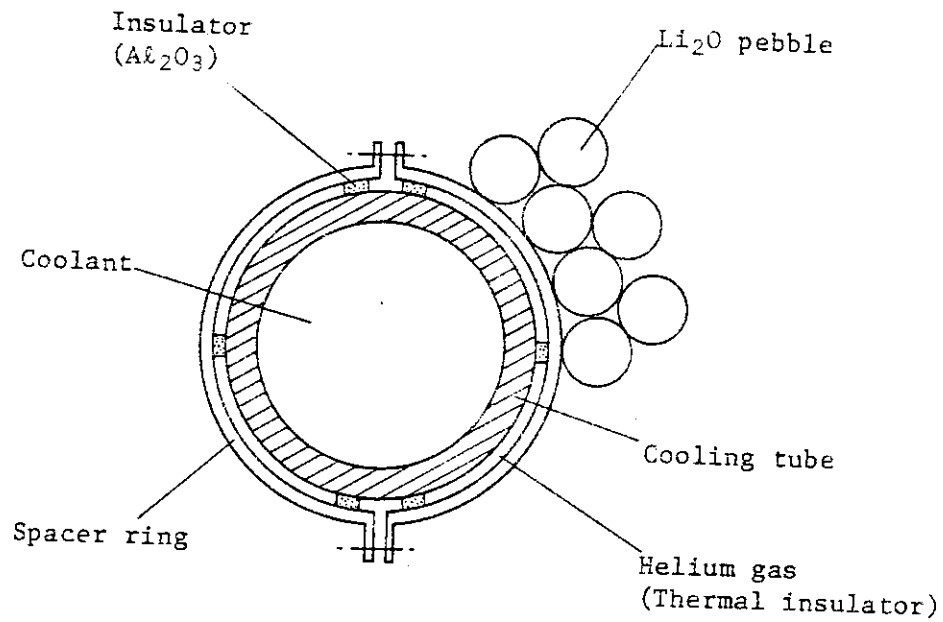


Fig. 10.3 Cooling tube structure in the breeding blanket

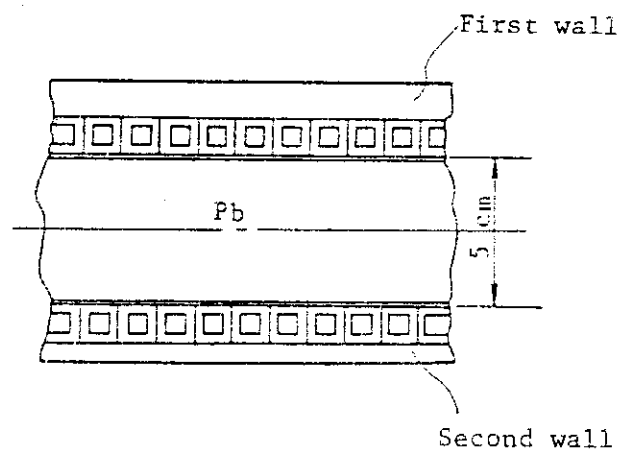


Fig. 10.4 Neutron multiplier region and first wall

## 11. First wall and tritium producing blanket (Batch tritium recovery)

### 11.1 Introduction

In the previous blanket design studies for INTOR, continuous tritium recovery scenario has been proposed based on economic and tritium availability considerations. However, design requirements associated with continuous tritium recovery such as the precise temperature control of breeder, lead to serious complexity of blanket design. A significant improvement of the simplicity and reliability is desired for tritium producing blanket.

In this section, batch-type tritium recovery scenario is offered as a solution of simple and reliable tritium producing blanket, and design feasibility studies have been performed.

The design philosophies adopted for accomplishing the simplicity and reliability are as follows:

- (i) Batch-type tritium recovery scenario is adopted to simplify the temperature control mechanism of breeder.
- (ii) To provide high reliability performance of shell effect, copper alloy (Cu-Be-Ni) which offers possible advantage over pure copper in the area of radiation damage resistance is used as a shell conductor material.
- (iii) Low temperature helium gas is selected as the coolant to avoid coolant/breeder reaction in accident.
- (iv) To achieve the high tritium breeding ratio, lithium oxide ( $\text{Li}_2\text{O}$ ) and beryllium are used as a tritium breeding material and a neutron multiplier, respectively.
- (v) To simplify the assembly/maintenance procedure of blanket and to avoid problems for vertical plasma stability, number of blanket modules is set to that of TF coils.

### 11.2 Selection of Blanket Concept

There are two major origins that reduces simplicity and reliability of blanket. One is the temperature control requirement of breeder (ex.  $400 \sim 1000^\circ\text{C}$  for  $\text{Li}_2\text{O}$ ) to ensure continuous in-situ tritium recovery during reactor operation. This factor imposes installation of thermal insulation gap to provide temperature difference between breeder and coolant tube. The other is the addition of neutron multiplier and shell conductor for passive plasma stabilization with their cooling mechanism and support structure. Application of beryllium plate potentially decreases design considerations, since it can be used as both neutron multiplier and shell conductor. However, limited ductility of beryllium relative to other structural materials imposes some constraints on design, fabrication and reliability of the shell structure. In the case of other low resistant metals such as copper and aluminum, neutron absorption in the material affects the tritium breeding performance.

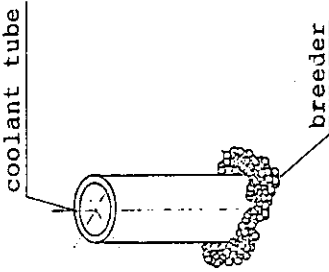
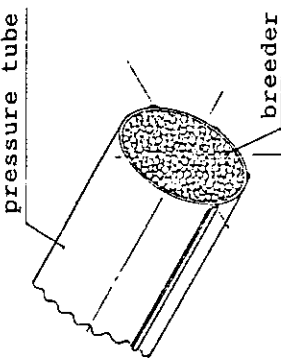
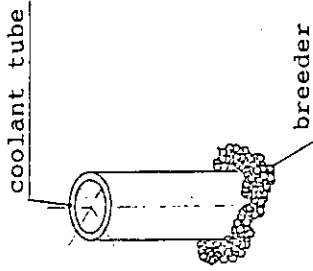
For the above reasons, design approaches in this selection study are focussed on simple and reliable blanket concept in the area of temperature control mechanism and neutron multiplier/shell conductor. Figure 11.2-1 shows an investigation of possible blanket concepts starting from simplification of temperature control mechanism of breeder. Elimination of thermal gap around cooling tube is essential for simple design of blanket.

As shown in Fig. 11.2-1 there are three options available for basic thermal hydraulic design of batch recovery blankets: (i) Water-cooled blanket, (ii) Directly-helium-cooled blanket, and (iii) Indirectly-helium-cooled blanket. Table 11.2-1 summarizes key features of these three-type design. Of these three concepts, indirectly-helium-cooled blanket appears most attractive and selected as the reference of the present study, because of its high potential of tritium breeding performance and easiness of periodic tritium recovery. In addition, it must be pointed out that this concept has some expansibility to a power reactor.

Figure 11.2-2 summarizes the major characteristics of this batch-type blanket, comparing with previous water-cooled blanket of continuous tritium recovery type. As is obvious from this figure, structure designs of breeder to structure interface can be simplified significantly, because low temperature operation of breeder allows direct contact of breeder with structure materials.

Figure 11.2-3 shows considerations to improve the reliability of shell conductor and to reduce the design complexity of neutron multiplier. In this blanket design copper alloy (Cu-Be-Ni) is selected as shell conductor material, since it exhibits smaller changes of mechanical and electrical properties by neutron irradiation than pure copper. As described above, plate-type multiplier increases design complexity because it must be cooled separately from the breeder. A homogenous breeder/multiplier mixture in the form of small spherical pebble is considered for this blanket design. This option has a potentiality of high tritium breeding performance compensating for neutron absorption by shell conductor material.

Table 11.2-1 Comparison of design approaches for batch recovery blanket

	Water-Cooled Blanket	Directly Helium-Cooled Blanket	Indirectly Helium-Cooled Blanket
<u>Concept</u>			
<u>Features</u>	<ul style="list-style-type: none"> <li>• advantages :               <ul style="list-style-type: none"> <li>• low temperature of structure materials</li> <li>• low pumping power</li> </ul> </li> <li>• disadvantages :               <ul style="list-style-type: none"> <li>• difficulty of precise coolant tube arrangement for breeder maximum temperature control</li> <li>• <math>\text{Li}_2\text{O}/\text{H}_2\text{O}</math> reaction</li> <li>• requirement of coolant detritiation system</li> <li>• change of coolant material to helium gas at tritium recovery operation</li> </ul> </li> </ul>	<ul style="list-style-type: none"> <li>• minimum design considerations on the breeder temperature control</li> <li>• reduction of tritium purge line</li> <li>• easiness of breeder heating for tritium recovery</li> <li>• complicated structure with pressure tube, sub header, manifold and so on</li> <li>• requirement of large piping spaces and high pumping power</li> <li>• large mass transport rate of <math>\text{Li}_2\text{O}</math></li> </ul>	<ul style="list-style-type: none"> <li>• high potential of tritium breeding performance</li> <li>• easiness of breeder heating for tritium recovery</li> <li>• difficulty of precise coolant tube arrangement for breeder maximum temperature control</li> <li>• requirement of large piping spaces and high pumping power</li> </ul>

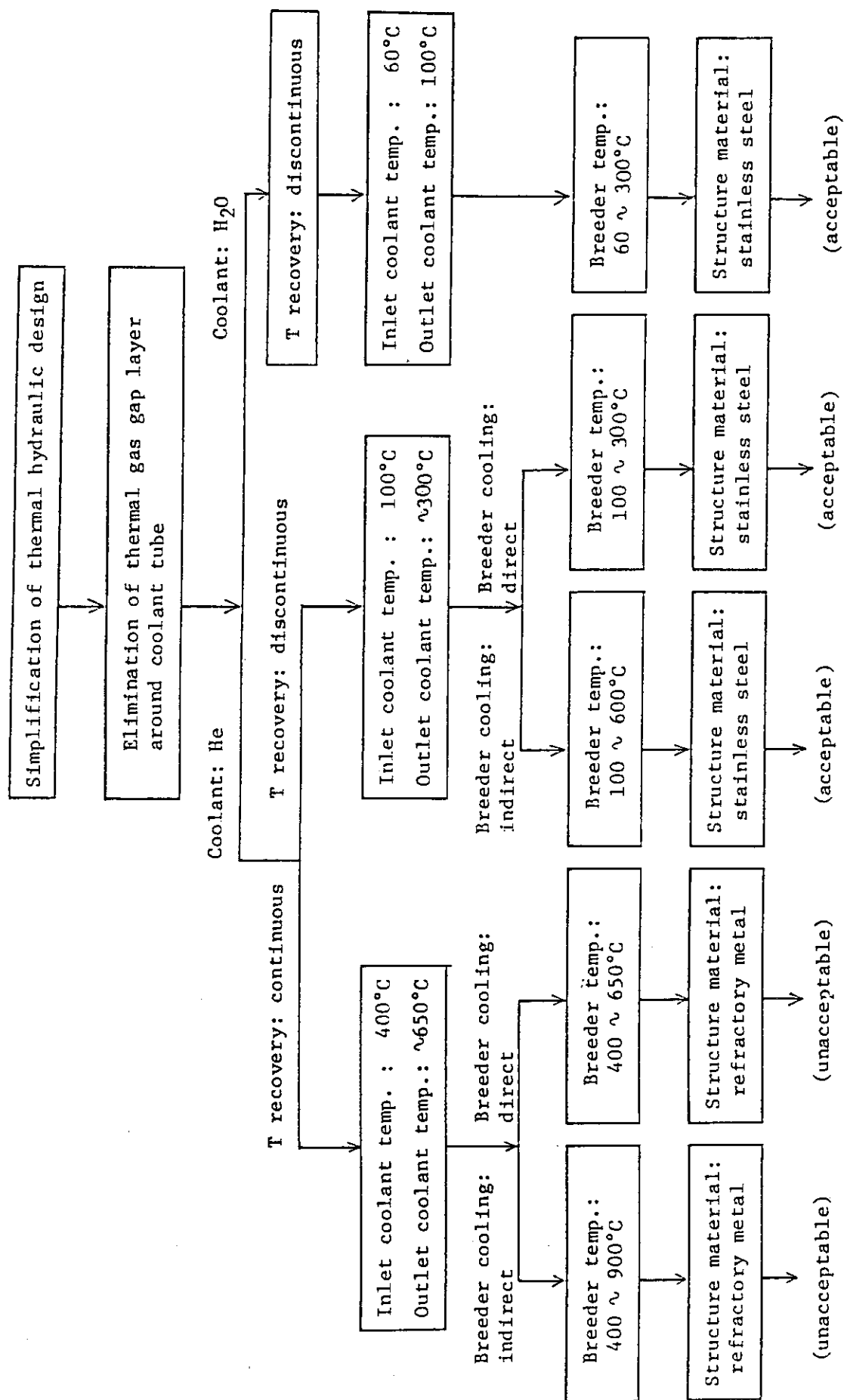
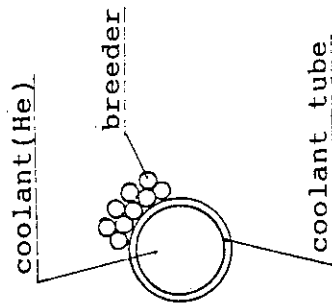


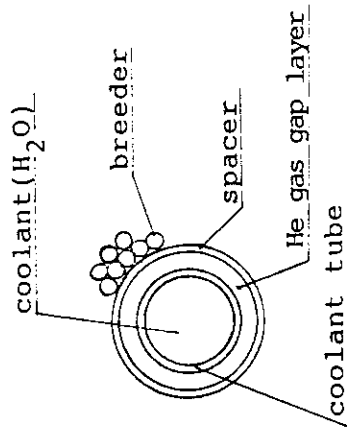
Fig. 11.2-1 Investigation of design concepts for batch recovery blanket

Indirectly Helium-cooled Blanket  
(batch tritium recovery)



Direct contact of breeder with coolant tube is accepted.  
During tritium recovery operation, high temperature ( $\sim 450^{\circ}\text{C}$ ) helium gas flows in the coolant tube to elevate breeder temperature.

Water-cooled Blanket  
(continuous tritium recovery)

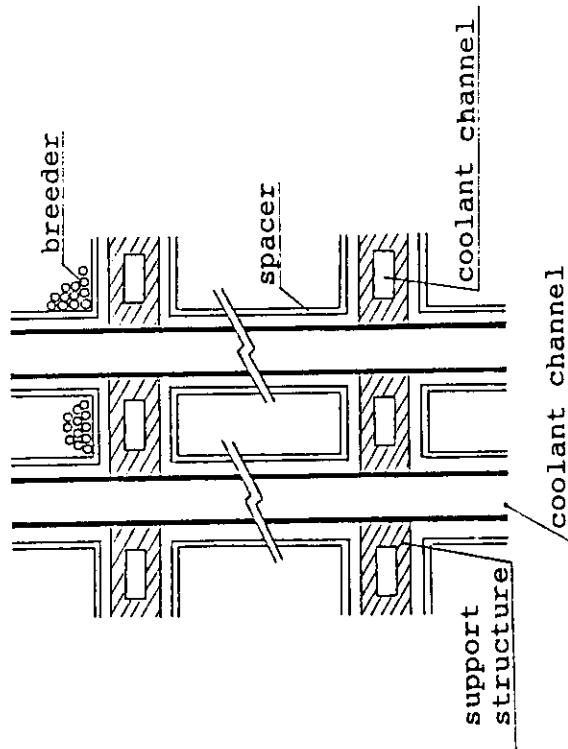


A spacer is installed around a cooling tube to provide thermal insulation gap of helium.

Concept of breeder-coolant tube interface

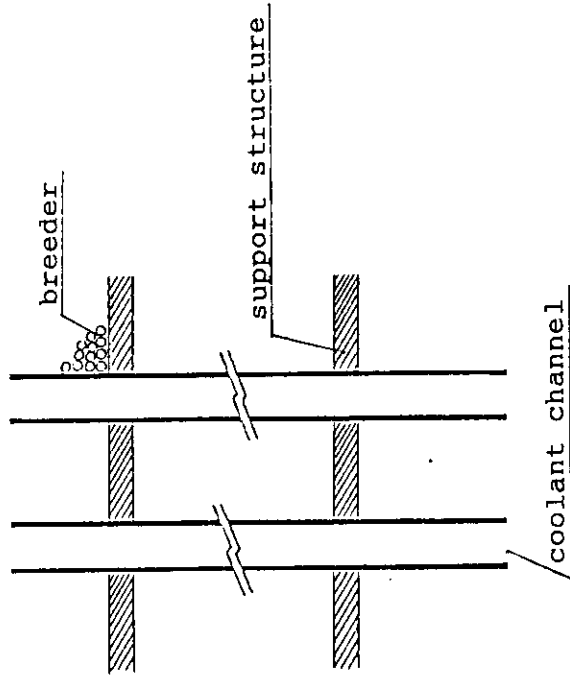
Fig. 11.2-2 Comparison of structure designs between water cooled blanket of continuous tritium recovery and helium cooled blanket of batch tritium recovery

Water-cooled Blanket  
(continuous tritium recovery)



Concept of  
support structure  
for Coolant tubes

Indirectly Helium-cooled Blanket  
(batch tritium recovery)



Cooling mechanism is required for the support structure of coolant tubes.

Thermal insulation gap at breeder to support interface is also required to control the breeder temperature above 400°C

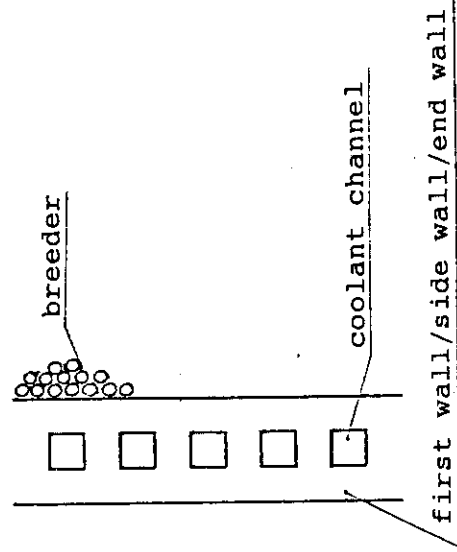
Maximum temperature control of support structure can be achieved by adjusted coolant tube pitch.

Existing refractory materials are potentially applicable to support structure, since the maximum temperature of breeder is at most 600°C or so.

Fig. 11.2-2 Comparison of structure designs between water cooled blanket of continuous tritium recovery and helium cooled blanket of batch tritium recovery (continued)

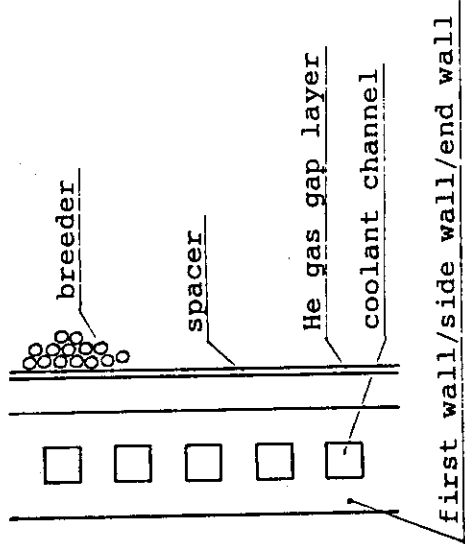


Indirectly Helium-cooled Blanket  
(batch tritium recovery)



Direct contact of breeder with vessel wall is accepted

Water-cooled Blanket  
(continuous tritium recovery)



Thermal insulation gap is required  
breeder to wall interfaces to  
control the breeder temperature  
above 400°C

Concept of  
breeder/wall  
interface

Comparison of structure designs between water cooled blanket of  
continuous tritium recovery and helium cooled blanket of batch  
tritium recovery (continued)

Fig. 11.2-2

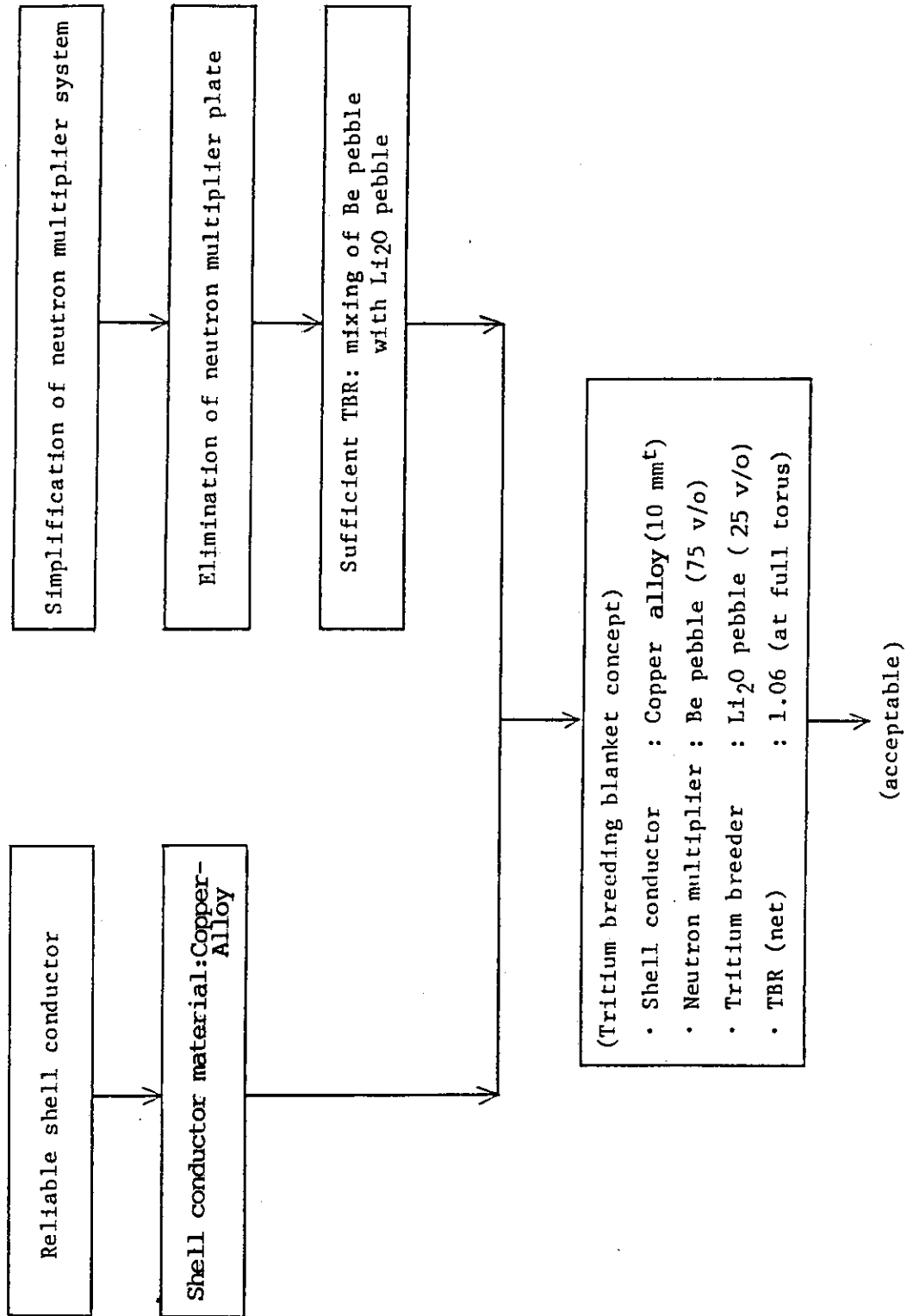


Fig. 11.2-3 Flow chart of breeding blanket simplification  
- shell conductor and neutron multiplier zone -

### 11.3 Design Description

#### 11.3.1 First Wall/Blanket Concept

Major design parameters of the first wall/tritium producing blanket (batch tritium recovery) are summarized in Tables 11.3-1 and 11.3-2. And the concept of the blanket is illustrated in Fig. 11.3-1. The first wall is integrated with a blanket vessel from the viewpoints of tritium breeding performance and structural simplicity. Rectangular coolant channel, which has a good cooling performance, is adopted for the first wall. And the channels run in toroidal direction for being expected their reinforcement effect to the internal pressure of the blanket vessel. Titanium modified austenitic stainless steel (PCA) and helium ( $100^{\circ}\text{C} \sim 300^{\circ}\text{C}$ , 4 MPa) are selected as structural material and coolant, respectively. The first wall includes the thickness of 2 mm eroded by sputtering with  $3 \text{ MW}\cdot\text{y}/\text{m}^2$  of neutron fluence.

Tritium producing blanket is installed in outer and top region of torus. In outer region, passive shell conductor of saddle type is provided for plasma vertical stabilization. Copper alloy (Cu-1.8Ni-0.3Be) of 30 mm thickness is chosen as a material of the shell conductor from the viewpoints of good fabricability and less sensitivity of mechanical property and electrical conductivity to neutron irradiation. This shell conductor is supported by second wall which is structurally integrated to and reinforces the first wall.

The number of blankets is 12 which is equal to the number of TF coils. And the width of a blanket module is decided also in consideration of maintainability and the performance of the shell conductor. The blanket has an internal wall in the toroidal center in order to stand its internal pressure.

The concept of tube-in-shell, BOT (Breeder Out of Tube), is selected for the blanket as illustrated in Fig. 11.3-2. Solid tritium breeder and neutron multiplier both in small spherical form are uniformly mixed and packed around cooling tubes. Lithium oxide ( $\text{Li}_2\text{O}$ ) is selected as the breeder material for its good breeding and thermal performances. And beryllium (Be) is selected as the neutron multiplier for its good neutronics and thermal performances.

Spherical forms of  $\text{Li}_2\text{O}$  and Be and 1 mm diameter for both spheres are adopted in order to avoid thermal crack and make it easy to fill them in the blanket.

Cooling tubes in the blanket run in poloidal direction. And the coolant is helium as same as the first and second walls. Temperature of the breeder is maintained below the maximum allowable temperature ( $1000^{\circ}\text{C}$ ) by proper arrangement of cooling tubes.

Tritium produced in the blanket is recovered in batch-mode after a certain period of plasma operation. During tritium recovery, a heater provided in cooling system is used to rise helium coolant temperature up to  $450^{\circ}\text{C}$ . Breeder material in the blanket is heated by this helium coolant up to the temperature required for tritium recovery. And another stream of helium gas purges and recovers the produced tritium from the blanket.

### 11.3.2 Blanket Support and Piping

#### (1) Blanket Support Structure

The tritium producing blanket is supported by the removable shield which is withdrawn together with it.

The blanket must be effectively supported against gravity, electromagnetic and seismic loads that will be encountered during the life of blanket. Furthermore, the support structure must be designed to release the thermal stress due to temperature difference between the blanket and the removable shield.

##### a) Design Conditions

The study of the blanket support structure is based on the following conditions:

##### (i) Weight and center of gravity of blanket

The blanket is about 30 tons in weight having its center of gravity at point G in Fig. 11.3-3.

##### (ii) Electromagnetic load

Electromagnetic loads act upon it as very large pulsed forces and torques during plasma disruption. The dominant electromagnetic forces are induced in the shell conductor region. Values of those are shown in Fig. 11.3-4.

##### (iii) Structural material temperatures

Since the maximum temperature difference between blanket and shield will be reached during batch tritium recovery operation. Structural material temperatures for thermal expansion are considered under that condition. Temperatures of the blanket and the shield were assumed to be 450°C and 50°C, respectively.

##### b) Support Structure

The blanket support structures are shown in Figs. 11.3-5 and 11.3-6. Support structures consist of a main-support and sub-supports. For supporting only dead weight, the most effective approach is to suspend it at the point over its center of gravity. But the main-support is provided near upper shell conductor in consideration of limited space between blanket and removable shield in upper region and also of supporting large electromagnetic forces. Its support is connected rigidly with the removable shield by bolts and a key. The sub-supports jugged from header box are connected with the shield by bolts. Bolt holes of them are larger than the diameter of the bolt to allow the thermal expansion of the blanket. In addition, some beams projected from center of the blanket end wall are inserted into the shield so that the blanket will not move toroidally.

## (2) Piping

Piping for the blanket has been designed with the following items:

- to permit thermal expansion
- to prevent neutron streaming
- to prevent thermal radiation loss from surfaces of pipes

Piping from the blanket to the access door is shown in Fig. 11.3-7. Temperature of coolant pipes will reach as high as 450°C during batch tritium recovery operation. So bellows are installed at penetration of the access door to absorb thermal expansion of pipes. And gaps between pipes and the shield are provided not to restrain pipes through the removable shield. Pipe penetration in the shield is prepared near the main-support to minimize the gap width.

To prevent the neutron streaming through pipes of helium coolant, coolant pipes are covered with duct shield outside the removable shield.

Thermal insulator such as layered-metal type is prepared around the coolant pipes in order to reduce thermal radiation loss from those surfaces.

### 11.3.3 Blanket Maintenance Concept

The removal concept of blanket is illustrated in Fig. 11.3-8. Number of blanket modules is equal to that of TF coils, and each blanket is replaced together with removable shield in a single straight-line radial motion. The removable shield is supported with support shelf provided in permanent shield. And as shown in Fig. 11.3-9, a part of the first wall whose erosion is negligible small is specified as permanent component in order to reduce the requirement of the maintenance.

Those concepts are developed based on a new design approach with a reliable, feasible and simple maintenance scheme described in detail in 12.4.3.

Table 11.3-1 Major Design Parameters of the First Wall  
of Tritium Producing Blanket  
(Batch Tritium Recovery)

---

Configuration	Integral with Blanket
Form	Ribbed Pannel
Structural Material	Titanium-modified Stainless Steel (PCA)
Coolant	Helium Gas
Flow Direction	Toroidal
Inlet Pressure	4.0 MPa
Inlet Temperature	100 °C
Outlet Temperature	300 °C
Maximum Velocity	63 m/s
Pressure Losses	<150 kPa
Total Pumping Power	30 MW
Wall Thickness	
Beginning-of-life	12.5 mm
End-of-life	10.5 mm
Coolant Channel	
Geometry	Rectangular
Size	5 mm <sup>w</sup> x 5 mm <sup>h</sup>
Pitch	7.5 mm
Maximum Wall Temperature	
during Normal Operation	400 °C

---

Table 11.3-2 Major Design Parameters of Tritium Producing Blanket (Batch Tritium Recovery) (1/2)

Blanket Type	Tube-in-Shell Type(BOT)
Thickness(including F/W)	50 cm
Location	Outboard and Top
Structure Material	Titanium-modified Stainless Steel (PCA)
Breeding Region	
Breeder	$\text{Li}_2\text{O}$ (natural)
Form	Spherical Pebble
Diameter	1 mm
Neutron Multiplier	Beryllium
Form	Spherical Pebble
Diameter	1 mm
Mixing Ratio	25v/o- $\text{Li}_2\text{O}$ /75v/o-Be
Packing Fraction	0.7(bulk) 0.3(near wall)
Acceptable Temperature Range	<1000 °C
Operating Temperature Range	100 °C - 600 °C
Minimum Temperature Control	none
Maximum Temperature Control	Proper Arrangement of Cooling Tube
Shell Conductor	Copper Alloy(Cu-Be-Ni)
Type	Saddle
Thickness	30 mm
Coolant	He
Inlet Pressure	4.0 MPa
Inlet/Outlet Temperature	100 °C/300 °C
Flow Direction	Poloidal
Tube ID/OD	20 mm/ 24 mm
Velocity	72 m/s
Pressure Loss	<150 kPa

Table 11.3-2 Major Design Parameters of Tritium Producing  
Blanket (Batch Tritium Recovery) (2/2)

---

Tritium Breeding Ratio	
Net TBR	0.61
Local TBR	1.56(without Cu Alloy)
	0.95(with Cu alloy)
Tritium Recovery	Discontinuous
Purge Gas	Helium
Pressure	0.1 MPa
Flow Rate	2400 Nm <sup>3</sup> /hr
Recovery Cycle	6 times per full- power operation of 1 yr
Recovery Time	1 day
Temperature	450 °C

---



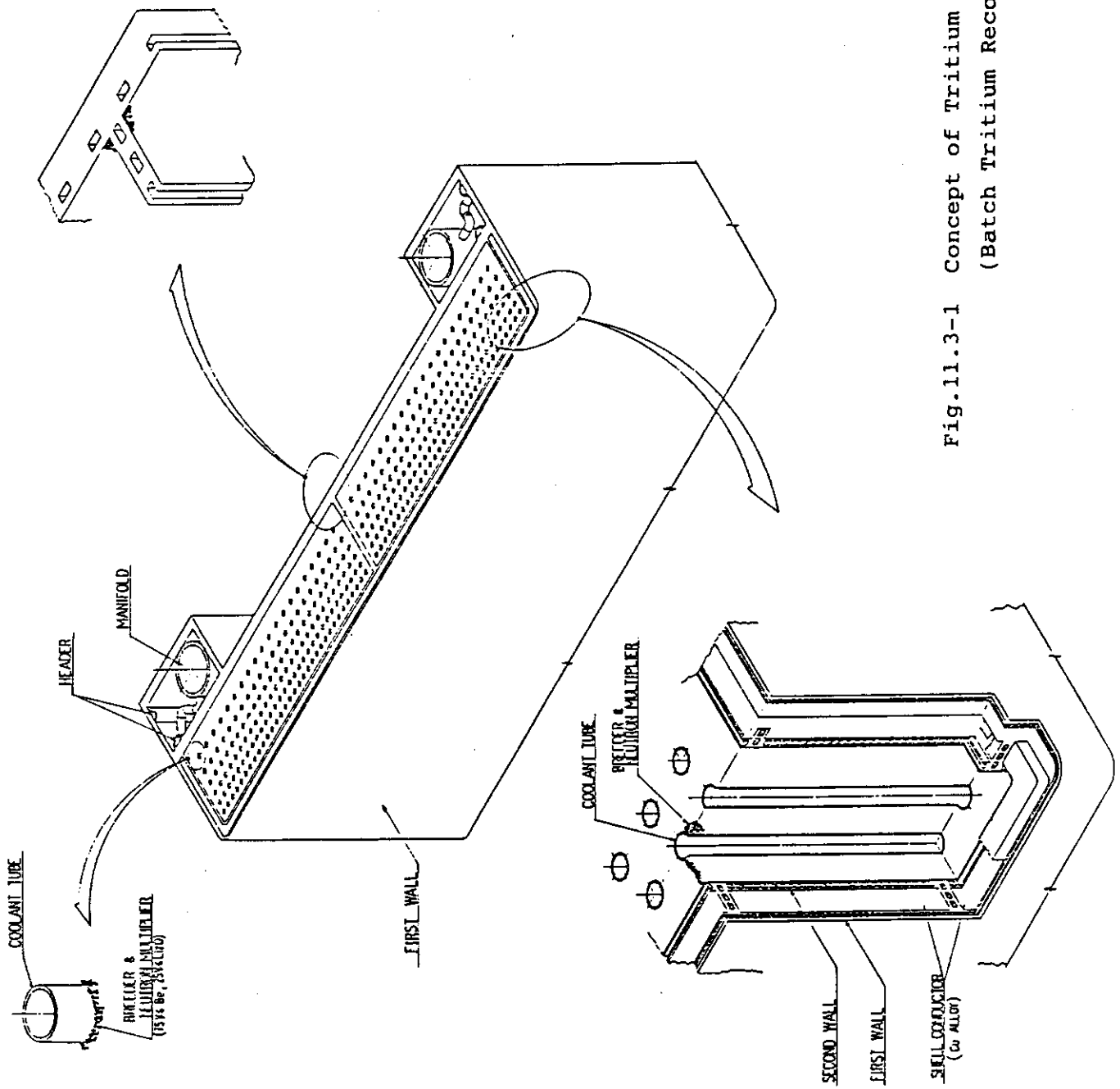
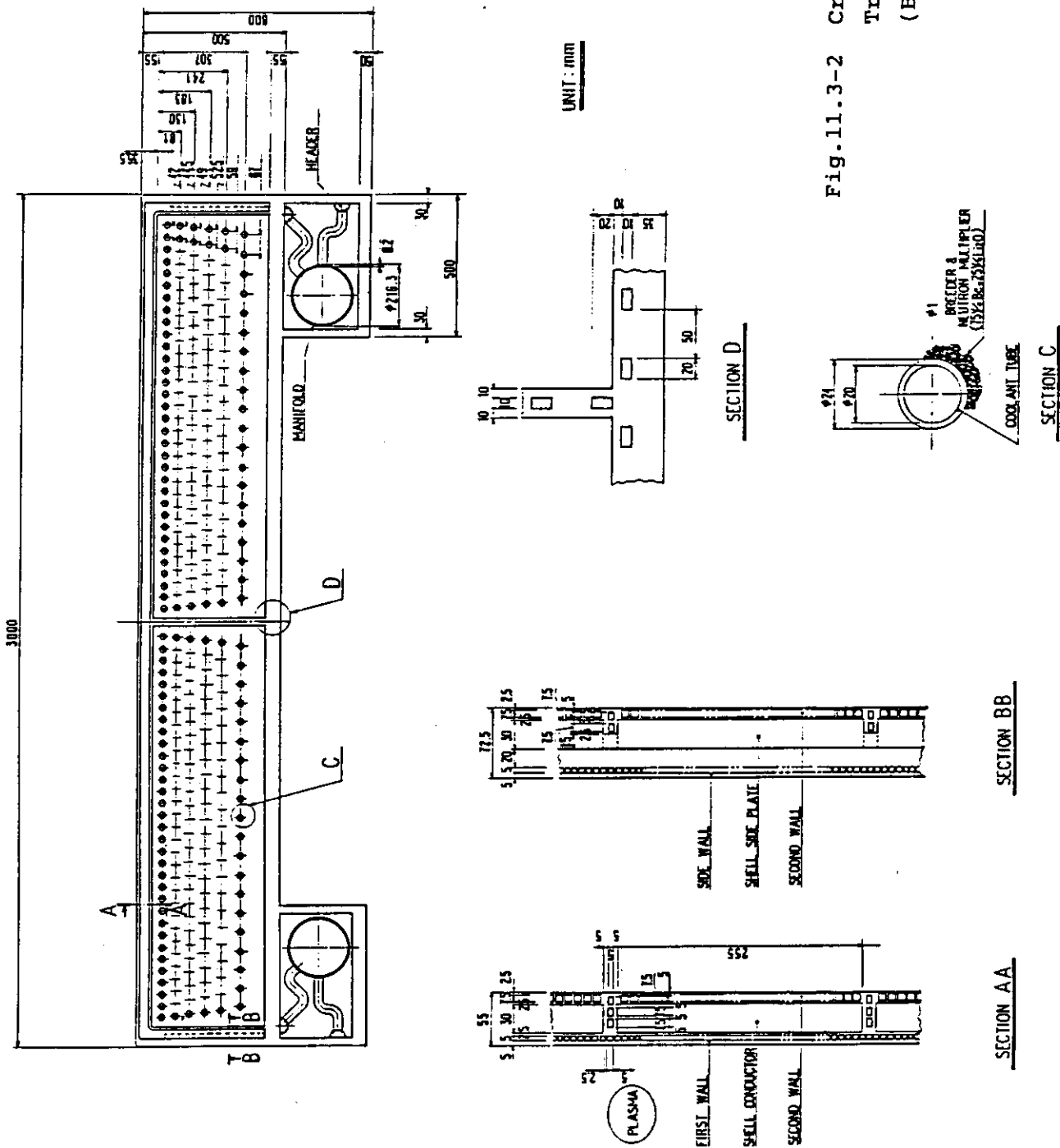


Fig.11.3-1 Concept of Tritium Producing Blanket  
(Batch Tritium Recovery)



**Fig. 11.3-2 Cross-Section of Tritium Producing blanket (Batch Tritium Recovery)**

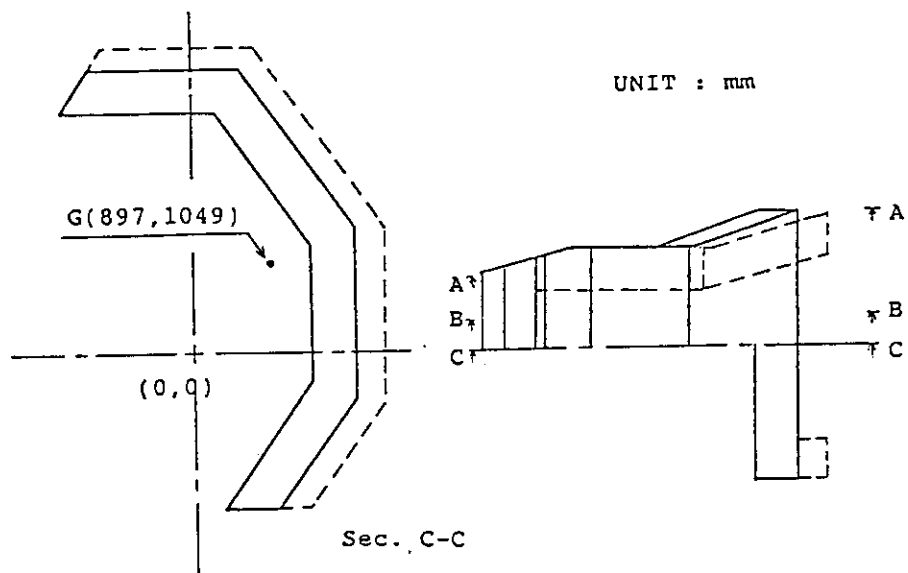


Fig. 11.3-3 Center of Gravity of Blanket.

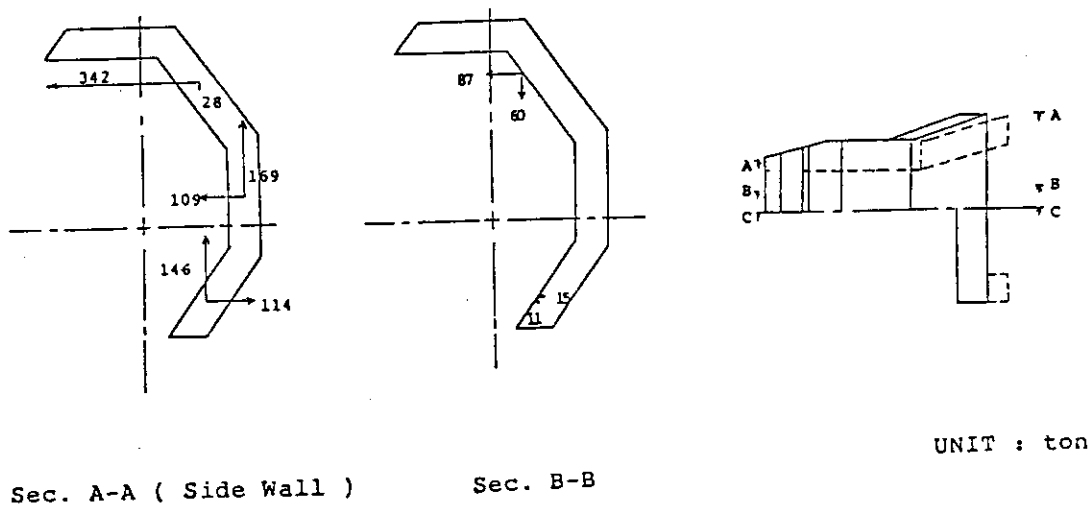


Fig. 11.3-4 Electromagnetic Loads of Blanket Shell Conductor.

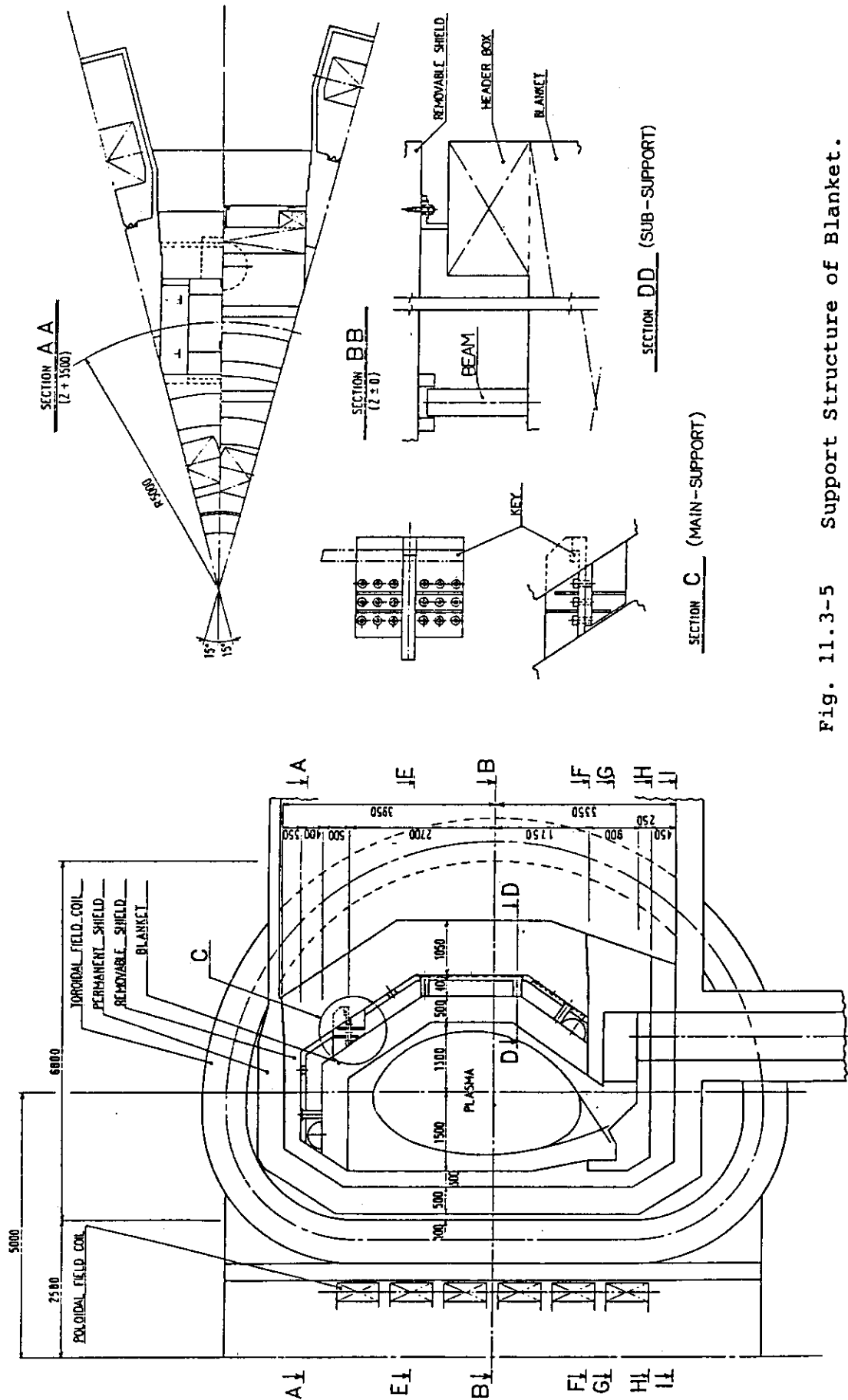


Fig. 11.3-5 Support Structure of Blanket.

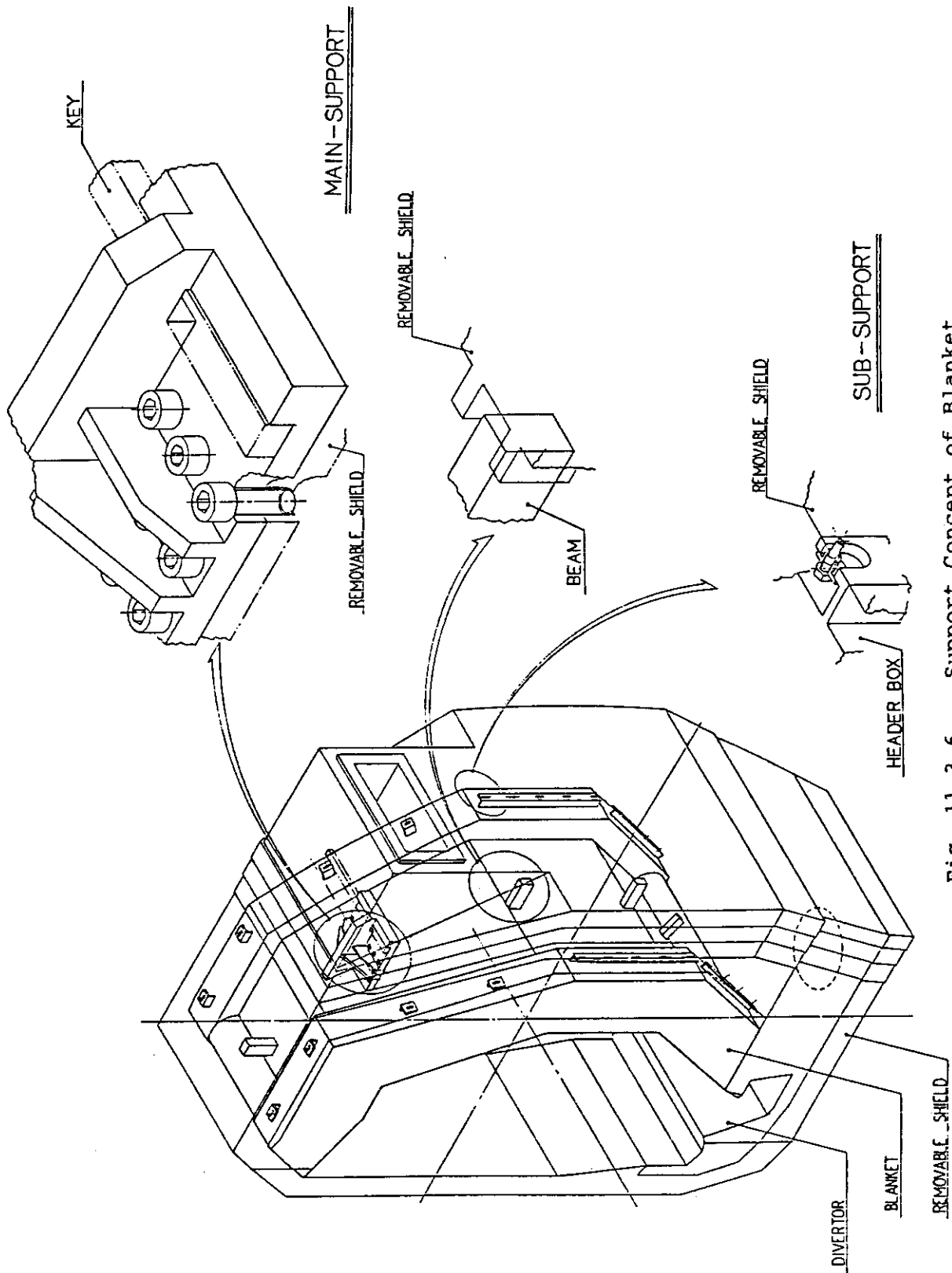


Fig. 11.3-6 Support Concept of Blanket.

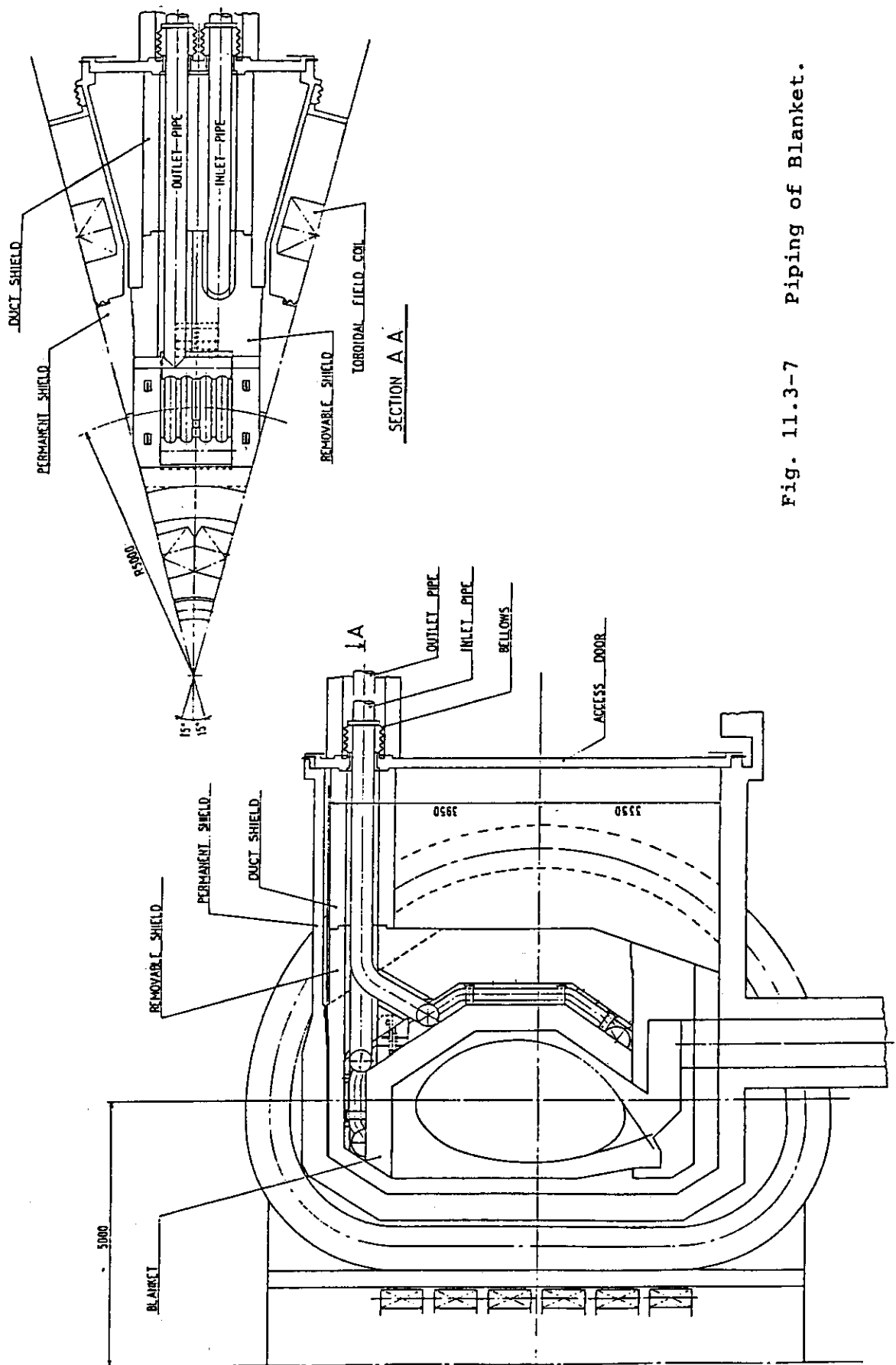


Fig. 11.3-7 Piping of Blanket.

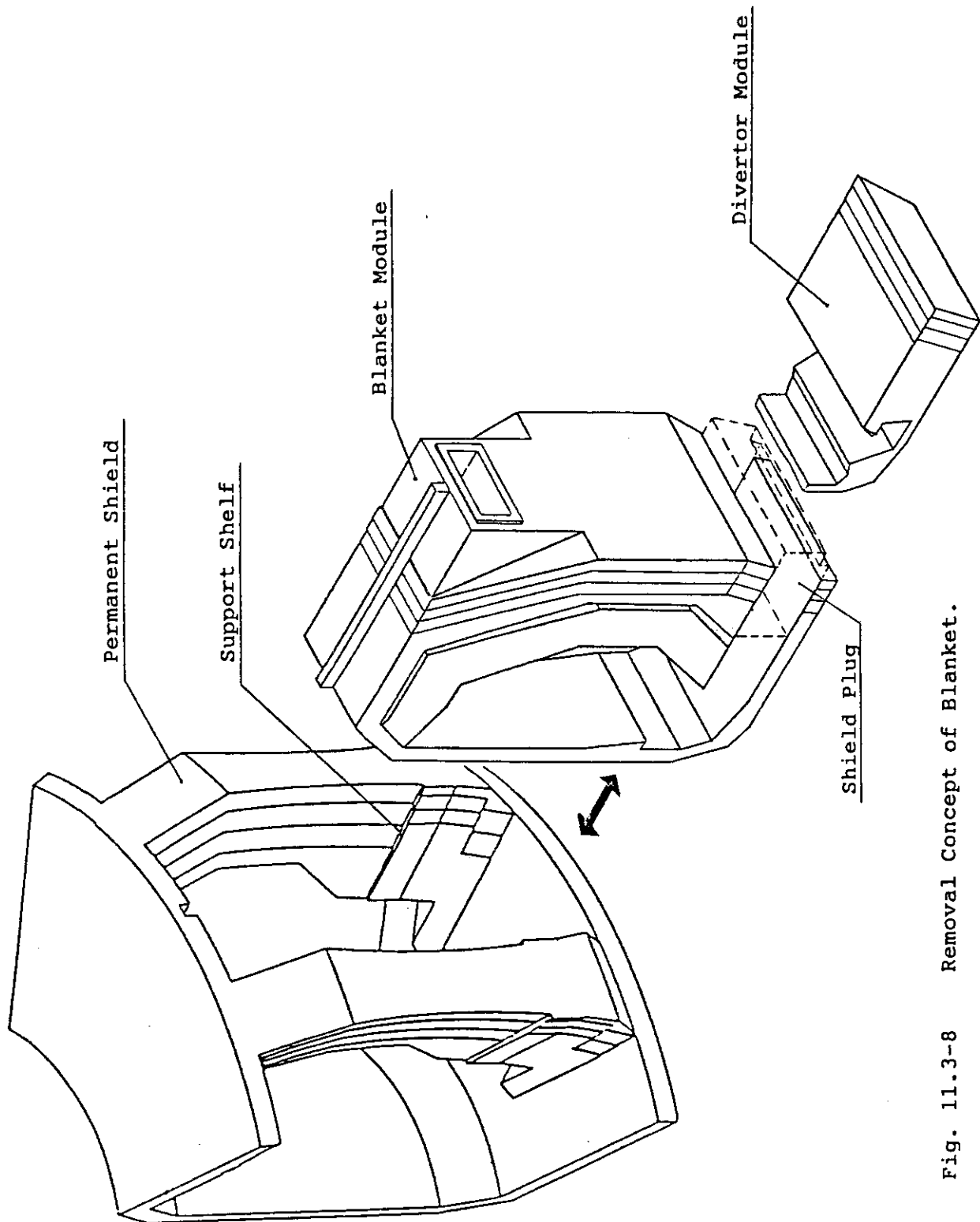


Fig. 11.3-8 Removal Concept of Blanket.

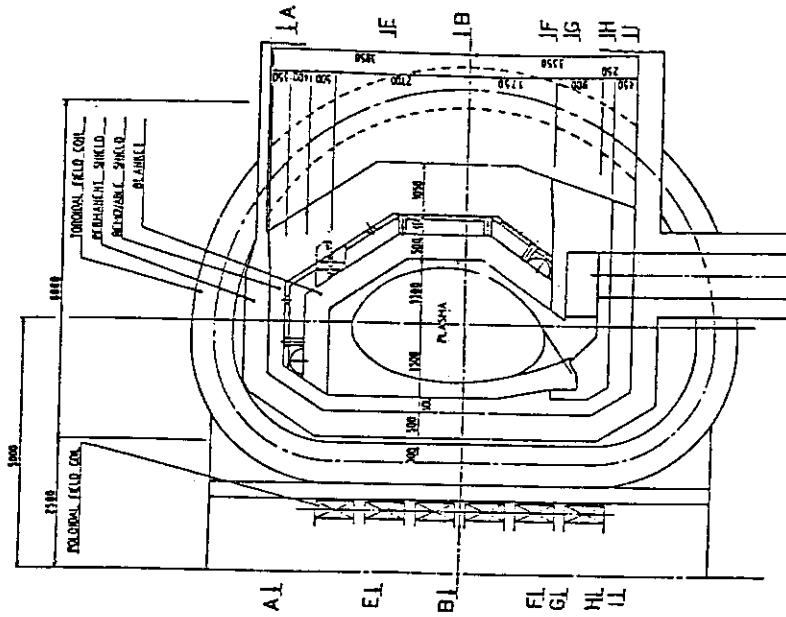
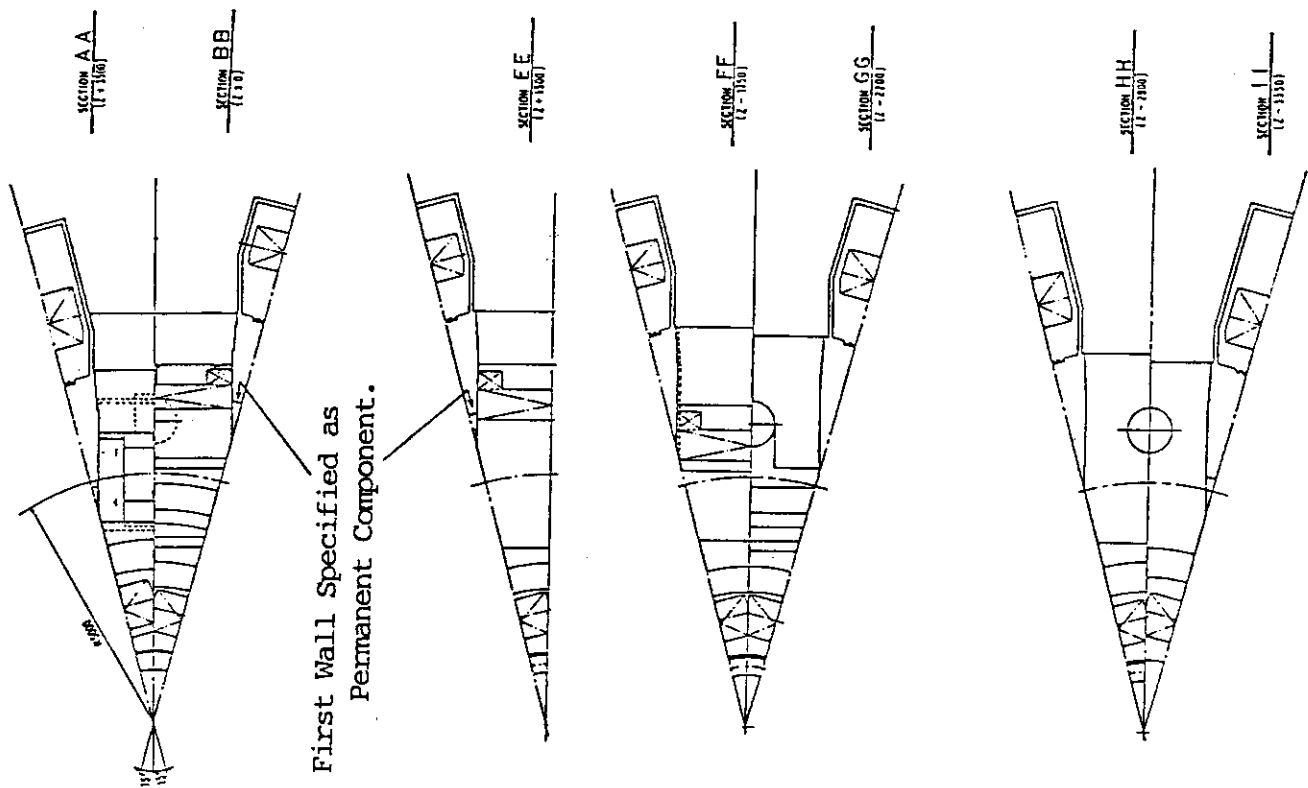


Fig. 11.3-9 Concept of Torus Configuration.



#### 11.4 Neutronics Analysis

In order to investigate tritium breeding and nuclear heating performances, parametric neutronics analyses have been carried out for batch-type tritium producing blanket.

##### (1) Analytical method and model

###### a) Analytical method

Neutronics analyses have been performed using one dimensional transport (SN) code, ANISN (-Apple 2), with infinite cylindrical model and  $S_8-P_5$  approximation. Coupled 42-group neutron and 21-group gamma-ray cross section sets (GICX40) based on the End F/B-III and IV nuclear data files were used in the analyses. Neutron wall load is  $1.24 \text{ MW/m}^2$ .

###### b) Analytical model

Blanket consists of typical two regions which are with shell conductor and without it. Therefore, the following two geometrical models were considered for ANISN:

- non-shell model for the region without shell conductor
- shell model for the region with shell conductor

Geometry of shell model is shown in Fig. 11.4-1. Geometry of non-shell model is almost the same as the shell model except for void region instead of shell conductor.

The following conditions were taken into consideration:

- (i) First wall is ribbed panel type.
- (ii) Breeder is lithium oxide ( $\text{Li}_2\text{O}$ ) pebble (85% T.D.). Breeder region in the blanket is filled with mixture of  $\text{Li}_2\text{O}$  pebbles and beryllium (Be) pebbles as neutron multiplier. The mixing ratio of  $\text{Li}_2\text{O}$  and Be has to be optimized to obtain high tritium breeding ratio (TBR). Figure 11.4-2 shows the dependency of TBR on the mixing ratio of Be. It is seen from the figure that optimized mixing ratio can exist between 70% and 90% of Be mixing ratio. In this blanket design, taken the burn-up effects of lithium atom into account, the mixing of Be-75%/Li<sub>2</sub>O-25% was adopted. Packing fraction of  $\text{Li}_2\text{O}$  and Be pebbles in breeder region is 70%.
- (iii) Although structural material is PCA, data of type 316 stainless steel are used in the analyses because the effect of minute inclusions within PCA is considered to be small.
- (iv) Coolant is helium gas.
- (v) Second wall is provided for supporting shell conductor and reinforcing first wall.
- (vi) Copper alloy (Cu-Be-Ni) of 30 mm thickness is selected as shell conductor material. Properties of pure Cu, however, are used in the analyses.

## (2) Results and discussion

## a) Local tritium breeding ratio

Table 11.4-1 summarizes the analytical results for the non-shell model. The local TBR for each case is remarkably high to be greater than 1.4. Figure 11.4-3 shows the dependency of TBR on effective thickness of stainless steel (first wall and second wall). The increase of the stainless steel thickness in 1 mm causes the TBR decrease in  $1.9 \times 10^{-2}$ . When mixed Be-Li<sub>2</sub>O pebbles are filled in a gap region between first wall and second walls (30 mm) with 70% packing fraction (Case A-3), the increase of TBR is at most 0.049. In practice, the packing fraction in the gap region will be lower than 70% because of wall effects of first and second walls. And, much improvement of TBR will not be expected. On the contrary, the penalty of structural complexity must be paid for charging breeder pebble into the gap region. Therefore, the gap is remained to be avoid region in this design. From above discussion, the reference batch-type tritium producing blanket is designed to contain the mixture of Be-75%/Li<sub>2</sub>O-25% in breeder region and void region between first and second walls. The thickness of first and second walls are 12.5 mm each for the reference design as shown in Fig. 11.4-4. Local TBR of non-shell region in this reference case (Case A-5 in Table 11.4-1) reaches up to 1.56.

Table 11.4-2 summarizes the results of calculation for the shell model. When the gap region of Case A-1 in Table 11.4-1 is replaced by shell conductor (Cu alloy), the TBR decreases from 1.43 to 0.91 (Case B-1). Figure 11.4-5 shows the effect of shell conductor thickness on TBR. If the thickness of shell conductor is decreased from 30 mm to 20 mm, the TBR increases to 1.04 (Case B-2). The decrease of the shell conductor thickness in 1 mm results in a TBR increase in  $1.35 \times 10^{-2}$ . The local TBR of shell conductor region in the reference batch-type blanket is 0.95 (Case B-3).

## b) Net tritium breeding ratio

Net TBR has been estimated using local TBR obtained above and effective coverage of blanket. The following items were assumed to evaluate the effective coverage:

- (i) The number of RF launchers is five. And width of 1.3 m and height of 1.5 m is considered for the area of each launcher.
- (ii) Permanent shield between blanket modules and side wall region of blanket are also considered as non-breeding region.

Table 11.4-3 shows the effective blanket coverage. As shown in this table, net TBR of 0.61 is obtained for reference INTOR design in which tritium breeding blanket is installed in top and out region of torus.

This batch-type blanket has high tritium breeding performance as described above. If this high performance tritium producing blanket is installed in full torus region, more than unity of net TBR can be obtained as shown in Table 11.4-3.

## c) Nuclear heating rate

The distribution of nuclear heating rates in stainless steel and  $\text{Li}_2\text{O}/\text{Be}$  for region without shell conductor are shown in Fig. 11.4-6 and Fig. 11.4-7, respectively. The maximum nuclear heating rate is 14.4 W/cc in stainless steel on first wall surface, and 7.83 W/cc in  $\text{Li}_2\text{O}/\text{Be}$ . In this case, the energy multiplication is 1.32.

For region with shell conductor, the maximum nuclear heating rates in shell conductor and in breeder are 15.1 W/cc and 4.72 W/cc, respectively. The energy multiplication is 1.18 in this case.

## (3) Conclusions

- (i) The local TBR in the region without shell conductor is 1.56 and in the region with shell conductor 0.95 for this batch-type tritium producing blanket.
- (ii) Net TBR of 0.61 can be obtained by installing this tritium producing blanket in outer and top regions of torus, which meets INTOR requirement.
- (iii) The installation of this high performance batch-type blanket in full torus region can bring net TBR of more than unity.

Table 11.4-1 Calculated TBR for Be.Li<sub>2</sub>O Mixed Blanket - Non-Shell Model -

Case No	First Wall Thickness (mm)	Gap Region* Materials	Thickness (mm)	Second Wall Thickness (mm)	Li <sup>6</sup> Enrichment in Breeder	T <sub>6</sub>	T <sub>7</sub>	Total
A-1	5 + 5 + 5	—	30	5 + 5 + 5	Natural	1.365	0.066	1.431
A-2	5 + 5 + 5	—	20	5 + 5 + 5	Natural	1.382	0.067	1.449
A-3	5 + 5 + 5	Li <sub>2</sub> O.Be	30	5 + 5 + 5	Natural	1.409	0.071	1.480
A-4	5 + 5 + 5	---	30	5 + 5 + 5	30 %	1.460	0.050	1.510
A-5	5 + 5 + 2.5	—	30	2.5+7.5+2.5	Natural	1.478	0.078	1.556

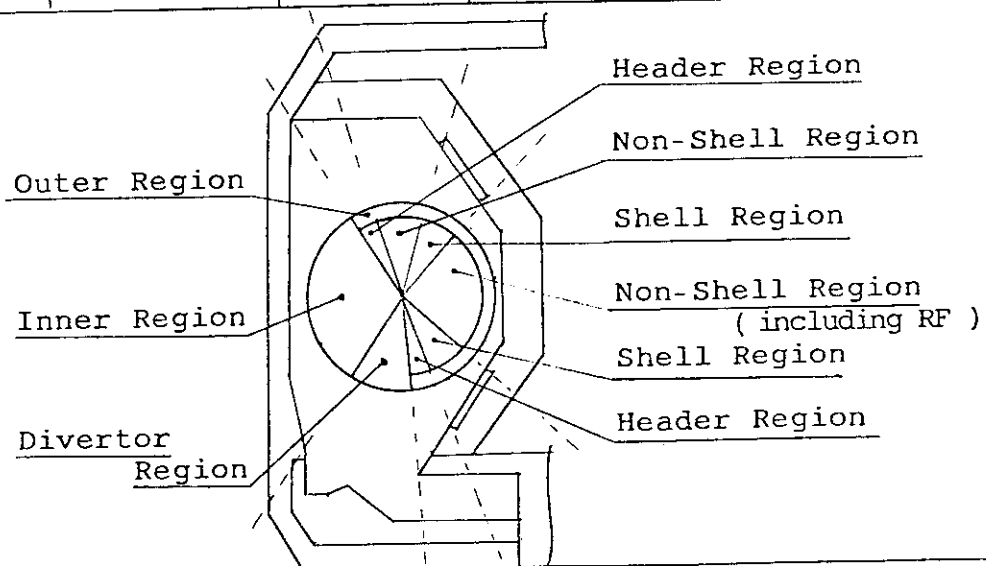
Gap Region\* = Region Between FW and SW

Table 11.4-2 Calculated TBR for Be.Li<sub>2</sub>O Mixed Blanket - SHELL Model -

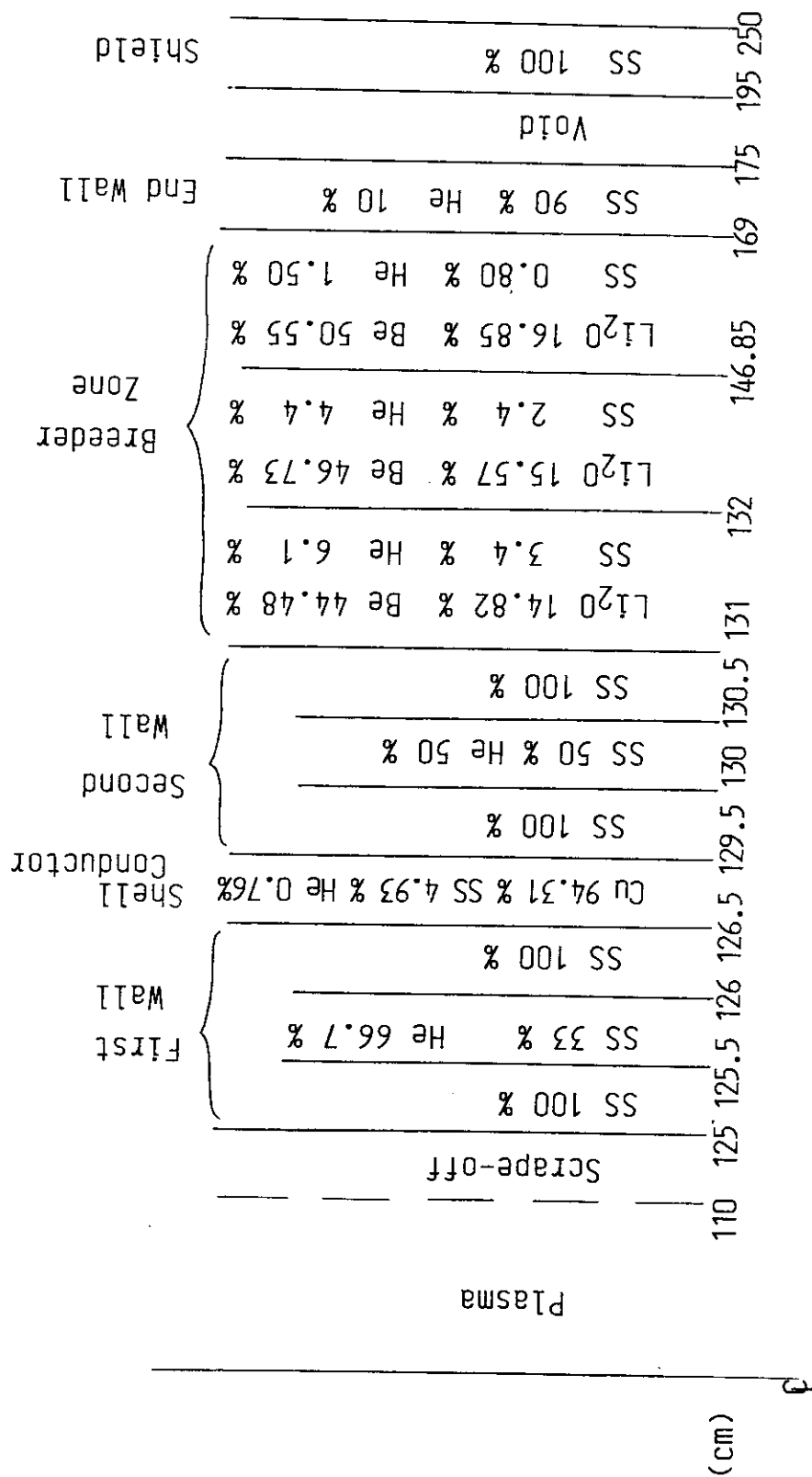
Case No	First Wall Thickness (mm)	Shell Plate Materials	Thickness (mm)	Second Wall Thickness (mm)	Li <sup>6</sup> Enrichment	T <sub>6</sub>	T <sub>7</sub>	Total
B-1	5 + 5 + 5	Cu	30	5 + 5 + 5	Natural	0.869	0.037	0.906
B-2	5 + 5 + 5	Cu	20	5 + 5 + 5	Natural	0.996	0.045	1.041
B-3	5 + 5 + 2.5	Cu	30	2.5+7.5+2.5	Natural	0.908	0.043	0.951

Table 11.4-3 The coverage and net TBR

Region			Coverage	Breeding region	Local TBR	Net TBR
Outer	Non-Shell	Breeder	0.283	0.283	1.556	0.61 (1.01)*
		Header	0.074			
		Side Wall	0.025			
		Permanent Shield	0.038			
		R F	0.051			
	Shell	Breeder	0.176	0.176	0.951	
		Side Wall	0.010			
		Permanent Shield	0.020			
Inner		Breeder	0.227	0 (0.227)*	0 (1.556x0.95 = 1.478)*	
		Side Wall	0.013			
Divertor		Breeder	0.079	0 (0.079)*	0 (1.556x0.5 = 0.778)	
		Side Wall	0.004			



\* in the case of the blanket installation in full torus region.

Fig.11.4-1 Calculated Model for Be/Li<sub>2</sub>O Mixture Zone Blanket

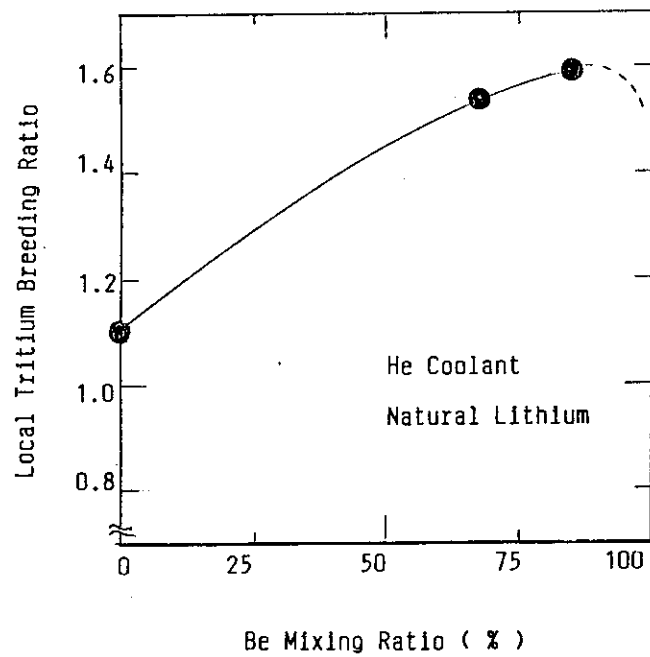


Fig.11.4-2 Dependence of Tritium Breeding Ratio on Be Mixing Ratio

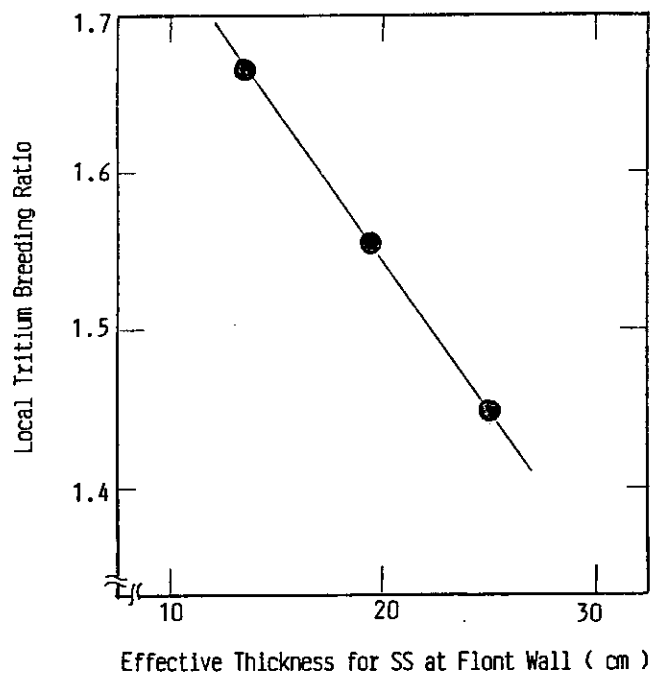


Fig.11.4-3 Effect of Front Wall (first Wall to Second Wall) Thickness on Tritium Breeding Ratio

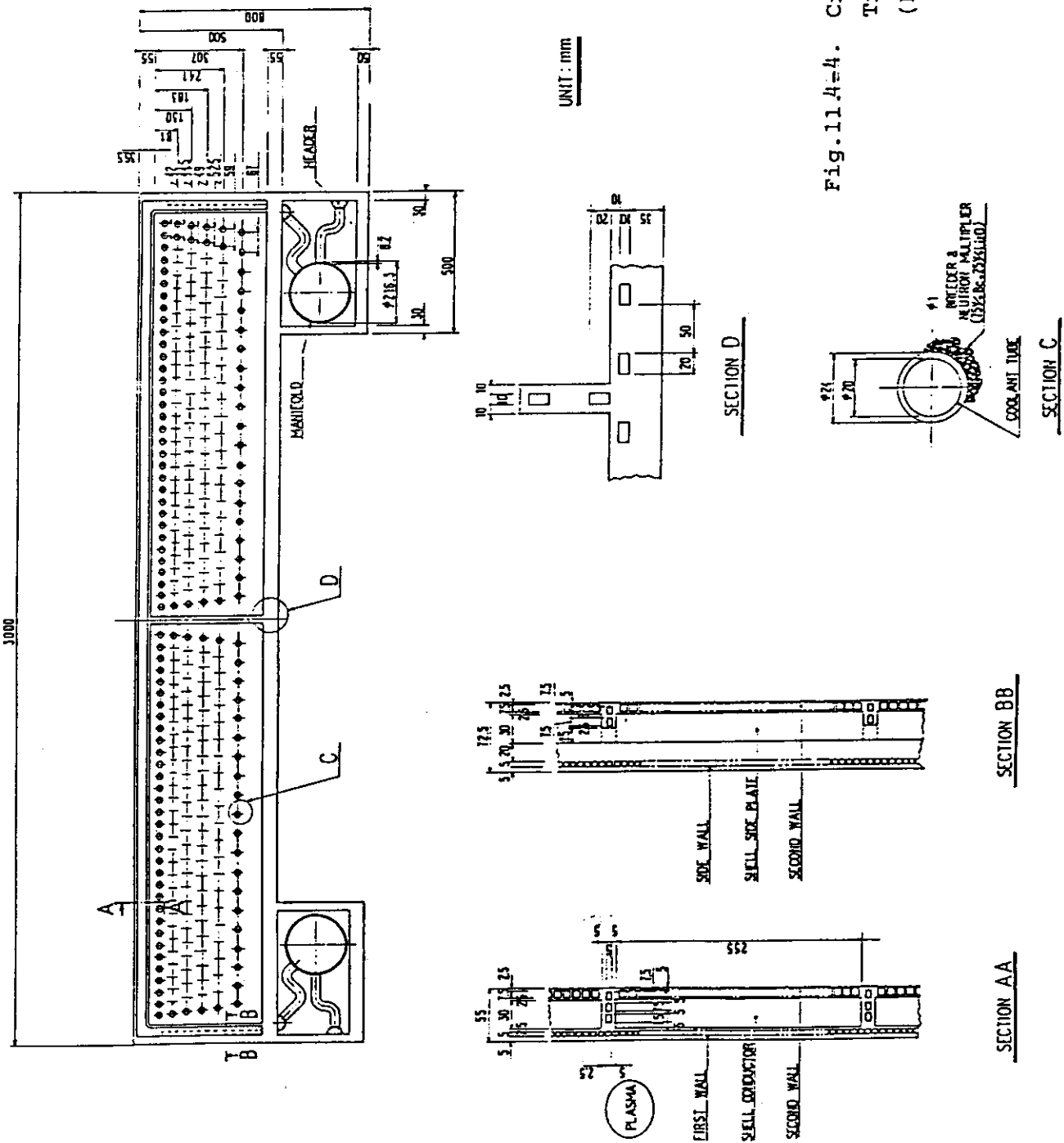


Fig.11.4=4. Cross-Section of  
Tritium Producing blanket  
(Batch Tritium Recovery)



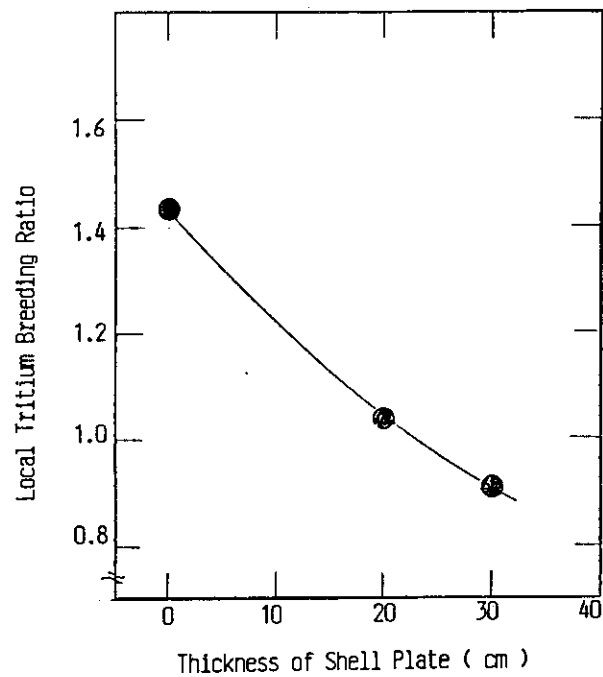
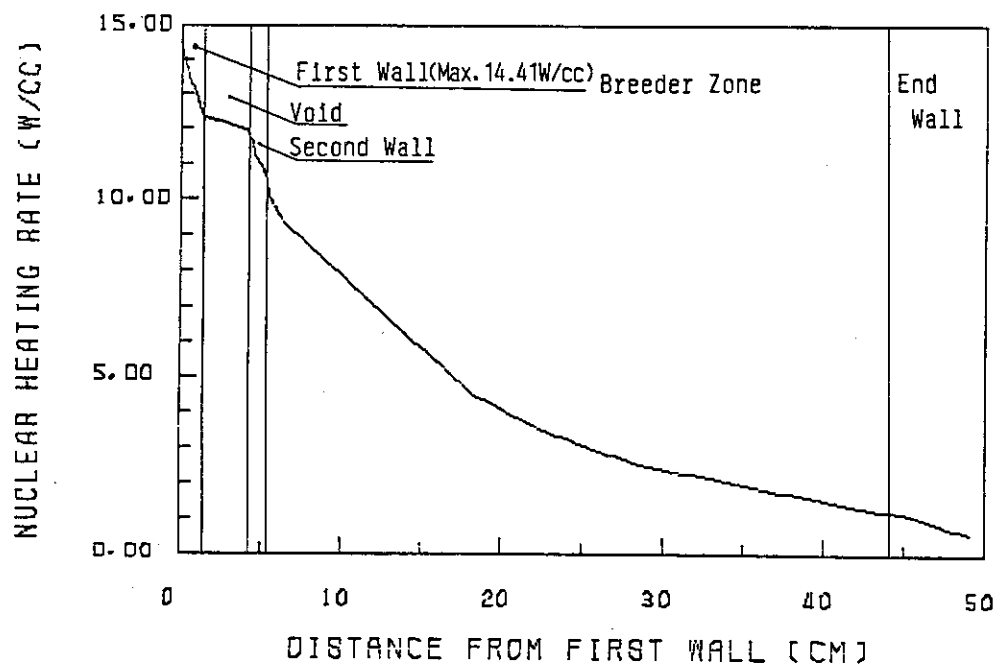


Fig. 11.4-5 Effect of Shell Thickness on Tritium Breeding Ratio

Fig. 11.4-6 Nuclear Heating Rates Distribution for SS  
in Tritium Breeding Blanket - He Cooled -

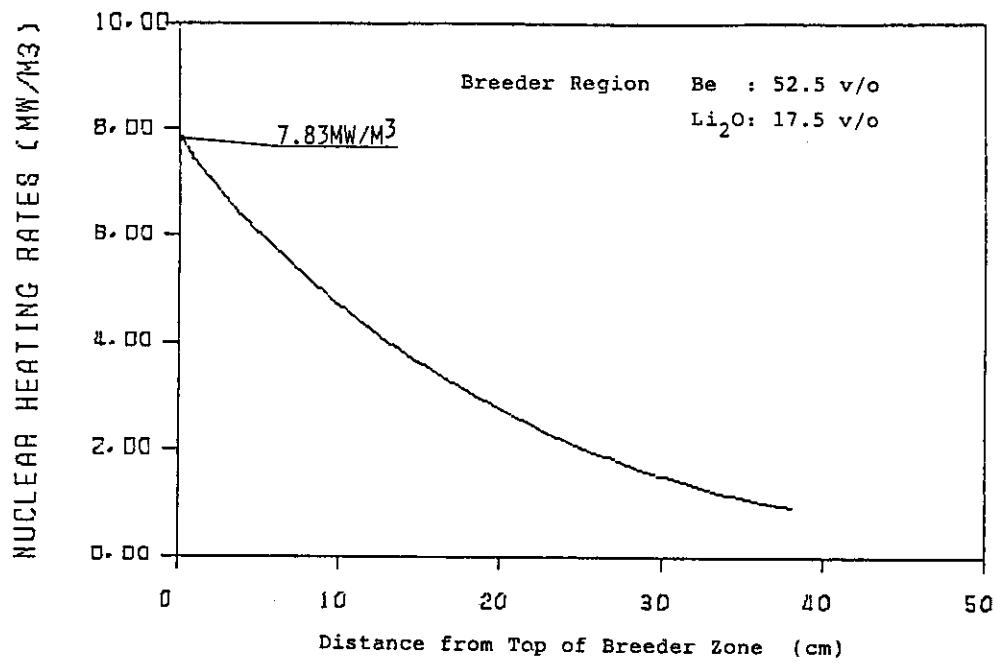


Fig. 11.4- 7 Nuclear Heating Rates Distribution of Breeder Region  
in Tritium Breeding Blanket - He cooled -

## 11.5 Thermal-hydraulic Analysis

### (1) Physical sputtering erosion

Heat load and particle load conditions of first wall are summarized in Table 11.5-1. Physical sputtering erosion thickness for stainless steel first wall was evaluated using these conditions.

#### (i) uniform distribution

As shown in Table 11.5-1, sputtering rate for stainless steel wall is  $2.3 \times 10^{18}$  atoms/m<sup>2</sup>/s with uniform flux and energy of charge exchange particles. Erosion thickness is, therefore, about 2.1 mm during the reactor lifetime of 3 MW-y/m<sup>2</sup>.

#### (ii) exponential distribution

Considering charge exchange particle flux distribution, it is expected that erosion thickness is maximized at the null point ( $Z = 0$ ) and reduces exponentially along poloidal field. The erosion thickness is about 4.1 mm at the null point, and about 1.2 mm at the bottom of the blanket region ( $Z = 0.3$  m). In the upper region ( $Z > 1.0$  m), it will be less than 0.1 mm. The maximum erosion thickness of the first wall integrated with the tritium producing blanket is, therefore, 1.2 mm. Armor materials may be necessary for the near divertor wall.

From the results of these investigations shown in Fig. 11.5-1, the first wall is designed to include the thickness of 2 mm for sputtering erosion during the reactor lifetime.

### (2) Thermal-hydraulic performances of first wall

Thermal-hydraulic analyses for the first wall have been carried out, and some thermal-hydraulic performances and the two dimensional temperature profile were clarified. In these analyses, steady state heat load conditions were assumed, because of long plasma burn time.

The maximum coolant velocity at the exit, the pressure loss, the maximum film temperature drop and the maximum temperature of the wall are summarized in Table 11.5-2. Coolant flow area and channel pitch of the first wall are also shown in the table. Coolant flows in toroidal direction between manifolds located behind the blanket end wall. A value of 4 m is assumed as the length of coolant channels. The pressure loss includes friction, entrance and exit losses. A value of 0.03 was used as the friction factor of coolant channels in consideration of surface roughness. The entrance and exit loss coefficients were assumed to be 0.5 and 1.0, respectively. Temperature profile in the first wall was obtained from a two dimensional thermal analysis. A model for the analysis and the result are shown in Figs. 11.5-2 and 11.5-3. It is considered that the maximum limits of coolant velocity, pressure loss and temperature of structural material are about 100 m/s, 150 kPa and 450°C, respectively. The thermal-hydraulic performances of this first wall shown in Table 11.5-2 satisfy the above design limits.

The heat generated in the shell conductor is removed by the coolant in the second wall. Performances of the second wall and other parts of blanket vessel were also evaluated, and they satisfy thermal-hydraulic requirements in the blanket design.

### (3) Disruption analysis

Thermal behaviors of the first wall during major plasma disruption were evaluated with a disruption analysis code. It was assumed that a plasma disruption occurred during plasma burning and the wall was being cooled by helium gas at 300°C. The initial temperature at the wall surface was, therefore, estimated to be about 400°C under the conditions of normal plasma operation. Since the first wall with tritium producing blanket is located in the part of outer and top of torus, the energy flux will be smaller than the peak energy flux. In this study, however, the value of the peak energy flux was used in consideration of uncertainty of the distribution for energy dissipation.

Disruption parameters and results of this analysis are summarized in Table 11.5-3, and the surface temperature responses during plasma disruption are shown in Fig. 11.5-4. Two cases of disruption time were considered. For the reference case, 20 msec of disruption time, the melt layer thickness is predicted to be about 20  $\mu\text{m}$  and the vaporized thickness is very small. For the alternative case, 5 msec of disruption time, they are about 100  $\mu\text{m}$  and 2  $\mu\text{m}$ , respectively. These values are almost correspond to those of water cooled first wall investigated for Phase 2A Part 1.

### (4) Thermal-hydraulics design of breeder region during normal operation

The breeder region of this blanket consists of homogeneously mixed  $\text{Li}_2\text{O}$  and beryllium pebbles. Mixing ratio of  $\text{Li}_2\text{O}$  and beryllium are 25% and 75% respectively, and the diameter of the pebbles are both 1 mm. Packing fraction is assumed to be 70% in bulk region and 30% in near wall region. The density of  $\text{Li}_2\text{O}$  is 85% T.D. and  $^6\text{Li}$  is not enriched. A blanket vessel is filled with helium gas at 0.1 MPa. Effective thermal conductivities shown in Fig. 11.5-5 were used for thermal analyses of breeder region.

Coolant for breeder region is helium gas that flows poloidally in tubes made of titanium modified stainless steel. Inlet pressure of coolant is 4 MPa, and the temperatures at the inlet and outlet are 100°C and 300°C, respectively. The length of coolant tubes is about 7 m. Adequate arrangement of coolant tubes in the blanket maintains the maximum temperature of breeder lower than 600°C. Since tritium produced in blanket is not recovered continuously, minimum temperature control is unnecessary in this blanket.

Although small diameter of coolant tubes is preferable to avoid the reduction of packed density due to wall effects, there is the limit from the view points of pressure loss and coolant velocity. Coolant tube pitches, friction losses and maximum coolant velocities have been calculated with various sizes of coolant tubes. The tube inner diameter

larger than about 17 mm is required to keep the value of friction loss less than 150 kPa and the maximum velocity less than 100 m/s as shown in Fig. 11.5-6. Coolant tubes with 20 mm of inner diameter and 2 mm of tube thickness were selected in this blanket design.

The arrangement with the coolant tube selected above is illustrated in Fig. 11.5-7. The maximum operating temperature is kept lower than 600°C to maintain integrity of breeder and neutron multiplier, sufficiently. The coolant tubes were arranged for a steady state condition to keep the temperature lower than the limit for any mode of plasma operation. The number of coolant tubes in a module is 322 in 6 tube arrays, and the pitches of tubes are between 42 mm and 67 mm.

Transient thermal analysis of breeder region has been carried out with cylindrical breeder unit cell models for the first and last coolant tube arrays. It was assumed that the duration of plasma burning is 1000 seconds and dwell time is 240 seconds with RF current drive. Responses of breeder temperature are shown in Fig. 11.5-8. It is found from the figure that the maximum breeder temperature in the blanket during normal operation is about 550°C. The temperature of breeder rises quickly, and the same temperature responses are repeated from the second pulse.

The thermal-hydraulic performances of the breeder region were evaluated in the same manner as the calculations for the first wall. Results of these calculations are summarized in Table 11.5-3. As shown in the table, the maximum velocity and the pressure loss are sufficiently small, and it is expected that the film temperature drop also cause no thermal-hydraulic and thermo-mechanical problems.

The results of this thermal-hydraulics design of breeder region indicate the good applicability of this blanket to INTOR.

##### (5) Heat-up of breeder region for batch tritium recovery

In this blanket design, tritium produced in blanket is recovered with helium purge gas stream during the reactor shutdown. Breeder must be heated up over 400°C for tritium recovery. Time required for heat-up of blanket was clarified from the results of transient thermal analysis. Breeder is heated up with helium gas in the primary cooling system shown in Fig. 11.5-9. Helium gas in the primary loop is heated by the heater between the circulator and the blanket, and bypasses coolers during tritium recovery. Inlet gas temperature rises from 50°C to 450°C by steps of 50°C an hour. The analysis has been carried out with cylindrical unit cell models for the first and last coolant tube arrays in the breeder region and the blanket end wall. Radiative heat loss to the shield at 50°C is considered for the model of blanket end wall.

Temperature responses at the outermost of exit side of unit cells are illustrated in Fig. 11.5-10. This figure shows that it is applicable to heat up by steps of 50°C an hour even in the rear breeder region in the blanket that will be heated up most slowly. In the end wall, the temperature will saturate at 434°C due to radiative heat loss. It is, however, high enough for tritium recovery. These results indicate that this heat-up method is applicable for tritium recovery of this type of blanket.

Table 11.5-1 Heat Load and Particle Load Conditions  
of First Wall

---

Radiation ( uniform distribution )	49 MW
Charge Exchange ( uniform/exponential distribution )	1 MW
Total Flux Density of C-X atoms	$1 \times 10^{20} \text{ 1/m}^2/\text{s}$
Sputtering Rate from Stainless Steel Wall for Uniform C-X Distribution	$2.3 \times 10^{18} \text{ a/m}^2/\text{s}$
Sputtering by Charged Particles	negligible
Ripple Alpha Particle Loss	not considered
First Wall Area	$375 \text{ m}^2$
Neutron Wall Load	$1.24 \text{ MW/m}^2$
Reactor Lifetime	$3 \text{ MW-y/m}^2$
Surface Heat Flux	$0.133 \text{ MW/m}^2$
Volumetric Heating Rates	$15 \text{ MW/m}^3$

---

Table 11.5-2 Thermal-hydraulic Performances of First Wall

Channel Area	5 mm <sup>w</sup> x 5 mm <sup>d</sup>
Channel Pitch	7.5 mm
Maximum Velocity	63 m/s
Re	39600
Nu	92
Heat Transfer Coefficients	3990
Maximum Film Temperature Drop	46 °C
Pressure Loss	142 kPa
Maximum Temperature of Wall	388 °C

Table 11.5-3 Surface Behaviors of First Wall during Major Plasma Disruption -peak-

Material	type 316 stainless steel	
Plasma Side Wall Thickness	5 mm	
Total Energy Flux	170 J/cm <sup>2</sup>	
Disruption Time	5 msec	20 msec
Maximum Surface Temperature	2770 K	1810 K
Maximum Melt Layer Thickness	99 μm	23 μm
Vaporized Thickness	1.7 μm	0.01 μm
Time of Melting Start	1.0 msec	15.8 msec
Time of Melting Terminate	12.3 msec	21.0 msec
Duration of Surface Melting	11.3 msec	5.2 msec

Table 11.5-4 Thermal-hydraulic Performances of Breeder Region in Tritium Producing Blanket

Tube Array No.	Maximum Coolant Velocity (m/s)	Pressure Loss (kPa)	Re	Nu	Heat Transfer Coefficient (W/m <sup>2</sup> K)	Film Temperature Drop (°C)
1	72	87	181000	311	3320	45
2	65	71	163000	287	3060	45
3	60	61	151000	270	2880	46
4	52	47	132000	242	2590	45
5	46	37	117000	219	2340	45
6	40	27	102000	197	2110	45



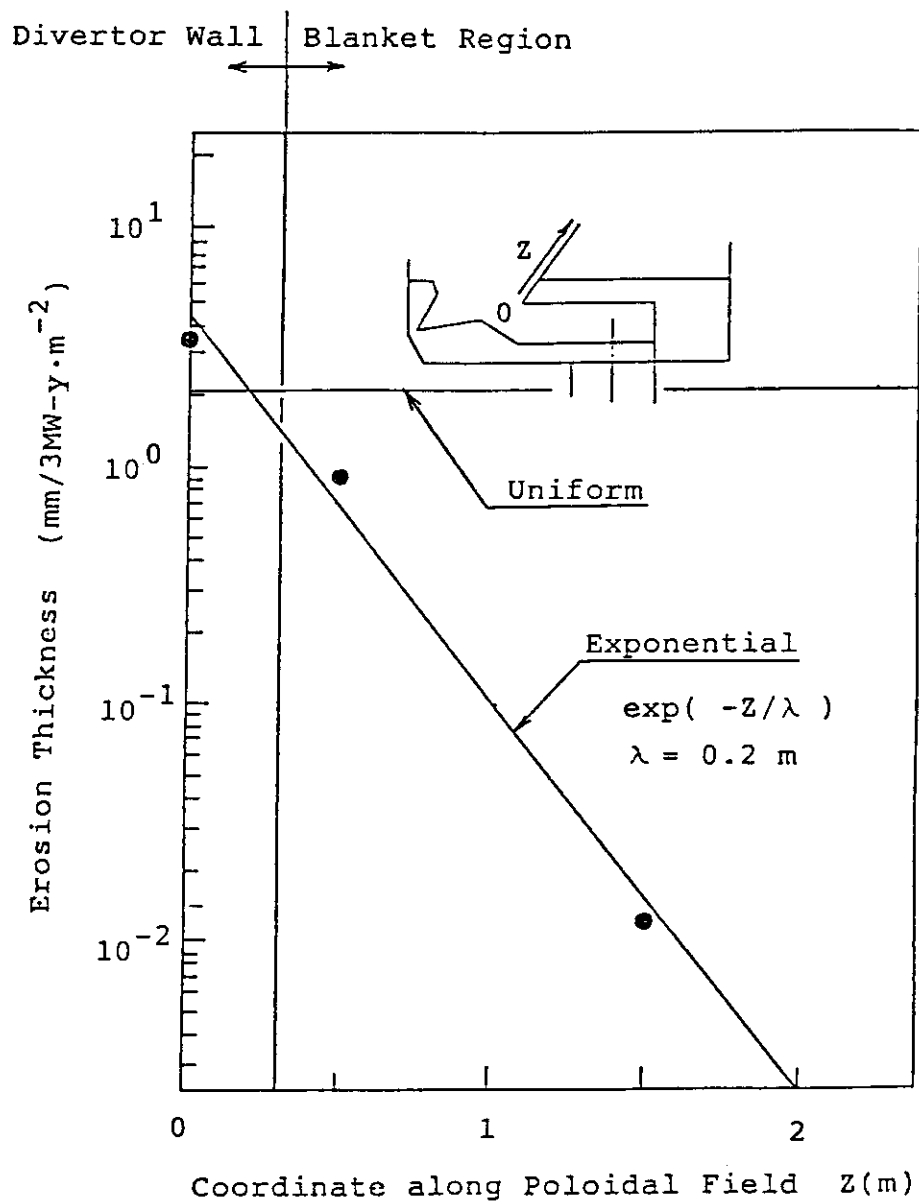


Fig. 11.5-1 Erosion Thickness of Stainless Steel First Wall

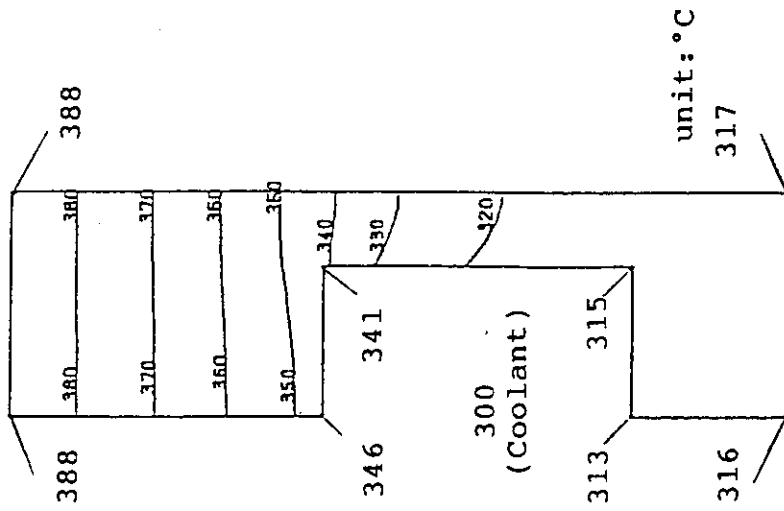


Fig. 11.5-3 Temperature Profile in First Wall

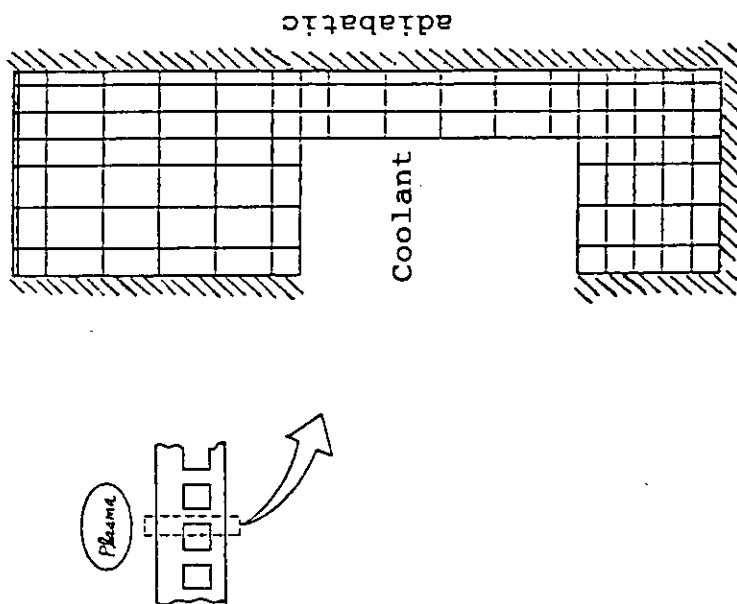


Fig. 11.5-2 Analytical Model

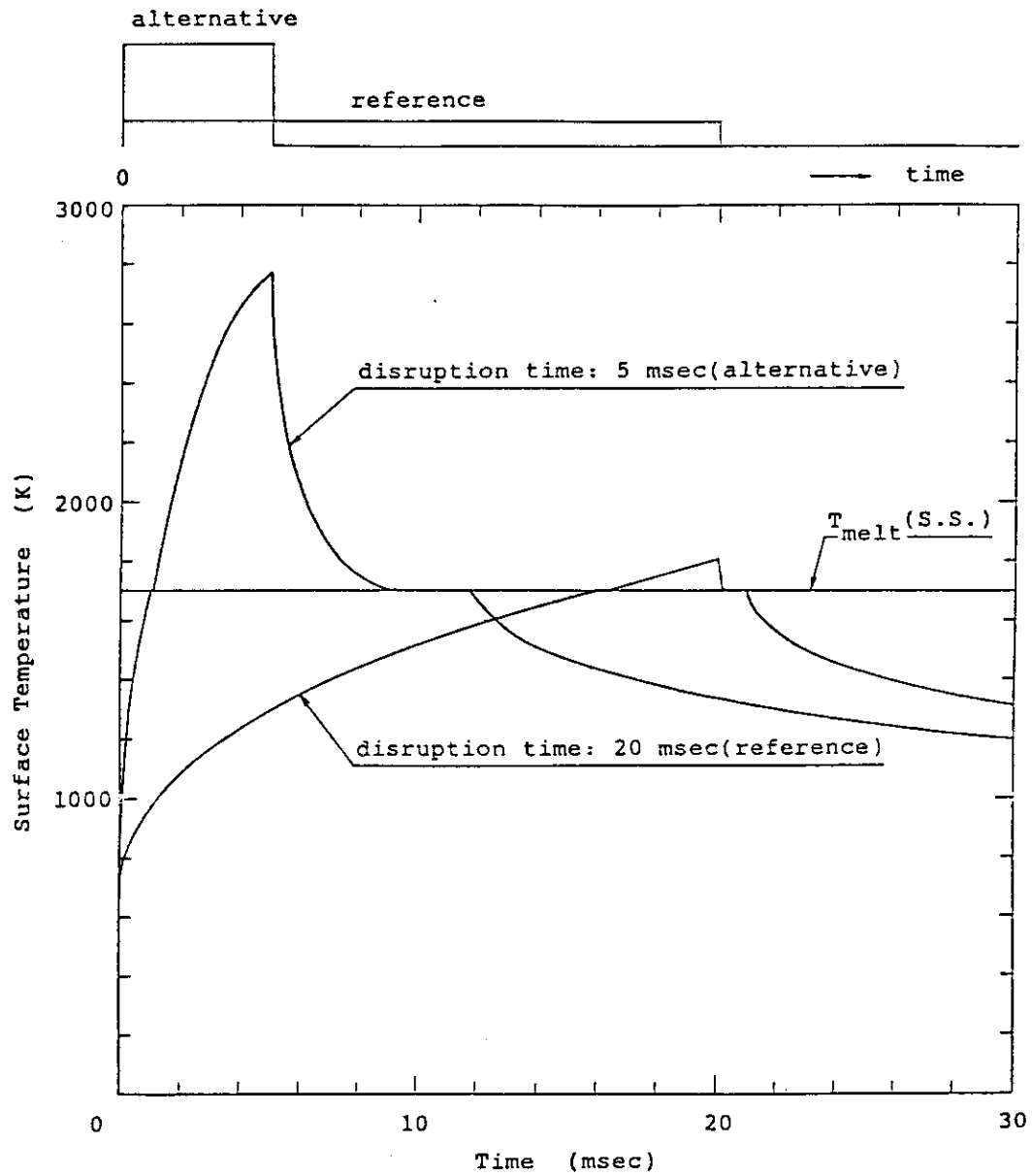


Fig. 11.5-4 Surface Temperature Responses of First Wall during Major Plasma Disruption

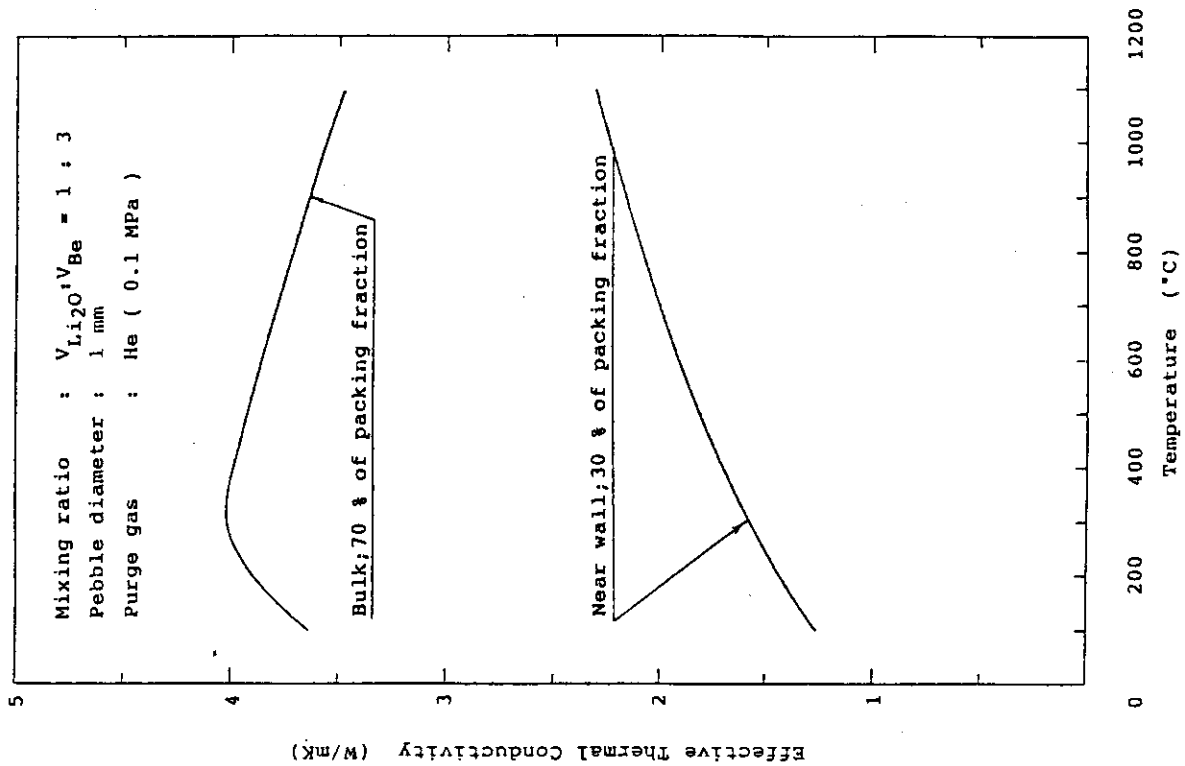


Fig. 11.5-5 Effective Thermal Conductivities of Breeder

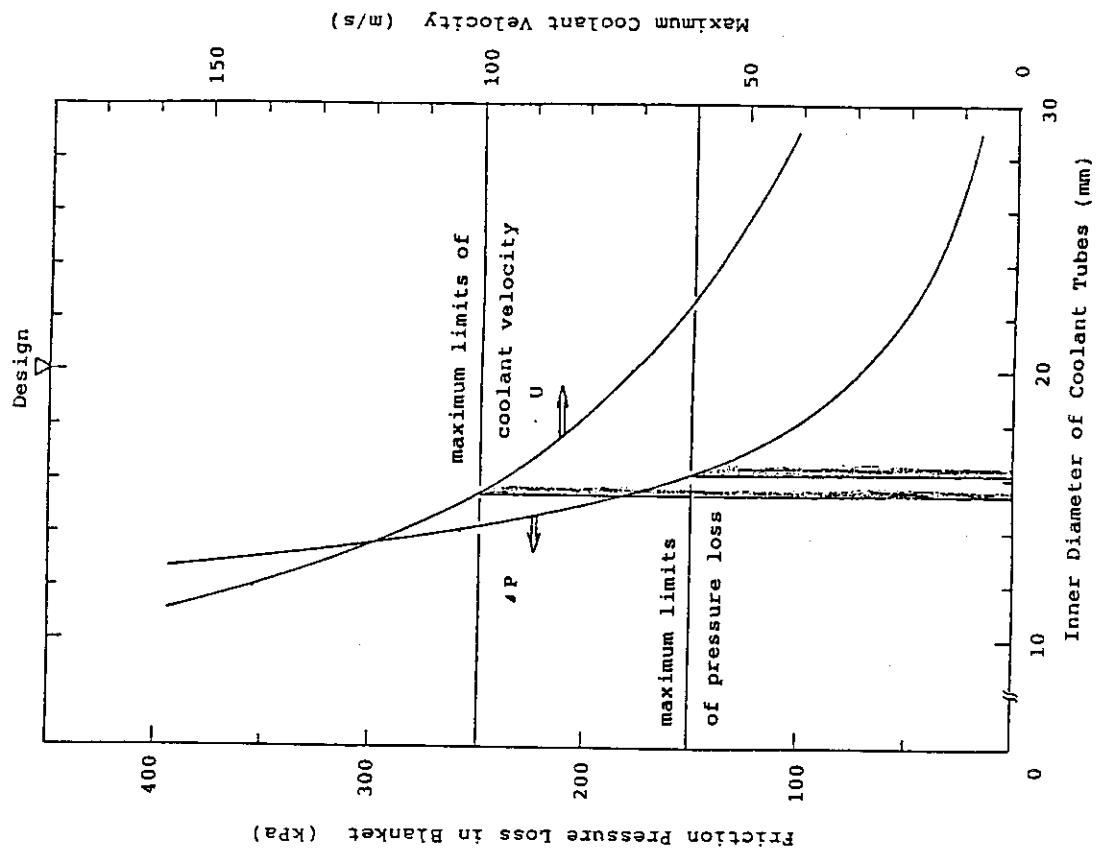


Fig.11.5-6 Friction Pressure Loss and Maximum Coolant Velocity in Tritium Producing Blanket

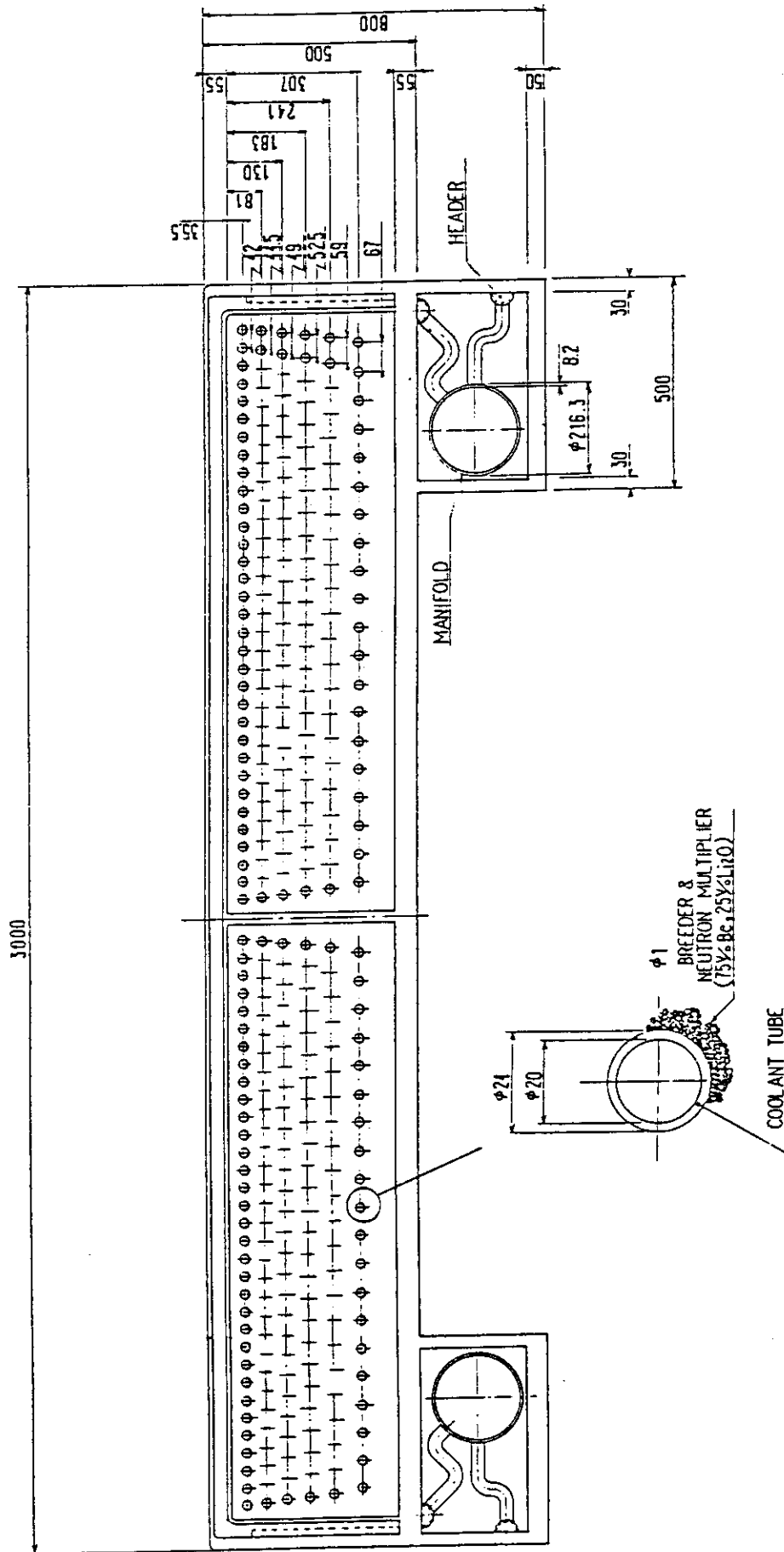


Fig. 11.5-7 Arrangements of Coolant Tubes in Tritium Producing Blanket  
- in the mid-plane -

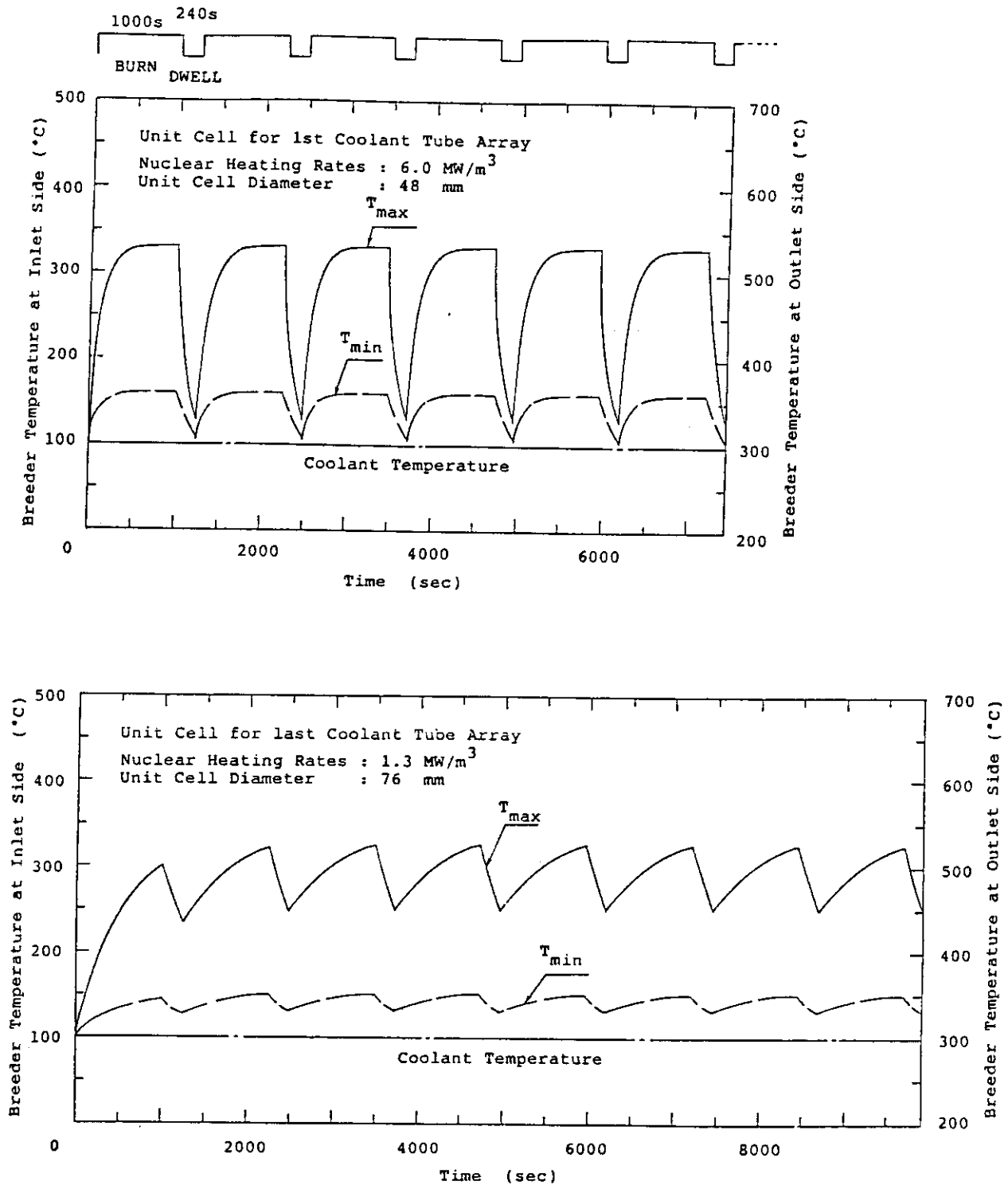


Fig. 11.5-8 Breeder Temperature Responses in Tritium Producing Blanket during Normal Operation

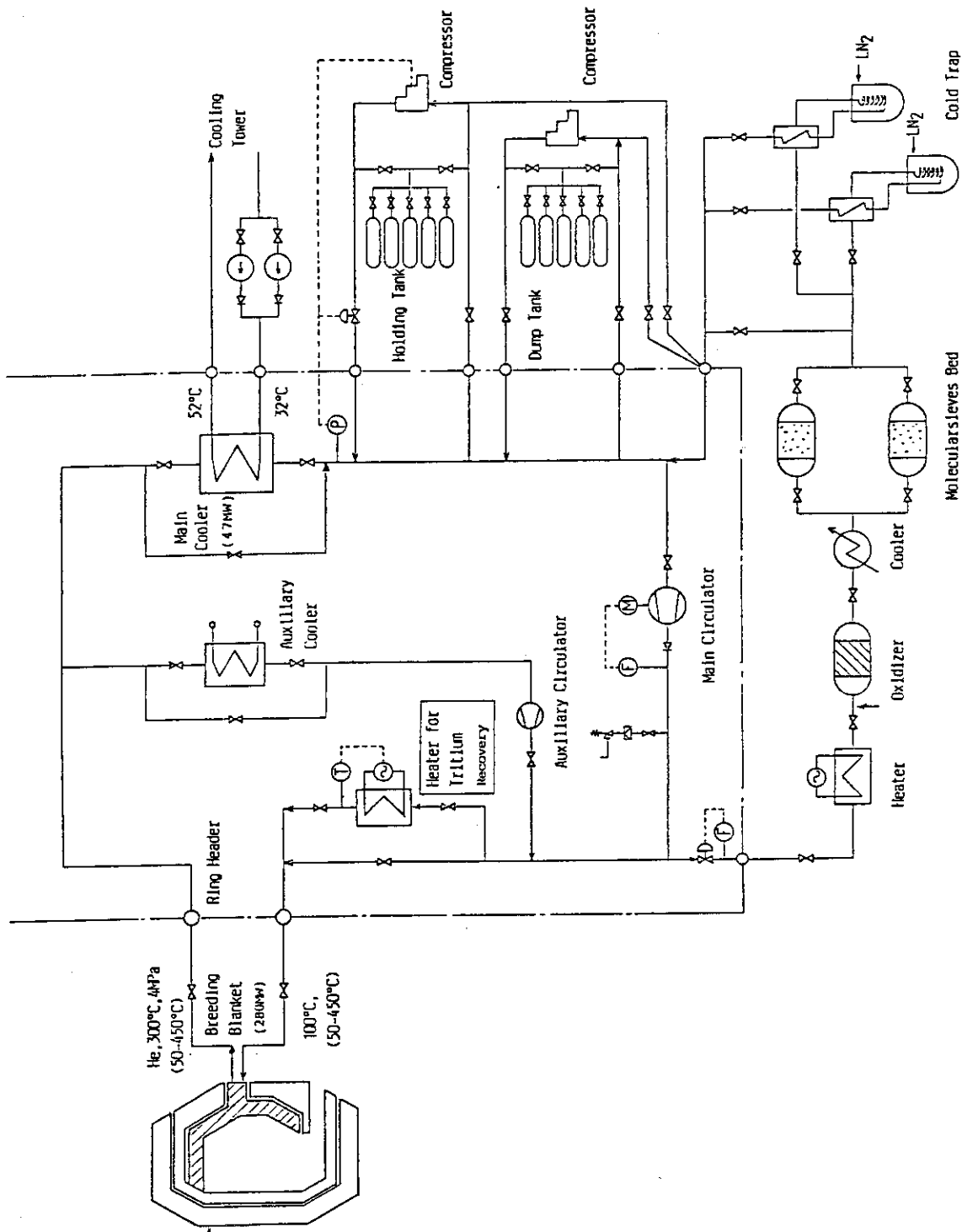


Fig. 11.5-9 Schematic Flow Diagram of Primary Cooling System for Tritium Producing Blanket

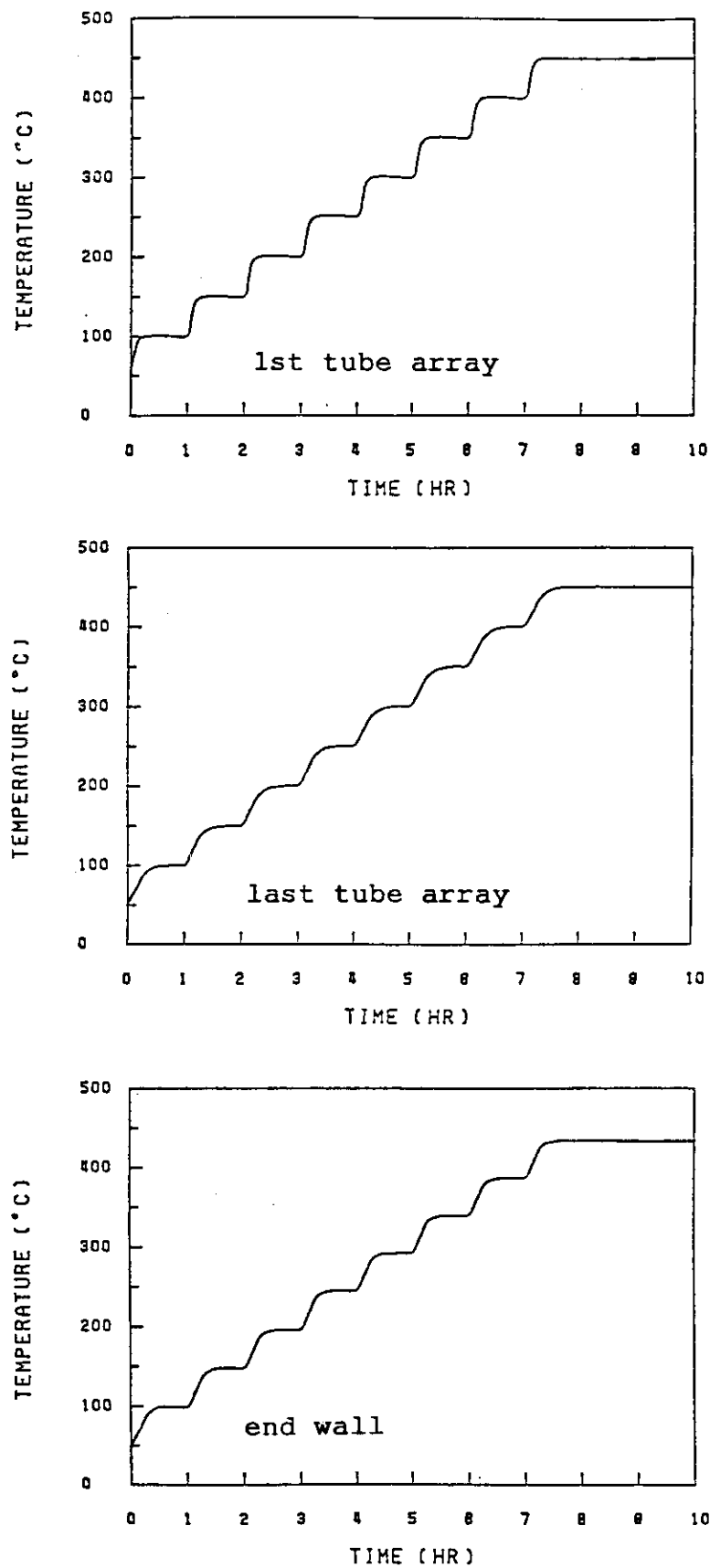


Fig. 11.5-10 Temperature Responses during Tritium Recovery at Coolant Exit End



## 11.6 Structural Analysis

Stress analyses of blanket have been carried out for loads of first wall coolant pressure, internal pressure of blanket vessel and thermal load. The internal pressure of blanket vessel is 0.1 MPa which is the pressure of helium filled in the blanket. Thermal load which brings temperature difference across the structural material consists of surface heat flux from plasma and volumetric heating due to neutron irradiation. Stress in the first wall due to its coolant pressure and thermal load is calculated by two-dimensional analysis at first here. Then the integrity of the blanket is evaluated by adding stress due to the internal pressure to those stresses.

Analytical conditions and model for two-dimensional analysis are shown in Table 11.6-1 and Fig. 11.6-1, respectively. Thermal stress is calculated by using the temperature profile obtained in two-dimensional thermal analysis in 11.5. Plane strain condition is assumed in the analysis. Stress intensity profiles are indicated in Fig. 11.6-2. Stress intensity due to coolant pressure (4 MPa) is small and not serious as shown in Fig. 11.6-2 a). Thermal stress mainly contributes to stress intensity due to both of coolant pressure and thermal load. Due to these loads, 177 MPa and 225 MPa are reached on the surface facing the plasma and on the corner of coolant channel, respectively. Stress on the corner of coolant channel, however, will be mitigated by structural consideration to avoid stress concentration, such as rounded structure.

Stress due to the internal pressure of blanket vessel is estimated using plate model whose four sides are clamped. In the calculation, reinforcement effect of second wall is included by consideration of equivalent plate thickness to conserve the second moment of area.

From those calculations, stress intensities in the first wall are estimated as indicated in Fig. 11.6-3. Primary stress intensity is due to the coolant pressure and the internal pressure of blanket vessel. And primary + secondary stress intensity is due to thermal load adding to those pressure loads. Allowable stress intensities for primary and primary + secondary ones are 165 MPa (1.5 Sm) and 330 MPa (3 Sm), respectively when stress evaluation follows ASME Code Section III. For fatigue evaluation, allowable value is about 420 MPa (2 Sa) for  $7.6 \times 10^4$  cycles (plasma burn time: 1000 sec) as shown in Fig. 11.6-4. As 3 Sm is smaller than 2 Sa, 3 Sm (330 MPa) is considered as the allowable value for primary + secondary stress intensity here. (In the case of 200 sec of plasma burn time for the adoption of OH heating, the number of cycles will be  $3.8 \times 10^5$  and the value of 2 Sa will be about 330 MPa. Therefore 3 Sm and 2 Sa are almost the same in this case.)

It is seen from Fig. 11.6-3 that stress intensities exceed the allowable values for full width (3000 mm) of tritium producing blanket. Stress intensities for the blanket with internal wall in this design, however, are lower than allowable values for both of primary and primary + secondary stress intensities. And integrity of the blanket is maintained.

Stress intensity on the second wall surface facing to breeder region due to the internal pressure of blanket vessel is also indicated in Fig. 11.6-3. As for stress intensities due to the internal pressure of blanket vessel, the one on the second wall surface is larger than those in the first wall. Though thermal stress must be included in stress evaluation, there remains enough margin to allowable stress intensities for the blanket design with internal wall, and the integrity of the second wall will be maintained.

In the future design, stresses due to electromagnetic force and temperature difference between first, second, side and end walls of blanket should be evaluated adding to the stresses considered above. Especially, temperature difference between first and end walls will be high in helium-cooled blanket, and thermal stress will be serious. Therefore structural and thermal-hydraulic considerations should be required to reduce the temperature differences, such as coolant flow control in coolant channels of blanket walls.

Table 11.6-1 Analytical Conditions for Two-Dimensional Stress Analysis

---

Structural Material	: PCA
Young's Modulus	: $1.71 \times 10^{-6}$ MPa *
Poisson's Ratio	: 0.3 *
Thermal Expansion Coefficient	: $17.9 \times 10^{-6}$ /K *
Temperature Profile	: obtained from thermal analysis (see Fig.11.5-3)
Coolant	: He
Pressure	: 4 MPa

---

\*) Properties of 316SS are used.

Note : Plane strain condition is assumed in the analysis.

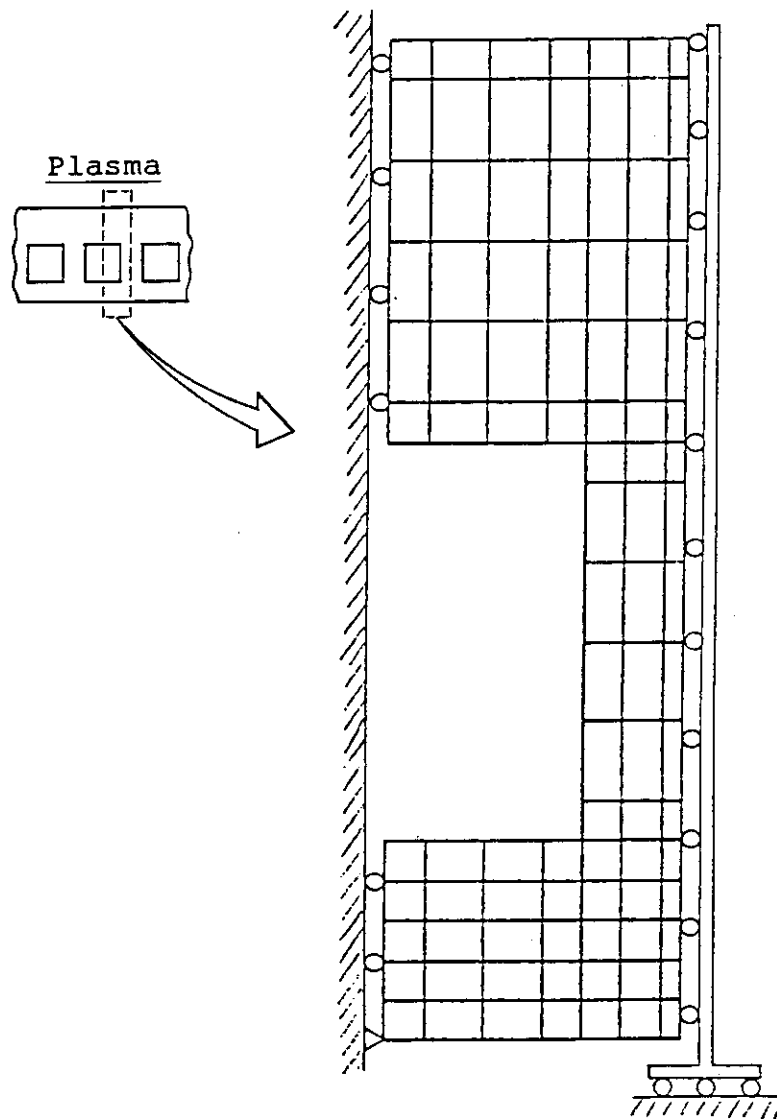


Fig.11.6-1 Analytical Model for Stress Analysis

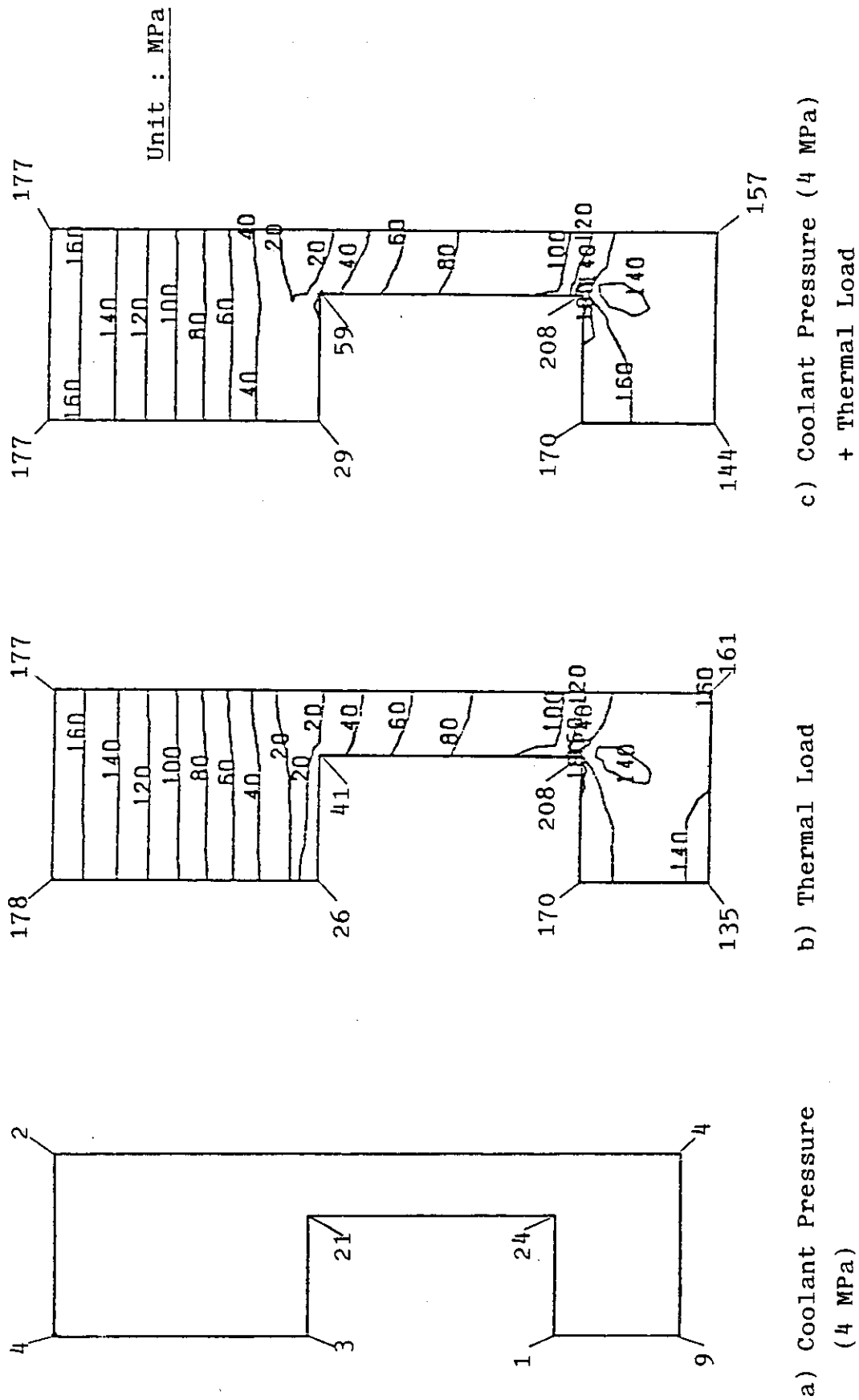


Fig.11.6-2 Stress Intensity Profiles in the First Wall

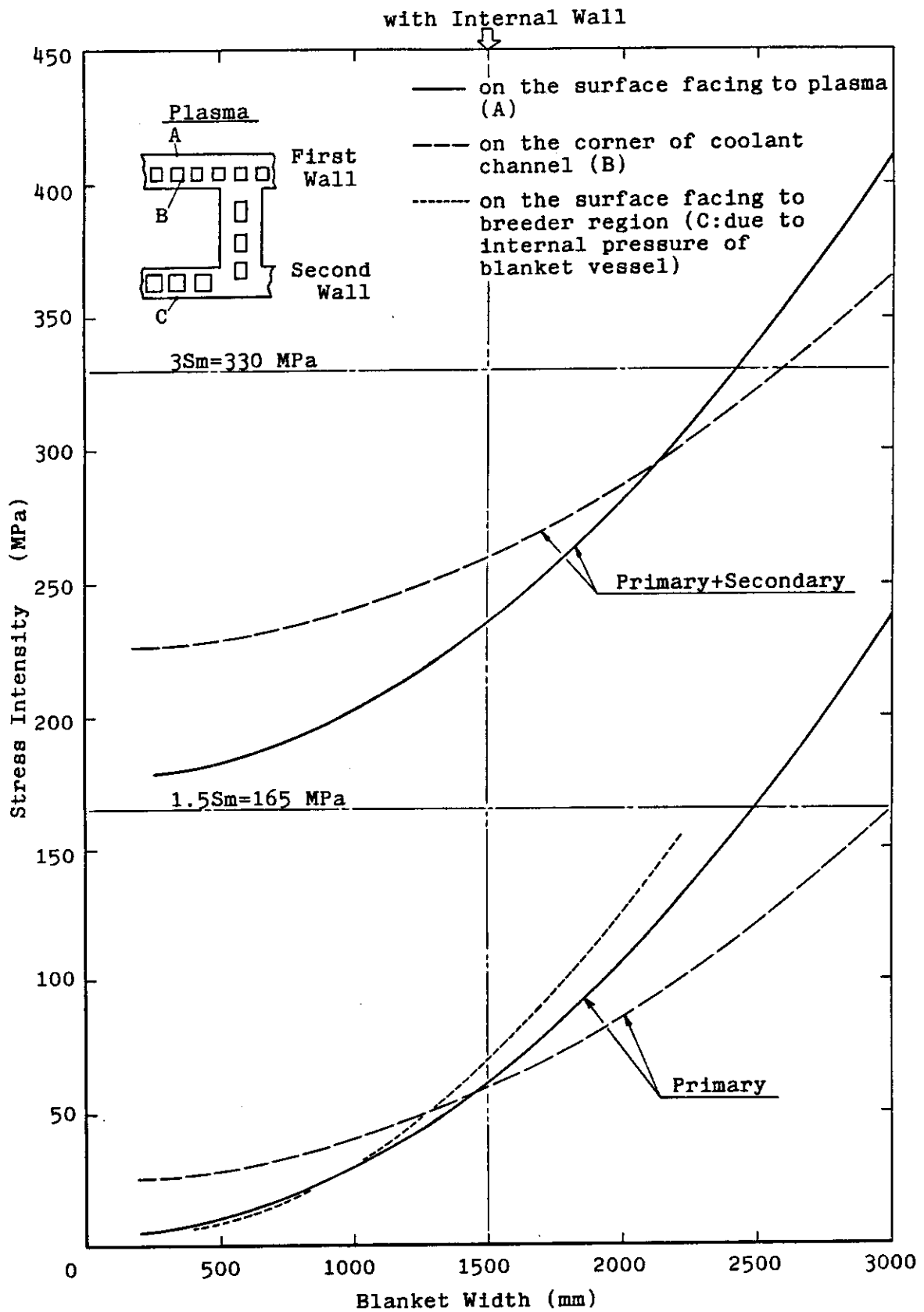


Fig.11.6-3 Stress Intensities in the First Wall

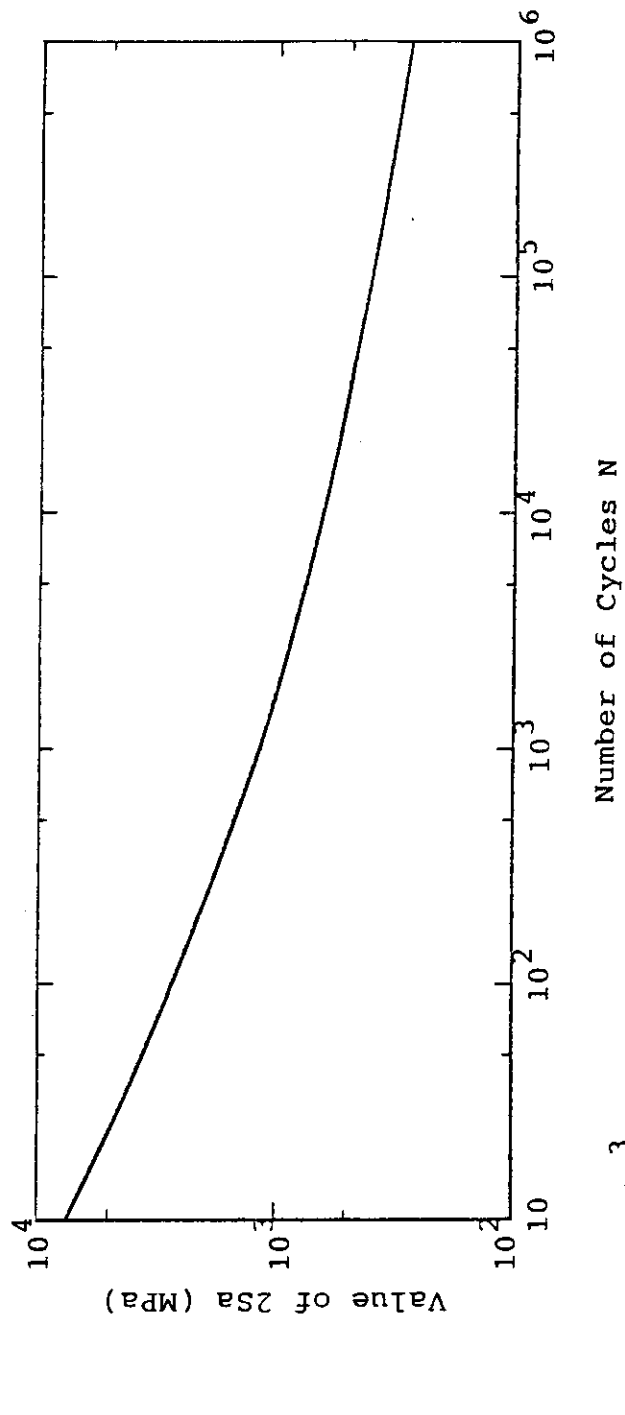


Fig.11.6-4 Design Fatigue Curve for Austenitic Steels

## 11.7 Tritium Recovery

In the batch-type tritium producing blanket, most part of breeding material ( $\text{Li}_2\text{O}$ ) is maintained at relatively low temperature during plasma operation. Most of produced tritium may remain in  $\text{Li}_2\text{O}$  grain. Even if produced tritium is released from grain, tritium reacts with  $\text{Li}_2\text{O}$  to stable  $\text{LiOT(S)}$ . Tritium recovery operation is performed periodically for the batch-type blanket. During the tritium recovery operation, breeding material is heated up to facilitate tritium migration within  $\text{Li}_2\text{O}$  grain and decomposition of  $\text{LiOT}$ , and released tritium is recovered by passing purge gas.

In this section, time and purge gas flow rate required for tritium recovery are estimated.

### (1) Analytical conditions

Table 11.7-1 shows analytical conditions for tritium recovery. It is assumed that breeding material is kept at  $450^\circ\text{C}$  during the recovery operation and recovery cycle is once every two months of full-power operation.

### (2) Time required for tritium recovery

Although there are uncertainties in the mechanism of tritium release from  $\text{Li}_2\text{O}$ , tritium release from  $\text{Li}_2\text{O}$  will be controlled by diffusion process within  $\text{Li}_2\text{O}$  grain and/or surface reaction process (e.g. decomposition of  $\text{LiOT(S)}$ ). A transfer process of tritium from the  $\text{Li}_2\text{O}$  surface to the bulk purge gas stream will also play an important role. Assuming each process as a rate limiting in tritium recovery operation, the time required for recovery was estimated.

#### 1) Tritium release from $\text{Li}_2\text{O}$

##### a) Diffusion within grain

Time dependence of tritium concentration, which is derived from diffusion equation in spherical approximation, is given by

$$\frac{C}{C_0} = \frac{6}{\pi^2} \sum_{n=1}^{\infty} \frac{1}{n^2} \exp \left( - \frac{n^2 \pi^2 D t}{\gamma^2} \right)$$

where  $C_0$  is initial tritium concentration in  $\text{Li}_2\text{O}$ . Average equivalent radius  $\gamma$  can be calculated from the density  $\rho$  and specific surface area  $\sigma$  of sintered  $\text{Li}_2\text{O}$ :

$$\gamma = 3/\sigma/\rho$$

The tritium diffusivity  $D$  in sintered  $\text{Li}_2\text{O}$  is expressed by [1]

$$D = 40.7 \exp (-1.85 \times 10^4/T) \quad [\text{cm}^2/\text{s}]$$

where  $T$  is the absolute temperature of  $\text{Li}_2\text{O}$ . Figure 11.7-1 shows the calculated time dependence of the tritium concentration in  $\text{Li}_2\text{O}$ .

About 99% of tritium within grain is released in 100 sec.

b) Decomposition at the surface

Tritium release rate from the  $\text{Li}_2\text{O}$  surface can be estimated from the decomposition rate of  $\text{LiOT(S)}$ . The tritium release rate from  $\text{Li}_2\text{O}$  is observed to be controlled by a first-order reaction. Then the  $\text{LiOT}$  concentration at the surface is expressed by

$$\frac{C}{C_0} = \exp(-kt)$$

The reaction rate constant  $k$  is given by [2]

$$k = 1.6 \times 10^3 \exp(-9.46 \times 10^3/T) \quad [1/\text{s}]$$

Figure 11.7-1 shows the decay of tritium concentration due to decomposition of  $\text{LiOT(S)}$  at the  $\text{Li}_2\text{O}$  surface. It is obvious from the figure that 99% of  $\text{LiOT(S)}$  is decomposed within about 23 minute.

2) Transport with purge gas

When the purge gas flow rate is relatively high, tritium recovery rate from blanket will be determined by tritium release rate from  $\text{Li}_2\text{O}$  (diffusion or decomposition). On the other hand, purge gas flow rate  $F$  will determine the recovery rate in the case of low flow rate. The time required for recovery in the latter case can be estimated by

$$t = I \cdot P_{\text{total}} / F \cdot P_{\text{T}_2\text{O}}$$

where  $I$  is tritium inventory in blanket, and  $P_{\text{total}}$  and  $P_{\text{T}_2\text{O}}$  are total pressure and  $\text{T}_2\text{O}$  partial pressure respectively. Considering a driving force of  $\text{T}_2\text{O}$  transportation from the surface of  $\text{Li}_2\text{O}$  to purge gas,  $P_{\text{T}_2\text{O}}$  is set to be 1/10 of the equilibrium  $\text{T}_2\text{O}$  pressure ( $\text{LiOT(S)} \rightleftharpoons \text{Li}_2\text{O(S)} + \text{T}_2\text{O(g)}$ ) calculated from JANAF thermochemical table [3]. Figure 11.7-2 shows the relation between the purge gas flow rate and the time required for the recovery. The time required for the tritium recovery is estimated to be 6 hours in the case of the purge gas flow rate of  $2400 \text{ Nm}^3/\text{hr}$ .

Total time required for tritium recovery operation is less than one day including 8 hours of heat-up time of blanket (see 11.5) and 6 hours of tritium extraction from the blanket. Table 11.7-2 summarize the results of above discussion and derived design parameters of tritium recovery system.

It must be noted that  $\text{T}_2$  gas will be released from  $\text{Li}_2\text{O}$  and permeate through coolant tubes of blanket into coolant during plasma operation. Continuous purge gas stream will be necessary to prevent permeation through the coolant tubes during plasma operation.

#### Reference

- [1] K. Okuno, et al., J. of Nuclear Materials, 116 (1983) 82-85.
- [2] H. Kudo, et al., J. of Inorganic Nuclear Chemistry, vol. 40 (1977) 363.
- [3] JANAF Thermochemical Tables, 2nd Ed., Nat. Stand. Ref. Data Ser., Nat. Bur. Stand. (US), 37 (1971).



Table 11.7-1 analytical conditions for tritium recovery

Parameter	Value
Tritium generation rate (Chemical form of tritium)	0.297 mol-T <sub>2</sub> or T <sub>2</sub> O/hr T <sub>2</sub> /T <sub>2</sub> O = 1/9 for Fusion power : 580 MW Dwell time : 240 sec Burn time : 1000 sec Breeding ratio : 0.6
Amount of Li <sub>2</sub> O	Total 27.5 ton
Temperature of breeder zone Normal operation	100 ~ 550°C
Tritium recovery operation	450°C
Temperature of coolant tube	170°C (inlet) ~ 370°C (outlet)
Dimension of tube (Breeder zone) (2nd wall)	690 M <sup>2</sup> x 2 MM <sup>t</sup> 120 M <sup>2</sup> x 2.5 MM <sup>t</sup>
Tritium recovery method	
Tritium recovery operation	Batch recovery (1 time/2 months)

Table 11.7-2 Design Parameters of Tritium Recovery System

Parameter	Value
(Normal operation)	
Tritium recovery rate	0.0297 mol-T <sub>2</sub> /hr (0.178 g-T <sub>2</sub> /hr)
Purge gas flow rate	200 Nm <sup>3</sup> -He/hr (1 ata)
T <sub>2</sub> gas concentration	3.3 vpm
(Tritium recovery operation)	
Amount of tritium	0.385 kmol-T <sub>2</sub> O/time (2.3 kg-T <sub>2</sub> )
Recovery cycle	1 time/2 months
Time for recovery	~ 6 hours
Purge gas flow rate	2400 Nm <sup>3</sup> /hr (1 ata)
Tritium inventory in blanket	Total 2.3 kg (before Recovery) 100 g (after Recovery)
Tritium permeation rate into coolant	~ 280 Ci/d Blanket 250 Ci/d Second wall 30 Ci/d

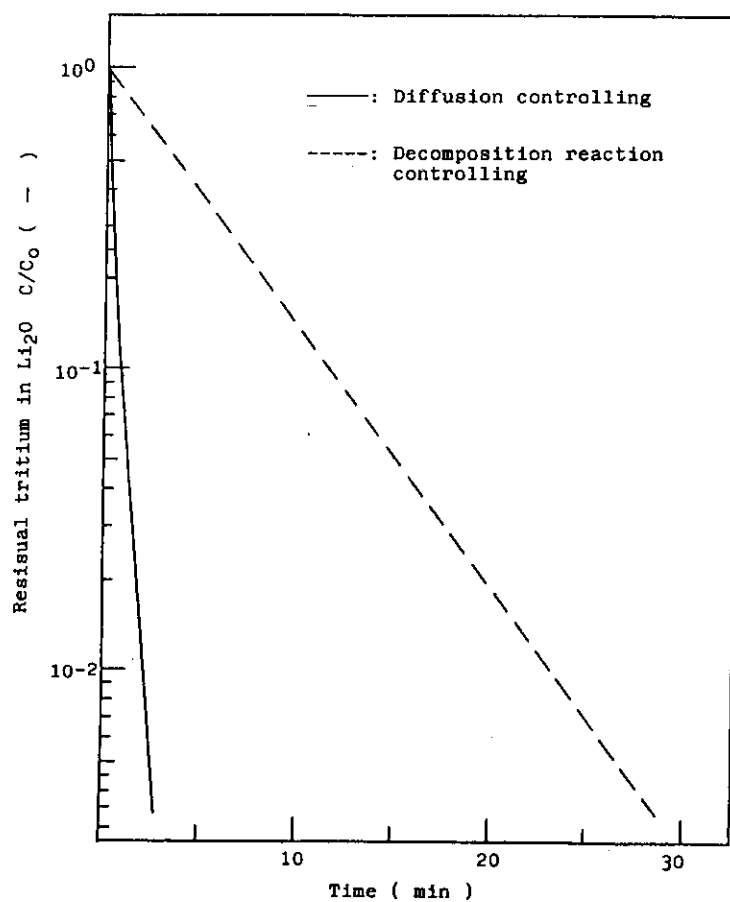
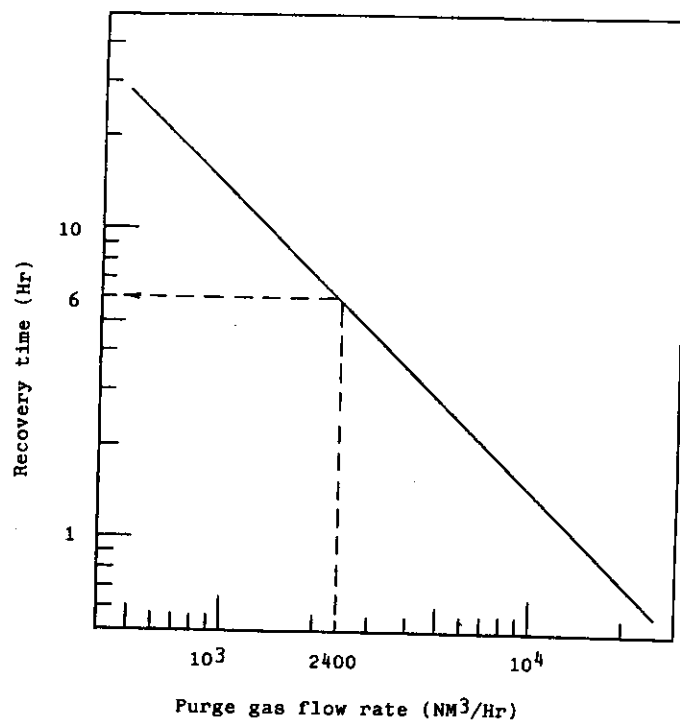
Fig.11.7-1 Tritium release from  $\text{Li}_2\text{O}$ 

Fig. 11.7-2 Relation between recovery time and purge gas flow rate

## 11.8 Tritium Permeation

Tritium permeates into primary coolant mainly through first wall subject to energetic tritium implantation. Although most of tritium in helium coolant can be removed by detritiation system, a part of it will be released to environment. The main tritium sources to environment are identified as follows:

- permeation through coolant tubes of heat exchangers into secondary coolant
- permeation through primary coolant pipes into reactor hall
- leakages with primary coolant to reactor hall

In this section, the tritium permeation rate into primary coolant and the release rate from coolant were estimated, and the countermeasures were discussed.

### (1) Tritium permeation into coolant

The tritium permeation rate through the first wall was calculated with the tritium transport analysis code. Unsteady-state diffusion equation with defect trapping was solved under boundary conditions of surface recombination controlling. Time dependence of the permeation rate and inventory in first wall were estimated.

Table 11.8-1 shows the major parameters for the calculations. One of the key parameters, the molecular sticking coefficient  $\alpha$ , has been reported to be in the range of 0.5 to  $5 \times 10^{-5}$ . Value of  $\alpha$  depends on surface conditions of first wall. In this study, values of 0.5 (clean surface) and  $5 \times 10^{-3}$  (average of data) were assumed for the parameter  $\alpha$ . Figures 11.8-1 and 11.8-2 show the calculated permeation rate and inventory for  $\alpha = 0.5$  and  $5 \times 10^{-3}$  respectively. The tritium permeation rates reach 8,000 ~ 90,000 Ci/day in less than 10 days. On the contrary, the tritium inventory at steady state is as low as 8 ~ 70 g. The relatively high permeation rate and the low tritium inventory are mainly due to the high coolant temperature (300°C).

However, there are large uncertainties for permeation parameter. Further experimental data are needed.

### (2) Tritium release from coolant

Primary coolant flow is bypassed to detritiation system where most of tritium in coolant is removed. However, a part of tritium permeates through coolant pipes and heat exchanger tubes, and leaks with coolant to environment. Table 11.8-2 shows analytical conditions for the calculation of the release rate. Figure 11.8-3 shows the estimated tritium release rate from coolant as a function of bypass ratio of detritiation system. Total tritium release rate is estimated to be in the range of 1 to 3 Ci/day for 5% of bypass ratio, resulting from mainly the permeation through coolant pipes.

This calculations are based on the data of bare stainless steel. In practice, the permeation rate may be reduced by natural formation of oxides on the surface of coolant pipes.

### (3) Conclusions

Although there are large uncertainties in the calculation parameters, the estimated permeation rates through first wall range from 8,000 to 90,000 Ci/day. Most of tritium in coolant can be removed by detritiation system of primary coolant. Detritiation system of helium coolant is much simpler than that of water coolant. The tritium release rate from primary coolant is estimated to be in the range of 1 to 3 Ci/day in the case of 5% bypass ratio.

The following design approaches are effective to reduce the tritium release from primary coolant.

- application of double tubes for primary coolant
- application of catalytic oxidizer in primary coolant line
- design of seals and components to minimize leaks

Table 11.8-1 Parameters for first wall permeation

Parameter	Unit	Values
Geometry		
Thickness (at the end of life)	mm	3
Surface area	m <sup>2</sup>	252
Thermal conditions		
Structure material	-	SUS316
Thermal conductivity	w/mk	18.2
Maximum temperature	°C	642
Minimum temperature	°C	618
Coolant		
Temperature (outlet)	°C	573
Thermal conductivity	w/mk	3990
Heat load		
Surface heat load	MW/m <sup>2</sup>	0.133
Average nuclear heating rate	MW/m <sup>3</sup>	15
Operating mode		
Burn time	sec	1000
Dwell time	sec	240
Dudy cycle	-	0.806
Operating period	day	60
Permeation parameters		
Diffusivity D <sub>0</sub>	cm <sup>2</sup> /s	2.15 x 10 <sup>-2</sup>
Ed	eV	0.59
Heat of transport	eV	-0.065
Solubility S <sub>0</sub>	n/cc.atm <sup>1/2</sup>	1.01 x 10 <sup>20</sup>
Es	eV	0.094
Trapping C <sub>T0</sub>	-	0.01
G <sub>T</sub>	n/cc.s	0
μ	1/s	0
Debye frequency ν <sub>0</sub>	1/s	10 <sup>13</sup>
ET	eV	0.85
Sticking coef. α in	-	0.5, 5 x 10 <sup>-3</sup>
α out	-	5 x 10 <sup>-3</sup>
Lattice parameter	cm	2.5 x 10 <sup>-8</sup>
Tritium flux	T/cm.s	3.41 x 10 <sup>16</sup>
Reflection coef.	-	0.635
Energy of particles	eV	200

Table 11.8-2 Parameters for tritium release from primary coolant

Parameter	Value
Tritium inleak into coolant	
First wall	7700 ~ 89700 Ci/day
Second wall	30 Ci/day
Blanket	250 Ci/day
Total	8000 ~ 90000 Ci/day
Heat exchanger	
Temperature of coolant tube	85 ~ 100°C
Heat transfer area	4800 m <sup>2</sup>
Thickness of tube	3.5 mm <sup>t</sup>
Permeation coefficient at 100°C	$3.33 \times 10^{-13}$ cc/cm·sec·Torr <sup>1/2</sup>
Coolant pipe	
Temperature of coolant pipe	300°C
Surface area of pipes	580 m <sup>2</sup>
Thickness of pipe	33 mm <sup>t</sup>
Permeation coefficient at 300°C	$5.77 \times 10^{-10}$ cc/cm·sec·Torr <sup>1/2</sup>
Primary coolant	
Inventory of primary coolant	2 Ton
Leak rate of primary coolant	0.01% / day
Detritiation	
Bypass rate	0.5 ~ 10%
Decontamination factor	20

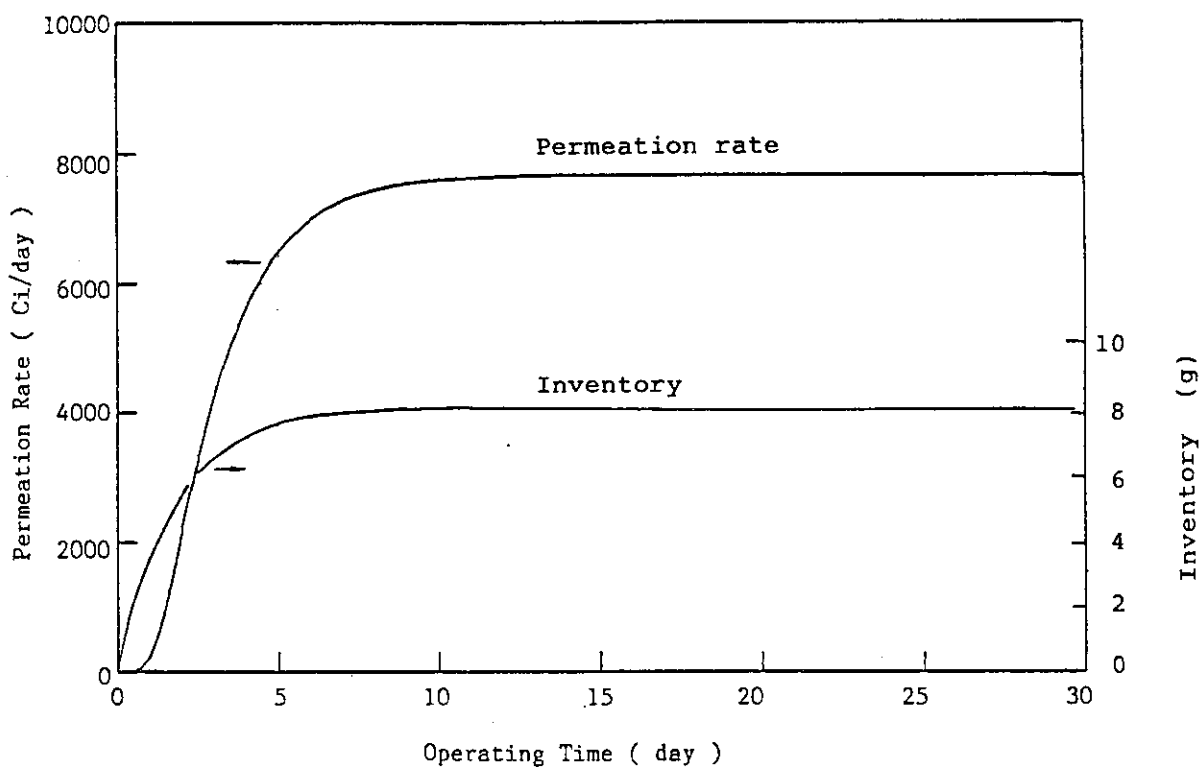


Fig. 11.8-1 Tritium Permeation rate and inventory in first wall  
( for  $\alpha = 0.5$  )

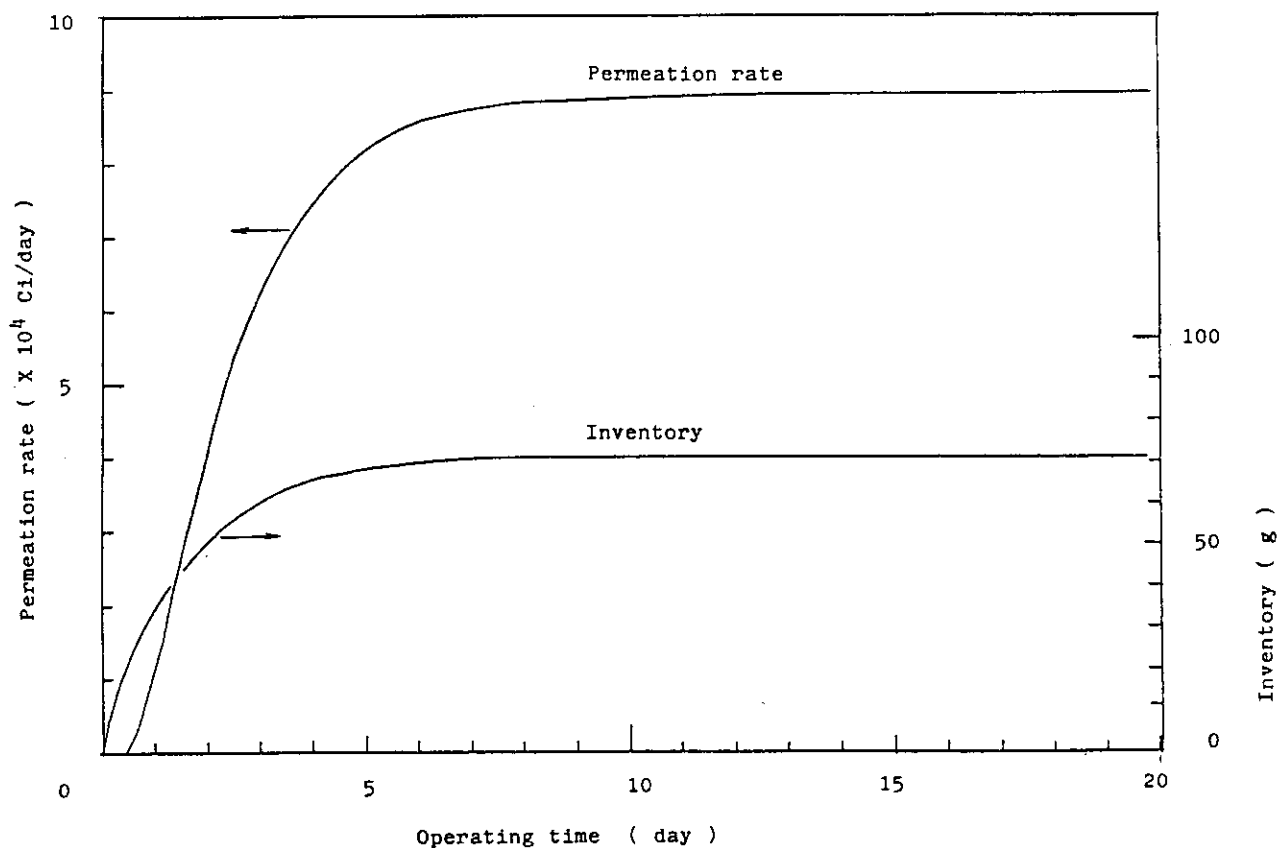


Fig. 11.8-2 Tritium permeation rate and inventory in first wall  
(  $\alpha = 5 \times 10^{-3}$  )

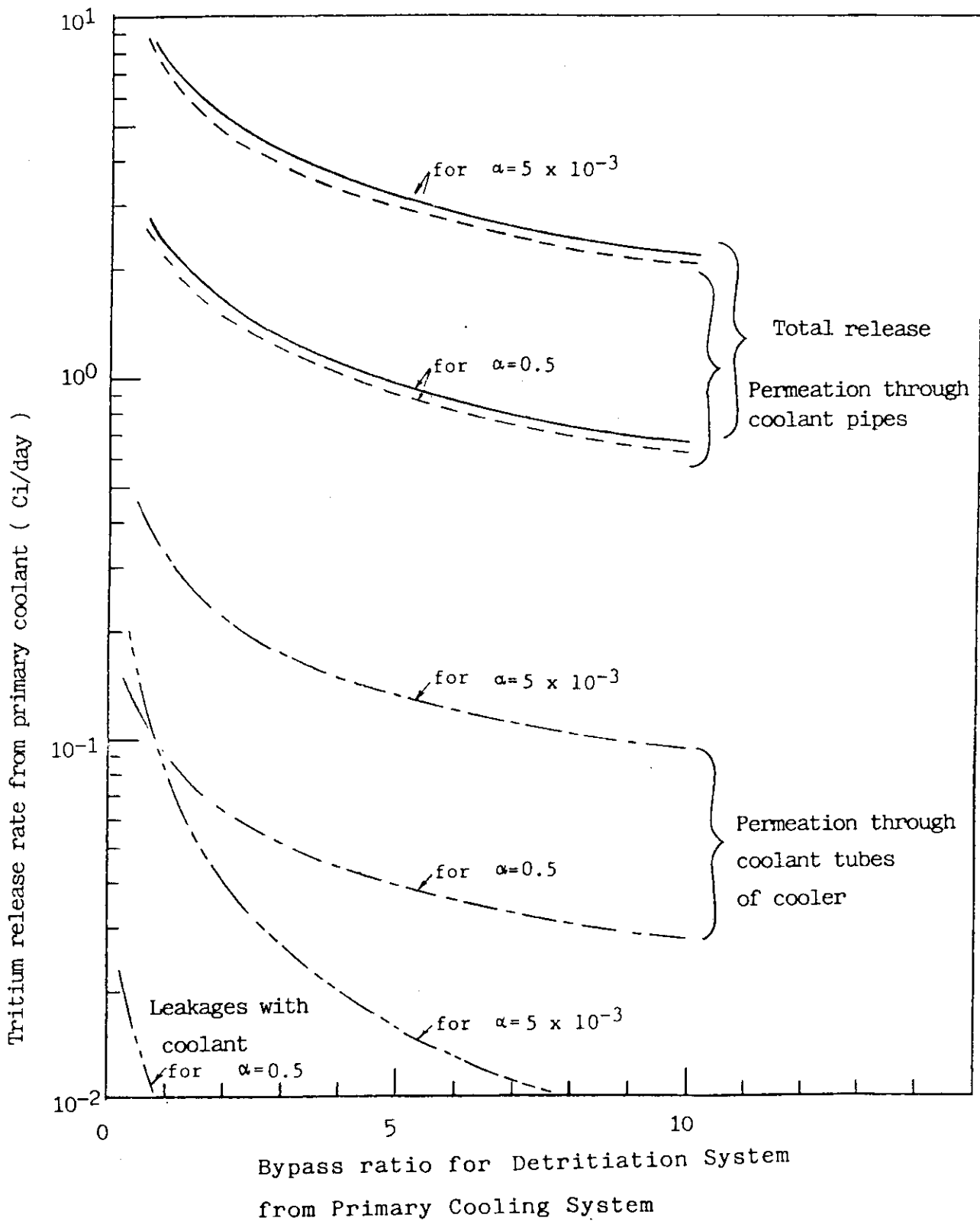


Fig. 11.8-3 Tritium release rate from primary coolant



## 12. Tritium and Vacuum

### 12.1 Tritium System

#### (1) Introduction

The INTOR tritium system (Fig. 12.1) is composed of all the subsystems of the device that have to process gases or liquids containing tritium in the form of  $T_2$  or  $T_2O$ . The different parts are then the following:

- plasma exhaust reprocessing system (P.E.R.S.)
- blanket exhaust processing system (considering the reference INTOR blanket with  $Li_2O$  as breeding material (B.R.S.))
- gaseous waste processing system (G.W.P.S.)
- atmosphere processing systems (E.C.S.<sup>1</sup>)
- coolant reprocessing system (C.R.S.).

#### (2) Plasma reprocessing system

The torus vacuum system is the source term for the plasma exhaust reprocessing system.

All lines coming from the torus are connected before going through cold traps in which impurities are solidified and sent to the waste processing line.

At a temperature of 35 K, H, D, T and He are in a gaseous form, whereas impurities are in solid form. Then, the processed gas is sent to the falling-film condenser in which H, D, T only are liquefied. The gaseous helium upstream is sent to the blanket processing line, while the liquid tritium-deuterium flow is sent to the isotopic separation system. This system includes five interconnected cryodistillation columns.

Three bottom flows for DT,  $D_2$  and  $T_2$  are driven to the torus feed processing line. The plasma exhaust isotopic separation columns system is interconnected with the cryodistillation column of the primary coolant and the detritiation system electrolysis cell of the blanket processing system, allowing, in this way, a complete autonomy of the tritium-handling system.

#### (3) Breeding tritium processing system

The reference breeding material is  $Li_2O$ , working in the temperature window 400-1000°C. Tritium formed inside the breeder may be recovered, by using helium as a sweeping gas. INTOR specifications stipulated a breeding ratio equal to 0.6, during Stages II and III of INTOR.

<sup>1</sup> ECS stands for Emergency Air Cleaning System.

The tritium recovering process from the blanket may be as follows:

Helium leaves the blanket at a temperature less than 600°C, which could be too high to be compatible with the compressor; so the first step of the process is to cool this gas down to a temperature compatible with the compressor material. This cooling is achieved in a countercurrent heat exchanger with helium entering inside the blanket. Tritium leaves the blanket mainly as  $T_2O$ , but a small fraction is in the form of  $T_2$ ; so the following step consists of converting this fraction into tritiated water on a catalytic bed, working at 200°C. The efficiency of such a reaction is higher than 99.99%, so the hypothesis that helium leaving the catalytic bed contains only water is reasonable. After this step, helium is cooled down to liquid nitrogen temperature to trap water as frost and to decrease the partial vapour pressure below  $10^{-4}$  Pa, giving a very good recovery efficiency. Leaving the cold trap, helium is heated again up to 400°C before re-entering the blanket.

The trapped water fraction is recovered, from time to time, by heating up the vessel to room temperature, with the aim of recovering tritiated water in liquid form. This water is directed to an electrolysis cell where the decomposition occurs. The oxygen flow is sent back to the catalytic bed. The tritium flow is directed to the purification of the fuel exhaust processing line.

#### (4) Tritium permeation into the primary water coolant

One of the potential source of tritium contamination is the spilled tritiated water. Tritium concentration level in the primary coolant strongly affects the size of detritiation system. Hence the tritium permeation rate is the key parameter to evaluate a feasible tritium separation method.

The best estimated permeation rate up to the present time is the steady-state rate of about 250 Ci/day most of which permeates through the first wall. The amount of permeation through the graphite limiter is negligible, since the active diffusion in the cooled limiter plate is unlikely due to the large activation energy for hydrogen migration. However, the time to reach the steady-state permeation rate will be beyond the INTOR mission period, it will be more longer if one takes the neutron damage traps into account. It is more appropriate to evaluate the transient-state permeation rate during the plant life time.

We analyzed the transient-state hydrogen isotopes migrations using the numerical code, TRIP (Tritium Reemission, Inventory and Permeation) based on Fickian diffusion equation<sup>1-3</sup>). TRIP allows us to deal with three hydrogen isotopes simultaneously, tritium decay and an arbitrary running mode like a pulsed operation under the following conditions:

- (a) Molecular recombination release and Sievert's law adsorption,
- (b) Fickian and thermal (Soret effect) diffusion in bulk materials, and
- (c) Interaction with material defect by Willson-Baskes' trapping-detrapping model.

For the calculation presented here, we used two sets of data base and a set of nominal INTOR conditions shown in Table 12.1 - 12.4. Though there are still large uncertainties among the experimental data, data base #1 of the stainless steel first wall is adapted as a reference because the tritium diffusion coefficients were directly measured. Graphite as the limiter material has two contradistinctive data sets, one for mobile tritium atoms and the other for almost stuck tritium atoms to the implanted site. Therefore the analytical results based on these data should be carefully applied to the detritiation system.

Transient-state permeation as a function of continuous operation time are shown in Fig. 12.2 - 12.5.

In comparison with a pulsed mode operation, tritium migration during the dwell time is found to be negligibly slow.

The results are summarized as follows:

- ① The permeation through the outboard first wall is no greater than 1 Ci/day after a 4.1 years continuous operation.
- ② The inboard first wall gives same order of permeation rate to the outboard first wall.
- ③ The data sets of hydrogen diffusivities and solubilities for stainless steel make difference of permeation rate by factor 4 as shown in Fig. 12.3.

Fig. 12.4 shows that the permeation will reduce by one order of magnitude if one uses the molecular sticking coefficient of  $\alpha=0.5$  as insisted in ref. 11.

The molecular sticking coefficient is the most critical parameter which has strong effects on the magnitude of tritium permeation.

- ④ There is no permeation through the graphite limiter if one uses the data set #1. Conversely, for the set #2 there is a rapid increase of permeation to the order of  $10^3$  Ci/day after 4 years continuous operation as shown Fig. 12.2.5. However, the above break-through may not be achieved if the graphite surface is more quickly eroded by bombarding hydrogen atoms than implanted with these atoms. Based on extremely limited data base, it is difficult to obtain more detailed conclusion.

- ⑤ When tritium permeation into the primary coolant during INTOR mission is under the transient-state, its rate is much less than that of steady-state level even though there is highly uncertainty in the graphite limiter.

## (5) Coolant

To ensure that the tritium levels in the primary coolant are maintained at a low enough level, a tritiated water recovery unit must be included in the tritium system design. Theoretically, all processes used to produce heavy water are suitable to extract tritium from the water coolant. But, taking into account the complexity of these processes, the choice is restricted to two or three processes: water distillation, isotopic exchange between water and hydrogen followed by cryogenic distillation, and electrolysis plus cryogenic distillation.

A small fraction of the coolant (depending on the tritium permeation flow rate) has to be processed. Before the tritium can be extracted, the activated materials must be removed.

## (6) Atmospheric tritium recovery

Significant part of the radiation dose received during maintenance in the reactor hall is due to the tritium. Tritium releases in the reactor hall is chronically supposed to be  $\sim 10$  Ci/day. Release during routine maintenance operations are estimated to be  $\sim 100$  Ci/day.

The maximum accidental release in the reactor hall was considered to be  $10^5$  Ci.

For tritium release of  $\sim 1$  Ci/day during personnel access maintenance, it is desirable that the tritium concentration level in the reactor room be kept in the range  $\leq 5 \times 10^{-6}$  Ci/m<sup>3</sup> for unsuited personnel. Therefore, the process flow rate will be  $> 2$  m<sup>3</sup>/s. This will be possible by a large ventilation system so long as the total amount of tritium does not exceed the waste limit.

For tritium release of large than  $10^2$  Ci/day, however, any personnel access is not permitted immediately. It is possible to use the emergency tritium clean up system (ECS) which is provided for the purpose of cleaning up a reactor hall in the case of accidental tritium release; for example, in loss of coolant accident. Leakage of tritiated water from the primary coolant circuit should be kept as low as possible.

Reduction of tritium concentration to the allowable level will be needed in order to minimize the tritium soaking effect of the reactor hall surface. For personnel access with the level of tritium concentration in the air greater than  $5 \times 10^{-6}$  Ci/m<sup>3</sup>, a significant time will be required before access is permitted.

Estimated water leakage into the reactor hall is in a range from 1 to 10 g/day.

## 12.2 Vacuum System

The reactor vacuum system as a whole includes: the torus, the SC magnet cryostats, the fuel pellet injector, and the special vacuum system for other components. Only the vacuum system for the torus is discussed here.

The pumping system of the toroidal chamber consists of 12 pumping units symmetrically placed relative to the reactor axis. Each pumping unit is connected with the divertor chamber by an exhaust duct of 1.0-1.2 m diameter and  $\sim 9$  m length. To provide the effective speed of the helium chamber pumping of  $2 \times 10^5$  l/s, each of the 12 pumps should pump helium at a speed of up to  $5 \times 10^4$  l/s.

The most attractive pumps to be used for the reactor system are listed below.

### Pumps for D-T mixture

- (a) Condensation pumps ( $\sim 4$  K): Their advantages are simple design and maintenance, short regeneration time and an unlimited number of regeneration cycles; their disadvantage is incompatibility with high radiation and heat fluxes.
- (b) Cryosorption pumps based on microporous adsorbents or condensed gases at 10-30 K: Their advantage is a higher working temperature; their disadvantages are incompatibility with high radiation and heat fluxes, and a relatively long regeneration time.
- (c) Sorption pumps based on non-evaporable metallic getters: Their advantage is that they can be arranged close to high radiation zones; their disadvantages are a relatively long regeneration time and a limited lifetime.

### Pumps for helium

Cryosorption pumps ( $\sim 4$  K) based on microporous adsorbents or condensed gases: The disadvantages of these pumps are the complicated technology of adsorbent deposition onto a substrate, the low mechanical strength limiting the number of regeneration cycles, and the low heat conductance limiting the sorption layer thickness and therefore sorption capacity. Helium can be pumped by means of adsorbent-based cryosorption pumps at 20 K, but in this case there is a substantial reduction both in specific pumping speed and in maximum sorption pump capacity. The development of a highly efficient pump on a condensed gas base is complicated because of the lack of sufficient experimental data on helium pumping and on helium mixtures with hydrogen nuclides.

With conventional cryosorption pumps of the refrigerator type the helium pumping speed reaches only 10-15% of the pumping speed for hydrogen; with modern cryopumps of the same type, however, the efficiency is up to 60%. It is unlikely that the helium pumping speed

can be increased by decreasing the cryosorption panel temperature or by using other cryosorbent materials.

Cryosorption pumps using microporous adsorbents, operated at  $\sim 4$  K, can pump either hydrogen mixtures or helium, but not both simultaneously. However, it has been shown that at the 4 K temperature required to cryosorb helium gas, these pumps actually pump the hydrogen isotopes by cryocondensation rather than by sorption. This solid hydrogen forms an effective hydrogen ice barrier between the gaseous helium and the cryosorption surface. Thus, these pumps are not acceptable for the torus vacuum system. Acceptable pumps are compound cryocondensation/cryosorption pumps. These consist of a cryocondensation panel working at 4 K, followed by a cryosorption panel also operating at 4 K. The hydrogen isotopes are efficiently pumped on the first-stage cryocondensation surface and the helium is pumped on the cryosorption panel. These compound cryopumps will meet all of the requirements of the torus vacuum system. The successful operation of compound cryopumps has recently been demonstrated. Pumps of this type will be used to pump helium and D-T mixtures in INTOR.

Two compound cryopumps are arranged in parallel in each of the 12 pumping units. There are two pumps in each unit, so that toroidal chamber pumping by 12 pumps and simultaneous regeneration of the other 12 pumps is provided. The regeneration time should be minimized in order to reduce tritium inventory in the reactor. The estimated time of continuous cryopanel operation is 2 hours, the tritium inventory in cryopumps being  $\sim 120$  g.

In addition to compound cryopumps, turbomolecular and "dry" mechanical pumps (Fig. 12.6) are included in the system. Their purpose is to pump air from the chamber and to provide the base pressure and pumping when the cryosorption pumps are regenerated. The development of oil-free turbomolecular pumps with a pumping speed of about  $(2-3) \times 10^4$  l/s is necessary for fusion devices of the INTOR type.

#### References

- 1) Baskes M.I. : SAND80-8201, Sandia National Lab, (1980)
- 2) Wilson K.L. and Baskes M.I. : J. Nucl. Mater., 76&77 (1978) 291
- 3) Baskes M.I. : *ibid.*, 92(1980) 318
- 4) Chaney K.F. and Powell G.W. : Metall. Trans., 1(1970) 2356
- 5) JAERI Group : "Tritium Group Rep-3, Tritium Permeation into Coolant", Rep. for INTOR Workshop, Phase IIA, Section III, (1981)9
- 6) Baskes M.I., Bauer W. and Wilson K.L. : J. Nucl. Mater., 111&112, (1982)663
- 7) Causey R.A., Elleman T.S. and Verghese K. : Carbon, 17(1979)323
- 8) Wilson K.L. : FED-INTOR/TRIT/82-5(USA) Appendix A, Sec. 1.1.3.
- 9) Haggmark L.G. and Biersack J.P. : J. Nucl. Mater., 85&86 (1979)1031
- 10) Look G.W. and Baskes M.I. : J. Nucl. Mater., 85&86(1979)995
- 11) Causey R.A. Holland D.F. and Sattler M.L. : Nucl. Technol/Fusion, 4(1983)64

Table 12.1 Hydrogen diffusivities and solubilities data base  
for the materials of this analysis

Material	Data Ba	$D^{\circ}$ <sup>(a)</sup> (cm /sec)	E (eV)	$S_0$ (atom/cm <sup>3</sup> .atm <sup>1/2</sup> )	Es (eV)	Ref
SS	①	$2.15 \times 10^{-2}$	0.59	$1.01 \times 10^{20}$	0.094	4), 5)
	②	$1.20 \times 10^{-1}$	0.61	$7.65 \times 10^{19}$	0.091	6)
C	①	$5.75 \times 10^2$	4.27	$4.85 \times 10^{15}$	-1.44	7)
	②	$9.90 \times 10^{-3}$	0.5	$7.9 \times 10^{20}$	0.05	8)

Table 12.2 Hydrogen total detrapping energies data base for the  
radiation damage material defect of this analysis<sup>(a)</sup>

	SS	C
ET (eV)	0.85	2.5

(a) from Ref. 8.

Table 12.3

## FIRST WALL REFERENCE PARAMETERS

Parameter	Reference value		
	Out board (BOL)	Out board (EOL)	Inboard (BOL)
Wall thickness (cm)	1.2	0.33	1.4
Wall area (m <sup>2</sup> )	266	266	114
Wall temperature (K)			
Plasma side surface	606	438	652
Coolant side surface	394	387	397
Implantation flux (atom/cm <sup>2</sup> .s)	$1.7 \times 10^{16}$ -T, $1.7 \times 10^{16}$ -D (e) 200 Calculated profile for Maxwellian energy distribution and cosine angular distribution for 200 eV D-T/SS <sup>(a)</sup> 0.62 <sup>(a)</sup>		
Implantation energy (eV)			
Depth profile			
Reflection coefficient			
Surface boundary condition	Recombination for both sides		
Molecular sticking coefficient	Plasma side: $\alpha_1 = 5 \times 10^{-3}$ , coolant side: $\alpha_2 = 0.5$		
Diffusivity, Solubility	Data Base ① <sup>(6)</sup>		
Heat of Transport (eV)	-0.065 (c)		
Trap	Present : $E_r = 0.85$ eV (d)		
Trap concentration			
	0.01 atom. fraction (Uniform and constant)		
Tritium decay	Included		

(a) from Ref. 10

(b) See Table 12.1.

(c) from Ref. 6

(d) from Ref. 8

(e) duty cycle = continuous.



Table 12.4 Limiter / Divertor Parameters

Parameter	C/Cu Brazed Limiter		C Armer of C/Cu Mechanically Attached Limiter	W/Cu Diverter
	Beginning-of-Life	End-of-Life		
Thickness (cm)	1.0/0.2	0.3/0.2	2.0	2.0/0.5
Area (m <sup>2</sup> )	32	32	32	10
Temperature (K)	Plasma side surface	473	443	730
	Material interface	425	418	430
	Coolant side surface	403	403	400
Implantation	Flux (atom/cm <sup>2</sup> sec)	3.9 × 10 <sup>18</sup> D-T (a)		3.35×10 <sup>18</sup> -T, 3.35×10 <sup>18</sup> -D
	Energy (eV)	97.5		135
	Depth profile	it is assumed to be same as first wall case		
	Reflection coeffi- cient	0 (b)		0.7 (b)
Surface molecular sticking coefficient	α = 0.5 for the both sides.			
Material data base	See Table 12.1 and 12.2			

(a) In these case, it is assumed that deuterium has same material properties as tritium, except for no  $\beta$ -decay.

(b) from Ref. 9

(c) duty cycle = continuous

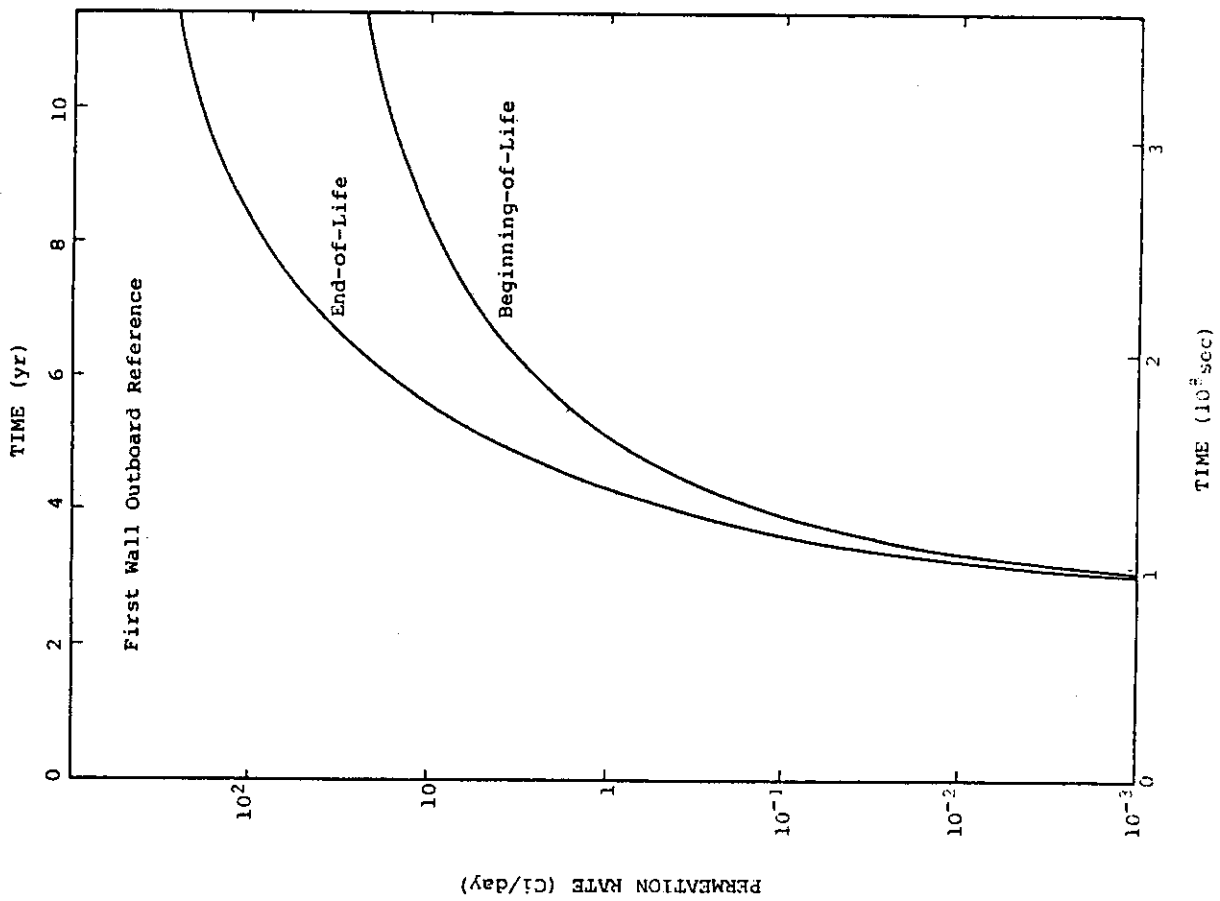


Fig. 12.2

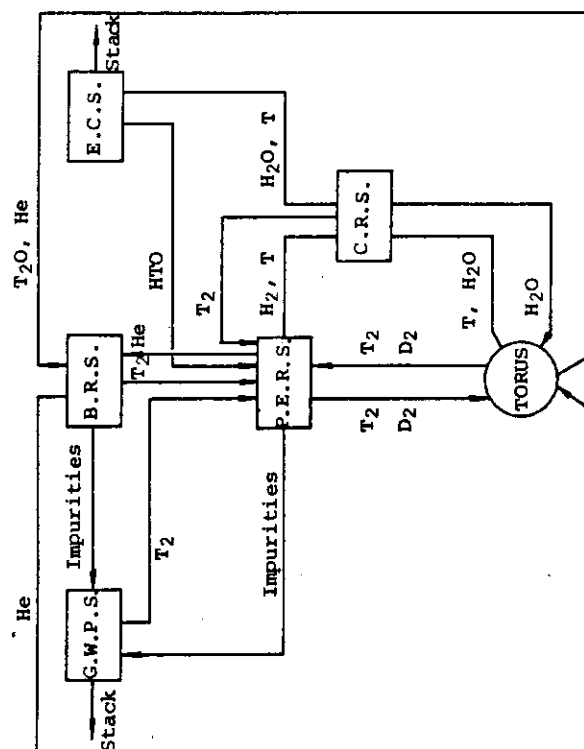


Fig. 12.1 Interconnections inside the tritium system

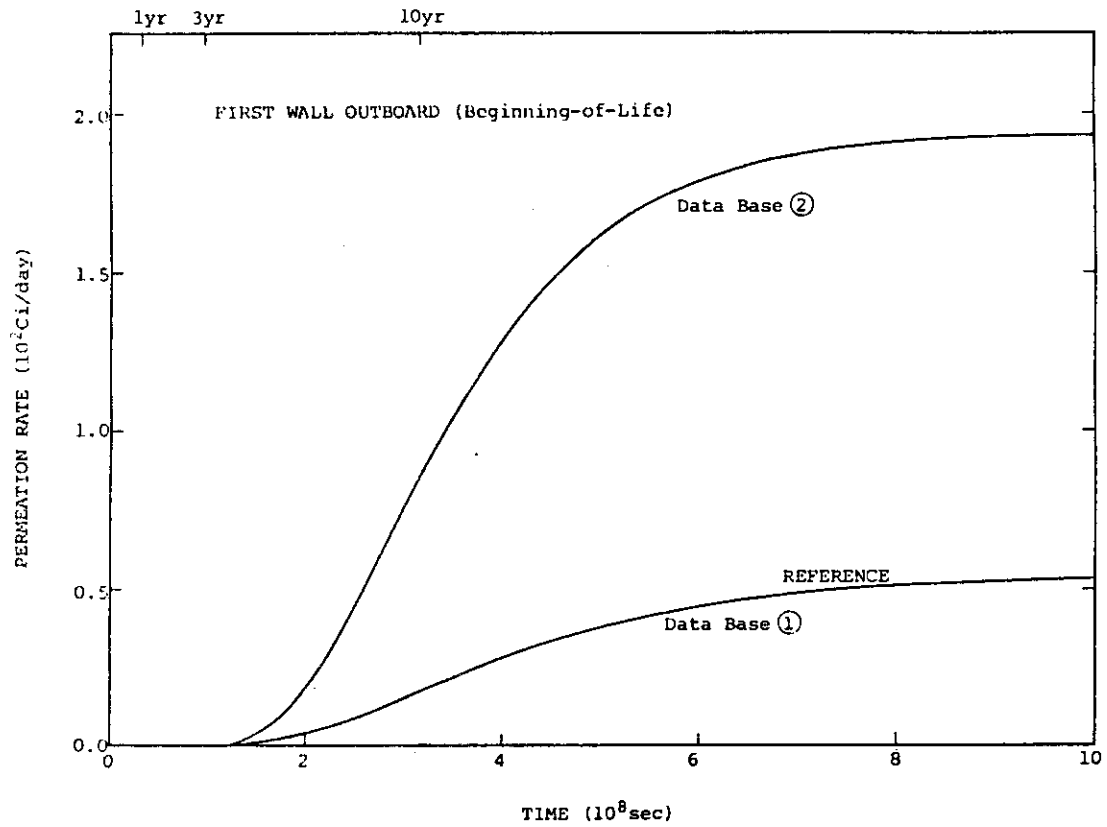


Fig. 12.3

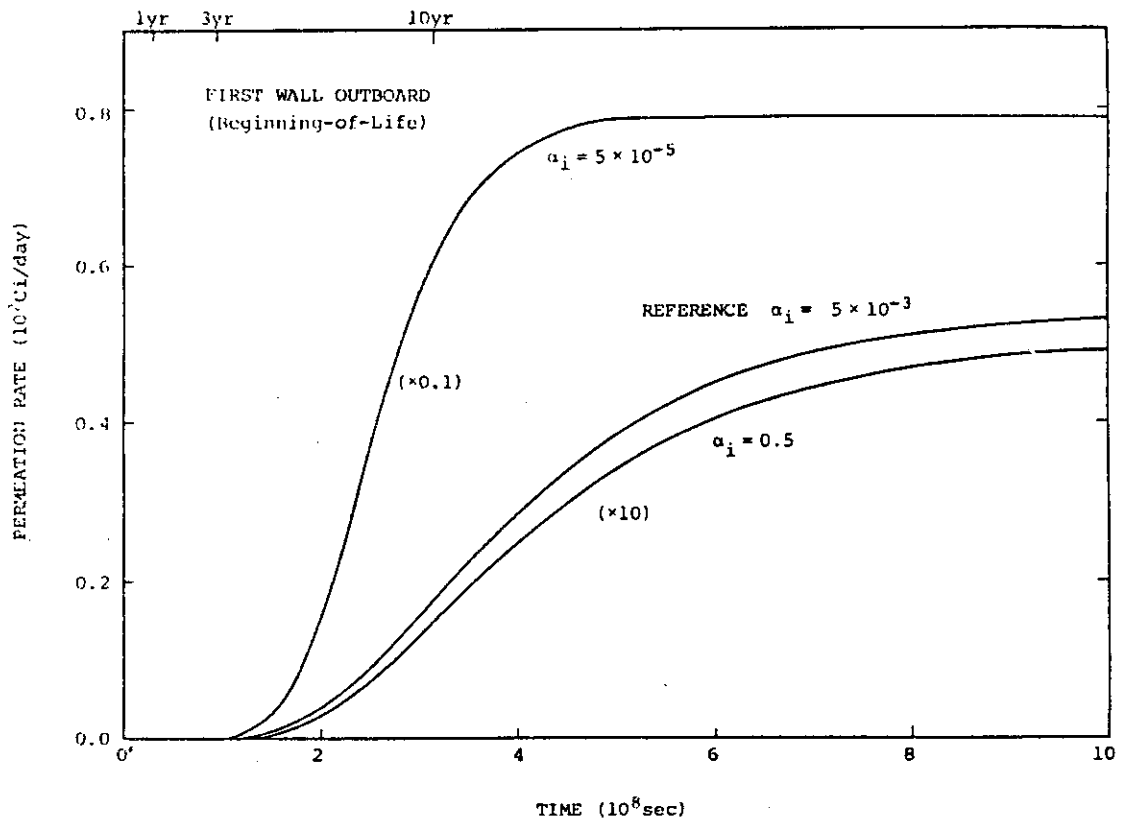


Fig. 12.4

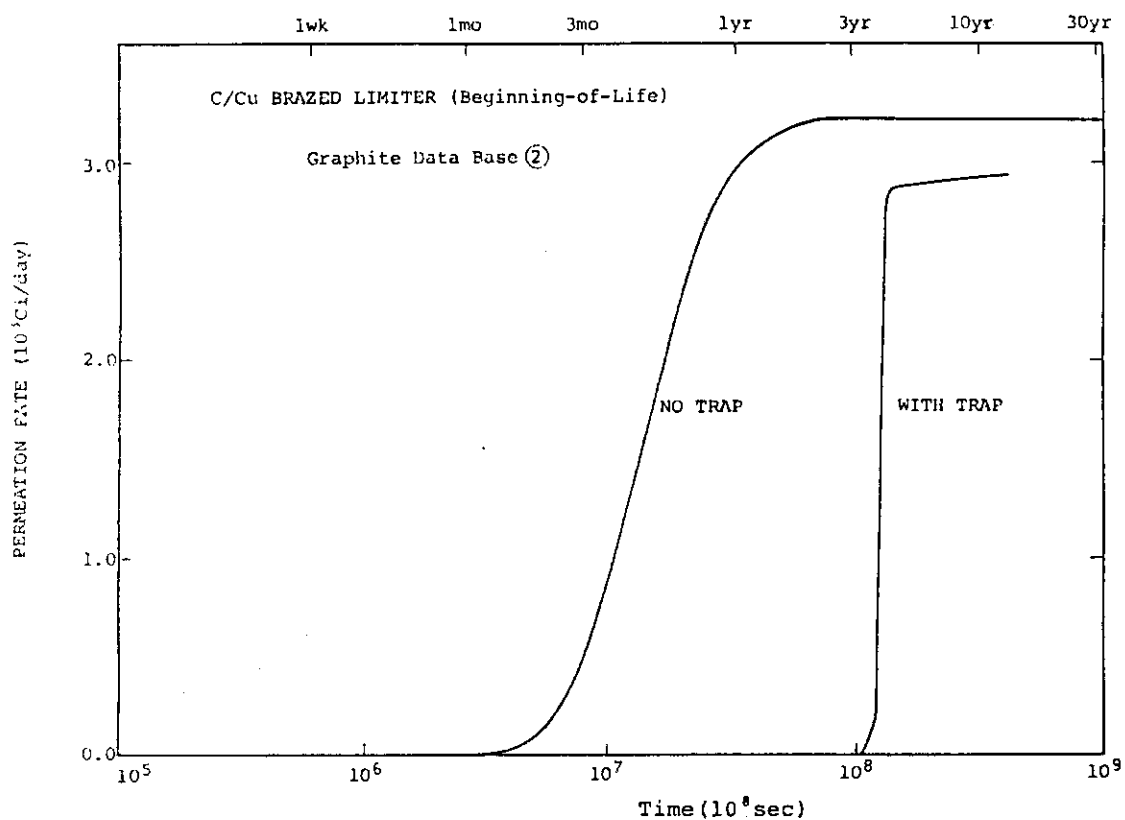


Fig. 12.5

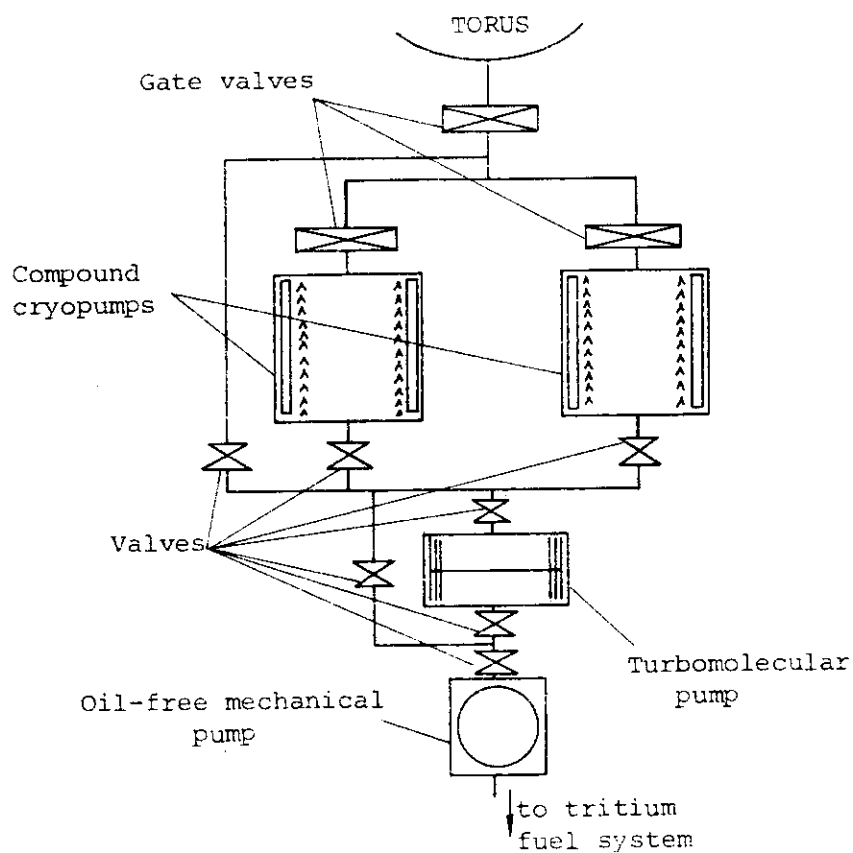


Fig. 12.6 Pumping unit of toroidal vacuum chamber

### 13. Radiation Shielding

#### 13.1 Shielding Criteria

##### 13.1.1 Biological Shielding Criteria

For personnel access, the dose rate of 2.5 mrem/h at 3 days after shutdown is proposed. At 3 days after shutdown,  $^{24}\text{Na}$  with the half life of 15 h which is produced in the reactor room concrete will decay to insignificant level.

The site boundary dose should be limited to 5 mrem/y.

##### 13.1.2 Components Protection

###### (1) Toroidal Field coils (TFC)

The shielding criteria employed for the design of Fusion Experimental Reactor (FER) should be applicable to INTOR. They are summarized in Table 13.1.1 and the bases for their derivation are described below.

The nuclear heating is proportional to the neutron flux in TFC. The maximum local nuclear heating rate in the superconductor can be as high as  $1 \text{ mW/cm}^3$ . At this value, there is little effect on stability and heat can be sufficiently removed. The total nuclear heating in the superconductor and the helium vessel should be smaller than 15 kW. This value was determined by the reasonable requirement for the refrigeration capacity.

The other three radiation damage related criteria are dependent on the neutron fluence in TFC. The radiation induced resistivity increase,  $\rho_r$  in the copper conductor should be limited to  $2.5 \times 10^{-8} \Omega \cdot \text{cm}$ . This  $\rho_r$  is reached when the displacement damage in copper becomes  $4 \times 10^{-4} \text{ dpa}$ (1). The value of the displacement damage rate causing  $\rho_r = 2.5 \times 10^{-8} \Omega \cdot \text{cm}$  differs between  $1 \times 10^{-4} \text{ dpa}$  and  $6 \times 10^{-4} \text{ dpa}$ (1)-(4). Intercomparison and evaluation of dpa to  $\rho_r$  conversion factor should be carried out to reduce the ambiguity in this factor. In addition, the recommended value of the energy dependent copper displacement damage cross section should be selected. Assuming 80% of the radiation induced resistivity increase of copper can be recovered by the room temperature annealing(5), the copper dpa rate criterion is set at  $4 \times 10^{-4} \text{ dpa/1 MW} \cdot \text{y/m}^2$ .

The superconductor fluence of the fast neutrons with energy greater than 0.1 MeV should be lower than  $2 \times 10^{18} \text{ n} \cdot \text{cm}^{-2}$  over the lifetime. This value is based on two experimental results.(3),(6)

The phase one report of INTOR(7) employed  $5 \times 10^9 \text{ rad}$  for the insulator dose based on irradiation tests results on epoxy/fibre-glass laminate (NEMA G-10). There is an irradiation data by Kato and Takamura(8) showing the applicability of polyimide up to  $1.1 \times 10^9 \text{ rad}$ . Based on the above two data,  $3 \times 10^9 \text{ rad}$  is adopted for the insulator dose limit.

Table 13.1.1 Shielding Criteria for Components

## Toroidal Field Coils (TFC)

- Maximum local heating rate in superconductor	1 mW/cm <sup>3</sup>
- Total nuclear heating in superconductor and helium case	15 kW
- Copper stabilizer displacement damage	$4 \times 10^{-4}$ dpa per 1 MW·y/m <sup>2</sup>
- Superconductor fast neutron fluence over lifetime*	$2 \times 10^{18}$ n·cm <sup>-2</sup>
- Insulator dose over lifetime*	$3 \times 10^9$ rad

## Cryopanel

- Total nuclear heating	5 kW
-------------------------	------

\* The lifetime fluence is 3 MW·y/m<sup>2</sup>

## 13.2 Optimization of shield thickness and composition

### 13.2.1 Objectives

A series of one-dimensional shielding calculations were performed to minimize the inboard shield thickness. Stainless steel SS316 and water were used as main shielding materials. The use of special materials such as tungsten as bulk shielding material was not considered. The radiation protection criteria for TF coils to consider are as follows:

Conductor fluence	$2 \times 10^{18}$ n/cm <sup>2</sup> /lifetime
Copper stabilizer dpa	$4 \times 10^{-4}$ dpa/(MW.y/m <sup>2</sup> )
Insulator dose	$3 \times 10^9$ rad/lifetime
Local nuclear heating rate	$1 \times 10^{-3}$ W/cm <sup>3</sup>
Total nuclear heating	15 kW

Radial build of the modified INTOR-J is shown in Fig. 13.2.1. A space of 80 cm thickness is reserved for inboard shielding region. Effective shield thickness, is however, about 70 cm since there must be clearance for component assembly and space for bellows.

### 13.2.2 Calculation method

One-dimensional transport ( $S_N$ ) code, ANISN<sup>(9)</sup> was used for the shielding calculation. A geometrical model in cylindrical geometry is shown in Fig. 13.2.2. Material composition for each region is shown in Table 13.2.1. The  $P_5$ - $S_8$  approximations, and a coupled 42-group neutron and 21-group gamma-ray cross section set (GICX40 library)<sup>(10)</sup> were used for calculations. Six calculational cases are shown in Table 13.2.2. In Case 1 to 4, volume fraction of SS316 in the removable shield and in the semi-permanent shield is varied. In Case 5, the B<sub>4</sub>C layer is excluded. In Case 6, <sup>10</sup>B is used in place of natural boron.

### 13.2.3 Calculation results

Radiation responses in inboard part of TF coils (TFC) are summarized in Table 13.2.2. Fluence dependent values are marginal as compared to the criteria. Flux dependent value, nuclear heating rate has a margin of about one order. Dependences of neutron fluence and total nuclear heating on material composition of shields are shown in Fig. 13.2.3 and Fig. 13.2.4, respectively. Shielding criteria are satisfied with the SS316 volume fraction between 80% and 90%. The B<sub>4</sub>C layer can be excluded from the shield.

### 13.2.4 Conclusions

- (1) It is possible to satisfy all the TFC shielding criteria with a 70 cm thick inboard shield including 10 cm thick helium vessel.
- (2) Fluence dependent responses are marginal compared to the criteria.
- (3) The SS316 volume fraction of 80-90% is required to satisfy the criteria.
- (4) High volume fraction of SS316 (e.g. 95%) in the removable shield, and low fraction (e.g. 70%) in the semi-permanent shield are effective from shielding point of view.
- (5) The B<sub>4</sub>C layer can be excluded from the shield.

Table 13.2.1 Material Composition for Inboard Shield used in One-dimensional Shielding Calculations

Region No.	Region	Composition (Volume Percent)	Remarks
1	Plasma	Vacuum	
2	Scrape-off Layer	Vacuum	
3	Removable Shield	316SS x% <sup>1)</sup> H <sub>2</sub> O y%	x,y: Parameters
4	Gap	Vacuum	
5	Semi-permanent Shield(SS Shield)	316SS a% <sup>1)</sup> H <sub>2</sub> O b%	a,b: Parameters
6	Semi-permanent Shield(B <sub>4</sub> C Shield)	316SS 5%, H <sub>2</sub> O 5% B <sub>4</sub> C 90%	<sup>N</sup> B or <sup>10</sup> B
7	Semi-permanent Shield(Shield Jacket)	316SS 95% H <sub>2</sub> O 5%	
8	Gap	Vacuum	
9	He Vessel	316SS 100%	
10	TFC Conductor	316SS 34% Cu 33%	
11	He Vessel	316SS 100%	

Note 1) See Table 13.2.2  
 $x + y = a + b = 100\%$



Table 13.2.2 Radiation Responses in the Inboard Toroidal Field Coils  
based on 1.24 MW/m<sup>2</sup> and 3 MWY/m<sup>2</sup>

Calculation Case	Fast Neutron Fluence (n/cm <sup>2</sup> /lifetime)	Copper dpa (dpa/lifetime)	Epoxy Dose (rad/lifetime)	Nuclear Heating Rate (W/cc)	TFC Total Nuclear Heating (kW)
① x = 90, a = 80 <sup>1)</sup> (av. SS = 85%) <sup>2)</sup>	1.18(+18) <sup>3)</sup>	7.22(-4)	1.71(+9)	1.81(-4)	7.02
② x = 90, a = 70 (av. SS = 80%)	1.20(+18)	7.52(-4)	1.76(+9)	1.83(-4)	7.38
③ x = 90, a = 90 (av. SS = 90%)	1.49(+18)	8.77(-4)	2.11(+9)	2.43(-4)	8.69
④ x = 95, a = 70 (av. SS = 83%)	1.09(+18)	6.83(-4)	not calculated	1.73(-4)	7.14
⑤ Replace <sup>N</sup> B <sub>4</sub> C with SS Shield (a = 80)	1.40(+18)	8.32(-4)	not calculated	2.29(-4)	8.57
⑥ Replace <sup>N</sup> B <sub>4</sub> C with <sup>10</sup> B <sub>4</sub> C	9.38(+17)	5.84(-4)	not calculated	1.34(-4)	5.59

Note 1) See Table 13.2.1  
 2) Average SS volume percent  
 3) Read as  $1.18 \times 10^{18}$

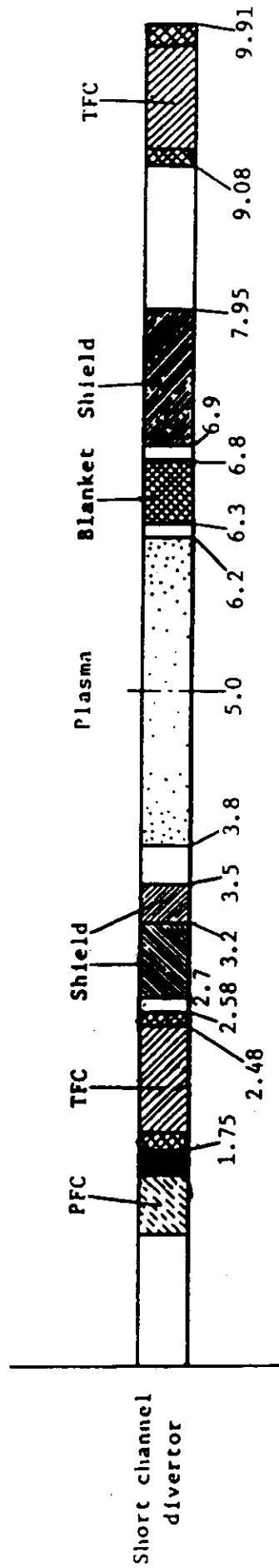


Fig.13.2.1 Radial Build for the Modified INTOR-J

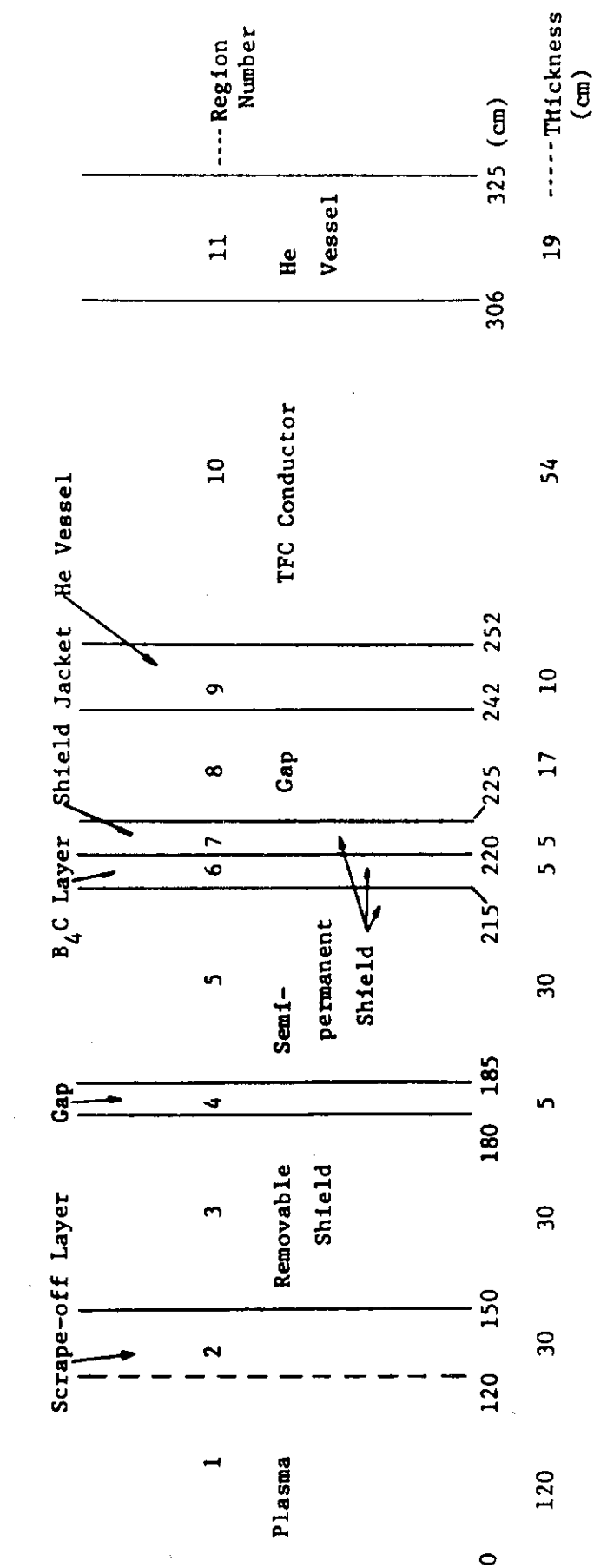


Fig.13.2.2 Infinite Cylindrical Model for One-dimensional Shielding Calculation

note : \* SS95% for Removable shield  
and 70% for Semi-permanent Shield  
+ Replace  $B_4C$  with SS80% Shield  
# Use  $B_4C$  with 100% B-10

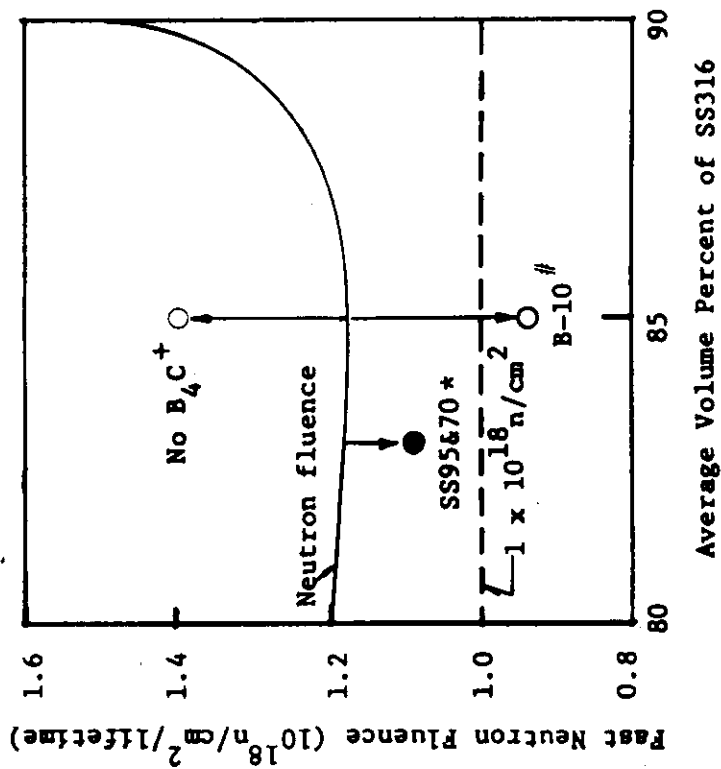


Fig.13.2.3 Dependence of Fast Neutron Fluence to Inboard TFC on Shield Material Composition

note : \* SS95% for Removable Shield  
and 70% for Semi-permanent Shield  
+ Replace  $B_4C$  with SS 80% Shield  
# Use  $B_4C$  with 100% B-10

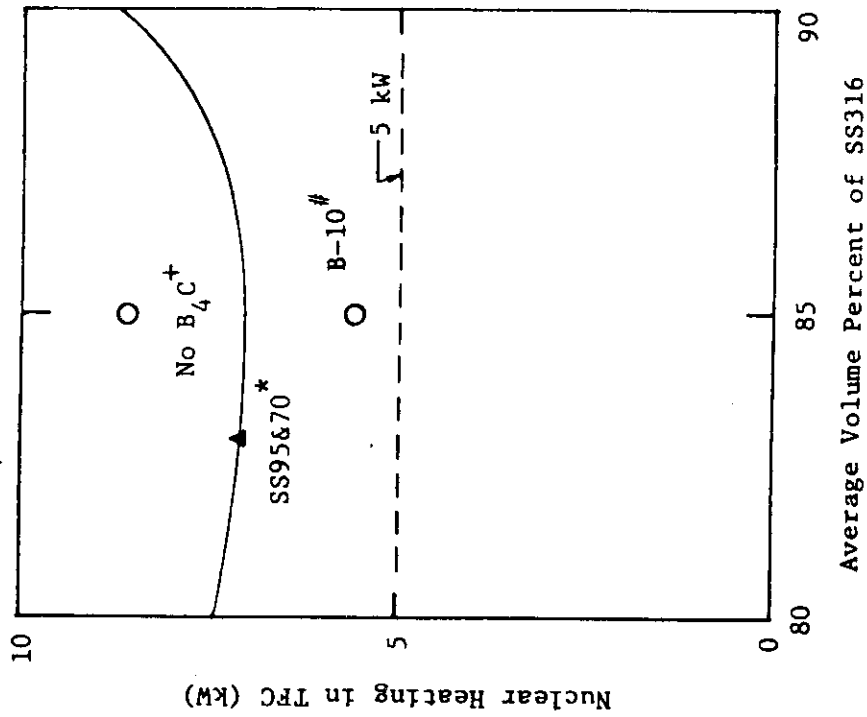


Fig.13.2.4 Dependence of TFC Nuclear Heating on Shield Material Composition

### 13.3 Local heterogeneous effects

#### 13.3.1 Objectives

Two-dimensional shielding calculations were performed to see the local heterogeneous effects of the inboard shield structures on the irradiation properties of the inboard legs of the TF coils. Two kinds of effects were analyzed: one was narrow gap streaming effect between adjacent shield modules, and the other was material heterogeneity effect. Local peaking factors were defined, comparing the results to those of the bulk shielding calculations. The radiation protection criteria of TF coils must be satisfied even if these local peakings are taken into account.

#### 13.3.2 Calculation methods

Two-dimensional transport ( $S_N$ ) code, DOT3.5<sup>(11)</sup> was used for analyzing the local heterogeneous effects. Two-dimensional geometrical models for narrow gap streaming calculations are shown in Fig. 13.3.1 which describe the inboard part of the reactor in X-Y coordinates. The first model has a narrow gap (0.5 cm width) between two adjacent modules in the removable shield region. The second model has a gap with a step (or a 90° bend) between the removable shield and the semi-permanent shield. The third model has a straight narrow gap between adjacent modules through the removable shield and the semi-permanent shield. The gap width is 0.5 cm for all the models.

Geometrical models for analyzing material heterogeneity effects are shown in Fig. 13.3.2. The first model has a 100% - SS316 region in the removable shield which represents shield vessel walls. The second model has a 100% - water region in the removable shield which represents a water coolant plenum in the shield module. The third and fourth models have a 100% - SS316 region and a 100% - water region through the removable shield and the semi-permanent shield, respectively.

Material composition for each region of the calculational models is shown in Table 13.3.1.

Calculational parameters for DOT3.5 were as follows:

- Order of Legendre expansion of scattering cross section ---  $P_3$
- Coupled 42-group neutron and 21-group gamma-ray cross section set (GICX 40 library)<sup>(10)</sup>
- Number of angles in quadrature set ---- 166 (131 directions in the forward hemisphere and 35 directions in the backward hemisphere)
- Isotropic fusion neutron source is assumed to be uniformly distributed in the plasma region.

At first, calculations were performed only for the first neutron energy group (15.0 - 13.72 MeV) to see local peaking effects because computing time was limited. Calculation with full neutron and gamma-ray groups was performed for the one case of the most severest peaking effect.

#### 13.3.3 Calculation results

##### 13.3.3.1 Narrow gap streaming effect

The 14 MeV neutron flux (the first neutron energy group) contour maps are shown in Fig. 13.3.3. A flux contour map for the bulk shielding is also shown in the figure for comparison. A local peaking factor is

defined as a ratio of the peak flux to the flux without gap streaming effect at the front surface of TFC helium vessel. The peaking factors for the three calculation cases are summarized in Table 13.3.2. Only the third case shows severe flux enhancement by neutron streaming effect. Calculation with full energy groups was performed for this geometry. Results of the neutron and gamma ray flux calculation are shown in Fig. 13.3.4. The severest streaming effect is observed in the 14 MeV neutron flux contour map. Flux distributions along the traverses perpendicular to the gap axis are shown in Fig. 13.3.5. Peaks at the center represent flux enhancement by the gap streaming. The local peaking factor, which is defined in this case as the ratio of the peak flux to the minimum flux at a traverse, is summarized in Table 13.3.3. Judging from the table, TFC irradiation properties which mainly depend on the fast neutron flux/fluence (copper stabilizer atomic displacement and insulator absorbed dose, etc.) are enhanced by 25%. Nuclear heating rate is enhanced by 40% as compared to the bulk shielding case.

#### 13.3.3.2 Material heterogeneity effect

The 14 MeV neutron flux contour maps for the four calculation cases are shown in Fig. 13.3.6. In the case of 100%-SS316, no local peaking effect is found. In the case of 100%-water, however, strong local peaking effect is found as shown in Table 13.3.4 since shielding capability of water against 14 MeV neutron is relatively weak.

#### 13.3.4 Conclusions

##### (1) Narrow gap streaming

If a narrow gap exists only in the removable shield, local peakings of the TFC radiation responses are small. However, if the gaps in the removable shield and in the semi-permanent shield form a straight path, the local peaking by gap streaming is rather high (about 40%). Therefore, structural consideration not to form a straight streaming path is required in the mechanical design of the shields.

##### (2) Heterogeneity effects

Coolant (water) plenum region may be a problem. It is desirable to consider not the form a straight path through the removable shield and the semi-permanent shield.

Table 13.3.1 Material Composition of Each Region  
for DOT3.5 Calculations

Region	Volume Fraction
Inner Removable Shield	SS 0.95    H <sub>2</sub> O 0.05
Inner Semi-permanent Shield	SS 0.7    H <sub>2</sub> O 0.3
Cryostat	SS 0.95    H <sub>2</sub> O 0.05
He Vessel of TFC	SS 1.0

Table 13.3.2 Local Peaking Factors of 14 MeV Neutron  
Flux by Gap Streaming Effect through  
Inboard Shields

	Gap <sup>(1)</sup> in Removable Shield		Gap <sup>(1)</sup> in Both Removable Shield and Semi-permanent Shield (Without Step)
	Without Step	With Step (Bend)	
Local Peaking Factor <sup>(2)</sup>	1.09	1.19	7.27

(1) Gap width = 0.5 cm

(2) At the front surface of TFC helium vessel

Table 13.3.3 Local Peaking Factors of Irradiation Properties by Gap<sup>(1)</sup> Streaming Effect through Inboard Shields

	Local Peaking Factor	
	Cyostat	He Vessel
14 MeV Neutron Flux	18.5	6.83
Fast Neutron Flux (E 70/MeV)	2.65	1.25
Total Neutron Flux	1.96	1.13
Total Gamma-Ray Flux	1.64	1.22
Nuclear Heating Rate of SS316	2.06	1.42

(1) Straight gap through the removable shield and the semi-permanent shield (gap width = 0.5 cm)

Table 13.3.4 Local Peaking Factors of 14 MeV Neutron Flux by Heterogeneity Effect in Inboard Shields

	100% - water Region <sup>(1)</sup> in Removable Shield	100% - water Region <sup>(1)</sup> in Both Removable and Semi-permanent Shield
Local Peaking Factor <sup>(2)</sup>	1.65	4.03

(1) Width = 10 cm

(2) At the front surface of TFC helium vessel



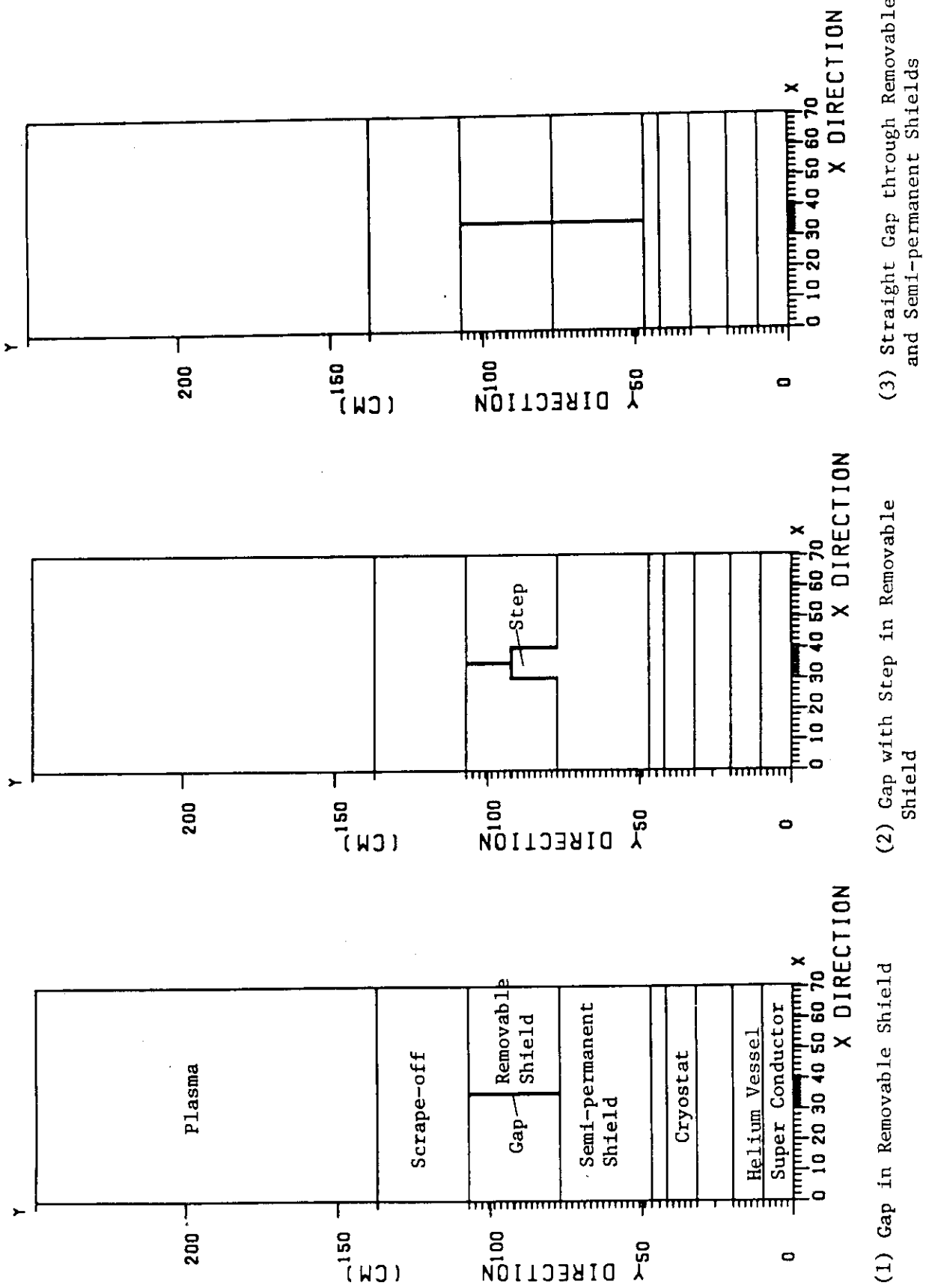


Fig.13.3.1 Two-dimensional Models for Gap Streaming Analysis of Inboard Shields

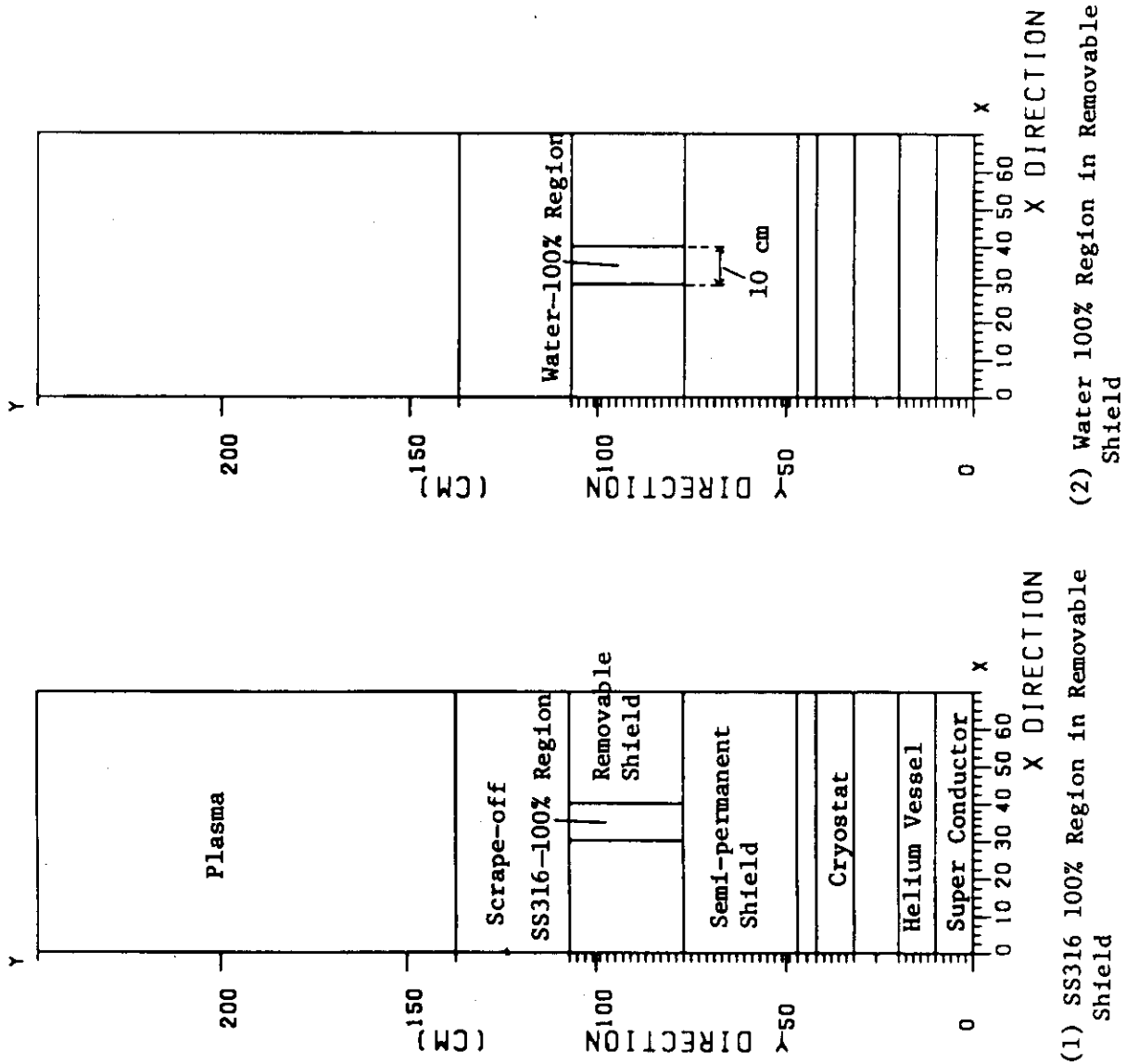


Fig.13.3.2 Two-dimensional Models for Heterogeneity Analysis of Inboard Shield

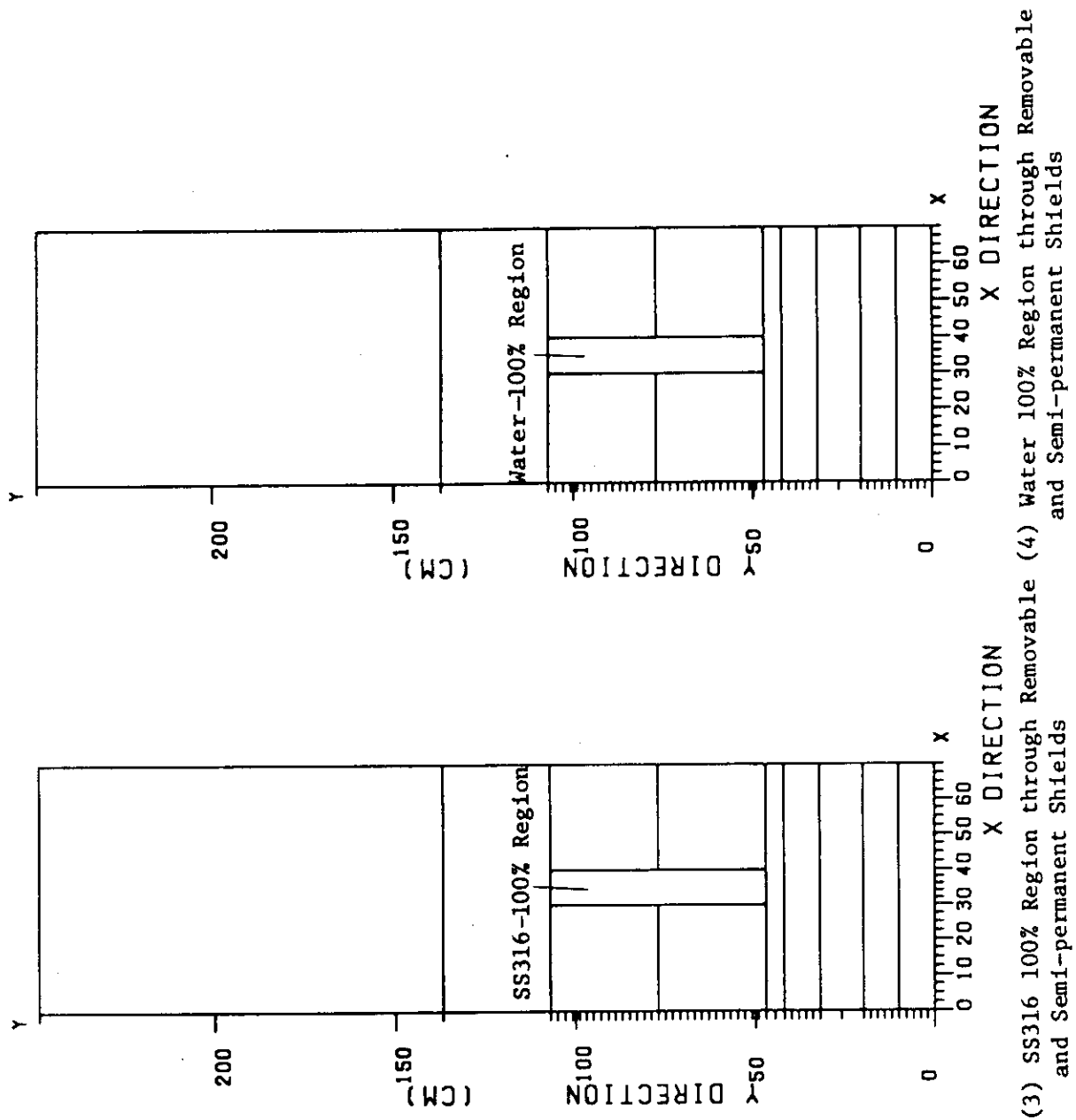
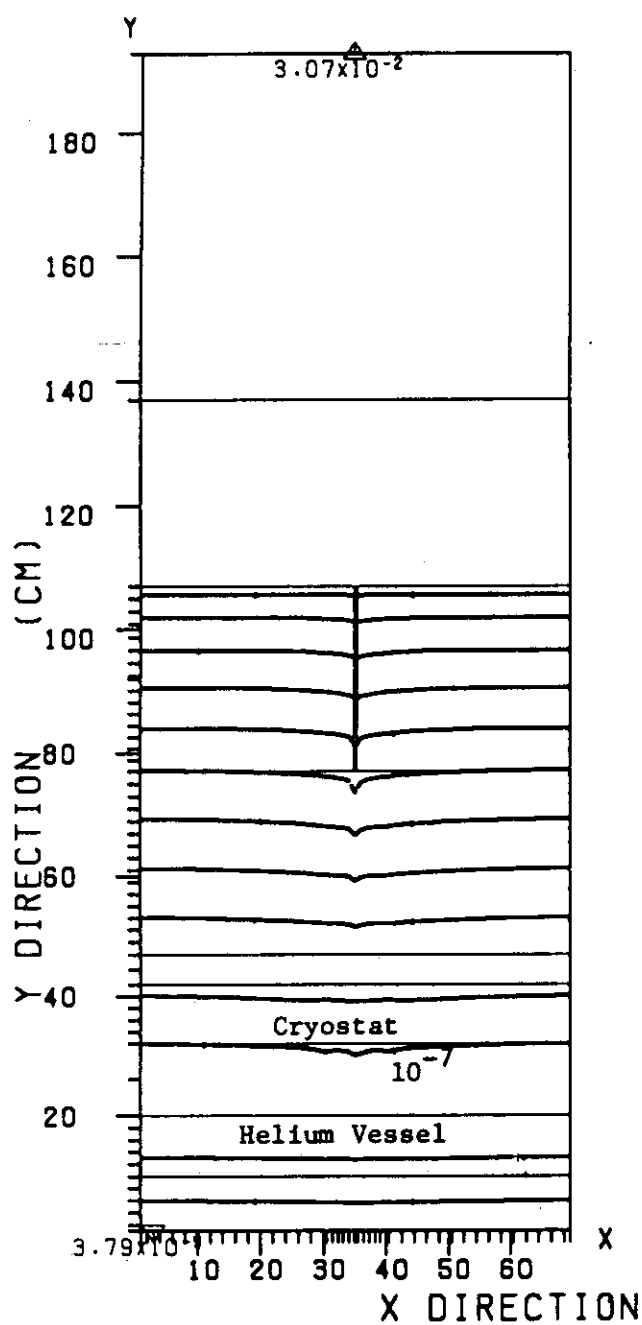
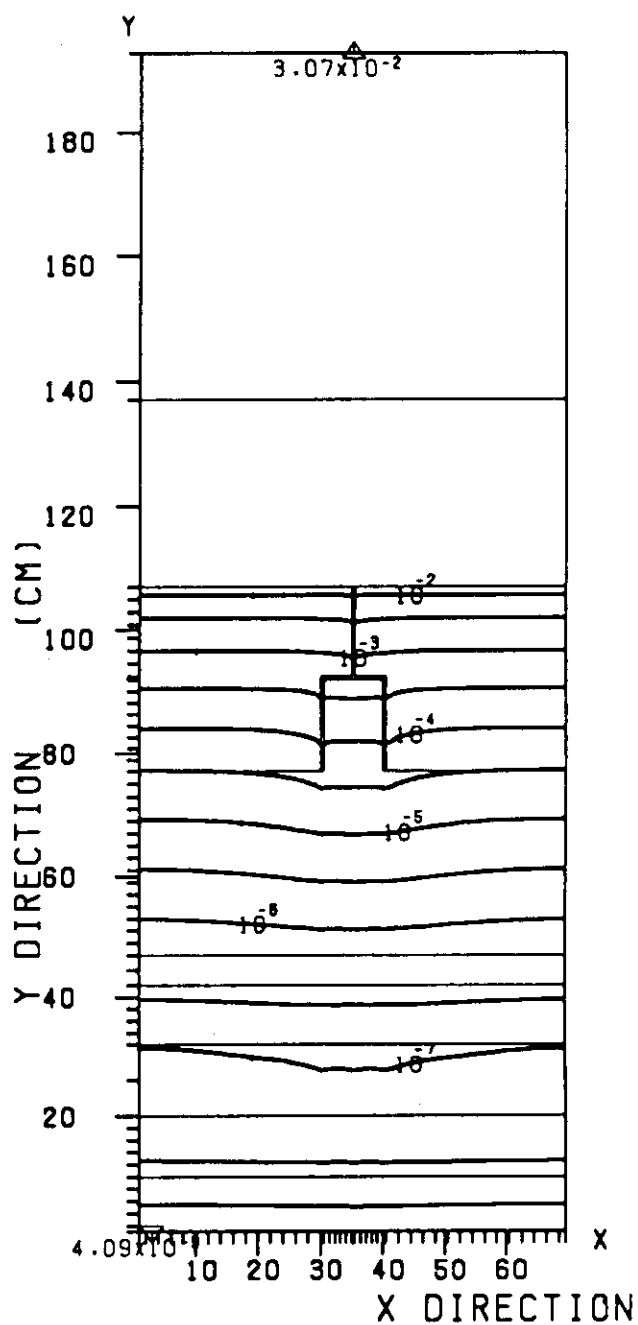


Fig.13.3.2 (cont'd)

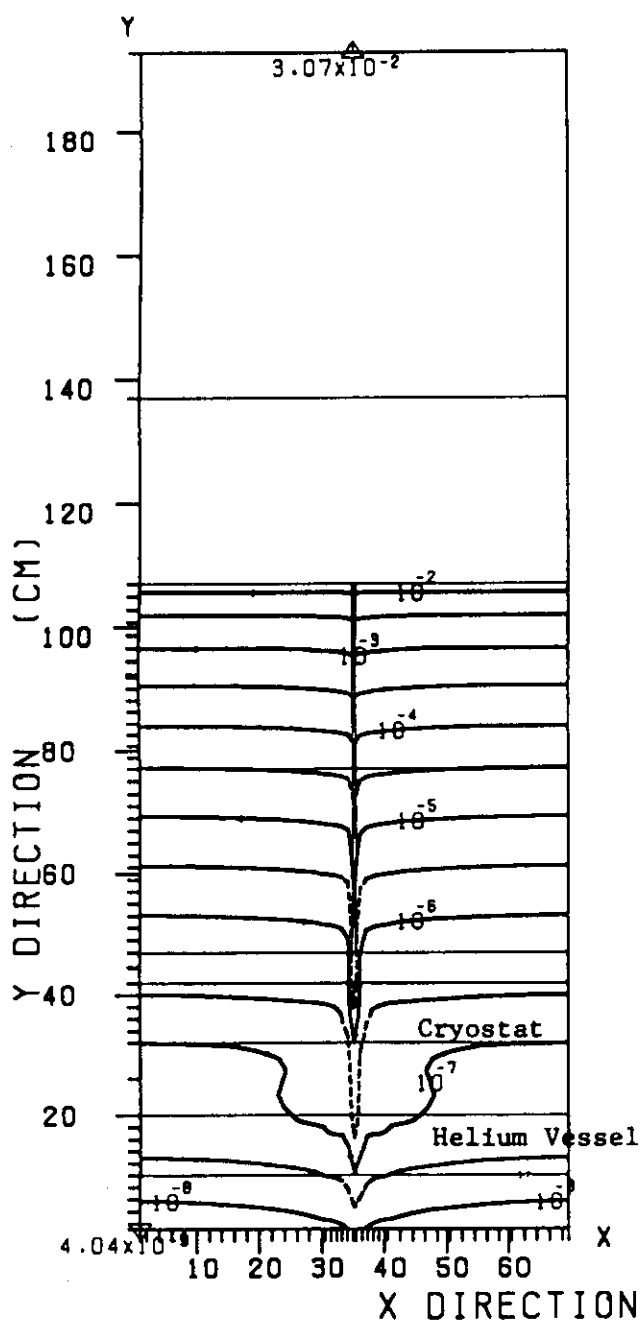


(1) Gap in Removable Shield

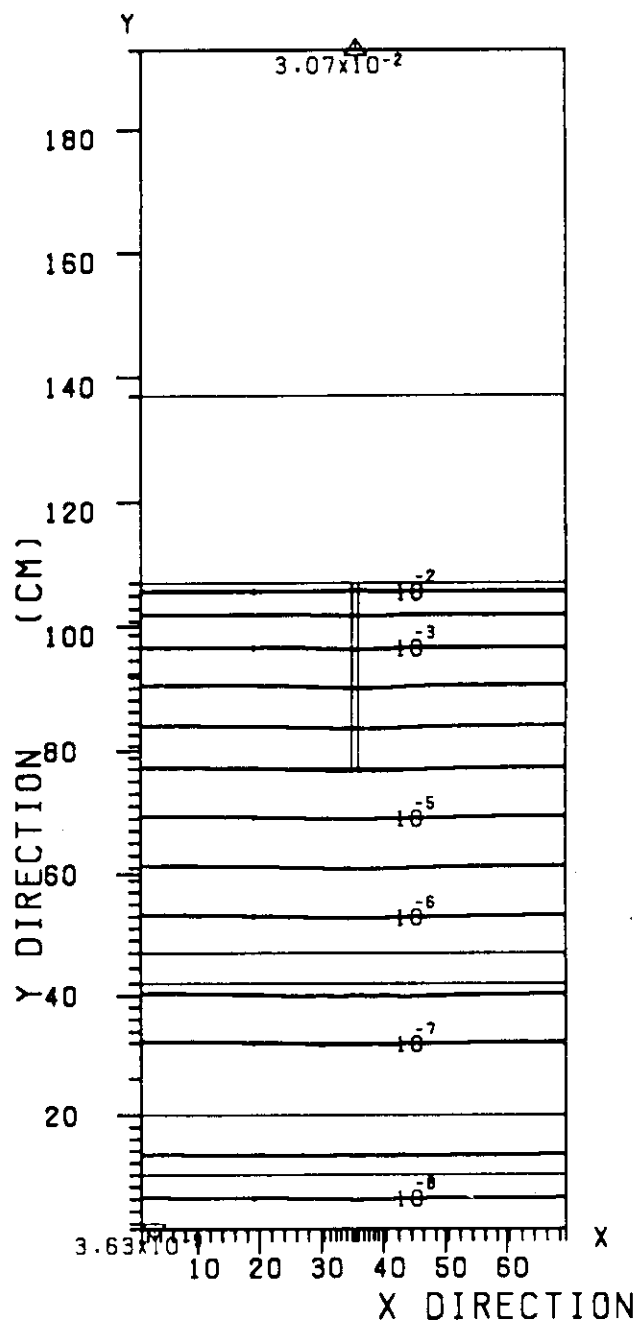


(2) Gap with Step in Removable Shield

Fig.13.3.3 14 MeV Neutron Flux Contour Maps from Gap Streaming Analysis of Inboard Shields



(3) Straight Gap through Removable and Semi-permanent Shields



(4) Bulk Shield without Gap

Fig.13.3.3 (cont'd)

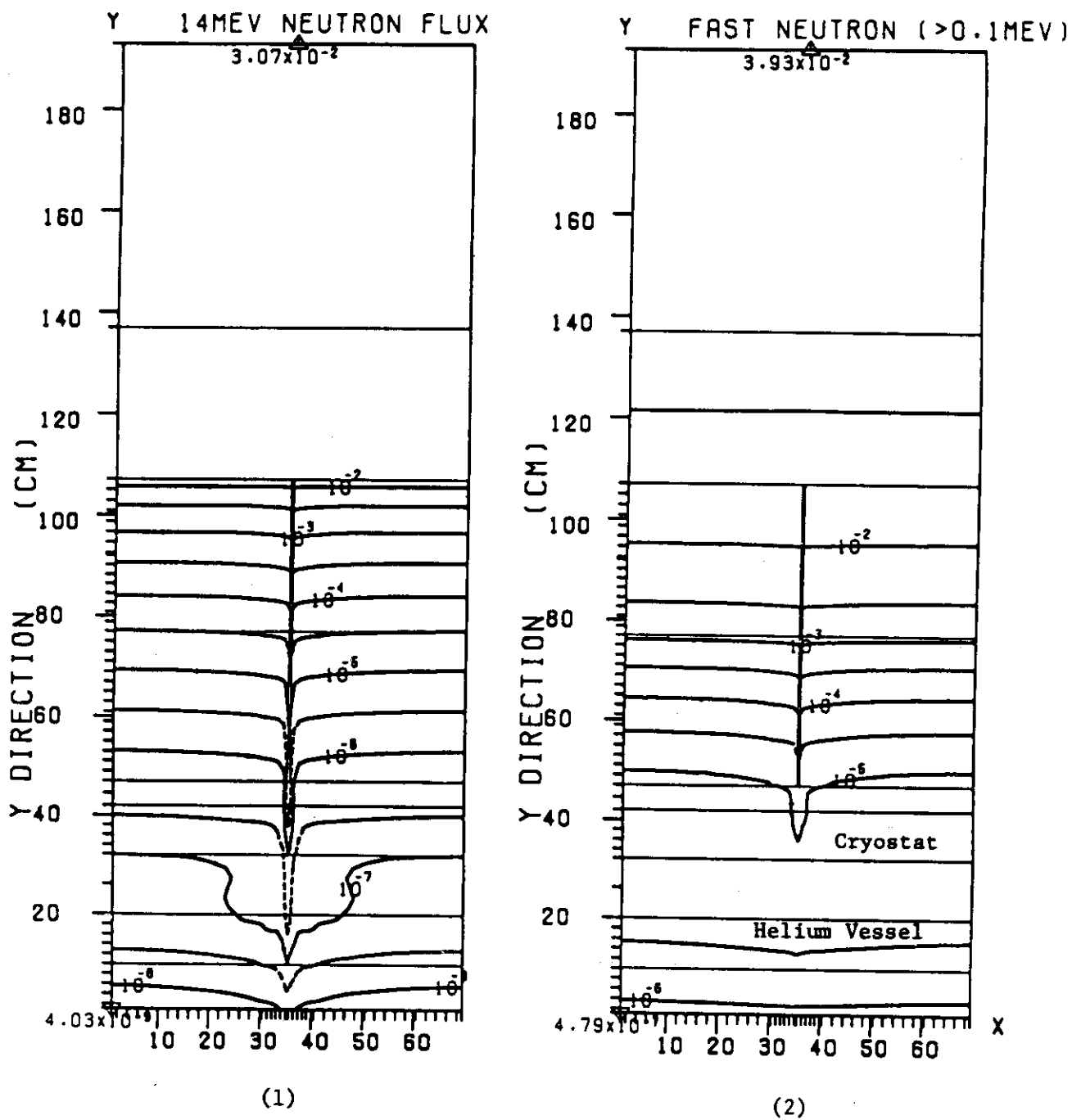


Fig.13.3.4 Flux Contour Maps for Gap through Removable and Semi-permanent Shields from Gap Streaming Analysis of Inboard Shields

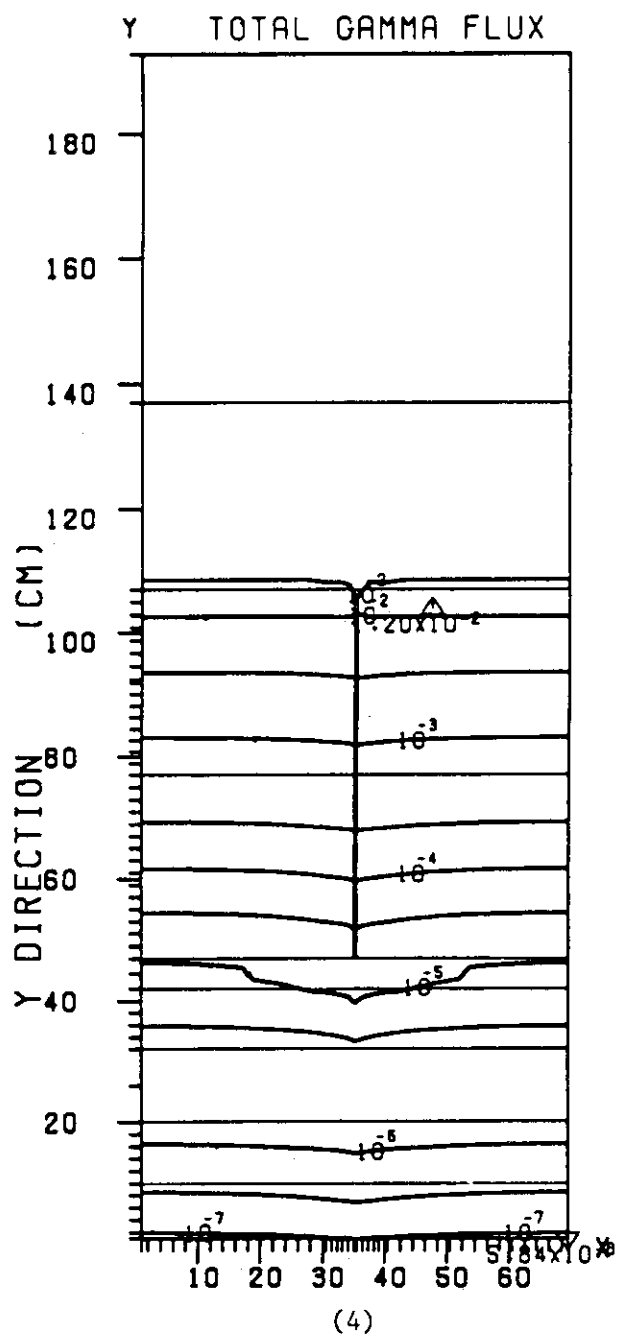
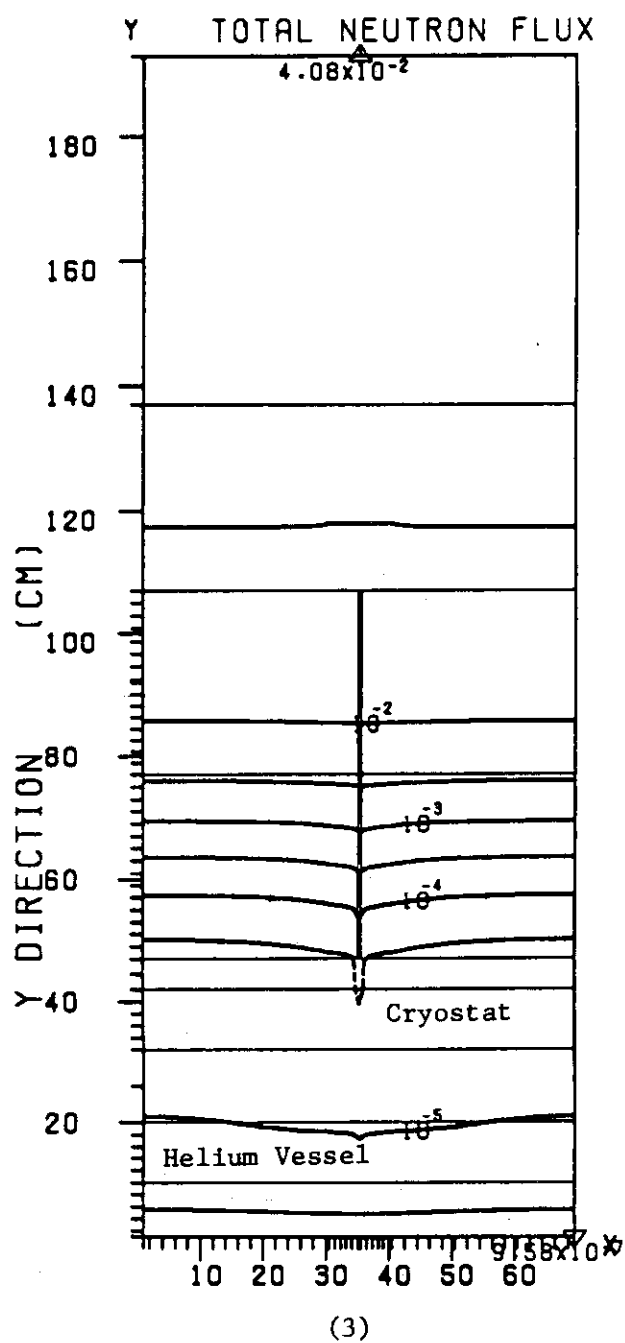
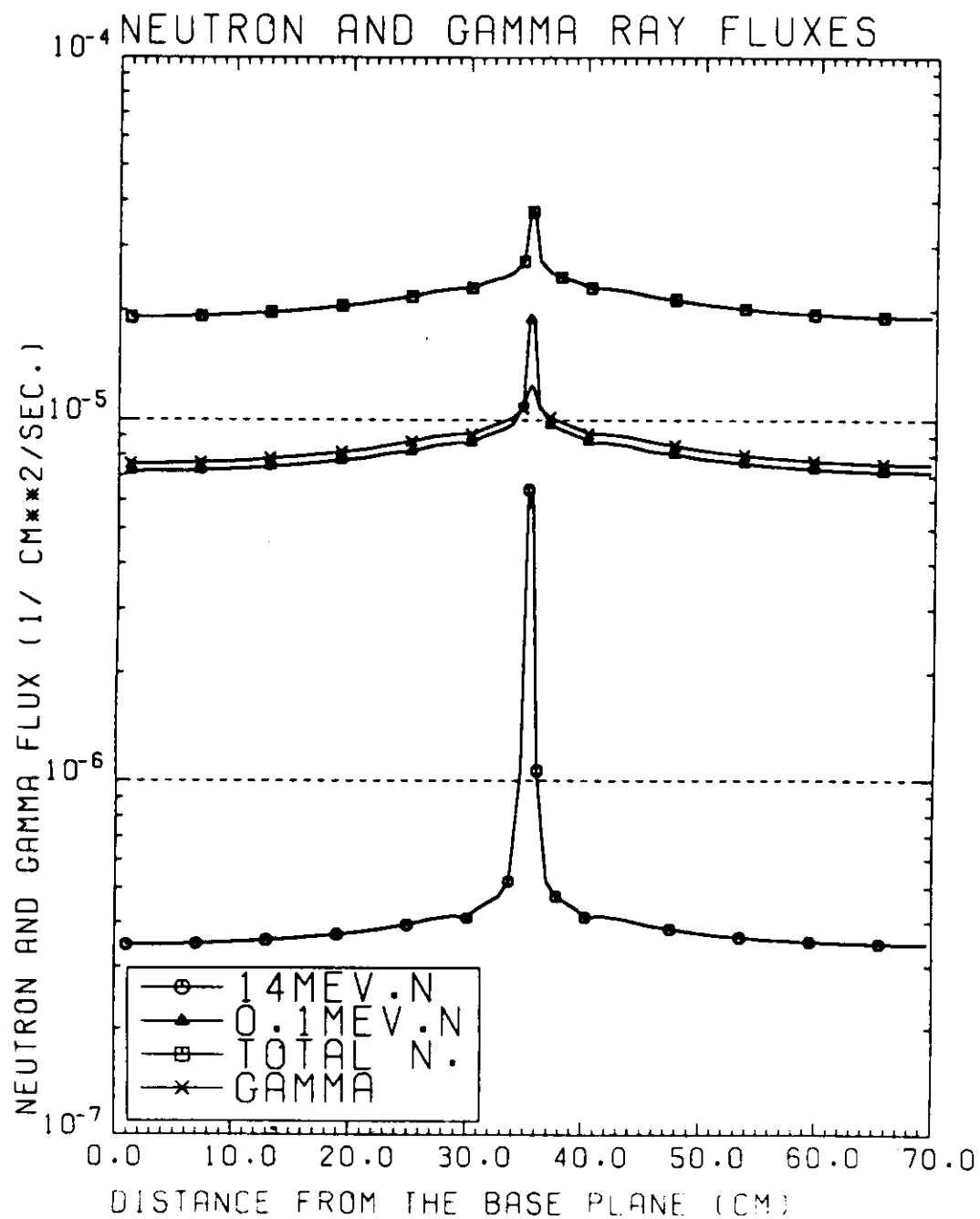


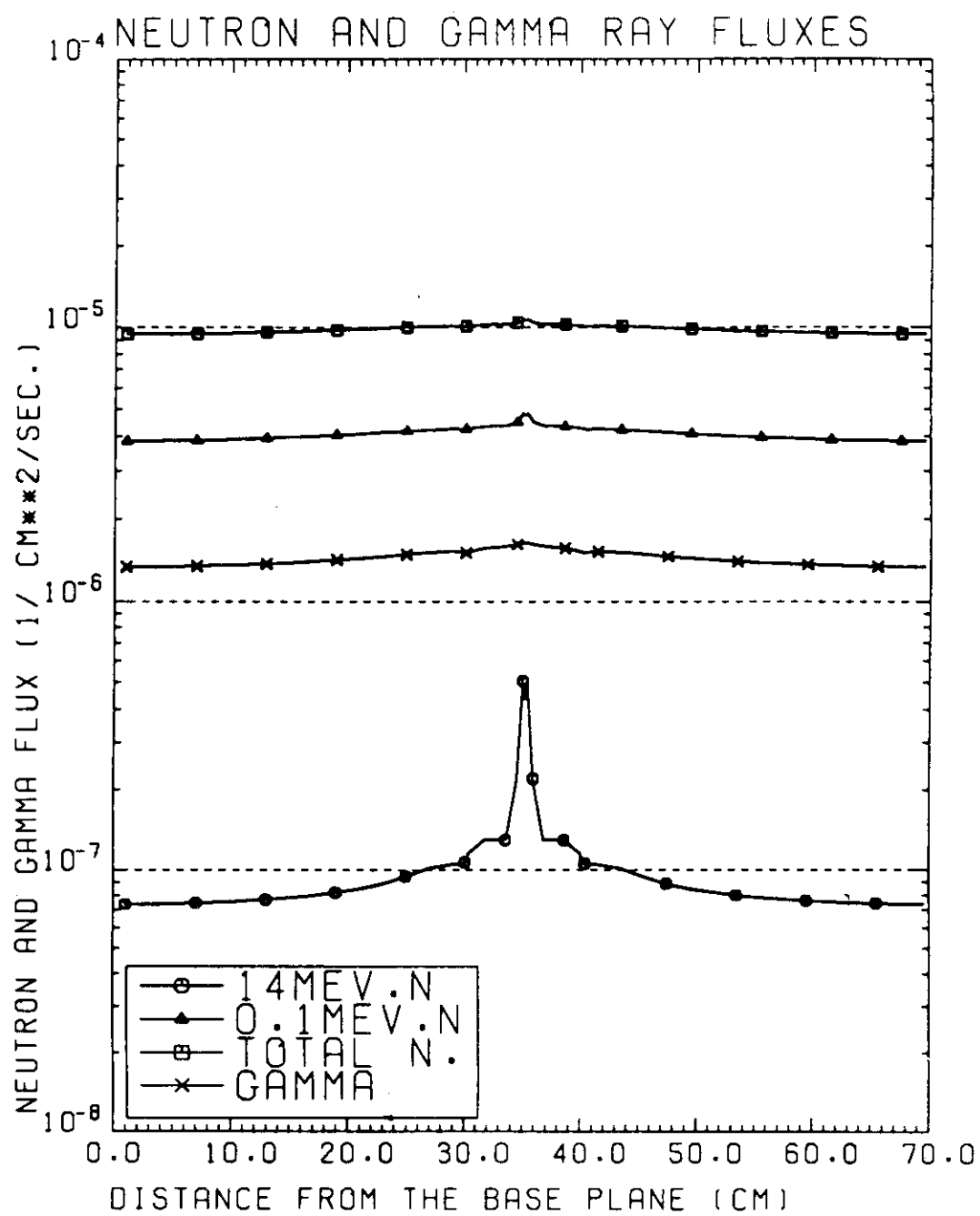
Fig.13.3.4 (cont'd)



(1) at Cryostat

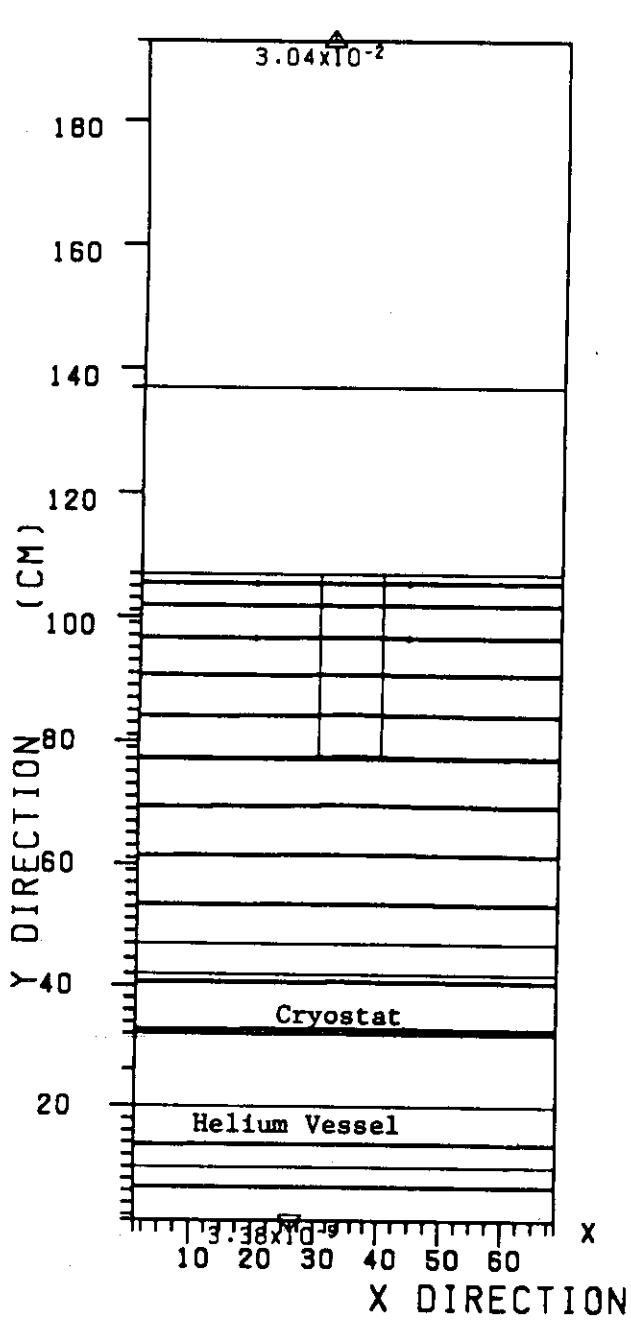
Fig.13.3.5 Flux Distribution along a Traverse Perpendicular to Gap Axis



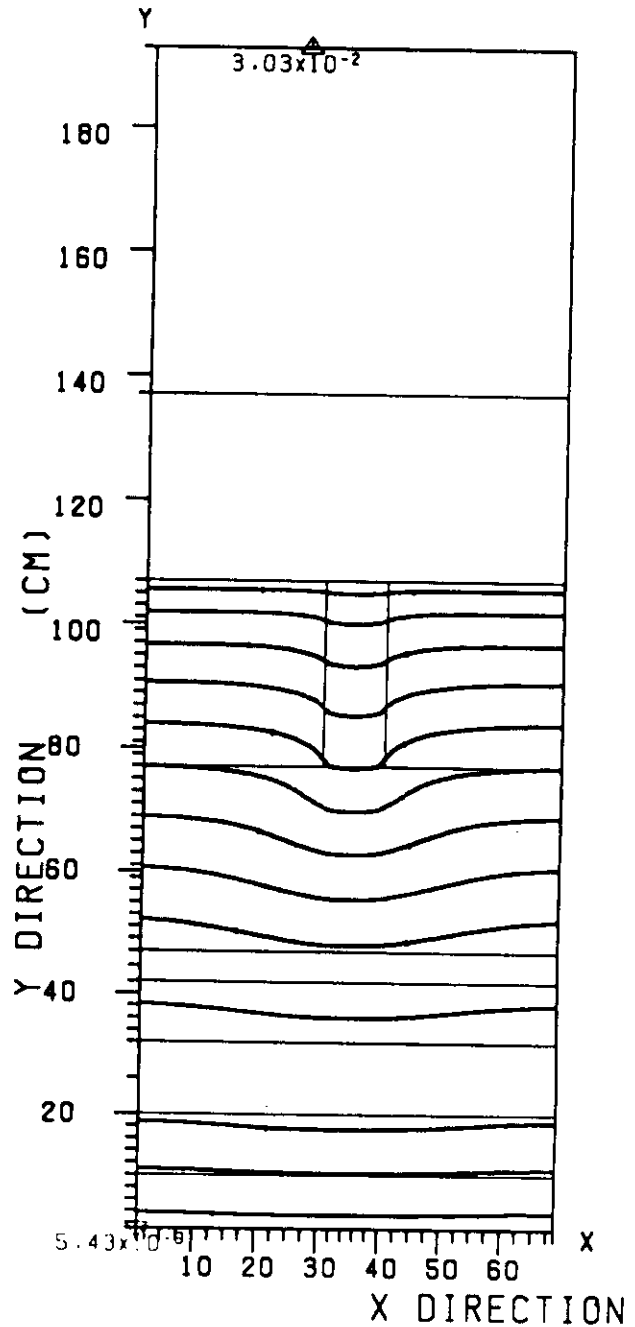


(2) at Helium Vessel

Fig.13.3.5 (cont'd)

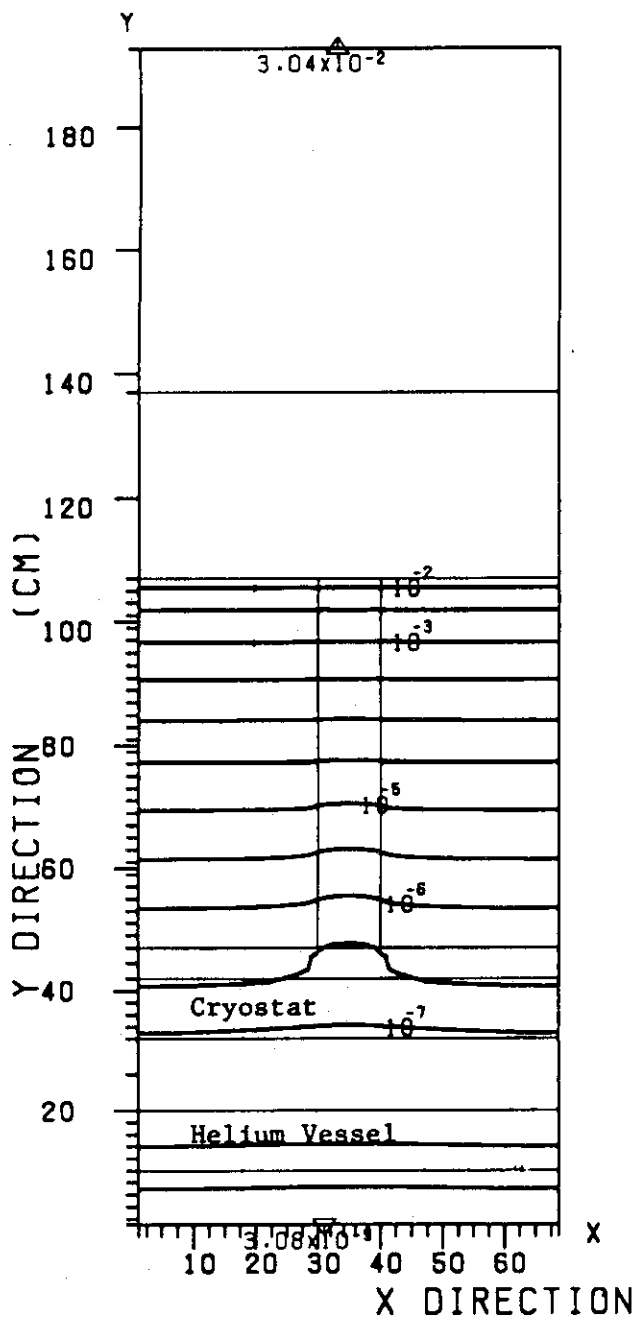


(1) SS316-100% Region in Removable Shield

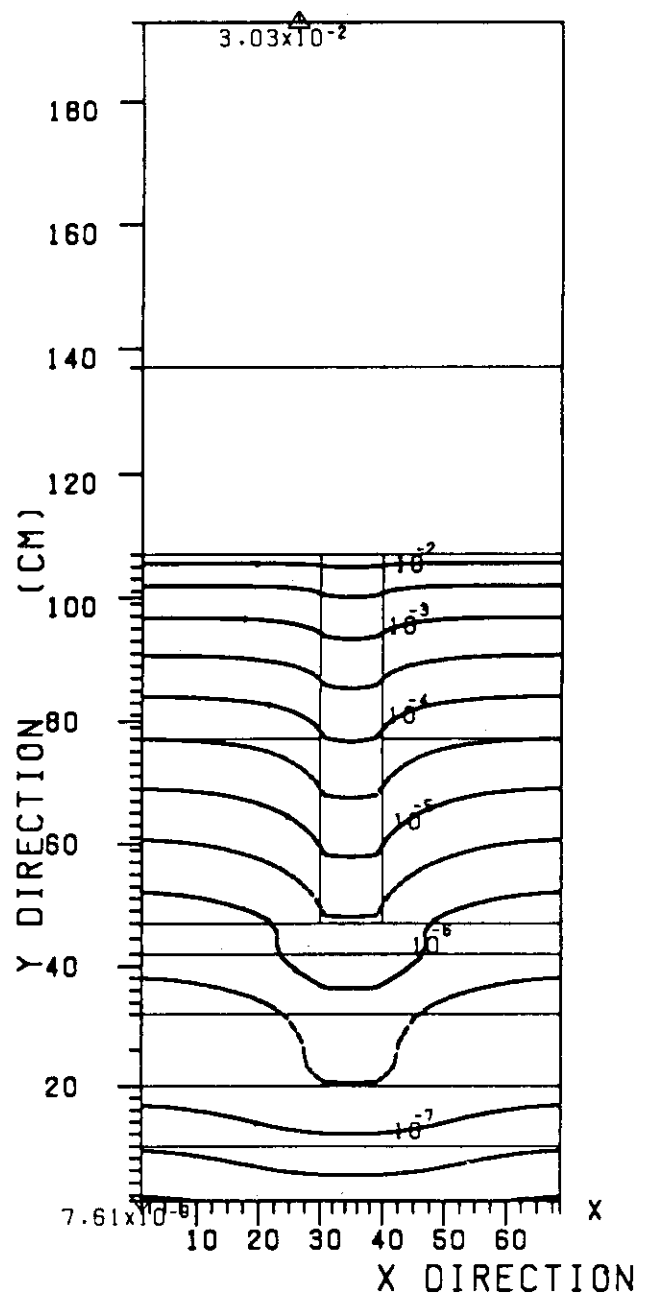


(2) Water-100% Region in Semi-permanent Shield

Fig.13.3.6 14 MeV Neutron Flux Contour Maps from Heterogeneity Analysis of Inboard Shields



(3) SS316-100% Region through Removable and Semi-permanent Shields



(4) Water-100% Region through Removable and Semi-permanent Shields

Fig.13.3.6 (cont'd)

Reference

- (1) C.E. Klabunde, R.R. Coltmon, Jr. and J.M. Williams, J. Nucl. Materials 85 & 86 (1979) 385-389
- (2) J.A. Horak and T.H. Blewitt, Nucl. Technol. 27 (1975) 416-438
- (3) B.S. Brown, J. Nucl. Materials 79 (1981) 1-14
- (4) M.W. Guinan and R.A. Van Konynenburg, UCID-19730, Lawrence Livermore Laboratory (1983)
- (5) R.E. Nygren, J. Nucl. Materials 103 & 104 (1981) 735
- (6) A.R. Sweedler, D.E. Cox and S. Moehlecke, J. Nucl. Mater. 72 (1978) 50
- (7) INTOR, International Tokamak Reactor, Phase One Report, International Atomic Energy Agency, Vienna (1982) 247
- (8) T. Kato and S. Takamura, Teionkogaku Gakkaishi, 18, No.4 (1983) 193
- (9) W.W. Engle, Jr., K-1693, Computing Technology Center, Oak Ridge National Laboratory (1967)
- (10) Y. Seki and H. Iida, JAERI-M 8818, Japan Atomic Energy Research Institute (1980)
- (11) W.A. Rhoades and F.R. Mynatt, ORNL/TM-4280, Oak Ridge National Laboratory (1973)

## 14. Facilities

### 14.1 Site criteria

The main criteria for the choice of a site are:

- (a) Sufficient area of land for buildings and services, and for an exclusion radius for the general public.
- (b) Appropriate land conditions from the points of view of seismic activity and ground load bearing.
- (c) Availability of large electric power supplies to provide pulsed power, including a line that provides a well-stabilized supply.
- (d) Availability of adequate water and cooling supplies for both the construction and operation phases.
- (e) Possibility of good arrangements for radioactive waste storage and disposal for very large pieces of equipment and slightly tritiated waste.
- (f) Satisfaction of the safety requirements for accidental release of tritium as gas or as oxide.
- (g) Availability of man-power resources required for the construction and operation of the reactor and for carrying out experiments, together with the associated housing and amenities.
- (h) Availability of transport for unusually large items of equipment during construction and repair, for tritium during operation, and for personnel for normal daily travel and for travelling abroad.
- (i) Proximity of a well-developed industrial base for the manufacturing of components.

### 14.2 Facility layout

A conceptual plant design study for the INTOR plant was undertaken to: define major buildings and their functional requirements; identify the radioactive boundary; and develop a preliminary plant arrangement.

The following criteria have been followed for the layout of the facilities:

- (a) Alternate positioning of the ICRF heating units.
- (b) Pellet fuelling devices on opposite positions as compared with the centreline of the torus, in order to facilitate fuel injection.
- (c) Test facilities near each other, in order to ease the transport of samples and test components to the hot cell area after irradiation.

The major features of the present arrangement are:

- (1) A centrally located, cylindrical tokamak building designed to withstand the maximum credible overpressure. The tokamak building would house the tokamak and major supporting equipment while allowing for the necessary maintenance and repair activities. The building may have to be designed to withstand high levels of seismic activity in order to meet important safety criteria on radioactive release.
- (2) Primary cooling loops are contained in an annulus within the main tokamak building. This arrangement is possible because a simple heat rejection system is used, without the high temperatures and pressures required by power-generating turbines. The removal of afterheat is not expected to be difficult and can be accomplished by circulating the primary coolant using either normal or emergency power sources. The tritium-processing system is also contained in an annulus within the tokamak building.

- (3) The repair and maintenance building is also a central part of the INTOR complex. This building is connected to the reactor building and the radwaste storage and cooling area by flexible joints so that the effect of earthquakes can be isolated. Radioactive materials are conveyed from the reactor building to the radwaste area through the repair and maintenance building. This configuration makes for simple radiation control zones.

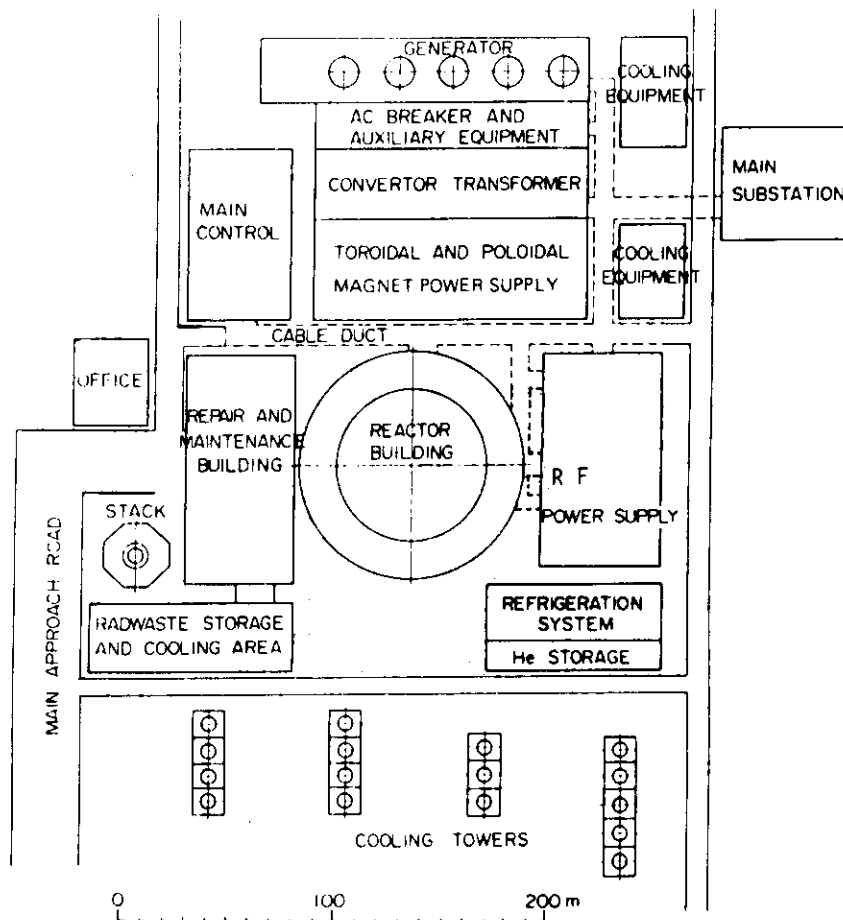


Fig. 14-1 INTOR plant layout

## 15. Cost

Capital and operation costs of the modified INTOR is estimated based on the cost analysis conducted in the Phase IIA Part 1 workshop. Table 15-1 and -2 show the estimation results comparing with the case 8 (ICRF 50 MW) in the Phase IIA Part 1 cost analysis. As a result of design modification, direct capital cost decreased by ~13%. This reduction is mainly contributed by the decrease of power supply capacity and weight of TF coil. The power supply capacity reduction is attained by the change of operation scenario, that is, the adoption of plasma current ramp up by RF instead of inductive ramp up. TF coil weight decrease by the virtue of the coil current density increase from  $25 \text{ A/mm}^2$  to  $30 \text{ A/mm}^2$ . The unit cost of TF coil is assumed to be unchanged. If the unit cost of TF coil should be increased with current density, weight reduction effect might be almost canceled.

Operation cost is greatly decreased (~40%) mainly by the reduction of fluence from  $6.6 \text{ MWY/m}^2$  to  $3 \text{ MWY/m}^2$ . Fluence reduction causes the decrease of maintenance and tritium costs. The total cost which is the sum of capital and operation cost decreased by about 25%.

Table 15-1 Capital Cost Evaluation (M\$ in 1982)

CASE		Case 8 50 MW ICRF	Modified INTOR
<u>1. Reactor systems</u>			
1.1	Torus (1st wall, blanket, shield, test modules, supports, pumping)	89	85
1.2	Magnets (TF, PF, supports)		
	TF	247	189
	PF	105	94
	Sup.	11	11
1.3	Divertor + auxiliaries	11	11
1.4	ICRF system (Launcher auxiliaries)	45	45
1.5	Fueling system	6	6
<u>2. Support system</u>			
2.1	Electrical TF, PF	143	70
2.2	Electrical ICRF	40	40
2.3	Tritium and fuel handling (plasma gas, blanket T)	194	194
2.4	Cooling systems, heat transport, colling tower	69	65
2.5	Instrumentation, control system: diagnostics, instrumentation and control computers	48	48
2.6	Maintenance equipment	28	28
<u>3. Facilities</u>			
3.1	Reactor building: reactor cell, hot cell	121	119
3.2	Other	59	59
<u>SUBTOTAL: Direct Costs</u>		1216	1063
<u>4. Indirect</u>			
4.1	Engineering	227	184
4.2	Installation, assembly	243	192
4.3	Contingency others	674	585
4.4	Design specific R + D	106	106
<u>TOTAL CAPTIAL COSTS</u>		2467	2130



Table 15-2 Operation Cost Evaluation (M\$ in 1982)

CASE	Case 8 50 MW ICRF	Modified INTOR
Tritium	418	190
Electricity	229	229
Material	53	53
Maintenance (5% of D.C.C. yr)	1034	480
Decomission (20% of D.C.C.)	243	213
<u>SUBTOTAL</u>	1977	1165
Contingency (5% of Subtotal)	99	58
<u>Operation Total</u> (Relative Value)	2076	1223
<u>TOTAL</u>	4543	3353

## Chapter XIII Operation and Test Program

### 1 Role of INTOR tests

INTOR is considered to be the major device in the fusion reactor development programme between the present generation of large tokamaks (TFTR, JET, JT-60, T-15) and a demonstration tokamak reactor (DEMO). Thus, whilst the design of INTOR must build on the knowledge gained in the existing research and development programmes in plasma physics and reactor technology, it is equally true that the construction of INTOR and the results of its test programme must provide a major part of the foundation on which DEMO is to be designed. It is therefore necessary to relate the design of INTOR and the specifications of its test programme to the needs of DEMO and to other complementary development programmes which may run in parallel.

DEMO is taken to be a tokamak reactor operating with plasma and blanket parameters extrapolated to a commercial fusion reactor and which will allow a reasonable estimate to be made of the commercial prospects of fusion power. It follows that DEMO will generate several hundred megawatts of electricity and produce net electrical power; it will also have a tritium-breeding blanket with a net breeding ratio greater than unity. DEMO must also demonstrate component and system reliability, availability and lifetime, as well as safe and environmentally acceptable operation under conditions approaching those required of a commercial reactor.

Table 1-1 compares the anticipated range of operating conditions for INTOR, DEMO and commercial reactors. The neutron and surface wall loadings possible with INTOR are less than those anticipated for DEMO by approximately a factor of two, and this has been a driving factor in the design of INTOR, since it is thought that a lower wall loading in INTOR would strongly reduce the value of blanket engineering tests. On the other hand, there are strong incentives for seeking steady-state operation of a commercial reactor.

The tasks which must be accomplished by INTOR and the complementary development programmes are as follows:

- (a) Demonstration of a plasma physics performance which can be extrapolated to DEMO conditions, and in particular the containment of a controlled D-T plasma for long pulse-lengths at optimum plasma parameters
- (b) Testing and development of reactor materials and components, and demonstration of their operation at high availability and reliability under conditions approaching those required for DEMO
- (c) Demonstration of the integration of all necessary components into an overall reactor system which can be safely and remotely maintained
- (d) Investigation of electricity generation and tritium breeding in INTOR in a local structure which is prototypical of DEMO

These requirements lead to a schedule for stage operation, described in Section 2, in which the successive stages are concerned with: (1) the achievement of the necessary plasma conditions and the operation of the basic INTOR device, (2) the testing and development of candidate first-wall and blanket materials and structures in test channels and modules, and (3) a more extensive testing of certain materials and components to neutron fluences approaching half of that expected in DEMO, together with a limited demonstration of electricity production. The major features of this test programme are described in Section 3.

### 1.1 Plasma physics experiments in INTOR and complementary programme

An extensive experimental and theoretical plasma physics programme should support the design and construction of INTOR and will supplement INTOR in providing the physics base necessary for DEMO. The present generation of tokamaks (JET, T-15, JT-60, TFTR) will provide preliminary information on the behaviour of reacting plasmas, plasma shaping, profile control, and alternative methods for auxiliary heating. A primary physics objective of INTOR is to investigate the operation of an ignited D-T plasma and to achieve long, controlled and reproducible burn with optimized plasma parameters. INTOR will also be used for performing certain plasma physics studies. These generally should be limited to experiments related to learning how to run INTOR as well as such investigations that require the unique capabilities of INTOR. Other physics experiments should be made in other plasma physics devices.

### 1.2 Technology testing in INTOR and complementary programme

A technology development programme for DEMO requires testing in both INTOR and simulation test facilities. Extensive screening of candidate materials and component design concepts will be carried out in test facilities which partially simulate the fusion environment prior to operation of INTOR. INTOR will then serve principally to provide component design verification tests with all synergistic effects in a true fusion environment. Testing in INTOR must be supplemented with tests in other facilities to provide the basis for design and construction of DEMO. Such a complementary test programme is necessary because specific types of tests can be simulated more readily in test facilities than in INTOR; in some cases they can only be done in test facilities.

The relation of INTOR to supporting and complementary technology and component test facilities is examined on a technology-by-technology basis in the following subsections.

#### (1) Materials

The basic properties of structural, breeding, insulating and other materials will be determined in test facilities. The behaviour of materials under irradiation will be investigated with accelerator-type neutron sources and in fission reactors, both of which will be able to achieve components end-of-life fluence levels, but not in a fusion radiation environment.

Accelerator neutron sources suffer from limitations on the number and size of samples, while fission reactor neutron spectra lack the important high-energy component associated with 14 MeV fusion neutrons. These test facilities will continue to be used to screen candidate materials for DEMO and commercial reactors. They will also be used to irradiate the few primary candidate materials to high fluences approaching those projected for DEMO. INTOR will then complement these test facilities by performing component element tests in a true fusion reactor environment and by irradiating a large number of samples of the primary candidate materials to fluence levels ( $\sim 3 \text{ MW}\cdot\text{a}/\text{m}^2$ ) approaching 1/3 to 1/2 of the end-of-life fluence for components in DEMO. These tests in INTOR will thus provide a benchmark for some interpreting and validating of the non-fusion irradiation data, and will contribute directly to the data base required for DEMO and subsequent commercial reactors.

(2) First wall/blanket

The thermomechanical and electromagnetic performance of first-wall/blanket elements can be tested in "separate effect" test stands to examine the response to normal surface and bulk heating loads, and to simulate off-normal conditions such as plasma disruption thermal and electromagnetic loads. A "multiple effect" facility can be constructed to investigate the thermomechanical and electromagnetic response to several simultaneous effects in a non-radiation environment. Tritium production capabilities of candidate tritium-breeding materials can be examined in simplified geometries in a 14 MeV neutron source facility. Tritium recovery can be investigated in special test stands and in fission reactors. One of the main objectives of INTOR is to provide simultaneous testing of thermomechanical and electromagnetic response, and tritium production and recovery for blanket assemblies in an actual fusion environment. Design verification and long-term reliability demonstration tests of first-wall/blanket elements and modules will provide an engineering data base for the design and construction of DEMO.

(3) Plasma heating

An integrated RF heating system and its reliability under sustained operation in a non-radiation environment can be demonstrated in test facilities. The integration of the heating system into a tokamak reactor system is an objective of INTOR. Information on neutron and plasma radiation effects upon components can be obtained from irradiation experiments in fission reactors and accelerators. Testing of advanced components can be carried out in INTOR. Also, the investigation of the performance of integrated heating systems under sustained operation with high availability in a fusion reactor radiation environment is an objective of INTOR.

## (4) Magnetism

Proof-of-principles testing of superconducting toroidal and poloidal field coils can be carried out in test facilities such as the LCP test facility and the planned 100 MJ pulsed coil test facility in the USA, and in the SC magnet test stand (SIMS) in the USSR. Experience with superconducting coils on tokamaks will be obtained from T-7, T-15 and Torus II. Beyond this level of testing, it is necessary to demonstrate: (1) an integrated magnetic system that functions in a tokamak fusion reactor environment, and (2) the reliability of that system under sustained operation. The investigation of these two items is an objective of INTOR. Since radiation effects upon materials properties can be studied separately, preliminary investigations could, in principle, be performed on a modified LCP test facility incorporating superconducting toroidal and poloidal coils and normal poloidal coils, a vacuum vessel/blanket/shield/structural system, and a means of simulating the electromagnetic and mechanical effects of plasma disruptions. However, such a modified LCP test facility would be complicated and costly. It is probably more feasible to study separate effects (e.g. fatigue and crack growth limits on large structural elements) in separate, single-purpose test facilities and then to rely upon INTOR for an integrated test of the complete magnetism system.

## (5) Tritium processing and containment

Most of the key issues involved in constructing and operating an integrated tritium processing system (excluding tritium recovery from the blanket) can be examined in facilities such as the Tritium Systems Test Assembly (TSTA). Such a facility can also deal with important aspects of tritium containment. INTOR will investigate the integration of the tritium processing system into a tokamak reactor system, including plasma exhaust, refueling and blanket tritium recovery.

## (6) Radiation shielding

The methods and basic nuclear data for radiation shielding can be validated by performing integral shield experiments with 14 MeV neutron sources. INTOR will verify the prediction capability for the design of an integrated radiation shield system and will provide engineering safety factors for the design of DEMO and subsequent commercial reactors.

## (7) Divertor collector plates

The thermomechanical and electromagnetic performance of integrated systems can be demonstrated under sustained operation in a non-radiation environment in test facilities. Neutron radiation damage effects on these components can be studied in fission reactors, but not with the important 14 MeV neutron component in the spectrum and not under the appropriate thermal and mechanical loadings. Erosion due to plasma interactions can be studied in plasma physics experiments and in accelerator

test facilities. Testing of several design concepts can be carried out in INTOR. The integration of these systems into a tokamak reactor system is an objective of INTOR, as is the investigation of the performance of these integrated components under sustained operation in a fusion reactor environment.

(8) Remote assembly/disassembly and maintenance

The tools and techniques for remote assembly/disassembly and maintenance can be developed and tested in test facilities, including a mock-up facility for INTOR. The investigation of remote maintainability of a tokamak in a radioactive environment is an objective of INTOR.

(9) Diagnostics, data acquisition and control

Diagnostics, data acquisition and control components can be tested in plasma experiments, in fission reactors and in other test facilities. The investigation of an integrated diagnostics, data acquisition and control system for a tokamak reactor and of the integration of such a system into a tokamak reactor are objectives of INTOR. Testing of advanced components can be done in INTOR. The investigation of the performance of such a system under sustained operation in a reactor environment is also an objective of INTOR.

## 2 Operation schedule

It is convenient to define three different stages of operation for INTOR, with emphasis on different aspects of the utilization of the device in each stage. During the first stage, the emphasis will be upon learning how to operate the device so as to obtain optimum performance. This will entail about one year of hydrogen plasma operation and engineering check-out, followed by about one year of D-T plasma operation. Calibration testing and some preliminary engineering testing may be performed.

The second stage will be devoted to engineering testing, with emphasis on a flexible test programme and with the objective of 25% availability. The duration of this stage will depend upon the exact test programme that will be developed ultimately for INTOR. At the present time, three years are anticipated for this stage of operation. This period would allow for initial testing and modification of a primary and back-up blanket concept by each of the four participating partners.

The third stage of operation differs from the second stage in that the emphasis is upon maximization of availability and fluence accumulation for performance testing of components. The objective of this stage is to obtain about  $3 \text{ MW}\cdot\text{a}/\text{m}^2$  of 14 MeV neutron fluence.

A representative schedule for staged operation is given in Table 2-1. The different INTOR testing objectives to be achieved during the various stages of operation are indicated in Table 2-2.

### 3 Test programme

A preliminary test plan has been developed to provide insight into the design and operational requirements that must be imposed on INTOR. This initial plan has been developed using judgements as to where INTOR fits into an international fusion development plan, as discussed in Section 1, and is considered an essential part of the development of a demonstration reactor.

The test plan is based on three stages of reactor operation, and the testing sequence is arranged to permit timely collection of data, as shown in Fig. 3-1. During Section I, emphasis is placed on plasma physics tests whose objective is the provision of a basis for the physics required for the DEMO reactor. In addition, these tests will provide the necessary experience and understanding of the INTOR plasma so as to permit long-pulse operation during Stages II and III when other tests requiring large fluences will be conducted. Most tests requiring frequent change-out will be performed during Stage II. This will provide a maximum amount of data early in the programme and will permit the use of a high-duty cycle during Stage III.

All material and module tests in INTOR can be fulfilled in about 12 m<sup>2</sup> of test area. A standard size of 1 m × 1 m has been defined for test channels and test modules. Two sectors of the machine incorporate six test pockets of 1 m<sup>2</sup> each. Some of the pockets (two or three) have to be opened to the plasma for surface materials tests. Other test units will be located behind the first wall and will not interact with the plasma. Test modules and test channels have equal dimensions, which facilitates interchange of test locations. Horizontal module and channel installation was selected as an approach that could provide the largest test area and minimum interference with other reactor components. A third sector is provided for plasma engineering and electricity generation tests.

### 3.1 Plasma operation in Stage-I and plasma experiments

During the initial stage of INTOR operation, the major objectives of the device will be the demonstration of plasma physics required for DEMO, as well as the demonstration of a number of the intrinsic reactor-relevant technologies in a fusion environment. Besides these specific programmatic objectives, however, the activities in Stage I are intended to prepare for the Stage-II engineering tests by establishing reliable operation of the device (25-50% availability) at the design parameters ( $\langle\beta\rangle \sim 5\%$ ,  $\sim 1000$  s burn pulse at 80% duty factor, and a neutron wall loading of  $1.3 \text{ MW/m}^2$ ). It is crucial, therefore, that the Stage-I schedule provide for the optimization of the tokamak, heating, fuelling and diagnostic systems as well as for remote maintenance capability.

In addition to the demonstration of DEMO characteristics, it is imperative that INTOR verify and expand the plasma physics data base for the ignition regime. This is important for establishing more detailed models to predict the plasma behaviour in future devices and thus to ensure reliable, optimized operation. Plasma physics experiments which are intended to provide such information will be performed during the final phase of Stage-I operation.

### 3.2 Plasma engineering tests

Plasma engineering tests for INTOR have not been defined yet. A test plan will have to include the information to be gathered from experiments on large tokamak machines now under construction and from the operation of INTOR during Stages I and II. Plasma engineering tests of plasma-wall interaction and long-pulse operation as well as plasma heating will be required for INTOR design. For a reliable operation of DEMO and of future power reactors, plasma control and operation should be as simple as possible. Examples of possible plasma engineering tests on INTOR are:

- (a) Tests of new impurity control and exhaust concepts under burning plasma conditions
- (b) Experiments for studying non-uniform energy deposition (during disruptions) on the divertor plates and the first wall
- (c) RF launcher tests
- (d) Optimization of burn control.

These tests may be performed at available experimental ports with a total area of about 3 to 5  $\text{m}^2$ . Plasma engineering tests which will require a drastic change of the INTOR configuration are unacceptable; however, some tests such as the application of helical winding or stability control coils may be feasible. Nonetheless, this kind of experiment should be performed by hydrogen tokamaks. Plasma engineering tests that will substantially alter the plasma operating characteristics



must be scheduled during Stage I. Only a limited number of such tests could possibly be performed during Stages II and III, since the engineering tests (e.g. for blanket, materials) require stable, reproducible and well-controlled plasma operation. A full 1/12th sector of the first wall/shield has been allocated to plasma engineering tests.

### 3.3 Blanket engineering tests

The primary purpose of blanket module tests in INTOR is to provide operating experience and design verification for extrapolation to a DEMO blanket design. The programme of blanket testing will provide basic engineering data in a fusion environment and deal with the following three main tests.

- (a) Blanket and engineering tests will emphasize confirmation of results predicated upon ex-machine tests. Tests will include 1 m<sup>2</sup> prototype blanket modules, tritium recovery capsules and tests of critical life-limiting elements of the blanket.
- (b) Critical element tests are used to provide closer simulation of DEMO reactor conditions and to permit use of accelerated testing. Long-term prototype blanket module demonstration tests are planned.
- (c) Short-term blanket tests will be used for design verification, and they require test periods ranging from about one month to two years. Demonstration tests are expected to be used to correlate testing results and analytical predictions for combined materials and synergistic effects, and to provide information on performance changes with irradiation. These test modules will be left in the reactor until the end of Stage III.

Should failure of a blanket test module occur, failure analysis would provide information on failure modes and guide design variation tests for design improvement efforts.

### 3.4 Materials testing-bulk properties

A bulk materials test programme has been defined to provide information for: (1) primary and back-up structural materials; (2) high heat flux materials; (3) insulators; (4) breeders; and (5) multipliers. Material properties of interest, the number of materials and variations, together with the number of test temperatures, fluences, duplications and other test conditions, resulted in the identification of 30 000 specimens for test in INTOR. Single-variable tests to characterize the effects of displacement rate, temperature and stress were included in defining requirements. Investigation of specimen volume requirements indicated that all 30 000 specimens could be tested in a single 1 m × 1 m test pocket

and resulted in identification of a 5-cm-diameter  $\times$  15-cm-long standard capsule to contain a varying number of specimens. This capsule can contain as many as 1440 swelling and phase stability specimens. One in-situ cyclic fatigue specimen fits in a single capsule. A total of 300 capsules are required to contain all 30 000 specimens. As many as 153 capsules can be in the reactor at a given time. At each change-out interval, 60 capsules are replaced. The temperature of each capsule can be controlled to operate at a specific level between 50°C and 700°C. Individual capsules can be removed without having to disconnect services. A second 1-m<sup>2</sup> test pocket will be used for single variable tests or to increase the fluence to the specimens.

INTOR is designed to achieve 3 MW·a·m<sup>-2</sup> (at the first wall) of neutron fluence with a high probability of success. Samples will be removed at 0.1, 1.0, 2.0, 3.0 MW·a·m<sup>-2</sup>.

### 3.5 Surface materials tests

Plasma-wall interaction is of great importance as it substantially affects the performance of the plasma and the integrity of the wall surfaces. INTOR studies have shown that the first-wall components and the divertor plates are eroded rather rapidly by plasma-wall interactions during the operation of the reactor, and that this erosion not only may be a problem for plasma operation but also is a life-limiting factor for components whose surfaces are exposed to the plasma. Plasma-wall interaction is expected to continue to be an important aspect of the design for DEMO and other devices that will follow INTOR. An extensive programme for surface testing in INTOR has been developed and is described in this section.

The objectives of the surface materials test programme are:

- (a) To obtain information that will enhance the data base needed for the design of DEMO and other reactors that will follow INTOR
- (b) To provide proof-of-concept tests for selected surface structures
- (c) To examine the performance reliability of selected surface structures.

INTOR will permit tests to be made in a fusion environment on the influence of synergistic effects on sample surface performance, to an extent that could not be achieved elsewhere. The synergistic effects are caused by the simultaneous irradiation of surfaces with neutrons, atoms, ions, electrons and photons. The synergistic effects may influence the sample surface performance with respect to particle retention/re-emission, plasma impurity release and surface erosion/impurity deposition.

INTOR will not be a substitute for simulation experiments, since the range of operating conditions is limited and therefore the results will be valid only for a narrow range of parameters which may not correspond to the expected DEMO conditions.

The most important surfaces are those of the first wall and of impurity control components such as divertor collector plates and limiters. The plan requires the use of about 5000 material specimens. Most specimens are 1 cm × 1 cm, but some larger samples will be required. The 1 cm × 1 cm samples can be tested in the allocated 1-m<sup>2</sup> test area, but the larger samples will have to be included in other areas, possibly as the first wall of other test modules and in the divertor chamber. Specimen locations, cleaning method, temperature, material and fluence levels are varied in the test programme.

### 3.6 Surveillance tests

The basic INTOR reactor components and operation will provide useful information. Monitoring failure rates, failure modes and maintenance times will permit improvements to be achieved for a DEMO reactor. Achievement of sufficient operation time in INTOR to provide reliability data for prediction of component failure rates in DEMO is a goal of INTOR.

### 3.7 Nuclear tests

INTOR will offer one of the first opportunities to perform important neutronics experiments in a radiation environment that is prototypical of a demonstration tokamak fusion reactor and in realistic blanket modules. INTOR will have not only higher fluxes than previous machines but also a significantly longer pulse time and a much higher duty factor. For planning purposes, this means that the neutron source can be considered to be almost steady state.

Neutronics information is required throughout the INTOR testing programme:

- (a) Testing of neutronics is required especially in the early stages of D-T burning for characterization of the basic machine performance. For example, the source intensities and the spatial variation of the source must be known. Traditionally, this area has been dealt with as part of the plasma-diagnostics studies.
- (b) The INTOR shield should be verified also in the early stages of D-T burning, at a low power level.
- (c) Neutronics information is required in proof-testing of various tritium-breeding blanket concepts. These studies include the determination of tritium breeding and nuclear heating.

- (d) Neutronics information is needed in providing important engineering data, such as: the radiation environment at sites where materials damage is studied, around sensitive structural components and at the magnets; the activation of various reactor components, especially the first wall and blankets; and radiation streaming through the shields and around various penetrations.
- (e) Neutronics information is needed to link the INTOR experiments with accelerator-based experiments, such as those using RTNS-II and FMIT, so that the whole body of information will be useful for the design of demonstration fusion breeders.
- (f) Neutronics experiments can provide important data for validating neutronics codes and various modelling approaches.

### 3.8 Electricity generation

One of the objectives of INTOR is to demonstrate the generation of electricity under reactor-relevant conditions. This does not necessitate the generation of net electricity, but can best be achieved by the production of 5 to 10 MW of electricity in an accessible out-board region of the reactor for a period of several months.

The main reason for producing electricity in INTOR is the verification that the necessary technology is available. Since the technology for producing electric power from heated steam is mature, the major technological problem is the recovery of heat from a blanket which will breed and safely contain tritium.

Electrical power generation at the end of Stage II and the beginning of Stage III should be accomplished by a special breeding blanket sector that is installed during the initial construction of INTOR, following successful blanket operating and module tests during Stage II. Simultaneous tritium and electrical power generation in a prototypical DEMO blanket sector should be performed at the end of Stage III.

### 3.9 Test module installation

The INTOR approach of test module installation was selected to minimize the effects of the test programme on the overall operation of INTOR. The complexity of past tokamak experiments has greatly limited the access to the reactor and constrained machine maintenance. To alleviate this problem, INTOR design has selected to radially extract shield/blanket sectors between magnets. This approach requires that open access be available around the reactor for transfer of RF launcher, shield sectors, divertors and other components. The INTOR test module installation approach has been developed to be compatible with the reactor design.

The major features of the approach are:

- Three dedicated test sectors
- Standardized test pockets (1 m<sup>2</sup>)
- Horizontal test module installation
- Independent replacement of test modules
- Isolation of most testing from the plasma vacuum.

### 3.10 Support facilities

Each test component inserted in the reactor will require support facilities whose size can be large. Therefore, scoping design studies are useful in assessing the impact of the test programme requirements on the INTOR reactor design. The support facilities can be located in the reactor building outside the magnets. However, in cases requiring large floor space, consideration should be given to locating the support facilities in the basement below the test area.

The test facility layout should be developed with the following aims:

- (a) To permit access for independent removal and installation of test modules
- (b) To provide clearance around the reactor for normal reactor maintenance equipment
- (c) To permit rearrangement of the modules within the test sectors without major revision of the support system components.

### 3.11 Post-irradiation examination (PIE) facility

Although some useful information can be obtained from test instruments during irradiation, most of the technologically important data on materials properties can be obtained only through post-irradiation examination (PIE) of the experiments.

The examination facilities (for the early PIE stages at least) must be located at the INTOR site in order to efficiently service the reactor, to minimize the time for change-out of modules and samples, and to reduce time delays and costs for shipping large irradiated components. Later post-irradiation examinations, especially those requiring very sophisticated and expensive equipment (such as electron microprobes or microscopes) or highly trained operators, could be done away from the INTOR site if appropriate facilities exist which can accommodate the workload.

Table 1-1 Anticipated reactor operating conditions

	INTOR	DEMO	COMMERCIAL
Thermal power (MW)	≈600	≈1000	4000
Gross electrical power (MW)	10	≈100	1000
Neutron wall loading (MW/m <sup>2</sup> )	1.24	2-3	3-6
Surface wall loading (MW/m <sup>2</sup> )	0.1	0.2-0.8 <sup>a</sup>	0.3-1.5 <sup>a</sup>
Burn time (s)	≈1000	≈1000	≈1000
Number of cycles	7.3×10 <sup>4</sup>	≈10 <sup>5</sup>	≈10 <sup>5</sup>
Integrated wall load (MW·a/m <sup>2</sup> )	3.0	10-20	15-30

<sup>a</sup> Depending on whether or not a divertor is necessary.

Table 2-1 INTOR staged operation schedule

Stage	Years	Emphasis	Availability	Annual 14 MeV neutron fluence <sup>a</sup> , (MW·a/m <sup>2</sup> )	Annual number of shots <sup>b</sup>	Total number of shots
IA	1	Hydrogen plasma operation	10%		$2.5 \times 10^3$	$2.5 \times 10^3$
IB	1	Engineering check-out				
		D-T plasma operation	15%	0.156	$3.8 \times 10^3$	$3.8 \times 10^3$
II	3	Engineering testing	25%	0.26	$6.3 \times 10^3$	$1.9 \times 10^4$
III	4	Upgraded engineering testing <sup>d</sup>	50%	0.52	$1.26 \times 10^4$	$5.04 \times 10^4$

<sup>a</sup> Based on 1000 s shots and 80% duty cycle  $\sim 600$  MW(th) flat-top power,  $1.3 \text{ MW/m}^2$  average neutron wall loading and the indicated availability.

<sup>b</sup> The requirement on Stage III is to accumulate  $\sim 3 \text{ MW}\cdot\text{a/m}^2$  after the end of Stage II. This could be achieved in several ways; the case given here is only a representative one.

Table 2-2 INTOR testing objectives

	Stage I	Stage II	Stage III
PHYSICS			
Ignition physics investigation	X		
Achievement of long, controlled, reproducible burns with optimized parameters	X		
High duty cycle	X		
Plasma physics experiments	X	X	
MATERIALS			
Materials bulk property investigation		X	X
Radiation damage investigation			X
Surface effects investigation	X	X	X
MAGNETICS			
Integrated magnetic system investigation	X		
Integration of magnetic system into tokamak reactor system	X		
Performance of magnetic system under sustained operation		X	X
PLASMA HEATING			
Integration of RF system into a tokamak reactor system	X		
Testing of RF components in fusion radiation environment	X	X	X
Performance of RF system under sustained operation		X	X
PLASMA FUELLING			
Integration of pellet injector into tokamak reactor system	X		
Testing of pellet injector components in fusion radiation environment	X	X	X
Performance of pellet injector system under sustained operation		X	X



Table 2-2 (cont.)

	Stage I	Stage II	Stage III
TRITIUM			
Integration of tritium-breeding system into tokamak reactor	X		
Investigation of tritium containment in tokamak reactor	X	X	
VACUUM			
Integration of vacuum pumping system into tokamak reactor system	X		
Performance of vacuum system under sustained operation in tokamak reactor		X	X
Component testing		X	X
BLANKET			
Integration of blanket system into tokamak reactor system	X	X	
Basic engineering data		X	
Tritium production and extraction		X	X
Electricity production		X	
DEMO prototypical blanket segment testing			X
Performance of blanket system under sustained operation in fusion reactor			X
Design concept testing		X	X
FIRST WALL, DIVERTOR			
Integration into tokamak reactor system	X		
Basic engineering data	X	X	
Performance under sustained operation in fusion reactor		X	X
Design concept testing		X	X
SHIELD			
Integration of shielding into tokamak reactor system	X		

Table 2-2 (cont.)

	Stage I	Stage II	Stage III
REMOTE MAINTENANCE			
Investigation of remote maintainability of tokamak reactor system	X	X	X
DIAGNOSTICS, DATA ACQUISITION, CONTROL			
Integration into tokamak reactor system	X		
Basic engineering data	X	X	
Investigation of integrated system under sustained operation	X	X	X
Component testing		X	

	YEARS OF OPERATION									
	1	2	3	4	5	6	7	8	9	10
	STAGE I		STAGE II				STAGE III			
PLASMA EXPERIMENTS										
PLASMA ENGINEERING										
BLANKET TESTING										
MODULE										
TRITIUM RECOVERY										
SPECIMEN										
ENGINEERING TESTS										
BULK MATERIALS										
SURFACE MATERIALS										
SHIELD VERIFICATION										
NEUTRONICS CHARACTERIZATION										
NUCLEAR TESTS										
REACTOR SURVEILLANCE										
ELECTRICITY PRODUCTION										
DEMO BLANKET SECTOR TEST										

Fig. 3-1 INTOR test schedule